Transactions of the ASME

TRANSACTIONS OF THE AMERICAN SOCIETY OF MECHANICAL ENGINEERS

VOLUME 77 JULY 1955 NUMBER 5

Transactions

of The American Society of Mechanical Engineers

Published on the tenth of every month, except March, June, September, and December

Published monthly by The American Society of Mechanical Engineers. Publication office at 20th and Northampton Streets, Easton, Pa. The editorial department is located at the headquarters of the Society, 29 West Thirty-Ninth Street, New York 18, N. Y. Cable address, "Dynamic," New York. Price $1.50 a copy, $12.00 a year for Transactions and the *Journal of Applied Mechanics;* to members and affiliates, $1.00 a copy, $6.00 a year. Add $1.50 for postage to all countries outside the United States, Canada, and Pan-American Union. Changes of address must be received at Society headquarters seven weeks before they are to be effective on the mailing list. Please send old as well as new address.... By-Law: The Society shall not be responsible for statements or opinions advanced in papers or...printed in its publications (B13, Par. 4).... Entered as second-class matter March 2, 1928, at the Post Office at Easton, Pa., under the Act of August 24, 1912....

Application of High-Speed Strain-Gage Torquemeter to Turbomachinery Research

By H. A. BUCKNER, JR.,[1] and J. J. REBESKE, JR.,[2] CLEVELAND, OHIO

In turbomachinery-component research, it is frequently impractical to obtain power measurements by conventional cradled dynamometers. This paper presents a description of a high-speed strain-gage torquemeter having the high accuracy required for this research and shows the application of this torquemeter to compressor and turbine setups. The paper also discusses pertinent factors for obtaining accurate measurements with the instrument.

Introduction

In turbomachinery-component research, an accurate measurement of power produced or consumed by the component is extremely vital. Because of the large equipment generally involved, being complicated in some cases by gear boxes, it frequently is impractical to cradle the equipment as required for conventional torque or power measurement. When components are investigated in an engine, the resulting complexities make power measurement by conventional means even more impractical. Under such circumstances, investigators have relied almost entirely upon measurement of gas-state change. In view of mass-flow and temperature gradients existing in turbomachinery as well as pulsating-flow conditions downstream of rotor-blade rows, these measurements often are subject to error.

In order to obtain torquemeters of the required accuracy (±0.5 per cent) at the high rotational speeds encountered (up to 17,000 rpm), the NACA Lewis Laboratory has designed, built, and investigated torquemeters of the strain-gage type. The first torquemeter was investigated dynamically on a special test stand where its accuracy compared favorably with that of a cradled dynamometer (1).[3] Since the initial investigation and development, strain-gage torquemeters have been built and used successfully on both compressor- and turbine-component setups where more conventional means of torque or power measurements were difficult or impractical. The present paper describes this torquemeter, discusses its use and accuracy in compressor and turbine research investigations, and discusses operating experience and latest developments obtained. The general range of applicability of the torquemeter in its present state also is discussed.

Description of Torquemeter

In general, torque-measuring instruments may be classified under one of the following three types: Torque-reaction type, angular-twist type, and surface-strain type. The torque-reaction type utilizes Newton's third law and requires the measurement of some external reaction force, as for example, the cradled dynamometer. The angular-twist type utilizes the familiar principle of measuring the angular deflection in a gage length of shaft, the angular deflection being proportional to torque transmitted. An example of this type is the optical torquemeter (2). The surface-strain type utilizes the principle that shaft torque and shaft-surface strain are proportional.

In the strain-gage torquemeter, the shaft-surface strain is measured by the use of suitably mounted bonded-wire strain gages, which are merely fine wires having the property of the resistance being very nearly a unique function of the strain applied. The readings are transmitted through slip rings to appropriate electronic equipment where shaft torque is read. The torquemeter consists of three basic components which will now be described in detail: The torsion shaft, the slip rings, and a self-balancing potentiometer.

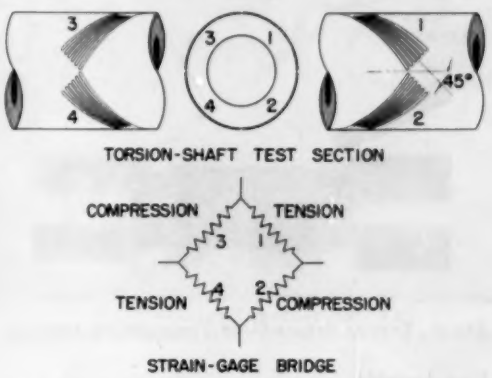

Fig. 1 Orientation of Strain Gages on Torsion-Shaft Test Section

(Advance-wire strain gages 1, 2, 3, and 4 are 350 ohms.)

Torsion Shaft

The torsion shaft consists of a hollow shaft especially designed to have practically measurable values of surface strain and on which are mounted strain gages on 45-deg helices, as recommended in reference (3) and as shown in Fig. 1. When so oriented on the torsion shaft the gages are subjected to the maximum tensile and compressive strains when torque is applied. With gages subjected to torque-induced strains of the same sign forming opposite arms of a Wheatstone bridge, the bridge is additively unbalanced when torque is applied. Further, such a device, while having maximum sensitivity to torsional stresses, is relatively (although not completely) insensitive to axial and bending stresses.

Torsion-shaft designs giving maximum values of torsional shearing stress on the order of 15,000 to 25,000 psi in steel shafts have been found to give excellent results when 350-ohm Advance-wire strain gages are used. The gages are cemented to the shaft with a bakelite cement. After the initial thermal-setting process has occurred, the shaft with the gages is baked over a period of time at temperatures slightly higher than the estimated shaft operating temperature until the resistance between the gages and

---

[1] Head, Turbine Aerodynamics Section A, National Advisory Committee for Aeronautics, Lewis Flight Propulsion Laboratory.

[2] Head, Turbine Aerodynamics Section B, National Advisory Committee for Aeronautics, Lewis Flight Propulsion Laboratory.

[3] Numbers in parentheses refer to the Bibliography at the end of the paper.

Contributed by the Gas Turbine Power Division and presented at the Semi-Annual Meeting, Pittsburgh, Pa., June 20–24, 1954, of The American Society of Mechanical Engineers.

Note: Statements and opinions advanced in papers are to be understood as individual expressions of their authors and not those of the Society. Manuscript received at ASME Headquarters, March 25, 1954. Paper No. 54—SA-23.

shaft at this temperature approaches 30 to 45 megohms. Twenty-gage flaminol-insulated copper wires soldered directly to the bridge ends are led through radial holes to the inside of the hollow shaft where a centering conduit carries the wires through the shafting to the slip-ring assembly. (The slip-ring assembly is wired with 24-gage cotton-covered enameled copper wire.) Connectors may be employed between the torsion shaft and slip-ring assembly as required by the assembly procedure of the particular setup, although it is generally best to minimize connections. An installation typical of those at NACA is shown in Fig. 2.

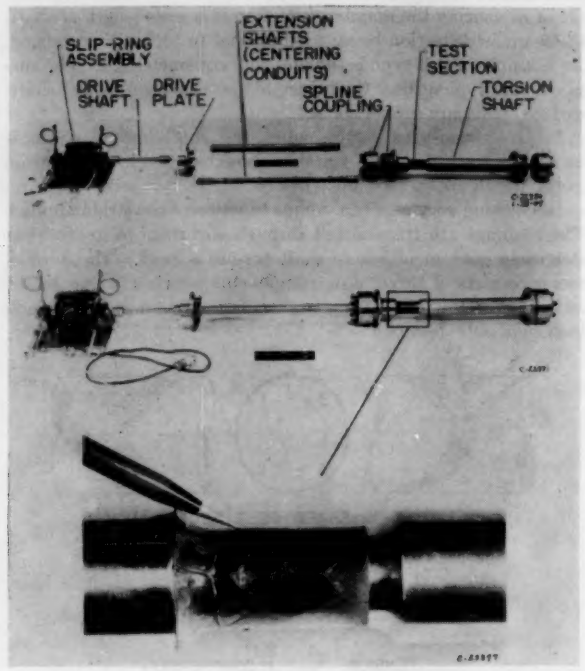

FIG. 2 TYPICAL STRAIN-GAGE TORQUEMETER ASSEMBLY

Slip-Ring Assembly

The slip-ring assembly, or pickup, consists of a separately mounted unit, driven by a hollow flexible coupling attached to the torsion shaft or its extension and through which pass the transmission wires as shown in Fig. 2.

Fig. 3 is a close-up view of the most recent and improved pickup. The slip rings consist of a series of monel washers having an axial width of 0.120 in. and an over-all diameter of 0.875 in. These monel rings are assembled with insulating washers in a laminated fashion on a hollow shaft over which an insulating sleeve has been placed. The insulating material is commercially available under the trade name "amphenol 200." The circumferential surfaces of the monel rings are ground after assembly as smooth as possible to a concentricity of ±0.0002 in. and the insulating washers are undercut. The shaft is mounted on ball bearings which are oil-mist-lubricated and the bearing chambers are scavenged to a subatmospheric pressure to minimize oil contamination of the slip rings.

The brushes, made of a mixture of 60 per cent silver and 40 per cent graphite, have a diameter of $^1/_8$ in. and a length of $^1/_8$ in. and are mounted on cantilevered leaf-type beryllium-copper springs. Two brushes spaced approximately 90 deg apart make contact with each of the slip rings. Each bank of brushes, Fig. 3, is pivoted and actuated by a spring-opposed direct-current solenoid so that the brushes contact the slip rings only when readings are taken. (An alternating-current solenoid was found unsatisfactory in that it influenced the torque readings.) Each bank of brushes is positioned by a bakelite support. Slightly different spring lengths are employed for the two banks to obtain different natural vibrational frequencies of the springs. This

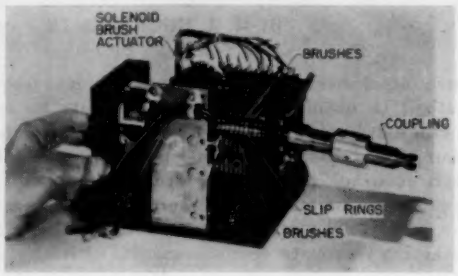

FIG. 3 SLIP-RING ASSEMBLY

procedure insures uninterrupted electric contact with the slip rings in case of critical vibration of the brush springs. Brush pressures are set by individual adjusting screws on the main brush support as shown in Fig. 3. Values of brush pressure of 20 to 40 psi have been found adequate for satisfactory brush and slip-ring life and for maintaining the series slip-ring resistance below 5 ohms at high-speed operation.

Although not shown in the figure, provisions have been made for flushing the slip rings with carbon tetrachloride during operation as dust or oil accumulates, a condition which is next to impossible to avoid in most installations. This is accomplished by providing a small horizontal tube with openings along the bottom above the slip-ring shaft; this tube is supplied carbon tetrachloride by remote-controlled methods such as a solenoid valve in conjunction with pressurized or gravity feed.

Torquemeter Circuit

The multiple bridge circuit of the torquemeter, Fig. 4, was conceived by Mr. Isadore Warshawsky of the Physics Division of the NACA Lewis Laboratory and virtually eliminates the effect of small contact resistance on the torquemeter readings. The basic theory is presented in detail in reference (4).

The circuit consists of a commercially available self-balancing potentiometer with a vacuum-tube amplifier whose output drives a sliding contact on the 20 Ω slide wire "S," Fig. 4, by means of a two-phase motor. Resistances R_7 and R_8, together with the 20Ω slide wire, form two main bridge arms. These two main bridge arms are shunted by R_6 which is a zero adjustment for the bridge. The other two main bridge arms are formed by R_1, R_4, and R_2, R_3, which are the strain gages mounted on the torsion shaft in the form of a Wheatstone bridge. The power corners of the main bridge are fed through auxiliary ratio resistors R_{10}, R_{11}, and R_{12}, R_{13}, which have the effect of distributing contact resistance in the main bridge arms in proportion to the resistance of the main arms adjacent to the power corners of the main bridge. This effectively reduces contact resistance to a second-order effect on the balance of the main bridge as long as the contact resitance is small.

In order to have a continuing check on the slip-ring resistance and resistance to ground of the strain-gage bridge during operation, a switching circuit is provided at position *xx* in Fig. 4 and allows the circuit to be opened at this point. With the slip rings and strain-gage bridge disconnected, the series resistance of slip rings AB, EF, and CD, may be obtained and also the resistance to ground may be measured. Thus periodic checks on the slip rings and strain-gage bridge during operation will indicate any malfunction of the torquemeter.

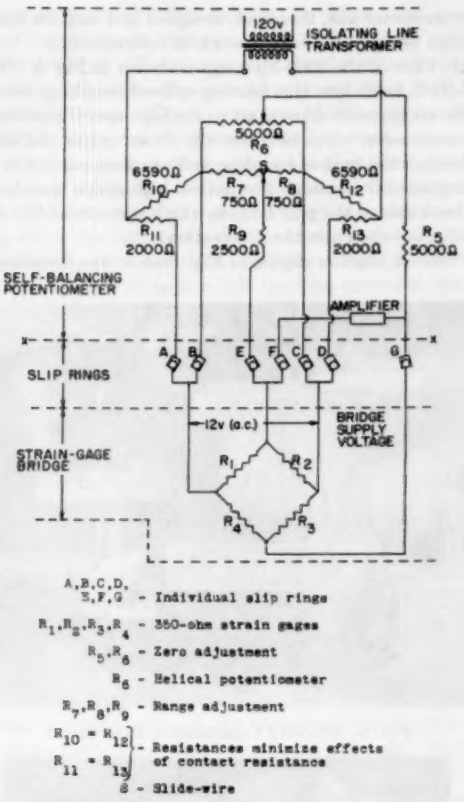

FIG. 4 BRIDGE CIRCUIT EMPLOYED IN STRAIN-GAGE TORQUEMETER

TORSION-SHAFT CALIBRATION

Reference (1) indicates that the dynamic characteristics of the torquemeter approach the static characteristics with a very high degree of accuracy so that a careful and accurate static calibration of the torsion shaft is the only calibration necessary to obtain accurate and reliable torque measurements. Extreme care should be exercised in the static calibration because under no circumstances can the accuracy of the torquemeter be greater than the accuracy of the static calibration. Consequently, the static-calibration apparatus should be examined carefully to determine whether it is capable of applying torques to the torsion shaft with the required degree of accuracy.

Because temperature affects the torsional modulus of elasticity as well as having a slight effect on the strain gages of the torsion shaft, the torsion shaft should be calibrated at the actual operating temperatures. It is also advisable to have the actual connecting cables and slip rings in the circuit during the static calibration so that resistances in the electric circuit during dynamic operation will be changed only by the variation in contact resistance. The final static-calibration equation should be determined by the method of "least squares" from the calibration data in order to eliminate any accidental error.

A typical torsion-shaft static-calibration setup is shown in Fig. 5. The apparatus consists of two pedestals, a ball-type bearing, a 60-in. moment arm, and suitable calibration weights. A thin steel ribbon, which makes contact with the surface of the moment-arm arc at a constant radius of 60 in., is used to attach the loading pan to the static-moment arm. The moment arm with the loading and counterbalance pans attached is first balanced and keyed to one end of the torsion shaft, which is then mounted between two pedestals. One end of the shaft is supported by a ball bearing located on the rear pedestal, and the other end is rigidly keyed to the front pedestal. After being mounted, the moment arm and the torsion shaft are adjusted to a horizontal position and the moment arm set perpendicular to the axis of the torsion shaft.

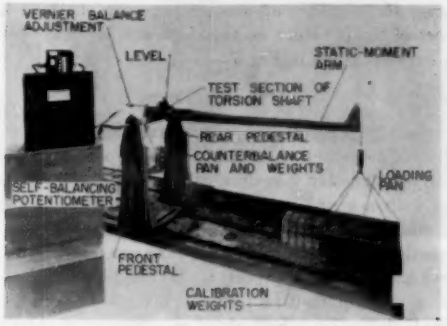

FIG. 5 TORSION-SHAFT APPARATUS FOR STATIC CALIBRATION

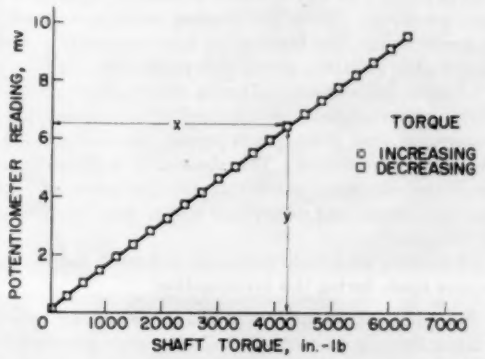

FIG. 6 STATIC CALIBRATION OF STRAIN-GAGE TORQUEMETER; TORSION-SHAFT TEMPERATURE, 73 F
(Equation for this calibration is $y = [150.37 \times 10^{-5}]\ x + 0.123$.)

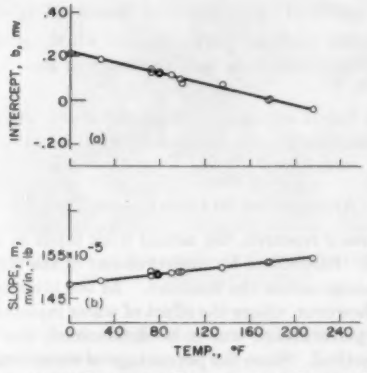

FIG. 7 VARIATION OF SLOPE AND INTERCEPT OF STATIC-CALIBRATION EQUATIONS WITH TORQUEMETER TORSION-SHAFT TEMPERATURE

In order to control the torsion-shaft temperature during calibration, an insulating box (not shown) is placed around the shaft; the shaft temperature is measured by a thermocouple mounted on the torsion shaft near the strain gages. Temperatures higher than ambient are produced by placing heating elements inside this box. (If electrical heating elements are used caution should be exercised to insure that no voltage is induced in the bridge by

stray magnetic fields.) Temperatures lower than ambient are obtained by use of solid carbon dioxide. In this manner, the torquemeter can be calibrated for the range of temperature usually encountered. The calibration is accomplished by placing weights on the loading pan and recording the potentiometer readings corresponding to the known torque. A typical calibration of a strain-gage torquemeter at one temperature is shown in Fig. 6. The effect of temperature on the slope and intercept of this calibration curve is given in Fig. 7.

Dynamic Tests

The strain-gage torquemeter was investigated under dynamic conditions in reference (1) in a special setup where a high-speed cradled dynamometer was driven by a low-speed motor in conjunction with a gear box, the torquemeter being built into the floating coupling between gear box and dynamometer. During this investigation the torquemeter was operated quite successfully over a range of shaft speed of 5000 to 17,000 rpm and over a wide range of torque with a probable accuracy of ±0.33 per cent of full-scale deflection. Successful operation with the brushes in continuous contact at speeds from 13,600 to 17,000 rpm for periods of about 5 hr was obtained without adjustment of brush-contact pressures. With the brushes solenoid-actuated, as in more recent setups, the brushes are in contact only a small percentage of the total time, giving very reasonable lengths of operation between adjustments. During the dynamic tests (1) the reliability of the torquemeter was checked by repeated calibration and operation over a six-month period; no change in the static calibration was observed. The absence of any significant performance trends with speed through the range of operation showed that speed and centrifugal effects were negligible in the range covered.

The following additional pertinent and more specific observations were made during this investigation:

1 Since full compensation for axial stress may not be achieved in practice because of small dissimilarity in characteristics of individual gages and of inaccuracies in orientation, it was concluded that the torquemeter should be used where no appreciable axial stress is present.

2 For best accuracy the torsion shaft should be designed for the highest torsional stress practical from a safety standpoint.

3 Erroneous readings were obtained when the minimum resistance between slip rings and ground was less than 30 to 45 megohms.

4 It was found advisable to keep the series brush to slip-ring contact resistance as low as possible and in any case below 5 ohms.

Application to Compressor Test Rig

In compressor research, the actual work input to the compressor is usually determined by measurement of the temperature or gas-stage change across the machine. In the investigation of reference (5), however, where the effect of water injection on over-all compressor performance was to be determined, this method was found impractical. Since the percentage of water evaporated was indeterminate, the evaluation of enthalpy increase for each of the constituents of the mixture at the compressor outlet (water droplets, water vapor, and air) could not be determined from conventional instrumentation. The assumption of complete evaporation and the use of conventional temperature measurements, for example, would introduce errors in computed work input as great as 40 per cent. Since the compressor was driven by a large 9000-hp low-speed motor in conjunction with a gear box, and the compressor itself was large and bulky, it was impractical to measure power input by conventional cradling means. A strain-gage torquemeter was, therefore, designed and built for this setup, the design being based on the work of reference (1).

A side view of the 9000-hp setup is shown in Fig. 8. The torsion shaft is built into the floating splined coupling, which connects the compressor drive shaft to the high-speed gear-box shaft. The transmission wires between the strain gages and slip rings pass through the hollow coupling and are then carried in special centering conduit through the hollow high-speed gear-box shaft to the back side of the gear box, on which is mounted the slip-ring assembly (not shown in the illustration).

The torsion shaft is shown in Fig. 9 as it was installed in the

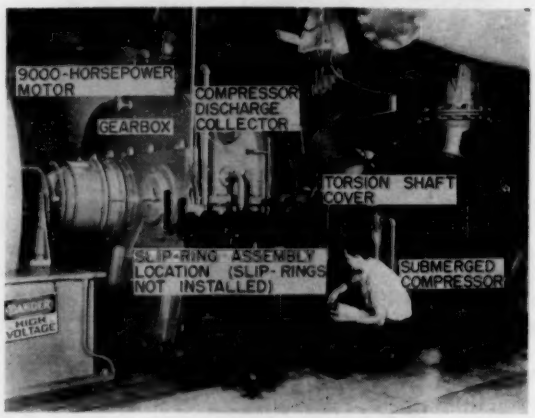

Fig. 8 9000-Hp Compressor Test Setup

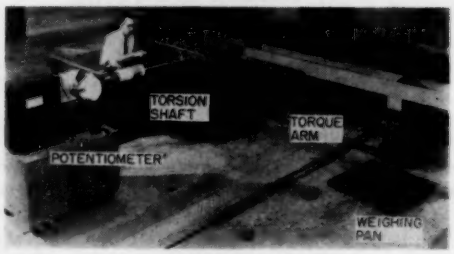

Fig. 9 Setup for Static Calibration of Torquemeter From 9000-Hp Compressor Test Stand

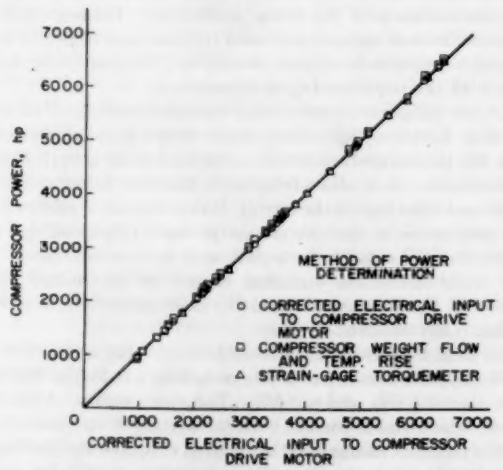

Fig. 10 Comparison of Power Measurements Made by Strain-Gage Torquemeter, Gas-State Change, and Wattmeter on 9000-Hp Compressor Setup

static-calibration rig. The section on which the gages are mounted has an inside diameter of 4.620 in. and an outside diameter of 5.000 in. The shaft was made of steel and is designed for a torsional shearing stress at the gage section of 6580 psi and speed of 11,500 rpm. The strain gages in this case are mounted on the inside surface of the thin-wall hollow shaft.

The calibration setup differs somewhat from that of reference (1) because of the larger torque involved and different coupling details. The left end of the shaft, Fig. 9, is clamped in a fixed position while the right end is free to rotate and is supported by ball bearings in contact with the hub periphery. These bearings are located so that no appreciable bending moments due to the torque arm and weights are transmitted to the torsion shaft. The counterbalanced torque arm in this case had a length of 97.38 in. from the shaft center to the point of suspension of the weighing pan.

The agreement among three different methods of measuring power input to the compressor (without water injection into the air stream) is shown in Fig. 10. Power measured by the strain-gage torquemeter is compared with that based on gas-state change and measured weight flow and with that calculated from electrical power input to the drive motor minus motor and gear-box losses. The gas-state change is based on the temperature rise measured by a large number of thermocouple probes and computed using data from Keenan and Kaye (6); the weight flow was measured with a calibrated adjustable orifice. The power input to the motor was measured with a polyphase wattmeter; the motor and gear-box losses were calculated on the basis of curves supplied by the respective manufacturers. In this particular case the maximum deviation between the torquemeter and either of the other two methods is less than 1 per cent of full scale. Part of this excellent agreement is undoubtedly accidental since neither of the other two methods is considered of that order of accuracy. It does, however, serve to illustrate that the strain-gage torquemeter gave excellent results in this installation.

Application to Turbine Test Rig

In turbine research, the measurement of power output by means of gas-state-change measurements poses somewhat more of a problem than in compressors. The Mach number and energy gradients are usually considerably larger at the turbine exit. Further, if the test is made at high temperature, it is difficult to measure the gas temperature with the required degree of accuracy because of radiation effects, physical difficulties encountered in getting probes to withstand the high temperature, and so forth. If the test is made at a low inlet temperature, the temperature change across the machine often becomes sufficiently small to make it difficult to measure. It has been customary, therefore, to measure the power by use of high-speed cradled dynamometers whenever possible.

A cold-air turbine-component setup was installed at the NACA several years ago which uses a 2000-hp low-speed eddy-current absorption device in conjunction with a gear box. A strain-gage torquemeter installation was made on this setup in a location similar to that in the compressor installation. The torsion shaft is built into the floating splined coupling connecting the turbine shaft to the high-speed gear-box shaft, Figs. 11(*a*) and (*b*). The torsion shaft at the gage section has an inner diameter of 2.012 in. and an outer diameter of 2.062 in. and is designed for a maximum torsional shearing stress of 25,000 psi at full torque. The installation of the slip-ring assembly at the opposite end of the gear-box high-speed shaft is shown in Fig. 11(*c*). The manner in which the assembly is attached to the gear box, the oil-supply and scavenging lines, and parts of the flushing system for spraying carbon tetrachloride on the slip rings may be seen. This location is convenient and provides excellent accessibility for minor adjustments and maintenance.

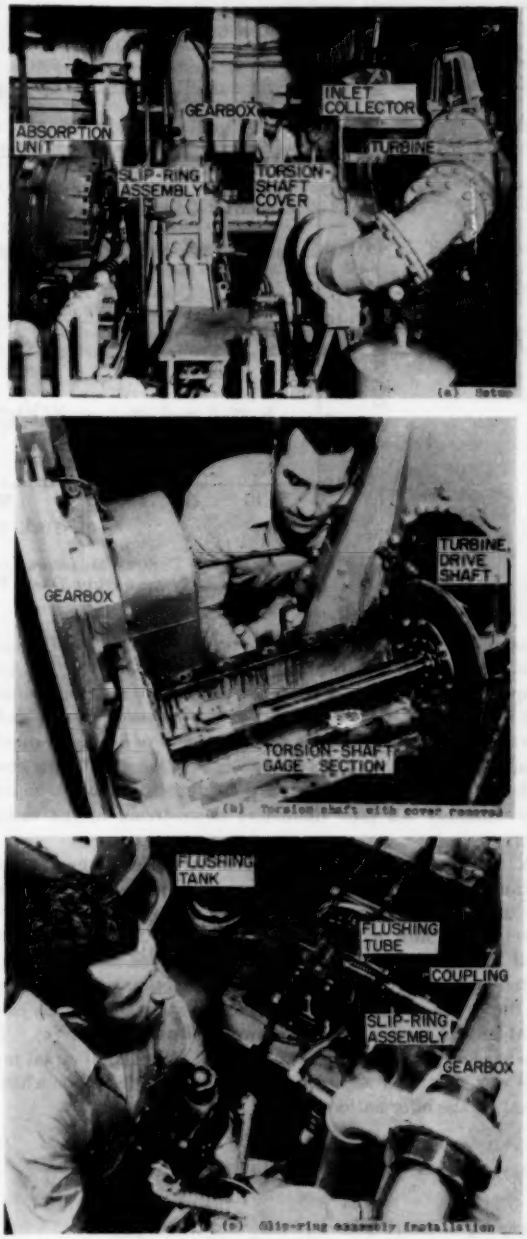

Fig. 11 Installation of Strain-Gage Torquemeter on 2000-Hp Turbine-Component Setup

A comparison between torque measured by the torquemeter and that computed from turbine temperature drop, weight flow, and rpm, including a correction for estimating bearing power loss, is shown in Fig. 12. The torque difference, expressed as a per cent of full-scale torque, is plotted against the ratio of torque to full-scale torque for three turbine configurations.

The turbine weight flow was measured with a submerged flat-plate orifice with an accuracy of 1 per cent. The turbine speed was measured with an electronic tachometer within an accuracy of ± 10 rpm. The temperature differential across the turbine was

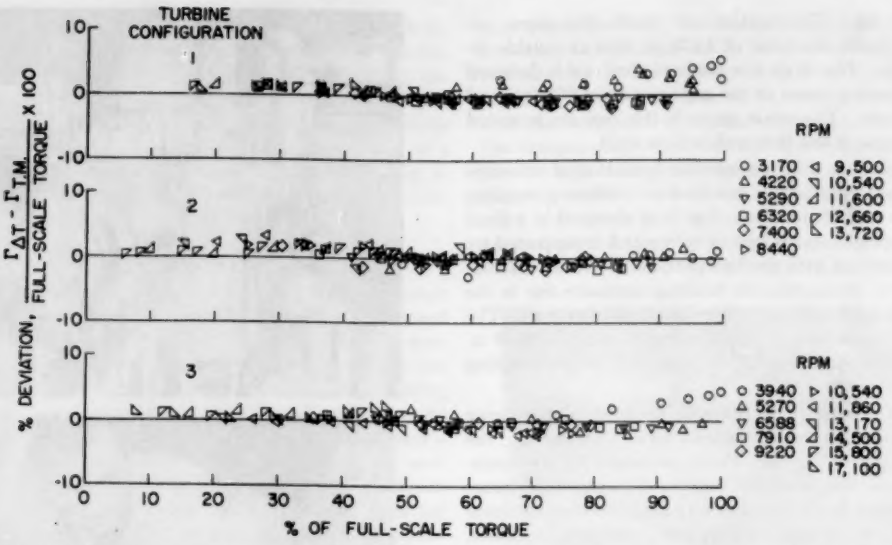

FIG. 12 COMPARISON OF TORQUE MEASURED BY STRAIN-GAGE TORQUEMETER WITH THAT CALCULATED FROM TEMPERATURE DROP, WEIGHT FLOW, AND ROTATIONAL SPEED

measured on a Rubicon potentiometer in conjunction with a spot-light galvanometer with a precision of ±0.2 deg F. The inlet temperature was obtained from two probes in the turbine annulus just upstream of the turbine stator, the probes having a total of five thermocouples located at the area center of five equal annular areas. The outlet temperature was indicated by a single probe with five thermocouples similarly located in the outlet annulus approximately 3.2 pipe diameters downstream of the turbine rotor.

A flow straightener consisting of a series of long slender rectangular tubes parallel to the turbine axis was located between the turbine rotor and the outlet measuring station to provide directions of flow within the range of yaw insensitivity of the fixed rake. All thermocouple probes were calibrated and corrected for recovery factor. The turbine inlet-air temperature was on the order of 600 deg R and the gas-state change was calculated on the basis of the data presented in reference (6). The bearing loss for the thrust bearing and four plain journal bearings was estimated according to the following equation which is based on the information in references (7, 8)

$$P_B = 0.016 \left(\frac{N}{1000}\right)^2$$

where P_B = bearing horsepower, and N = rpm.

The maximum bearing correction amounted to approximately 0.4 per cent of full-scale torque; therefore, the thrust-bearing power was assumed not to vary with thrust load in view of the relatively small magnitude of the bearing correction. In spite of precautions taken to insure accurate temperature measurements, it is difficult to estimate the accuracy of these measurements because of large temperature and mass-flow gradients which cause the true mass-averaged temperature drop to vary from the measured area-averaged temperature drop. The order of agreement between the two methods for the three turbine configurations is quite good, being on the order of 2 per cent of full-scale torque. In view of the difficulties involved in making accurate temperature measurements, the torquemeter values are considered to be the true values. As a matter of interest, the reproducibility on this turbine setup using the strain-gage torquemeter is of the order of 0.5 per cent in efficiency at or near design work output.

In several years of experience with the strain-gage torquemeter on this setup, the following items have been found necessary for successful results:

1 Precautions must be taken during assembly to avoid any short circuits to ground or between wires.

2 For maximum life, brushes should be kept in contact with the slip rings only long enough to take readings.

3 During operation, slip-ring resistance and resistance to ground should be checked fairly frequently and if the series resistance of a pair of slip rings is greater than 5 ohms, steps should be taken to remedy the trouble. Excessive slip-ring resistance is usually the result of contamination which can be eliminated easily by remotely flushing with carbon tetrachloride.

4 During static calibration, great care should be taken in making connections as they are in the installation. The "zero" adjustment on the Brown potentiometer should not be changed after static calibration; if the zero in the final installation does not check the static-calibration zero, the trouble should be located and remedied.

Excellent results have been obtained over a period of several years with this torquemeter application at operational speeds up to 17,000 rpm. The static calibration has been checked periodically and found to duplicate the original calibration, even after several sudden accelerations and decelerations when shaft torque exceeded full scale. The slip-ring assembly now in use requires only a reasonable amount of maintenance; operating time between brush adjustments and regrinding of the slip rings is usually on the order of 50 and several hundred hours, respectively.

CONCLUSION

The strain-gage torquemeter has been applied successfully to high-speed-turbomachinery research where a high degree of accuracy is required. Satisfactory life and accuracy have been obtained for rotational speeds up to 17,000 rpm. This maximum speed is not a limit, but is as high as has been obtained in these installations.

On the basis of this experience, the strain-gage torquemeter

appears to have a wide range of applicability to high-speed equipment. It could be used, for instance, to measure compressor or turbine power in a turbojet or turbine-propeller engine, propeller power and, with different gage arrangements, propeller thrust in turbine-propeller engines, and to measure shaft power in many large stationary applications.

Acknowledgments

The authors wish to acknowledge the assistance obtained in various phases of this work from Messrs. Seth Wise, Robert Y. Wong, William L. Beede, Joseph R. Withee, and other members of the Lewis Laboratory staff.

BIBLIOGRAPHY

1 "Investigation of a NACA High-Speed Strain-Gage Torquemeter," by J. J. Rebeske, Jr., NACA TN 2003, January, 1950.

2 "Investigation of a NACA High-Speed Optical Torquemeter," by J. J. Rebeske, Jr., NACA TN 2118, June, 1950.

3 "The Bonded Wire-Gage Torquemeter," by A. C. Ruge and Ruge DeForest, Proceedings of the Society for Experimental Stress Analysis, vol. 1, no. 2, 1943, pp. 68–72; paper presented before joint meeting SESA and ASME, New York, N. Y., Dec. 2–4, 1943.

4 "A Multiple Bridge for Elimination of Contact-Resistance Errors in Resistance Strain-Gage Measurements," by I. Warshawsky, NACA TN 1031, 1946.

5 "Some Investigations With Wet Compression," by J. T. Hamrick and W. L. Beede, Trans. ASME, vol. 75, 1953, pp. 409–420.

6 "Thermodynamic Properties of Air," by J. Keenan and J. Kaye, John Wiley & Sons, Inc., New York, N. Y., 1945.

7 "Thrust Bearings," by F. C. Lynn and R. Shephard, Trans. ASME, vol. 60, 1938, pp. 245–252.

8 "Lubrication," by A. E. Norton, first edition, McGraw-Hill Book Company, Inc., New York, N. Y., and London, England, 1942, p. 131.

The Combustion-Efficiency Problem of the Turbojet at High Altitude

By W. T. OLSON,[1] J. H. CHILDS,[1] AND E. R. JONASH,[1] CLEVELAND, OHIO

This paper discusses NACA research on the single problem of combustion efficiency of turbojet engines at high altitudes. Representative results of investigations with turbojet combustors are presented to illustrate the trends obtained with the following categories of variables: (*a*) Combustor operating variables, (*b*) combustor design variables, and (*c*) fuel variables. The data indicate that as the environment of the combustor becomes one of low pressure and low temperature at high altitude, low combustion efficiencies and limited values of obtainable temperature rise are encountered. Increased cross-sectional area of combustor for a given weight flow of air decreased velocities and facilitated high combustion efficiency at altitude. For the design of the liner, increased volume in the flame zone and gradual admission of the air into the combustion space were shown to aid combustion by helping to provide that localized fuel-air mixtures of correct composition exist sufficiently long for ignition and combustion to occur. For high combustion efficiency to occur, all of the fuel must be involved in this manner, and it was shown that the combustor design, the fuel injection, and the fuel volatility must be matched if optimum combustion efficiency is to be achieved. Further, it was shown that, for a given combustor, fuel injector, and fuel volatility, fuels of higher flame speed and/or lower ignition temperatures gave higher combustion efficiency at high-altitude operating conditions.

Introduction

THE value of an aircraft propulsion system is measured in terms of the reliable delivery of required thrust for a minimum of fuel-consumption rate, engine weight, engine frontal area, and engine cost. For turbojet engines, these factors impose many requirements on the combustion chamber, the principal ones being stability and reliability of operation, high combustion efficiency, small volume or size, minimum pressure drop, minimum weight, a preferred pattern of outlet-temperature distribution, strength and durability, ease of ignition, ability to utilize a variety of fuels, and ease of manufacture. Many of these requirements are in conflict with one another, such as high combustion efficiency versus minimum combustor size. Although NACA research on turbojet combustors necessarily has involved most of these requirements, the present paper is restricted intentionally to only that part of research on turbojet combustion that has been concerned with combustion efficiency at high altitude.

It is commonly understood that the effective operating regime of the turbojet engine is high flight speed and high altitude. Further, the service requirements of turbojet engines plainly call for effective operation at even higher and higher altitudes. Experience has shown that, as operating altitudes are increased progressively above about 25,000 ft, the effects of altitude on combustion efficiency ultimately result in severe penalties in thrust and specific-fuel consumption. The problem of maintaining high combustion efficiency is one of the most important problems of altitude operation.

The research approach to the problem has involved both systematic investigations of the effect of individual variables on combustor performance, and attempts to relate fundamental combustion parameters such as fuel-spray characteristics, ignition limits, and flame speeds, to the observed combustor performance. Consequently, this paper will describe and discuss the individual effects of different variables on turbojet combustion efficiency. These variables are, for convenience, listed as operational variables (fuel-air ratio, and combustor inlet-air pressure, temperature, and velocity), design variables, and fuel variables. Although the shortcomings of trying to isolate variables or to apply fundamental data to a total process as complicated as the combustion process in a high-heat-release burner are recognized, nevertheless an appreciation and an understanding of the combustion problem at altitude has been gained in this way.

The data that will be presented are selected from a broad range of studies with many different combustors and are believed to be illustrative of the trends obtained. The data were obtained by operating individual combustors in test rigs supplied with air and exhaust services that permitted control of combustor inlet-air pressures, temperatures, and flow rates. Typical methods are described in references (1, 2).[2] Certain trends thus obtained have been verified with full-scale engine operation in research facilities that simulate altitude conditions.

The Turbojet Combustor

The technique that is used to obtain the required combustion in turbine engines is dictated largely by the necessity of establishing a low-velocity zone having a fuel-air ratio near the stoichiometric value. The need for such a zone is evident from Figs. 1 and 2. Fig. 1 (reference 3) shows the inflammability limits of quiescent gasoline-air mixtures obtained in simple bench-scale laboratory apparatus. For a given pressure, ignition is possible over only a limited range of fuel-air ratios near the stoichiometric, and this range decreases with decrease in pressure. There is, too, a pressure below which ignition is not possible at any fuel-air ratio, although this limiting pressure is a function of apparatus. If combustion is to occur at all in a turbine engine, the pressure and fuel-air ratio in the burning zone must lie within the envelope shown in Fig. 1.

In Fig. 2 another variable, velocity, is plotted as a function of fuel-air ratio. The lowest curve (4) in the figure shows flame velocities typical of mixtures of hydrocarbon fuels and air; if the flow velocity in the fuel-air mixture everywhere exceeds about 2 fps, the flame will be extinguished. The upper curve (5) delineates the limits for combustion of mixtures of vaporized gasoline and air burning downstream of a perforated plate positioned normal to the flow in a 2-in-diam tube; combustion could

[1] National Advisory Committee for Aeronautics, Lewis Flight Propulsion Laboratory.

Contributed by the Gas Turbine Power Division and presented at the Semi-Annual Meeting, Pittsburgh, Pa., June 20–24, 1954, of The American Society of Mechanical Engineers.

Note: Statements and opinions advanced in papers are to be understood as individual expressions of their authors and not those of the Society. Manuscript received at ASME Headquarters, March 25, 1954. Paper No. 54—SA-24.

[2] Numbers in parentheses refer to the Bibliography at the end of the paper.

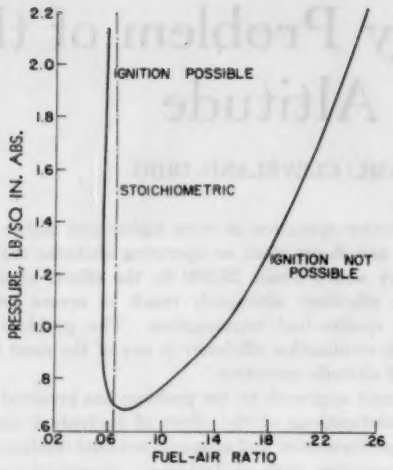

FIG. 1 INFLAMMABILITY LIMITS OF GASOLINE-AIR MIXTURES

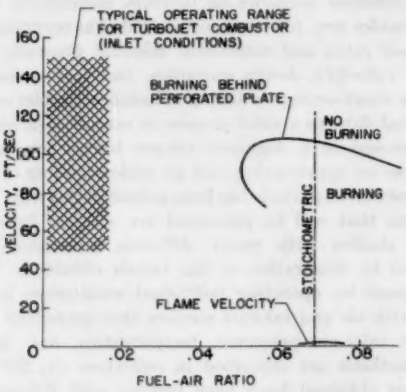

FIG. 2 COMBUSTION LIMITS

be maintained at fuel-air ratios and velocities corresponding to points lying beneath the upper curve. At these conditions the perforated plate not only provided adequate shielded zones where the velocity and fuel-air ratio correspond to values below the normal flame speeds shown by the lower curve, but also provided turbulence, which, together with additional turbulence arising from the shear between unburned gas and higher-velocity burned gas, extended the burning area, or flame surface, to produce the higher burning rates associated with turbulent flame. If combustion is to be maintained and to be completed in a reasonable length in a combustor, the local velocities and fuel-air ratios in the burning zone should correspond to points lying beneath the upper curve in Fig. 2.

The shaded area in the figure indicates the range of over-all fuel-air ratios and velocities typical of current turbojet combustors. These values of fuel-air ratio and velocity were computed by methods described in a subsequent section of this paper and are approximate average values of these parameters within the combustors. The high over-all velocities are required so that the combustor will not exceed the diameter set for the engine by other components. It is evident from Fig. 2 that the combustor geometry should produce within the combustion zone fuel-air ratios that are much higher and velocities that are preferably much lower than the approximate average values lying within the shaded area in Fig. 2.

In both annular and tubular combustors the air is admitted into the burning zone through perforations in a combustor liner; the passage of the air through these perforations is indicated by the arrows in Fig. 3. The fuel is injected as a liquid spray at the upstream end by means of pressure-atomizing nozzles. Most of the air is by-passed around the upstream end of the combustor and admitted farther downstream; only a fraction of the total air flow is, therefore, admitted directly through the perforations into the burning zone. These first essentials in combustor design produce both the high fuel-air ratios shown to

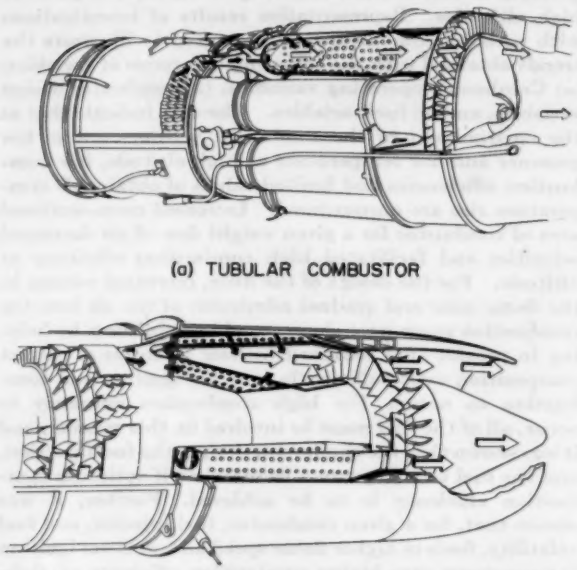

FIG. 3 CUTAWAY DRAWINGS OF TURBOJET ENGINES SHOWING COMBUSTORS

be necessary by the data in Figs. 1 and 2, and the low local velocities shown to be necessary by the data in Fig. 2.

The general development of turbojet combustors and some important observations on their performance have been described by Whittle (6), Mock (7), Lloyd (8), Watson and Clarke (9), Nerad (10), and Way (11).

In the turbojet combustor a big problem, as previously stated, is one of maintaining a high combustion efficiency in addition to a high rate of heat release. Because of the requirement of a high heat-release rate and the attendant high velocities that must be employed in the combustor, thermodynamic equilibrium is not achieved within the combustor; and combustion efficiencies below 100 per cent frequently are obtained at adverse operating conditions. Fig. 4 shows a plot of the combustion efficiencies obtained with a typical turbojet combustor over a range of simulated flight altitudes and engine-rotor speeds. The efficiency decreases progressively with increase in altitude and with decrease in engine-rotor speed. Above the dotted curve the engine is inoperable because the combustor cannot supply heat at the required rate to operate the turbine. The general phenomena and trends exhibited in Fig. 4 are encountered in all aircraft turbine engines.

Fig. 5 shows a plot of combustion efficiency versus altitude for three different turbojet combustors operating at simulated rated engine-rotor speed. With each combustor the efficiency is very close to 100 per cent at sea level and decreases at an accelerat-

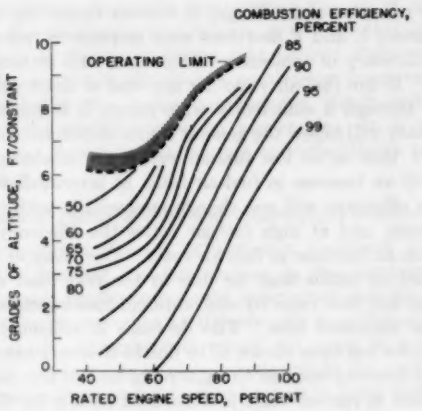

FIG. 4 COMBUSTION EFFICIENCIES AND ALTITUDE OPERATING LIMITS OF TURBOJET COMBUSTOR AT VARIOUS SIMULATED FLIGHT CONDITIONS

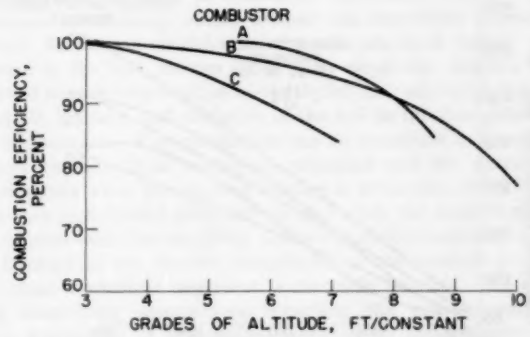

FIG. 5 EFFECT OF SIMULATED FLIGHT ALTITUDE ON COMBUSTION EFFICIENCY OF THREE TURBOJET COMBUSTORS AT SIMULATED RATED ENGINE SPEED

ing rate as altitude is increased. The subsequent discussion will examine the effect of combustor operating variables, design variables, and fuel on combustion efficiency.

EFFECT OF COMBUSTOR OPERATING VARIABLES

The operating variables that would be expected to affect combustor performance include, of course, the static pressure and temperature of the incoming air. Another variable, the mixture composition, is expressed herein by the fuel-air ratio; that is, the weight ratio of the total fuel flow to the total air flow. Actual values of the mixture composition vary considerably throughout the combustion space and probably are not directly proportional to the over-all fuel-air ratio. However, since the over-all fuel-air ratio is the only measurement of mixture composition available from most experimental studies, it must suffice herein as an index of the mixture composition. Still another important variable is the velocity of flow of the incoming air. This velocity is roughly inversely proportional to the residence time of the fuel-air mixture in the combustion space, and it is also important in determining heat and mass-transfer rates. The velocity of the incoming air is another variable which varies markedly in different parts of the combustion space, so it will be expressed herein by a reference velocity, which is only approximately proportional to actual values of velocity of the air entering the combustion space. This reference velocity is simply the volume flow through the combustor divided by the maximum cross-sectional area of the combustor flow passage. It is the fictitious velocity that would exist if the air passed through the maximum cross section of the combustor with a uniform velocity profile and with its density unchanged from the value at the combustor inlet.

Effect of Inlet Pressure

The effect of the inlet static pressure on combustion efficiency for constant inlet temperature, constant reference velocity, and constant fuel-air ratio is shown in Fig. 6 (reference 1). The efficiency decreases at an accelerating rate as the inlet pressure decreases. At high values of inlet pressure the efficiency approaches 100 per cent.

The data in Fig. 6 were obtained with an annular combustor of early U. S. design. Although the quantitative values of efficiency apply only for this particular combustor operating at the specified conditions, the same general trend of efficiency with variation in inlet pressure has been obtained with a large number of liquid-fuel combustors of both the annular and tubular types. If the combustor's design is better, or if the constant operating variables of inlet temperature, reference velocity, and fuel-air ratio are more favorable, then the combustion-efficiency curve will be displaced toward lower pressures; the curve will retain its characteristic shape, however.

Effect of Inlet Temperature

The effect of inlet static temperature on combustion efficiency for constant inlet pressure, constant reference velocity, and constant fuel-air ratio is shown in Fig. 7 (reference 1). A decrease in the inlet temperature has an effect analogous to that shown in Fig. 6 for a decrease in inlet pressure; that is, the efficiency decreases at an accelerating rate as the inlet temperature decreases.

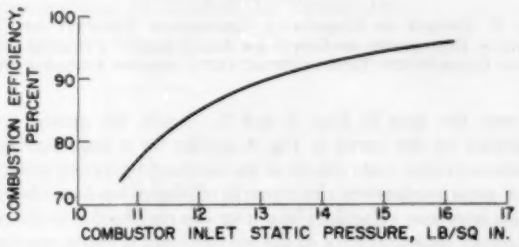

FIG. 6 EFFECT OF COMBUSTOR INLET STATIC PRESSURE ON COMBUSTION EFFICIENCY AT CONSTANT INLET TEMPERATURE, CONSTANT REFERENCE VELOCITY, AND CONSTANT FUEL-AIR RATIO

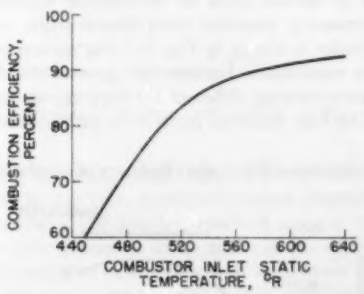

FIG. 7 EFFECT OF COMBUSTOR INLET STATIC TEMPERATURE ON COMBUSTION EFFICIENCY AT CONSTANT INLET STATIC PRESSURE, CONSTANT REFERENCE VELOCITY, AND CONSTANT FUEL-AIR RATIO

The data in Fig. 7 were obtained with the same combustor as the data in Fig. 6; the constant reference velocity and fuel-air

ratio were the same as for Fig. 6; and the inlet pressure was held constant. Again, the general trend shown by the curve in Fig. 7 applies to a large number of liquid-fuel turbojet combustors over wide ranges of the constant operating variables. The effect of inlet-air temperature on combustion efficiency is at least in part associated with vaporization of the fuel spray. As will be discussed later, the magnitude of the effect is, accordingly, dependent upon the volatility characteristics of the fuel and the atomization characteristics of the fuel injector.

Effect of Reference Velocity

The effect of the reference velocity on combustion efficiency for constant inlet pressure, constant inlet temperature, and constant fuel-air ratio is shown in Fig. 8 (reference 1). The efficiency decreases at an accelerating rate as the reference velocity increases. These data were obtained with the same combustor

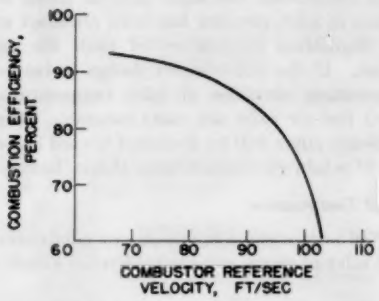

FIG. 8 EFFECT OF COMBUSTOR REFERENCE VELOCITY ON COMBUSTION EFFICIENCY AT CONSTANT INLET STATIC PRESSURE, CONSTANT INLET STATIC TEMPERATURE, AND CONSTANT FUEL-AIR RATIO

as were the data in Figs. 6 and 7. Again, the general trend indicated by the curve of Fig. 8 applies for a large number of combustors over wide ranges of the constant operating variables. With some combustors a decrease in efficiency has been observed at low reference velocities; this decrease may be due to the poor fuel-spray characteristics of the conventional injection nozzles at the attendant very low fuel-flow rates.

Effect of Fuel-Air Ratio

The effect of fuel-air ratio on combustion efficiency for constant inlet pressure, constant inlet temperature, and constant reference velocity is shown in Fig. 9. Curves are presented for four different combustors because the general trends shown by the curves are somewhat different for various combustors within the range of fuel-air ratios of interest in current aircraft turbine engines.

At a fuel-air ratio of 0.017 the efficiency of combustor D is substantially constant with changes in fuel-air ratio; the efficiency of combustors E and F decreases with increase in fuel-air ratio; and the efficiency of combustor G increases with increase in fuel-air ratio. If the fuel-air ratio for any one of these combustors is varied through a sufficiently wide range, it is probable that the efficiency will follow the general trends shown for combustors E and F; that is, at low fuel-air ratios the efficiency will increase with an increase in fuel-air ratio, at intermediate fuel-air ratios the efficiency will not change appreciably with change in fuel-air ratio, and at high fuel-air ratios the efficiency will decrease with an increase in fuel-air ratio. Decreases in efficiency at low fuel-air ratios may be due to the poor fuel spray developed at low flow rates by conventional fuel-injection nozzles, as will be discussed later. The decrease in efficiency at high fuel-air ratios has been shown to be due to overenrichment of the important burning zone at the upstream end of the combustor.

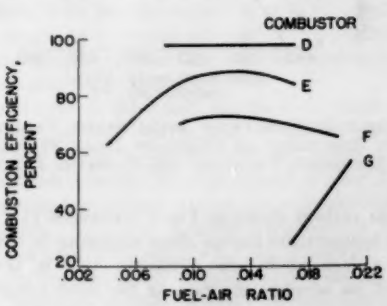

FIG. 9 EFFECT OF FUEL-AIR RATIO ON COMBUSTION EFFICIENCY OF FOUR TURBOJET COMBUSTORS AT CONSTANT INLET PRESSURE, CONSTANT INLET TEMPERATURE, AND CONSTANT REFERENCE VELOCITY

The effect of fuel-air ratio is illustrated further by the curves in Fig. 10 (reference 1). Temperature rise through the combustor is plotted against fuel-air ratio in Fig. 10 and dashed lines of constant combustion efficiency are indicated on the grid.

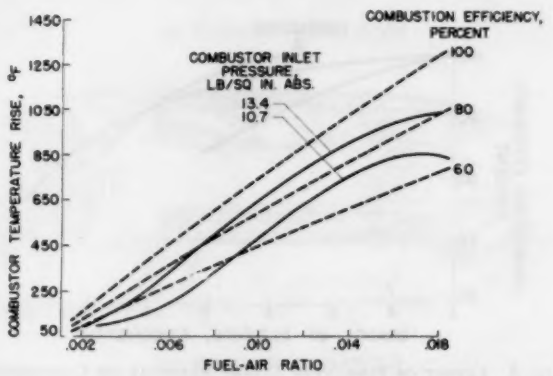

FIG. 10 EFFECT OF FUEL-AIR RATIO ON TEMPERATURE RISE THROUGH COMBUSTOR AT CONSTANT INLET PRESSURE, CONSTANT INLET TEMPERATURE, AND CONSTANT REFERENCE VELOCITY

By interpolating between the dashed lines, the efficiency can be estimated for any point on the solid combustor-operating curves. The two solid curves were obtained with the combustor used to obtain the data of Figs. 6 to 8; for Fig. 10 the combustor operated at two different sets of fixed operating variables of inlet pressure, inlet temperature, and reference velocity. For operation along the upper curve the inlet pressure was 13.4 psia; the inlet temperature and the reference velocity were held constant. For operation along the lower curve, the inlet pressure was 10.7 psia, and the inlet temperature and reference velocity were the same as for the upper curve. Inspection of the upper curve shows the general trends mentioned in the foregoing; that is, the efficiency is approximately constant at about 90 per cent in the intermediate fuel-air ratio range of 0.01 to 0.015, and the efficiency decreases at low and at high fuel-air ratios.

The same general trends also are exhibited by the lower curve in Fig. 10. The decrease in efficiency with increase in fuel-air ratio at high values of fuel-air ratio is so pronounced for the lower curve, that the temperature rise actually begins to decrease with increase in fuel-air ratio. This phenomenon results in a maximum in the curve of temperature rise against fuel-air ratio; that is, there exists a maximum obtainable temperature rise (850 deg F for the lower curve in Fig. 10) that cannot be exceeded with this combustor at these particular operating conditions.

The maximum obtainable temperature rise is, of course, an index of the maximum heat-release rate that this combustor can achieve at these conditions. At desired flight conditions where the maximum obtainable combustor temperature rise would be below the value required for steady-state engine operation, the engine would be inoperable. It is this phenomenon that results in the altitude operating limits previously noted, Fig. 4.

Explanation of Effects of Combustor Operating Variables

As previously indicated, if sufficient residence time were allowed the burning fuel-air mixture in the combustor, then thermodynamic equilibrium would be attained and the efficiency would always be very close to 100 per cent provided combustion occurred at all. (Combustion would not occur in a very thin film of the combustible in close proximity to the cold walls of the combustor liner, and this would result in some slight loss in efficiency.)

The data presented in Figs. 6 to 8 indicated that the combustion efficiency of turbojet combustors decreases at an accelerating rate with a decrease in combustor-inlet pressure or temperature and with an increase in combustor reference velocity. This decrease in efficiency occurs because the conversion processes, which liberate as sensible enthalpy the chemical energy contained in the fuel, are too slow. The conversion processes involved include vaporization of the liquid fuel, mixing of the fuel and air, ignition, and oxidation of the fuel to the final products of combustion. The combustion can be visualized as a competition between these conversion processes and the quenching that occurs when the reacting mixture is swept out of the burning zone and diluted with cold air and when the mixture comes in contact with the relatively cool walls of the combustor liner.

Because of the obvious complexity of the over-all process, no exact theoretical treatment is currently possible. By making simplifying assumptions regarding the turbojet-combustion mechanism it is possible, however, to apply theoretical consideration in the analysis of this combustion process. If the rate of any one of the conversion processes is substantially less than the rates of the others, then this one process will govern the over-all rate and hence will determine the combustion efficiency. The effects on combustion efficiency of the inlet pressure, inlet temperature, and reference velocity have been considered to be the result of their effect on the rate of the chemical reaction. These variables affect the collision frequency of the reacting molecules and also determine the residence time of the reacting mixture within the combustor.

Theoretical treatment has been made at the NACA laboratory with the simplifying assumption that a second-order chemical reaction is the over-all-rate determining step. Longwell and his associates (12) also have utilized second-order-reaction equations to explain the flame-stability phenomena observed with flame holders of the type used in ramjet combustion chambers. In addition, Avery and Hart (13) have suggested that chemical-reaction kinetics control the performance of jet-engine combustors.

It also was observed that combustion efficiency first increased and then decreased with an increase in fuel-air ratio. The trends are believed to be associated with the formation of inflammable or noninflammable fuel-air ratios in the primary zone and are therefore largely dependent upon the atomization characteristics of the fuel-injection system. Fuel atomization and vaporization will be discussed more completely in a later section of this paper.

Effect of Design Variables

The general trends discussed in the preceding section are essentially the same for the various turbojet combustors. The absolute values of efficiency and obtainable temperature rise for given operating conditions vary, however, with the combustor design. Good combustor design, of course, must favor the combustion-conversion processes previously discussed. The design features necessary for high combustion efficiency are obvious only if the exact contribution of each individual process to combustor performance were known. Such is not the case, and further, compromise to meet the many combustor requirements as enumerated in the Introduction must be included in any acceptable combustor design.

Several design variables have been investigated by the NACA for their effect on combustion efficiency and obtainable temperature rise. They are: combustor size and shape; total open area, distribution, size, and shape of air-admission holes in the walls of the combustor liner; and fuel-injection methods. An examination of the trends observed with these variables assists in understanding the part played by each of the individual processes that contribute to combustion efficiency.

Combustor Size

Concerning combustor size, the combustor must have a sufficiently high heat-release rate to meet the power requirements of the engine. This requirement introduces the immediate question of whether combustor volume is the single limiting factor in altitude operation. Partly to answer this question, a simple diffusion flame of propane in air, Fig. 11, was burned at reduced pressures and the volume required to effect a given rate of heat release per unit time determined from photographic measurements of the reaction-zone volume (14).

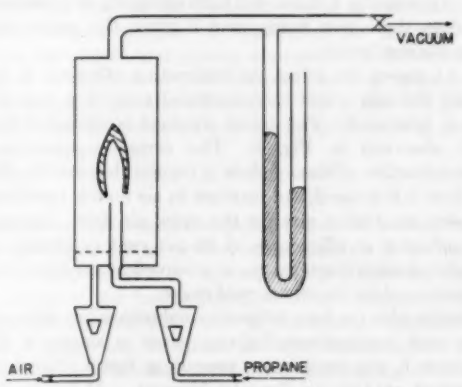

Fig. 11 Diffusion-Flame Apparatus Reference (14)

The volume in cubic inches required to release 1000 Btu per hr, computed in this way, is plotted against pressure in Fig. 12. At pressures above 120 mm the reaction zone of the flame was too thin to allow estimates to be made of its volume, although the curve extrapolates reasonably well to a value corresponding to 7×10^6 Btu per hr per cu ft at 1 atm, a value cited in reference (10) and based on an estimate of flame thickness for a flame propagating in a tube at a known rate.

Also shown in Fig. 12 is the volume available for the same heat-release rate in a turbojet combustor at the design fuel-flow rates and assuming 100 per cent combustion efficiency. It is noted that the combustor affords sufficient volume for the flame alone, although the volume required increases from less than 1 per cent of that available at sea level to about 10 per cent of the combustor at 65,000 ft for the combustor heat-release rates currently used.

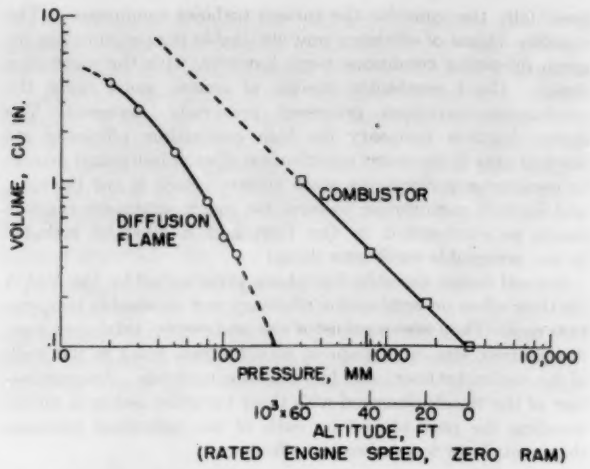

FIG. 12 EFFECT OF PRESSURE ON VOLUME REQUIRED BY DIFFUSION FLAME TO RELEASE 1000 BTU PER HR AND CORRESPONDING VOLUME AVAILABLE IN TURBOJET COMBUSTOR AT DESIGN FUEL FLOW RATES, REFERENCE (14)

In another experiment a wick lamp was substituted for the propane flame in similar apparatus and the entire apparatus was immersed in a calorimeter so that combustion efficiency could be measured. The results are shown in Fig. 13 and are compared with the same turbojet combustor. The diffusion flame burned at 100 per cent efficiency down to the blowout limit. Apparently, a flame will burn efficiently at pressures much lower than those now being used if given the proper environment in the combustor.

Fig. 14 shows the effect on combustion efficiency as the airflow rate through a unit cross-sectional area of a typical combustor is increased. The trend obtained is similar to that previously observed in Fig. 8. The curves representing constant combustion efficiency show a regular decrease in efficiency as air flow is increased; an increase in air flow is tantamount to decreasing combustor size for the same air flow. Operation of this combustor at efficiencies of 90 per cent or greater, over a reasonable temperature range, is achieved at air flows less than those indicated by the 90 per cent curve.

A similar plot for four different combustors but with only the 90 per cent combustion-efficiency curve is shown in Fig. 15. Combustor K was used in the preceding figure. Combustor H was limited at high air flows by blowout. At low air flows or low fuel flows (low temperature rise), H was limited by decreasing combustion efficiency because this combustor, unlike the other three, had a fixed-orifice fuel nozzle.

Decreased combustor size for a constant reference velocity also has been shown to reduce combustion efficiency if the ratio of combustion-zone volume to surface becomes small enough. Reasons for this effect of combustion-zone volume are discussed in a subsequent section. It may be concluded that combustor cross section should be maximized without exceeding the size of the other engine components. No comment can be made here about length.

Design of Primary Zone

A most important design consideration for stable and efficient combustion is, of course, the primary combustion zone, where that portion of the air that is to burn the fuel should be admixed. This zone is where low velocities and reverse flows afford sufficient residence time for initiation of flame and "piloting." Flow characteristics present in the primary zone of a typical

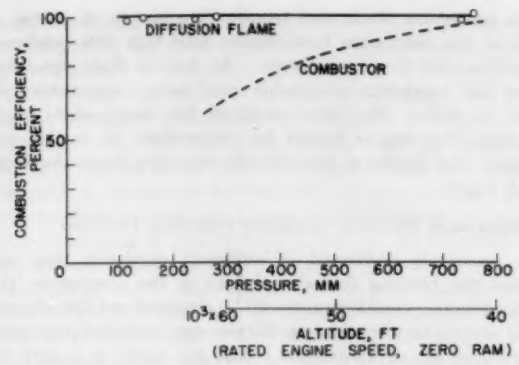

FIG. 13 EFFECT OF PRESSURE ON COMBUSTION EFFICIENCIES OF DIFFUSION FLAME AND TURBOJET COMBUSTOR, REFERENCE (14)

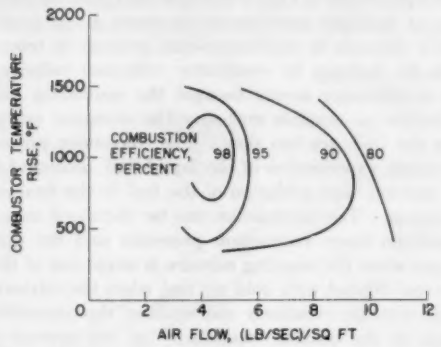

FIG. 14 EFFECT OF AIR FLOW PER MAXIMUM CROSS-SECTIONAL AREA ON COMBUSTION EFFICIENCY OF TURBOJET COMBUSTOR

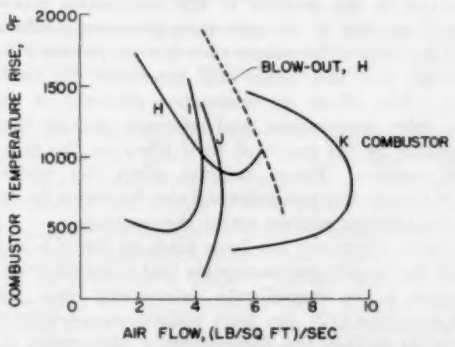

FIG. 15 LIMITING AIR FLOW PER MAXIMUM CROSS-SECTIONAL AREA FOR SEVERAL TURBOJET COMBUSTORS. COMBUSTION EFFICIENCY, 90 PER CENT

tubular combustor are illustrated in Fig. 16. These patterns were observed by flowing balsa dust in air through transparent combustors. A region of high turbulence, resulting from the impingement of air-entry jets, is seen near the center of the combustor. In the upstream, or primary zone, of the combustor reverse flow and large-scale eddies are apparent. The flow patterns shown were found to vary more with time than with operating conditions in the particular combustor investigated. Other visual studies of flow in similar combustors are described in reference (11).

One important design consideration for the combustor primary

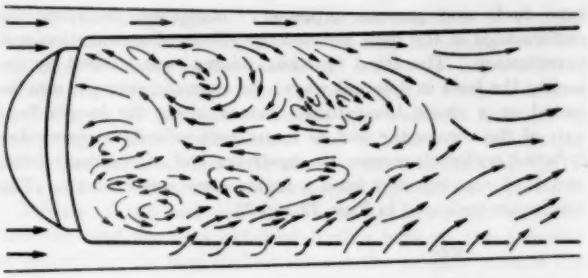

FIG. 16 AIR-FLOW PATTERN IN TUBULAR TURBOJET COMBUSTOR UNDER NONBURNING CONDITIONS

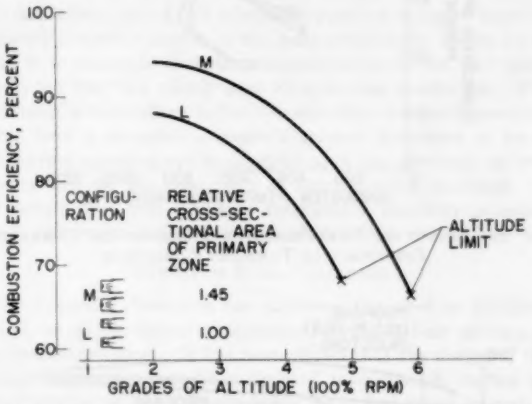

FIG. 17 EFFECT OF SIZE OF PRIMARY ZONE ON COMBUSTION EFFICIENCY OF TURBOJET COMBUSTOR

zone is its size. Combustion efficiency at simulated full engine speed is plotted against grades of altitude in Fig. 17 for two double-annular combustors. The two combustors were identical in all respects except that the cross-sectional area of the primary zone of combustor M was 45 per cent greater than that of combustor L. Longitudinal cross-sectional views of the upstream end of the combustor liner are included in Fig. 17 to indicate the fuel nozzles and the relative size of the combustion zones. It is noted that combustor M exhibits higher combustion efficiency at all altitudes than combustor L. The altitude operating limits for these combustors are designated by a symbol at the end of each curve. It is seen that these limits are in the same order as the efficiencies.

Possible reasons for the improvement in the combustion efficiency and altitude operating limits with the larger primary zone are that (*a*) a smaller portion of the fuel spray impinges on the wall; (*b*) lower local velocities are afforded; (*c*) a larger quantity of material burns in the low-velocity region of the combustor; and (*d*) quenching of chemical reactions by the cold walls is reduced. With respect to (*d*) it is significant to recall Fig. 12 in which the volume of a diffusion flame is shown to increase as pressure decreases.

Another important design consideration for the combustor primary zone is the distribution of open area along the length of the combustor. In order to determine the criteria for optimum size and distribution of the openings in the liner wall, systematic investigations were made in several different annular turbojet combustors both of proprietary manufacture and of NACA design.

Some results from one of these studies are presented in Fig. 18 as representative of the findings. The combustion efficiencies

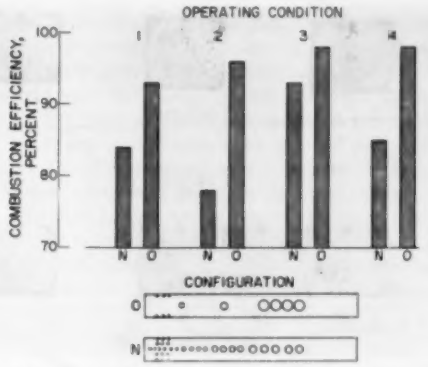

FIG. 18 EFFECT OF DISTRIBUTION OF LINER PERFORATIONS ON COMBUSTION EFFICIENCY OF TURBOJET COMBUSTOR AT FOUR COMBUSTOR OPERATING CONDITIONS

of two different configurations of an annular combustor are compared at each of four different operating conditions. The sketches in the lower part of the figure show an element of surface for each combustor liner; the smaller holes are at the fuel-nozzle end. The total open area of the holes for each combustor liner was identical. It is noted that combustor O produced higher combustion efficiencies than did combustor N. Thus a distribution of open area that allows less air into the upstream end or burning zone is to be preferred. This gradual admission of air aids in insuring that over a range of fuel flows, especially at low fuel flows such as at high altitude, correct mixtures for combustion will exist in the upstream end of the combustor.

Pressure loss, as such, in the combustor for the purpose of generating turbulence and mixing appears to be subordinate in importance to the factors just discussed as long as reasonable values of pressure loss are maintained. It is how the pressure loss is used, that is, how and where the air is directed in the combustor, that is important.

Fuel Injection

If satisfactory combustion requires the existence of localized fuel-air ratios that are at or near stoichiometric in the primary zone for all combinations of engine speed and altitude, then the manner in which the fuel is admitted to the combustor can be expected to be fully as important as the manner in which air is admitted. Important variables are the configuration of the spray because it influences distribution and mixing of the fuel, and injection pressure because it affects drop-size distribution as well as the distribution and mixing of the fuel.

The influence of fuel-spray configuration on combustion efficiency is illustrated in Fig. 19, which shows the combustion efficiency of a tubular combustor plotted against fuel-flow rate for two types of spray nozzles using kerosene-type fuel (15). The data for the lower curve were obtained with a hollow-cone fixed-orifice-type fuel nozzle. A loss of efficiency accompanies the collapse of the spray cone at low fuel flows with this nozzle. The data for the upper curve were obtained with a conventional nozzle to which had been added a small divergent section at the exit of the fuel orifice. At low rates of fuel flow the fuel appears to follow the divergent cone and forms a wide-angle spray as shown in Fig. 19. The combustion efficiencies obtained with the modified nozzle clearly indicate that large improvements in combustion efficiency can be achieved by the use of a nozzle that maintains a preferred fuel-spray configuration, especially at low fuel flows such as are encountered at high altitude.

The effects of fuel-injection pressure on combustor performance have been studied by using fuel nozzles of different rated capaci-

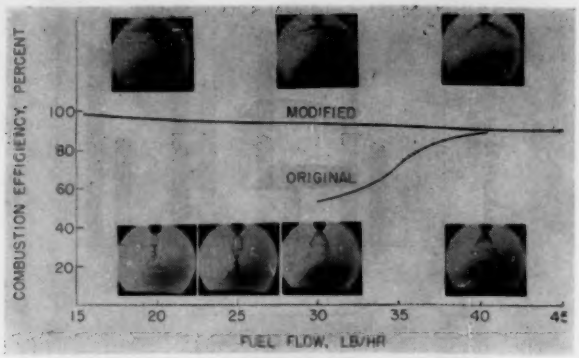

FIG. 19 EFFECT OF FUEL-SPRAY CONFIGURATION ON COMBUSTION EFFICIENCY OF TURBOJET COMBUSTOR (REFERENCE 15)

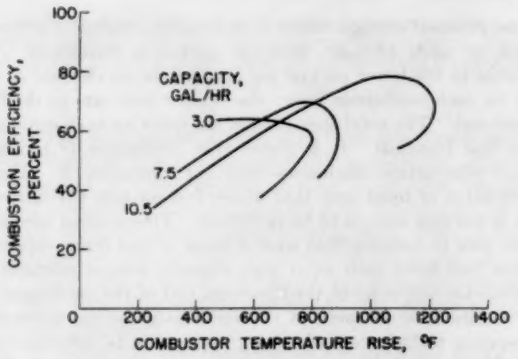

FIG. 20 EFFECT OF CAPACITY OF FUEL-INJECTION NOZZLES ON COMBUSTION EFFICIENCY OF TURBOJET COMBUSTOR

ties (rated at 100 psi fuel pressure) in order to vary the injection pressure. Some of the trends are illustrated in Fig. 20, a plot of combustion efficiency against combustor temperature rise for an annular combustor operated on gasoline at fixed inlet-air conditions. The operating conditions were selected deliberately to give marginal operation for this combustor. The data indicate that the 3-gph nozzle gave the highest combustion efficiency at low values of temperature rise, with the 7.5 and the 10.5-gph nozzles giving higher combustion efficiencies at higher values of temperature rise. The higher the injection pressure, that is, the smaller the nozzle, the lower were the temperature-rise limits encountered, however.

This trend is illustrated further in Fig. 21 where the data of Fig. 20, with results for additional fuel nozzles included, are plotted as combustion efficiency against combustor temperature rise for different values of fuel-injection pressure differential. From these and other similar data it may be concluded that at severe operating conditions increased fuel-injection pressure aids combustion efficiency at low fuel flows; however, it is possible to atomize the fuel too well and to reach a condition where cdditional fuel gives no additional heat release in the combustor. The combustor was designed for gasoline and 10.5-gph nozzles. Apparently, the fine atomization and rapid vaporization with the small nozzles caused a fuel-air mixture in the primary zone that was too rich to burn at higher fuel flows.

An attempt was made to study the individual effects on combustor performance of fuel atomization, vaporization, and distribution in another investigation. In this research a tubular combustor was operated with two fuels, JP-1 (a kerosene-type fuel) and gaseous propane. Comparison between the performance of the fuels isolated the effects of atomization and vaporization. The third function, mixing, was studied by injecting the fuels in different ways; for example, propane was injected as a single low-velocity stream along the longitudinal axis of the combustor and as many high-velocity streams distributed uniformly across the upstream end of the combustor, and JP-1 was injected from a hollow-cone spray nozzle. The results are indicated in Figs. 22 and 23.

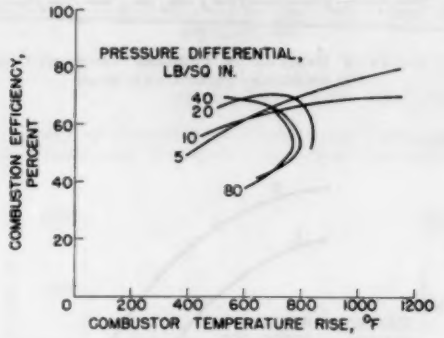

FIG. 21 EFFECT OF FUEL-INJECTION PRESSURE ON COMBUSTION EFFICIENCY OF TURBOJET COMBUSTOR

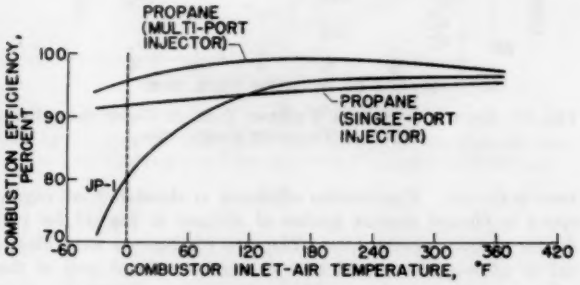

FIG. 22 EFFECT OF INLET-AIR TEMPERATURE ON COMBUSTION EFFICIENCY FOR GASEOUS AND LIQUID FUELS IN TURBOJET COMBUSTOR

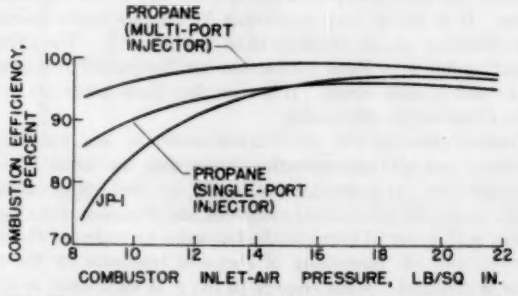

FIG. 23 EFFECT OF INLET-AIR PRESSURE ON COMBUSTION EFFICIENCY FOR GASEOUS AND LIQUID FUELS IN TURBOJET COMBUSTOR

In Fig. 22, a plot of combustion efficiency against combustor inlet-air temperature for the three injection schemes, it is seen that combustion efficiency with propane is less affected by a decrease in inlet temperature. This result may be because the temperature effects on atomization and vaporization rates are not present.

In Fig. 23 the curves line up in the same order when pressure is the variable as they did when temperature was the variable

in the preceding figure. The multiport injection of propane consistently gave the highest efficiencies, indicating the importance of mixing of fuel and air as well as the importance of eliminating atomization and vaporization. From evidence of this type, it has been concluded that when the functions of atomization and vaporization are eliminated, combustion efficiencies are much less influenced by the decreased inlet pressures and temperatures corresponding to high-altitude operation.

Mixing of the fuel and air is also an important variable, however, and the data obtained further indicate the necessity of controlling the local fuel-air ratio in the primary zone of the combustor. It also was apparent in this research that not all of the depreciation in combustion efficiency at altitude could be ascribed solely to the fuel-preparation processes.

From the research on fuel injection completed, it is concluded that fuel admission and air admission must be designed together to insure correct mixtures in the combustion zone. With liquid fuels, it is desirable that the characteristics of the fuel spray should not vary too widely over all operating conditions. This conclusion is a corollary to the concept that the fixed geometry of the liner is intended to provide gradual admission of air so that correct mixtures can be established in the upstream or low-velocity end of the combustor at any operating condition. A fuel nozzle that will maintain satisfactory injection pressures over a wide range of fuel flows is indicated from the studies.

Effect of Fuel Variables

The foregoing discussion has indicated the need of adequate control, at all conditions of operation, of the fuel-air mixture in the combustion zone. It has been shown that the design of the turbojet combustor has been directed toward such control by proper choice of the air-admission and fuel-injection-system design. If it is assumed that the combustion process occurs in the vapor phase, a final control of the fuel-air mixture must depend on the vaporization properties of the fuel. Further, the combustion process itself, even at optimum fuel-air mixture conditions, would be expected to be influenced by certain combustion characteristics relating to the composition of the fuel, such as flame speed or ignition temperature.

Effect of Volatility

At conditions favorable for combustion it has been seen that combustion efficiency may be relatively insensitive to changes in operating and design variables; similarly, under such conditions, satisfactory combustion efficiency may be obtained with fuels of widely varying properties. At adverse conditions of operation, however, there are significant effects of fuel properties on combustion efficiency. Three typical hydrocarbon-fuel mixtures, varying both in volatility and in composition, are shown in Table 1.

TABLE 1 PHYSICAL DATA OF FUELS TESTED IN ANNULAR COMBUSTORS

Fuel	Boiling range, deg F	Composition, per cent by volume: Aromatics	Paraffins, cycloparaffins
Aviation gasoline, AN-F-28	104–328	14	86
Kerosene type, AN-F-32	314–480	11	89
Diesel oil	364–664	19	81

Aviation gasoline represents a typical reciprocating-engine fuel, which has been used in some turbojet engines; kerosene, a turbojet-engine fuel; and diesel oil, the less volatile components of petroleum which could be utilized in turbojet engines. The combustion-efficiency performance of the three fuels in an annular combustor is shown in Fig. 24. These data illustrate a trend of combustion efficiency with simulated flight altitude that has been observed with many fuels in many different combustors. The actual values of combustion efficiency, of course, would depend upon the design factors and upon the operating conditions. The data indicate that the combustion efficiencies of these fuels tend to converge near 100 per cent combustion efficiency at low-altitude conditions. As altitude is increased, the combustion efficiencies begin to decrease rapidly, and significant differences in combustion efficiency among the fuels are observed. The least-volatile fuel, diesel oil, burns with the lowest combustion efficiency, and the most-volatile fuel, aviation gasoline, burns with the highest combustion efficiency.

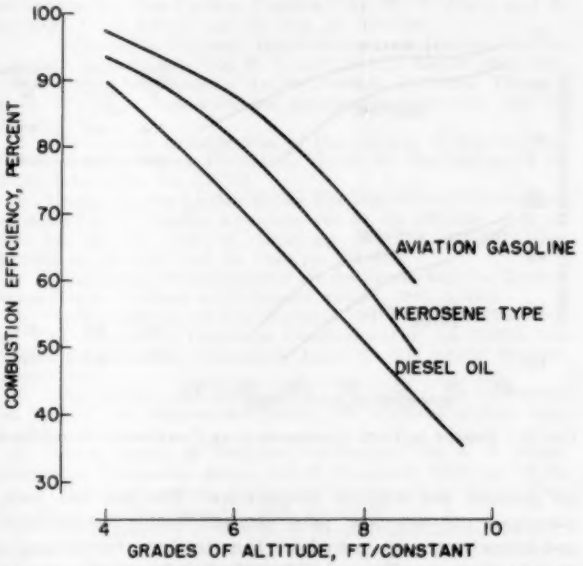

Fig. 24 Variation of Combustion Efficiency With Increasing Altitude at Constant Engine Speed With Three Fuels

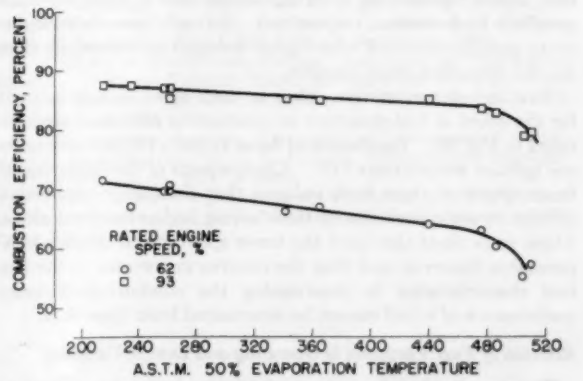

Fig. 25 Effect of ASTM 50 Per Cent Evaporation Temperature of Several Mixed Hydrocarbon Fuels on Combustion Efficiency in Single Tubular Combustion

The trend of combustion efficiency with fuel volatility noted in Fig. 24 has been observed in other combustor types. Tests with several mixed hydrocarbon fuels in a single tubular combustor at adverse operating conditions indicated the relationship between combustion efficiency and the ASTM 50 per cent boiling temperature shown in Fig. 25. The combustion efficiency decreased with an increase in the boiling temperature of the

fuel. The mixed fuels represented in Fig. 25 varied also in hydrocarbon composition, containing up to 33 per cent aromatic hydrocarbons, and in viscosity, varying from 0.5 to 3.5 centistokes (at 100 F). Thus the trend shown is not necessarily one of volatility alone, although it is believed that volatility was the most significant variable investigated.

Effect of Fuel Type

The effect of hydrocarbon composition on combustion efficiency has been investigated in another tubular combustor with pure hydrocarbons. Fig. 26 presents combustion-efficiency data for four pure paraffinic hydrocarbons tested over a wide range of reference velocities at adverse conditions of combustor inlet-

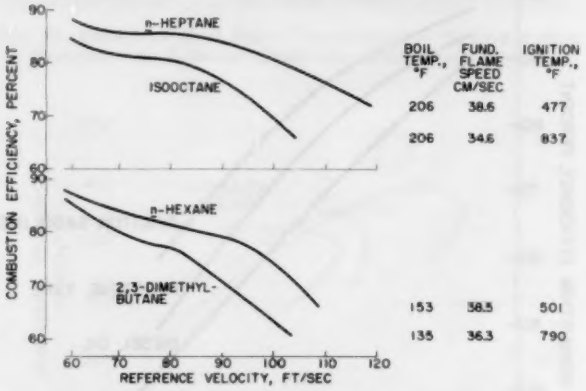

FIG. 26 EFFECT OF FUEL COMPOSITION ON COMBUSTION EFFICIENCY

air pressure and inlet-air temperature. The first two fuels, n-heptane and isooctane, have identical boiling temperatures, and hence vary only in hydrocarbon structure, representing a straight-chain paraffin and a branched-chain paraffin, respectively. The n-hexane and 2, 3-dimethylbutane have almost equivalent boiling temperatures and vary, similarly, in structure, again representing a straight-chain and a branched-chain paraffinic hydrocarbon, respectively. In both cases the straight-chain paraffin operated with higher combustion efficiencies than did the branched-chain paraffin.

Two fuel characteristics, either or both of which may account for the effect of fuel structure on combustion efficiency, are indicated in Fig. 26: Fundamental flame velocity (4), and spontaneous ignition temperature (16). Comparisons of the fundamental flame speeds of these fuels indicate that the higher combustion efficiencies are observed with fuels having higher flame velocities. These same fuels also have the lower spontaneous ignition temperatures, however, and thus the relative importance of the two fuel characteristics in determining the combustion-efficiency performance of a fuel cannot be ascertained from these data.

Relation of Fuel Variables to Operating and Design Variables

The trends that have been determined can be applied to many combustors and many combustor operating conditions. Exceptions do exist, however, and the relative combustion efficiencies of fuels are frequently altered by a different choice of combustor design or operating condition. As an illustration there is plotted in Fig. 27 the variation of combustion efficiency with combustor temperature rise for two fuels, gasoline and diesel oil, and two combustor inlet-air temperatures. With a combustor inlet-air temperature of 240 F, the more volatile gasoline gave higher combustion efficiencies throughout the range of combustor temperature rise. When the inlet-air temperature was reduced to 150 F, however, the gasoline gave a maximum combustion efficiency at a temperature rise of about 1200 deg F. As the fuel-flow rate to the combustor was increased in an attempt to obtain higher values of combustor temperature rise, a rapid decrease in the combustion efficiency of gasoline occurred. This decrease was followed by a marked reduction in obtainable temperature rise and, finally, by flame blowout.

The occurrence of limiting values of combustor temperature rise, accompanied by decreases in combustion efficiency, has been attributed to the presence of overrich fuel-air mixtures in the primary combustion zone. This condition will be encountered, then, at the high fuel-flow rate accompanying high-tempera-

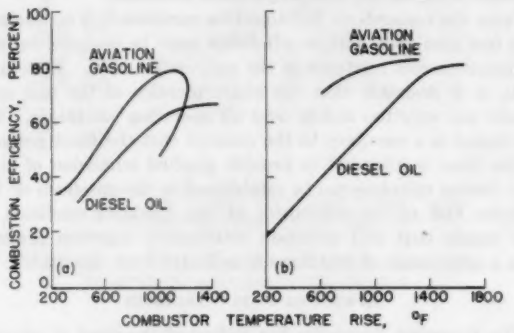

FIG. 27 VARIATION OF COMBUSTION EFFICIENCY WITH COMBUSTOR TEMPERATURE RISE FOR TWO FUELS
(*a*, Inlet-air temperature, 150 F; *b*, inlet-air temperature, 240 F.)

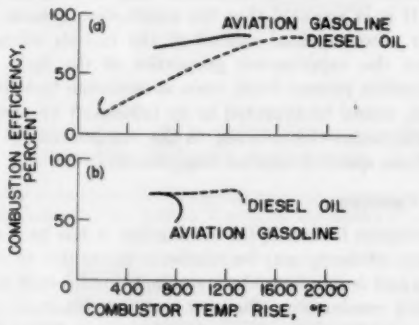

FIG. 28 EFFECT OF FUEL-NOZZLE DESIGN AND FUEL COMPOSITION ON COMBUSTION EFFICIENCY
(*a*, 10.5-gph nozzle; *b*, 3.0-gph nozzle.)

ture-rise operation and with a more volatile fuel [Fig. 27(*a*) gasoline].

A similar explanation has been applied to trends of combustion efficiency with varying fuel-injection-nozzle characteristics, as previously discussed. Data illustrating the variation of combustion efficiency with combustor temperature rise for two fuels, gasoline and diesel oil, are compared for operation with two different fuel-injection systems (3.0 and 10.5-gph nozzles) in Fig. 28. With the larger fuel-injection nozzles, higher-combustion-efficiency performance was obtained with the more volatile fuel, gasoline. With the smaller nozzle, however, the overrich-mixture conditions, provided by the improved atomization characteristics, resulted in better performance with the less-volatile fuel, diesel oil. It should be noted, however, that even the improved combustion efficiency of diesel oil with the smaller nozzles did not quite equal the improved com-

bustion efficiency of gasoline with the larger nozzles, indicating that optimum fuel-injection conditions will not necessarily eliminate the effect of fuel properties on combustion efficiency.

It should not be inferred from the foregoing discussion that volatility and hydrocarbon composition, or structure, are the only fuel variables that may have an effect on combustion efficiency in a turbojet combustor. The effects of these particular variables have been investigated more intensively (17). Other variables such as viscosity and surface tension also may affect the combustion efficiency—for example by affecting the fuel-atomization characteristics.

It may be concluded that certain fuel properties significantly affect the combustion efficiency of a combustor at adverse conditions of operation. The trends that have been determined indicate (*a*) that combustion efficiency generally increases with an increase in fuel volatility; and (*b*) straight-chain paraffins operate with higher combustion efficiencies than do branched-chain paraffins. Considerations of fuel availability and of other turbojet-performance factors obviously require certain compromises to obtain the optimum combination of fuel and combustor design.

Conclusion

In conclusion, the research data reviewed herein have shown that as the environment of the combustor becomes one of low pressure and low temperature at high altitude, low combustion efficiencies and limited values of obtainable temperature rise are encountered. The reason for low efficiencies at high altitudes is related to the increased time required to convert the fuel and air "reactants" in the chemical process as pressure and temperature are lowered. Systematic research on combustors and fuels and comparison of the results with results from basic studies have led to at least a qualitative understanding of what is required for successful combustor performance.

The necessary criteria for achieving stability of operation and high combustion efficiency over a wide range of operating conditions are (*a*) that localized fuel and air mixtures having fuel-air ratios at or near stoichiometric values exist somewhere in the combustor; (*b*) that these localized mixtures of correct composition exist sufficiently long for ignition and combustion to occur; and (*c*) that all of the fuel entering the combustor be involved in just this manner.

Design features that aid in establishing the criteria described previously include a wide upstream end, or primary zone, gradual admission of the primary air, and constant-pressure fuel nozzles. It has been observed that it is necessary to match the combustor design, the fuel nozzles, and the fuel to insure satisfactory fuel-air ratios in the primary zone at all operating conditions. Fuels that burn faster, or ignite at lower temperatures, or both, would alleviate the combustion-efficiency problem, although appreciable changes in this regard cannot be made without jeopardizing the fuel-supply problem.

Finally, it is again stated that the authors recognize that much work remains to be done on the problem of combustion efficiency at high altitude, and, further, that this paper has not discussed at all the many other combustor problems that require solution concurrently with the efficiency problem.

Bibliography

1 "Effect of Combustor-Inlet Conditions on Performance of an Annular Turbojet Combustor," by J. H. Childs, R. J. McCafferty, and O. W. Surine, NACA Rep No. 881, July, 1947.

2 "Temperature Measurements and Combustion Efficiency in Combustors for Gas-Turbine Engines," by W. T. Olson and E. Bernardo, Trans. ASME, vol. 70, 1948, pp. 329–334.

3 "Relationship Between Inflammables and Ignition Sources in Aircraft Environments," by W. E. Scull, NACA Report 1019, 1951.

4 "Flame Propagation. Active Particle Diffusion Theory," by D. M. Simon, *Industrial and Engineering Chemistry*, vol. 43, 1951, p. 2718.

5 "Preliminary Investigation of Combustion in Flowing Gas With Various Turbulence Promoters," by G. W. Haddock and J. H. Childs, NACA RM No. E8C02.

6 "James Clayton Lecture Before The Institution of Mechanical Engineers," by F. Whittle, *Aeroplane*, vol. 69, pp. 445–448; Oct. 19, 1945, pp. 451–452, Oct. 12, 1945, pp. 288–290, 503–507; Oct. 19, 1945, pp. 210–212; Oct. 26, 1945, pp. 328–329.

7 "Engineering Development of the Jet Engine and Gas Turbine Burner," by F. C. Mock, *SAE Journal*, vol. 54, 1946, p. 218.

8 "Combustion in the Gas Turbine," by P. Lloyd, The Institution of Mechanical Engineers, Development of the British Gas Turbine Jet Unit, War Emergency Issue No. 12, ASME Reprint, January, 1947.

9 "Combustion and Combustion Equipment for Aeroplane Gas Turbine," by Watson and Clarke, The Institute of Fuel, May 28, 1947.

10 "Some Aspects of Turbojet Combustion," by A. J. Nerad, *Aeronautical Engineering Review*, vol. 8, December, 1949, pp. 24–26.

11 "Turbojet Combustion Chamber Problems," by Stuart Way, *Aero Digest*, vol. 60, February, 1950, pp. 52–54.

12 "Flame Stability in Bluff Body Recirculation Zones," by J. P. Longwell, E. E. Frost, and M. A. Weiss, *Industrial and Engineering Chemistry*, vol. 45, 1954, pp. 1629–1633.

13 "Combustor Performance With Instantaneous Mixing," by W. H. Avery and R. W. Hart, *Industrial and Engineering Chemistry*, vol. 45, 1953, pp. 1634–1637.

14 "Combustion Efficiencies in Hydrocarbon-Air Systems at Reduced Pressures," by R. R. Hibbard, I. L. Drell, A. J. Metzler, and A. E. Spakowski, NACA RM E50G14, September, 1950.

15 "Effects of Fuel-Nozzle Carbon Deposition on Combustion Efficiency of Single Tubular Type, Reverse-Flow Turbojet Combustor at Simulated Altitude Conditions," by R. T. Dittrich, NACA TN 1618, June, 1948.

16 "Spontaneous Ignition Temperatures. Commercial Fluids and Pure Hydrocarbons," by J. L. Jackson, *Industrial and Engineering Chemistry*, vol. 43, 1951, p. 2869.

17 "Effect of Fuel Properties on the Performance of the Turbine Engine Combustor," by L. C. Gibbons and E. R. Jonash, ASME Paper No. 48—A-104.

Heat Transfer From Spheres to a Rarefied Gas in Subsonic Flow

By L. L. KAVANAU,[1] BERKELEY, CALIF.

Experimental over-all average heat-transfer coefficients for spheres in a subsonic air stream are presented for the slip-flow region in the range of Mach number M, and Reynolds number Re (based on diameter), $0.1 \leqslant \mathbf{M}_1 \leqslant 0.69$ and $1.75 \leqslant \mathbf{Re}_1 \leqslant 124$. A simplified analysis is presented which yields the convective heat-transfer coefficient for a rarefied gas by means of a correction to the continuum coefficient at the same Reynolds number. Comparison of this analysis is made with an existing theory for cylinders. An expression for the nondimensional over-all average heat-transfer coefficient for spheres in a rarefied subsonic flow is given as

$$\mathbf{Nu}_{avg} = \frac{\mathbf{Nu}^{\circ}_{avg}}{1 + 3.42 \dfrac{\mathbf{M}_1}{\mathbf{Re}_1 \mathbf{Pr}} \mathbf{Nu}^{\circ}_{avg}}$$

Nomenclature

The following nomenclature is used in the paper:

- A = surface area of sphere, sq ft
- a = speed of sound, fps
- c, c_p = specific heat, Btu/lb deg F
- D = sphere diameter, ft
- h = heat-transfer convection coefficient, Btu/hr sq ft deg F
- h_c = average over-all convection coefficient, Btu/hr sq ft deg F
- h_r = average over-all radiation coefficient, Btu/hr sq ft deg F
- J_1, Y_1 = Bessel functions of first kind, order 1
- k = thermal conductivity, Btu/hr ft deg F
- l = molecular mean free path, ft
- $\mathbf{M}$ = Mach number (U/a), dimensionless
- n = U_1/U_{avg}, dimensionless
- Nu = Nusselt number (hx/k), dimensionless
- p_i = impact pressure on probe, microns of Hg
- p_s = nozzle wall static pressure, microns of Hg
- Pr = Prandtl number $(\mu c_p/k = 0.72$ for air), dimensionless
- q = heat flux, Btu/hr sq ft
- Re = Reynolds number $(U\rho x/\mu)$, dimensionless
- Re_1 = free-stream Reynolds number $(U_1\rho_1 D/\mu)$, dimensionless
- Re_2 = free-stream Reynolds number behind normal shock wave in supersonic flow $(U_2\rho_2 D/\mu_2)$, identical to Re_1 for subsonic flow, dimensionless
- t = temperature, deg F
- t_e = surface equilibrium temperature due to convection, deg F
- t_e' = surface equilibrium temperature due to convection, radiation, and conduction, deg F
- t_w = tunnel wall temperature, deg F
- t_i = initial temperature of sphere, deg F
- T = absolute temperature, deg R
- U = velocity, fps
- V = volume of sphere, cu ft
- u = arbitrary variable of integration
- w = specific weight of sphere, lb/cu ft
- x = characteristic length, ft (diameter of sphere, diameter of cylinder)
- y = distance along outward normal from surface, ft
- α = thermal accommodation coefficient, dimensionless
- β = parameter $\sqrt{\frac{2}{n}\,\mathrm{Re}\,\mathrm{Pr}}$, dimensionless
- γ = ratio of specific heats, dimensionless
- η = cylinder diameter/2.5l
- θ = parameter, $1.996 \dfrac{2-\alpha}{\alpha} \dfrac{\gamma}{\gamma+1}$, dimensionless
- λ = temperature jump distance $(\theta l/\mathrm{Pr})$, ft
- μ = absolute viscosity, lb sec/sq ft
- ρ = mass density, lb sec^2/ft^4
- τ = time, hr

Subscripts

- 0 = stagnation conditions
- 1 = free-stream conditions
- avg = an integrated average
- e = surface equilibrium conditions
- w = surface conditions
- $(y = 0)$ = stream conditions adjacent to surface

Superscript

- $^{\circ}$ = continuum conditions

Introduction

The calculation of convective heat transfer between a gas and an immersed body becomes increasingly difficult when the mean free path of the gas is not negligible compared to significant body dimensions (1).[2] Occurrence of this gas rarefaction decreases the heat-transfer coefficient below its continuum value. This effect is apparently primarily due to the temperature-jump condition at the surface, analogous to the slip velocity at the surface, which occurs at low pressures. This temperature jump introduces an effective thermal contact resistance at the surface.

Convective heat transfer from spheres to a rarefied gas has been treated analytically and experimentally in references (1 to 4). The experimental results of reference (4) gave heat-transfer coefficients in the slip-flow region below continuum values. These results were determined under supersonic-flow conditions. Since there existed a curved detached shock wave, some doubt remained as to the effect of the shock wave and possibly other compressibility phenomena on the results. It was considered desirable to obtain heat-transfer data from spheres at subsonic Mach numbers in the slip-flow region.

[1] Research Engineer, Department of Engineering, University of California. Presently with Theoretical Analysis Dept., Missile System Division, Lockheed Aircraft Corporation, Van Nuys, Calif.

Contributed by the Heat Transfer Division and presented at the Semi-Annual Meeting, Pittsburgh, Pa., June 20–24, 1954, of The American Society of Mechanical Engineers.

Note: Statements and opinions advanced in papers are to be understood as individual expressions of their authors and not those of the Society. Manuscript received at ASME Headquarters, April 14, 1954. Paper No. 54—SA-52.

[2] Numbers in parentheses refer to the Bibliography at the end of the paper.

It is the purpose of this paper to present over-all average heat-transfer data from spheres to a rarefied air stream for a range of variables $0.1 \leqslant M_1 \leqslant 0.69$ and $1.75 \leqslant Re_1 \leqslant 124$, and to present a simplified analysis which predicts the trends of these data by means of a rarefaction correction to the continuum solution. Comparison of the analysis also will be made with an existing closed-form solution for the heat transfer from a circular cylinder in rarefied-gas flow (2).

The flow region of the present experimental investigation together with that reported in reference (2) are shown in Fig. 1, for comparison with the range of earlier investigations reported in reference (5).

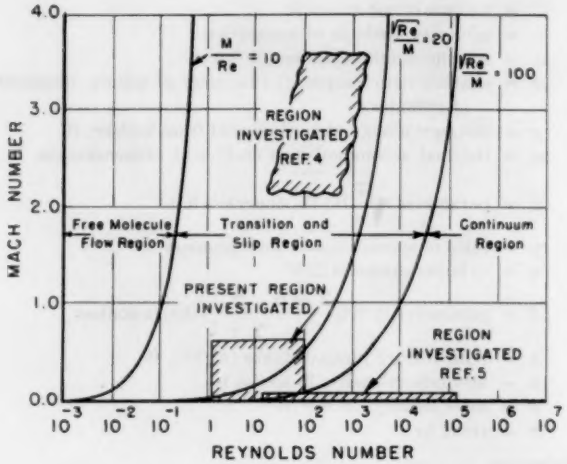

FIG. 1 INVESTIGATED FLOW REGION

ANALYSIS

If one considers the temperature jump in the slip-flow region as an effective thermal contact resistance at the surface over and above the thermal resistance due to the viscous boundary layer, then the heat-transfer coefficient at low pressures can be determined to the first order by a correction to the continuum heat-transfer coefficient at the same Reynolds number.

Consider a surface placed in a continuum flow so that heat is transferred between the surface and the stream. At any particular instant the surface temperature is assumed uniform and equal to t_w°. The heat flux will be

$$q = -k_{y=0} \left.\frac{\partial t}{\partial y}\right)_{y=0} = h_c^\circ (t_w^\circ - t_e^\circ) \quad \ldots\ldots [1]$$

where $\partial t/\partial y$ is the gradient of temperature normal to the surface, k is the heat conductivity, h_c is the convective heat-transfer coefficient, and t_e is the equilibrium temperature of the surface. The subscript $y = 0$ identifies the properties of the air evaluated at the surface and zero superscript signifies continuum conditions.

Now if the air stream is rarefied while holding the Reynolds number constant, the additional resistance to heat transfer as a result of the temperature jump will present itself so that we may define a total convective heat-transfer coefficient incorporating both the thermal boundary layer and temperature-jump resistances by writing

$$q = h_c (t_w - t_e) \quad \ldots\ldots [2]$$

where t_w and t_e are the surface temperature and equilibrium surface temperature, respectively.

The first-order temperature-jump boundary condition may be written as

$$t_{y=0} - t_w = \lambda \left.\frac{\partial t}{\partial y}\right)_{y=0} \quad \ldots\ldots [3]$$

where

$$t_{y=0} \quad \text{and} \quad \left.\frac{\partial t}{\partial y}\right)_{y=0}$$

are the temperature and gradient of temperature in the layer of gas immediately adjacent to the surface. The quantity λ is the temperature-jump distance defined from kinetic theory (6) by the formula

$$\lambda = 1.996 \frac{2 - \alpha}{\alpha} \frac{\gamma}{\gamma + 1} \frac{l}{\mathrm{Pr}}$$

or

$$\lambda = \frac{\theta l}{\mathrm{Pr}} \quad \ldots\ldots [4]$$

with $l = 1.48x(\mathbf{M}/\mathrm{Re})$, α the accommodation coefficient, γ the ratio of specific heats, Pr the Prandtl number, and

$$\theta = 1.996 \frac{2 - \alpha}{\alpha} \frac{\gamma}{\gamma + 1}$$

This first-order temperature-jump condition requires that $t_e = t_e^\circ$. It is now further assumed that q, the heat transferred between the surface at temperature t_w and the gas at temperature t_1 for the case of a surface-temperature jump, is the same as the heat transferred between a sphere at temperature $t_{y=0}$ and the gas at temperature t_1 under conditions of no temperature jump. In other words, Equation [1] is assumed valid with $t_w^\circ = t_{y=0}$.

Combinations of Equations [1], [2], [3] give

$$\frac{h_c^\circ}{h_c} = 1 + \frac{\lambda h_c^\circ}{k_{y=0}} \quad \ldots\ldots [5]$$

Substituting Equation [4] in Equation [5] yields

$$\frac{h_c^\circ}{h_c} = 1 + 1.48\,\theta \frac{h_c^\circ x}{k_{y=0}} \cdot \frac{\mathbf{M}}{\mathrm{Re\,Pr}} \quad \ldots\ldots [6]$$

or

$$\frac{\mathrm{Nu}^\circ}{\mathrm{Nu}} = 1 + 1.48\,\theta \frac{\mathbf{M}}{\mathrm{Re\,Pr}} \mathrm{Nu}^\circ \quad \ldots\ldots [7]$$

where Nu° and Nu are the local Nusselt numbers for continuum and rarefied flows, respectively.

Comparison With Existing Cylinder Theory

As with all approximate analyses, it would be advantageous to evaluate the foregoing method by means of a comparison with other solutions. It is possible to do this for the case of a circular cylinder since reliable continuum heat-transfer data exist (5) and a closed-form solution has been obtained for the slip-flow region (2).

The comparisons of Equation [7] with the theory of reference (2) is shown in Table 1 where the nondimensional heat-transfer coefficient (Nu_{avg}) is given for various Reynolds numbers with η as the parameter. The term η is defined as the ratio of cylinder diameter to 2.5 mean free paths of the gas. Closer agreement could not be expected.

TABLE 1 HEAT-TRANSFER COEFFICIENTS FOR CIRCULAR CYLINDERS AS GIVEN IN REFERENCE (2). COEFFICIENTS IN PARENTHESES WERE OBTAINED FROM EQUATION [7]

η	0.2	0.5	1.0	2.5	5.0	10
Re	N_{Nusv}					
0.672	0.160 (0.165)	0.304 (0.309)	0.435 (0.436)	0.583 (0.579)	0.651 (0.650)	0.679 (0.693)
1.344	0.167 (0.172)	0.329 (0.335)	0.488 (0.489)	0.690 (0.677)	0.780 (0.776)	0.824 (0.841)
6.72	0.180 (0.187)	0.392 (0.396)	0.650 (0.634)	1.03 (0.99)	1.24 (1.22)	1.35 (1.38)
67.2	0.192 (0.201)	0.453 (0.468)	0.837 (0.839)	...	...	...
672	...	...	0.932 (0.976)	2.12 (2.19)	...	...
6720	...	...	...	...	4.38 (4.74)	7.15 (8.57)

Experimental Equipment and Procedure

Wind Tunnel

The required low-density gas stream was provided by the No. 3 wind tunnel located at Berkeley. The constructional features and general operating characteristics of the tunnel are contained in reference (7). An axisymmetric, subsonic nozzle was employed in the investigation, giving a range of Mach numbers, 0.1 to 0.69, and a static pressure range of 36 to 3300 microns Hg. The nozzle used had an exit diameter of 9 in. The design of this nozzle is described in reference (8).

The four spheres and the impact-pressure probe were mounted on a rotary selector (8) which in turn was supported in the tunnel test chamber by a traversing mechanism (7) capable of axial, lateral, and vertical movement with respect to the nozzle. With this versatile mounting system, any of the five objects on the rotary selector could be moved into the flow field as required, without alteration of the flow.

Experimental Method

The over-all average heat-transfer coefficients were determined by the transient technique described in reference (4). Briefly, the method is as follows: The rate of change of heat in a small body of sensibly uniform internal temperature distribution is equated to the heat loss by convection and radiation to give

$$-cwV\frac{dt}{d\tau} = h_c A(t - t_a) + h_r A(t - t_a) \quad [8]$$

with the boundary conditions

$$t = t_i; \quad \tau = 0$$
$$t = t_a'; \quad \tau \to \infty$$

where t_i is the initial sphere temperature and t_a' is the equilibrium temperature for the combined effects of radiation and convection. If the difference between the absolute surface temperature and the absolute temperature of the surroundings is not great, Equation [8] may be integrated for h_c and h_r not functions of the temperature to yield

$$\frac{t - t_a'}{t_i - t_a'} = \exp\left[-\frac{A(h_c + h_r)\tau}{cwV}\right] \quad [9]$$

where the equilibrium temperature t_a' is

$$t_a' = \frac{h_c t_a + h_r t_a}{h_c + h_r} \quad [10]$$

and the equilibrium temperature due to convection heat transfer alone is given from Equation [10] as

$$t_a = t_a' + \frac{h_r}{h_c}(t_a' - t_a) \quad [11]$$

It is necessary to determine the radiation heat-transfer coefficient h_c independently by making transient cooling runs at no flow with tunnel pressures reduced to the order of 0.1 micron Hg, so that free-convection currents are eliminated. The heat balance in this case becomes

$$-cwV\frac{dt}{d\tau} = h_r A(t - t_a) \quad [12]$$

and the solution for the boundary conditions

$$t = t_i; \quad \tau = 0$$
$$t = t_a; \quad \tau \to \infty$$

becomes

$$\frac{t - t_a}{t_i - t_a} = \exp\left(-\frac{Ah_r\tau}{cwV}\right) \quad [13]$$

Making use of the temperature-time histories on a semilogarithmic plot as suggested by Equation [9] and Equation [13], the radiation heat-transfer coefficient h_r and the sum of the radiation and convection coefficients, $h_c + h_r$, are obtained. The quantity t_a is measured by means of a thermocouple placed on the tunnel wall and t_a' is that equilibrium temperature attained by the sphere after a very long time. The equilibrium temperature for convection only may then be calculated from Equation [11]. The heat-transfer coefficient resulting from convection alone h_c is the arithmetic difference between the two experimentally determined coefficients $h_c + h_r$ and h_r.

Sphere Models

The spheres were made of silver and were mounted on hollow drawn glass stings as shown in Fig. 2. B and S No. 40 iron- and-constantan wires were made into thermocouples and soft-soldered into the centers of the spheres and were then led out through the glass stings to larger wires on the sting support leading to the recording potentiometer. The spheres are further described in reference (4).

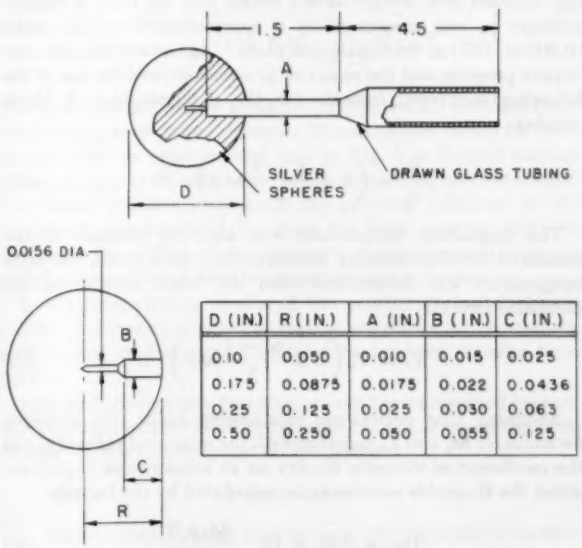

D (IN.)	R (IN.)	A (IN.)	B (IN.)	C (IN.)
0.10	0.050	0.010	0.015	0.025
0.175	0.0875	0.0175	0.022	0.0436
0.25	0.125	0.025	0.030	0.063
0.50	0.250	0.050	0.055	0.125

FIG. 2 DIMENSIONS OF HEAT-TRANSFER SPHERES

Experimental Procedure

The sphere in question was heated initially to a temperature of approximately 120 to 150 F by means of a radiation furnace consisting of a 100-watt lamp encased in several radiation shields and mounted near the nozzle in the test chamber. This radiant energy was sufficient to give the sphere a 10-deg F temperature rise in approximately 10 sec. The sphere was then removed from the furnace and traversed into the air stream on the nozzle center line with its forward stagnation point tangent to the exit plane of the nozzle. The temperature-time history of the sphere for this position was recorded by means of the recording potentiometer.

Instrumentation

All pressures were measured by a precision U-tube manometer (9) to an accuracy of ±1 micron Hg for pressures up to 400 microns and ±¼ per cent for pressures above 400 microns.

Sphere temperatures were measured by an iron-constantan thermocouple and recorded by a Leeds and Northrup potentiometer to an accuracy of ±0.017 millivolts (±0.5 deg F) and 2.5 per cent in time. The tunnel wall temperature t_w and settling chamber temperature t_0 were measured by copper-constantan thermocouples located in the settling chamber and recorded with a Brown 16-point recording potentiometer to ±0.03 millivolt (±1.4 deg F).

In addition to the foregoing special instrumentation, the standard tunnel equipment and instrumentation as described in reference (7) were utilized.

Reduction of Experimental Data

Flow System

The flow parameters required in the data presentation are Mach number and Reynolds numbers evaluated at the center of the nozzle-exit plane. These values were determined in the following manner: The static pressure p_e was measured by a wall orifice in the constant-area section of the nozzle and the total or impact pressure p_i was measured by a source-shaped impact probe (0.300 in. OD) at the nozzle-exit plane. Agreement between this impact pressure and the reservoir pressure allowed the use of the following isentropic formula for the determination of Mach number

$$\frac{p_i}{p_e} = \left(1 + \frac{\gamma - 1}{2} \mathbf{M}_1^2\right)^{\frac{\gamma}{\gamma - 1}} \quad \ldots\ldots [14]$$

The stagnation temperature was assumed identical to the measured settling-chamber temperature. As a result, the state temperature was determined from the Mach number by the adiabatic formula

$$T_1 = T_0 \left(1 + \frac{\gamma - 1}{2} \mathbf{M}_1^2\right)^{-1} \quad \ldots\ldots [15]$$

Assuming that perfect-gas relationship holds, the foregoing formulas for $\mathbf{M}_1$ and T_1, together with the measured value of p_e and the coefficient of viscosity for dry air at temperature T_1 (10) enabled the Reynolds number to be calculated by the formula

$$\mathrm{Re}_1 = 6.64 \times 10^{-6} \frac{\mathbf{M}_1 p_e D}{\mu_1 \sqrt{T_1}} \quad \ldots\ldots [16]$$

No nozzle blocking corrections were applied.

Thermal System

The reduction of the thermal data was accomplished by means of the method outlined in the Experimental Method section to result in the values of the convection coefficients h_c. The final results are given in the dimensionless form of the Nusselt number

$$\mathrm{Nu}_{av_2} = \frac{h_c D}{k_e}$$

wherein the thermal conductivity of the air is evaluated at the equilibrium temperature of the sphere. A typical plot of log $(t - t_e')$ versus τ appears in Fig. 3.

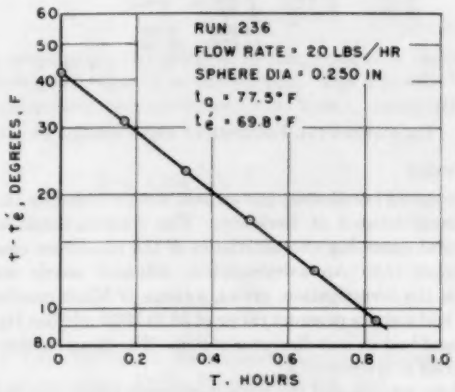

Fig. 3 Typical Plot of Sphere Temperature With Time

Sources of Error

Flow System

Errors incurred in the determination of the Mach and Reynolds numbers were due primarily to the inaccuracy of the instrumentation used to measure the pressures and temperature required in Equations [14] and [16]. The maximum relative errors of these quantities vary from 0.1 to 25 per cent.

Thermal System

The errors attendant to the determination of the heat-transfer coefficients h_c reside in the measurement of the time-temperature history of the cooling body and in the separate determination of the equilibrium temperature t_e'. These errors are thus determined by the least count of the recording potentiometers. The largest least count, ±0.52 deg F, when associated with the smallest temperature difference measured and used in the computation, 5 deg F, gives a possible error of 10 per cent. In addition, the error due to time measurement is 2.5 per cent. The radiation-conduction correction which is accounted for experimentally in independent runs is subject to the same errors as result from instrumentation. Since the radiation-conduction correction may amount to 50 per cent of the total heat-transfer coefficient, $h_c + h_r$ in the worst case, the maximum uncertainty in the determination of h_c may possibly be 25 per cent. This uncertainty in h_c will be transmitted directly to the Nusselt number with any other error incurred in the value of the thermal conductivity of the air.

Discussion of Experimental Results

The foregoing analysis results in an expression for the dimensionless local heat-transfer coefficient for the case of slip flow by virtue of an effective thermal-contact resistance resulting from the temperature-jump boundary condition. The result appears as a function of the dimensionless local heat-transfer coefficient for continuum flow and the local Mach, Reynolds, and Prandtl numbers.

It is given as

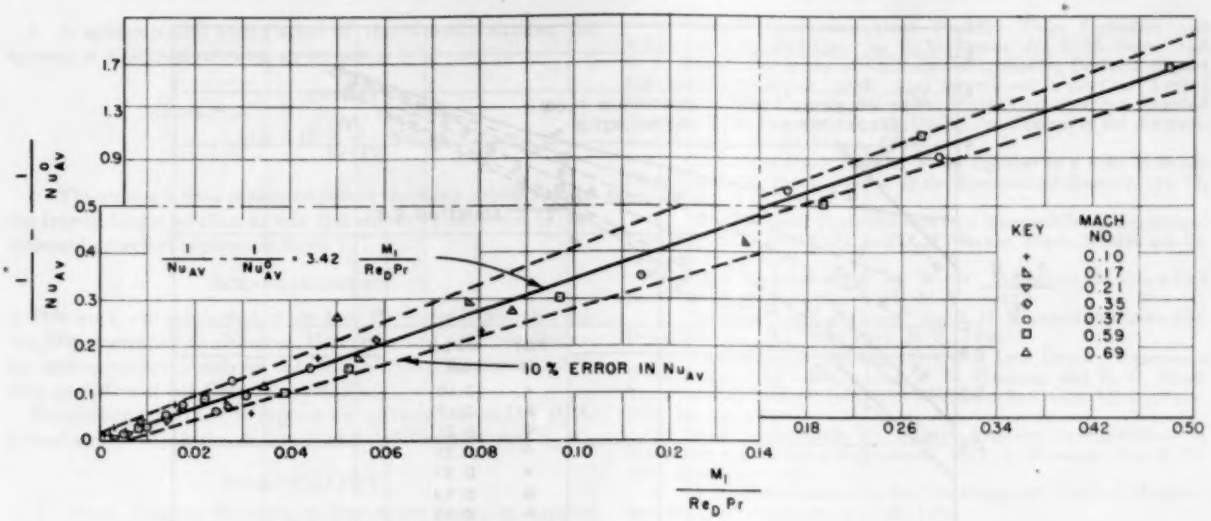

FIG. 4 CORRELATION OF HEAT TRANSFER FROM SPHERES IN RAREFIED SUBSONIC AIR STREAM

$$Nu = \frac{Nu^{\circ}}{1 + 1.48\theta \frac{M}{Re\,Pr} Nu^{\circ}} \quad \ldots\ldots [17a]$$

or

$$\left(\frac{1}{Nu} - \frac{1}{Nu^{\circ}}\right) = 1.48\theta \frac{M}{Re\,Pr} \quad \ldots\ldots [17b]$$

The experimental data are in the form of over-all average heat-transfer coefficients on spheres and exact prediction of these results cannot be extracted from the foregoing simplified analysis. However, one could expect that Equation [17*b*] would give a method of correlating the data, in so far as it reduces to the continuum value for small $M/(Re\,Pr)$ and gives a solution for large $M/(Re\,Pr)$ which resembles the free molecule solution of Equation [3], i.e.

$$\frac{Nu}{Re\,Pr} = \frac{f(\gamma, \alpha)}{M}$$

for small M.

For our particular application to over-all average heat transfer from spheres, we shall utilize the continuum solution from reference (2) as the specification for $Nu_{avg}{}^{\circ}$ which gives

$$Nu_{avg}{}^{\circ} = \left(\frac{h_{avg} D}{k}\right)^{\circ} = 2 + \frac{2}{\pi^2} \int_0^{\infty} \frac{(1 - e^{-\pi u^2})(1 + u^4)^{-1}}{J_1{}^2(\beta, u) + Y_1{}^2(\beta, u)} \frac{du}{u} \quad \ldots\ldots [18]$$

where

$$\beta = \sqrt{\frac{2}{n} Re\,Pr}, \quad n = U_1/U_{avg}$$

with U_1 the free-stream velocity and U_{avg} the average velocity over the sphere. The experimental data are correlated as

$$\frac{1}{Nu_{avg}} - \frac{1}{Nu_{avg}{}^{\circ}} \text{ versus } \frac{M}{Re\,Pr}$$

and appear in Fig. 4 with $n = 1.3$. The value of $n = 1.3$ was chosen merely to match the solution to the data for small $M/(Re\,Pr)$. The data correlate as a straight line of slope equal to 3.42 as determined by the method of least squares. It may be seen in Fig. 4 that better than 90 per cent of all the experimental data lie within a 10 per cent error by Nu_{avg} of this line. This, in general, is within the accuracy of measurement of the data.

The foregoing empirically determined constant, 3.42, enables one to write an expression for the heat transfer for spheres in a slightly rarefied subsonic air stream as

$$Nu_{avg} = \frac{Nu_{avg}{}^{\circ}}{1 + 3.42 \frac{M_1}{Re_1\,Pr} Nu_{avg}{}^{\circ}} \quad \ldots\ldots [19]$$

The superimposed plot of Equation [19] as well as the theoretical results for spheres from references (2) and (3) are shown for comparison with the experimental data in Fig. 5 as Nusselt number versus Reynolds number with Mach number as the parameter. This figure presents graphically the growing influence of the rarefaction parameter M/Re upon the heat transfer and also illustrates the ability of the proposed rarefaction correction to match the continuum and free molecule-flow solutions.

In Fig. 6 analytical results of the continuum low Reynolds number and free molecule-flow regions are shown for comparison with known existing experimental data for heat transfer from spheres.

Temperature-recovery factors have not been presented because the instrumentation used prevented obtaining an acceptable accuracy in the measurement of this quantity.

CONCLUSIONS

1 Experimental average over-all heat-transfer coefficients were obtained for spheres in a rarefied subsonic air stream where the Mach number and Reynolds number varied from 0.1 to 0.69 and 1.7 to 124, respectively.

2 A simplified analysis is presented which corrects continuum heat-transfer results for rarefaction by considering the temperature-jump boundary condition as an effective thermal-contact resistance. This analysis compares favorably to results for a cylinder given in reference (2).

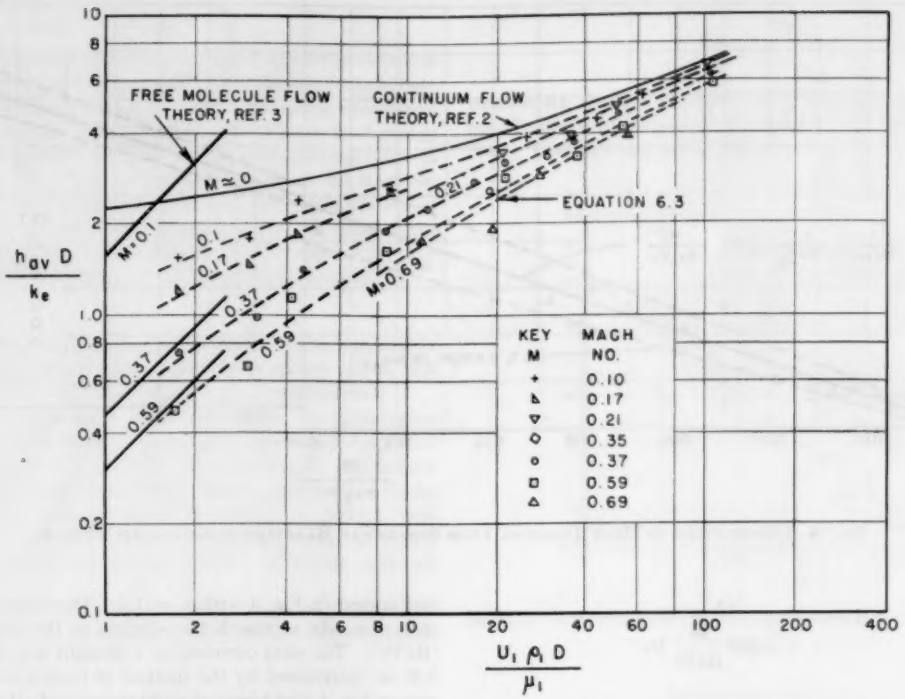

FIG. 5 AVERAGE HEAT-TRANSFER COEFFICIENTS FOR SPHERES IN SUBSONIC FLOW TO RAREFIED AIR

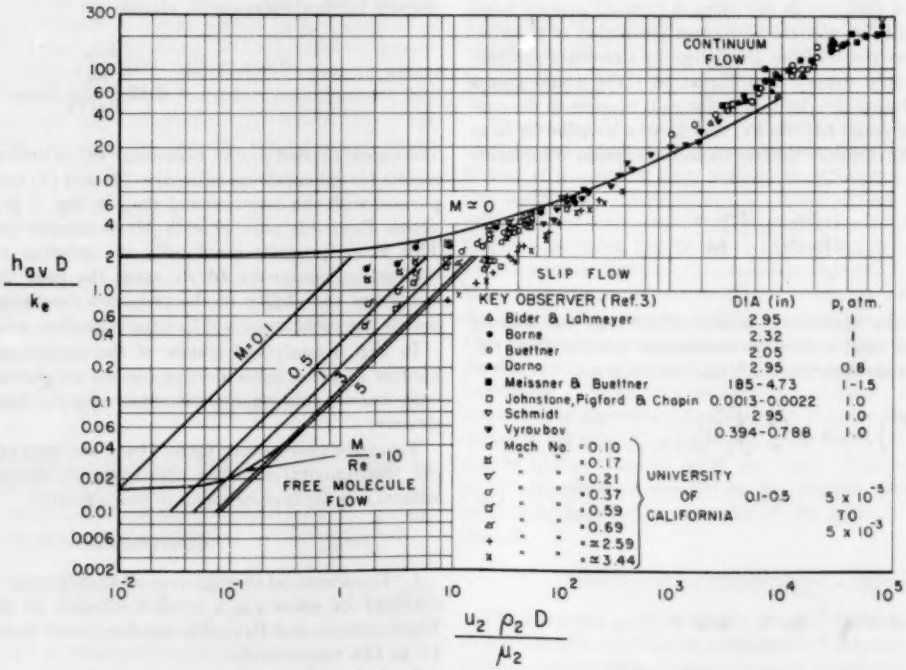

FIG. 6 AVERAGE HEAT-TRANSFER COEFFICIENT FOR SPHERES IN AIR

3 A semiempirical formulation of the Nusselt number for spheres in a rarefied subsonic air stream is

$$Nu_{avg} = \frac{Nu_{avg}^{\circ}}{1 + 3.42 \dfrac{M_1}{Re_1 Pr} Nu_{avg}^{\circ}}$$

4 The subsonic data presented follow the same trends toward the free-molecule solution as was first shown in reference (4) for spheres in rarefied supersonic flows.

ACKNOWLEDGMENTS

This work was conducted at the Low Pressures Research Project, Department of Engineering, University of California, Berkeley, and sponsored jointly by the Office of Naval Research (USN) and the Office of Air Research (USAF).

The author would like to express his appreciation to Drs. S. A. Schaaf and R. M. Drake, Jr., for their helpful suggestions.

BIBLIOGRAPHY

1 "Heat Transfer Problems in High-Speed Flows in Rarefied Gases," by R. M. Drake, Jr., and E. D. Kane, General Discussion of Heat Transfer, London, England, September, 1951; also, University of California Engineering Projects Report HE-150-73, October, 1950.

2 "Forced Convection Heat Transfer From Cylinders and Spheres in a Rarefied Gas," by R. M. Drake, Jr., F. M. Sauer, and S. A. Schaaf, University of California Engineering Projects Report HE-150-74, November, 1950. Also reproduced in part as "Forced Convection Heat Transfer From Horizontal Cylinders in a Rarefied Gas," by F. M. Sauer and R. M. Drake, Jr., *Journal of the Aeronautical Sciences*, vol. 20, March, 1953.

3 "Convective Heat Transfer From Spheres in a Free Molecule Flow," by F. M. Sauer, *Journal of the Aeronautical Sciences*, vol. 18, May, 1951.

4 "Heat Transfer From Spheres to a Rarefied Gas in Supersonic Flow," by R. M. Drake, Jr., and G. H. Backer, Trans. ASME, vol. 74, 1952, pp. 1241–1249.

5 "Heat Transmission," by W. H. McAdams, McGraw-Hill Book Company, Inc., New York, N. Y., 1942.

6 "Kinetic Theory of Gases," by E. H. Kennard, McGraw-Hill Book Company, Inc., New York, N. Y., 1938.

7 "Design and Initial Operation of a Low Density Supersonic Wind Tunnel," by S. A. Schaaf, D. O. Horning, and E. D. Kane, Trans. of Heat Transfer and Fluid Mechanics Institute, ASME, June, 1949, pp. 223–242.

8 "New Experiments on Impact Pressure Interpretation in Supersonic and Subsonic Airstreams," by F. S. Sherman, NACA TN 2995, September, 1953.

9 "A Precision Manometer for Low Pressures," by G. J. Maslach, *Rev. Sci. Instruments*, vol. 23, July, 1952.

10 "The NBS-NACA Tables of Thermal Properties of Dry Air," December, 1950.

11 "Gas Dynamics Tables for Air," by H. W. Emmonds, Dover Publications, New York, N. Y., 1947.

A Note on Limiting Laminar Nusselt Number in Ducts With Constant Temperature Gradient by Analogy to Thin-Plate Theory

By S. M. MARCO[1] and L. S. HAN,[2] COLUMBUS, OHIO

In this paper it is pointed out that the existing solutions for the deflections of thin plates under uniform lateral load and simply supported along all edges can be applied to the determination of the limiting temperature distributions in a fluid flowing in laminar motion in ducts of the same cross sections as those of the plates. The direct application of this solution is permissible only when (*a*) the axial temperature gradient is constant, with respect to both flow length and cross-section position. This implies uniform heating or cooling. (*b*) The cross section is a polygon. When the cross-section boundary contains curves, the constants of integration must be adjusted so that the boundary condition of nonslip flow is satisfied. Since the temperature and velocity distributions obtained by this analogy are expressed analytically, values of local heat transfer at any point in the cross-section boundary can be calculated. Examples are given for four cross sections, namely, rectangular, equilateral triangular, right-angled isosceles triangular, and semicircular. The heat-transfer distributions on the boundaries are calculated for square and equilateral triangular cross sections.

Nomenclature

The following nomenclature is used in the paper:

a = a dimension of cross section, ft
b = a dimension of cross section, ft
c = specific heat, Btu per (lb-deg F)
c_1 = axial temperature gradient ($\partial t/\partial z$), deg F per ft
c_2 = axial pressure gradient ($\partial p/\partial z$), (lb/sq ft) per ft
D_e = equivalent hydraulic diameter, (4 × cross-sectional area divided by the perimeter), ft
D = flexural rigidity of a plate, lb-ft
h = heat-transfer coefficient, Btu per (deg F-sq ft-hr)
k = thermal conductivity of fluid, Btu per (deg F-sq ft-hr per ft)
L = length, ft
m, n = indexes, integers
p = pressure, psf
q = rate of heat transfer, Btu per hr
q_0 = load intensity, psf
r = radius, ft
S = heat-transfer area, sq ft (perimeter of cross section × unit length), sq ft
t = temperature, deg F
u = velocity, ft/hr
w = deflection of a plate, ft
x, y = co-ordinates in plane of cross section of duct or plate
z = axial-flow direction
α = thermal diffusivity ($k/c\rho$)
β = angular co-ordinates, radians (rad)
γ = aspect ratio (a/b)
∇^2 = Laplacian operator $\left(\frac{\partial^2}{\partial x^2} + \frac{\partial^2}{\partial y^2}\right)$, $\left(\frac{\partial^2}{\partial r^2} + \frac{1}{r}\frac{\partial}{\partial r} + \frac{1}{r^2}\frac{\partial^2}{\partial \beta^2}\right)$
θ = temperature difference between fluid and wall, deg F
μ = viscosity, lb-hr per sq ft
ν = Poisson's ratio
ρ = density of fluid, lb/cu ft

Subscripts

avg = average
lim = limiting value
m = denotes mixed mean
s = denotes conditions at wall

Introduction

The need for compact heat exchangers of high effectiveness has greatly stimulated interest in the heat-transfer and friction characteristics for tubes of various cross sections. Experimental data are being added constantly to the already abundant literature on the in-tube flow in both laminar and turbulent regions. In the turbulent region there seems to be sufficient evidence to indicate that the heat-transfer coefficients can be estimated with assured accuracy from the established correlations. When the Reynolds number is low or L/D_e is large, prediction of laminar heat transfer becomes rather uncertain as is evidenced in a recent investigation (1)[3] by Kays and London. It was demonstrated therein that for long ducts the Nusselt number approaches a limit which is strongly influenced by the geometry of the cross section—for example, the aspect ratio $\gamma(a/b)$, in the case of a rectangular-cross-section channel. The determination of these limiting Nusselt numbers then became the subject of a paper by Clark and Kays (2) wherein two extreme cases, uniform surface temperature and uniform heating or cooling, i.e., $\partial t/\partial z$ = const, were treated by numerical solution of the differential equations of motion and heat transfer. Tests were performed which essentially substantiate the analytical results.

These two extreme cases, uniform surface temperature and uni-

[1] Chairman, Department of Mechanical Engineering, The Ohio State University. Assoc. Mem. ASME.

[2] Research Associate, Department of Mechanical Engineering, The Ohio State University.

Contributed by the Heat Transfer Division and presented at the Semi-Annual Meeting, Pittsburgh, Pa., June 20–24, 1954, of The American Society of Mechanical Engineers.

Note: Statements and opinions advanced in papers are to be understood as individual expressions of their authors and not those of the Society. Manuscript received at ASME Headquarters, April 14, 1954. Paper No. 54—SA-46.

[3] Numbers in parentheses refer to the Bibliography at the end of the paper.

form heating or cooling, constitute the limits within which virtually all laminar heat-transfer processes take place. For the uniform-temperature case, only two solutions are known, one for a circular tube and the other for a parallel gap. For the uniform-heating case, although great mathematical simplifications result, limited numbers of solutions have been published. For a circular tube subjected to a constant temperature gradient, the solution was first given by Nusselt.[4] Glaser as cited in (2) worked out solutions for a square and a gap by the method of finite differences; Clark and Kays (2) computed values for rectangular cross sections of various aspect ratios and for both constant-heat-input and constant-wall-temperature conditions. Jakob (4) shows the solution for an annulus.

In reference to the solutions indicated by Clark and Kays (2) and also by Glaser (2), although the numerical procedure yields reasonably accurate results when average quantities such as the mixed mean temperatures are involved, the method is not readily adaptable to finding the local values of heat-transfer coefficients. This is because much greater error would be incurred in computing the local temperature gradients as is pointed out by Clark and Kays (2). A knowledge of the variation of local heat-transfer coefficients is important since more exact calculation of the thermal efficiencies of extended surfaces which constitute a part of the duct enclosures may be made.

To supplement the findings reported in the foregoing and for the purpose of further investigation, exact solutions for tubes of rectangular, equilateral triangular, right-angled isosceles triangular, and semicircular cross sections with constant axial temperature gradient are given in this paper. The first two of these cross sections are commonly encountered in heat-exchanger work. The right-angled isosceles triangular cross section occurs when an extended surface is inserted in the diagonal direction of a square cross-sectional tube. In a similar manner, the semicircular cross section may be obtained if a diametral extended surface is used in a circular cross section.

Analysis

Considering constant physical properties and constant temperature gradient in the axial direction, the equations of motion and heat transfer for fully established velocity and temperature profiles may be written as

$$\nabla^2 t = c_1 u/\alpha \quad [1]$$

$$\nabla^2 u = c_2/\mu \quad [2]$$

with the boundary conditions

$$u_s = 0$$

$$t_s = t_0 + c_1 z$$

where t_0 is the wall temperature at $z = 0$ and subscript s denotes conditions at the wall.

Defining $\theta = t - (t_0 + c_1 z)$, Equation [1] and the corresponding boundary condition become

$$\nabla^2 \theta = c_1 u/\alpha \quad [3]$$

and

$$\theta_s = 0$$

While it is generally recognized that Equation [2] can be solved for usually encountered cross sections by using analogous solutions of torsional problems, the solution of Equation [1] or [3] has been considered difficult. However, when Equations [2] and [3] are combined giving

$$\nabla^2(\nabla^2\theta) = \nabla^2(c_1 u/\alpha)$$

or

$$\nabla^4 \theta = c_1 c_2/\mu\alpha \quad [4]$$

one notes that c_1, c_2, α, and μ are all constant, being independent of x and y, and that Equation [4] shows a striking similarity to the well-known Lagrange's equation in the small-deflection theory of thin plates subjected to a uniform load. The Lagrange equation reads

$$\nabla^4 w = q_0/D \quad [5]$$

Solutions of Equation [5] are too numerous to mention here. Now if the boundary conditions which must be satisfied by Equation [4] are also to be satisfied by Equation [5], then the solutions of Equations [4] and [5] are identical. The boundary conditions for Equation [4] may be stated as

$$\theta_s = 0$$

$$(\nabla^2\theta)_s = 0$$

The first states that the fluid must attain the wall temperature which is $t_0 + c_1 z$ and hence $\theta = t - (t_0 + c_1 z) = 0$; and the second condition comes from Equation [3] which states that the velocity

$$u = \frac{\alpha}{c_1} \nabla^2 \theta$$

must be zero. Thus a solution of Equation [4] satisfying the conditions just described must be the solution of Equations [2] and [3] since then the velocity u may be obtained by means of Equation [3].

Equations [4] and [5] can be made identical if w is replaced by θ and q_0/D by $c_1 c_2/\alpha\mu$. The corresponding boundary conditions for Equation [5] are

$$w_s = 0$$

and

$$(\nabla^2 w)_s = 0$$

These boundary conditions mean that the deflection w must be zero at the supported edges and that the plate must be simply supported for a plate of a polygonal shape.[5]

Thus the solution of Equation [5] may be transformed into that of Equation [4] by the foregoing substitutions. It must be cautioned, however, that the direct substitutions as stated may not lead to a correct solution of Equation [4] when the cross section contains curves, even when the boundaries of the corresponding thin plate are simply supported[5] and consequently adjustments of the integration constants are necessary so that the boundary condition of $(\nabla^2\theta)_s = 0$ is satisfied. The resultant expression, however, does not represent a solution for the deflection of any actual thin plate. An example [4] is shown indicating this fact.

Examples

Rectangular Cross Section. Consider the flow cross section as shown in Fig. 1. The solution of Equation [5] for a corresponding plate is of the standard form[6]

$$w = \frac{16 q_0}{\pi^6 D} \sum_{m=1,3,5\cdots}^{\infty} \sum_{n=1,3,5\cdots}^{\infty} \frac{\sin\frac{m\pi x}{a} \sin\frac{n\pi y}{b}}{mn\left(\frac{m^2}{a^2} + \frac{n^2}{b^2}\right)^2} \quad [6]$$

[4] Reference (3), p. 622.

[5] Reference (5), p. 100.

[6] Ibid., p. 118.

Substituting $c_1c_2/\mu\alpha$ for q_0/D and θ for w, the corresponding solution for θ is therefore

$$\theta = \frac{16c_1c_2}{\pi^6\alpha\mu}\sum_{m=1,3,5\cdots}^{\infty}\sum_{n=1,3,5\cdots}^{\infty}\frac{\sin\frac{m\pi x}{a}\sin\frac{n\pi y}{b}}{mn\left(\frac{m^2}{a^2}+\frac{n^2}{b^2}\right)^2} \quad \ldots\ldots [7]$$

Expression [7] for θ evidently satisfies the condition of $\theta_s = 0$ when $x = 0, a$ and $y = 0, b$.

The velocity u is then given by

$$u = \frac{\alpha}{c_1}\nabla^2\theta = -\frac{16c_2}{\pi^4\mu}\sum_{m=1,3,5\cdots}^{\infty}\sum_{n=1,3,5\cdots}^{\infty}\frac{\sin\frac{m\pi x}{a}\sin\frac{n\pi y}{b}}{mn\left(\frac{m^2}{a^2}+\frac{n^2}{b^2}\right)} \quad \ldots [8]$$

It will be noted that u also satisfies the condition of $u_s = (\nabla^2\theta)_s = 0$ at $x = 0, a$ and $y = 0, b$. Furthermore, u as represented by

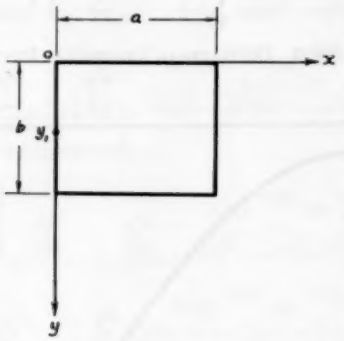

FIG. 1 RECTANGULAR DUCT

Equation [8] will satisfy Equation [2] since Equation [7] satisfies Equation [5].

Equations [7] and [8] are sufficient to determine the limiting Nusselt number. By definition, the Nusselt number is

$$\mathrm{Nu}_{\lim} = hD_e/k \quad \ldots\ldots [9]$$

where the heat-transfer coefficient h is defined as

$$h = q/S(t_s - t_m) \quad \ldots\ldots [10]$$

The heat-transfer rate q and the mixed mean temperature t_m are evaluated by the following integrals

$$q = c\rho\int\int_A u\frac{\partial t}{\partial z}\,dx\,dy \quad \ldots\ldots [11]$$

$$t_m = \left[\int\int_A ut\,dx\,dy\right]\Big/\left[\int\int_A u\,dx\,dy\right] \quad \ldots\ldots [12]$$

or

$$t_m - t_s = \left[\int\int_A u\theta\,dx\,dy\right]\Big/\left[\int\int_A u\,dx\,dy\right] \quad \ldots [13]$$

Hence the expression for the Nusselt number may be written as

$$\mathrm{Nu}_{\lim} = -\left(\frac{D_e}{S}\right)\left(\frac{c\rho}{k}\right)c_1\left[\int\int_A u\,dx\,dy\right]^2\Big/\left[\int\int_A u\theta\,dx\,dy\right] \quad \ldots\ldots [14]$$

Equation [14] is a general expression and is applicable to any cross section. With θ and u expressed by Equations [7] and [8], respectively, and for a rectangular cross section

$$D_e = 2ab/(a+b)$$
$$S = 2(a+b) \quad \ldots\ldots [15]$$

the limiting Nusselt number obtained by performing the integrations shown in Equation [14] over the entire cross section becomes

$$\mathrm{Nu}_{\lim} = \frac{64}{(1+\gamma)^2\pi^2}\frac{\left[\sum_{m=1,3,5\cdots}^{\infty}\sum_{n=1,3,5\cdots}^{\infty}\frac{1}{m^2n^2(m^2+n^2\gamma^2)}\right]^2}{\left[\sum_{m=1,3,5\cdots}^{\infty}\sum_{n=1,3,5\cdots}^{\infty}\frac{1}{m^2n^2(m^2+n^2\gamma^2)^3}\right]} \quad \ldots\ldots [16]$$

The series converge quite rapidly and a few terms are sufficient for an approximation.

Equation [16] is a general formula and can be applied for any aspect ratios. For instance, if $\gamma = 0$, which corresponds to the case of a gap, the limiting Nusselt number is

$$\mathrm{Nu}_{\lim} = \frac{64}{\pi^2}\frac{\left[\sum_{n=1,3,5\cdots}^{\infty}\left(\sum_{m=1,3,5\cdots}^{\infty}\frac{1}{m^4}\right)\frac{1}{n^2}\right]^2}{\left[\sum_{m=1,3,5\cdots}^{\infty}\left(\sum_{n=1,3,5\cdots}^{\infty}\frac{1}{n^2}\right)\frac{1}{m^8}\right]}$$

since

$$\sum_{m=1,3,5\cdots}^{\infty}\frac{1}{m^2} = \frac{\pi^2}{8}$$

and

$$\sum_{m=1,3,5\cdots}^{\infty}\frac{1}{m^4} = \frac{\pi^4}{96}$$

The limiting Nusselt number is then

$$\mathrm{Nu}_{\lim} = \frac{64}{\pi^2}\left(\frac{\pi^2}{8}\frac{\pi^4}{96}\right)^2\Big/\left[\frac{\pi^2}{8}\sum_{m=1,3,5\cdots}^{\infty}\frac{1}{m^8}\right]$$
$$= \frac{\pi^8}{12\times 96}\left[1+\frac{1}{3^8}+\frac{1}{5^8}+\ldots.\right]^{-1} = 8.21$$

For $\gamma = 1$, and 2, the Nusselt numbers are 3.60, and 4.125, respectively. When these values were compared with those reported in (2), surprisingly good agreement is observed owing to the care and the small net employed in the finite-difference method.

Equation [7] also may be used to determine the peripheral variation of the heat-transfer coefficient h, by a mere process of differentiation to calculate the local temperature gradient. Because of symmetry, for $\gamma = 1$, only one eighth (0 to y_1, Fig. 1) of the periphery needs to be dealt with. The temperature gradient along the boundary $x = 0$ is obtained by differentiating θ in Equation [7] with respect to x and then setting $x = 0$

$$\left(\frac{\partial\theta}{\partial x}\right)_{x=0} = \frac{16c_1c_2}{\pi^5\mu\alpha}a^2\sum_{m=1,3,5\cdots}^{\infty}\sum_{n=1,3,5\cdots}^{\infty}\frac{\sin\frac{n\pi y}{b}}{n(m^2+n^2)^2} \quad \ldots [17]$$

To determine the average temperature gradient $(\partial\theta/\partial x)_{x=0,\,\mathrm{avg}}$ Equation [17] is integrated from 0 to y_1 and divided by $b/2$ or $a/2$. The result is

$$\left(\frac{\partial\theta}{\partial x}\right)_{x=0,\text{avg}} = \frac{32c_1c_2}{\pi^4\mu\alpha}\, a^3 \sum_{m=1,3,5\cdots}^{\infty} \sum_{n=1,3,5\cdots}^{\infty} \frac{1}{n^2(m^2+n^2)^2} \quad [18]$$

The ratio of local-to-average heat-transfer coefficient is then given by

$$h_{\text{local}}/h_{\text{avg}} = \left(\frac{\partial\theta}{\partial x}\right)_{x=0,y} \Bigg/ \left(\frac{\partial\theta}{\partial x}\right)_{x=0,\text{avg}}$$

$$= \frac{\pi}{2} \frac{\sum_{m=1,3,5\cdots}^{\infty} \sum_{n=1,3,5\cdots}^{\infty} \frac{\sin\frac{n\pi y}{b}}{n(m^2+n^2)^2}}{\sum_{m=1,3,5\cdots}^{\infty} \sum_{n=1,3,5\cdots}^{\infty} \frac{1}{n^2(m^2+n^2)^2}} \quad [19]$$

From Equation [19], the values of $h_{\text{local}}/h_{\text{avg}}$ are computed for various points between 0 and y_1. The values are tabulated in Table 1 and also shown graphically in Fig. 2.

TABLE 1 VARIATION OF LOCAL-TO-AVERAGE HEAT-TRANSFER COEFFICIENT FROM 0 TO y_1 (FIG. 1) FOR A SQUARE CROSS SECTION

(y/b)	$(h_{\text{local}}/h_{\text{avg}})$
1/12	0.427
1/6	0.809
1/4	1.121
1/3	1.350
2/5	1.481
1/2	1.535

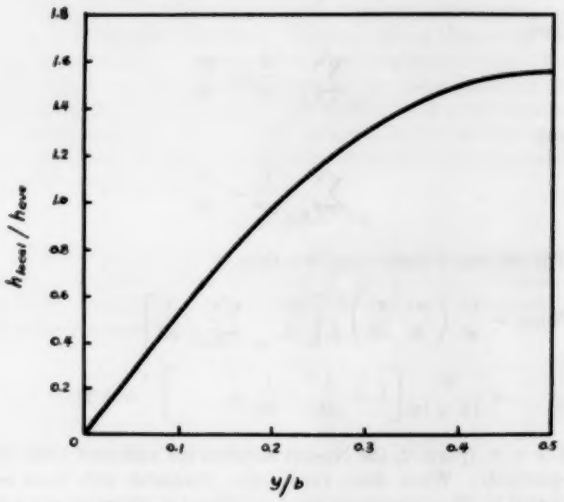

FIG. 2 HEAT-TRANSFER DISTRIBUTION IN A SQUARE DUCT

Equilateral Triangular Cross Section (Fig. 3). The solution of Equation [5] for a plate of this shape and satisfying the boundary conditions of $w_s = 0$ and $(\nabla^2 w)_s = 0$ is[7]

$$w = \frac{q_0}{64aD}\left[x^3 - 3xy^2 - a(x^2+y^2) + \frac{4}{27}a^3\right]\left[\frac{4}{9}a^2 - x^2 - y^2\right] \quad [20]$$

With the substitutions mentioned previously, the corresponding solutions of Equations [4] and [3] are

$$\theta = \frac{c_1c_2}{64a\alpha\mu}\left[x^3 - 3xy^2 - a(x^2+y^2) + \frac{4}{27}a^3\right]\left[\frac{4}{9}a^2 - x^2 - y^2\right] \quad [21]$$

[7] Reference (5), p. 293.

and

$$u = -\frac{c_2}{4a\mu}\left[x^3 - 3xy^2 - a(x^2+y^2) + \frac{4}{27}a^3\right] \quad [22]$$

From Equation [21] a simple expression for the variation of the local heat-transfer coefficient can be obtained in a manner similar to that for a rectangular cross section. Thus the temperature

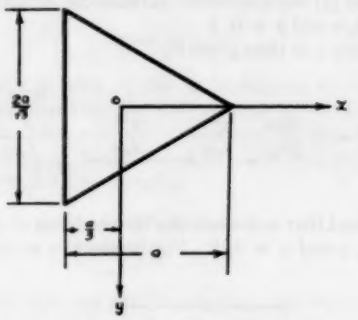

FIG. 3 EQUILATERAL TRIANGULAR DUCT

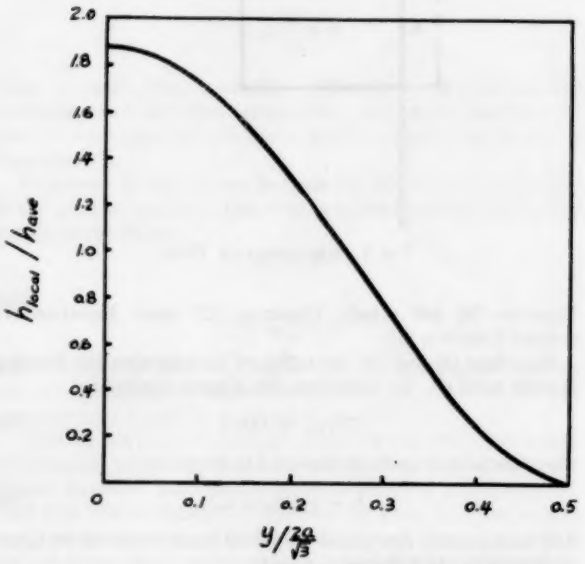

FIG 4 HEAT-TRANSFER DISTRIBUTION IN AN EQUILATERAL TRIANGULAR DUCT

gradients $(\partial\theta/\partial x)_{x=-a/3}$, for one sixth of the periphery, define the entire periphery

$$\frac{h_{\text{local}}}{h_{\text{avg}}} = \frac{\left(\frac{\partial\theta}{\partial x}\right)_{x=-a/3,y}}{\left(\frac{\partial\theta}{\partial x}\right)_{x=-a/3,\text{avg}}} = \frac{15}{8}\left[1 - \left(y\Big/\frac{a}{\sqrt{3}}\right)^2\right]^2 \quad [23]$$

This expression is shown in Fig. 4.

Right-Angled Isosceles Triangle (Fig. 5). The solution[8] for θ is

[8] Reference (5) p. 296.

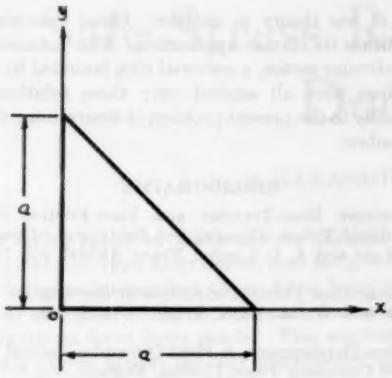

FIG. 5 RIGHT-ANGLED TRIANGULAR DUCT

$$\theta = \left(\frac{16a^4}{\pi^6}\right)\left(\frac{c_1c_2}{\alpha\mu}\right)\left\{\sum_{m=1,3,5\cdots}^{\infty}\sum_{n=2,4,6\cdots}^{\infty}\frac{n\sin\frac{m\pi x}{a}\sin\frac{n\pi y}{a}}{m(n^2-m^2)(m^2+n^2)^2} + \sum_{m=2,4,6\cdots}^{\infty}\sum_{n=1,3,5\cdots}^{\infty}\frac{m\sin\frac{m\pi x}{a}\sin\frac{n\pi y}{a}}{n(m^2-n^2)(m^2+n^2)^2}\right\} \quad [24]$$

The velocity u is consequently

$$u = -\frac{16a^2c_2}{\pi^4\mu}\left\{\sum_{m=1,3,5\cdots}^{\infty}\sum_{n=2,4,6\cdots}^{\infty}\frac{n\sin\frac{m\pi x}{a}\sin\frac{n\pi y}{a}}{m(n^2-m^2)(m^2+n^2)} + \sum_{m=2,4,6\cdots}^{\infty}\sum_{n=1,3,5\cdots}^{\infty}\frac{m\sin\frac{m\pi x}{a}\sin\frac{n\pi y}{a}}{n(m^2-n^2)(m^2+n^2)}\right\} \quad [25]$$

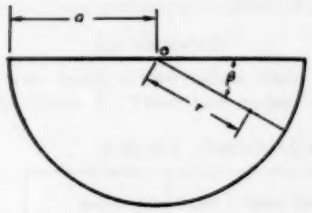

FIG. 6 SEMICIRCULAR DUCT

Semicircular Cross Section (Fig. 6). This example is different from the previous ones in that the boundary contains an arc. The solution of Equation [5] is given in reference (5).[9] As stated before, the application of the solution of Equation [5] is not exactly identical to that of Equation [4], because of different boundary conditions. The solution of Equation [5] is

$$w = \frac{q_0a^4}{D}\sum_{m=1,3,5\cdots}^{\infty}\left\{\frac{4r^4}{a^4}\frac{1}{m\pi(16-m^2)(4-m^2)} + \frac{r^m}{a^m}\frac{m+5+\nu}{m\pi(16-m^2)(2+m)\left[m+\frac{1}{2}(1+\nu)\right]} - \frac{r^{m+2}}{a^{m+2}}\frac{m+3+\nu}{m\pi(4+m)(4-m^2)\left[m+\frac{1}{2}(1+\nu)\right]}\right\}\sin m\beta \quad [26]$$

[9] Reference (5), page 273.

This solution cannot be adapted to that of Equation [4] by the substitutions indicated, since upon substitution, the condition of $(\nabla^2\theta)_r = 0$ is not satisfied. However, when the solution represented by Equation [26] is examined, the boundary condition of zero moment along its curved boundary is

$$\frac{\partial^2 w}{\partial r^2} + \nu\left(\frac{1}{r}\frac{\partial w}{\partial r} + \frac{1}{r^2}\frac{\partial^2 w}{\partial\beta^2}\right) = 0$$

hence, if one sets $\nu = 1$, this boundary condition becomes

$$\nabla^2 w = 0$$

and the corresponding solution of Equation [4] is now

$$\theta = \frac{c_1c_2}{\alpha\mu}a^4\sum_{m=1,3,5\cdots}^{\infty}\left\{\frac{4r^4}{a^4}\frac{1}{m\pi(16-m^2)(4-m^2)} + \frac{r^m}{a^m}\frac{m+6}{m\pi(16-m^2)(2+m)(m+1)} - \frac{r^{m+2}}{a^{m+2}}\frac{1}{m\pi(4-m^2)(m+1)}\right\}\sin m\beta \quad [27]$$

Thus, by using Equation [3], the velocity u is given by

$$u = -\frac{c_2}{\mu}a^4\sum_{m=1,3,5\cdots}^{\infty}\left\{\frac{4r^2}{a^4}\frac{1}{m\pi(4-m^2)} - \frac{4r^m}{a^{m+2}}\frac{1}{m\pi(4-m^2)}\right\}\sin m\beta \quad [28]$$

This expression can be checked by substituting it into Equation [2], resulting in

$$\nabla^2 u = \frac{c_2}{\mu}\sum_{m=1,3,5\cdots}^{\infty}\frac{4}{m\pi}\sin m\beta$$

since

$$\sum_{m=1,3,5\cdots}^{\infty}\frac{4}{m\pi}\sin m\beta = 1$$

the solution is verified.

Circular Cross Section. For a circular plate with radius a, the solution for a simply supported and uniformly loaded plate is [10]

$$w = \frac{q_0}{64D}(a^2-r^2)\left(\frac{5+\nu}{1+\nu}a^2-r^2\right)$$

which satisfies the equation

$$\nabla^4 w = q_0/D \quad [5]$$

Converting the solution to that for θ

$$\theta = \frac{c_1c_2}{64\mu\alpha}(a^2-r^2)\left(\frac{5+\nu}{1+\nu}a^2-r^2\right) \quad [29]$$

This solution must satisfy the condition of

(a) $\theta = 0$ at $r = a$

(b) $\nabla^2\theta = 0$ at $r = a$

The first condition is already satisfied; the latter is not but can be made so by writing

$$\nabla^2\theta = 16r^2 - 4a^2 - 4\left(\frac{5+\nu}{1+\nu}\right)a^2 = 0$$

[10] Reference (5), equation [67], p. 62.

at $r = a$, or

$$12 - 4\left(\frac{5+\nu}{1+\nu}\right) = 0$$

or

$$\nu = 1$$

hence

$$\theta = \frac{c_1 c_2}{64\alpha\mu}(a^2 - r^2)(3a^2 - r^2) \quad \ldots\ldots\ldots\ldots [30]$$

The velocity u is then, by Equation [3]

$$u = \frac{c_2}{4\mu}(r^2 - a^2)$$

The expression for θ is identical to that given in reference (3).[11]

The foregoing examples were shown here to indicate the direct correlation of one theory to another. Other examples may be cited to indicate its further application. For instance, the solutions for a circular sector, a sectorial ring bounded by two radii, and an ellipse were all worked out; these solutions may be adapted readily to the present problem of determining the limiting Nusselt numbers.

[11] Reference (5), page 622.

BIBLIOGRAPHY

1 "Convective Heat-Transfer and Flow-Friction Behavior of Small Cylindrical Tubes—Circular and Rectangular Cross Section," by W. M. Kays and A. L. London, Trans. ASME, vol. 74, 1952, pp. 1179–1189.

2 "Laminar-Flow Forced Convection in Rectangular Tubes," by S. H. Clark and W. M. Kays, Trans. ASME, vol. 75, 1953, pp. 859–866.

3 "Modern Developments in Fluid Dynamics," edited by S. Goldstein, Oxford University Press, London, England, vol. 2, 1938, p. 622.

4 "Heat Transfer," by Max Jakob, John Wiley & Sons, Inc., New York, N. Y., 1949, p. 464.

5 "Theory of Plates and Shells," by S. Timoshenko, McGraw-Hill Book Company, Inc., New York, N. Y., 1940.

Safe Stress Range for Deformation Due to Fatigue

By M. KAWAMOTO[1] and K. NISHIOKA,[2] KYOTO, JAPAN

The safe stress range of materials for fatigue is determined from both fatigue destruction and fatigue deformation. On fatigue destruction there have been many investigations, hitherto, while on fatigue deformation only a few investigations have been made. The authors believe that the safe stress range, usually considered for fatigue deformation, is incorrect for some materials and discuss this matter as it was presented in their experiments.

Introduction

DESIGNERS must always use the diagram as shown in Fig. 1(*a* or *b*), which gives the safe stress range of materials for fatigue. There is no doubt that the fatigue limit *A-B-T* in the diagram can be determined by endurance tests. But how is the yield limit *R-B-S* in the diagram to be determined? Usually the yield limit in the diagram has been determined as the maximum stress (mean stress + stress amplitude) to be equal to the static yield limit; that is, *R-B-S* in Fig. 1(*a*) is drawn as the straight line parallel to the abscissa, or that in Fig. 1(*b*) is inclined at 45 deg to the co-ordinate axis.

The foregoing method for determining the yield limit *R-B-S* is based upon the supposition that the yield limit under alternating stress is always equal to that under static stress. But this supposition is incorrect as shown in our experiments. The relation is quite similar for elastic limit. Then we attempted to obtain the true yield limit and the true elastic limit for fatigue from experiments and to derive the experimental formulas of them.

Experiments

Experiments were made on two carbon steels and two spring steels shown in Table 1. These two carbon steels and the spring steel SUP4 were applied to repeated torsion tests, and the spring steel SUP3 was exposed to repeated bending tests (plane bending).

The forms and dimensions of specimens are shown in Fig. 2. Testing machines, used for these tests, were driven at 2000–2600 rpm and stopped at some intervals to measure the deformation of specimens. Measurements were made statically by the optical-lever method with the mirrors attached at both ends of gage length. Of course, if stress is reversed completely as in case C of Fig. 3, no permanent deformation occurs, so for the experiments in this paper the stress applied is always the pulsating one as in cases A and B of the same figure. Also, it must be noted that the stresses in this paper are always nominal values which are calculated by considering the materials as perfectly elastic. Therefore those stresses beyond the elastic limit have no physical meaning, but they have practical meaning in actual machine design.

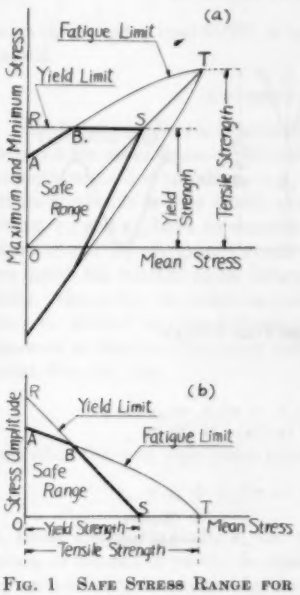

Fig. 1 Safe Stress Range for Fatigue

The relation between deformation of specimens and number of stress repetitions is shown, as an example, in Fig. 4 for the mild steel 5637 under pulsating torsional stress of $\tau_m = \tau_a$. As seen in the figure, increasing rate of fatigue deformation is very large at the beginning of stress repetitions and it decreases gradually. When the applied stress is less than the fatigue limit, deformation finally becomes constant, and when it is larger than the fatigue limit, deformation increases steadily until destruction.

In Fig. 4, when the applied stress is larger, the increase of

TABLE 1 CHEMICAL COMPOSITION AND HEAT-TREATMENT OF MATERIALS

Material	Mark	Heat Treatment	Chemical Composition, per cent						
			C	Mn	Si	S	P	Cu	Cr
Carbon Steel	5637	As received	0.10	0.62	0.16	0.040	0.044	—	—
	2245	Oil quenched from 820-840°C, tempered at 550°C	0.61	0.61	0.25	0.026	0.044	—	—
Spring Steel	SUP3	Oil quenched from 850°C, tempered at 475°C	0.85	0.47	0.33	0.015	0.022	0.20	0.32
	SUP4	Ditto	1.03	0.51	0.32	0.046	0.040	0.19	0.23

[1] Professor of Mechanical Engineering, Kyoto University.
[2] Graduate Student, Kyoto University.

Contributed by the Machine Design Division and presented at the Semi-Annual Meeting, Pittsburgh, Pa., June 20–24, 1954, of The American Society of Mechanical Engineers.

Note: Statements and opinions advanced in papers are to be understood as individual expressions of their authors and not those of the Society. Manuscript received at ASME Headquarters, March 31, 1953. Paper No. 54—SA-10.

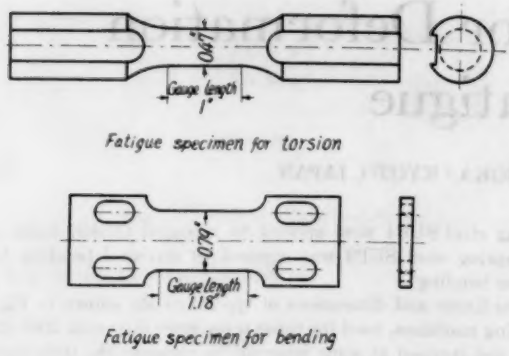

FIG. 2 FATIGUE SPECIMENS

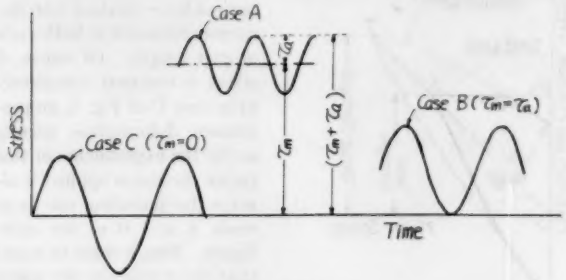

FIG. 3 STRESS-TIME CYCLES

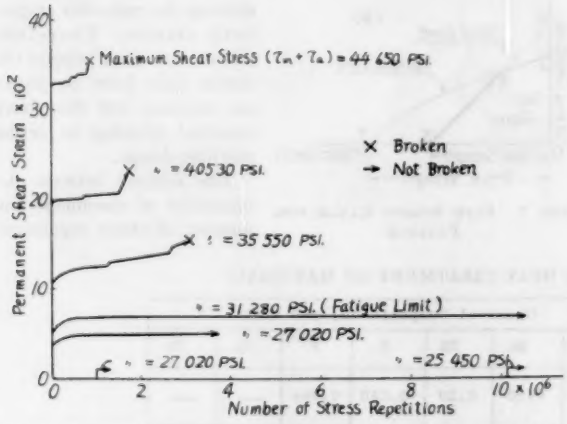

FIG. 4 FATIGUE DEFORMATION OF MILD STEEL 5637 AT REPEATED TORSION TESTS

deformation is somewhat stepwise, but this is a special characteristic of mild steel; that is, in hard steel and spring steel, deformation always increased smoothly.

Fig. 5(*a*) is a stress-strain diagram representing the results of Fig. 4. Here the results of static tests are added for the sake of comparison. For the results of fatigue tests in the figure, the ordinate represents the maximum shear stress (mean stress τ_m + stress amplitude τ_a) and the abscissa represents the shear strain of broken specimens at the time just before failure or the shear strain of the unbroken specimens after large stress repetitions. Similar results obtained for the hard steel 2245 and the spring steel SUP4 are shown in Figs. 5(*b*) and 5(*c*), respectively.

From these figures we can see that deformation in fatigue tests is greater than that in static tests, even when the maximum

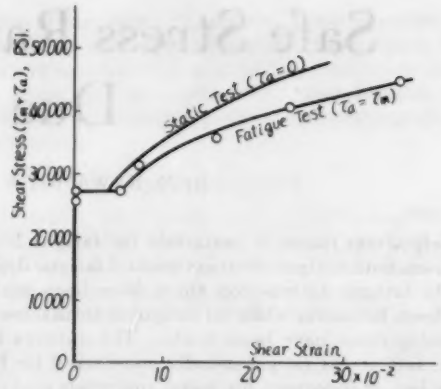

FIG. 5(*a*) STRESS-STRAIN DIAGRAM FOR MILD STEEL 5637 UNDER STATIC AND FATIGUE TORSION TESTS

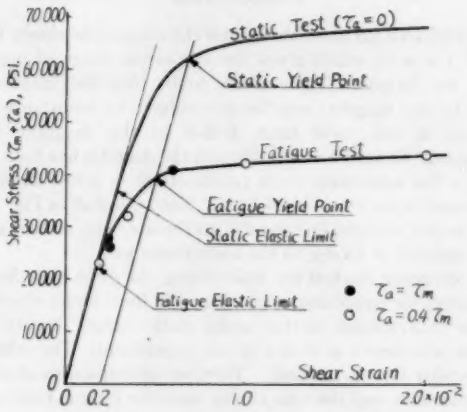

FIG. 5(*b*) STRESS-STRAIN DIAGRAM FOR HARD STEEL 2245 UNDER STATIC AND FATIGUE TORSION TESTS

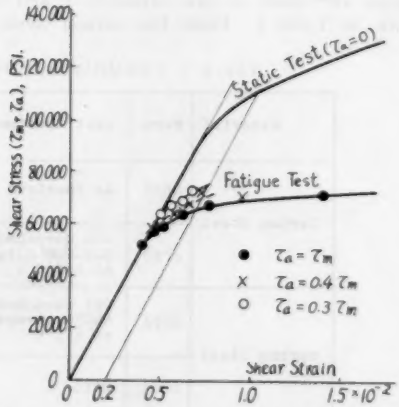

FIG. 5(*c*) STRESS-STRAIN DIAGRAM FOR SPRING STEEL SUP4 UNDER STATIC AND FATIGUE TORSION TESTS

stresses applied in both tests are equal. Then we defined the fatigue elastic limit as the alternating stress under which permanent strain begins to appear. Similarly, we defined the fatigue yield limit as the nominal value of the alternating stress which causes 0.2 per cent permanent strain. Of course the maximum stresses ($\tau_m + \tau_a$) at fatigue elastic limits or fatigue yield limits depend

TABLE 2 VALUES OF $\tau_m + \tau_a$ AT YIELD POINTS AND ELASTIC LIMITS FOR FATIGUE AND STATIC TORSION TESTS

Material			Hard Steel 2245	Spring Steel SUP4
at Yield Point τ_s, PSI.	for Fatigue	when $\tau_a = \tau_m$	39800	64300
		when $\tau_a = 0.4\tau_m$	39800	68500
		when $\tau_a = 0.3\tau_m$	———	73200
	for Static	when $\tau_a = 0$	62900	109500
at Elastic Limit τ_e, PSI.	for Fatigue	when $\tau_a = \tau_m$	22800	54800
		when $\tau_a = 0.4\tau_m$	22800	59700
		when $\tau_a = 0.3\tau_m$	———	62000
	for Static	when $\tau_a = 0$	37000	93900

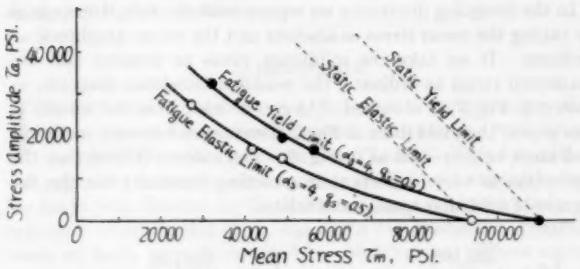

FIG. 6(a) RESULTS ON HARD STEEL 2245

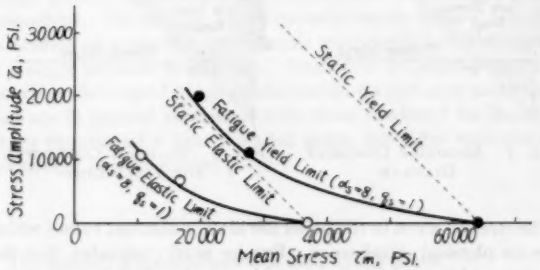

FIG. 6(b) RESULTS ON SPRING STEEL SUP4

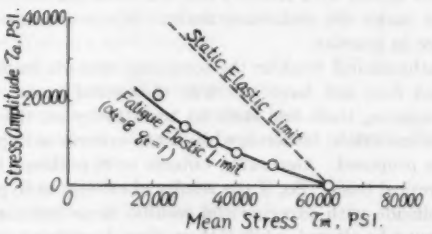

FIG. 6(c) RESULTS ON SPRING STEEL SUP3

on the ratio of τ_a to τ_m. Table 2 shows those values obtained from Figs. 5(*b*) and 5(*c*). For the material with clear yield point, the fatigue yield point coincides with the static yield point as seen in Fig. 5(*a*).

Showing the results of Table 2 in diagrams like Fig. 1(*b*), we obtain Figs. 6(*a*) and 6(*b*). As seen in these figures, the fatigue yield limit or the fatigue elastic limit is very different from the static yield limit or the static elastic limit, which usually has been taken incorrectly as the fatigue yield limit or the fatigue elastic limit. Fig. 6(*c*) shows the similar results for repeated bending tests on the spring steel SUP3, in which only elastic limits are obtained.

CONSIDERATION

Now let us consider the expression which represents the relation between the mean stress σ_m, the stress amplitude σ_a, and the permanent strain due to fatigue ϵ_{fp}. In the special case when the stress amplitude is very small, that is, $\sigma_a = 0$, the relation between σ_m and ϵ_{fp} have to coincide with that between the static stress σ and the permanent strain due to static stress ϵ_p. Then we derive the relation under fatigue tests from that under static tests. Generally, the relations between σ and ϵ_p in static tests may be divided into the following two cases, depending on the presence or absence of the clear yield point: When the clear yield point does not exist

$$\epsilon_p = A_i(\sigma - \sigma_e)^{n_i}, \quad \sigma \geqq \sigma_e \ldots\ldots\ldots\ldots [1]$$

and when the clear yield point exists

$$\epsilon_p = \epsilon_s + A_i'(\sigma - \sigma_s)^{n_i'}, \quad \sigma \geqq \sigma_s \ldots\ldots\ldots [1a]$$

σ_e being the elastic limit, σ_s the yield point, and ϵ_s the plastic strain at the end of yield. In these equations, A_i, n_i, A_i', and n_i' are constants determined by static tests. Applying these relations to the case of fatigue, we substitute $\sigma_m + k_i\sigma_a$ for σ in Equations [1] and [1a], that is

$$\sigma = \sigma_m + k_i\sigma_a \ldots\ldots\ldots\ldots\ldots [2]$$

In Equation [2], if $k_i = 1$, σ becomes equal to $\sigma_m + \sigma_a$; therefore in this case it means that fatigue deformation is determined only by the maximum value of the applied alternating stress. However, the fatigue deformation cannot be considered to depend only on the maximum stress $\sigma_m + \sigma_a$, but it may be considered to be greatly influenced by the stress amplitude σ_a; that is, the deformation under alternating stress perhaps will be larger by the cyclical action of σ_a than the deformation under static stress $\sigma_m + \sigma_a$. Therefore k_i in Equation [1] is considered to be a dimensionless value greater than 1. Further, since the effect of σ_a on fatigue deformation should become greater with the increase of the mean stress σ_m, we put k_i as follows

$$k_i = \alpha_i \left(\frac{\sigma_m}{\sigma_e}\right)^{q_i} \ldots\ldots\ldots\ldots [3]$$

or

$$k_i = \alpha_i' \left(\frac{\sigma_m}{\sigma_s}\right)^{q_i'} \ldots\ldots\ldots\ldots [3a]$$

where α_i, q_i, α_i', and q_i' are constants having dimensionless value, the former, Equation [3], being for materials without a clear yield

point, the latter, Equation [3a], for those with a clear yield point. Applying the relations of Equations [2], [3], and [3a] into Equations [1] and [1a], the permanent strain due to fatigue ϵ_{fp} can be obtained as follows

$$\epsilon_{fp} = A_t \left[\sigma_m + \alpha_t \left(\frac{\sigma_m}{\sigma_e} \right)^{q_t} \sigma_a - \sigma_s \right]^{n_t} \quad \ldots\ldots [4]$$

or

$$\epsilon_{fp} = \epsilon_s + A_t' \left[\sigma_m + \alpha_t' \left(\frac{\sigma_m}{\sigma_s} \right)^{q_t'} \sigma_a - \sigma_s \right]^{n_t'} \quad \ldots [4a]$$

In these equations, the constants α_t, q_t, α_t', and q_t' should be determined from fatigue tests, while A_t, n_t, A_t', and n_t' from static tests as mentioned previously. As known from the foregoing experimental results, the permanent strain resulting from fatigue cannot be observed in the material with a clear yield point when the maximum stress $\sigma_m + \sigma_a$ is less than σ_s. Therefore Equation [4a] is applicable under the condition of $\sigma_m + \sigma_a > \sigma_s$. In the materials without clear yield points, however, Equation [4] is applicable even when $\sigma_m + \sigma_a < \sigma_s$. Then, putting $\epsilon_{fp} = 0$ in Equation [4], the condition under which fatigue deformation begins to appear is obtained as follows

$$\sigma_m + \alpha_t \left(\frac{\sigma_m}{\sigma_e} \right)^{q_t} \sigma_a - \sigma_s = 0 \quad \ldots\ldots [5]$$

If the permanent strain due to fatigue ϵ_{fp} of Equation [4] is equal to the static permanent strain ϵ_p of Equation [1] at the yield point σ_s, the following relation can be obtained

$$\sigma_m + \alpha_t \left(\frac{\sigma_m}{\sigma_s} \right)^{q_t} \sigma_a - \sigma_s = 0 \quad \ldots\ldots [6]$$

Similarly, to Equations [4], [5], and [6] we can obtain the relations between the mean shear stress τ_m, the shear-stress amplitude τ_a, and the permanent shear strain due to fatigue γ_{fp}; that is

$$\gamma_{fp} = A_s \left\{ \tau_m + \alpha_s \left(\frac{\tau_m}{\tau_e} \right)^{q_s} \tau_a - \tau_s \right\}^{n_s} \quad \ldots\ldots [7]$$

$$\tau_m + \alpha_s \left(\frac{\tau_m}{\tau_e} \right)^{q_s} \tau_a - \tau_s = 0 \quad \ldots\ldots [8]$$

$$\tau_m + \alpha_s \left(\frac{\tau_m}{\tau_s} \right)^{q_s} \tau_a - \tau_s = 0 \quad \ldots\ldots [9]$$

where constants A_s and n_s are determined by static torsion tests and constants α_s and q_s from fatigue torsion tests.

The curves shown in Figs. 6 (a, b, c) are drawn from calculation by Equations [5], [6], [8], and [9], taking the values of constants α_t, q_t or α_s, q_s as shown in those figures. We can see that the results of calculation are in good agreement with the results of experiments, and the values of constants for the carbon steel are twice as large as those for the spring steels. Thus the foregoing constants are proved to be appropriate to express the safe stress range for fatigue deformation.

Conclusion

In materials with clear yield points the fatigue yield points coincide with the static yield points, while in materials without clear yield points, the fatigue yield points or fatigue elastic limits are lower than those in static tests. Therefore, in the latter case, the safe stress range for fatigue deformation must be smaller than that usually accepted and it can be represented by the constants proposed by the authors.

References

1 "Yielding of Carbon Steel Specimens Subjected to Repeated Tensile Stresses," by A. Ono, Transactions of the Japan Society of Mechanical Engineers, vol. 2, 1936, p. 457.

2 "The Elastic Limits of Iron and Steel Under Cyclical Variations of Stress," by L. Barstow, Royal Society of London, England, Philosophical Transactions, series A, vol. 210, 1910, p. 35.

3 "On the Fatigue Deformation of Metals," by M. Itihara and Y. Ishihara, *Nippon Kinzoku Gakkai-Si*, vol. 6, 1942, p. 405.

Appendix

In the foregoing discussion we represented the safe stress range by taking the mean stress as abscissa and the stress amplitude as ordinate. If we take the minimum stress as abscissa and the maximum stress as ordinate, the modified Goodman diagram, as shown in Fig. 7, is obtained. As can be seen from the results of this paper, the yield limit in Fig. 7 is erroneous for some materials and must be corrected as in Fig. 8. The authors believe that the correction is very important in practice, especially for the designers of vehicular springs and others.

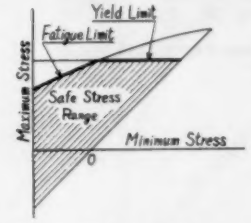

Fig. 7 Modified Goodman Diagram

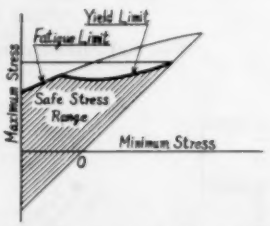

Fig. 8 Diagram Corrected for Yield Limit

The stresses given in the paper are always nominal values which have no physical significance. But we must remember that the stresses used in every fatigue problem on bending or torsion are always nominal values, because stress-strain diagrams at fatigue tests do not accord with Hooke's law, but show elastic hysteresis loops even under the endurance limits. Nominal stresses have significance in practice.

The mathematical work in the foregoing study is empirical in nature and does not have the true theoretical basis. In the authors' opinion, there has been no true theory on the fatigue strength of materials, hitherto, while many criteria or hypotheses have been proposed. Generally, criteria or hypotheses have no true theoretical basis. So, if the results of criteria or hypotheses do not coincide with experimental results, those criteria or hypotheses must be altered, while if they coincide with experimental results, they are justified and useful in practice.

In the paper the authors have obtained a new fatigue elastic limit or new fatigue yield limit from experiments. The mathematical procedure is a criterion to obtain the expressions for the fatigue elastic limit and the fatigue yield limit. Then the expressions obtained have no true theoretical basis and are empirical in nature but they must be useful in practical machine design.

Dynamic Loads on Spur and Helical-Gear Teeth

By J. B. RESWICK,[1] CAMBRIDGE, MASS.

A simple model gives physical insight into the dynamic behavior of gears. Relationships developed from consideration of this model indicate that design criteria are significantly different in heavily loaded gears from those which are very lightly loaded. Results show that dynamic loads may be ignored in many heavily loaded gears, but that dynamic loads provide an important basis for the design of lightly loaded gears.

Introduction

In 1931 the ASME Special Research Committee on the Strength of Gear Teeth issued a Research Publication entitled "Dynamic Loads on Gear Teeth." This committee was organized under the chairmanship of Wilfred Lewis and after his death was directed by Earle Buckingham. After a study of extensive experimental data, equations for predicting dynamic loads on teeth were formulated by Buckingham. These equations are presented in some detail elsewhere.[2] The results of many tests, as well as the general acceptance of his equations for design practice, have laid a substantial basis for Buckingham's relationships. The author, in the material which follows, attempts to develop an expression for dynamic tooth loads based on a study of a single physical mechanism. From first principles, equations have been developed which predict values for dynamic tooth loads that are in general agreement with those predicted by Buckingham's equations for lightly loaded gears, but differ somewhat in the case of heavily loaded gears.

Nomenclature

The following nomenclature is used in the paper:

c = parabolic cam constant; $c = e/d^2$, in.$^{-1}$
D = pitch diameter, in.
d = length of effective parabolic cam, in.
E = Young's modulus, psi
e = effective tooth error . . . $e = (e_m + \delta_t)$, in.
e_m = manufactured tooth error, in.
F = force acting along pressure line, lb
F_W = maximum allowable load along pressure line for infinite wear life, lb
f = face width of gear, in.
i_g = number of teeth on gear
i_p = number of teeth on pinion
J = moment of inertia, in-lb-sec^2
K = wear factor
k = tooth-spring constant, lb/in.
k_a = tooth stiffness in axial plane for helical gearing, lb/in.
k_f = materials coefficient or tooth spring constant per inch of face width, psi
m = effective mass of gears, $1/m = R_p^2/J_p + R_g^2/J_g$, lb-sec^2/in.
m_f = effective mass of gears per inch of face width, lb-sec^2/in.^{2}
n = stress-concentration factor
P = transmitted power, in-lb/sec
P_c = circular pitch, in.
P_d = diametral pitch, in.$^{-1}$
P_{dn} = diametral pitch in normal plane for helical gears, in.$^{-1}$
Q = gear diameter ratio, $\dfrac{2D_g}{D_g + D_p} = \dfrac{2i_g}{i_g + i_p} = \dfrac{2r}{r+1}$
R = gear-pitch radius, in.
R_f = radius of fillet at tooth root, in.
r = speed ratio, $r = D_g/D_p = i_g/i_p = \omega_p/\omega_g$
t = time, sec
T = tangentially applied load, lb
T_B = maximum allowable tangential bending load for infinite life, lb
T_d = total actual tangential load acting on tooth, lb
T_i = dynamic increment load, lb
T_{max} = maximum instantaneous tangential load, lb
T_s = static component of dynamic load, lb
T_t = tangentially applied load at pitch line calculated from transmitted power, lb
T_W = maximum allowable tangential wear load for infinite life, lb
v = pitch-line velocity of engagement of gears, ips
Y = Lewis form factor
z = elastic form factor based on Lewis factor, $z = Y/(0.761 + 7.25\,Y)$
β = frequency ratio, $\beta = \dfrac{v\sqrt{c/e}}{\omega_n}$; $\beta_a = \dfrac{v\sqrt{c/e}}{\omega_{na}}$; $\beta_b = \dfrac{v\sqrt{c/e}}{\omega_{nb}}$
θ = pressure angle, deg
δ = total deflection of a pair of teeth under load, in.
δ_d = total deflection of a pair of teeth under load, T_d, in.
δ_t = total deflection of a pair of teeth under load, T_t, in.
σ_e = flexural endurance limit in reverse bending, psi
ω = angular velocity, sec^{-1}
ω_{nb} = natural frequency of unloaded gear system, $\omega_{nb} = \sqrt{\dfrac{k}{m}}$, sec^{-1}
ω_{na} = natural frequency of loaded gear system, $\omega_{na} = \sqrt{\dfrac{2k}{m}}$, sec^{-1}
ρ = mass density of gear material $\rho = \dfrac{\gamma}{g}$, lb sec^2/in.^{4}
γ = weight density of gear material, lb/in.^{3}

---

[1] Assistant Professor, Department of Mechanical Engineering, Massachusetts Institute of Technology. Mem. ASME.

[2] "Analytical Mechanics of Gears," by E. Buckingham, McGraw-Hill Book Company, Inc., New York, N. Y., 1949.

Contributed by the Machine Design Division and presented at the Semi-Annual Meeting, Pittsburgh, Pa., June 20–24, 1954, of The American Society of Mechanical Engineers.

Note: Statements and opinions advanced in papers are to be understood as individual expressions of their authors and not those of the Society. Manuscript received at ASME Headquarters, March 1, 1954. Paper No. 54—SA-9.

Gear-Tooth Loads

The stresses due to elastic deformation of gear teeth provide the basis for design. In order to evaluate these stresses, the loads producing them must be known. The loading program on a single gear tooth is highly involved and is subject to many factors. The following excerpt from Buckingham[3] gives a good idea of those factors which affect dynamic tooth loads:

"Errors on gear-tooth profiles, caused by elastic deformation under load or by inaccuracies of production, or both, act to change the relative velocities of the mating members. This varying velocity of the rotating members results in a varying load cycle on the teeth of the gears; the amount of this load variation depends largely upon the extent of the effective masses of the revolving gears, the extent of the effective errors, and the speed of the gears."

The tangential force acting at the pitch point which has a moment equal to that determined from the transmitted power is

$$T_t = \frac{P}{\omega_p R_p} = \frac{P}{\omega_g R_g} \quad \ldots\ldots [1]$$

where

P = power, in-lb/sec
R = radius, in.
ω = angular velocity, rad/sec (rps)
T_t = tangential load, lb

Tooth Deflections

The total deflection, Fig. 1, which occurs when a pair of teeth are in contact at the pitch point is composed of bending, shear, and compressive deformations. A complete and useful analytical expression for this deflection has not yet been proposed. Buckingham[4] has suggested an expression, Equation [2], which involves certain of the pertinent parameters and which gives results that agree reasonably well with test data

$$\delta = \frac{T}{f}\left[\frac{E_1 z_1 + E_2 z_2}{E_1 z_1 E_2 z_2}\right] \quad \ldots\ldots [2]$$

$$z = \frac{Y}{0.761 + 7.25Y}$$

where

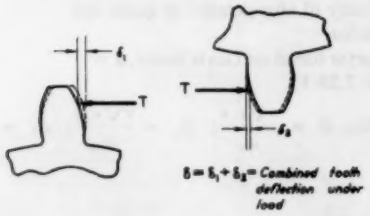

Fig. 1 Tooth Deflection Under Load

δ = total elastic deformation of pair of mating tooth profiles, in.
T = applied tangential load, lb
f = face width, in.
E = modulus of elasticity, psi
Y = Lewis tooth form factor (see Tables 3 and 4)

Equation [2] may be used to define the equivalent tooth-pair spring constant k (lb/in)

$$k = \frac{T}{\delta} = \left[\frac{E_1 z_1 E_2 z_2}{E_1 z_1 + E_1 z_1}\right] f \quad \ldots\ldots [3]$$

Table 1 gives average values of z which may be used for initial calculations; note that variations from average values are less than 10 per cent.

TABLE 1 AVERAGE VALUES OF z

	20-deg full depth form		20-deg stub tooth form		14½-deg involute form	
	Range	Average	Range	Average	Range	Average
z based on contact at end of tooth.....	0.097–0.113	0.103	0.103–0.116	0.108	0.092–0.109	0.100
based on contact at middle of tooth	.....	.115	.....	.118	.....	.118

A materials coefficient or tooth spring constant per inch of face width may be defined from Equation [3]

$$k_f = \frac{k}{f} = \left[\frac{E_1 z_1 E_2 z_2}{E_1 z_1 + E_2 z_2}\right]$$

A useful table of values for k_f may be derived from the average values of z, Table 2.

TABLE 2 VALUES[a] OF k_f, PSI

Materials of gears	$\theta = 14\frac{1}{2}°$	$\theta = 20°$ full depth	$\theta = 20°$ stub teeth
Gray iron and gray iron.....	0.80×10^6	0.83×10^6	0.86×10^6
Gray iron and steel.....	1.10×10^6	1.14×10^6	1.18×10^6
Steel and steel.....	1.60×10^6	1.66×10^6	1.72×10^6

[a] "Gear Tooth Loads," by Earle Buckingham, published by the U. S. Navy, p. 15.

Dynamic Tooth Loads—Simplified Analog

Consider two masses m_1 and m_2, Fig. 2, which are constrained to move in a horizontal direction. They are loaded initially with a force T_t and are held in static equilibrium by contact at tooth ① only. Variables x_1 and x_2 are measured from their static equilibrium positions. Tooth ① is deflected an amount

$$\delta_i = \frac{T_t}{k}$$

where T_t = tangential load due to transmitted power, k = elastic-deformation constant.

A cam ③ with a parabolic contour having zero slope at point

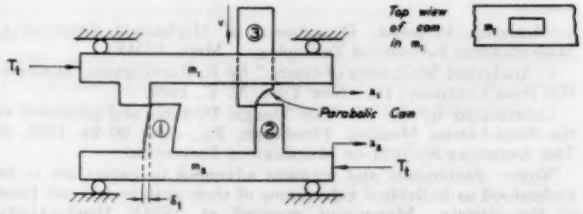

Fig. 2 Basic Mechanism Used to Simulate Gears in Action

[3] See footnote 2, p. 426.
[4] Footnote 2, p. 432

of contact with tooth ② which may slide vertically in mass ① is suddenly given a downward velocity v. The cam quickly takes over all or part of the load depending on δ_i, and the ensuing relative motion of the masses is to be studied.

The analogy of this system with actual gear engagement is as follows: Consider two gears transmitting power at the instant before a tooth engagement occurs. If the contact ratio lies between 1 and 2 (as is common for most spur gears), the load will be carried by two teeth near the pitch point as shown in Fig. 3.

FIG. 3 GEARS AT INSTANT BEFORE TOOTH ENGAGEMENT

Even if the gears are perfect, there will be an initial interference at the tip of the tooth coming into engagement equal to the amount of the deflection of the pair of teeth supporting the load. If, in addition, there is an error in tooth form such that the driving tooth is a little ahead of its theoretical position, the interference will be increased. Thus

$$e = e_m + \delta_i \quad [4]$$

where

e = effective error, in.
e_m = manufactured error,[5] in.
δ_i = transmitted load deflection; $\delta_i = \frac{T_i}{k}$

It may be seen that the full load must be shared by the teeth coming into engagement in an exceedingly short time. The corners of interference actually are worn off during the initial period of operation so that the tooth corners become cams. Since inertia forces are proportional to acceleration, it seems reasonable to assume that high spots which would produce high local stresses would be worn off. The result would tend toward a cam of constant acceleration.

For gears of infinite moment of inertia, it is clear that the engaging teeth would be deflected by the amount of the effective error (manufactured error plus transmitted tooth deflection) and this would comprise the total tooth load. However, the inertias of most gears are small enough so that they are accelerated because of this interference and an involved relative motion results.

The model under study is equipped with a parabolic or constant-acceleration cam which is suddenly moved downward at the pitch-line velocity of engagement v. The rise on this cam is made equal to the effective error e. Thus a disturbance which is analogous to that introduced into the gear during tooth engagement is introduced in the model.

Tooth ② on the model represents the combined elasticity of the two actual gear teeth coming into engagement. At any instant the force acting on the end of tooth ② will be equal to its deflection times its "spring" constant

$$T = k(x - x_2) \quad [5]$$

and the maximum value of load on the tooth will equal the maximum deflection times the spring constant. The motion of the model resulting from the disturbance of tooth engagement will be studied in order to determine the maximum tooth deflection during vibration.

[5] The manufactured error is taken as the amount a perfect rack would move ahead of its theoretical position when driven under no load by a gear having a tooth error.

ANALYSIS OF MODEL

An exact analysis of the basic mechanism for all possible modes of operation is very difficult since the resulting equations are nonlinear due to the fact that at certain times the load is carried by two pairs of teeth (or more, depending on the contact ratio), while at other times only a single pair of teeth may support the load. This is determined mainly by the ratio of δ_i to e_m. Two special cases which essentially bracket the practical range of operation of most gears will be analyzed. The first case is that which represents a heavily loaded gear with small tooth error. Under these conditions the load is carried by two pairs of teeth during tooth engagement. The second case considered is that of a pair of gears operating at very light load. Here only a single pair of teeth will be involved in the tooth engagement.

The following assumptions are made:

1 $\delta_i >> e_m$. This assumption applies to the first case mentioned, i.e., the case of heavily loaded gears with very small manufacturing error.

2 Error is introduced with constant acceleration, Fig. 4.

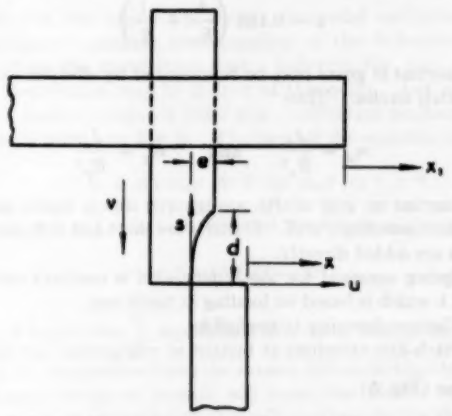

FIG. 4 CONSTANT-ACCELERATION CAM USED TO REPRESENT ACTION OF TOOTH ERROR AT INSTANT OF TOOTH ENGAGEMENT

Equation of cam

$$u = cs^2 \quad [6]$$

when $u = e$, $s = d$ = a constant to be determined from actual gear engagement

$$\therefore c = \frac{e}{d^2} \quad [7]$$

Now

$$\dot{u} = 2cs\dot{s}$$

and

$$\ddot{u} = 2cs\ddot{s} + 2c\dot{s}^2$$

for

v = const (pitch-line velocity of engagement)

$$\dot{s} = v$$

$$\ddot{s} = 0$$

$$\ddot{u} = 2cv^2 = \text{const} \quad [8]$$

The value c has been observed to be a constant for a given size and tooth form of gear. Thus for constant velocity of engagement a greater error will take longer to be introduced. Buckingham[6] has proposed an equation for c which agrees with experimental results. He studies the distance a rack moves when engaged by a tooth having an error. During the time the error is introduced, both rack and gear move a certain distance. However, the rack will move an amount equal to the error e ahead of where it would have been had the gear been perfect. The amount the pitch circle of the gear has moved during this time is taken as the effective cam length d. A study of the geometry gives the following

$$c = \left(\frac{1}{R_p} + \frac{1}{R_g}\right) \frac{\tan\theta\,(1 - \cos\theta)}{\theta^2}$$

where R = radius, in.; θ = pressure angle, radians.

For $\theta = 14.5°$

$$c = 0.129\left(\frac{1}{R_p} + \frac{1}{R_g}\right)$$

For $\theta = 20°$

$$c = 0.183\left(\frac{1}{R_p} + \frac{1}{R_g}\right)$$

3 Inertias of gears may be represented by effective masses at their pitch circles. Thus

$$m_p = \frac{J_p}{R_p^2} \quad \text{and} \quad m_g = \frac{J_g}{R_g^2}$$

4 Inertias on gear shafts are ignored unless shafts and couplings are exceedingly stiff. If shafts are short and stiff, associated inertias are added directly.

5 Spring constant for tooth deflection is constant and equal to that k which is based on loading at tooth end.

6 Viscous damping is negligible.

7 Pitch-line velocities at instant of engagement are equal.

Define (Fig. 5)

$$x_r = x_2 - x_1 \qquad [9]$$

$$x - x_1 = u = c(s^2) = c(v^2t^2) \qquad [10]$$

Isolate rigid bodies, Fig. 6.

Equations of motion

$$T_1 - T_i + kx_r - kx + kx_2 = m_1\ddot{x}_1$$

$$T_i - kx_r - T_i + kx - kx_2 = m_2\ddot{x}_2$$

$$m_1\ddot{x}_1 - 2kx_r = -kcv^2t^2$$

$$m_2\ddot{x}_2 + 2kx_r = +kcv^2t^2$$

Dividing through by m_1 and m_2 and then subtracting upper equation from lower

$$\ddot{x}_r + 2k\left(\frac{1}{m_1} + \frac{1}{m_2}\right)x_r = \left(\frac{1}{m_1} + \frac{1}{m_2}\right)kcv^2t^2$$

Let

$$\frac{1}{m} = \frac{1}{m_1} + \frac{1}{m_2}$$

Then

$$m\ddot{x}_r + 2kx_r = kcv^2t^2 \qquad [11]$$

[6] Footnote 2, pp. 428–430.

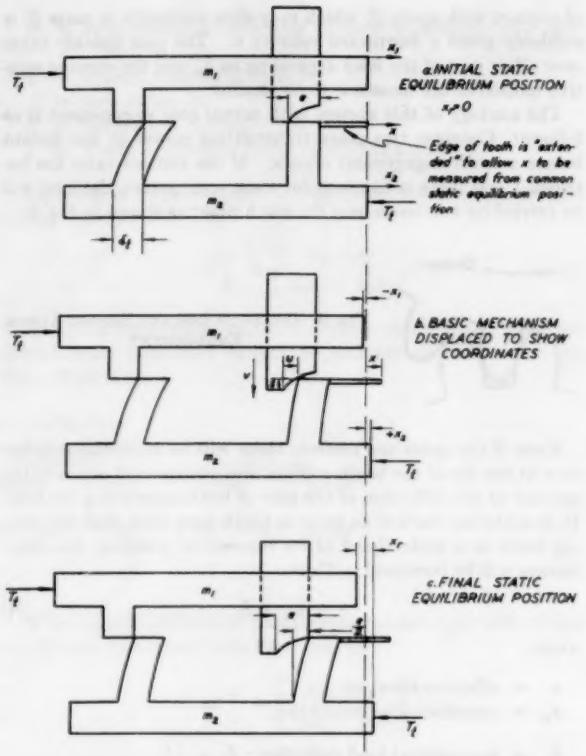

FIG. 5 CO-ORDINATES DEFINED

(a, Initial static equilibrium position at commencement of tooth engagement; b, Basic mechanism displaced to show co-ordinates; c, Final static equilibrium position for motion after tooth engagement is complete.)

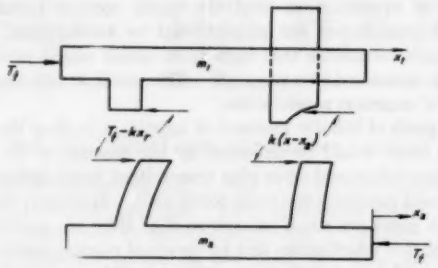

FIG. 6 ISOLATION OF RIGID BODIES

Equation [11] has a solution composed of a transient part (complementary) and a steady-state part (particular)

$$x_r = x_{r1} + x_{r2}$$

The complementary solution is of form

$$x_{r1} = C\cos\omega_{n_2}t$$

where

$$\omega_{n_2} = \sqrt{\frac{2k}{m}}$$

A particular solution of the following form may be assumed

$$x_{r_2} = acv^2t^2 + b$$

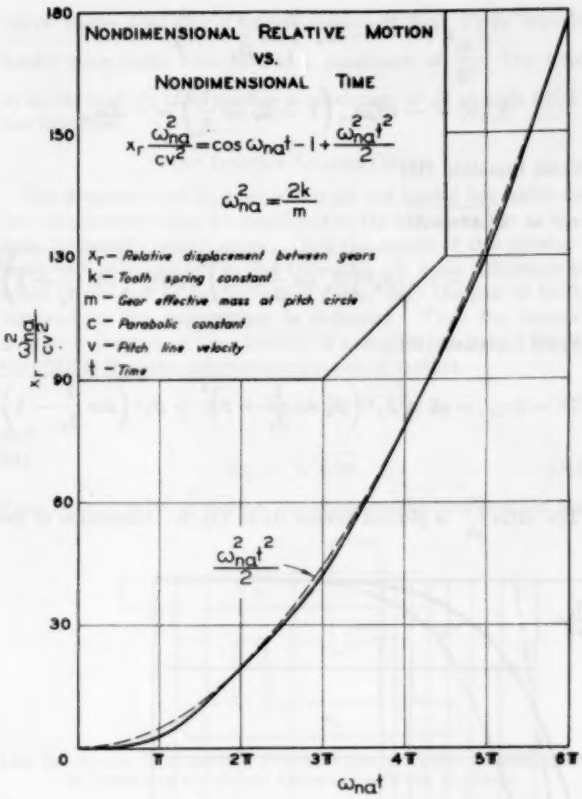

FIG. 7 SOLUTION OF EQUATION [12] IN NONDIMENSIONAL TERMS

Substitution into Equation [11] gives

$$a = 1/2$$

$$b = -\frac{mcv^2}{2k} = -\frac{cv^2}{\omega_{na}^2}$$

The complete (general) solution form is

$$x_r = C \cos \omega_{na} t + \frac{cv^2 t^2}{2} - \frac{cv^2}{\omega_{na}^2}$$

C may be determined from initial conditions

$$x_r = 0 \text{ at } t = 0$$

$$\therefore C = \frac{cv^2}{\omega_{na}^2}$$

The complete solution of Equation [11] is then

$$x_r = \frac{cv^2}{\omega_{na}^2}\left[(\cos \omega_{na} t - 1) + \frac{\omega_{na}^2 t^2}{2}\right] \ldots\ldots [12]$$

A plot of $x_r \Big/ \frac{cv^2}{\omega_{na}^2}$ versus $\omega_{na} t$ appears in Fig. 7. The motion is seen to be a cosine oscillation whose peaks touch a parabola.

After the cam has reached its maximum rise a new mode of vibration results. Referring to Fig. 4, it may be seen that the cam ceases to act after a time t_1

$$t_1 = \frac{d}{v} = \frac{1}{v}\sqrt{\frac{e}{c}} \ldots\ldots [13]$$

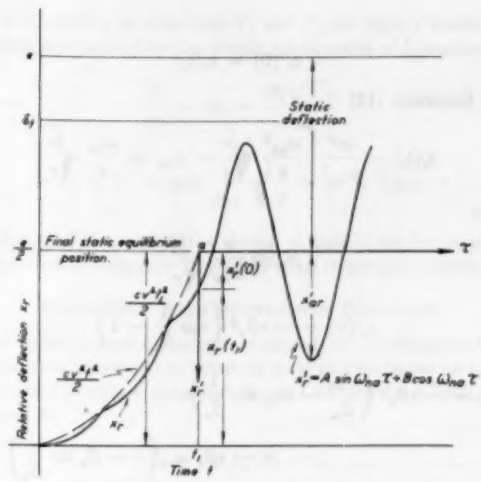

FIG. 8 RELATIVE MOTION OF GEAR MASSES SHOWING TRANSITION FROM TOOTH-ERROR FORCED MOTION TO FREE VIBRATION ABOUT AN EQUILIBRIUM POSITION

At this time the masses will start a sinusoidal oscillation about an equilibrium position corresponding to the deflection of the teeth under the transmitted load. Refer to Fig. 5(c). A new set of co-ordinates may be defined at this point. Let x_r' be the relative motion measured from this equilibrium position. This position is point a on Fig. 8. The form of the equation is

$$x_r' = A \sin \omega_{na} \tau + B \cos \omega_{na} \tau \text{ for } \tau > 0 \ldots\ldots [14]$$

where $\tau = 0$ at $t = t_1$, and the total amplitude x_{ar}' is given by

$$x_{ar}' = \sqrt{A^2 + B^2} \ldots\ldots [15]$$

If x_{ar}' is larger than $\frac{e}{2}$, separation will occur and under the action of the transmitted force the masses will come together again. The kinetic energy on impact will equal the kinetic energy on leaving and the sinusoidal motion will continue during the period of contact. The maximum resulting force will be given by

$$T_d = T_s + T_i = k(x - x_2) = k\left(\frac{e}{2} + x_{ar}'\right) \ldots\ldots [16]$$

whether or not separation occurs. Fig. 5 shows that $x - x_2$ becomes $e/2 + x_{ar}'$, where $e/2$ is the final static equilibrium position for motion after tooth engagement is complete. Also indicated is the fact that results of this analysis for heavily loaded gears will hold for values of e_m from zero to $e_m \leqq \delta_t$.

The term x_{ar}' may be evaluated from initial conditions existing at time $t = t_1$ or $\tau = 0$ (see Fig. 8)

$$x_r'(0) = \frac{cv^2 t_1^2}{2} - x_r(t_1)$$

but

$$t_1 = \frac{1}{v}\sqrt{\frac{e}{c}}$$

and

$$x_r'(0) = \frac{cv^2 t_1^2}{2} - \frac{cv^2}{\omega_{na}^2}\left(\cos \frac{\omega_{na}}{v}\sqrt{\frac{e}{c}} - 1\right) - \frac{cv^2 t_1^2}{2}$$

now

$$\dot{x}_r'(0) = \dot{x}_r(t_1)$$

From Equation [12]

$$\dot{x}_r(t_1) = \frac{cv^2}{\omega_{ns}^2}\left[\frac{\omega_{ns}^2}{v}\sqrt{\frac{e}{c}} - \omega_{ns}\sin\frac{\omega_{ns}}{v}\sqrt{\frac{e}{c}}\right]$$

Define

$$\beta_s \equiv \frac{v}{\omega_{ns}}\sqrt{\frac{c}{e}}$$

$$x_r'(0) = -e\beta_s^2\left(\cos\frac{1}{\beta_s} - 1\right) \quad \ldots\ldots\ldots\ldots [17]$$

$$\dot{x}_r'(0) = -e\beta_s^2\left(\frac{\omega_{ns}}{\beta_s} - \omega_{ns}\sin\frac{1}{\beta_s}\right)$$

$$= -e\beta_s\,\omega_{ns}\left(1 - \beta_s\sin\frac{1}{\beta_s}\right) \quad \ldots [18]$$

Introducing these initial conditions into Equation [14] and its derivative

$$x_r'(0) = -e\beta_s^2\left(\cos\frac{1}{\beta_s} - 1\right) = B$$

$$\dot{x}_r'(0) = -e\beta_s\omega_{ns}\left(1 - \beta_s\sin\frac{1}{\beta_s}\right) = -A\omega_{ns}$$

From Equation [15]

$$x_{ar}' = \sqrt{A^2 + B^2}$$

$$= e\sqrt{\beta_s^2\left(\beta_s\sin\frac{1}{\beta_s} - 1\right)^2 + \beta_s^4\left(\cos\frac{1}{\beta_s} - 1\right)^2}$$

From Equation [16]

$$T_i = kx_{ar}' = ek\sqrt{\beta_s^2\left(\beta_s\sin\frac{1}{\beta_s} - 1\right)^2 + \beta_s^4\left(\cos\frac{1}{\beta_s} - 1\right)^2} \quad \ldots [19]$$

The ratio $\frac{T_i}{ek}$ is plotted versus β in Fig. 9. Inspection of this

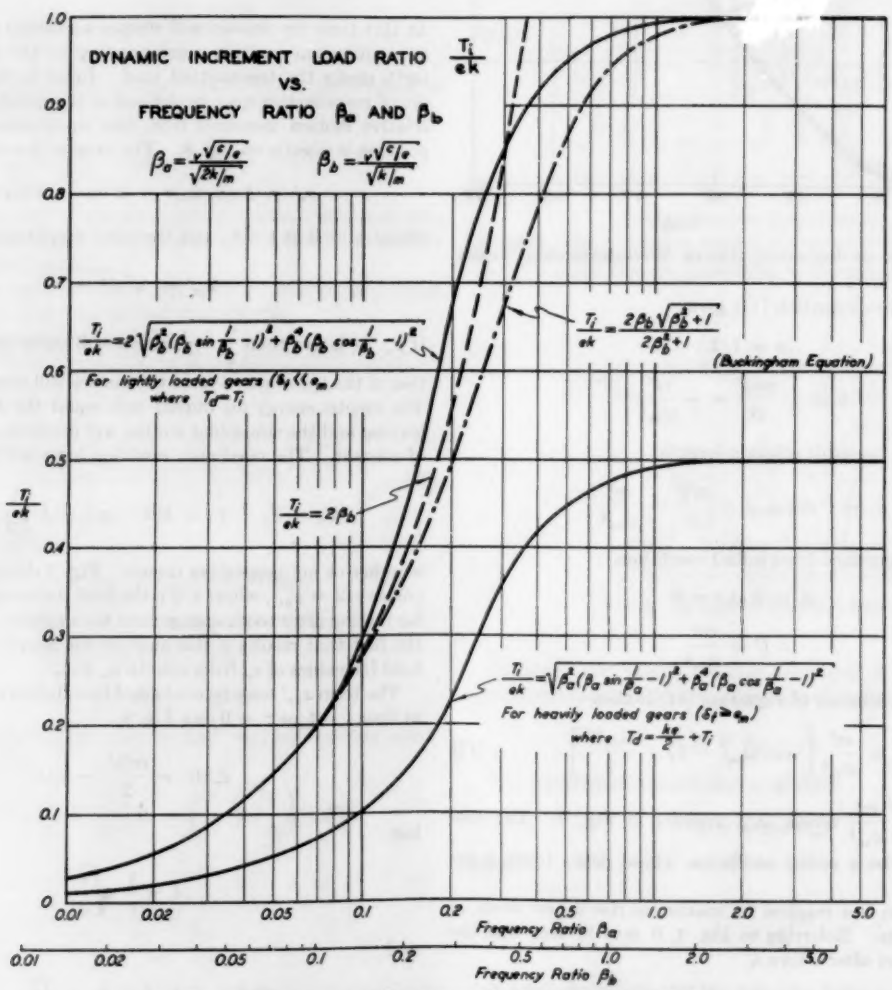

FIG. 9 SOLUTIONS OF EQUATIONS [19], [24], [25], AND [31]
(Load ratio T_i/ek versus ratio of pitch-line velocity to natural frequencies as derived is compared with an approximate form and with Buckingham's formulations.)

figure shows that the dynamic increment load T_i in heavily loaded gears varies from zero to a maximum of $\frac{ek}{2}$. The total dynamic load T_d then reaches a maximum of ek at high pitch-line velocities.

Very Lightly Loaded Gears

The dynamic loads in gears which are not loaded but which do have tooth errors may be developed in the same manner as was done for heavily loaded gears. Only the results of this development will be presented in the following. A basic difference is noted in the case of lightly loaded gears; only the pair of teeth involved in the engagement is deflected. Thus the natural frequency depends on the elasticity of a single tooth pair. Equation [20] is then the differential equation of motion

$$m\ddot{x}_r + kx_r = kcv^2t^2 \quad [20]$$

and

$$\omega_{nb} = \sqrt{k/m} \quad [21]$$

Since no load is being carried, the static equilibrium position for

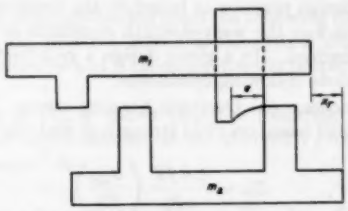

Fig. 10 Static Equilibrium Position After Tooth Engagement Is Complete for Basic Mechanism With No Load

motion after engagement is completed is given by Equation [22] and is illustrated in Fig. 10.

At $t = t_1$

$$x - x_2 = x_r = e \quad \text{st. def.} = e - x_r = 0 \quad [22]$$

The solution of Equation [20] in this case is given by Equation [23]

$$x_r = \frac{2cv^2}{\omega_{nb}^2}\left[(\cos \omega_{nb}t - 1) + \frac{\omega_{nb}^2t^2}{2}\right] \quad [23]$$

and after inserting initial conditions in the equation which corresponds to Equation [15], the dynamic increment load is found to be given by Equation [24]

$$\frac{T_i}{ek} = 2\sqrt{\beta_b^2\left(\beta_b \sin\frac{1}{\beta_b} - 1\right)^2 + \beta_b^4\left(\cos\frac{1}{\beta_b} - 1\right)^2} \quad [24]$$

Since the static deflection is zero

$$T_d = T_i$$

Lightly loaded gears will inevitably separate during dynamic vibration. It is assumed that results obtained when separation is not considered will still be valid since the teeth will strike the backs of neighboring teeth and bounce back (assuming no losses) with the same velocity with which they separated. Thus a sinusoidal motion during contact will resume as if uninterrupted. Fig. 11 is intended to show this situation.

Equation [24] is plotted in Fig. 9. Inspection of this figure shows that the dynamic increment load T_i varies from zero to a maximum of ek. Since the static load is zero in this case, the total dynamic load T_d reaches ek for very high velocities. This is in agreement with intuition.

It is interesting to note that T_i and T_d for lightly loaded gear may be approximated by the simple relationship of Equation [25]

$$\frac{T_i}{ek} = 2\beta_b = \frac{2v\sqrt{c/e}}{\omega_{nb}}$$

$$T_i = T_d = 2ekv\frac{1}{\omega_{nb}}\sqrt{\frac{c}{e}} = 2v\sqrt{kmec} \quad [25]$$

Equation [25] is useful in the design of lightly loaded gears if it is noted that no values of T_d greater than ek are permissible.

Comparison With Buckingham Equations

The dynamic-load equations proposed by Buckingham[3] may be written in terms of the symbols used in this paper as follows (the symbol f with a subscript is used to denote a force, as in footnote 2)

$$T_i = \sqrt{f_a(2f_2 - f_a)} \quad [26]$$

where

$$f_a = \frac{f_1f_2}{f_1 + f_2} \quad [27]$$

$$f_1 = 2cmv^2 \quad [28]$$

$$f_2 = ek \quad [29]$$

The frequency ratio β_b may be defined in terms of f_1 and f_2

$$\beta_b^2 = \frac{f_1}{2f_2} \quad [30]$$

Equation [31] results when Equation [26] is solved in terms of Equation [30]

$$T_i = 2f_2\beta_b\frac{\sqrt{\beta_b^2 + 1}}{2\beta_b^2 + 1}$$

or

$$\frac{T_i}{ek} = 2\beta_b\frac{\sqrt{\beta_b^2 + 1}}{2\beta_b^2 + 1} \quad [31]$$

Equation [31] is plotted in Fig. 9 and shows a significant devia-

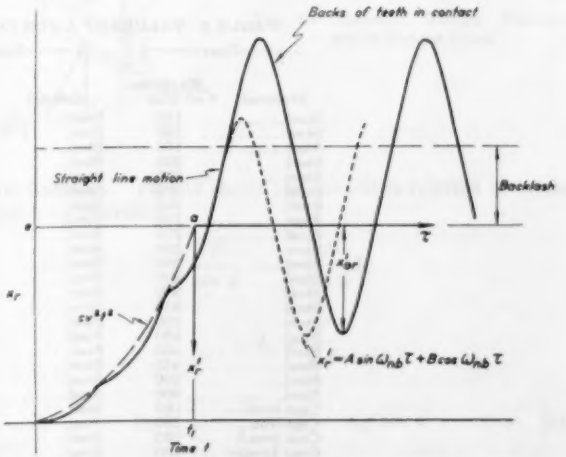

Fig. 11 Relative Motion of Unloaded Gear Masses Showing Motion Across Backlash Region. Sinusoidal Results Based on Initial Conditions at t_1 Are Applicable

TABLE 3[a] VALUES OF Y WITH LOAD AT TIP OF TOOTH

No. of teeth, i	14½°	20° full depth	20° stub	Internal gears: Spur pinion	Internal gears: Internal gear
12	0.211	0.245	0.311	0.327	—
13	0.223	0.261	0.324	0.327	—
14	0.236	0.276	0.339	0.330	—
15	0.245	0.289	0.349	0.330	—
16	0.255	0.295	0.361	0.333	—
17	0.264	0.302	0.368	0.342	—
18	0.270	0.308	0.377	0.349	—
19	0.276	0.314	0.386	0.358	—
20	0.283	0.320	0.393	0.364	—
21	0.289	0.327	0.399	0.371	—
22	0.292	0.330	0.405	0.374	—
24	0.298	0.336	0.415	0.383	—
26	0.308	0.346	0.424	0.393	—
28	0.314	0.352	0.430	0.399	0.691
30	0.317	0.358	0.437	0.405	0.679
34	0.327	0.371	0.446	0.415	0.660
38	0.333	0.383	0.456	0.424	0.644
43	0.339	0.396	0.462	0.430	0.628
50	0.346	0.408	0.474	0.437	0.613
60	0.355	0.421	0.484	0.446	0.597
75	0.361	0.434	0.496	0.452	0.581
100	0.368	0.446	0.506	0.462	0.566
150	0.374	0.459	0.518	0.468	0.550
300	0.383	0.471	0.534	0.478	0.534
Rack	0.390	0.484	0.550	—	—

[a] Footnote 3, p. 64.

TABLE 4[a] VALUES OF Y WITH LOAD NEAR MIDDLE OF TOOTH

No. of teeth, i	14½°	20° full depth	20° stub	Internal gears: Spur pinion	Internal gears: Internal gear
12	0.355	0.415	0.496	0.650	—
13	0.377	0.443	0.515	0.654	—
14	0.399	0.468	0.540	0.657	—
15	0.415	0.490	0.556	0.660	—
16	0.430	0.503	0.578	0.663	—
17	0.446	0.512	0.588	0.676	—
18	0.459	0.522	0.603	0.685	—
19	0.471	0.534	0.616	0.698	—
20	0.481	0.544	0.628	0.707	—
21	0.490	0.553	0.638	0.716	—
22	0.496	0.559	0.647	0.723	—
24	0.509	0.572	0.663	0.732	—
26	0.522	0.588	0.679	0.742	—
28	0.534	0.597	0.688	0.751	1.257
30	0.540	0.606	0.698	0.760	1.241
34	0.553	0.628	0.713	0.773	1.216
38	0.566	0.650	0.729	0.786	1.194
43	0.575	0.672	0.738	0.795	1.169
50	0.588	0.694	0.757	0.814	1.144
60	0.603	0.713	0.773	0.817	1.119
75	0.613	0.735	0.792	0.829	1.093
100	0.622	0.755	0.807	0.842	1.068
150	0.635	0.779	0.829	0.855	1.043
300	0.650	0.801	0.855	0.867	1.021
Rack	0.660	0.823	0.880	—	—

[a] Footnote 3, p. 65.

tion from Equation [24] only in the range of β_b between 0.1 and 1.0. The over-all agreement is thought to be good in the case of lightly loaded gears. However, Equation [31] does not indicate a reduction in increment load when gears are heavily loaded.

TABLE 5[a] VALUES OF BENDING ENDURANCE LIMITS, σ_e

Material	Bhn	Reversed bending	One-way bending
Cast iron	180	8000	12000
Phosphor bronze	100	16000	24000
Steel	150	24000	36000
Steel	200	33000	50000
Steel	240	40000	60000
Steel	280	46000	70000
Steel	320	53000	80000
Steel	360	60000	90000
Steel	400	66000	100000

[a] Footnote 3, p. 65.

Design Approach

The wear strength of a pair of gears of specified tooth form, material, diameter, and speed ratio depends only on face width. The bending strength has an additional dependence on actual tooth size or diametral pitch. For this reason, gears usually are designed first from the wear point of view. This permits the design of the gear "blank." The application of the bending criterion then allows a decision on diametral pitch.

Standard design practice as based on the bending-stress equations of Lewis and the wear-strength equations of Buckingham will be summarized. In a given design a gear tooth must meet each of the three following conditions:

Design Practice. (*a*) Overload bending stress: T_0 = allowable bending load based on yield strength of material

$$T_0 = \frac{1.6\,fY}{nP_d}\left(\frac{\sigma_{yp}}{\text{FS}}\right) \qquad [32]$$

$$T_{\max} \leq T_0$$

FS = factor of safety

(*b*) Dynamic bending stress: T_B = allowable bending load based on reverse-bending endurance limit

$$T_B = \frac{1.6\,fY}{nP_d}(\sigma_e) \qquad [33]$$

$$n = 1 + \frac{0.075\,P_c}{R_f}$$

TABLE 6 VALUES OF K FOR COMPUTING LIMITING WEAR LOAD

Gear: Material	Gear: Hardness, Bhn	Pinion: Material	Pinion: Hardness, Bhn	Surface endurance limit, psi	Value of K: Involute 14½°	Value of K: Involute 20°
Steel	150	Steel	150	50000	30	41
Steel	150	Steel	200	60000	43	58
Steel	150	Steel	250	70000	58	79
Steel	200	Steel	200	70000	58	79
Steel	200	Steel	250	80000	76	103
Steel	200	Steel	300	90000	96	131
Steel	250	Steel	250	90000	96	131
Steel	250	Steel	300	100000	119	162
Steel	250	Steel	350	110000	144	196
Steel	300	Steel	300	110000	144	196
Steel	300	Steel	350	120000	171	233
Steel	300	Steel	400	125000	186	254
Steel	350	Steel	350	130000	201	275
Steel	350	Steel	400	140000	233	318
Steel	350	Steel	450	145000	250	342
Steel	450	Steel	450	170000	344	470
Steel	450	Steel	500	175000	364	497
Steel	450	Steel	600	180000	385	526
Steel	500	Steel	500	190000	430	588
Steel	600	Steel	600	230000	630	861
Cast iron	180	Steel	150	50000	44	60
Cast iron	180	Steel	200	70000	87	119
Cast iron	180	Steel	250	90000	144	196
Gear bronze	100	Steel	150	50000	46	62
Gear bronze	100	Steel	200	70000	91	124
Gear bronze	100	Steel	250	85000	135	184
Cast iron	180	Cast iron	180	90000	193	264
Metal	...	Nonmetallic	(34)	32000	189	258

Some values of Y are given in Tables 3 and 4; some values of σ_e are given in Table 5.

For infinite life

$$T_d \leq T_B$$

(c) Wear: T_W = allowable wear load based on lower surface endurance limit of the two materials

$$T_W = KQD_p f \cos\theta \quad [34]$$

Some values of K are given in Table 6.

For infinite life

$$T_d \leq T_W$$

Design Equations for Lightly Loaded Gears

The equations that have been presented permit a direct analytical check of an existing or proposed gear design. However, certain simplifications of the design equations must be made in order to solve them directly, rather than by trial, for unknown design parameters such as face width, hardness, and diametral pitch.

In the case of lightly loaded gears the following simplification is useful where the effective inertia of the system depends only on the gears themselves and is therefore directly proportional to their face width.

Inspection of Fig. 9 shows that the following equations for T_i are a good approximation of the derived T_i over almost the complete range of β_b

$$\frac{T_i}{ek} = 2\beta_b \quad \text{or} \quad T_i = 2v\sqrt{mc(ke_m + T_i)} \quad \text{for} \quad \beta_b < 0.5 \quad [35]$$

$$\frac{T_i}{ek} = 1.0 \quad \text{or} \quad T_i = (ke_m + T_i) \quad \text{for} \quad \beta_b > 0.5 \quad [36]$$

Since gears are lightly loaded and $ke_m \gg T_i$, Equation [30] may be approximated by

$$T_i = 2vf\sqrt{cm_f k_f e_m} \quad [37]$$

where

m_f = effective mass per inch of face width (lb sec²/in.²)

$$\frac{1}{m_f} = \frac{2}{\rho\pi}\left[\frac{1}{R_p^2} + \frac{1}{R_g^2}\right]$$

k_f = spring constant per inch of face width, psi
e_m = manufactured error, in.
f = face width, in.
c = parabolic constant, in.$^{-1}$
v = pitch-line velocity, ips
T_i = increment load, lb

Likewise, Equation [36] becomes for $\beta_b > 0.5$

$$T_i = fk_f e_m \quad [38]$$

Now

$$T_d = T_i \leq KQD_p f\cos\theta$$

$$2vf\sqrt{cm_f k_f e_m} \leq KQD_p f\cos\theta$$

$$\therefore K \geq \frac{2v\sqrt{cm_f k_f e_m}}{QD_p\cos\theta} \quad \text{for} \quad \beta_b < 0.5 \quad [39]$$

and

$$K \geq \frac{k_f e_m}{QD_p\cos\theta} \quad \text{for} \quad \beta_b > 0.5 \quad [40]$$

Equations [39] and [40] will determine the minimum K factor and thus the minimum hardness appropriate for a chosen gear diameter, all other parameters having been fixed. It is interesting to note that for these lightly loaded gears the dynamic load varies linearly with face width, while the allowable load also varies linearly. Thus the face width is independent of the wear criterion.

The face width of lightly loaded gears is also independent of the bending criteria since the allowable bending load based on the flexural endurance limit varies directly with the face width. Application of the bending criteria will yield a result for the diametral pitch only. Usually the wear criterion demands a hardness resulting in a high value of the endurance limit. Thus reasonable diametral pitches often result in large safety factors in bending. Face width may be determined from other considerations including gear blank stiffness and overload estimate.

Helical Gearing

Dynamic increment forces will occur in helical gearing from the same causes as in spur gearing. The tooth engagement is quite different, however, for contact occurs first at a point and then develops into line contact gradually. This, coupled with the increased difficulty of expressing the gear-tooth spring constant and the possibility of axial motion of the gear masses, makes the application of spur-gear analysis to helical gears somewhat questionable. However, results so obtained have been substantiated by experience. In the absence of a more complete investigation, equations will be formulated from those already derived for spur gears.

The velocity of engagement in the normal plane which controls the speed with which the error is introduced is given by

$$v_n = v\cos\psi$$

It will be assumed that the gears are free to vibrate only about their axis of rotation and therefore the effective tooth stiffness in the axial plane k_a is of interest in determining the system natural frequency. Fig. 12 shows the quantities referred to in the following derivation

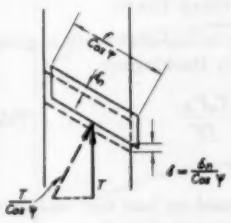

Fig. 12 Helical Tooth Deflections Under Load

$$\frac{T}{\cos\psi} = k_f\frac{f}{\cos\psi}\delta_n$$

$$\therefore \delta_n = \frac{T}{k_f f}$$

$$k_a = \frac{T}{\delta} = \frac{T}{\delta_n}\cos\psi = k_f f\cos\psi \quad [41]$$

Since the actual contact is not on the pitch line but lies on a curved line across the teeth, deflections will be greater than pre-

dicted by k_s. Buckingham[7] suggests multiplying Equation [41] by cos ψ to account for this.

$$k_s = k_f f \cos^2 \psi \quad [42]$$

Fig. 9 may now be applied to helical gearing by substitution of analogous quantities. It is interesting to note that β_a and β_b by inference remain unchanged

$$\beta_a = \frac{v\sqrt{\frac{c}{e}}}{\sqrt{\frac{2k}{m}}} \text{ for spur gears}$$

$$\beta_a = \frac{v\cos\psi\sqrt{\frac{c}{e}}}{\sqrt{\frac{2k\cos^2\psi}{m}}} = \frac{v\sqrt{\frac{c}{e}}}{\sqrt{\frac{2k}{m}}} \text{ for helical gears}$$

Since the effective tooth stiffness is different, the ordinate in Fig. 9

$$\frac{T_i}{ek}$$

should be interpreted as

$$\frac{T_i}{ek\cos^2\psi}$$

For lightly loaded gears the equation for values of $\beta_b < 0.1$ is then

$$\frac{T_i}{ek\cos^2\psi} = 2\beta_b = \frac{2v\sqrt{\frac{c}{e}}}{\sqrt{\frac{k}{m}}} \quad [43]$$

or

$$T_i = 2v\cos^2\psi\sqrt{mcek} \quad [44]$$

As before for lightly loaded gears only

$$T_d = T_i$$

Strength of Helical-Gear Teeth

The maximum bending stress for a helical-gear tooth is given by the following equation suggested by Buckingham

$$\sigma = 1.3\left(\frac{n}{1.6}\right)\frac{T_d P_{dn}}{fY} \quad [45]$$

where

Y = beam factor for spur gears based on load near middle of tooth and on the virtual number of teeth i_s

$$i_s = \frac{\text{actual number of teeth}}{\cos^3\psi}$$

P_{dn} = diametral pitch in normal plane

$$P_{dn} = \frac{P_d}{\cos\psi}$$

$$n = 1 + \frac{0.075\,P_d}{R_f}$$

f = face width in axial plane

T_d = total tangential load in axial plane

The wear-strength equation may be modified for helical gears as follows

$$T_W = \frac{D_p f k Q\cos\theta}{\cos^2\psi} \quad [46]$$

where constants are the same as for spur gears and ψ = helix angle.

As in the case of spur gears, the design criterion is based on yield strength, bending fatigue, and wear strength, with each being considered independently.

Conclusions

1 Equations for predicting total dynamic loads in heavily loaded gear teeth have been developed. The term "heavily loaded gears" is applied to those gears in which the deflection due to the steady power load is equal to or greater than the manufacturing tooth error. The dynamic-load equations for such gears indicate that the dynamic load varies from a minimum of one half the effective tooth error (static deflection plus manufacturing error) times the elastic constant of the tooth to a maximum value equal to the effective error times the elastic tooth constant.

In many heavily loaded gears the total dynamic load may be actually less than the static load determined from the transmitted power. The full static load must be taken by a single pair of teeth when in contact near the pitch point in gears having a contact ratio between one and two. Therefore the static load may often be used as the maximum load in the design of heavily loaded gears. The fact that initial wear failure usually commences near the center of the tooth surface substantiates this argument.

2 Equations predicting total dynamic loads in lightly loaded gear teeth have been presented. The term "lightly loaded gears" applies to those gears in which the deflection due to the steady power load is very much smaller than the manufacturing error. The dynamic load equations for such gears indicate that the dynamic load varies from a minimum of zero to a maximum value equal to the effective error times the elastic tooth constant. These equations are in general agreement with those proposed by Buckingham.

3 Simplified equations for dynamic loads in lightly loaded gears in which the effective inertia is due only to the inertia of the gears themselves have been proposed. These equations indicate that the face width of such gears is independent of endurance criteria. Application of wear criteria yields a suitable value for material hardness, while the bending strength determines a maximum diametral pitch.

Further Investigations

There are many directions in which analysis based on transient vibrations might be pursued. Some that come to mind include: More precise description of tooth elastic constants and how they vary; investigations of gears with medium loads including their nonlinear operation; investigations of dynamic loads in gears with contact ratios greater than 2; and also, very important, a more exact description of the nature of tooth errors which cause dynamic loads.

Probably the most significant step that might be taken would be to apply the basic mechanism of this paper to the problem of very high speed gears, where the assumption that the transient solution dies out before the following tooth engagement takes place must no longer be valid. The application of an analog computer wherein a simulated error would be introduced repetitively at high speed might produce results in this area.

Acknowledgment

The author wishes to acknowledge the encouragement and helpful suggestions of Prof. John A. Hrones of M.I.T. and Prof. Arthur D. Brickman of Pennsylvania State College.

[7] Footnote 2, p. 456

The Grinding of Titanium Alloys

By C. T. YANG[1] and M. C. SHAW,[2] CAMBRIDGE, MASS.

When titanium is ground under conventional conditions the rate of wheel wear is abnormally high and the finish produced is poor. Improvement in surface finish accompanies a decrease in wheel-wear rate. A study of the influence of a wide variety of operating and grinding-wheel variables reveals the most important quantities to be grinding-wheel speed, type of abrasive, and grinding fluid. When a wheel speed of 1500 to 2000 fpm is used with a suitable fluid and a white-aluminum-oxide wheel of conventional hardness, grain size, and bonding, greatly improved results are obtained. All of the observations that have been made can be explained in terms of the assumption that bonding between titanium chips and abrasive grains is of major importance. While most of the experiments and discussion are centered around the surface-grinding operation, cylindrical grinding and the cut-off operations also are considered.

Introduction

TITANIUM is a metal belonging to the tin group of the periodic table that resembles iron in many of its properties. It is strong but light. Until recently titanium alloys were not used for structural applications owing to their high cost. At present, after much research, relatively large quantities of titanium are available for engineering experimentation.

The structural alloys of titanium are ductile, light in weight, and have good fatigue strength and high corrosion resistance. The strength-weight ratio of titanium alloys is the highest among all structural materials. Titanium alloys have high melting points which would suggest good strength properties at elevated temperatures. However, the strength of titanium falls rapidly at temperatures above about 800 F. The properties of titanium are compared with other common metals in Table 1

The thermal conductivity and specific heat of titanium alloys are usually low which accounts to a large extent for the difficulties experienced in machining and grinding these alloys. The thermal combination of importance with regard to tool-tip temperature will later be seen to be ($k\rho c$) where k is the heat conductivity and ρc is the volume specific heat of the workpiece material. Until recently stainless steel had the lowest values of ($k\rho c$) normally experienced in cutting and this gave rise to high cutting temperatures. From Table 1 the quantity ($k\rho c$) for titanium is seen to be even lower than that for stainless steel.

Similar to iron, titanium exhibits an allotropic transformation at 1625 F, changing from a hexagonal close-packed structure (α-phase), stable at lower temperatures, to a body-centered cubic structure (β-phase). While pure titanium cannot be hardened by heat-treatment, it can be hardened by cold work. Inasmuch as the work-hardening exponent is found to be very nearly that for mild steel, Fig. 1, the difficulty experienced in cutting and grinding titanium cannot be attributed to an abnormally strong tendency to work-harden.

Nitrogen, oxygen, carbon, and iron will go into solution in titanium in the molten state, and tend to make the metal harder, stronger, and less ductile. The influence of nitrogen and oxygen on hardness is approximately additive. Titanium alloys contain-

TABLE 1 PROPERTIES OF COMMERCIALLY PURE TITANIUM AND OTHER STRUCTURAL METALS

Property	Metal: 75A Titanium	SAE 1020 Steel	18-8 Stainless Steel	75ST Aluminum
Structure	HCP	BCC	FCC	FCC
Specific Weight ρ lb/cu in	0.16	0.28	0.28	0.10
Ultimate tensile strength (annealed), psi	80,000	50,000	90,000	12,000
Youngs modulus, E, psi x 10^{-6}	16	30	30	10
Shear modulus, G, psi x 10^{-6}	6	11.5	11.5	4
Melting point, °F	3200	2600	2600	1220
Coefficient of linear expansion, per °F x 10^{6}	5	6.6	9	13
Thermal conductivity k, BTU/in/sec/(°F/in) x 10^{4}	2.0	7.5	2.2	16
Specific heat, c BTU/lb/°F	.13	.13	.12	.21
Volume specific heat, ρc, BTU/in^3/°F	.021	.036	.034	.021
Thermal diffusivity, $K = \frac{k}{\rho c}$, in^2/sec.	.0095	.021	.0065	.076
$k\rho c$, (BTU/in^{2}°F)^2/sec x 10^{6}	4.2	27.	7.5	34

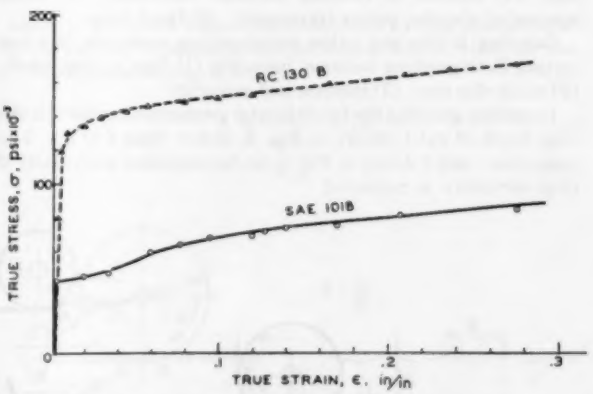

FIG. 1 TRUE STRESS—TRUE STRAIN TENSILE CURVES FOR TITANIUM RC 130B AND AISI 1018 STEEL

(Dimensions of tensile specimen corresponded to ASTM standard, 0.505 in. diam.)

[1] Assistant Professor, Department of Mechanical Engineering, Massachusetts Institute of Technology.

[2] Professor, Department of Mechanical Engineering, Massachusetts Institute of Technology. Mem. ASME.

Contributed by the Metal Processing Research Committee and presented at a joint session with the Production Engineering Division at the Semi-Annual Meeting, Pittsburgh, Pa., June 20–24, 1954, of THE AMERICAN SOCIETY OF MECHANICAL ENGINEERS.

NOTE: Statements and opinions advanced in papers are to be understood as individual expressions of their authors and not those of the Society. Manuscript received at ASME Headquarters, April 15, 1954. Paper No. 54—SA-57.

ing large quantities of chromium or iron in solution can be quenched and age-hardened. Large quantities of chromium and iron tend to stabilize the β-phase of titanium at room temperature.

Titanium has some interesting chemical properties. It is characterized by a strong affinity with compounds containing nitrogen, oxygen, carbon, and halogens, especially at elevated temperatures. This makes it difficult to refine titanium since it has a strong tendency to react with the usual refractory materials, all of which have negative oxygen or carbon ions at their surfaces.

At a temperature of 1475 F titanium will burn with incandescence in an atmosphere of pure nitrogen to form TiN. At a temperature of 1125 F titanium may be burned to TiO_2 in pure oxygen or at 2200 F in air. At high temperatures oxygen reacts with titanium in preference to nitrogen.

Inasmuch as molten titanium reacts readily with refractory oxides, it would be expected to react with the glasses used as bonding materials in vitrified grinding wheels. Titanium also will form strong bonds with aluminum oxide or silicon carbide at temperatures as low as 1800 F. Titanium will decompose water at elevated temperatures releasing nascent hydrogen. Titanium as well as zirconium has the property of absorbing hydrogen at high temperatures. This hydrogen forms interstitial hydrides, the lattice of the metal being expanded and as a result becoming more reactive.

Grinding Theory

The nature of surface grinding is shown schematically in Fig. 2, the pertinent operating variables being as follows:

1 Wheel speed, V, fpm
2 Wheel depth of cut, d, in.
3 Table speed, v, ipm
4 Axial feed, d_a, ipp

In addition to these there are certain characteristics of the grinding wheel which influence its performance. These wheel variables include (1) external dimensions; (2) abrasive type; (3) abrasive size; (4) amount of bonding material (hardness); (5) mean spacing of abrasive points (openness); (6) bond type.

Grinding is like any other metal-cutting operation, but has certain distinguishing features, including (1) high cutting speed; (2) small chip size; (3) random tool geometry.

In surface grinding the fundamental geometrical variable is the chip depth of cut t, shown in Fig. 3, rather than d or d_a. The quantities l and t shown in Fig. 3 can be expressed analytically if chip curvature is neglected

$$l = \sqrt{Dd} \quad [1]$$

$$t = \sqrt{\frac{4v}{VCr}}\sqrt{\frac{d}{D}} \quad [2]$$

where D is wheel diameter, C is number of cutting points per square inch of wheel surface, r is mean width to depth ratio of individual grinding scratches.

The derivations for these equations and those to follow are to be found elsewhere.[3,4,5] The value of r is usually between 10 and 15, while C is found to vary with dressing technique, structural number, and particularly, grain size. For a No. 60 grain size, C is about 3000 cutting points per sq in. of wheel surface.

The total force to which a grit is subjected during grinding will vary directly with t. Thus the tendency for an entire grain to leave the wheel will vary directly with t. The influence of grinding and wheel variables on the relative tendency for grains to leave the wheel, i.e., relative wheel hardness, may be determined conveniently from Equation [2].

The quantity t is found to have a still more important influence on the energy associated with the grinding operation. The energy per unit volume of metal removed is a convenient quantity to consider when judging the efficiency of the grinding operation. In surface grinding the energy per unit volume is

$$u = \frac{F_P V}{vbd}, \text{ in-lb/cu in.} \quad [3]$$

where F_P is the tangential force on the wheel that is responsible for the power consumed and b is the axial width of cut. A typical curve of u plotted against t for steel is shown in Fig. 4.

The energy per unit volume is of particular significance regarding the temperature to which ground surfaces are subjected. The mean temperature rise on the finished surface can be shown to be

$$\bar{\theta}_s = \frac{u}{24J(c_1\rho_1)} R_1 \quad [4]$$

where

$$R_1 = \frac{1}{1 + 1.328\sqrt{\frac{K_1\gamma}{Vt}}} \quad [5]$$

[3] "The Size Effect in Metal Cutting," by W. R. Backer, E. R. Marshall, and M. C. Shaw, Trans. ASME, vol. 74, 1952, p. 51.
[4] "Surface Temperatures in Grinding," by J. O. Outwater and M. C. Shaw, Trans. ASME, vol. 74, 1952, p. 73.
[5] "On the Analysis of Cutting-Tool Temperatures," by E. G. Loewen and M. C. Shaw, Trans. ASME, vol. 76, 1954, p. 217.

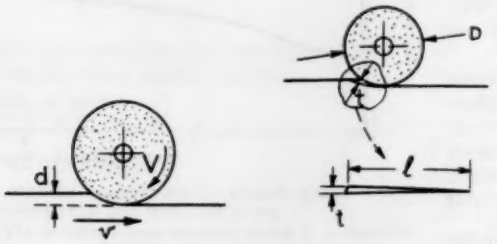

Fig. 2 Surface Grinding

Fig. 3 Shape of Individual Chip in Surface-Grinding Operation

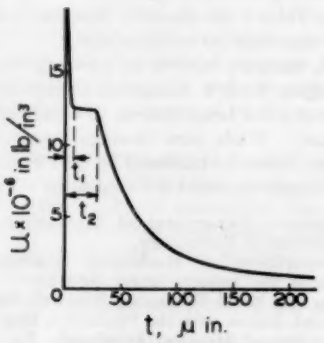

Fig. 4 Variation of Grinding Energy Per Unit Volume u, With Undeformed Chip Thickness t, for Mild Steel

J is the mechanical equivalent of heat, $(c_1\rho_1)$ is volume specific heat of metal cut, K_1 is thermal diffusivity of workpiece, and γ is strain in chip. The effect of t on the mean temperature of the ground surface $\bar{\theta}_s$, can be obtained from Equations [4] and [5] by use of the u-versus-t plot, Fig. 4.

The mean temperature on the tool face, which is another important quantity, is given by the following expression[5] under equilibrium conditions

$$\bar{\theta}_t = \frac{u}{J}\sqrt{\frac{Vt}{\gamma k_2\rho_2 c_2}}\left[A\mu\sqrt{\frac{t\sec\alpha}{a}} + B\right] + \theta_0{}^1 \ldots\ldots [6]$$

where

u = energy per unit volume
J = mechanical equivalent of heat
t = depth of layer removed
γ = strain in the chip
k_2 = thermal conductivity of work
$(\rho_2 c_2)$ = volume specific heat of work
μ = coefficient of friction between chip and tool
α = rake angle
a = length of contact along tool face
A, B = const
$\theta_0{}^1$ = ambient temperature of tool

This equation shows that under equilibrium conditions the tool-face temperature depends upon a particular product of thermal properties of the workpiece $(k\rho c)$.

However, in the case of the abrasive grains of a grinding wheel, we do not have steady-state conditions. The temperature on the face of a grain will rise while it is cutting, but will fall exponentially when it ceases to cut. The temperature variation will be as shown in Fig. 5, the temperature remaining at the ambient value

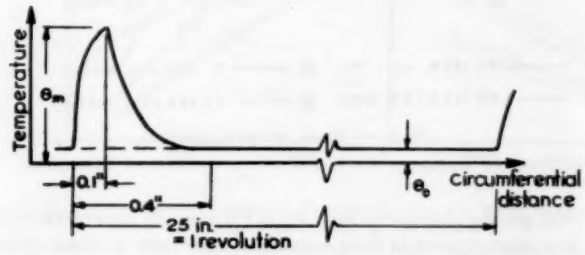

FIG. 5 VARIATION OF TEMPERATURE OF ABRASIVE GRAIN WITH PERIPHERAL DISTANCE TRAVELED

during most of the cycle. Analysis shows the time it takes the temperature to fall, to within 1 per cent of the ambient value, to be about three times the period of heating which is the time of cutting. For an average surface-grinding condition with an 8-in-diam wheel the arc of contact l will be about 0.1 in., the cooling distance about 0.3 in., and the peripheral length of the wheel for which it is at ambient temperature will be about 25 in. The grain is thus seen to be at the ambient temperature over 98 per cent of the time it takes to make a revolution. Because of this relatively long time at ambient temperature we should expect the ambient temperature to be much lower than the peak temperature at the end of the cut, θ_m. At the same time the peak temperature should be far more important with regard to grinding performance than the ambient temperature.

By following a series of steps similar to those used to derive Equation [6], the peak temperature in grinding is found to be

$$\theta_m = \sqrt{\frac{\pi}{4}}\,\frac{u_f}{J}\sqrt{\frac{Vl}{k_3\rho_3 c_3}}\left(\frac{rt^2}{A}\right) + \theta_0 \ldots\ldots [7]$$

where

k_3 = thermal conductivity of abrasive
$(\rho_3 c_3)$ = volume specific heat of abrasive
u_f = friction energy per unit volume
A = area of contact between chip and abrasive
θ_0 = ambient temperature of abrasive

The quantity rt^2/A will remain nearly constant as will the ratio u_f/u and hence we may write

$$\theta_m - \theta_0 \sim u\sqrt{\frac{Vl}{k_3\rho_3 c_3}} \ldots\ldots [8]$$

Thus the temperature of an abrasive grain should be influenced by $(k\rho c)$ for the abrasive rather than for the workpiece, and the cutting speed V, length of cut l, and energy per unit volume u, also are seen to be important.

The quantity t may be shown to correlate well with the finish produced in surface grinding although it is not physically responsible for surface roughness. Assuming no built-up edge and no welding between chip and grit, we may calculate the mean peak-to-valley distance $\bar{h}$ for the finished surface. In Fig. 6 the mean height of the scratches left behind is $\bar{h}$ and the distance AB is then

$$\text{AB} = 2\sqrt{D\bar{h}} \ldots\ldots [9]$$

The time for the work to feed a distance AB will be

$$\frac{2\sqrt{D\bar{h}}}{v}$$

and the number of grits N_{AB}, which will sweep through a given line on the surface of an axial width $1/\sqrt{C}$, as it moves through distance AB will be

$$N_{AB} = \frac{2\sqrt{D\bar{h}}}{v}\,V\sqrt{C} \ldots\ldots [10]$$

where $1/\sqrt{C}$ is the mean distance between cutting points, since C is the number of cutting points per square inch of wheel surface.

The distance $\bar{x}$, Fig. 6, will be

$$\bar{x} = \frac{1}{\dfrac{\sqrt{C}}{N_{AB}}} = r\bar{h} \ldots\ldots [11]$$

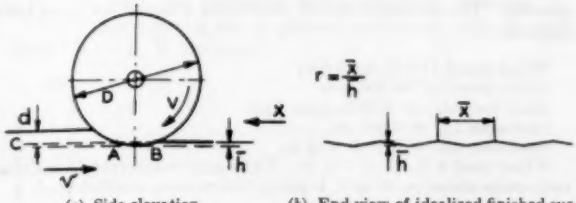

(a) Side elevation

(b) End view of idealized finished surface looking in direction x shown in Fig. 8(a)

FIG. 6 DIAGRAM FOR USE IN COMPUTING MEAN SURFACE ROUGHNESS, $\bar{h}$

where $r = \bar{x}/\bar{h}$ and hence

$$\bar{h} = \left[\frac{v}{2Vr\sqrt{C}\sqrt{D}}\right]^{2/3} \ldots\ldots [12]$$

From Equations [2] and [12] we obtain

$$\bar{h} = \frac{t^{4/3}}{4d^{1/3}} \quad [13]$$

This does not mean that $\bar{h}$ depends on t and d, for actually $\bar{h}$ depends on quantities equivalent to the combination of t and d given in Equation [13] but actually not on t and d. The actual mean peak-to-valley distance ($\bar{h}_a$) will differ from $\bar{h}$ owing to the fact that the abrasive grains are not spaced uniformly in a grinding wheel and also because of the formation of built-up edge. However, we should expect $\bar{h}_a$ to be proportional to $\bar{h}$ and hence

$$\bar{h}_a \sim \frac{t^{4/3}}{d^{1/3}} \quad [14]$$

This tells us that the surface roughness produced in a grinding operation should be expected to vary a little more rapidly than linearly with grain depth of cut t but only slightly with wheel depth of cut d.

The equations for surface grinding given in the foregoing can be rederived for internal and external grinding, yielding

$$l = \sqrt{\frac{Dd}{1 \mp D/D_W}} \quad [15]$$

$$t = \sqrt{\frac{4v}{VCr}}\sqrt{\frac{d}{D} \mp \frac{d}{D_W}} = \sqrt{\frac{4vd}{VCrl}} \quad [16]$$

$$\bar{h} \sim \frac{t^{4/3}}{d^{1/3}} \quad [17]$$

$$\bar{h} \sim \left[\frac{v}{VrC}\sqrt{\frac{1}{D} \mp \frac{1}{D_W}}\right]^{3/4} \quad [18]$$

All other equations discussed previously remain unchanged. In these equations, D_W is the diameter of the workpiece (which equals infinity for surface grinding) and the minus signs are for internal grinding while the plus signs are for external grinding.

of the volume of metal removed to the corresponding volume of wheel consumed is a convenient measure of grinding performance and this "grinding factor" will be designated by the symbol G in the following discussion.

Representative results for a variety of operating conditions are shown in Fig. 7. For all alloys tested the wheel speed was optimum with regard to grinding factor G at values between 1500 and 2000 fpm (lower values for harder alloys). This is in contrast

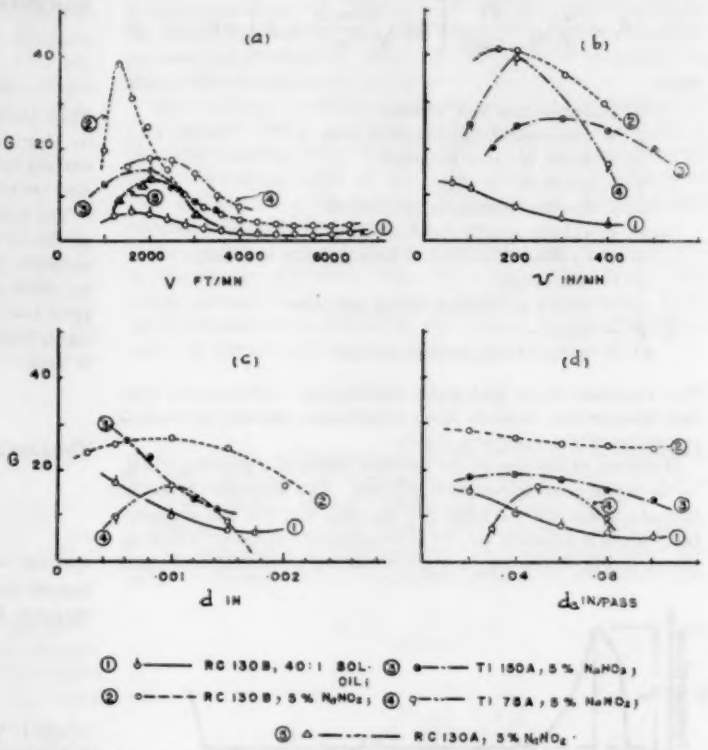

FIG. 7 VARIATION OF GRINDING FACTOR G, WITH OPERATING VARIABLES

OPERATING VARIABLES

In order to study the influence of the principal operating variables upon wheel wear, surface finish, and specific grinding energy u, pieces of the titanium alloys described in Table 2 were surface-ground. The standard set of conditions adopted for these tests follows:

Wheel speed (V) = 2000 fpm
Table speed (v) = 400 ipm
Axial feed (d_a) = 0.05 in/pass (ipp)
Downfeed (d) = 0.001 in.
Specimen size = 2 × 2 × 4 in.
Wheel used 8 × 3/4 × 1 1/4 in. Light-gray monocrystalline aluminum-oxide abrasive, 60 grit, L grade, 5 structure, vitrified bond

In making a test, a single variable was changed from the foregoing set of conditions and the effect noted.

Each test was continued until 0.02 in. was removed from the surface by taking off successive layers each 0.001 in. thick and the amount of wheel consumed was determined from the change in wheel diameter as measured by a micrometer. The ratio

with general practice for steel where V is normally about 6000 fpm. The improvement in G as a result of a decrease in wheel speed from 6000 to 2000 fpm was found to correspond to a factor of from 5 to 10. All other variables (table speed, wheel depth of cut, and table cross-feed) were found to lie within the conventional range of values for steel. Satisfactory wheel life was found in surface-grinding all titanium alloys when the operating conditions were close to the following:

Wheel speed (V) = 2000 fpm
Table feed (v) = 200 ipm
Wheel depth of cut (d) = 0.001 in
Cross-feed (d_a) = 0.05 ipp

TABLE 2 COMPOSITION AND PHYSICAL PROPERTIES OF TITANIUM ALLOYS INVESTIGATED

Titanium Alloys Investigated

Alloy Designation	Chemical Composition								Tensile Strength, psi		%	Hardness	
	Ti	N_2	O_2	Fe	C	Mn	Al	Cr	Ultimate	Yield	Elongation	R_C	Brinell
Ti 75A	99.4	.10	.20	.20	.05	-	-	-	87,000	75,000	22	10	160
RC 130B	99.3	-	-	-	.11	3.5	3.0	-	150,000	140,000	17	28	260
Ti 150A	95.3	.10	.30	1.5	.05	-	-	2.7	152,000	120,000	12	30	270
RC 130A	92	-	-	-	.13	7.9	-	-	130,000	115,000	19	29	265

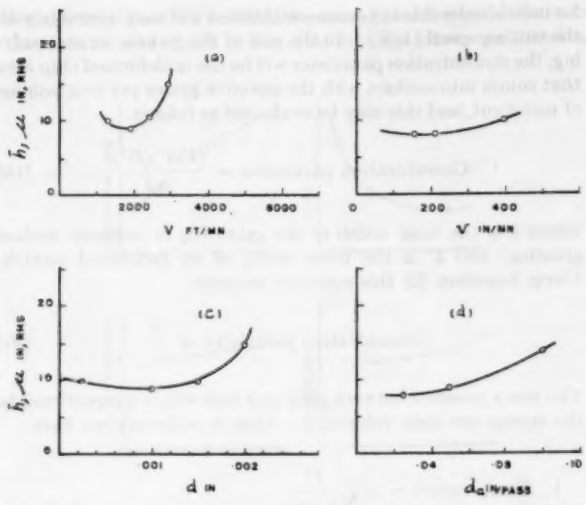

FIG. 8 VARIATION OF SURFACE FINISH IN MICROINCHES RMS WITH OPERATING VARIABLES

(Work material, RC 130B; cutting fluid, 5 per cent sodium-nitrite solution; wheel speed V, 2000 fpm; table speed v, 400 ipm; wheel depth of cut d, 0.001 in.; cross-feed d_e, 0.05 ipp.)

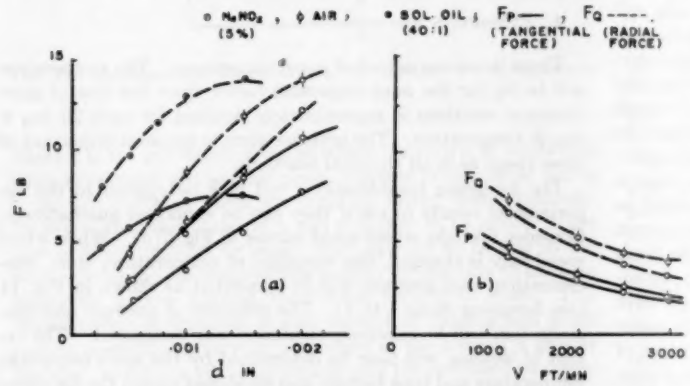

FIG. 9 VARIATION OF GRINDING FORCES F_P AND F_Q WITH WHEEL SPEED V, AND WHEEL DEPTH OF CUT d

(Wheel speed V, 2000 fpm; work material, RC 130B; table speed v, 400 ipm; wheel depth of cut d, 0.001 in.; cross-feed, 0.05 ipp.)

The grinding fluid was found to have an important influence upon the quantitative values but the foregoing qualitative picture was the same for all fluids. The role of the grinding fluid will be discussed in detail in a later paper.

The surface finish produced was found to vary directly with G. When G was large the finish was good and vice versa. Representative surface-roughness data are shown in Fig. 8. No difficulty was found in producing finishes of 16 microinches, when grinding under conditions to give good wheel life, and it may be stated that under such conditions it is no more difficult to produce good finishes on titanium alloys than on steel.

The variation of grinding forces with down feed and wheel speed are shown in Fig. 9 and the corresponding specific-energy curve is shown in Fig. 10. These data will be discussed later.

When a number of ground titanium-alloy surfaces were examined metallographically no grinding damage was observed. From our experience it would appear to be conservative to state that titanium alloys show no greater tendency to develop microcracks or exhibit surface transformation as a result of grinding than do hardened alloy steels.

WHEEL VARIABLES

In addition to the operating variables already discussed, a number of quantities are associated with the grinding wheel itself that influence grinding performance. Results of a large number of tests upon a wide variety of wheels enables the following observations to be made:

Abrasive Type. (*a*) When wheel speed is decreased to the vicinity of 2000 fpm, aluminum-oxide wheels give better results (higher values of G) than either black or green silicon-carbide wheels.

(*b*) The optimum speed for silicon carbide is higher than that for aluminum oxide.

(*c*) Both the white friable and light-gray types of aluminum oxide gave better results than the tougher brown forms.

(*d*) The grinding energy for silicon carbide and aluminum oxide were very nearly the same when grinding titanium alloys. This is in contrast to results on steel where the grinding energy with silicon carbide is about twice as high as that for aluminum oxide. The radial component of force which reflects the resistance to penetration was less for SiC (particularly the green variety) which indicates sharper fracture surfaces for SiC in accordance with fractometry.

Abrasive Size. (*e*) In tests on wheels of different grain size, wheels of 60 grit were found to give better results than those containing larger or smaller abrasive grains.

Wheel Hardness. (*f*) Wheels of medium hardness (approximately L grade) were found best. When hard wheels were used, difficulty due to wheel chipping was experienced with the softer titanium alloys.

Bond Type. (*g*) The vitrified bond was found to give better results than a resinoid bond.

Dressing Technique. (*h*) Several different dressing techniques using a diamond failed to show any significant difference in performance.

In all cases the surface finish was found to vary inversely with rate of wear regardless of the values of t or d obtaining.

There seems to be little point in presenting the large mass of data upon which the foregoing observations are based. The general observation that might be made regarding the choice of wheel variables for titanium grinding is that general HSS tool-grinding practice be followed except for the wheel grade which should be harder for titanium grinding. This calls for vitrified white-aluminum-oxide wheels of medium grain size, hardness, and openness of structure.

The foregoing results are in general agreement with those obtained by Dr. L. P. Tarasov.[8]

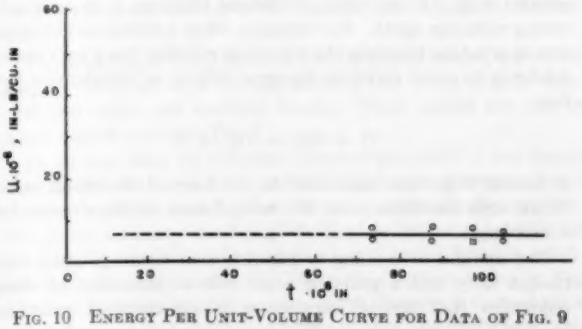

FIG. 10 ENERGY PER UNIT-VOLUME CURVE FOR DATA OF FIG. 9

[8] "How to Grind Titanium," by L. P. Tarasov, *American Machinist*, vol. 96, 1952, p. 135.

Discussion

The foregoing results reveal that in grinding titanium alloys there are two quantities of major interest—the rate of wheel wear and the finish produced. It also has been observed that these quantities are not independent but closely related.

A grinding wheel that is properly operating is expected to exhibit some wear. As the sharp edges of the abrasive grain are worn smooth in use the grain is expected to shed small regions to provide new sharp-edged fracture surfaces. When all of the weak regions within the grain have been fractured, the entire grain is supposed to leave the wheel. This calls for a bonding arrangement that is not too strong, for otherwise large forces and high surface temperatures may develop before the used grain is disposed of. At the same time the bond must not be too weak for then the largest chip depth of cut (t) that may be taken by even a sharp grain may be too small to be practical. In grinding ordinary materials the rate of abrasive wear is not great. In grinding ordinary mild steel a G-factor of over 100 is to be expected while a value of over 30 can be achieved when grinding hard tool steel.

In grinding ordinary steels and tool steels there is relatively little welding or bonding between the abrasive surfaces and the chips The oxygen in the air is responsible for this. The freshly cut metal immediately reacts with oxygen to form a very thin oxide film that is capable of largely preventing the chip from welding to the abrasive grain. This greatly limits the rate of wear for if strong welds are allowed to form the abrasive frequently will break instead of the weldment and abrasive particles will leave with the chips in a steady stream. The important role that oxygen plays in the grinding of ordinary steel may be illustrated dramatically by grinding in a nitrogen atmosphere. Under such conditions the grinding forces have been observed to increase by as much as twenty-five fold and wheel wear becomes catastrophic. The forces are observed to be a little higher when pure water is used as a cutting fluid than when grinding in air. This could be due to the water excluding oxygen from the tool. However, even the small amount of water vapor normally present in the air is sufficient to cause a noticeable increase in grinding forces. In addition to the possibility of water merely adsorbing on the abrasive grains and thus excluding oxygen, it is also possible for the water to decompose into its elements under the extreme conditions of temperature and pressure obtaining at the tips of abrasive grains. The hydrogen thus liberated could act as a very effective weld promoter.

When titanium alloys are ground in air the rate of wear is unusually high. When grinding under ordinary conditions the G-factor may be as low as 0.5, and even lower when pure water is used as a cutting fluid. At the temperatures reached at the tips of the grinding points, the freshly cut titanium has a strong tendency to weld or bond (react) to most anything it comes in contact with. Under these conditions titanium is an extremely strong reducing agent. For example, when a silicon-carbide abrasive is grinding titanium the following reaction has a very strong tendency to occur owing to the great affinity of titanium for carbon

$$\mathrm{Ti} + \mathrm{SiC} \rightarrow \mathrm{TiC} + \mathrm{Si}$$

A similar reduction can occur in the case of aluminum oxide. When such reactions occur the rate of wear of the abrasive becomes large.

The amount of welding or bonding that occurs between a titanium alloy and a grinding wheel will be influenced by those quantities that are of importance in all chemical reactions, namely, (1) temperature, (2) time, (3) concentration of reactants, (4) pressure. The mean temperature between chip and abrasive grain has been given in Equation [8]. The time available for individual welds to become established will vary inversely with the cutting speed ($1/V$). In the case of the process we are studying, the concentration parameter will be the undeformed chip area that comes into contact with the abrasive grains per unit volume of metal cut, and this may be evaluated as follows

$$\text{Concentration parameter} = \frac{(VbC)(lb')}{vbd} \quad \ldots\ldots [19]$$

where b is the total width of the grind (d_a in ordinary surface grinding) and b' is the mean width of an individual scratch. Using Equation [2] this equation becomes

$$\text{Concentration parameter} = \frac{2}{t} \quad \ldots\ldots [20]$$

The mean pressure between chip and tool will be proportional to the energy per unit volume, u. Thus in summary we have

1 Temperature $\sim u\sqrt{\dfrac{Vl}{k_3\rho_3 c_3}}$

2 Time $\sim \dfrac{1}{V}$

3 Concentration $\sim \dfrac{1}{t}$ (where t is given by Equation [2])

4 Pressure $\sim u$

These items are not all of equal importance. The temperature will be by far the most important factor since the rate of most chemical reactions is approximately doubled for each 20 deg F rise in temperature. The pressure term is the least important of these items as in all chemical reactions.

The foregoing considerations will now be applied to the experimental results to see if they can be explained qualitatively. Consider first the wheel-speed curves in Fig. 7(a). When wheel speed only is changed, the variation of temperature, time, concentration, and pressure will be somewhat as shown in Fig. 11 (see foregoing items 1 to 4). The influence of pressure and concentration will be relatively small and may be ignored. The extent of welding will then be determined by the more important temperature and time factors, and we should expect the life curve to have an optimum as shown in Fig. 11(e) if wear is the predominant action. However, as the value of V is decreased, t will increase and a value will be reached at which entire grains will be forced from the wheel as a result of the load per grain becoming excessive. This will alter the life curve as shown by the dotted curve in Fig. 11(e).

The speed corresponding to optimum point A will depend upon the welding and strength characteristics of the metal-abrasive combination as well as upon the thermal properties of the work and abrasive. We should expect point A to move to the left whenever greater temperatures at the grit-chip interface are involved. For example, maximum point A should occur at a lower speed for titanium than for steel when both are ground with the same abrasive, inasmuch as the temperatures will be much greater in the case of titanium. Similarly, we should expect point A to lie farther to the right for silicon carbide than for aluminum oxide in view of the fact that the quantity ($k_3\rho_3 c_3$) for silicon carbide is appreciably greater than that for aluminum oxide. The data in Fig. 7(a) are in good qualitative agreement with the foregoing picture. The fact that the optimum speed for weaker Ti 75A is greater than that for stronger RC 130B may be explained by the fact that the temperature in grinding RC 130B will be greater than that arising when Ti 75A is ground.

From the energy per unit-volume u-curve shown in Fig. 10 it is

evident that titanium exhibits the same general type of curve as that for the steel shown in Fig. 4 in the region between t_1 and t_2,

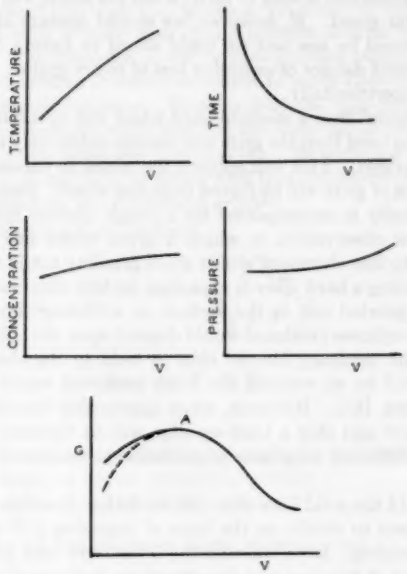

FIG. 11 QUALITATIVE EXPLANATION OF WHEEL WEAR-VELOCITY CURVES

where t_1 is the grit depth of cut at which the chip is so small that rubbing between grit and specimen becomes predominant and t_2 is the grit depth at which the grinding energy drops suddenly. However, the magnitudes of t_1 and t_2 appear to be greater in the case of titanium than for steel. This appears to be due to the tendency for the inhomogeneities present in titanium to have an inherently greater spacing than those present in steel. This characteristic of titanium is also evident in turning and other cutting operations involving large chips in the form of a greater tendency to deform inhomogeneously and the increased tendency to produce discontinuous chips.

The magnitude of u in the horizontal region is seen to be about 6×10^6 in-lb/cu in. for titanium but about twice this value for steel, Figs. 4 and 10. In grinding operations the total energy per unit volume u is divided about equally between shear energy per unit volume u_s and friction energy per unit volume u_f. Furthermore, the shear energy per unit volume is related to the shear stress on the shear plane τ, and the strain in the chip γ, as follows

$$u_s = \frac{u}{2} = \tau\gamma \quad \ldots\ldots\ldots\ldots\ldots\ldots [21]$$

Since the strain in a grinding chip is about 3 we have from Equation [21]

$$\tau \simeq \frac{u}{6} \quad \ldots\ldots\ldots\ldots\ldots\ldots [22]$$

From this equation and the previously mentioned values of u the values of τ to be expected on the shear plane when cutting in the horizontal region of the u-versus-t curve will be

$$\text{For steel:} \quad \tau_{max} = \frac{12 \times 10^6}{6} = 2 \times 10^6 \text{ psi}$$

$$\text{For titanium:} \quad \tau_{max} = \frac{6 \times 10^6}{6} = 1 \times 10^6 \text{ psi}$$

In an earlier paper[3] it is shown that the theoretical strength of a metal (the shear stress that a specimen possessing no lattice imperfections should exhibit) might be expected to be about

$$\tau_{max} = \frac{G}{2\pi} \text{ psi} \quad \ldots\ldots\ldots\ldots\ldots\ldots [23]$$

where G is the shear modulus of the metal. For steel the value of G is about 11.5×10^6 psi and hence τ_{max} is seen to be 1.83×10^6 psi from Equation [23]. For titanium alloys G is approximately 6×10^6 psi and hence τ_{max} should be expected to be 0.95×10^6 psi. These values are seen to be in good agreement with those computed from Equation [22] and this might be considered to represent additional confirmation of the concept expressed in footnote 3 that the horizontal region of the u-versus-t curve corresponds to the cutting of specimens that are so small as to have a perfect lattice arrangement without imperfections throughout their volume.

Owing to the fact that t_1 appears to be greater for titanium than steel there is real danger of operating in the region of very high u to the left of t_1 unless the cutting conditions are adjusted to give large values of t. Normally with steel, values of t to the left of t_1 are involved only in internal grinding operations in which t is unusually small, i.e., during spark out. In grinding titanium the chip depth of cut t should be made unusually large. This requirement is satisfied automatically when the wheel speed is decreased from the conventional 6000 fpm to about 2000 fpm and other operating variables are maintained at conventional values for steel.

Let us next consider the importance of changing the table speed when grinding titanium at about 2000 fpm. In Fig. 12 the expected variation in temperature, time, concentration, and pressure with a change in table speed v is shown. From these characteristics it is evident that less wear should be expected from all points of view as the value of v increases. This would suggest a life curve in which G increases monatomically with increased v. However, as v is increased, t also will increase, and a point eventually will be reached beyond which entire grains will become displaced from the wheel as a result of the force per grit becoming greater than the average grit can withstand. The value of G will then decrease with increased t. From these two considerations we should expect the general life curve to exhibit an optimum as shown in Fig. 12(c). The optimum point A should be expected to lie farther to the left as the strength of the alloy cut increases or the effectiveness of the cutting fluid used decreases. These observations are seen to be in general agreement with the curves of Fig. 7(b) where the optimum of curve 1 is obviously to the left of curve 2 which corresponds to an identical test with more effective fluid.

The cases where wheel depth of cut d and axial feed d_a are varied may be analyzed in a similar manner and when this is done optimum values are similarly found. These results are also in general agreement with Fig. 7.

In the test data for different abrasive materials it was found that the 38A, 32A, and AA types of aluminum oxide were superior to other varieties investigated. These particular abrasive materials contain many small imperfections so that it is possible for very small portions to chip away when a strong bond is established between chip and tool. This action is represented in Fig. 13 where the cross-hatched portion of the abrasive is that which is chipped away when the forces between chip and grit reach high enough values as a result of the dulling of the cutting point and simultaneous increase in the weld area. The major difference be-

tween the white friable, 38A, AA, and light-gray 32A abrasive particles and other aluminum-oxide types appears to lie in the greater number and hence smaller mean spacing of imperfections in the case of the 38A, AA, and 32A materials.

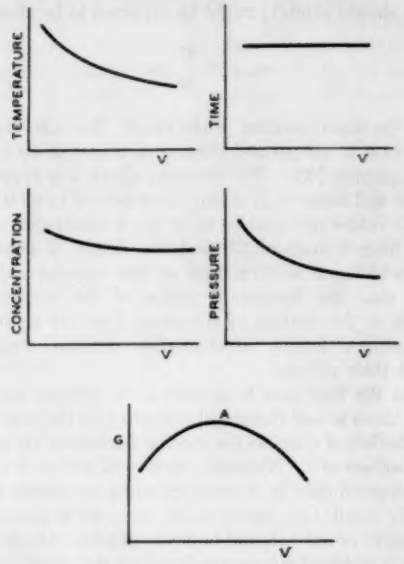

FIG. 12 QUALITATIVE EXPLANATION OF WHEEL WEAR-TABLE SPEED CURVES

The reason that aluminum oxide is superior to silicon carbide in grinding titanium alloys undoubtedly is due to the greater tendency for titanium to react with SiC than Al_2O_3. It has been explained already that the reason the optimum speed for silicon carbide is greater than that for aluminum oxide lies in the fact that silicon carbide has a far higher value for ($k\rho c$) than aluminum oxide.

There are two important considerations with regard to grain size. The maximum force that a single grain can withstand, and hence the maximum value of t that can be used without loss of entire grains, varies directly with the grain size. Furthermore, the mean force required to cause a grain to penetrate the surface prior to removing the chip will increase with grain size. Thus there should be an optimum grain size corresponding to a value of t dictated by other considerations. If the grain size is smaller

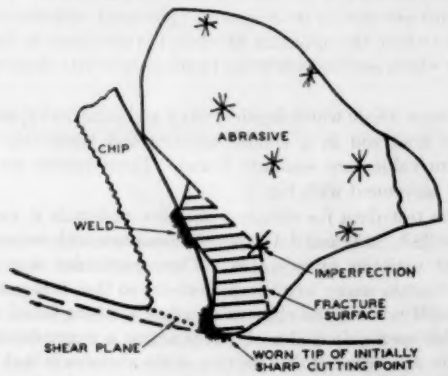

FIG. 13 MANNER IN WHICH PORTIONS OF ABRASIVE GRAINS MAY FRACTURE AND LEAVE SYSTEM AS RESULT OF ADHESION BETWEEN CHIP AND ABRASIVE GRAIN

than this optimum there will be a tendency for entire grains to leave the wheel, while on the other hand, if the grain size is greater than the optimum, the force to penetrate will be excessive. The optimum grain size is seen to be 60 when the wheel was operating at optimum speed. If, however, we should operate at a higher speed, t would be less and we could afford to have a finer-grain wheel without danger of excessive loss of entire grains. This was verified experimentally.

It was found that a medium-hard wheel was optimum. If the wheel is too hard then the grits will become excessively dull before being dislodged. This will subject the wheel to excessive stress and clumps of grits will be forced from the wheel. Such chipping action usually is accompanied by a rough chatter finish. The paradoxical observation in which a given wheel has a greater tendency to lose clumps of grains when grinding a soft alloy than when grinding a hard alloy is explained by this observation.

It was pointed out in the section on surface-grinding theory that the roughness produced would depend upon the chip depth of cut and the tendency for the chip to weld to the abrasive. If there should be no welding the finish produced would be given by Equation [13]. However, when appreciable bonding occurs between grit and chip a built-up edge will be obtained that will produce additional roughness proportional to the size of the built-up edge.

In Fig. 14 the solid lines show the variation of surface finish we might expect to obtain on the basis of Equation [13] in the absence of welding. If we consider the G-factor to vary inversely as the amount of bonding and the size of the built-up edge, we can sketch the resultant surface-finish curves to be expected by making the distance between the solid and dotted curves inversely proportional to the G-factors from Fig. 7. These resultant curves are seen to be in good qualitative agreement with those of Fig. 8 and it is evident that the built-up edge plays a very significant role in determining the finish that is produced in grinding titanium alloys. The role of the built-up edge is, in fact, so important in titanium grinding that the surface roughness varies directly with the rate of wear of the grinding wheel.

In Fig. 7 a considerable variation in results is evident with different grinding fluids. The role of the grinding fluid will not be discussed here but will be treated in a separate paper.

OTHER GRINDING OPERATIONS

The results that have been obtained already for surface grind-

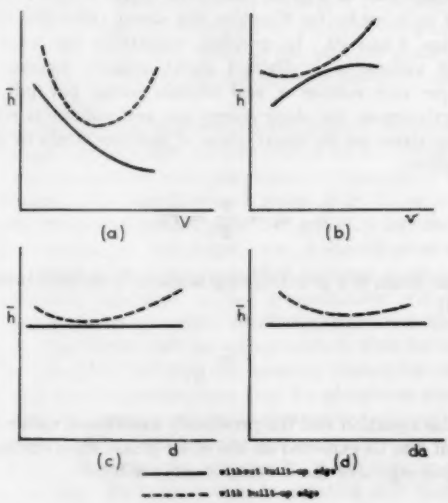

FIG. 14 VARIATION OF SURFACE FINISH DUE TO GRINDING GEOMETRY AND BUILT-UP EDGE

ing may be applied readily to other grinding operations, provided differences in geometry are taken into account. Let us first consider how this may be done for a cylindrical-grinding operation. A good wheel in surface grinding was found to be 32A60-L5-VBE, and such a wheel also should perform well in cylindrical-grinding. The diameter of the surface-grinding wheel was 8 in. but we will assume it more convenient to use a 12-in-diam wheel on our cylindrical grinder. In order that the chip-abrasive temperature be the same when grinding the same metal we need only keep V and l the same, see Equation [8]. In surface grinding we found the best speed to be about 2000 fpm and therefore we shall use this speed on the cylindrical grinder.

From Equation [15] we have

$$l_{\text{cyl grinder}} = \sqrt{\frac{12d_c}{1 + \frac{12}{D_W}}}$$

$$l_{\text{sur grinder}} = \sqrt{8d_s}$$

where

D_W = diameter of workpiece to be ground cylindrically
d_c = depth of cut on cylindrical grinder
d_s = depth of cut on surface grinder

If these two arc lengths are to be the same we have

$$d_c = \frac{2}{3}\left(1 + \frac{12}{D_W}\right) d_s$$

Or, if the work diameter to be cylindrically ground is 4 in.

$$d_c = \frac{8}{3}\, d_s$$

Since in surface grinding it was found advisable to make d_s = 0.001 in., we shall here make d_c 0.0027 in.

From Equation [19] and the fact that we are using the same wheel it is evident that if

$$(vd)_{\text{cyl}} = (vd)_{\text{sur}}$$

then the chip depth of cut t will be the same for the two operations. In surface grinding it was found advisable to make v about 300 ipm and therefore, v_{cyl} should be about 300 ÷ 2.7 = 110 ipm. In surface grinding it was found convenient to make the axial feed 0.05 ipp. If we now require the cross section removed in cylindrical and surface grinding to be the same we have for cylindrical grinding

$$d_a = \frac{0.05}{2.7} = 0.018 \text{ ipr}$$

In the foregoing procedure we have made all cylindrical-grinding quantities equivalent to those for optimum surface grinding, and we should therefore find these cylindrical-grinding operating conditions also to be optimum. The results of the foregoing analysis are summarized for convenience in Table 3.

These recommended conditions for cylindrical grinding of titanium alloys are seen to involve unusually low values of wheel speed and work speed. If an increased production rate is required d_a may be doubled with little loss of life conditions. The surface finish produced under these conditions also should be good. As we have seen in surface grinding, the value of chip depth of cut obtaining in this case is sufficiently small to provide good finish, and the best finish possible for a given value of t is obtained under conditions to give maximum wheel life.

Unfortunately, a cylindrical-grinding machine was not available that could be operated with variable wheel speed. However, two wheel speeds lower than the usual value of 6000 fpm were provided by sets of pulleys. Wheel-life data obtained in this manner are shown plotted against work speed in Fig. 15 under a variety of operating conditions. From these data the following is evident:

1 The same type of abrasive that gave best results in surface grinding was found best in cylindrical grinding.
2 Wheel life was better at 2000 fpm than at 3200 fpm.
3 The best work speed when cylindrical grinding at 2000 fpm was very low, being less than 35 fpm.

TABLE 3 PREDICTED OPTIMUM OPERATING CONDITIONS FOR CYLINDRICALLY GRINDING TITANIUM ALLOYS

Quantity	Surface Grinding	Cylindrical Grinding
Wheel Speed, V, fpm	2000	2000
Depth of cut d, in	0.0010	0.0027
Feed rate, v, ipm	300	110
Axial feed, d_a in/pass (or ipr)	0.050	0.018
Wheel diameter D, in	8	12
Work diameter, D_w, in	∞	4

These results are seen to be in general agreement with the foregoing conditions predicted from surface-grinding results.

The centerless-grinding operation is merely a special type of cylindrical grinding, and for each cylindrical-grinding variable there is a corresponding quantity in centerless grinding. For optimum performance the centerless-grinding variables should be determined from the optimum surface-grinding conditions using the method employed to obtain Table 3.

The internal-grinding operation may be treated in a similar manner.

While all grinding operations involving a cross-feed have been found to give best results at wheel speeds in the vicinity of 2000 fpm, when grinding titanium alloys, those operations in which the work is not fed across the wheel give best results at higher speeds. Thus titanium alloys are best snagged at speeds in the vicinity

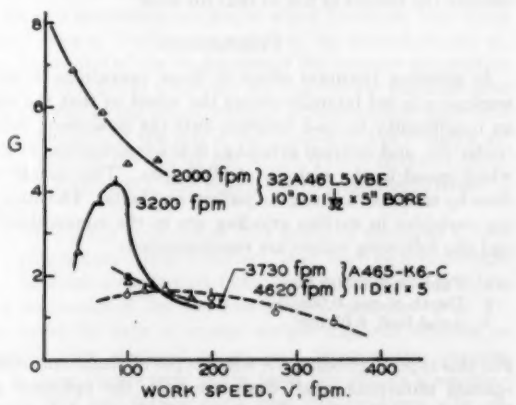

FIG. 15 VARIATION OF GRINDING FACTOR G, WITH WORK SPEED IN CYLINDRICAL GRINDING WITH DIFFERENT GRINDING WHEELS AND AT DIFFERENT GRINDING SPEEDS
(Work material, RC 130B; depth of cut d, 0.0005 in.; axial feed d_a, 0.050 ipr; work diameter D_w, 2 in.; fluid, 5 per cent $NaNO_3$.)

of 7000 to 9000 fpm. Similarly, cut-off wheels should be operated at speeds in the same vicinity. In these cases the same spot on the workpiece is ground continuously without chance to cool

periodically as in the case of cylindrical or surface grinding. This causes the ambient workpiece temperature to become unusually high which in turn causes a decrease in the resistance the metal offers to being cut since titanium has an unusual tendency toward decreased strength at elevated temperatures.

Safety Considerations

Attempts to ignite chips of different size with a torch revealed that while grinding chips ignite more easily than larger chips, it takes a very intense source of heat to get them to burn. Combustible cutting oil present in ordinary steel chips would appear to be far easier to ignite than a group of dry titanium chips.

In another series of tests an electric furnace was used to determine the relative temperatures at which titanium and magnesium chips could be ignited. In these tests the temperature of the furnace was increased slowly until the chips burst into flame. The titanium chips were found to ignite in air at an average temperature of 1140 F while similar magnesium chips were found to burn at 1030 F. No significant difference was observed in combustibility of different titanium alloys.

Some experiments were made to determine the best way to extinguish a titanium fire in grinding chips. However, no good method was ascertained. While a commercial sodium-chloride-base fire-extinguishing powder caused the fire at the surface of the chips to be extinguished, the fire still continued beneath the surface until all chips were consumed.

There appears to be no physiological hazard associated with titanium alloys. The literature contains no clear evidence of any adverse effects on the health of persons engaged in the fabrication of titanium alloys.

In summary, it might be stated that titanium alloys present little danger and what little danger there is lies in the limited combustibility of the material. While it is not nearly as combustible as magnesium, it would be wise to exercise reasonable precaution and not allow large quantities of chips to accumulate on or about machine tools. This is particularly true of grinding chips, and those that are apt to be saturated with oil are slightly more undesirable. The use of water-base cutting fluids eliminates the little danger there is of having a fire ignite in titanium grinding chips and the adoption of lower grinding-wheel speeds further reduces the hazard of fire to that for steel.

Conclusions

In grinding titanium alloys in those operations in which the workpiece is fed laterally across the wheel so that the metal has an opportunity to cool between cuts (as in surface, cylindrical, centerless, and internal grinding) it is advantageous to lower the wheel speed to the vicinity of 2000 fpm. This usually may be done by means of a change of pulleys and belts. The other operating variables in surface grinding are in the conventional range, and the following values are recommended:

1 Table speed, 300 ipm
2 Depth of cut, 0.001 in.
3 Axial feed, 0.05 ipp

For this type of grinding the white types of aluminum oxide which contain numerous small flaws are best, the optimum grit size being about 60. A medium-hard wheel (about L grade) with medium spacing should be used. Wheels with vitrified bond have been found satisfactory. A wheel having the designation AA-60-L8-V or the equivalent will give good results.

Water-base cutting fluids containing ionizable salts of the alkali and heavy metals give improved grinding performance. Under these conditions wheel life will be equivalent to that used in grinding hard steel and surface finish will be as good as can be obtained in grinding steels under conventional conditions.

While it may appear on first thought that a decrease of cutting speed might result in a decreased production rate or an increase in surface roughness, this is not true. The production rate is independent of wheel speed and depends only on the table speed and axial feed which are still maintained in the conventional range. While a decrease in wheel speed will cause the chip depth of cut to increase, the surface finish does not vary with this quantity alone but also varies with the size of the built-up edge that results from welding between chip and tool. In fact, the influence of the decreased build-up with decreased wheel speed causes a greater effect upon surface finish than the accompanying increase in chip depth of cut. The net effect is therefore an improvement in surface finish with decreased wheel speed. The best finish in all cases has been found under conditions that provide the lowest rate of wheel wear and not under conditions to give minimum chip depth of cut.

In cylindrical and centerless grinding, the wheel speed also should be about 2000 fpm and the other operating variables adjusted to correspond to those recommended for surface grinding by following the procedure used in conjunction with the formulation of Table 3. This calls for an unusually low work speed but corresponding greater radial depth of cut. The same sort of wheel and fluid that has been recommended for surface grinding should be used in internal and in centerless grinding.

There is little difference in the grindability of the several titanium alloys tested in this investigation. The soft Ti 75A alloy does give somewhat better wheel life than the harder alloys, however.

In those processes in which the wheel grinds continuously in one region of the workpiece such as in the snagging and cut-off operations, higher cutting speeds are called for. For example, good results were obtained in the cut-off operation with a silicon-carbide wheel of 60-grain size when operating at 7000 fpm using a water solution of sodium nitrite.

While titanium alloys do not present an undue industrial hazard it is advisable to exercise good housekeeping practice and not allow the chips to accumulate on or about the machines. The use of a water-base cutting fluid is recommended as another safeguard against fire in addition to offering the best means for discouraging wheel wear and at the same time promoting improved surface finish.

Acknowledgment

This paper is based upon work performed by the Machine Tool Laboratory at the Massachusetts Institute of Technology under Contract No. DA-19-020-ORD-835 for the Ordnance Corps, U. S. Army, with technical supervision by the Watertown Arsenal Laboratory.

Discussion

W. E. Fraser.[7] The authors have presented an excellent explanation of the reasons why titanium and its alloys cannot be ground in the same manner as conventional materials. It does much to rationalize the entirely different approach to grinding required by this material.

Since the aircraft industry at this time has been the principal user of titanium, the writer wishes to discuss this paper from an aircraft-engine-manufacturing viewpoint.

His company was required to obtain an interim solution to many manufacturing problems in the use of titanium, one of most difficult being the grinding of this material.

Similar reduced-speed surface-grinding tests were conducted by us on a much smaller scale and, with a similar set of operating

[7] Metal Cutting Specialist, Aircraft Accessory Turbine Department, General Electric Company, Lynn, Mass.

conditions, it was our experience that at least 0.020-in. stock removal in 0.001-in. increments was necessary to condition or break in a grinding wheel properly before measurements could be taken to obtain consistent wheel-life data.

Our tests were conducted only on Ti 150A material, but it is felt that a similar break-in period would be required on test-grinding any titanium alloy and that an insufficient break-in period would introduce an error in G-ratio calculations.

The authors' inference that titanium alloys show no greater tendency to develop microcracks than hardened alloy steels might be qualified in that we feel this is true only at reduced wheel speed.

In certain cases when it became necessary for us to grind titanium parts at standard speeds, it was very difficult to eliminate burning and resultant cracking. A peculiar characteristic of this cracking was that it sometimes would not develop for as long as 24 hr and when it did, it was very difficult to observe with the naked eye. A 1-min etch with 10 per cent hydrofluoric acid by volume of the area questioned would permit proper inspection.

This cracking was more pronounced when aluminum-oxide wheels were used and could be minimized by the careful use of silicon carbide wheels.

Exceptions must be taken with the authors' Safety Consideration, in that we feel that a definite fire hazard exists when titanium is ground at standard wheel speeds, using conventional grinding oils. The writer has had experience with certain oil vapors igniting, even when titanium is ground at reduced speed and it is our practice to discourage the use of oils on all titanium grinding until more is known about this subject.

The finishes obtained by the authors in their test work were exceptionally good, much better than we were able to obtain in our test and production work. Finishes obtained in our work were approximately 35 to 40 microinches finish.

A finish characteristic we observed on this material, more noticeable on the pure metal than on the alloy, was its tendency to smear and fishtail when ground even at reduced grinding-wheel speeds.

This has led us to consider using single-point-tool techniques, such as precision boring, when possible. The finishes obtained were sometimes as good, if not better, than those obtained when grinding.

In general, our experience in cylindrical and internal-grinding titanium alloys is similar to that of the authors. It might be mentioned that we have found it advantageous to leave less stock for finish-grinding on these operations. If our setup will permit it, 0.005 to 0.007 in. is left on for finish-grinding instead of the conventional 0.010 to 0.015 in., which greatly reduces the problem of cylindrical and internal or any grinding operation on this material.

R. S. Hahn.[8] The authors have presented some interesting data which should be very helpful to those engaged in grinding titanium alloys. Of especial interest are the curves given in Fig. 7. Fig. 7(a) shows an optimum wheel speed when considering the amount of wheel wear. This factor, G, is sometimes of interest in production grinding. However, it would appear that there are certain types of production-grinding operations in which the wheel wear is a minor expense compared to the time required to grind a given part, i.e., the production rate. Here one is interested in the metal removal per unit time. At low wheel speeds the rate of metal removal naturally would be low and likewise the rate of dulling of the wheel. At high wheel speeds the rate of metal removal would be high for a sharp freshly dressed wheel but would quickly drop due to rapid dulling, resulting in an average over-all rate of metal removal for the workpiece which again may be low. At some intermediate wheel speed one would expect an optimum.

It would be interesting if the authors would supply data showing the average rate of metal removal versus wheel speed. Presumably this would depend also on the quantity of work material removed. In view of the foregoing, the optimum wheel speed, when the production rate is of primary concern, may not be 2000 fpm. Furthermore, it may vary with the amount of stock to be removed and the size of wheel.

J. L. Jessup.[9] The writer wishes to compliment the authors on their concise explanation of this complex subject.

Whatever disagreement the writer has found between the results of work by his group and the authors' conclusions probably can be resolved around the fact that the work done by the former has been on form grinding, which, by the nature of the wheel shape, will require a little more consideration of the forces involved, the chip shape, grit geometry, and so on, than does the grinding with a cylindrical surface on the wheel.

Some confirmation of the fact that the heat developed on the ground surface is relatively constant and depends to some extent on the rate of wheel breakdown is shown in Fig. 16 of this discussion. These macros were made of the cross sections of the root forms on compressor turbine blades. They were ground on a two-wheel root-form grinder where the speed of the wheels could be changed and, for the purpose of this test, the speed of the right-hand wheel was one half that of the left-hand wheel. This one variation was the only one made in an otherwise normal grinding cycle. Note the narrowing of the burn line on the left-hand side near the concave portion of the form. This area of the wheel broke down at the highest rate and therefore showed a considerable reduction in the heat generated.

Breakdown is undesirable at any time in form-grinding, and is particularly so in the highly accurate size control required of these parts—hence one of the apparent disagreements in our work and that of the authors. We found that wheels of "R," "S," and "T" hardness worked very well on form-grinding when used with the proper coolants.

In order to understand the reasons for the apparent discrepancy in the two recommendations for wheel hardness, look again at the mechanics of the forces applied on an individual grit at, let us say, the center of the 10-deg side of the concave vee-portion of the form. This grit is subjected not only to the cutting forces normal to the axis of the wheel, but also to very high compressive stresses (particularly if the grit is dull) owing to the wedging action of the walls of the vee as the wheel travels between them. In order to hold the grit in the wheel, harder bonds were found to be necessary.

Some evidence has been found that grinding produces a very shallow highly tensile-stressed surface that may be a contributing cause of some aircraft-part failures even when the grinding has been accomplished by the best-known methods. Fig. 17, herewith, shows the type of ground surface that was obtained on blades which were destined to go into experimental engines. A series of these blades were taken from lots run on a semiproduction schedule and fatigue tests were run on them. In all, about 50 blades were run and the results of these tests are shown in Fig. 18.

Note that in the "as-ground" condition, the endurance limit for a fatigue life of 10-million cycles of reversed stress was about 40,000 psi. Observe also that this is about 57 per cent of the value of the broached blades.

[8] Consulting Engineer, The Heald Machine Company, Worcester, Mass. Mem. ASME.

[9] Project Engineer in Charge, Machinery Experimental Department, Ex-Cell-O Corp., Detroit, Mich.

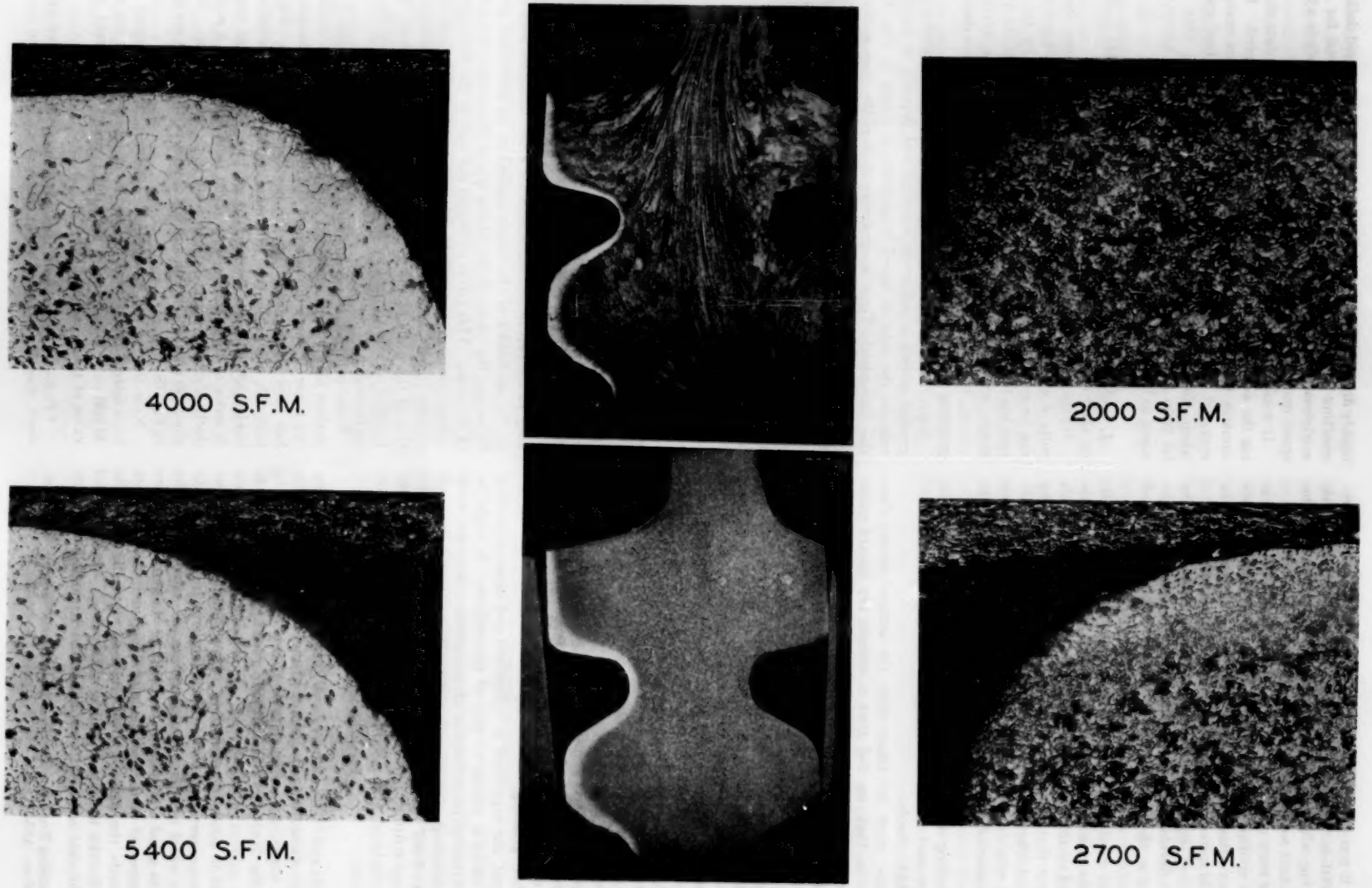

FIG. 16 EFFECT OF WHEEL SPEED ON FORM-GRINDING TITANIUM ALLOYS
(Coolant: Ucon H-660.)

A group of the blades, taken from the production line, was shotpeened according to the AMS-2430 specification. The results of the fatigue tests of these blades was startling to say the least. The entire series showed an endurance limit of 60,000 psi for the required 10-million cycles.

We had noted that all the fatigue failures that had occurred below 70,000 psi were airfoil failures. It was felt that this indication showed the need for some form of surface-working on the airfoil section, since it was finished by belt-grinding. Of course, shotpeening could not be used here since a finish of 15 microinches rms was specified on these surfaces. The type of finishing method finally agreed upon was vapor-honing with a grit mixture that would produce a finish just under the 15-microinch requirement.

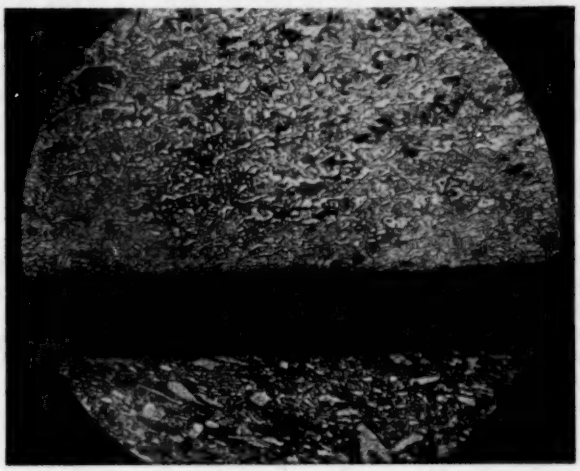

FIG. 17 TYPICAL GROUND SURFACE ON EXPERIMENTAL ENGINE BLADES

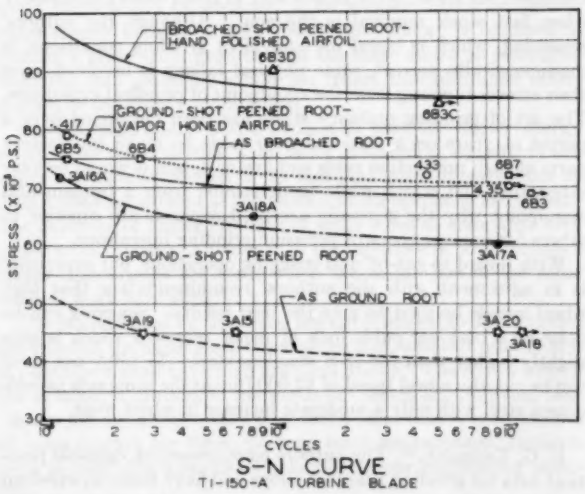

FIG. 18 *S-N* CURVE FOR TI 150A TURBINE BLADE

Note the improved endurance limit of these blades. In the interest of clarity not all the 50 test blades are shown on the *S-N* curve. One blade, in particular, ran a total of 20,400,000 cycles at a stress in excess of 70,000 psi, on step tests, before failure at 87,000 psi. This blade is out of the ordinary perhaps, but it does show that the material can and will exhibit a very high endurance limit if it is handled properly.

O. P. LOWREY.[10] The best proof or verification of the excellent work done by the authors on the subject of titanium grinding will, of course, come from application of the data presented in the subject paper to large production operations where highest quality and production economics are critical controlling factors.

Based on early contact with Dr. L. P. Tarasov of the Norton Company, and Prof. M. C. Shaw, a Methods Development Project was set up at Pratt & Whitney Aircraft to verify initial research data and incorporate its use in feasible production operations. Resultant current production operations on our principal titanium material, Ti 150A, is good testimony to the accuracy of the subject paper. Two typical production operations, at Pratt & Whitney Aircraft, the setup being based on information in the paper, are as follows:

1 Material—Ti 150A
Part—10-in-long compressor blade
Operation—to grind 0.0025 in. off per blade side, leaving a finish of 25 rms
Machine—Pratt & Whitney airfoil belt grinder
Belt—50-grit aluminum oxide, $^5/_8$ in. × 90 in.
Belt speed—2250 sfpm
Coolant—Straight chlorinated oil, viscosity 200 sec, 300°F flash point
Feed—0.062 in. feed per revolution
Work speed—150 ipm (average)

2 Material—Ti 150A
Part—20-in-diam spacer—a thin-wall section, very flexible and difficult to grind with a total run out tolerance of ±0.0005 in. on ground flanges when in free state
Finish—20 rms
Wheel speed—1750 sfpm
Work speed—200 sfpm
Depth of cut—0.0002 in. per pass
Traverse—4.2 ipm
Cross-feed—0.088 in. per revolution of work
Wheel—32A60L5VBE
Coolant—Half molar sodium-nitrite solution

It will be noted that some compromises were made with Massachusetts Institute of Technology experimental data in the interest of production feasibility—such compromises are desirably indicated in the paper.

In the examples given, and on the many other jobs set up in production, good finish, as stated in the paper, has been the key index to good wheel life and other favorable operating conditions, as well as indicating a minimum part damage condition. Owing to the unstable nature of the original raw titanium forgings used in machining, any serious deviations from the data recommended by the authors tended to magnify the original material faults, while closer adherence to the "best practice methods" allowed meeting of the desired physical requirements in the finished parts. Therefore, early in our experience it was recognized, as we gained control over proper application of machining conditions, that material variations were the cause of production problems initially blamed on such factors as "grinding damage." Such experience indicates the importance of strong laboratory control of the raw stock as a corollary to good production development practices.

It is unfortunate that coolant data on grinding were not available at the time of publication of this paper. Our coolant work indicated that sodium nitrite was the best of the ionizable salts owing to its high solubility. Sodium nitrite could be used in concentrations of 5 to 9 times the concentration of barium nitrate, for an example.

[10] Supervisor, Methods Development, Production Engineering, Pratt & Whitney Aircraft, Division of United Aircraft Corporation, East Hartford, Conn.

L. P. TARASOV.[11] This paper confirms what had been discovered previously about the highly unorthodox grinding characteristics of titanium and its alloys, but it goes further in providing force data and in furnishing a more detailed explanation of the observed variation of G with wheel and table speed. However, although some of the results are in satisfactory agreement with those obtained by the writer, others are not and the question arises as to the possible origins of such discrepancies.

For example, we have not found any substantial difference between the grinding factors for RC-130-B and Ti 150A at a wheel speed of 1600 fpm such as is indicated by curves 2 and 3 in Fig. 7(a). The only significant difference in the grinding conditions was that we did considerably more grinding in each test run in order to get greater accuracy in the wheel-wear measurements. With the total downfeed limited to 0.020 in. as used by the authors, the wheel wear on the diameter must have been only about 0.4×10^{-3} in. for $G = 40$ and 0.8×10^{-3} in. for $G = 20$. In these circumstances, it would not require much error in wheel-diameter measurement or much unavoidable fluctuation in the wheel wear itself to lead to considerable variation in the grinding factor. Another possibility worth mentioning is that Ti 150A was apparently not ground at speeds between 1000 and 2000 fpm, so that a sharp peak between these speeds could have been missed completely.

It is true that the authors state there was little difference in the grindability but a superficial examination of the curves may lead the hasty reader to the opposite conclusion.

In working with Ti 150A, we have observed repeatedly a sharp drop in G when either the unit downfeed or the unit cross-feed was increased. Curve 3 in Fig. 7(c) does behave in this fashion but the same curve in Fig. 7(d) shows very little effect of increased cross feed. In view of such discrepancies there is definite need for an accurate redetermination of the effect upon G of each of the variables of Fig. 7 for the principal titanium alloys. Such a study would show whether the curves do cross over in the manner indicated by the authors and whether the shapes of the curves are affected so markedly by the type of alloy ground. Incidentally, these curves do not bear out the statement made in the text that Ti 75A gave somewhat better wheel life (higher G) than did the harder alloys.

The authors do not state whether any pregrinding was done in order to break in the wheel to an equilibrium condition after dressing. Experience has shown that this is a vital step in obtaining significant results, all the more so when the total amount of grinding done is relatively small.

The authors repeatedly refer to wheel depth of cut when actually downfeed is meant. The two differ by the radial wheel wear, and when this is large, the two are significantly different. The use of the wrong term leads to a certain amount of confusion, as when the statement is made that "0.02 in. was removed from the surface by taking off successive layers each 0.001 in. thick." Taken literally, this would mean that the unit down-feed would be adjusted beforehand for each test run to compensate for the as yet unknown wheel wear. Presumably, the authors actually used a total downfeed of 0.02 in. so that the amount of material removed was smaller as determined by the wheel wear. This distinction between feed and depth of cut is an important one to keep in mind when dealing with low-grindability materials. For example, grinding costs involve volumetric rate of cut, not volumetric rate of feed, and if the two terms are used indiscriminately, it is easy to make the wrong calculation.

We have never observed any cracking when precision-grinding titanium alloys but have had considerable difficulty with cracking in abrasive cutoff tests, where this occurred in such fashion that it could be attributed only to large variations in the quality of the bar stock. As generally happens, the problem of surface damage is a more serious one when actual parts are ground in the shop than when experimental work is done on small laboratory test samples.

The surface-roughness values reported by the authors are far lower than we have been able to obtain under the same grinding conditions, and our figures seem to be substantiated by industrial experience. A possible clue to the discrepancy is that recent measurements of the same ground titanium surfaces on the authors' profilometer and on three profilometers at the writer's company resulted in considerably higher values on the latter instruments. Our experience indicates that 35 microinches would be a more realistic figure for an alloy like Ti 150A when the unit downfeed is 0.001 in. and the unit cross-feed is 0.050 in., using a suitable aluminum-oxide wheel at 1600 fpm in conjunction with sodium-nitrite solution. Cutting either of the unit feeds in half, or increasing the wheel speed to 2000 fpm, brought the roughness down to about 25 microinches. Only by using a 100-grit wheel dressed for finish-grinding and reducing the unit downfeed to 0.0001 in. were we able to get down to 10 microinches.

Exception must be taken to the authors' tentative recommendations for cylindrical grinding, which are based on conditions found satisfactory for surface grinding. Their method involves a very high infeed and a very low traverse rate, which leads to a volumetric rate of feed of only 0.005 cu in. per min. By using a diametral infeed of 0.0005 in., a traverse rate of 0.3 ipr, a work speed of 55 fpm, a wheel speed of 2000 fpm, and the same type of grinding fluid as used by the authors, we have obtained grinding ratios of 6 or 7 with satisfactory finish and ten times as much stock removal per unit time. A J or K-grade wheel should be used, L being somewhat too hard for our conditions.

The method employed by the authors for deducing suitable cylindrical-grinding conditions on the basis of surface-grinding experience should be equally applicable to ordinary steels, yet it is universally accepted that entirely different conditions, involving a traverse rate per revolution roughly equal to two thirds of the wheel thickness, is the proper way to grind steels cylindrically when fast stock removal is the goal. Although the authors' reasoning, which is based on equivalent grinding conditions, is mathematically correct, some physical fallacy is involved since their answer is wrong from the standpoint of practical experience. The art of grinding ordinary steels has been developed over a period of years on a trial-and-error basis to make satisfactory parts at high production rates and low cost, and it would be very interesting and worth while to determine from a fundamental standpoint why the generally accepted methods are superior to others for various types of precision-grinding operations.

With regard to cut-off and snagging operations, our experience is in agreement with the authors' recommendation that high wheel speeds be used to give the best results. Snagging can be done at a cost per cubic inch of metal removed which is only slightly higher than for 18-8 stainless steel. Ti 150A bar stock can be cut at a wheel speed of 12,000 fpm at the same rate as cold-drawn steel with only a moderate increase in wheel wear.

E. G. THOMSEN.[12] The authors have presented valuable practical data for grinding titanium alloys and have made an excellent analysis of the grinding variables to be considered in grinding these alloys. The conclusion, i.e., of using lowered wheel speeds, rather than conventional speeds, is of particular importance since such departure from practice could not be anticipated when examining the mechanical properties of these alloys.

The analysis leading to the relationships giving the peak tem-

[11] Research and Development Department, Norton Company, Worcester, Mass.

[12] Professor of Mechanical Engineering, University of California, Berkeley, Calif.

perature of the workpiece and grinding wheel should, however, in the opinion of the writer, be accepted only as qualitative in view of the assumptions that were necessary in the derivation. This is because of the heterogeneous composition of the grinding wheel and the fact that each abrasive particle during cutting presents a local infinitesimal heat source. The thermal group $k\rho c$ for the workpiece or for the abrasive particles, however, is probably the correct variable which explains the high tool-tip temperature when grinding dry, even though heat transfer to the ambient temperature has been neglected and the workpiece is treated as an infinite body. When using cutting fluids, however, the workpiece-abrasive particle interfacial temperature is lowered through heat absorption by the fluid. This introduces a local heat-transfer coefficient not included in the analysis by the authors and hence may lead to a different criterion for the peak temperature from that given by the authors. The fact that titanium will bond to the abrasive particles and that it shows a low G-value even when using water as a coolant, as mentioned by the authors, indicates, however, that the tool-point temperature is high and that the thermal group $k\rho c$ may be substantially correct even for indicating peak temperatures under these conditions.

While the comparison of the maximum shearing stress in grinding with the theoretical maximum shearing stress of the material sounds convincing, it should be borne in mind that consideration of workpiece deformation may lead to a somewhat similar result. Referring to Fig. 4 of the paper, it is visualizable that the flat portion of the curve u versus t, and even for larger t, is a region of chip thickness where instability occurs and that the abrasive grains do not remove the chips cleanly but that successive passes are required. One could visualize that an abrasive grain could distort the work surface in the first pass and that the passage of successive grains would remove the work material. This would have the effect of demanding the removal of work material which is in a highly work-hardened state. Hence the energy required to cut a given chip would be that due to distortion of the work surface and also to the removal of a previously highly work-hardened chip. Therefore the calculated specific energy for very small chips would be expected to be greater than with thicker chips merely because greater plastic-flow energy is required to remove a given chip, even though the shear strain as calculated from the chip geometry would not reflect this additional deformation or the energy requirement.

Such considerations would explain in part the higher energy required for metal cutting when using small chips (size effect) and which has been attributed to the fact that fewer imperfections or dislocations are present as the volume of the specimen is reduced.[3] The evidence of higher strength of small wires as compared with larger wires, quoted as evidence in the reference is not conclusive unless comparisons are made when the metals are in the same state of work-hardening.

The points raised by the writer are not intended to detract from the value of the paper since the analysis is of excellent quality and the data presented have high practical utility. The writer merely has in mind to caution, in the words of Gilbert and Sullivan, that "things are not always what they seem," and that it is sometimes of value to look for other, perhaps more conventional, explanations in ascribing anomalous behavior to our engineering materials.

Authors' Closure

The authors wish to acknowledge the valuable remarks of the several discussers. Only a few of the points considered require further comment.

The observation independently made by Messrs. Fraser, Jessup, and Tarasov, that grinding damage can be obtained when grinding titanium alloys at high speeds is well taken. The statement that grinding damage was not experienced with titanium alloys referred to grinding at reduced wheel speeds where the surface temperatures experienced are very much reduced. As Mr. Fraser points out, damage should be expected to be greater with aluminum-oxide wheels than with silicon-carbide wheels at conventional grinding speeds (6000 fpm). This is because ($k\rho c$) for aluminum oxide is less than that for silicon carbide and hence the temperature at the ground surface will be higher for an aluminum-oxide wheel in accordance with Equation [8]. This higher temperature will most likely induce more surface damage.

With regard to Dr. Hahn's question concerning the rate of metal removal at different wheel speeds it should have been emphasized that all comparisons were made on the basis of the same rate of metal removal. When the wheel speed is varied the rate of metal removal does not change unless the table feed (v) is altered. Instead, the size of the individual chips (t) increases. What is recommended in the paper is that titanium alloys be ground at about $^1/_3$ conventional wheel speed (V), but under otherwise conventional conditions, including table feed (v). This will result in the same rate of metal removal but an increase in mean chip size of $\sqrt{3}$ (from Equation [2]). From Equation [13] the increase in the mean peak-to-valley distance $\bar{h}$ (without BUE) would be $(\sqrt{3})^{4/3} = 2.1$. However, the decreased tendency for titanium to form a large built-up edge neutralizes this increased tendency toward surface roughness and one ends up with surfaces that are smoother than those for steel ground under conventional conditions.

The observation made by Dr. Tarasov that the cylindrical grinding conditions recommended for titanium do not agree with those in general use for steel and hence cannot be correct would appear to be open to question. If this argument were extended to surface grinding we would be led to the conclusion that what is recommended for the surface grinding of titanium could not likewise be correct since it differs from proved practice for steel. The need for different grinding conditions for steel and titanium lies in the relative importance of welding and the consequent difference in the rate of wheel wear when grinding the two materials. Dr. Tarasov's suspicion that in Fig. 7(a) the peak values of G might be inaccurate for a total downfeed of 0.020 in., since the diametrical wheel wear would then be only about 0.0004 in., is correct. It should have been stated that whenever the change in wheel diameter was less than 0.001 in. an additional 0.020 in. downfeed or more was used in the determination of G.

The authors concur with Mr. Fraser and Dr. Tarasov that a "break-in" period is necessary in order to obtain reproducible G values. For all tests reported in this paper a break-in of four 0.001 in. downfeeds (0.004 in.) was used before measuring the initial wheel diameter.

As Professor Thomsen correctly points out the equations presented are far closer to being true qualitatively than quantitatively. However, this is of little importance since the absolute values obtained are of little value and are difficult to interpret. As in practically all engineering calculations the qualitative aspects of the results are most useful. For example, what we should really like to know is what variables influence chip size (t) and to what degree. The knowledge that the mean chip size is precisely $^1/_4$ micron is of relatively little value.

Professor Thomsen is qualitatively correct in stating that the specific energy required to produce small chips should be expected to be larger than that required to produce large chips due to subsurface working and differences in strain hardening. These items are given minor consideration in previous discussions of the size effect since they are believed to be small compared with the experimentally observed increases in specific energy. By conventional standards an increase in strength due to strain hardening of 50 per cent is very large indeed for the largest of strains.

If a subsurface layer as great as the layer actually removed in the form of a chip (t) were to be as fully strained as the metal in the chip, the resulting increase in shear energy would be 100 per cent. If these two conditions were assumed to be the only ones to exist we might, therefore, expect an extreme increase in specific shear energy of 150 per cent for grinding chips over turning chips. The observed increase in specific energy in going from turning chips to grinding chips is, however, some 3000 to 4000 per cent. The effects of subsurface working and strain hardening were included in the previous discussions of size effect by assuming a greater amount of friction energy relative to shear energy. By taking the specific friction energy to be twice as large for grinding as for turning (i.e., 100 per cent increase in specific friction energy), it was thought a reasonable allowance had been made for subsurface working and possible additional strain hardening. If there were no increase in strength with decrease in specimen size, then it would be necessary that a layer 30 to 40 times the undeformed chip thickness (t) be as fully deformed as the metal in the chip in order to account for the observed increase in specific energy in going from turning to fine grinding chips.

Working-Stress Criteria for Nuclear Power Plants

By B. F. LANGER,[1] PITTSBURGH, PA.

There are two respects in which strength calculations for nuclear-power-plant components may differ from calculations made for conventional heat-power or process equipment. One is the greater importance of thermal stresses resulting from the generation of heat inside the material of the structure, and the other is the frequent use of unfamiliar materials. In this paper a method is proposed for combining the stresses produced by fluid pressure with those produced by thermal gradients in order to arrive at a practical estimate of the factor of safety in a structure such as a pressure vessel. Because of the relaxation of thermal stress it is possible to show that certain operating conditions are really safe even though a simple addition of pressure stress and thermal stress gives too high a value. A discussion is given of the relative importance in reactor design of such physical properties as ductility, creep, endurance limit, creep-rupture strength, impact strength, and notch sensitivity.

Nomenclature

The following nomenclature is used in the paper:

- ϵ = unit strain
- σ = unidimensional stress
- S = stress intensity of combined stresses as calculated by shear-energy theory
- F = factor of safety
- k = theoretical stress-concentration factor
- q = notch-sensitivity index
- k_f = effective stress-concentration factor
- N = number of cycles (also used as subscript)

Subscripts

- p refers to stress or strain produced by load
- t refers to stress or strain produced by thermal gradient
- o refers to steady component of fluctuating stress
- v refers to variable component of fluctuating stress
- u refers to stress at ultimate strength of material
- e refers to stress at endurance limit of material
- 1,2 refer to principal stresses

Introduction

The design of a piece of apparatus for adequate strength involves much more than just the calculation of a maximum stress and the comparison of this calculated stress with known physical properties. Much has been written on the subject of working stresses and strength theories. Particular mention should be made of the summary by C. R. Soderberg (1).[2]

These methods are of course just as applicable to a nuclear power plant as to any other design problem. In nuclear power plants, however, there are two factors which make re-examination of the problem necessary. One is the great importance of thermal stress resulting from the generation of heat inside the material of the structure and the other is the frequent use of unfamiliar materials. In the construction of a reactor core, properties such as neutron-absorption cross section and corrosion resistance often preclude the use of ordinary structural material. The materials which are allowable are apt to be completely unfamiliar to design engineers and therefore must be studied thoroughly from the standpoint of physical properties such as ductility, creep, endurance limit, notch sensitivity, impact strength, and creep-rupture strength.

Thermal Stress

In a power reactor intense radiation generates heat inside the material of the core and surrounding components, whereas in conventional power and process equipment the heat is applied to one side of a wall and transmitted through it. In a reactor the rate of heat generation can change very rapidly whereas in most conventional equipment the rate of temperature rise is limited by the rate at which fuel can be supplied.

The ASME Boiler Code makes little mention of thermal stress. In Section VIII, Par. UG-22, it does list "The effect of temperature gradients on maximum stress" as one of the loadings to be considered in designing a vessel, but these gradients do not appear directly in the Code formulas for calculating allowable working pressure. The supposition is that the allowable working stresses are sufficiently conservative so that thermal gradients normally expected during operation will not cause trouble. In designing a power reactor, however, one of the first problems which presents itself is the allowable thickness of structural members close to the core, and in the core itself. If these members are too thick, the heat generated in them cannot be removed fast enough and high thermal stresses will result. A conservative approach would be to limit these stresses to the values allowed by the Code for pressure stresses. This method, however, places an unnecessary handicap on the design because high thermal stresses produce plastic flow, which reduces the stresses automatically to safe values. For steady-state conditions, therefore, we could almost ignore thermal stresses, and merely watch to see that the plastic flow does not produce objectionable dimensional changes, strains beyond the ductile limit of the material, or temperatures so high as to damage its metallurgical structure.

What happens, though, during power changes? A metal cannot be stressed back and forth through its yield point too many times without producing fatigue failure. The endurance limit of the material is therefore the best starting point in the search for an allowable working stress. It is the starting point but not the final answer. Published values of endurance limit are obtained from tests using complete stress reversal for millions of cycles. Thermal transients seldom reverse the direction of stress at all, and large power changes may occur thousands of times, but not millions of times during the life of a plant. Therefore the peak calculated thermal stress should not be compared to the known endurance limit of the material. The expected stress range during

[1] Consulting Engineer, Atomic Power Division, Westinghouse Electric Corporation. Mem. ASME.

[2] Numbers in parentheses refer to the Bibliography at the end of the paper.

Contributed by the Power Division and presented at a joint session of the Power and Metals Engineering Divisions, Semi-Annual Meeting, Pittsburgh, Pa., June 20–24, 1954, of The American Society of Mechanical Engineers.

Note: Statements and opinions advanced in papers are to be understood as individual expressions of their authors and not those of the Society. Manuscript received at ASME Headquarters, April 23, 1954. Paper No. 54—SA-59.

power variations should be calculated, and this range used in one of the well-known methods for combining alternating and steady stress (1, 4). The fatigue data used should be taken from the upper branch of the usual diagram of stress versus number of cycles so that credit is taken for the fact that the expected number of cycles is small. To be realistic, account also must be taken of the reduction of stress produced by plastic flow of the material (5).

Stress Range

To visualize the effect of stress range and yielding on a material, let us consider the simple case of a thick-walled ring which is loaded at its inner circumference by a uniformly distributed radial pressure, Fig. 1. This pressure produces hoop stress in the ring which is quite similar to that which occurs in the wall of a pressure vessel. Such a stress never must be allowed to become larger than the yield point of the material since yielding tends to increase rather than decrease the magnitude of the stress.

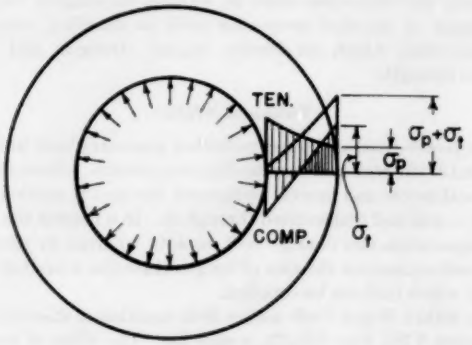

FIG. 1

Now let us suppose that in addition to the radial load, the inner circumference of the ring is heated to a temperature higher than that of the outer circumference. This heating will produce additional hoop tension at the outer circumference and this tension will add directly to the tension from the radial load, provided all stress values are within the yield point. If, however, the sum of the tensions produced by the radial load and by the thermal gradient add up to a value greater than the yield point, the actual total stress at the outer surface of the ring will be less than the sum of the two stresses which would be calculated by conventional methods, since the yielding of the material will tend to relieve the portion of the stress produced by the thermal gradient.

Let

ϵ_p = strain in outer fiber produced by radial load
ϵ_t = strain in outer fiber produced by thermal gradient
σ_p = stress in outer fiber produced by radial load
σ_t = stress in outer fiber produced by thermal gradient
σ_o = steady component of fluctuating stress
σ_v = variable component of fluctuating stress
σ_u = ultimate strength of material
σ_e = endurance limit of material
F = factor of safety

Let us suppose that the temperature of the ring fluctuates between the condition of uniform temperature and one where the inside is hotter than the outside, but the radial load remains constant. If $\sigma_p + \sigma_t$ is less than the yield point of the material, the stress in the outer fiber fluctuates as shown in Fig. 2. This stress history can be separated into a steady and a variable component. The steady component is $\sigma_o = \sigma_p + \sigma_t/2$. The variable component is $\sigma_v = \sigma_t/2$. The possibility of cracking at the outer circumference is tested by plotting this condition on a diagram such as that shown in Fig. 3. In this diagram the steady stress is plotted along

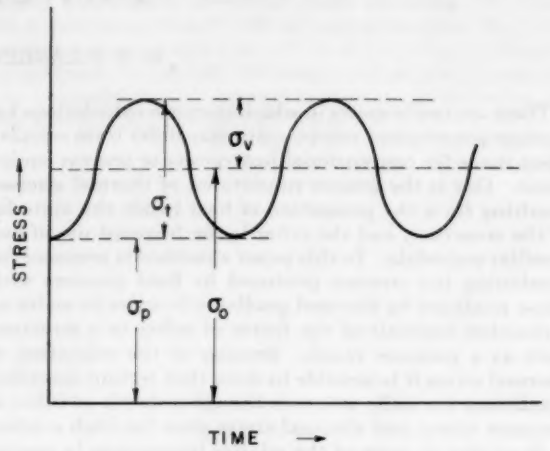

FIG. 2

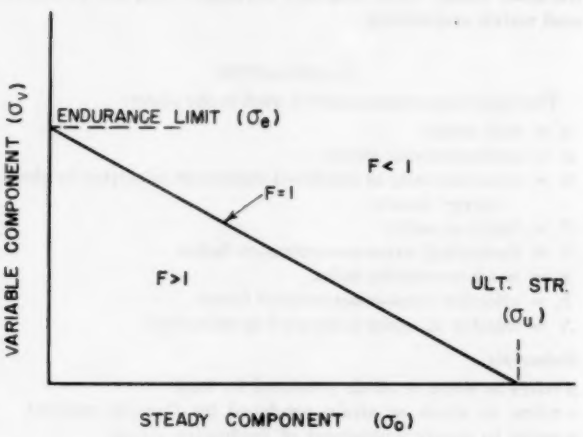

FIG. 3

the horizontal axis and the variable-stress component is plotted along the vertical axis. A straight line joins the points representing the endurance limit on the vertical axis and the ultimate strength of the material on the horizontal axis. If the calculated stress condition falls inside this line the condition is safe, whereas if it falls outside of the line, failure is to be expected. The equation of this line is

$$\frac{\sigma_v}{\sigma_e} + \frac{\sigma_o}{\sigma_u} = 1 \quad \ldots\ldots\ldots\ldots\ldots\ldots [1]$$

Conditions which fall on this line have a factor of safety of unity. The factor of safety F, for a given set of conditions can be calculated from

$$F = \frac{1}{\frac{\sigma_v}{\sigma_e} + \frac{\sigma_o}{\sigma_u}} \quad \ldots\ldots\ldots\ldots\ldots\ldots [2]$$

Case of Hoop Stress Above Yield Point

Let us now consider the case where the addition of the thermal

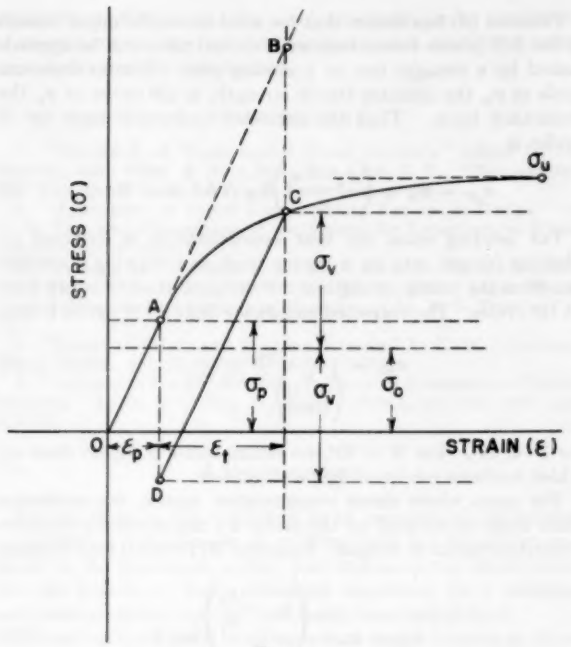

FIG. 4

stress σ_t to the pressure stress σ_p brings the hoop stress in the ring above the yield point of the material. The history of such a case can be traced on a stress-strain diagram for the material such as is shown in Fig. 4. Instead of calculating σ_p and σ_t as stresses, it is now necessary to consider them as unit strains. As the strain increases from ϵ_p to $\epsilon_p + \epsilon_t$, the stress does not continue to increase along the straight line *O-A-B* in this diagram but follows the yielding shown by the curve *O-A-C*. When the temperature drops back to its initial condition the strain decreases again from $\epsilon_p + \epsilon_t$ to ϵ_p. The stress, however, as a result of work hardening of the material, follows the straight line *C-D*. Further temperature cycles cause the stress and strain to fluctuate back and forth along the line *C-D*. Therefore, in calculating the steady and variable components of stress, we must decrease σ_o by an amount corresponding to the distance *B-C* in Fig. 4.

Thermal-Cycling Test

This type of analysis explains some observed phenomena which look unreasonable when less carefully analyzed. One example was a thermal-cycling test on type 347 stainless steel.[3] A thick-walled steel cylinder was heated externally with an induction coil and cooled internally with high-pressure water. The stress on the inside of the tube due to water pressure was 2280 psi. The heating was cycled in such a way that the sum of pressure plus thermal stress on the inside of the tube varied between 17,280 and 80,000 psi when calculated on the assumption that no yielding occurred. The physical properties of the material were:

Ultimate tensile strength, psi	75000
0.2 per cent yield point, psi	30000
Endurance limit, psi	35000

The test was continued for 15,000 cycles with no evidence of cracking. Thus this material survived 15,000 applications of a stress which appeared to be higher than its ultimate strength. When analyzed by the method just described, however, the survival of the test specimen is not surprising. It may be estimated from Equation [8] of this paper that the fatigue limit for 15,000 cycles is about 47,000 psi instead of 35,000 psi. If no yielding were assumed, the steady-stress component σ_o would be 48,640 psi and the alternating component σ_v would be 31,360 psi. The factor of safety would be

$$F = \frac{1}{\frac{48,640}{75,000} + \frac{31,360}{47,000}} = 0.76$$

If yielding is assumed, the steady component drops to about zero and the factor of safety is

$$F = \frac{1}{0 + \frac{31,360}{47,000}} = 1.50$$

Cases of Combined Stresses and Stress Concentrations

In the foregoing discussion a simple system was assumed in which stress occurred in only one dimension and no stress concentration occurred. The same general method can be applied to more complicated situations where combined stresses and stress concentrations must be considered. The following method is proposed as a general procedure for determining the adequacy of an application of this type. In this procedure, principal stresses are combined into a quantity S, called "intensity of stress," in accordance with the shear-energy theory of failure (1, 2), and stress concentration is assumed to affect only σ_v, the fluctuating component of stress:

1 Calculate the principal stresses, σ_1 and σ_2, for the combined thermal and pressure effects, using the smallest thermal gradient which will occur during the operating cycle. Call these $\sigma_{1\,\min}$, $\sigma_{2\,\min}$.

2 Repeat step 1 for the largest thermal gradient which is expected. Call these $\sigma_{1\,\max}$, $\sigma_{2\,\max}$.

3 Find steady (σ_{1o}, σ_{2o}) and variable (σ_{1v}, σ_{2v}) components, where

$$\left.\begin{aligned} \sigma_{1o} &= \frac{\sigma_{1\,\max} + \sigma_{1\,\min}}{2}, \quad \sigma_{2o} = \frac{\sigma_{2\,\max} + \sigma_{2\,\min}}{2} \\ \sigma_{1v} &= \frac{\sigma_{1\,\max} - \sigma_{1\,\min}}{2}, \quad \sigma_{2v} = \frac{\sigma_{2\,\max} - \sigma_{2\,\min}}{2} \end{aligned}\right\} \quad \ldots [3]$$

4 Find actual stress-concentration factor k_f for each principal stress, using theoretical factor k and sensitivity index for material q, in the formula

$$k_f = 1 + q(k - 1) \quad \ldots [4]$$

5 Calculate intensity of steady stress S_o from

$$S_o = \sqrt{\sigma_{1o}^2 + \sigma_{2o}^2 - \sigma_{1o}\sigma_{2o}} \quad \ldots [5]$$

and intensity of variable stress from

$$S_v = \sqrt{(k_{1f}\sigma_{1v})^2 + (k_{2f}\sigma_{2v})^2 - k_{1f}\sigma_{1v}k_{2f}\sigma_{2v}} \quad \ldots [6]$$

If $S_o + S_v$ is greater than the yield point of the material, $S_o + S_v$ arbitrarily should be reduced to the stress value which falls on the stress-strain curve of the material, Fig. 4.

6 Select S_u and S_e from the known physical properties of the material, where S_u is the steady stress which would produce failure (ultimate strength) and S_e is the endurance limit for complete reversal at the expected number of cycles.

7 The factor of safety of the application is then

$$F = \frac{1}{\frac{S_v}{S_e} + \frac{S_o}{S_u}} \quad \ldots [7]$$

[3] These tests were made by Mr. D. Frederick at the Westinghouse Atomic Power Division.

An acceptable factor of safety must, of course, be greater than unity. Just how much greater it should be depends on the conservatism of the calculations, the consequences of failure, and similar considerations which must be evaluated by the designer for each problem.

Relative Importance of Various Physical Properties

In testing and evaluating a new material for use in a reactor structure it is necessary to know which properties are most desirable and important for the service. The required nuclear properties and corrosion resistance so limit the choice of materials that it is not possible to select them on the basis of physical properties. The few allowable materials must be studied carefully and then used by the mechanical designer within their limitations. It is seldom that nuclear and chemical limitations will allow the addition of alloying elements for the purpose of improving the physical properties. In this section the relative importance of various physical properties for use in reactor design will be discussed.

Ductility

The discussion of thermal stresses covered in the first part of this paper leads immediately to the conclusion that ductility is one of the most important and desirable properties of a reactor material. Many cases arise in which the sum of pressure and thermal stresses cannot be kept within the yield point of the material and we depend upon the ductility to relieve the peak stresses. The same situation also exists in most welded structures where weld shrinkage produces residual stress considerably in excess of the yield point. In the structural supports and shields of a large power reactor there are apt to be field welds which cannot be stress-relieved to eliminate residual stress and in which we must place our whole dependence on the ductility of the material to prevent cracking. Examples have been found where a high-ductility low-yield-point material did not fail, but another material with about 4 times the yield strength but much lower ductility did develop cracks, even though both were subjected to the same operating conditions. In a reactor structure it is usually easy to limit the stress resulting from static load and fluid pressure to very low values, but the stresses caused by thermal gradients and weld shrinkage are not so easily controlled.

For the special case of mobile reactors for naval use, a ductile material has the added advantage of its resistance to high-impact shock. Brittle materials are avoided wherever possible for naval use and the same rule should apply to reactors for naval application.

Creep

Extensive creep testing of materials for reactor use is not as essential at the present time as might be supposed. Creep is most important in a member such as a turbine blade in which centrifugal force produces a high stress which is not relieved by creeping of the material. In the reactors which already have reached the operation or even detail design stage, the stresses produced by steady loads are not apt to be excessive and creep distortion of a material is really advantageous in that it relieves thermal stresses. Approximate knowledge of creep characteristics is of course useful and necessary but the creep rate is not apt to become the limiting factor in a reactor design.

Endurance Limit

The number of thermal cycles to which a reactor plant will be subjected may be several thousand but will not be as high as a million. Therefore it is important to explore the upper branch of the usual fatigue-limit curve to obtain an endurance limit which is not overly pessimistic.

Peterson (3) has shown that for axial stress the upper branch of the *S-N* (stress versus number of cycles) curve can be approximated by a straight line on a semilog plot. It runs from one cycle at σ_u, the ultimate tensile strength, to 10^6 cycles at σ_e, the endurance limit. Thus the corrected endurance limit for N cycles is

$$\sigma_{eN} = \sigma_u - \left(\frac{\sigma_u - \sigma_e}{6}\right)\log N \text{ for } N < 10^6 \quad [8]$$

For bending cases the best approximation is obtained by plotting fatigue data on a log-log basis and drawing a straight line from the tensile strength at 10^3 cycles to the endurance limit at 10^6 cycles. The corrected endurance limit for N cycles is then

$$\sigma_{eN} = \frac{\sigma_u}{\left(\frac{N}{1000}\right)^{1/3 \log \frac{\sigma_u}{\sigma_e}}} \quad [9]$$

for $N < 10^6$. For $N < 10^3$ the failure stress is higher than σ_u, which has been confirmed by bending tests.

For cases where stress concentration occurs, the endurance limit must be reduced by the factor k_f, the effective stress-concentration factor in fatigue. Equation [8] for axial load becomes

$$\sigma_{eN} = \sigma_u - \left(\frac{\sigma_u - \frac{\sigma_e}{k_f}}{6}\right)\log N \quad [10]$$

and Equation [9] for bending load becomes

$$\sigma_{eN} = \frac{\sigma_u}{\left(\frac{N}{1000}\right)^{1/3 \log \frac{k_f \sigma_u}{\sigma_e}}} \quad [11]$$

Creep Rupture

Creep-rupture properties at the expected operating temperature must be investigated for any material used in a reactor because of the long periods of time during which the reactor must operate at full temperature. Short-time tensile tests, even at high temperature, are not a safe criterion on which to base working stresses since some materials such as precipitation-hardened stainless steel are affected by very long exposure to high temperature.

Impact Strength

Impact strength is of importance in a naval reactor just as it is in any other equipment for use on a naval vessel, but there is nothing peculiar to the reactor itself which makes impact resistance of particular importance.

Notch Sensitivity

The stress concentration in a member is determined entirely by the geometry of the member and the applied system of forces. Thus in a notched bar the ratio between peak stress and average stress is the same whether the bar is made of glass or low-carbon steel. However, the ability of the glass rod to carry static tensile load has been decreased by the notch much more than the ability of the steel rod to carry such a load has been decreased. Different materials have different degrees of notch sensitivity and any one material is quite apt to have different notch sensitivities for different types of loading and for different sizes of notch. The correlation between ductility and notch sensitivity under steady load is quite good. The same relation does not hold at all, however, for notch sensitivity in fatigue or impact. For example, annealed copper is ductile in tension, tough in impact, but highly notch-sensitive in fatigue. Cast iron has almost no ductility, is weak in impact, but has almost no notch sensitivity in fatigue. For use in stationary reactors it is important to know the notch

sensitivity in fatigue and the notch sensitivity under conditions of creep rupture. For naval applications notch sensitivity under impact also must be investigated.

BIBLIOGRAPHY

1 "Handbook of Experimental Stress Analysis," edited by M. Hetenyi, John Wiley & Sons, Inc., New York, N. Y., 1950; chapter 10, "Working Stresses," by C. R. Soderberg, p. 438.

2 "Application of Stress Concentration Factors in Design," by R. E. Peterson, Proceedings of the Society for Experimental Stress Analysis, vol. I, 1943, p. 118.

3 "Fatigue and Fracture of Metals," edited by W. M. Murray, John Wiley & Sons, Inc., New York, N. Y., 1952; paper No. 4, "Brittle Fracture and Fatigue in Machinery," by R. E. Peterson, p. 74.

4 "Factor of Safety and Working Stresses," by C. R. Soderberg, Trans. ASME, vol. 52, paper APM-52-2 1930,.

5 "A Study of the Effects of Cyclic Thermal Stresses on a Ductile Material," by L. F. Coffin, Jr., Trans. ASME, vol. 76, 1954, pp. 931-950.

Discussion

FRANK BONI.[4] The author is to be commended for having established a valuable set of working tools for the design engineer in the petroleum, utility, and nuclear-power fields where the significance of high calculated combined fluid pressure and thermal stresses has not previously been well defined.

The author's work will be of more than casual interest to those concerned with the evaluation of stresses produced in austenitic stainless steels which suffer from low thermal conductivity plus high thermal expansion since the high calculated combined stress for these metals, generally being greater than the yield point, does not materialize and strain becomes the design criterion. Fig. 4 of the paper can be used to illustrate this statement, noting that the actual stress is not at point B as calculated on an elastic basis but at point C on the stress-strain diagram. If the operation of the system is cyclic, the resulting inelastic strains may be totaled and used to predict the life of the equipment according to Coffin's theory (5) that there is some limiting total inelastic strain.

The literature has been enriched by the author's significant addition and again we wish to emphasize the noteworthy recent work by Dr. Coffin. As a net result of all these works the engineer has certainly been enlightened regarding the problem of thermal stress fatigue.

D. K. DAVIES.[5] The author has made a frontal attack on a problem which has been plaguing pressure-vessel designers and particularly code-writing bodies for a period of several years. Much progress has been made recently in this field and, although we cannot say at present that solutions to all of our problems are available, we know much more about this problem than we did as recently as three years ago.

It is fortunate that work done by Mr. L. F. Coffin, Jr.[6], with the same material as that used by the author in his illustration, has recently been made available. Several areas exist in which direct comparisons can be made between the author's example and the work of Mr. Coffin and his associates at KAPL.[7]

For specimens cycled in uniaxial thermal fatigue, failure points on the strain versus cycles to failure curve may be approximated by the expression — $N^{1/2}\,\Delta_{\epsilon_p} = 0.36$, where N represents the number of cycles to failure and Δ_{ϵ_p} represents the total plastic-strain change per cycle. A comparison with this expression has been made of the example cited by the author where a tube cycled between 17,280 and 80,000 psi had not failed at 15,000 cycles. The expression given in the foregoing by Mr. Coffin would predict that approximately 160,000 cycles could be expected for this strain range before failure occurred; this, of course, is in agreement with the author's conclusions that a stress calculated to be in excess of the ultimate tensile strength of the material is of little significance in this type of service.

Much work has been done recently at Lehigh University and at the University of Illinois on fatigue-strength investigations for pressure-vessel steels. These investigations are utilizing both stress versus cycles to failure and strain versus cycles to failure data, in efforts to obtain fatigue properties of these steels.

The author has chosen to use an approach to the problem which entails the calculation of equivalent stresses and the use of a modified Goodman diagram for predicting the interdependence of stress range and cycles to failure. Most present-day investigators prefer to work directly with strains rather than to revert to equivalent stresses. In this way, for instance, Mr. Coffin has found that the number of cycles to failure for type 347 material is dependent primarily upon the plastic strain and is not influenced at the outset by the elastic strain. This is borne out in part by the long familar rule of thumb—that the endurance limit for a structural quality steel may be approximated by its yield strength so that fatigue failure is not expected where plastic strain is not encountered.

One item which should be pointed out with respect to the author's use of the Goodman diagram in predicting cycles to failure is that data for plotting the Goodman diagram were obtained from constant-temperature strain cycles. Mr. Coffin has found in his tests by making direct comparisons between constant-temperature strain cycles and thermal strain cycles that the constant temperature mechanically strained specimens always exhibited fatigue lives approximately four times as long as thermally cycled specimens. On this basis designers should not use published data on fatigue of materials for use in designing equipment subject to thermal cycling without close examination of the methods of testing and without comparison with the best available thermal-fatigue data.

In connection with the author's remarks concerning the effects of stress-concentration factors, it is felt that more work must be done in the plastic range before the true effects of strain concentration can be evaluated in fatigue service with large strains since plastic strain has a tendency to localize very seriously at notches or other series-type inhomogeneities. Recent results of thermal-cycling tests of models of heat exchangers and other equipment have indicated that effects such as this may be far more serious in the plastic range than have been heretofore believed.

AUTHOR'S CLOSURE

The author is in complete agreement with the comments of Messrs. Boni and Davies and thanks them for their contributions. The work of Dr. Coffin, to whom they both refer, is being followed with great interest and it is hoped that it will eventually result in the establishment of a firm basis for the prediction of failure from plastic cycling in specific materials.

The approach to the problem through the calculation of equivalent stresses was chosen because it is more familiar to the designer who is in the habit of calculating stresses and then comparing these stresses to known mechanical properties. The chief purpose of writing the paper was to point out how unnecessarily conservative this approach can be.

---

[4] The Griscom-Russell Company, Massillon, Ohio.

[5] Atomic Energy Division, The Babcock & Wilcox Company, Akron, Ohio. Assoc. Mem. ASME.

[6] "The Problem of Thermal Stress Fatigue in Austenitic Steels at Elevated Temperatures," by L. F. Coffin, Jr., ASTM Preprint Paper No. 100-A, to be published.

[7] Knolls Atomic Power Laboratory Report KAPL 1070, February 1, 1954.

The Thermal Design of Nuclear Power Reactors

By N. J. PALLADINO,[1] PITTSBURGH, PA.

This paper presents the development of relationships between maximum fuel-element surface temperatures, coolant temperature rise, flow, pumping power, and operating steam temperatures for use in the design of a power-producing nuclear reactor. The heat output of a power-producing reactor is generally limited by the maximum metal-surface temperature which can be utilized without incurring excessive corrosion or dangerous conditions of boiling. The design of a reactor on the basis of maximum metal-surface temperature is particularly important in view of the fact that heat is not generated uniformly throughout the reactor and because of the fact that tolerances which must be established for manufacturing purposes may lead to further increases in hot-spot temperatures.

Nomenclature

The following nomenclature is used in the paper:

A_f = total coolant-flow area in core normal to direction of flow, sq ft
A_s = total heat-transfer area of core, sq ft
b = constant of proportionality (see Equation [34]), kw
c_p = specific heat at constant pressure, Btu/lb deg F
C = cost of power, $/kwhr
C_r = cost of reactor core, dollars
C_v = cost of reactor vessel, dollars
D = diameter of core, ft
D_e = equivalent diameter, ft
e_g = over-all steam-turbine and generator efficiency
e_p = pump efficiency
f = friction factor
F_1 = ratio of system pressure drop to core and reactor-vessel pressure drop
F_2 = ratio of core and reactor-vessel pressure drop to core-friction pressure drop
$F_{\Delta T}$ = hot-channel factor applied to coolant temperature rise through core to account for nonuniform radial heat generation and average dimensional deviations from design conditions (Appendix 1)
F_θ = hot-channel factor applied to coolant-film temperature drop for nonuniform radial heat generation and average and local dimensional deviations from design conditions (Appendix 1)
G = mass flow through channel, lb/hr sq ft
h = coolant-film heat-transfer coefficient, Btu/hr deg F sq ft
H = fluid pumping power applied to coolant, hp
k = thermal conductivity, Btu ft/hr deg F sq ft
k_1 = cost factor for boiler and steam plant based on heat flow through boiler in kw, $/kw
k_2 = cost factor for pumps based on inlet power requirements in kw, $/kw
k_3 = cost factor for piping and associated equipment based on reactor heat output in kw, $/kw
L_0 = length or height of core, ft
L = length of flow passage = nL_0, ft
L_s = full-load lifetime of plant, years
$M = N\dfrac{\left(1+\dfrac{\beta L_s}{\gamma N}\right)}{\left(1+\dfrac{\beta L_s}{\gamma}\right)}$, Equation [5]
$m = 1 + \beta L_s/\gamma$, Equation [38]
n = number of coolant passes through core, assuming equal flow areas in each pass
N = number of cores per plant lifetime
Q_b = heat flow through boiler, kw
Q_f = fluid pumping power applied to coolant, kw
Q_0 = net power generated by plant, kw
Q_p = power supplied to pump = Q_f/e_p, kw
Q_r = thermal output from reactor, kw
R = ratio of thermal power used for pumping to thermal output of reactor = $\dfrac{Q_p}{e_g Q_r}$
R_c = the value of R expended in core and reactor vessel
R_m = optimum value of R
R_p = value of R expended in primary reactor loop exclusive of core and reactor vessel = $R - R_c$
T_1 = coolant inlet temperature to core, deg F
T_2 = coolant outlet temperature from core, deg F
T_s = saturated-steam temperature from boiler, deg F
T_{sm} = maximum fuel-element surface temperature in core, deg F
T_{smc} = maximum fuel-element surface temperature in a single channel, deg F
W_s = coolant flow through plant system, lb/hr
WP = wetted perimeter, ft
Z = operating cost, $/kwhr
α = portion of core cross section used for flow
β = interest rate, per cent per year
γ = utilization factor of reactor core, $\dfrac{\text{full load life of core}}{\text{actual life of core}}$
ΔP_c = pressure drop through core and reactor vessel, psf
ΔP_{fr} = core friction pressure drop, psf
ΔP_s = system pressure drop, psf
ΔT = coolant temperature rise through the core = $(T_2 - T_1)$, deg F
θ_a = average coolant-film temperature drop in core, deg F
θ_{a1} = average coolant-film temperature drop in a single channel, deg F
θ_b = logarithmic-mean temperature difference in boiler, deg F

---

[1] Manager, Reactor Design Subdivision, Reactor Department, Westinghouse Electric Corporation, Atomic Power Division, Pittsburgh, Pa. Mem. ASME.

Contributed by the Power Division and presented at a joint session of the Power and Metals Engineering Divisions at the Semi-Annual Meeting, Pittsburgh, Pa., June 20–24, 1954, of The American Society of Mechanical Engineers.

Note: Statements and opinions advanced in papers are to be understood as individual expressions of their authors and not those of the Society. Manuscript received at ASME Headquarters, April 13, 1954. Paper No. 54—SA-58.

θ_{m1} = maximum coolant-film temperature drop in a single channel, deg F
ρ_p = coolant density at pumps, lb/ft³
ρ_r = mean coolant density in core, lb/ft³
μ = viscosity of coolant in core, lb/ft hr

Introduction

As is true for any heat engine, the design of a power-producing nuclear reactor requires the integration of four important factors affecting its economic application to a given service; these factors are thermal performance, limitations on materials, fuel requirements, and control requirements. These factors bear even a closer relationship to each other in a nuclear reactor than is found in the usual heat engine.

The heat in a nuclear reactor is evolved from the fissioning of uranium, principally U-235, under bombardment by neutrons. This heat arises from the loss of kinetic energy of the fission fragments to the surrounding materials, from the loss of kinetic energy of the two to three high-speed neutrons emitted during each fission, and from the absorption of alpha, beta, and gamma rays in the reactor materials. The reaction once started is maintained by absorption of the fission neutrons in atoms of the remaining uranium. These high-speed fission neutrons, however, are not as effective as slow (thermal-energy) neutrons in producing further fission in U-235; therefore they must be slowed down to thermal energies. The slowing down is accomplished by having the neutrons collide with nuclei of a moderator made up largely of one of the light elements, whose mass is not too much greater than that of the neutron; heavy elements would cause the neutrons to rebound without appreciable loss of their incident velocity. In order for the neutrons, released from fission, to maintain the reaction even after being slowed down, they must be formed at a sufficient rate to balance neutrons lost by escape from the reactor, by nonfission capture in U-238 or structural materials, and by fission capture in the U-235. The amount of U-235 required for production of these neutrons in a given-size reactor is known as the critical mass; the associated size of the reactor core is known as the critical size.

Inasmuch as the reactor consumes U-235 during operation, an excess of this nuclear fuel must be provided; otherwise the reactor becomes subcritical and the chain reaction stops. The effect of this excess fissionable material is counteracted by the insertion of control rods containing materials of high-neutron-absorbing properties such as boron or cadmium. These control rods also are used for shutting down the reactor.

In usual practice, the core or active portion of the reactor is made of uranium-bearing fuel elements with flow passages around the elements for circulation of a coolant. The coolant is moved through these passages, out of the reactor to a heat exchanger where the heat is extracted and applied to water to form steam, and through pumps back to the reactor. In the core, the fuel elements are generally clad by a metallic sheath to protect the uranium against oxidation or corrosion by the coolant and to prevent escape of radioactive fission products which would contaminate the coolant stream.

In order to conserve the fuel inventory necessary for making the reactor critical, it becomes clear that the materials used in the core must have low-neutron-absorbing properties. As a consequence, the number of materials that can be used to clad the fuel elements is limited; for effective production of power the available materials may have to be operated at temperature levels close to the limiting temperatures for good structural properties and resistance to oxidation or corrosion. Therefore the operating temperature of the fuel elements becomes one of the major limitations on the thermal performance of the plant. This temperature is not the same for all fuel elements in the reactor because of the uneven production of heat by the nuclear reactions in the core, arising from the diffusion of neutrons outward from the center of the core and the absorption of neutrons in control rods. In an unreflected cubical core, for example, the normal heat-generation pattern follows a cosine distribution along all directions parallel to the exterior surfaces of the core. In a cylindrical core this pattern follows a cosine distribution axially and a J_o Bessel distribution radially.

Design Parameters

The fuel-element temperature generally of particular interest is the maximum surface temperature because of its effect on corrosion and oxidation and its effect on the maximum fuel-element operating-temperature level. For flow in a channel in which the heat is generated in cosine pattern the expression for this temperature as indicated below is dependent upon three basic reactor characteristics, core coolant inlet temperature T_1, coolant temperature rise ΔT, and average film drop θ_a, all related to core dimensions and over-all plant requirements. This expression is developed in Appendix 1

$$T_{sm} = T_1 + F_{\Delta T}\frac{\Delta T}{2} + 1/2\sqrt{F_{\Delta T}^2\,\Delta T^2 + F_\theta^2\pi^2\theta_a^2} \quad \ldots [1]$$

As a consequence the process of core design proceeds as an iteration process whereby the core dimensions are varied in accordance with plant requirements, and values for maximum fuel-element surface temperature are computed for comparison with the limiting value. The variables entering into this process can be combined in a number of interesting arrangements most of which involve implicit combinations of parameters not readily amenable to computation. In Appendixes 2 through 4 are developed explicit relationships for the core parameters which have been found useful in the design of a core using an incompressible coolant in the turbulent range with equal flow in all channels. These relationships may be summarized for a cylindrical core as follows:

Average Temperature Rise in Core

$$\Delta T = 0.008\left[\frac{F_1F_2}{\rho_p\rho_r}\frac{L_0}{D}\frac{1}{H}\right]^{0.357}\frac{\mu^{0.0714}}{D_e^{0.429}}\frac{Q_r}{c_p}\frac{n}{\alpha^{0.643}}\frac{1}{D^{0.929}} \quad \ldots [2]$$

This equation shows that, for a given coolant, the temperature rise ΔT through a reactor is directly proportional to the thermal output of the reactor Q_r, to the number of times n the coolant passes through the core, and to the 0.357 power of the length-to-diameter ratio of the core L_0/D; it is inversely proportional to the 0.357 power of the fluid pumping power H applied to the coolant, to the 0.429 power of the equivalent diameter D_e of the coolant channels, to the 0.929 power of the core diameter D, and to the 0.643 power of the portion α of the core cross section used for flow.

Average Coolant-Film Temperature Drop in Core

$$\theta_a = \frac{58.2\,Q_r^{0.2}\,\Delta T^{0.8}\,D_e^{1.2}\,c_p^{0.4}\,\mu^{0.4}}{D^{1.4}(L_0/D)\,k^{0.6}\,\alpha^{0.2}\,n^{0.8}} \quad \ldots [3]$$

This equation shows that, except for the fluid pumping power H, the coolant-film temperature drop in the core θ_a involves the same core characteristics, but in different combination, as does the coolant temperature rise ΔT. In addition, it depends upon the 0.8 power of ΔT computed from Equation [2].

Coolant Inlet Temperature to Core as Determined From Heat-Exchanger Design for Saturated-Steam Production

$$T_1 = T_s + \frac{\Delta T}{[e^{\Delta T/\theta_b} - 1]} \quad \ldots\ldots\ldots\ldots\ldots\ldots [4]$$

This equation shows that the inlet temperature to the reactor T_1 is related to the desired temperature of the steam in the power plant T_s, the coolant temperature rise in the core ΔT, and the temperature drop θ_b across the heat-exchange surface in the boiler. The computation of T_1 thus becomes explicit after ΔT has been computed and the steam temperature and boiler characteristics have been assumed.

It is to be noted that Equations [2] and [3] require only the assumption of consistent core dimensions for explicit determination of the values for ΔT and θ_s. Other combinations of these parameters usually involve in the determination of one of them, an assumed value of the other. Such an assumption is usually difficult to make because of the common dependence of these parameters on the same core dimensions as indicated. By use of Equations [2] and [3] this problem is avoided. Thus, from Equations [2], [3], and [4] the values required in Equation [1] can be computed directly from assumed core design and plant variables.

It is to be noted that the coolant temperature rise through the core and hence the coolant-film temperature drop and the core-inlet coolant temperature are dependent upon the amount of power assigned to pumping the coolant around the system. An economic value for this pumping power, however, can be established by consideration of the various costs and performance characteristics of plant components. An equation for determining the optimum thermal energy to be assigned to pumping power as a percentage of core thermal output is developed in Appendix 5 for pumps driven electrically from the main plant generator

$$R_m = R_p + \frac{1 - R_p(1 - e_g e_p)}{3(1 - e_g e_p) + \dfrac{2Q_r[k_1 + e_g k_2 + k_3(1 - e_g e_p)]}{C_v + MC_r}} \quad \ldots [5]$$

where

$$M = N\left[\frac{1 + \beta L_s/\gamma N}{1 + \beta L_s/\gamma}\right]$$

This equation indicates that the ratio of thermal power used for pumping to the thermal output of the reactor is related to the costs of all system components, to the number of cores used per plant lifetime, and to the generator and pump efficiencies. The expression $L_s/\gamma N$ defines the average life of a reactor core in years.

Design Procedure

By use of these equations the core characteristics can be determined for a given desired plant output once the moderator, coolant, and cladding materials have been chosen. Several general criteria can be established for selection of these materials but particular choices of these materials for a given core design will depend upon the application.

A moderator, besides being light, should have low neutron-absorbing properties to avoid parasitic loss of neutrons and should have a sufficient density or compactness of atoms to provide the necessary moderation. This density requirement eliminates the use of gases, particularly hydrogen and helium, as moderators except at prohibitively high pressures. Hydrogen and its isotope, heavy hydrogen, can be used, however, in the form of water and heavy water. Among the remaining light elements which might be used for moderating are lithium, beryllium, boron, and carbon. Lithium and boron have high-absorption cross sections and therefore can be eliminated. This leaves as moderators of practical importance water, heavy water, beryllium and its compounds, and carbon in various forms.

In a practical reactor the core is surrounded by a reflector of inert material having good scattering but low-absorption properties. A certain number of neutrons leaving the core are returned to the core by the reflector and assist in the chain reaction. The reflector material is often the same as the core-moderating material so that fast neutrons entering the reflector can be slowed down and returned to the core as thermal neutrons. The reflector contains no fissionable material but it may contain fertile materials such as thorium or U-238 to absorb neutrons in the reflector to produce other fissionable materials for further use.

The coolant also must have (*a*) low neutron-absorbing properties, but unless also used as a moderator, it need not be limited to materials containing light elements; (*b*) it must not react with the moderator or the uranium or the available cladding materials; (*c*) it should have better-than-average heat-transfer characteristics; (*d*) it should not decompose under irradiation.

Among the coolants to be considered are air and water. Both of these materials present severe oxidation and corrosion problems. Water makes a particularly attractive coolant because it also can be used as a moderator. The use of water as a coolant, however, requires a pressurized reactor-coolant system for operation at significant temperatures. The use of either air or water as coolants necessitates the use of a uranium cladding material with low neutron-absorbing properties, but satisfactory for operation at high enough temperatures to produce reasonable thermodynamic efficiencies for the plant. Aluminum has been used successfully at moderate temperatures with both air and water cooling but it is not practical for high-temperature operation in water or air. Zirconium can be used as a cladding material in high-temperature water if the appropriate impurities are controlled properly.

Looking further for coolants, helium bears consideration for certain applications. Helium meets requirements (*a*, *b*, and *d*) listed in the foregoing; but in order to meet requirement (*c*) it requires large amounts of pumping power which might be practical only in restricted applications. Certain liquid metals such as sodium and sodium-potassium alloys have been used successfully as reactor coolants; the liquid-metal coolants usually introduce special handling and design problems peculiar to their chemistry. Organic coolants are not attractive because they tend to decompose in a reactor radiation field.

Upon selection of the moderator, the cladding and the coolant, the core dimensions and thermal characteristics can be computed for the desired plant output by use of the following procedure:

1 Make an estimate of the plant efficiency, to determine the desired core output.

2 Estimate R_p, the per cent of the reactor thermal output to be assigned to pumping the coolant through the primary reactor loop exclusive of the core and reactor vessel and compute H, the fluid pumping power applied to the coolant based on cost and performance limitations defined in Equation [5] and the relationship of Equation [32] in Appendix 5.

3 Estimate F_2, the ratio of core and reactor-vessel pressure drop to core-friction pressure drop and compute F_1, the ratio of system pressure drop to core and reactor-vessel pressure drop from $F_1 = R/(R - R_p)$.

4 Determine the heat-generation pattern considering the control-rod configurations to be used in the core.

5 Estimate the effect of manufacturing tolerances and of local maximum-to-average heat-transfer coefficients for their influence on hot-spot characteristics similar to the influence of the heat-generation pattern in the core.

6 Combine the influence of steps 4 and 5 to yield the effective peak-to-average power-generation factors defined as $F_{\Delta T}$ and F_θ.

7 Determine the percentage of the core to be utilized for passage of the coolant from considerations of the critical mass requirements of the core.[2]

8 Using Equations [1 to 4], proceed with a study of the various steam conditions and core dimensions, such as core diameter, flow-passage hydraulic diameter, and number of coolant passes through the core, for their influence on maximum fuel-element temperature. Equation [1] must be applied to each pass separately for a multipass core. The length-to-diameter ratio is generally fixed at about 1 to 1 by the desire for minimum critical mass requirements.

These performance computations usually must be accompanied by mechanical-arrangement layouts for evaluation of assumed core dimensions and flow arrangements and by nuclear computations on uranium requirements. Thus the design of the reactor core involves extensive parallel efforts on all aspects of the problem. The relationships presented herein assist in clarifying the nature and direction that such efforts should assume. These relationships will require modification when different design assumptions apply, as is the case where apportionment of flow among coolant channels or between coolant passes in the core is not made uniform; in general, however, the methods used here can be applied. Cores utilizing a nuclear reflector can generally be treated by modifying the heat-generation peak-to-average factors, and by appropriate extension of the cosine heat-generation pattern in the axial direction over the core so that the heat-generation rates at the ends of the core match the level brought about by the reflector.

Appendix 1

Development of Expression for Maximum Fuel-Element Surface Temperature

Assumption. Heat-generation pattern follows cosine distribution.

Basic Equations. In an average core channel with a cosine heat-generation pattern cooled by uniform flow, the maximum metal-surface temperature is given by the equation[3]

$$T_{sma} = T_1 + \frac{\Delta T}{2} + 1/2\sqrt{\Delta T^2 + 4\,\theta_{a1}^2} \quad [6]$$

For a cosine distribution it can be shown that

$$\frac{\theta_{m1}}{\theta_{a1}} = \frac{\pi}{2} \quad [7]$$

Solution. Combining Equations [6] and [7] yields

$$T_{sma} = T_1 + \frac{\Delta T}{2} + 1/2\sqrt{\Delta T^2 + \pi^2\,\theta_{a1}^2} \quad [8]$$

The hottest channel has a higher value of ΔT by the factor $F_{\Delta T}$ which takes into account the maximum-to-average radial heat-generation distribution and the average dimensional deviations from design conditions in the coolant passages and fuel elements.

The hottest channel similarly has a higher coolant-film temperature drop than θ_a by the amount F_θ which takes into account the maximum-to-average radial heat-generation distribution and the average and local dimensional deviations from design conditions in the coolant passages and fuel elements as well as independent local variations in heat-transfer coefficients around the surface of the fuel elements.

Applying these factors to Equation [8] the maximum fuel-element surface temperature in the core becomes

$$T_{sm} = T_1 + F_{\Delta T}\frac{\Delta T}{2} + 1/2\sqrt{F_{\Delta T}^2\Delta T^2 + F_\theta^2\pi^2\theta_a^2} \quad [1]$$

Appendix 2

Development of Expression for Coolant Temperature Rise in a Nuclear Reactor

Assumptions. Uniform flow in all fuel-element passages; uniform apportionment of core cross section for flow among the coolant passes.

Basic Equations Used:

$$\text{Fluid pumping power} = H = \frac{W_e\Delta P_e}{33{,}000\ (60)\rho_p} \quad [9]$$

Define

$$F_1 = \frac{\Delta P_s}{\Delta P_e} \quad \text{and} \quad F_2 = \frac{\Delta P_e}{\Delta P_{fr}} \quad [10]$$

Core friction pressure drop

$$\frac{\Delta P_{fr}}{\rho_r} = \frac{4f\ L\ G^2}{2g\ D_e\rho_r^2\ (3600)^2} \quad [11]$$

Core friction factor

$$f = \frac{0.046}{Re^{0.2}} = \frac{0.046\,\mu^{0.2}}{G^{0.2}\,D_e^{0.2}} \quad [12]$$

For uniform flow in all fuel-element passages

$$W_e = \frac{A_f G}{n} \quad [13]$$

Core heat-balance equation

$$Q_r = \frac{W_e c_p \Delta T}{3413} = \frac{A_f G c_p \Delta T}{n(3413)} \quad [14]$$

Core flow area

$$A_f = \frac{\pi D^2}{4}\alpha \quad [15]$$

Solution:

1 Substitute Equation [10] in Equation [9] to obtain

$$H = \frac{W_e F_1 F_2 \rho_r}{1.98 \times 10^6 \rho_p}\left(\frac{\Delta P_{fr}}{\rho_r}\right) \quad [16]$$

2 Substitute Equation [12] in Equation [11] to obtain

$$\frac{\Delta P_{fr}}{\rho_r} = 2.2 \times 10^{-10}\frac{\mu^{0.2}G^{1.8}L}{D_e^{1.2}\,\rho_r^2} \quad [17]$$

3 Substitute Equations [13] and [17] in Equation [16] to obtain

$$H = 1.11 \times 10^{-16}\frac{A_f}{n}\frac{G^{2.8}L}{\rho_p\rho_r}\frac{\mu^{0.2}F_1F_2}{D_e^{1.2}} \quad [18]$$

---

[2] "The Elements of Nuclear Theory," by S. Glasstone and M. C. Edlund, D. Van Nostrand Company, Inc., New York, N. Y., 1954, p. 222.

[3] "The Science and Engineering of Nuclear Power," by Clark D. Goodman, Addison-Wesley Press, Inc., Cambridge, Mass., 1948, vol. 2, p. 138.

4 Combine Equations [14], [15], and [18], simplify using $L = nL_0$, and transpose to obtain

$$\Delta T = 0.008\left[\frac{F_1F_2}{\rho_s\rho_r}\frac{l_0}{D}\frac{1}{H}\right]^{0.357}\frac{\mu^{0.0714}}{D_e^{0.429}}\frac{Q_r}{c_p}\frac{n}{\alpha^{0.643}}\frac{1}{D^{0.929}} \quad [2]$$

Appendix 3

DEVELOPMENT OF EXPRESSION FOR COOLANT FILM DROP

Added Assumptions: Turbulent flow; heat transfer over entire length of core.

Basic Equations Used: Basic heat-transfer equation

$$Q_r = \frac{hA_s\theta_a}{3413} \quad [19]$$

Heat-transfer correlation for turbulent flow[4]

$$\frac{hD_e}{k} = 0.023\left[\frac{GD_e}{\mu}\right]^{0.8}\left[\frac{c_p\mu}{k}\right]^{0.4} \quad [20]$$

By definition, equivalent diameter is

$$D_e = \frac{4A_f}{WP} = \frac{4A_fL_0}{A_s} \quad [21]$$

Hence

$$A_s = \frac{4A_fL_0}{D_e} \quad [22]$$

Solution:

1 Substitute Equation [20] in Equation [19] using Equation [22] for A_s to obtain

$$Q_r = 2.7 \times 10^{-5}\frac{A_fL_0k^{0.6}G^{0.8}c_p^{0.4}}{D_e^{1.2}\mu^{0.4}}\theta_a \quad [23]$$

[4] "Heat Transmission," by W. H. McAdams, McGraw-Hill Book Company, Inc., New York, N. Y., 1942, p. 168.

2 Combine Equations [14] and [15] with Equation [23], transpose, and simplify to obtain

$$\theta_a = \frac{58.2\,Q_r^{0.2}\Delta T^{0.8}D_e^{1.2}c_p^{0.4}\mu^{0.4}}{D^{1.4}(L_0/D)k^{0.6}\alpha^{0.2}n^{0.8}} \quad [3]$$

Appendix 4

DEVELOPMENT OF EXPRESSION FOR COOLANT-INLET TEMPERATURE

Assumptions. Dry and saturated steam leaves the boiler; heat added by the coolant pumps balances boiler feedwater-heating requirements in the boiler (refer to Fig. 1).

Basic Equations. Logarithmic-mean temperature difference in the boiler is

$$\theta_b = \frac{(T_2 - T_s) - (T_1 - T_s)}{\ln\left[\frac{T_2 - T_s}{T_1 - T_s}\right]} = \frac{T_2 - T_1}{\ln\left[\frac{T_2 - T_s}{T_1 - T_s}\right]} \quad [24]$$

Solution. Transposing Equation [24] yields

$$\ln\left[\frac{T_2 - T_s}{T_1 - T_s}\right] = \frac{\Delta T}{\theta_b} \quad [25]$$

so that

$$e^{\Delta T/\theta_b} = \frac{T_2 - T_s}{T_1 - T_s} = \frac{\Delta T + T_1 - T_s}{T_1 - T_s} \quad [26]$$

Simplifying and transposing Equation [26] yields

$$T_1 = T_s + \frac{\Delta T}{[e^{\Delta T/\theta_b} - 1]} \quad [4]$$

Appendix 5

EXPRESSION FOR OPTIMUM THERMAL ENERGY TO BE ASSIGNED TO REACTOR COOLANT PUMPING POWER

Assumptions. The following assumptions are made (see Fig. 1):

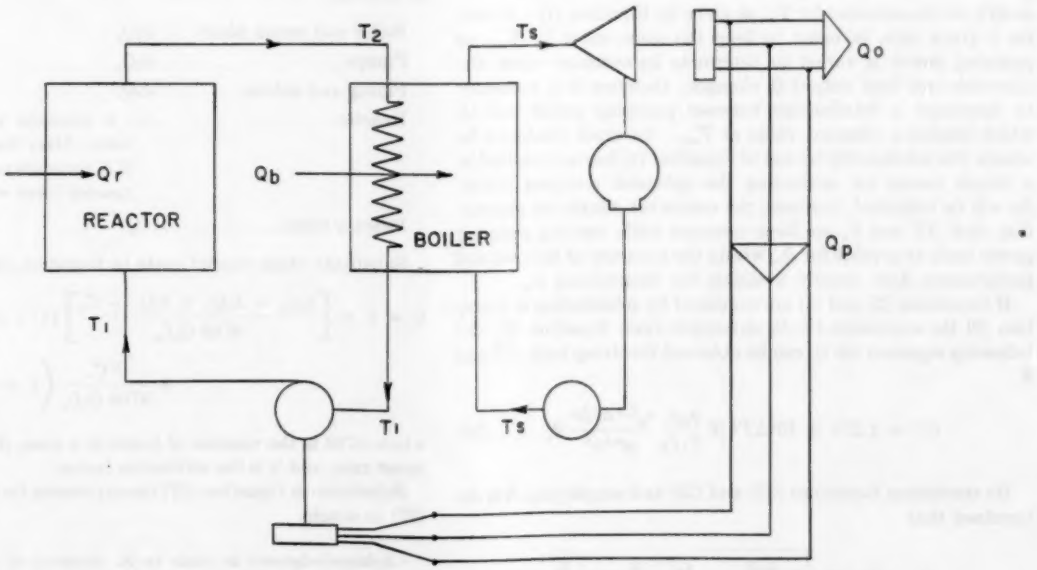

FIG. 1 LINE DIAGRAM OF REACTOR PLANT

Reactor core and vessel dimensions are fixed.

Costs of pumps are proportional to their power ratings.

Desired steam temperature is fixed.

The maximum metal-surface temperature in the core is to be a fixed value regardless of the pumping power used in the system.

The mass flow rates through piping, valves, and boiler tubes are maintained constant regardless of the pumping power.

Basic Equations. By energy balance

$$Q_b = \frac{Q_0}{e_g} + \frac{Q_p}{e_g} = Q_r + Q_f \quad \ldots\ldots [27]$$

By definition

$$Q_f = e_p Q_p \quad \ldots\ldots [28]$$

By definition

$$H = Q_f/(0.746) = e_p Q_p/(0.746) \quad \ldots\ldots [29]$$

By definition

$$R = \text{new variable} = \frac{Q_p}{e_g Q_r} \quad \ldots\ldots [30]$$

$$\left.\begin{aligned} \text{Cost of power} = C &= \frac{\text{operating cost}}{\text{per kwhr}} \\ &\quad + \frac{\text{capital cost + interest charges}}{\text{lifetime kwhr output}} \\ C &= Z + \frac{\text{capital cost + interest charges}}{Q_0 L_s} \end{aligned}\right\} \quad [31]$$

Solution. Combining Equations [29] and [30] yields

$$H = \frac{Q_p e_p}{0.746}\frac{Q_r}{Q_r} = \frac{R e_g e_p}{0.746} Q_r \quad \ldots\ldots [32]$$

For given reactor-core dimensions and a given steam temperature from the boiler there is only one pumping power for a given core output Q_r that provides the necessary ΔT, θ_a, and T_1 to satisfy the requirement for T_{sm} as given by Equation [1]. Hence, for a given core, in order to keep the same value for T_{sm}, as pumping power is varied to determine its optimum value, the allowable core heat output Q_r changes; therefore it is necessary to determine a relationship between pumping power and Q_r which implies a constant value of T_{sm}. An exact treatment to obtain this relationship by use of Equation [1] has not resulted in a simple means for estimating the optimum pumping power. As will be indicated, however, the somewhat restrictive assumption that ΔT and θ_a are kept constant while varying pumping power leads to a value for R_m within the accuracy of the cost and performance data usually available for determining R_m.

If Equations [2] and [3] are combined by substituting in Equation [2] the expression for D_s obtainable from Equation [3], the following equation for Q_r can be obtained involving both ΔT and θ

$$Q_r^3 = 1.275 \times 10^4 \Delta T^2 H \frac{\rho_p \rho_r}{F_1 F_2} \frac{c_p^{2.4} \alpha^2 D^4}{\mu^{0.4} n^2} \theta_a \quad \ldots\ldots [33]$$

By combining Equations [32] and [33] and simplifying, it is determined that

$$Q_r = 98 \Delta T \sqrt{\theta_a \frac{\rho_p \rho_r}{F_2} e_g e_p \frac{c_p^{1.2}}{\mu^{0.2}} \frac{\alpha}{n} D^2 \sqrt{\frac{R}{F_1}}} \quad \ldots\ldots [33a]$$

where

$$R/F_1 = R_c$$

Thus

$$Q_r = b\sqrt{R_s} = b\sqrt{R - R_p} \quad \ldots\ldots [34][5]$$

where b is a constant of proportionality indicated by Equation [33a] in which ΔT and θ_a are kept constant. (If all the parameters indicated in Equation [33a] are kept constant, then it can be shown that D_s is being varied inversely proportional to the twelfth root of R. An increase in R from 0.1 to 0.2 would indicate a decrease of about only 3 1/2 per cent in D_s; hence the basis of the analysis that the core dimensions are fixed is not markedly affected by the assumption that ΔT and θ_a are kept constant.)

By combining Equations [27], [28], and [30] obtain

$$Q_0 = Q_r e_g [1 - R(1 - e_g e_p)] \quad \ldots\ldots [35]$$

Combining Equations [34] and [35] yields

$$Q_0 = b e_g \sqrt{R - R_p}\,[1 - R(1 - e_g e_p)] \quad \ldots\ldots [36]$$

It can be shown that R_p is a constant if the pressure drop through the primary circuit (exclusive of the core and reactor vessel) is constant regardless of the flow. If this pressure drop, however, is to be held constant the size of equipment must increase with flow. In order to maintain a constant pressure drop in the boiler for a given flow rate per tube, the number of tubes in the boiler must be increased, proportional to the system coolant flow. Since the ΔT in the core and hence approximately the ΔT in the boiler is maintained constant, the boiler output Q_b is proportional to the system flow. Hence, if the cost of the boiler is assumed proportional to the number of tubes, the cost of the boiler can be established as approximately $= k_3 Q_b$.

If the pressure drop in the piping is maintained constant, it can be assumed that the cost of piping and associated primary-system equipment is approximately proportional to the flow and hence reactor output. The cost of the piping and associated primary-system equipment thus becomes $= k_3 Q_r$.

On the foregoing basis, if the cost of pumps is assumed to be proportional to their rated power, the following capital costs can be defined:

Boiler and steam plant	$k_1 Q_b$
Pumps	$k_2 Q_p$
Piping and valves	$k_3 Q_r$
Reactor	C_r, a constant value for a given core. Over the life of the plant if N cores are used the cost of the reactor cores $= NC_r$
Reactor vessel	C_v

Substitute these capital costs in Equation [31] to obtain

$$C = Z + \left[\frac{k_1 Q_b + k_2 Q_p + k_3 Q_r + C_v}{8760\, Q_0 L_s}\right](1 + \beta L_s/\gamma) + \frac{NC_r}{8760\, Q_0 L_s}\left(1 + \frac{\beta L_s}{\gamma N}\right) \quad \ldots\ldots [37]$$

where 8760 is the number of hours in a year, β is the annual interest rate, and γ is the utilization factor.

Substitute in Equation [37] the expression for Q_b from Equation [27] to obtain

[5] Acknowledgment is made to A. Amorosi of Argonne National Laboratory for his initial development of the square-root relationship between Q_r and R.

$$C = Z + m\,\frac{[(k_1/e_g)(Q_0 + Q_p) + k_2Q_p + k_3Q_r + MC_r + C_v]}{8760\,Q_0L_s} \quad \ldots\ldots [38]$$

where

$$m = 1 + \beta L_s/\gamma$$

and

$$M = N\,\frac{\left(1 + \dfrac{\beta L_s}{\gamma N}\right)}{\left(1 + \dfrac{\beta L_s}{\gamma}\right)}$$

Combining Equations [30] and [38] and simplifying yields

$$C = Z + m\left[\frac{\dfrac{k_1}{e_g}\,Q_0 + Q_r\,[(k + e_gk_3]R + k_3] + MC_r + C_v}{8760\,Q_0L_s}\right] \quad \ldots\ldots [39]$$

Substitute in Equation [39] the expression for Q_0 from Equation [35] and the expression for Q_r from Equation [34] to obtain

$$C = Z + \frac{m}{8760}\left[\frac{k_1}{e_gL_s} + \frac{[k_1 + e_gk_2]R + k_3}{e_g[1 - R(1 - e_ge_p)]L_s} + \frac{MC_r + C_v}{be_g\sqrt{R - R_p}\,[1 - R(1 - e_ge_p)]L_s}\right] \quad \ldots\ldots [40]$$

Differentiate Equation [40] with respect to R and set the derivative equal to zero to obtain the expression for R at which C is a minimum. Upon simplification, by the use of $Q_r/\sqrt{R - R_p}$ for the value of b, the expression for R_m becomes

$$R_m = R_p + \frac{1 - R_p(1 - e_ge_p)}{3(1 - e_ge_p) + \dfrac{2Q_r[k_1 + e_gk_2 + k_3(1 - e_ge_p)]}{C_v + MC_r}} \quad \ldots [5]$$

where

$$M = N\,\frac{1 + \beta L_s/\gamma N}{1 + \beta L_s/\gamma}$$

Discussion

ALFRED AMOROSI.[6] The author has boiled down what is usually a complicated and tedious procedure of thermal design of reactors. When a person first starts to work in the field of reactor design he usually takes the standard heat-transfer, pressure-drop, and flow equations; then for assumed values of velocity and heat generation, he proceeds to plot an endless number of curves of surface temperature versus distance through the reactor. He also calculates pressure drop and pumping power as a function of velocity. The curves are then studied in an attempt to optimize conditions. The trouble is that the basic heat-transfer and fluid-flow equations are not expressed in terms of the true independent reactor-system variables. The author has done an excellent job in reducing the thermal design of reactor to eliminate much of the cut-and-try work.

Anyone who has attempted to design a reactor also will appreciate the straightforward design procedure given at the end of the paper.

Some judgment should be exercised in determining the correct value for various factors such as $F_{\Delta T}$ and F_θ. It might appear that these factors should have the same value. However, a more careful inspection will reveal that the hot-channel factor to be applied on film temperature drop is sensitive to local variations (such as a localized disturbance of heat generation or flow), whereas the temperature-rise factor is not.

AUTHOR'S CLOSURE

The author wishes to thank Mr. Amorosi for his comments. Mr. Amorosi was among the first to recognize the need for relationships such as developed here and was instrumental in establishing early approaches to their derivation. His comments regarding the hot-channel factors $F_{\Delta T}$ and F_θ are both valid and appropriate.

---

[6] Associate Director, Reactor Engineering Division, Argonne National Laboratory, Lemont, Ill. Mem. ASME.

Graphical Representation of the Frictional Losses in Commercial Pipe of Air and Steam Flowing Turbulently at Low Pressure

By W. C. KNAPP[1] and J. W. METZGER,[2] PHILADELPHIA, PA.

Frequently, design investigations in the field of fluid flow require the rapid evaluation of pressure losses in pipes at various conditions of temperature and pressure. This discussion presents a graphical solution for determining frictional losses in pipes of various sizes carrying air and steam, together with the mathematical analysis from which it is evolved. Similar investigations carried out for other fluids may yield comparable graphical solutions, the utilization of which would aid materially in increasing the usefulness of fluid-flow data.

Nomenclature

The following nomenclature is used in the paper:

A = area, sq ft
a = coefficient in exponential equation for viscosity
C, C' = correction factors used on graph (with proper subscripts)
D, d = diameter of pipe, ft, in., respectively
F, F_1, F_2 = friction loss, components of friction loss, respectively, in. H_2O/100-ft pipe
F', F'' = friction loss, feet of fluid, inches of fluid, respectively
f = friction factor, unitless
f_n = function
g = gravitational acceleration conversion factor, ft/hr²
K, K' = simplification coefficients used for plotting graphs
K_1, K_2 = constants in equation relating f to Reynolds number
L = length, ft
n = exponent in equation relating f to Reynolds number
P = pressure, psf
P_h = pressure, in. Hg
P_{mm} = pressure, mm Hg
R = gas constant, ft-lb/lb deg F
Re = Reynolds number
T = absolute temperature, Rankine
T_k = absolute temperature, Kelvin
T_{k0} = absolute temperature, Kelvin for 0 C
$t_F°, t_C°$ = temperature Fahrenheit and Centigrade, respectively
V = velocity of fluid, ft/hr
v = specific volume, cu ft per hr
W = rate of flow of fluid, lb per hr
x = exponent in exponential equation for viscosity
λ = mean free path of air molecules, in.
μ, μ_0 = viscosity of fluid, centipoises
ρ = density of fluid, pcf
ΔP = pressure drop, psf

Introduction

Numerous graphical aids for the determination of friction losses in pipe lines are available in the literature. For the engineer who requires their use incidental to other problems, they appear to be unsatisfactory in some one respect. Some are limited to values at fixed conditions of pressure and temperature; others, while sufficiently flexible to permit consideration of varied conditions, require a distractingly large number of computations. The former were evolved from the latter more fundamental methods. Similarly, a more flexible graph, capable of yielding reliable values, can be developed using only the basic data now available in the literature. The variables involved may be incorporated into a single mathematical expression which in turn can be reduced to a graphical representation which is relatively simple to use.

Preliminary Analysis

A gas or vapor flowing isothermally in a horizontal pipe or tube will suffer friction loss. Further, it may expand and it may increase its kinetic energy. Assuming that all three conditions are present, they may be represented by the equation (1)[3]

$$vdP + \frac{VdV}{g} + \frac{4fV^2dL}{2gD} = 0 \quad \ldots\ldots\ldots\ldots [1]$$

Dividing through by $V^2/2g$, making the necessary substitutions, and integrating between suitable limits (2) yields

$$P_1^2 - P_2^2 = \frac{W^2RT}{gA^2}\left(2\log_e\frac{V_2}{V_1} + \frac{4fL}{D}\right) \quad \ldots\ldots [2]$$

For the analysis of the graph, it may be assumed that V_2/V_1 will approach unity, permitting the first term in the parentheses to be omitted

$$(P_1 - P_2)(P_1 + P_2) = \frac{W^2RT}{gA^2}\left(\frac{4fL}{D}\right) \quad \ldots\ldots\ldots [3]$$

Average values may be assigned to the appropriate factors and the following relations noted

$$P_{avg} = \rho_{avg}RT = \frac{P_1 + P_2}{2}, \quad W = \rho_{avg}V_{avg}A$$

then

$$P_1 - P_2 = \frac{\rho_{avg}V_{avg}^2A^2P_{avg}}{gA^2}\,\frac{4fL}{2D\left(\frac{P_1 + P_2}{2}\right)}$$

---

[1] Mechanical Engineer, C. H. Wheeler Manufacturing Company.

[2] Mechanical Engineer, C. H. Wheeler Manufacturing Company. Assoc. Mem. ASME.

Contributed by the Process Industries Division and presented at the Semi-Annual Meeting, Pittsburgh, Pa., June 20–24, 1954, of The American Society of Mechanical Engineers.

Note: Statements and opinions advanced in papers are to be understood as individual expressions of their authors and not those of the Society. Manuscript received at ASME Headquarters, January 25, 1954. Paper No. 54—SA-17.

[3] Numbers in parentheses refer to the Bibliography at the end of the paper.

$$\Delta P = \frac{\rho_{ave} V_{ave}^2}{g} \frac{4fL}{2D}$$

$$F' = \frac{\Delta P}{\rho_{ave}} = \frac{4W^2 fL}{2g\left(\frac{\pi^2 D^4}{16}\right)\rho_{ave}^2 D}$$

$$F' = \frac{32W^2 fL}{g\pi^2 \rho_{ave}^2 D^5} \text{ ft of fluid} \quad \ldots\ldots [4]$$

The Fanning equation, in the form thus evolved, is chosen as the basic equation from which the graphs are to be developed because the weight rate of flow is a commonly used datum in problems related to the flow of air and steam. The length is taken as 100 ft. Introducing the numerical values of the constants

$$F' = \frac{32W^2 f \times 100 \times 12}{4.16995 \times 10^8 \times 9.8696 \rho^2 D^5} \text{ in. of fluid}$$

In order to give the pressure drop in inches of water the equation is multiplied by the ratio of the density of the fluid to that of water at 68 F

$$F = \frac{32W^2 f \times 100 \times 12}{4.16995 \times 10^8 \times 9.8696 \rho^2 D^5} \left(\frac{\rho}{62.31}\right)$$

$$F = 1.4975 \times 10^{-7} \frac{fW^2}{\rho D^5} \text{ in. } H_2O \quad \ldots\ldots [5]$$

Equation [5] is basically the equation to be graphed. However, in their present forms, several of the variables do not lend themselves readily to a graphical representation. The conditions of operating temperature and pressure, pipe diameter, and fluid-flow rate are the factors which are apt to be known, and efforts may be directed toward expressing the pressure drop in terms of these variables.

The friction factor f is a function of the Reynolds number and, therefore, of the rate of flow and viscosity of the fluid and the diameter of the pipe

$$f = f_n(\text{Re}) = f_n\left(\frac{4W}{\pi D\mu}\right)$$

In the literature their relation is usually illustrated by a graphical plot of log Re versus log f. Fig. 1 (3) is such a plot illustrating the data of a number of observers for clean pipes of steel and cast iron. The equation (4) given for the representation is

$$\frac{1}{\sqrt{f}} = 3.2 \log(\text{Re}\sqrt{f}) + 1.2$$

which is not suitable for use in the equation under discussion. A more satisfactory form used by a number of researchers relates f to the Reynolds number by an empirical equation of the form

$$f = K_1 + \frac{K_2}{(\text{Re})^n}$$

Assuming that by substitution of the proper values for K_1, K_2, and n it is possible to derive a formula which approximates the curve of Fig. 1; a series of values may be tried which finally yield

$$f = 0.00157 + \frac{0.101}{(\text{Re})^{0.282}} \quad \ldots\ldots [6]$$

The encircled points in Fig. 1 indicate the values of f obtained by use of the formula thus derived. Incorporating the value of f into Equation [5]

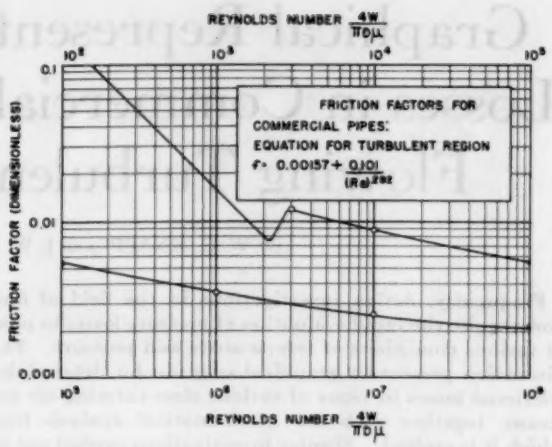

Fig. 1 Friction Factors for Isothermal Flow Data of Drew, Koo, and McAdams

(Plot points are solutions of given equation.)

$$F = 1.4975 \times 10^{-7}\left[0.00157 + \frac{0.101}{(\text{Re})^{0.282}}\right]\frac{W^2}{\rho D^5} \quad \ldots\ldots [7]$$

Incorporation of the Reynolds Number

The Reynolds number is given by $4W/\pi D\mu$. Of the terms in the expression, only μ is not readily evaluated. However, μ varies as a function of the temperature and at low pressures is essentially independent of the pressure. The relation of viscosity to temperature is most accurately expressed by Sutherland's equation. However, in order to minimize the complexity of the friction-drop equation, use is made of the exponential relation (5)

$$\mu = aT_k^x$$

where a and x are constants characteristic of the gas. The equation has been tested and verified by W. Licht, Jr., and D. G. Strechert (6). The exponential equation is incorporated into the friction-loss formula by the following adaptation

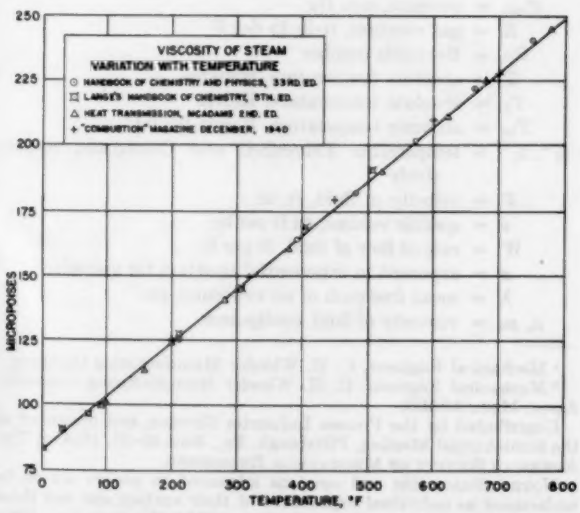

Fig. 2 Viscosity Variation of Steam With Temperature at Atmospheric Pressure

$$\frac{\mu}{\mu_0} = \frac{aT_k^x}{aT_{k_0}^x}$$

$$\mu = \mu_0 \left(\frac{T_k}{T_{k_0}}\right) \quad \ldots\ldots [8]$$

Thus, if the viscosity at 0 C and the exponent for the temperature ratio are known, viscosity may be evaluated at any desired temperature. For air (7), $\mu_0 = 0.01709$ centipoise and $x = 0.768$. The values of μ_0 and x for steam are established from data gathered from other sources and are plotted, Fig. 2. The plot points lie in an essentially straight line, the derived equation for which is

$$\mu = 0.207 t_F^\circ + 83.2 \text{ micropoises}$$

over the range plotted. At 32 F (0 C) the value of viscosity is $\mu = 0.00898$ centipoise. Since the plot is a straight line, μ must be a linear function of the temperature. For steam then, $\mu_0 = 0.00898$ centipoise and $x = 1.0$. The foregoing evaluation is verified as substantially correct by additional data (8) for μ and x. In order to retain English units, the viscosity is expressed in terms of the Fahrenheit temperature

$$\mu = \mu_0 \left(\frac{T_k}{273.1}\right)^x = \mu_0 \left(\frac{273.1 + t_C^\circ}{273.1}\right)^x$$

$$\mu = \mu_0 \left(1 + \frac{t_C^\circ}{273.1}\right) = \mu_0 \left[1 + \frac{5/9(t_F^\circ - 32)}{273.1}\right]^x$$

$$\mu = \mu_0 \left[1 + \frac{t_F^\circ - 32}{491.6}\right]^x \text{ centipoises} \quad \ldots\ldots [9]$$

For air

$$\mu = 0.01709 \left[1 + \frac{t_F^\circ - 32}{491.6}\right]^{0.768} \quad \ldots\ldots [10]$$

For steam

$$\mu = 0.00898 \left[1 + \frac{t_F^\circ - 32}{491.6}\right]^{1.00} \quad \ldots\ldots [11]$$

Writing Equation [9] into Equation [7]

$$F = 1.4975 \times 10^{-7} \left\{ 0.00157 + \left[\frac{0.101}{\frac{4W}{2.42\pi D\mu_0 \left(1 + \frac{t_F^\circ - 32}{491.6}\right)^x}}\right]^{0.282} \right\} \frac{W^2}{D^5} \quad [12]$$

Note that the conversion factor 2.42 has been introduced to convert centipoises to lb/hr-ft in order to keep the Reynolds number unitless.

There remains only the density to be expressed in terms of pressure and temperature. It is subject to variation with either of these factors. Their relationship is contained in the characteristic equation of a perfect gas

$$\rho = \frac{P}{RT} = \frac{144(0.4912)P_b}{R(459 + t_F^\circ)}$$

$$\rho = \frac{70.7328 P_b}{R(459.6 + t_F^\circ)} \quad \ldots\ldots [13]$$

For air $R = 53.35$ ft-lb/lb deg F

$$\rho = 1.3258 \frac{P_b}{(459.6 + t_F^\circ)} \quad \ldots\ldots [14]$$

For steam

$$R = 85.71 \text{ ft-lb/lb deg F}$$

$$\rho = 0.8253 \frac{P_b}{(459.6 + t_F^\circ)}$$

Writing Equation [13] into Equation [12] yields the final form of the general equation from which the graphs are evolved

$$F = \frac{1.4975 \times 10^{-7} W^2}{\left[\frac{70.7328 P_b}{R(459.6 + t_F^\circ)}\right] D^5} \left\{ 0.00157 + \frac{0.101}{\left[\frac{4W}{2.42\pi D\mu_0 \left(1 + \frac{t_F^\circ - 32}{491.6}\right)^x}\right]^{0.282}} \right\} \quad \ldots\ldots [15]$$

DEVELOPMENT OF THE GRAPHS

In order to plot the equation, the constants are evaluated and combined to provide separate similar equations for the air and the steam. The final equation derived for air is

$$F = \frac{1.4975 \times 10^{-7} (459.6 + t_F^\circ) W^2}{1.3258 P_b D^5} \left\{ 0.00157 + \frac{0.101}{\left[\frac{4W}{2.42\pi D \times 0.01709 \left(1 + \frac{t_F^\circ - 32}{491.6}\right)^{0.768}}\right]^{0.282}} \right\}$$

$$F = \frac{1.1295 \times 10^{-7} (459.6 + t_F^\circ) W^2}{P_b D^5} \left\{ 0.00157 + 0.038424 \left[\frac{D}{W} \left(1 + \frac{t_F^\circ - 32}{491.6}\right)^{0.768}\right]^{0.282} \right\} \quad [16]$$

The problem of plotting the pressure-drop graph from the equation derived can be approached by first separating F into the sum of two components F_1 and F_2 such that $F = F_1 + F_2$ when

$$F_1 = \frac{1.1295 \times 10^{-7} (459.6 + t_F^\circ) W^2}{P_b D^5} \times 0.00157 \quad \ldots [17]$$

$$F_2 = \frac{1.1295 \times 10^{-7} (459.6 + t_F^\circ) W^2}{P_b D^5} \times 0.038424 \left[\frac{D}{W} \left(1 + \frac{t_F^\circ - 32}{491.6}\right)^{0.768}\right]^{0.282} \quad \ldots\ldots [18]$$

Base values may be assigned to the variables

$$P_b = 1 \text{ in. Hg}, \quad t_F^\circ = 68^\circ, \text{ and } D = 10/12 \text{ ft}$$

The equations then reduce to

$$F_1 = \frac{1.1295 \times 10^{-7} (527.6) W^2}{1 \times \left(\frac{10}{12}\right)^5} \times 0.00157 = 2.3281 \times 10^{-7} W^2$$

$$F_2 = \frac{1.1295 \times 10^{-7} (527.6) W^2}{1 \times \left(\frac{10}{12}\right)^5} \times 0.038424 \left[\frac{5}{6W} (1.05578)\right]^{0.282}$$

$$= 5.4960 \times 10^{-6} W^{1.718}$$

Using these base values, various rates of flow may be assumed

for W and the resultant components F_1 and F_2 may be plotted for their corresponding flow rates.

The friction loss varies inversely with the operating pressure of the system. Hence, if the base value of friction loss is multiplied by the ratio of the base pressure divided by the desired pressure, the friction loss for any desired pressure will result. Since the base pressure is taken as unity, it is necessary only to divide the pressure loss, corrected for temperature and diameter when necessary, by the desired operating pressure. The equation

$$F = \frac{F_1 + F_2}{P_b}$$

represents the evaluation of F when all variables have their base values except the pressure.

The powers to which D is raised in each of the Equations [17] and [18] are different. In Equation [17] D is raised to the fifth power. By a treatment similar to that applied to the operating pressure, the correction factor necessary to find the pressure loss in a pipe of any diameter is given by

$$C_{D1} = \frac{10^5}{d^5} \quad \ldots\ldots [19]$$

In Equation [18], by combining exponents, D is raised to the 4.718 power. The correction factor will be

$$C_{D2} = \frac{10^{4.718}}{d^{4.718}} \quad \ldots\ldots [20]$$

For each of these Equations [19] and [20], the correction factor can be plotted as a function of the diameter. The equation

$$F = \frac{(F_1 C_{D1}) + (F_2 C_{D2})}{P_b}$$

represents the evaluation of F when temperature is the only variable retaining its base value.

As with pressure and diameter, the change of F with the temperature can be determined by a ratio of the temperatures involved. For Equation [17]

$$C_{T1} = \frac{459.6 + t_F^\circ}{459.6 + 68} \quad \ldots\ldots [21]$$

A more complex formula is required for the correction of temperature in Equation [18]

$$C_{T2} = \frac{459.6 + t_F^\circ}{459.6 + 68} \left[\frac{\left(1 + \frac{t_F^\circ - 32}{491.6}\right)^{0.216576}}{\left(1 + \frac{68 - 32}{491.6}\right)^{0.216576}} \right]$$

$$C_{T2} = KC_{T1} \left(1 + \frac{t_F^\circ - 32}{491.6}\right)^{0.216576} \quad \ldots\ldots [22]$$

Equations [21] and [22] can be solved and the correction factors can be plotted as functions of their corresponding temperatures.

The final equation of the graphic factors for any assumed pressure, temperature, and diameter is

$$F = \frac{(F_1 C_{D1} C_{T1}) + (F_2 C_{D2} C_{T2})}{P_b}$$

for air, when the correction factors corresponding to these conditions are determined from the graph for any desired rate of flow.

The final equation derived for steam is

$$F = \frac{1.4975 \times 10^{-7}(459.6 + t_F^\circ)W^2}{0.8253\, P_b\, D^5} \left\{ 0.00157 + \frac{0.101}{\left[\frac{4W}{2.42\,\pi D \times 0.00898 \left(1 + \frac{t_F^\circ - 32}{491.6}\right)} \right]^{0.262}} \right\}$$

$$F = \frac{1.8145 \times 10^{-7}(459.6 + t_F^\circ)W^2}{P_b\, D^5} \times \left[0.00157 + 0.032048 \left\{ \frac{D}{W} \left(1 + \frac{t_F^\circ - 32}{491.6}\right) \right\}^{0.262} \right] \ldots [23]$$

A set of separate curves similar to those developed for air could be plotted for steam. However, on a single graph, the greater number of curves would tend to be confusing. In order to simplify the graphs the equation for steam can be related to the equation for air by determining the differences between the two equations and then inserting the resultant differences in one of the correction factors only. It is most convenient to incorporate the differences into the temperature-correction factor. When the pressure loss for steam F is separated into the sum of $F_1 + F_2$

$$F_1 = \frac{1.8145 \times 10^{-7}(459.6 + t_F^\circ)W^2}{P_b\, D^5} \times 0.00157 \ldots [24]$$

$$F_2 = \frac{1.8145 \times 10^{-7}(459.6 + t_F^\circ)W^2}{P_b\, D^5} \times 0.032048 \left[\frac{D}{W} \left(1 + \frac{t_F^\circ - 32}{491.6}\right) \right]^{0.262} \ldots\ldots [25]$$

Comparison of Equation [24] with Equation [17] reveals that for steam $F_1 > F_1$ for air by

$$\frac{1.8145}{1.1295} = 1.60646$$

Similarly, from comparison of Equations [25] and [18], for steam $F_2 > F_2$ for air by

$$\frac{1.8145 \times 0.032048 \left(1 + \frac{36}{491.6}\right)^{0.262}}{1.1295 \times 0.038425 \left(1 + \frac{36}{491.6}\right)^{0.216576}} = 1.346$$

Thus the incorporation of these factors into the temperature-correction factors enables the original values of F_1 and F_2 for air to be used to determine the pressure drop for steam as well.

Further examination of Equations [24] and [25] indicates that both P_b and D are identical in value with the same factors in Equations [17] and [18]. Therefore the pressure may be treated mathematically in the same manner as for air and the diameter-correction curve for air may be applied intact to the evaluation of pressure loss for steam systems.

The corrections for temperature are determined in a manner similar to that used for the air curves but are further modified by the corrections carried over from the revaluation of F_1 and F_2 for steam.

For Equation [24]

$$C_{T1}' = 1.60646 \times \frac{459.6 + t_F^\circ}{459.6 + 68}$$

$$C_{T1}' = 1.60646 \times C_{T1} \quad \ldots\ldots [26]$$

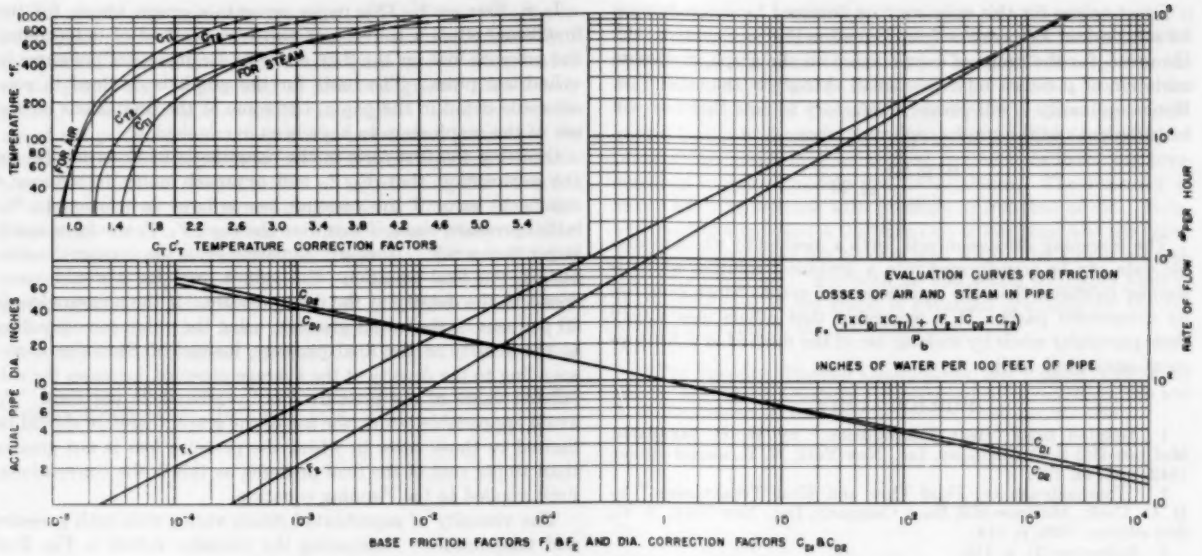

FIG. 3 EVALUATION CURVES FOR FRICTION LOSSES OF AIR AND STEAM IN PIPE
(Note that P_b in given equation is actual pressure, in. Hg.)

and for Equation [25]

$$C_{T2}' = 1.346 \times \frac{459.6 + t_F°}{459.6 + 68} \left[\frac{\left(1 + \frac{t_F° - 32}{491.6}\right)^{0.282}}{\left(1 + \frac{68 - 32}{491.6}\right)^{0.282}} \right]$$

$$C_{T2}' = K' C_{T1}' \left(1 + \frac{t_F° - 32}{491.6}\right)^{0.282} \quad \ldots\ldots\ldots [27]$$

Equations [26] and [27] may be plotted on the graph containing the temperature-correction factors for air. The graph, Fig. 3, is then complete.

Illustrative Problem

Consider a brief example to illustrate the use of the graph. It is desired to determine the loss in pressure in a pipe connecting a jet ejector to a condenser. An estimate places the air being removed at 370 lb per hr. The suction line is 12 in. diam and 10 ft in length. The ejector maintains a pressure of 2.5 in Hg, and the air being removed will have a temperature of 100 F. From the flow rate of 370 lb per hr, the graph yields $F_1 = 3.19 \times 10^{-2}$, and $F_2 = 0.142$. For the given diameter obtain $C_{D1} = 0.402$ and $C_{D2} = 0.423$, and for the given temperature obtain $C_{T1} = 1.06$ and $C_{T2} = 1.075$. The pressure loss will be

$$F = \frac{L}{100} \frac{1}{P_b} [(F_1 C_{D1} C_{T1}) + (F_2 C_{D2} C_{T2})]$$

$$F = \frac{10}{100} \times \frac{1}{2.5} [1.36 \times 10^{-2} + 6.46 \times 10^{-2}]$$

$$F = 0.00313 \text{ in. } H_2O \text{ (total)}$$

The accuracy of this method is limited only by the accuracy of the data upon which it is based and the resolution possible in reading the graph. The most uncertain factor is the friction-factor curve; all experimental data upon which the friction-factor curve, Fig. 1, are based, are described as plotting within plus or minus 10 per cent of the values represented by the curve. The lack of greater accuracy is most probably due to the fact that the curve fails to recognize the effect of tube size and tube roughness upon the friction factor. The relative roughness is generally considered an important criterion in more accurate evaluations of the friction factors. The plot adopted for this study apparently endeavors to provide a single curve which approximates the possible factors with an error less than or equal to 10 per cent.

Limits of Applicability

It is necessary to define the limit beyond which the graphs will not furnish correct results. Investigation to determine whether or not the use of a very low pressure will result in molecular flow yields the relationship (9)

$$P_{mm} \lambda = 1.945 \times 10^{-2}$$

Only when the mean free path of air molecules λ exceeds the diameter of the pipe will molecular flow occur. If 0.1 in. of mercury is assumed to be the minimum pressure applied to the graphs, the dimension in inches at which the mean free path equals the diameter is given by

$$\lambda = d = \frac{1.945 \times 10^{-2}}{0.1 \times 25.4} = 7.66 \times 10^{-4} \text{ in.}$$

Therefore, in no case is there a molecular flow.

Although the graphs are developed from an equation involving turbulent flow, the ranges across which the various factors extend permit selections of pressure, temperature, and pipe diameter such that the Reynolds number resulting would fall below 3000. As may be seen in Fig. 1, the flow is then laminar and the corresponding friction factors are evaluated differently. Therefore some simple method to determine whether or not the flow is turbulent is needed. If the Reynolds number is taken as 3000 in the equation

$$\text{Re} = \frac{4\,W}{2.42\,\pi D \mu}$$

it is possible to write the ratio

$$\frac{W}{d} = 475.17\,\mu$$

Exact values for this ratio may be obtained by determining μ for any desired temperature from Equation [10] or Equation [11]. However, for the range of temperature on the graph, maximum variation of μ causes relatively small changes in the ratio W/d. Hence ordinarily it will prove satisfactory to note that flow will be turbulent and the graphs applicable when

$$\frac{W \text{ lb/hr}}{d \text{ in.}} \geqq 20$$

The foregoing discussion sets forth a method by which available data can be transformed into a graphical solution which is simpler to utilize than the equations and graphs which comprise its component parts. It is suggested that others may satisfy their particular needs by making use of the method or a development analogical to it.

BIBLIOGRAPHY

1 Adapted from "Heat Transmission," by W. H. McAdams, McGraw-Hill Book Company, Inc., New York, N. Y., second edition, 1942, pp. 114, 127.

2 "Thermodynamics, Fluid Flow and Heat Transmission," by H. O. Croft, McGraw-Hill Book Company, Inc., New York, N. Y., first edition, 1938, p. 114.

3 Reference (1), p. 118.

4 "Fluid Flow in Clean Round Straight Pipe—II Commercial Steel Pipe Lines," by B. Miller, discussion by T. B. Drew and R. P. Genereaux, Trans. AICE, vol. 32, 1936, pp. 17–19.

5 "Scientific Foundations of Vacuum Technique," by S. Dushman, John Wiley & Sons, Inc., New York, N. Y., 1949, p. 34.

6 "The Variation of the Viscosity of Gases and Vapors With Temperature," by W. Licht, Jr., and D. G. Strechert, *Journal of Physical Chemistry*, vol. 48, 1944, p. 23.

7 "Chemical Engineers' Handbook," by J. H. Perry, McGraw-Hill Book Company, Inc., New York, N. Y., second edition, 1941, p. 792.

8 Reference (5), pp. 36–37.

9 "High Vacua, Principles, Production, and Measurement," by Swami Jnanananda, D. Van Nostrand Company, Inc., New York, N. Y., 1947, p. 31.

Discussion

GEORGE KARNOFSKY.[4] The method of graphing standard friction-loss data applied to air and steam conceived by the authors will make a useful addition to the handbooks. The final charts may be used easily and have the correct precision.

Although the title states that the paper is concerned with low pressures, these are nowhere defined except in the section, Limits of Applicability. Here it is pointed out that the pressure cannot be so low that the flow is molecular. The upper pressure limit would appear to be determined by the applicability of the perfect-gas law, which is assumed to apply.

The average gas density which must be used in applying these charts is correctly denoted as ρ_{avg} in Equation [4], but from then on the subscript is not used, and in the illustrative problem the pressure drop is small enough that this point is of no consequence. When the pressure drop is large, an average value of P_b (which is not clearly defined as the average pressure) must be assumed and the problem solved by trial.

The illustrative problem would be improved if the values of F_1, F_2, etc., as given, were those read from the graphs instead of calculated values. The graphs cannot be read with a precision better than about 10 per cent, but this is about the correct precision for the empirical friction-factor equation on which the charts are based.

The derivation of the statement that W/d approximates 20 when the Reynolds number is 3000 is not clear. In any case, this seems like an unnecessary simplification.

[4] Chemical Plants Division, Blaw-Knox Company, Pittsburgh, Pa.

L. S. STINSON.[5] This paper presents a graph which, for the first time, offers a convenient and easy method of determining the pressure loss for the flow of air or steam at low pressures in cylindrical pipes. The basis for the graph is outlined in considerable detail in the paper, but some of the limitations on the use of the graph seem to have been overlooked.

Omitting the first term in the parenthesis in Equation [2] on the assumption that V_2/V_1 will approach unity introduces a significant error if the pressure loss is large in relation to the initial pressure, since, if this were the case, V_2/V_1 would be much larger than unity. Also, ρ in Equation [4] is the average density, but, in the final equations, the values used for ρ would correspond to the density at the final pressure. If the pressure loss is 20 per cent of the initial pressure, using the value corresponding to the density at the final pressure, instead of the value corresponding to the density at the average pressure, increases the calculated value of the pressure loss by around 26 per cent. To avoid appreciable errors, the use of the graph therefore should be limited to those cases in which the pressure loss is not greater than 10 per cent of the final pressure, as this is the conventional limit applied to the Fanning equation.

The viscosity of superheated steam varies with both pressure and temperature. Comparing the viscosity values in Fig. 2 of the paper with the viscosity values for steam given in Fig. 16, Part 5, Chapter 4, "Flow Measurement by Means of Standardized Nozzles and Orifice Plates" of the ASME Power Test Codes published in 1940, indicates the viscosity values for steam used in the final equation in the paper corresponding to those for superheated steam at around 25 psia pressure. Since the numerical value for the viscosity of steam at 800 psia, 600 F, is approximately 1.79 times that for the viscosity of steam at 25 psia, 600 F, the graph for steam should not be used for pressures higher than, say, around 100 psia or so.

With the proper limitations established, the graph will be of considerable practical value, and the authors are to be congratulated for contributing these useful data.

AUTHORS' CLOSURE

The authors wish to express their thanks to Messrs. Karnofsky and Stinson for their written discussions and to all those who participated in the discussions at the Semi-Annual Meeting; their comments have suggested several addenda which should lend additional value to the paper.

In the Preliminary Analysis of the paper it was assumed that values of V_2/V_1 approach unity. Implicit in such an assumption is the condition that should the pressure drop exceed approximately ten per cent of the average pressure, appreciable error may be introduced. Further, while in the mathematical analysis average values were assigned, in actual practice the user of the graph is apt to know or to have assumed one of the terminal values of the pressure. Although such a value is acceptable for use with the graph, it can readily be seen that a large pressure drop may separate the assumed terminal pressure from the average pressure by a considerable amount. It would appear then, that a large pressure drop would invalidate the use of the graph, but such is not the case. In the event that a problem solved with the aid of the graph appears to have a large pressure drop compared to the operating pressure, one may check the percentage ratio of pressure drop to operating pressure. If the ratio yields a value greater than ten per cent, a more accurate solution may be obtained by dividing the length of pipe involved into several smaller lengths and solving them in tandem sequence, each as a separate problem. The sum of the individual pressure drops of the separate problems will yield the desired total pressure drop.

[5] Elliott Company, Jeannette, Pa.

The graph was originally intended to apply to problems involving turbulent flow at subatmospheric pressures. Actually, if the factors involved are weighed with some care, the application of the graph may be extended to pressures greater than atmospheric. The analysis upon which the graph is based involves the use of the perfect-gas law. At low pressures real gases obey the law rather well but as pressure increases to multiples of an atmosphere they deviate. One method of representing the deviation of a real-gas from the perfect-gas law is by the use of a compressibility factor. A general reduced-pressure compressibility chart[6] for various reduced temperatures may be consulted to determine the degree of departure of air or steam from the perfect-gas law at pressures greater than atmospheric. If a limit of 5 per cent deviation from the perfect-gas law is observed for air, it is possible to extend the use of the graph for air to about 30 atmospheres. Actually, the value of 30 atmospheres is conservative but since the viscosity of air also increases[7] with pressure to a maximum of about 4 per cent at 30 atmospheres, the maximum net error will be in excess of 5 per cent but less than the 10 per cent to which the graph is accurate. Assuming a tolerance of 5 per cent deviation from the perfect-gas law for steam, the pressure-loss graph may be applied to problems involving pressures up to approximately five atmospheres. The viscosity of steam tends to increase with pressure as did that of air. However, at five atmospheres the variation is less than one per cent.[7] Hence the maximum net error is well within the 10 per cent allowed for the graph. For both air and steam the upper limit of the applicability of the graph is governed primarily by the adherence of the gas to the perfect-gas law.

[6] "Chemical Engineering Thermodynamics," by B. F. Dodge, McGraw-Hill Book Co., Inc., New York, N. Y.

[7] "The Viscosity, Thermal Conductivity, and Prandtl Number for Air, O_2, N_2, NO, H_2, CO, CO_2, H_2O, He, and A," by J. Hilsenrath and Y. S. Touloukian, Trans. ASME, vol. 76, 1954, pp. 967–985.

Fanning Friction Factors for Air Flow at Low Absolute Pressures in Cylindrical Pipes

By W. J. BOHNET[1] AND L. S. STINSON[2]

As there are no published data verifying the theoretical Fanning friction factors for streamline flow of air at low absolute pressures, an investigation was made of the pressure drops in 6 to 18-in-diam pipe lines in which room-temperature air was flowing at absolute pressures varying from 50 microns Hg to 1 mm Hg. The large number of pressure-drop readings taken at various rates of flow permits developing friction-factor curves for this type of flow. These are presented in this paper.

Introduction

IN designing a large vacuum system to be operated at an absolute pressure between 50 microns Hg and 1 mm Hg, one of the uncertainties encountered in determining the size of the cylindrical pipe lines to be used is the reliability of existing friction-factor data. Since the cost of maintaining a low absolute pressure in a large system evolving gases is high, a low pressure drop in the pipe lines connecting the system to the vacuum-producing equipment is extremely desirable. This, in turn, indicates that the gas flow should be streamline or viscous flow rather than turbulent flow since the pressure drop with streamline flow is always lower than it is with turbulent flow. Calculations to determine the size of the pipe line to insure getting a low pressure drop with streamline flow usually are made by using the Fanning equation in which the Hagen-Poiseuille friction factor f (16 divided by the Reynolds number) is used. This friction factor was derived from the conventional equation expressing Poiseuille's law of viscous flow. While tests, having a rather high experimental error, with hydrocarbon oils[3] and tests with air in small-diameter tubes for Reynolds numbers higher than 1250[4] tend to verify it, there are no published data verifying its accuracy for gas flows at low absolute pressures where the flow may be a combination of streamline and free molecular flow.[5]

This problem was encountered in designing a magnesium-producing plant which was built in 1943, near Spokane, Wash., as this plant required vacuum piping of capacities and lengths never before attempted. After a small amount of experimental work and with the advice and suggestions generously furnished by others with some experience in this field, the pipe-line sizes were selected with some misgivings relative to their being of sufficient size to give low pressure drops.

Two of the four sections of this plant included an 18-in-diam manifold approximately 410 ft long which operated at around 100 microns Hg abs pressure with a gas flow in it, equivalent to 10 lb per hr of 70 F dry air (16,900 cfm at 100 microns Hg). These sections also included a 12-in-diam manifold approximately 418 ft long which operated at around 800 microns Hg abs pressure with a gas flow in it, equivalent to 47 lb per hr of 70 F dry air (9940 cfm at 800 microns Hg), and several 8 and 6-in-diam secondary manifolds approximately 70 ft long which operated at about these same absolute pressures with smaller flows. The other two sections of the plant had slightly shorter manifolds. When a reduction in the production of magnesium in 1944 permitted part of the plant to be shut down, it was decided to make a rather extensive investigation of pressure drops to see if data could be secured which would permit a more accurate determination of pipe-line sizes for future vacuum systems of this kind.

Test Arrangements

A half-section of the plant which contained the longest sections of the main manifolds and which was not in use was selected for this test work. To determine accurately the inside diameter of the large pipe lines in it and to check the condition of the inside walls, three $1^3/_4$-in-diam holes were cut in both the 18 and the 12-in. pipe lines. Measurements were taken of the wall thickness adjacent to the holes, and the outside circumferences also were measured. The condition of the inside walls was observed through the holes. With one exception, the inside walls were found to be smooth although covered with a very light deposit of white dust. The exception was a point in the 18-in. line which was not in the test section but was between the test section and the steam-jet air ejectors used to produce vacuum. At this location there was a layer of black material approximately 8-in. across and 1-in. deep in the center. The length of this deposit was not determined.

The absolute-pressure gages used were the small portable Stokes' McLeod type. These were cleaned thoroughly and then checked against a Columbia Model laboratory standard McLeod gage before the tests, rechecked once during the tests, and rechecked again after the completion of the tests. Cold traps were used when checking the gages and when taking the test readings. The traps consisted of a glass U-tube submerged in a mixture of acetone and carbon-dioxide ice in a Dewar flask. The reading of the portable McLeod gages was rather difficult, particularly so when attempting to determine small pressure changes in the absolute-pressure range below 300 microns Hg. Additional calibration marks were inscribed on the scales to facilitate reading in this range; however, some difficulty was still encountered in checking the readings.

Gage connections consisted of a $^1/_4$-in. standard pipe nipple welded to the outside of the pipe over a $^3/_8$-in-diam hole previously

[1] Research Engineer, Metals Research Laboratories, Electro-Metallurgical Company, Niagara Falls, N. Y.

[2] Development Contracts Department, Elliott Company, Jeannette, Pa.

[3] "The Flow of Fluids Through Commercial Pipe Lines," by R. E. Wilson, W. H. MacAdams, and M. Seltzer, *Industrial and Engineering Chemistry*, vol. 14, 1922, pp. 105–119.

[4] "Similarity of Motion in Relation to the Surface Friction of Fluids," by T. E. Stanton and J. R. Pannell, Philosophical Transactions of the Royal Society of London, England, series A, vol. 214, 1914, p. 199.

[5] "Calculations for High Vacuum Systems," by W. P. Dryer, *Chemical Engineering*, vol. 54, 1947, pp. 127–131.

Contributed by the Process Industries Division and presented at the Semi-Annual Meeting, Pittsburgh, Pa., June 20–24, 1954, of The American Society of Mechanical Engineers.

Note: Statements and opinions advanced in papers are to be understood as individual expressions of their authors and not those of the Society. Manuscript received at ASME Headquarters, February 2, 1954. Paper No. 54—SA-16.

drilled through the pipe wall. Before welding, all projections were removed from the inside of the pipe wall.

All of the lubricated plug valves segregating each test line from the rest of the system were greased and rotated to distribute the grease. The 18 and the 12-in. test lines were checked for air-tightness by evacuating to low absolute pressure, completely closing them off, and observing the pressure rise. It was found there was some leakage through the center valves connecting the 18 and 12-in. manifolds in this section of the plant to similar 18 and 12-in. manifolds in the immediately adjacent section of the plant. This leakage was believed due to the fact that these center valves were the only segregating valves which were not lubricated plug valves. Therefore it was decided to operate the steam-jet air ejectors serving the manifolds in the adjacent plant section and maintain a relatively low absolute pressure in these manifolds so as to reduce greatly the leakage through the center valves. With this arrangement the pressure rise in the test manifolds was reduced to a maximum of 10 microns Hg per min based on both 1-hr and 3-hr tests. This indicated the air leakage into the full section lengths, which are more than twice the length of the test lines, was quite small as it was only 0.036 lb per hr for the 18-in. line and 0.018 lb per hr for the 12-in. line. It is believed most of this small amount of leakage was through the center valves. Leakage through these valves did not affect the pressure-drop readings in any way, as it entered the manifolds outside of the test sections and did not go through them.

To measure the temperature of the air flowing in the pipe lines, holes approximately 1 in. in diam were cut at about the center of each test section, and after proper cleaning a $1^1/_4$-in. standard pipe fitting was welded to the outside of the pipe. A thermometer was then inserted into the pipe line through a rubber stopper fitted into the $1^1/_4$-in. pipe fitting.

The air flow through the pipe lines was measured by means of a set of small flow nozzles of the Heat Exchange Institute type.[6] The nozzles were screwed into fittings previously welded in the extreme end of each test line, as illustrated in Figs. 1 to 3. The operating absolute-pressure level was changed by using a similar set of nozzles to admit air in the lines beyond the test sections and near the steam-jet air ejectors. The flow nozzles used had nominal flows of 2.5, 5.0, 20.0, 25.0, and 50.0 lb per hr. These nominal values were corrected to the correct values for the observed upstream temperature and pressure of the air. The air was assumed dry, and the weight of water vapor in the air was ignored as wet and dry-bulb observations of the air admitted to the flow nozzles indicated the weight of water vapor in it varied from a minimum of 0.005 to a maximum of 0.007 lb per lb of air and this was regarded as insignificant.

One condition that was undesirable for the tests but which could not be avoided was that all of the lines tested were manifolds and had a few smaller lines, equally spaced, branching from

[6] "History of the Development, Manufacture, and Calibration of HEI Standard Flow Nozzles," by H. S. Bean, W. H. Reynolds, and R. M. Johnson, Heat Exchange Institute, first edition, 1946, p. 6.

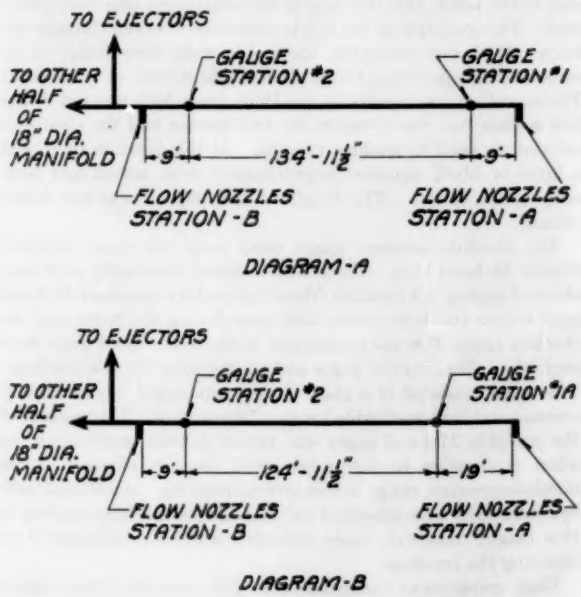

FIG. 1 TEST ARRANGEMENTS FOR 18-IN. LINE

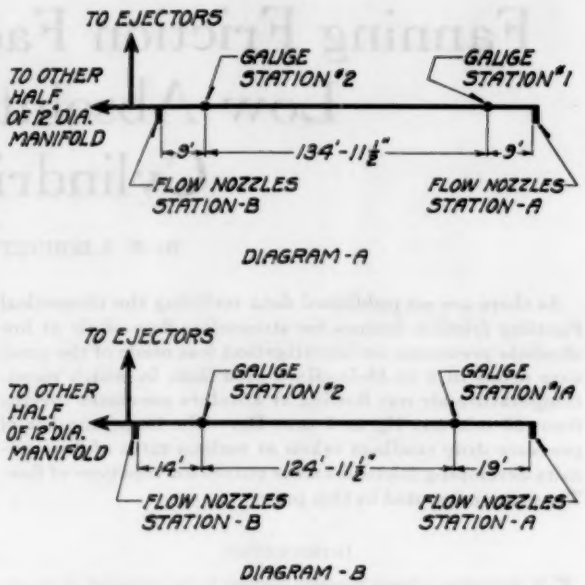

FIG. 2 TEST ARRANGEMENTS FOR 12-IN. LINE

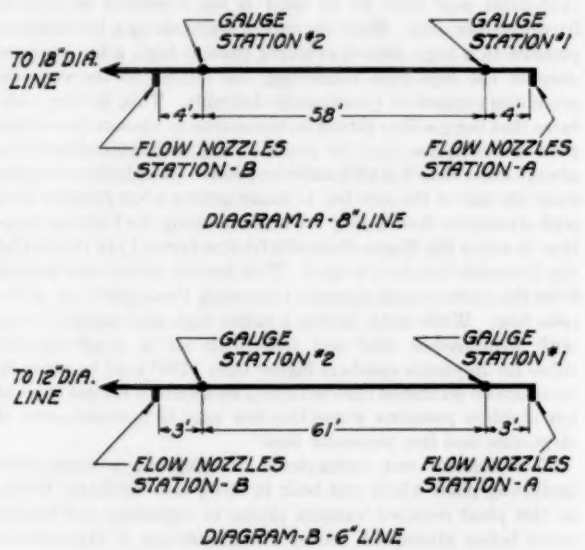

FIG. 3 TEST ARRANGEMENTS FOR 8 AND 6-IN. LINES

them so that they did not have continuous wall surface on one side. For example, the 18-in. test section had six 8-in. lines branching from it, and the 12-in. test section had six 6-in. lines branching from it. Both the 8 and the 6-in. test sections had four 6-in. lines branching from them.

Pressure-Drop Readings

Fig. 1, diagram A, shows the length of the 18-in. line tested and the location of the gage connections and flow nozzles for the pressure-drop readings given in Table 1, first test, and Table 2, first check test. Fig. 1, diagram B, is a similar diagram for the pressure-drop readings given in Table 3, second check test. This third test was run on the same 18-in. test section to see if the location of the gage connection at station No. 1 relative to the location of flow nozzles at station A had any influence on the pressure readings.

Fig. 2, diagram A, shows the length of the 12-in. line tested and the location of the gage connections and flow nozzles for the pressure-drop readings given in Table 4, first test, and Table 5, first check test. Fig. 2, diagram B, is a similar diagram for the pressure-drop readings given in Table 6, second check test. This test was run on the same 12-in. test section to see if the location of the gage connection at station No. 1 relative to the location of the flow nozzles at station A had any influence on the pressure readings.

Fig. 3, diagram A, shows the length of the 8-in. line tested and the location of the gage connections and the flow nozzles for the pressure-drop readings given in Table 7, first test, and Table 8, first check test. Fig. 3, diagram B, shows the length of the 6-in. line tested and the location of the gage connections and flow nozzles for the pressure-drop readings given in Table 9.

The air temperature given in the tables is the temperature of the air upstream of the flow nozzles at station A. The temperature of the air measured in the test sections is not given in the tables as it was either the same or appreciably less than 1 deg F different from the temperature of the air admitted through the flow nozzles.

TABLE 1 FIRST TEST ON 18-IN. LINE

18" diameter standard weight pipe - 17.192" I.D.

Length of test section - 134.958'

Average inlet air temperature - 56F

Barometric pressure - 713 MM Hg

Date of test - 10/12/44

Air Flow #/hr. at Station A	Pressure in Microns Hg Station 1 P_1	Station 2 P_2	$P_1 - P_2$	Air Flow #/hr. at Station B	Calculated f Values	Reynolds Number
2.38	85	58	27	0	0.551	49.4
4.76	109	73	36	0	0.232	98.8
19.05	238	175	63	0	0.057	395.5
23.77	297	245	52	0	0.039	493.0
47.55	530	440	90	0	0.030	987.0
2.38	97	68	29	2.38	0.683	49.4
4.76	109	83	26	2.38	0.173	98.8
19.05	254	213	41	2.38	0.041	395.5
23.77	308	266	43	2.38	0.035	493.0
47.55	530	455	75	2.38	0.026	987.0
2.38	109	83	26	4.76	0.714	49.4
4.76	121	98	23	4.76	0.179	98.8
19.05	297	230	67	4.76	0.077	395.5
23.77	345	282	63	4.76	0.055	493.0
47.55	570	460	110	4.76	0.041	987.0
2.38	210	180	30	19.05	1.674	49.4
4.76	238	212	26	19.05	0.419	98.8
19.05	355	335	20	19.05	0.030	395.5
23.77	460	380	80	19.05	0.095	493.0

TABLE 2 FIRST CHECK TEST ON 18-IN. LINE

18" diameter standard weight pipe - 17.192" I.D.

Length of test section - 134.958'

Average inlet air temperature - 64F

Barometric pressure - 710 MM Hg

Date of test - 10/24/44

Air Flow #/hr. at Station A	Pressure in Microns Hg Station 1 P_1	Station 2 P_2	$P_1 - P_2$	Air Flow #/hr. at Station B	Calculated f Values	Reynolds Number
2.35	79	48	31	0	0.570	48.0
4.69	109	68	41	0	0.264	95.6
18.78	238	175	63	0	0.059	383.0
23.46	312	230	82	0	0.065	479.0
46.9	530	432	98	0	0.034	956.0
2.35	97	63	34	2.35	0.787	48.0
4.69	120	84	36	2.35	0.267	95.6
18.78	274	200	74	2.35	0.079	383.0
23.46	330	255	75	2.35	0.064	479.0
46.9	540	450	90	2.35	0.033	956.0
2.35	105	75	30	4.69	0.855	48.0
4.69	138	94	44	4.69	0.371	95.6
18.78	298	225	73	4.69	0.087	383.0
23.46	332	269	63	4.69	0.070	479.0
46.9	565	470	95	4.69	0.036	956.0
2.35	205	165	40	18.78	2.128	48.0
4.69	238	202	36	18.78	0.576	95.6
18.78	380	315	65	18.78	0.102	383.0
23.46	430	360	70	18.78	0.081	479.0
2.35	237	215	22	23.46	1.438	48.0
4.69	268	235	33	23.46	0.603	95.6
18.78	415	360	55	23.46	0.097	383.0
23.46	470	410	60	23.46	0.077	479.0

TABLE 3 SECOND CHECK TEST ON 18-IN. LINE

18" diameter standard weight pipe - 17.192" I.D.

Length of test section - 134.958'

Average inlet air temperature - 48F

Barometric pressure - 705.4 MM Hg

Date of test - 11/8/44

Air Flow #/hr. at Station A	Pressure in Microns Hg Station 1A P_1	Station 2 P_2	$P_1 - P_2$	Air Flow #/hr. at Station B	Calculated f Values	Reynolds Number
2.38	120	104	16	0	0.563	50.2
4.75	150	109	41	0	0.420	100.1
19.03	280	213	67	0	0.081	401.0
23.77	327	255	72	0	0.066	501.0
47.54	567	480	87	0	0.036	1001.0
2.38	138	130	8	5.0	0.337	50.2
4.75	165	148	17	5.0	0.211	100.1
19.03	298	260	38	5.0	0.052	401.0
23.77	345	295	50	5.0	0.051	501.0
47.54	590	530	60	5.0	0.027	1001.0
2.38	268	234	34	25.0	2.682	50.2
4.75	298	260	38	25.0	0.840	100.1
19.03	427	390	37	25.0	0.074	401.0
23.77	482	430	52	25.0	0.075	501.0
2.38	495	470	25	50.0	3.788	50.2
4.75	500	480	20	50.0	0.778	100.1

Calculations

As the observed pressure drops were, in most cases, more than

TABLE 4 FIRST TEST ON 12-IN. LINE

12" diameter standard weight pipe - 12.0" I.D.

Length of test section - 134.958'

Average inlet air temperature - 60F

Barometric pressure - 709 MM Hg

Date of test - 10/13/44

Air Flow #/hr. at Station A	Pressure in Microns Hg Station 1 P_1	Station 2 P_2	$P_1 - P_2$	Air Flow #/hr. at Station B	Calculated f Values	Reynolds Number
2.35	238	225	13	0	0.145	69.2
4.7	327	277	50	0	0.182	138.3
18.8	585	480	105	0	0.042	554.5
23.5	700	545	155	0	0.047	692.0
2.35	297	275	22	2.35	0.305	69.2
4.7	355	320	35	2.35	0.143	138.3
18.8	640	525	115	2.35	0.051	554.5
23.5	750	585	165	2.35	0.053	692.0
2.35	355	310	45	4.7	0.724	69.2
4.7	412	360	52	4.7	0.243	138.3
18.8	700	550	150	4.7	0.071	554.5
23.5	755	620	135	4.7	0.045	692.0
2.35	585	530	55	18.8	1.484	69.2
4.7	640	565	75	18.8	0.546	138.3
2.35	640	600	40	23.5	1.198	69.2
4.7	700	630	70	23.5	0.562	138.3

TABLE 5 FIRST CHECK TEST ON 12-IN. LINE

12" diameter standard weight pipe - 12" I.D.

Length of test section - 134.958'

Average inlet air temperature - 58F

Barometric pressure - 710 MM Hg

Date of test - 10/24/44

Air Flow #/hr. at Station A	Pressure in Microns Hg Station 1 P_1	Station 2 P_2	$P_1 - P_2$	Air Flow #/hr. at Station B	Calculated f Values	Reynolds Number
2.36	268	210	58	0	0.671	69.8
4.72	330	265	65	0	0.232	139.8
18.9	620	470	150	0	0.061	559.0
23.6	685	515	170	0	0.049	697.8
2.36	315	260	55	2.36	0.767	69.8
4.72	385	308	77	2.36	0.321	139.8
18.9	640	510	130	2.36	0.056	559.0
23.6	710	570	140	2.36	0.043	697.8
2.36	360	308	52	4.72	0.836	69.8
4.72	412	350	62	4.72	0.284	139.8
18.9	675	540	135	4.72	0.062	559.0
23.6	745	600	145	4.72	0.047	697.8
2.36	585	515	70	18.9	1.862	69.8
4.72	615	545	70	18.9	0.489	139.8
18.9	870	750	120	18.9	0.073	559.0
2.36	640	590	50	23.6	1.487	69.8
4.72	685	630	55	23.6	0.433	139.8

TABLE 6 SECOND CHECK TEST ON 12-IN. LINE

12" diameter standard weight pipe - 12" I.D.

Length of test section - 134.958'

Average inlet air temperature - 48F

Barometric pressure - 705.5 MM Hg

Date of test - 11/7/44

Air Flow #/hr. at Station A	Pressure in Microns Hg Station 1A P_1	Station 2 P_2	$P_1 - P_2$	Air Flow #/hr. at Station B	Calculated f Values	Reynolds Number
2.38	245	213	32	0	0.382	71.9
4.75	308	260	48	0	0.178	143.5
19.03	585	475	110	0	0.047	575.0
23.77	650	535	115	0	0.036	719.0
2.38	327	295	32	5.0	0.515	71.9
4.75	375	325	50	5.0	0.229	143.5
19.03	630	520	110	5.0	0.052	575.0
23.77	700	590	110	5.0	0.037	719.0
2.38	500	455	45	25.0	1.122	71.9
4.75	530	480	50	25.0	0.332	143.5
19.03	740	655	85	25.0	0.048	575.0
23.77	820	735	85	25.0	0.034	719.0
2.38	700	680	20	50.0	0.722	71.9
4.75	755	700	55	50.0	0.524	143.5

TABLE 7 FIRST TEST ON 8-IN. LINE

8" diameter standard weight pipe - 7.981" I.D.

Length of test section - 58'

Average inlet air temperature - 60F

Barometric pressure - 711 MM Hg

Date of test - 10/11/44

Air Flow #/hr. at Station A	Pressure in Microns Hg Station 1 P_1	Station 2 P_2	$P_1 - P_2$	Air Flow #/hr. at Station B	Calculated f Values	Reynolds Number
2.36	210	85	125	0	0.270	104.5
4.71	285	135	150	0	0.115	208.3
18.84	700	415	285	0	0.036	835.0
23.55	830	510	320	0	0.031	1043.0
2.36	210	105	105	2.36	0.240	104.5
4.71	285	145	140	2.36	0.110	208.3
18.84	700	420	280	2.36	0.036	835.0
23.55	820	510	310	2.36	0.030	1043.0
2.36	210	110	100	4.71	0.232	104.5
4.71	300	150	150	4.71	0.123	208.3
18.84	700	430	270	4.71	0.035	835.0
23.55	820	525	295	4.71	0.029	1043.0
2.36	250	208	42	18.84	0.140	104.5
4.71	330	245	85	18.84	0.089	208.3
18.84	755	450	305	18.84	0.042	835.0
4.71	355	275	80	23.55	0.092	208.3
18.84	700	475	225	23.55	0.030	835.0

TABLE 8 FIRST CHECK TEST ON 8-IN. LINE

8" diameter standard weight pipe - 7.981" I.D.

Length of test section - 58'

Average inlet air temperature - 56F

Barometric pressure - 713 MM Hg

Date of test - 10/12/44

Air Flow #/hr. at Station A	Pressure in Microns Hg Station 1 P_1	Station 2 P_2	$P_1 - P_2$	Air Flow #/hr. at Station B	Calculated f Values	Reynolds Number
2.38	191	136	55	0	0.200	106.3
4.76	285	135	150	0	0.113	212.5
19.05	700	420	280	0	0.038	851.0
23.77	820	510	310	0	0.030	1062.0
2.38	210	104	106	2.38	0.239	106.3
4.76	275	150	125	2.38	0.096	212.5
19.05	700	425	275	2.38	0.035	851.0
23.77	820	525	295	2.38	0.029	1062.0
2.38	210	109	101	4.76	0.232	106.3
4.76	285	150	135	4.76	0.106	212.5
19.05	700	425	275	4.76	0.035	851.0
23.77	830	525	305	4.76	0.030	1062.0
2.38	263	213	50	19.05	0.171	106.3
4.76	355	240	115	19.05	0.123	212.5
19.05	700	460	240	19.05	0.031	851.0
23.77	820	550	270	19.05	0.027	1062.0

TABLE 9 FIRST TEST ON 6-IN. LINE

6" diameter standard weight pipe - 6.065" I.D.

Length of test section - 61'

Average inlet air temperature - 56F

Barometric pressure - 713 MM Hg

Date of test - 10/12/44

Air Flow #/hr. at Station A	Pressure in Microns Hg Station 1 P_1	Station 2 P_2	$P_1 - P_2$	Air Flow #/hr. at Station B	Calculated f Values	Reynolds Number
2.38	412	255	157	0	0.182	139.8
4.76	565	385	180	0	0.074	279.6
19.05	1130	770	660	0	0.039	1118.0
2.38	427	288	139	2.38	0.172	139.8
4.76	565	360	205	2.38	0.082	279.6
19.05	1320	770	550	2.38	0.031	1118.0
2.38	450	330	120	4.76	0.163	139.8
4.76	585	390	195	4.76	0.083	279.6
19.05	1320	800	520	4.76	0.030	1118.0
2.38	665	530	125	19.05	0.258	139.6
4.76	760	570	190	19.05	0.110	279.6
19.05	1380	850	530	19.05	0.032	1118.0

10 per cent of the final absolute pressure, the conventional equation for large pressure drops, which is

$$P_1^2 - P_2^2 = \frac{2w^2RT}{gA^2} \log_e \frac{P_1}{P_2} + \frac{4fRTw^2L}{gA^2D} \quad \ldots\ldots [1]$$

was equated for f as follows

$$f = \frac{(P_1^2 - P_2^2)gA^2D}{4RTw^2L} - \frac{D}{2L} \log_e \frac{P_1}{P_2} \quad \ldots\ldots [2]$$

where

P_1 = initial pressure, psfa
P_2 = final pressure, psfa
w = weight of fluid flowing past a given section, lb per sec
R = perfect gas constant = 53.3 for air
T = temperature, deg R
L = length of line, ft
D = inside diameter of pipe, ft
g = dimensional consistency factor = 32.174
A = area of pipe, sq ft
f = friction factor

This equation was solved for f for each of the 150 sets of pressure-drop readings taken. Each f-value was then plotted against the corresponding Reynolds number $R_D = DV\rho/\mu$, where D is the internal diameter of the pipe in feet, V the average velocity in feet per second, ρ the density in pounds per cubic foot at the average absolute pressure, and μ the absolute viscosity in pounds per foot-second.

Fig. 4 shows an envelope enclosing all but five of the f-values for the 58 pressure-drop readings taken on the 18-in. line. The heavy line is a curve through the average of the enclosed f-values. Fig. 5 shows an envelope enclosing all but one of the f-values for the 47 pressure-drop readings taken on the 12-in. line. The heavy line is a curve through the average of the enclosed f-values.

Fig. 6 shows an envelope enclosing all but two of the f-values for the 45 pressure-drop readings taken on the 8 and 6-in. lines. The heavy lines are a curve drawn through the average of the enclosed f-values for the 8-in. line and a curve drawn through the average of the enclosed f-values for the 6-in. line. The f-values not enclosed in the envelopes were rejected after an analysis of the data indicated that these values were based on readings less accurate than the others.

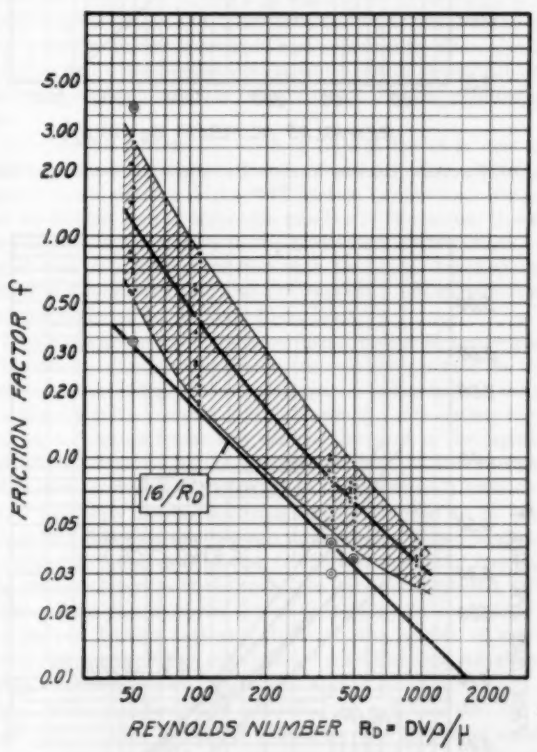

FIG. 4 FRICTION FACTOR VERSUS REYNOLDS NUMBER FOR 18-IN. PIPE

Fig. 7 shows the average curves of Figs. 4, 5, and 6. Fig. 8 shows an average of the average curves for the 18 and 12-in. lines and an average of the average curves for the 8 and 6-in. lines.

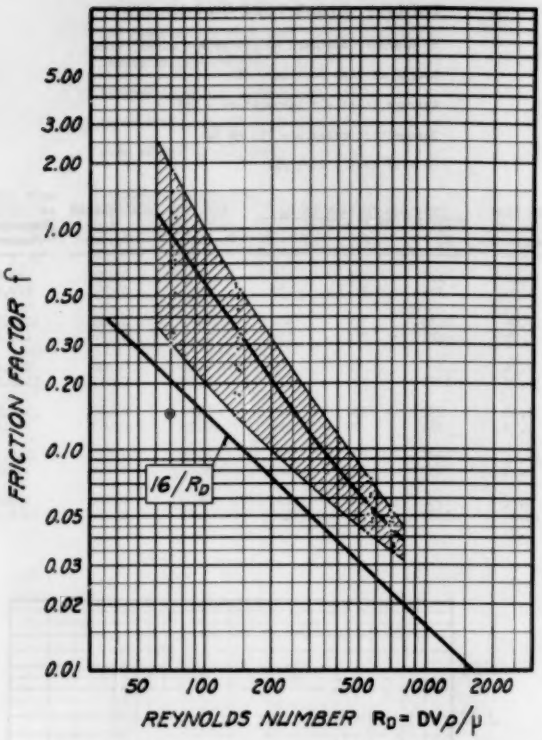

FIG. 5 FRICTION FACTOR VERSUS REYNOLDS NUMBER FOR 12-IN. PIPE

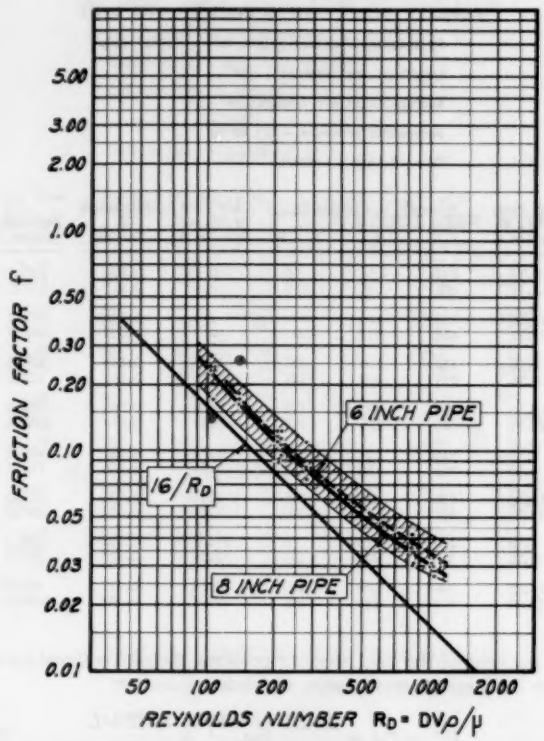

FIG. 6 FRICTION FACTOR VERSUS REYNOLDS NUMBER FOR 8 AND 6-IN. PIPES

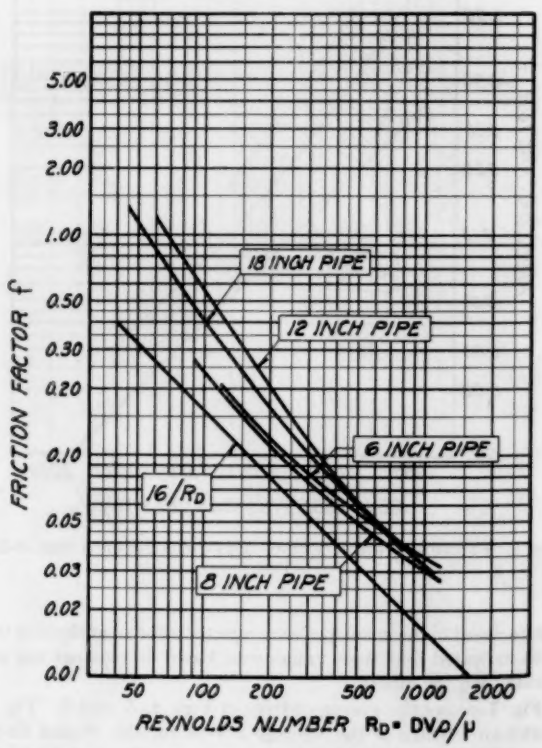

FIG. 7 AVERAGE FRICTION FACTOR VERSUS REYNOLDS NUMBER FOR 18, 12, 8, AND 6-IN. PIPES

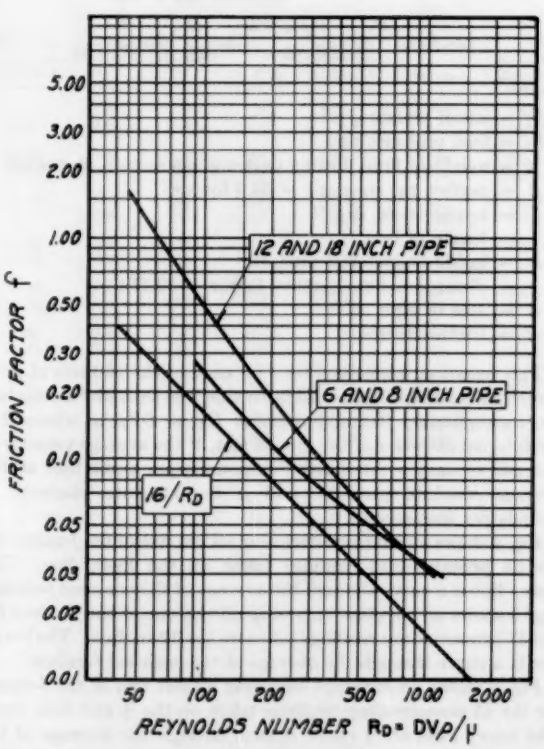

FIG. 8 FRICTION FACTOR FOR STREAMLINE FLOW OF GAS AT ABSOLUTE PRESSURES FROM 50 MICRONS HG TO 1 MM HG

Discussion of Results

Moving gage station No. 1 from a location 9 ft from the flow nozzles at station A to a location 19 ft from the flow nozzles at station A had no discernible effect on the pressure-drop readings.

In calculating the f-values it was found the right-hand expression in Equation [2] had little significance as it only changed the value of f in the third decimal figure. It was therefore omitted as being considerably less than the possible error in the absolute-pressure readings and, in most cases, less than could be plotted accurately.

The effect of not having a continuous wall surface in one side of the test pipe lines could not be determined. It seems probable that this condition may have caused a slight disturbance in the air flow and hence produced a slightly higher pressure drop than would have been the case with continuous wall surface.

The spread in the f-values was greater than expected. It is believed this is due to the difficulty of reading accurately the portable McLeod gages used to determine the absolute pressures, and to the inaccuracy of these gages. When checking the portable gages against the standard gage it was found the readings of the portable gages were inaccurate by as much as 10 per cent. To correct for this inaccuracy simultaneous readings were taken over a wide range in absolute pressures with both the portable gages and the standard gage connected to the same absolute-pressure source. The readings of each of the portable gages were then plotted against the readings of the standard gage and a curve averaged through the resulting points for each portable gage. All of the test absolute-pressure readings, as read, were then corrected from these curves. This reduced the errors in the test readings but the wide spread in the f-values indicates it did not eliminate them. It is significant, however, that even with this wide spread in f-values all but four of the 150 values were higher than the f-values of the Hagen-Poiseuille friction-factor curve.

Conclusion

These tests indicate that, for streamline flow of gases in circular pipes at absolute pressures between 50 microns Hg and 1 mm Hg, the values of f shown by the Hagen-Poiseuille friction-factor curve (f equals 16 divided by the Reynolds number) are too low and should be approximately 50 to 100 per cent larger. For practical work, where low pressure drops are essential, the friction factors shown in Fig. 8 should be used to determine the pipe-line sizes.

Acknowledgment

The authors wish to thank the Electro-Metallurgical Company and the Reconstruction Finance Corporation for their permission to publish the data from these tests.

Discussion

H. W. Iversen.[7] The difference between the authors' results and the accepted friction factors in laminar flow is very disturbing, particularly when sweeping conclusions are made from a five-fold scatter of results. The test conditions should be examined for possible causes of the differences.

(*a*) Slip-flow and free-molecule flow effects are present in low-pressure gas flow. Brown, DiNardo, Cheng, and Sherwood[8] summarize the analytical form of the correction to the Hagen-Poiseuille equation to include the slip and free-molecule flow effects. They also correlate experimental results of laminar gas flow in pipes from capillary size to 8 in. diam. The flow correction is

$$F = \frac{f_0}{f}$$

where

f_0 = normal laminar-flow friction factor of 16 divided by the Reynolds number

f = actual friction factor including slip and molecular flow effects

According to the analysis by which it is derived, F is always equal to or greater than 1. When slip and free-molecule flow become important, the actual friction factor is less than the normal Fanning friction factor. The authors' test results, when interpreted in terms of the correction factor F, show all but a few of the values of F to be less than 1. In addition, the authors' results in terms of F show as much scatter in the correlation used by Brown, et al., as in the friction-factor results of Figs. 4 through 8. Thus there is some doubt as to the accuracy of the authors' results.

However, Brown, et al., also list values of F less than 1 for the larger-sized pipes of 2, 4, and 8 in. diam in the same range of the correlating variables as the authors' tests. The trend of the two sets of results, the authors' and those reported by Brown, et al., indicates that a phenomenon exists which should be investigated further to establish accurate friction factors for low-pressure gas flow.

(*b*) The side outlets, i.e., six 8-in. lines in the 18-in. test section, introduce a possible added resistance effect, which, if present, would result in higher-test friction factors than the normal 16 divided by the Reynolds number. The writer checked the influence of side outlets in the laboratory. The system consisted of a $^1/_2$-in-ID test section with six $^7/_{32}$-in. blanked stub outlets in a 50-in. length. The fluid was oil. The system represented a model of the authors' 18-in. line.

Within the accuracy of the experiment, no significant increase in the flow resistance, or friction factor, was observed for the tube with the blanked stub outlets as compared to the smooth tubing at a flow Reynolds number of 50. Hence the side outlets of the authors' test setups apparently are not the cause of the reported high friction factors, unless laminar gas flow at low pressures differs from laminar liquid flow at the same Reynolds number.

(*c*) The pipe interior condition, while reported to be clean except for a thin dust film, is open to question. One deposit was mentioned as found downstream of the test section of one pipe. The complete interiors of the test pipes were not inspected. Reduction of the pipe diameter due to deposit layers would tend to increase test friction factors. However, the scatter of results should not appear if the pipe interior condition did not change during the tests.

(*d*) Of the measured flow variables, the only one that can be questioned seriously is that of pressure. The scatter of results does not permit any detection of a consistent erroneous pressure measurement. When the weight rate of flow divided by the mean pressure is plotted as a function of the pressure difference, assuming the log term in the compressible-flow equation to be negligible, the results should fall on a line passing through the origin. This was done for all the test results. The plot for the results from the 18 in. and from the 12-in. pipes showed a tendency to intercept the pressure-difference co-ordinate axis at a value greater than zero. No conclusion may be drawn from this, other than to point out that the pressure measurements are open to question.

[7] Associate Professor, University of California, Berkeley, Calif. Assoc. Mem. ASME.

[8] "The Flow of Gases in Pipes at Low Pressures," by G. P. Brown, A. DiNardo, G. K. Cheng, and T. K. Sherwood, *Journal of Applied Physics*, vol. 17, 1946, pp. 802–813.

GEORGE KARNOFSKY.[9] The authors are to be congratulated for performing an imaginative experiment on an important problem and reporting it lucidly.

The most striking fact revealed by the data is not so much the deviation of the average results from the theoretical Fanning friction factor, but instead, the wide dispersion of the data from any simple correlation. Since the experimentation was done under difficult conditions, the data are subject to question. For example, the authors changed flow rate by inserting standard nozzles at test stations. Was the system brought to atmospheric pressure each time to change these nozzles? If so, it is hard to believe as many as 20 observations could have been made in a day with the system in a steady state each time.

Although it had no effect on the final calculations, Equations [1] and [2] are slightly in error. The first term to the right of the equality of Equation [1] should have the coefficient 4 instead of 2 for viscous flow, as is discussed by Walker, Lewis, McAdams, and Gilliland.[10] However, this term is insignificant in the final calculation, even when doubled.

Since the authors reported their results as a friction-factor versus Reynolds-number correlation, they must have used data for the viscosity of air. The source of these data is not revealed. This is an important omission since the whole validity of their conclusion, that friction factors are higher than theoretical, depends on the correctness of their viscosity data.

J. W. METZGER.[11] Available experimental data pertaining to fluid flow at very low pressures are exceedingly meager, particularly in the case of tubing or piping of a size encountered in industrial installations. Therefore the results of the tests summarized in the foregoing paper constitute an original contribution to the body of knowledge of the behavior of a flowing fluid and should be of increasing value as the application of high-vacuum technology to industrial processes continues to grow in importance. Metallurgy, electronics, nuclear physics, and other sciences are constantly demanding larger vacuum systems designed to operate at higher vacuums. Although many such systems operate in the molecular flow regime, they require backing systems in which the pressures are of an order in which laminar flow may exist. In spite of the increasing demand for vacuum equipment, design is still dependent largely upon theoretical formulas for the sizing of connecting piping. After determining the theoretical size requirements, designers introduce a liberal "safety factor" in the selection of vacuum plumbing. When the need arises for a more careful evaluation of optimum pipe sizes, experimental data certainly will prove to be invaluable.

Vacuum equipment of the type described, with such a tremendous throughput capacity (1,690,000 micron cu ft per min at 100 microns) is exceedingly rare. For instance, contrast this throughput with the 43,000 micron cu ft per min at 100 microns of the Kinney DVD 181420 rotary mechanical pump, which is one of the largest sizes. Such a large throughput can be obtained only by the use of multistage steam ejectors. Therefore these tests, conducted on a magnesium-reduction plant built during the second world war, represent the utilization of a singular opportunity to obtain such pressure-drop data.

According to the text of the paper the measurements were obtained using a Stokes' McLeod gage. While this type gage has the advantage of being an absolute-pressure-reading gage and therefore consistent in its readings in the absence of condensable vapors, there may have been some merit in the use of one of the secondary-type gages. These are of a class which makes use of the various properties of a fluid which are dependent upon the pressure when the latter is low. Their greatest advantage, lacking in the McLeod gage, is that they read continuously. At least two of the continuous-reading gages are reasonably well suited to the pressure regions covered by the tests. Both were existent at the time the tests were conducted although they may have been difficult to obtain commercially. Both depend upon the thermal conductivity of the low-pressure gas.

One, the vacuum thermocouple gage, indicates the temperature variations of a radiant wire as the pressure varies. The other, the Pirani gage, measures the changes in resistance of a hot filament as the pressure varies. Although both gages can span the range of pressures encountered in the tests, their calibration is not linear but is crowded at either end of their useful scales. Further, the Pirani gage, particularly, is subject to variation in its calibration; a factor which might have been a source of difficulty if it had been used in the tests. Thus each of the gages has its limitations as well as its advantages and careful consideration may have been required to determine the most satisfactory gage for the tests. If the tests could be repeated at present, it is probable that the National Research "Alphatron" gage would be preferable. It is continuous reading and has linear calibration up to about 25 mm of mercury.

A review of many sources revealed that actual experiments with low-pressure fluid flow are very rare. L. A. Bromley and C. R. Alancraig[12] authored an article which contains a series of data on copper tubing of 2.866 in. ID. The data were taken on the tubing alone and with cores of various sizes inserted to form the annuli. Alancraig is also the author of an unpublished Master of Science thesis in Chemical Engineering at the University of California, on the topic of "Pressure Drop for High Vacuum Flows Through Annular Sections." Dr. R. K. Wakerling of the Radiation Laboratory of the University of California, and co-editor of "Vacuum Equipment and Techniques," in a personal communication states that there is classified material in the AEC project on the viscous flow of gases at low pressures.

Unfortunately, since the work by the present authors appears to be original, it is impossible to make direct comparisons, but by using the equations given in their paper, it is possible to calculate the friction factors corresponding to the data given in the paper by Bromley and Alancraig and compare the results to draw some general conclusions. The 3-in. copper tube, without a core, and carrying a flow of 589 micron liters per sec through a 5-ft length from $P = 16.2\mu$ to $P = 7.01\mu$ yielded a friction factor of 10.8 at a Reynolds number of 0.89. Thus the factor obtained is less than the theoretical value obtained by solving 16/Re. Other values, when plotted, indicate that as the Reynolds number decreases the actual friction factor diverges from the theoretical more and more widely from a common point at a Reynolds number of about $3^1/_2$ and a friction factor of about $4^1/_2$, assuming that the experimental values extrapolate as a straight line. Accepting the correctness of the approximate limits of the flow regimes in terms of the mean free path divided by pipe diameter to be

$$\lambda/D < 0.01 \qquad \text{for viscous flow}$$

$$0.01 < \lambda/D < 15 \qquad \text{for transitional flow}$$

as given by R. G. Folsom,[13] in his paper on nozzle flow at low

[9] Chemical Plants Division, Blaw-Knox Company, Pittsburgh, Pa.

[10] "Principles of Chemical Engineering," third edition, McGraw-Hill Book Company, Inc., New York, N. Y., 1937, p. 90.

[11] Mechanical Engineer, C. H. Wheeler Manufacturing Company, Philadelphia, Pa. Assoc. Mem. ASME.

[12] "Pressure Drop for High Vacuum Flow of Air Through Angular Sections," by L. A. Bromley and C. R. Alancraig, *Chemical Engineering Progress*, vol. 48, 1952.

[13] "Nozzle Characteristics in High-Vacuum Flows—Rarefied Gas Dynamics," by R. G. Folsom, Trans. ASME, vol. 74, 1952, pp. 915–918.

pressures, the data for the copper tubing all fall within the transitional-flow regime. By contrast, all the data taken on the magnesium-plant piping fall in the viscous-flow regime. Apparently the differences in the friction factors may be attributed to the differences in the flow mechanisms. This may be confirmed by comparing the pressure-loss formulas for viscous flow and molecular flow. For viscous flow

$$\Delta P_V = \frac{4QL}{D^4\overline{P}}$$

For molecular flow

$$\Delta P_M = \frac{QL}{6.5D^3}$$

Hence

$$\Delta P_V = \frac{26}{D\overline{P}}\ \Delta P_M$$

It may be seen that as diameter and average pressure decrease, the theoretical value of the pressure loss by viscous flow becomes large compared with that determined by molecular flow. Although the theoretical formulas may not conform to the actual observable data, they represent analyses which will approximate the experimental values rather closely for the regions to which they apply.

The work of the authors has extended knowledge of the viscous flow of gases to very nearly the lowest pressure at which it can exist. Barely beyond the limit of their tests, flow behavior becomes partly molecular in character and is referred to as transitional. Much work remains to be done in the investigation of flow at very low pressures and the authors' contribution should serve as a model as well as an incentive for further research.

Authors' Closure

The authors wish to thank Messrs. Iversen, Karnofsky, and Metzger for their interesting and helpful discussions.

With reference to Professor Iversen's discussion, the authors would like to point out that most of the analysis and test results of Brown, et al., are for a different type of flow from that reported in our paper. Mellen[14] states that, if the average pressure in microns mercury is equal too, or less than, seven divided by the pipe diameter in inches, then, with small error, the flow can be considered as free molecular, and, if the average pressure in microns mercury is equal to, or greater than, 220 divided by the pipe diameter in inches, the flow is predominantly viscous. At pressures between these, both types of flow would coexist. Application of these criteria to the test runs reported in Table 2 by Brown, et al., shows that of the total 137 runs, 27 are in the free-molecular-flow region, 77 are in the region where both flows coexist, and only 33 are in the region where viscous flow predominates. Also, the values of Brown's friction factors are quite high in the free-molecular-flow region, reduce and tend to approach 1 in the region where both flows coexist, and continue to reduce and go down to a low value of 0.73 where the flow is predominantly viscous. The average pressure during all of our tests was more than five times the value of 220 divided by the pipe diameter in inches, which would indicate that the flow is either predominantly viscous, or completely viscous flow. The pattern of the friction values just pointed out would, therefore, indicate that for our tests, friction values would be substantially less than one.

[14] "Flow of Low Pressure Gases," by G. L. Mellen, *Chemical Engineering*, vol. 56, May, 1949, p. 122.

Professor Iversen's qualified conclusion that the side outlets of the manifolds were apparently not the cause of the higher friction factors is quite interesting. Since the gas velocities were quite low, it seems probable that the effect of the side outlets on the friction factors is minor. In any event, since most large industrial-process systems using absolute pressures in the range reported in the paper use vacuum manifolds and not single pipe lines, the friction-factor data reported can safely be used in most cases to determine the manifold sizes and may have a small factor of safety in it when used to determine single pipe-line sizes.

As the entire length of the interior of the manifolds could not be inspected to determine the condition of the inside walls, it was assumed, after examining the visible areas about the pressure, temperature, and orifice openings, that there were no deposits of any kind in the sections tested. With 12 in. and 18-in-diam lines, it would take a rather substantial deposit to cause enough of a reduction in the pipe-line cross-section area to make more than a minor change in the friction factors. Friction-factor data on lines that are not completely clean and smooth are probably of more practical value than those on smooth clean lines, since, with most industrial-process vacuum systems, the vacuum lines are not smooth clean lines after the systems have been in operation a year or so.

As stated in the paper, the authors believe the scatter in the friction values was due to possible inaccuracy in the pressure readings. However, since an error did not appear as the result of the pressure readings being either consistently high or consistently low, the averaging of a large number of test results minimizes this possibility. While it would have been desirable to procure and use absolute pressure gages of laboratory accuracy for the tests, the time available for running the tests made it impossible to do so. Therefore, to minimize any error during the interim of such an extensive test schedule, the gages used were calibrated at the start, once during the tests, and also at the end of the program. Since there were exceptionally few times when competent technical help was available for test work, and the free use of a portion of a multimillion-dollar plant was permitted, and the time interval during which this golden opportunity existed was limited, it was necessary either to run these tests with the available absolute-pressure gages or to pass up the opportunity.

In answer to Mr. Karnofsky's question, none of the systems was brought back to atmospheric pressure when a flow nozzle was changed. At each flow-nozzle station, one end of a 2-in-diam nipple was welded into the test line, and a 2-in. gate valve was screwed onto the other end. A flow nozzle was screwed into the outside end of the gate valve. This gate valve was closed when a nozzle was changed so that only a very small volume in the body of the gate valve was brought to atmospheric pressure when a nozzle was changed. For each test the nozzle with the smallest flow was used first and the rate of flow progressively increased. To be sure the system had reached an equilibrium condition after each nozzle change, simultaneous absolute-pressure readings were taken at intervals but not recorded as test readings until three consecutive readings at each point were approximately the same. The average of each of these three readings was then recorded as the test readings.

The use by Walker, et al., of 4 instead of 2 as the coefficient in the first term to the right of the equality in Equation [1] is based on the flow having no slip at the wall and a true parabolic velocity distribution so that the average kinetic energy is V^2/g instead of $V^2/2g$. This may be true for highly viscous fluids such as heavy oils, but the authors feel sure it is not true for air flow with very low density. At the time the tests were run several attempts were made to determine velocity distribution

by taking pitot-tube readings at short intervals across both the 18-in. and the 12-in-diam test lines. So much difficulty was encountered in trying to determine accurately the very small pressure differences involved, that the authors felt these results were not reliable enough to report in the paper. However, there was a definite pattern of flat velocity distribution in about the center two thirds of the test lines for several different rates of flow, and for that reason the coefficient 2 was used in Equation [1]. As Mr. Karnofsky pointed out, this point is immaterial as a few calculations established the fact that the maximum value of the right-hand expression in Equation [2] was around 0.003 so that, as stated in the paper, the value of this expression changes the f-values appreciably less than the possible error in the absolute-pressure readings and, in most cases, less than can be plotted accurately.

Mr. Karnofsky is correct in stating that the authors' failure to include in the paper the values used for the viscosity of air in the Reynolds numbers' calculations is an important omission. The authors appreciate his calling attention to this omission. The viscosity values used were taken from Fig. 14 on page 25 of Part 5, Chapter 4, "Flow Measurement by Means of Standardized Nozzles and Orifice Plates," of the ASME Power Test Code published in 1940. As very little is known about the viscosity of air at low absolute pressures, these values may not be correct. They were used with the thought that, if anyone wishing to use an f-value recommended in the paper uses these same data to obtain the viscosity value for his Reynolds-number calculation, he will get a Reynolds number consistent with those used in plotting the f-values.

Both types of secondary gages mentioned by Mr. Metzger were on hand and available at the time the tests were run. In fact, originally, Pirani gages were used in production work and a thermocouple gage used for checking. However, these gages frequently go out of calibration without any warning. Continually checking and frequently recalibrating them required so much time that their use in production work was discontinued and McLeod gages used in their place. This past unsatisfactory experience with these secondary gages led to the use of the McLeod gages for the tests.

As Mr. Metzger points out, there have been many investigations of fluid flow in both the free-molecular-flow range and the transitional range in which free molecular and viscous flow coexist, for example, that of Dryer,[15] but very little previous investigation of fluid flow in the absolute-pressure range immediately above the transitional range, where the flow is either predominantly viscous or completely viscous.

[15] "Calculations for High Vacuum Systems," by W. P. Dryer, *Chemical Engineering*, vol. 54, 1947, pp. 127–131, and "Rough Evacuation of Vacuum Systems," by W. P. Dryer, *Chemical Engineering*, vol. 55, 1947, pp. 122–124.

Interaction of Friction and Temperature at the Chip-Tool Interface in Metal Machining

By F. F. LING[1] and EDWARD SAIBEL,[2] PITTSBURGH, PA.

The significance of chip-tool interface friction-temperature characteristics in metal machining is pointed out. For orthogonal metal machining with Type 2 chip an approximate analysis of the interface temperature, or cutting temperature, is given for linear friction-temperature characteristics and small rake angles. In the analysis, the coefficient of friction and the temperature are expressed in terms of the cutting velocity, the physical properties of the material, and constants obtained from the data of Chao and Trigger (1).[3]

Nomenclature

The following nomenclature is used in the paper:

a = average thermal diffusivity
b = half-width of chip
C = average specific heat
K = average thermal conductivity
F = frictional force
q_1 = heat liberated at shear zone
q_2 = heat liberated at chip-tool interface
r = ratio of δ to δ_c
R = $Vb/4a$
S_s = dynamic shear stress
t = time
T = dimensionless temperature ($\equiv \theta/\theta_0$)
V = cutting velocity
V_c = chip velocity
α = rake angle
γ = average density
δ = thickness of cut
δ_c = thickness of chip
ϵ = shear strain
ϕ = shear angle
σ_1 = fraction of q_1 going into workpiece
σ_2 = fraction of q_2 going into chip
θ = average temperature of chip-tool interface (cutting temperature) above ambient
θ_0 = ambient temperature
θ_s = average temperature of shear zone above ambient
μ = coefficient of friction

Introduction

The existence of a correlation between chip-tool interface friction and temperature, or cutting temperature, has been observed in recent years. The data of Chao and Trigger as well as those of other authors shows this phenomenon. In the study of metallic friction one of the present authors has observed that, in kinetic friction between metallic surfaces at elevated temperatures, the coefficient of friction decreases with increase of interface temperature. While the true mechanism involved has yet to be discovered, it may be ventured that at higher temperatures a lower yield strength of the material and more ready oxidation are the principal causes of lower frictional resistance.

This observation has prompted the authors to take into consideration the variation of friction and cutting temperature in putting forth an approximate analysis of the cutting temperatures for orthogonal metal machining. The analysis is limited to linear friction-temperature characteristics and small rake angles. Published analyses on cutting temperatures (2, 3) do not account for the variation of friction with cutting temperature. By incorporating the friction-temperature characteristics, the authors believe the metal-machining problem has been brought to a more fundamental basis in that all the dependent variables are expressible in terms of only dependent variables. For instance, in calculating the shear-zone temperature, which is a component part of the cutting temperature, Chao and Trigger (4) express it in terms of the so-called thermal number $V\delta/a$, which is equal to $4\delta R/b$, and another proportionality factor which depends on the shear angle, etc.

By introducing the friction-temperature characteristic as a basic factor, by virtue of the fact that it is characteristic of a given chip-tool combination, the coefficient of friction is expressed in terms of cutting velocity and other physical properties. Thus the shear angle, through its empirical relation with the coefficient of friction, and other dependent variables such as δ_c, which is a function of the shear angle and rake angle, can be expressed in terms of only independent variables, namely, cutting velocity and physical properties including the friction-temperature characteristics.

Friction-Temperature Characteristics

Referring to Fig. 1, which shows the elements in an orthogonal metal-machining model, the problem is to find θ while considering

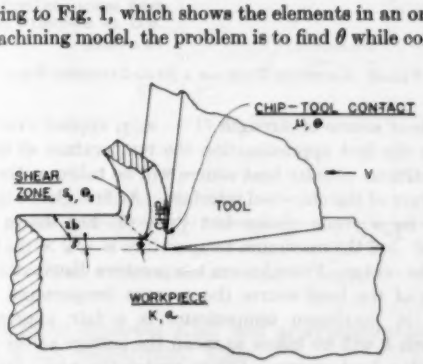

Fig. 1 Model of Orthogonal Metal Machining With Type 2 Chip

[1] Project Engineer, Department of Mechanical Engineering, Carnegie Institute of Technology. Assoc. Mem. ASME.

[2] Professor of Mechanics, Department of Mathematics, Carnegie Institute of Technology. Mem. ASME.

[3] Numbers in parentheses refer to Bibliography at end of paper.

Contributed by the Production Engineering Division and presented at a joint session with the Research Committee on Metal Processing at the Semi-Annual Meeting, Pittsburgh, Pa., June 20–24, 1954, of The American Society of Mechanical Engineers.

Note: Statements and opinions advanced in papers are to be understood as individual expressions of their authors and not those of the Society. Manuscript received at ASME Headquarters, December 11, 1953. Paper No. 54—SA-2.

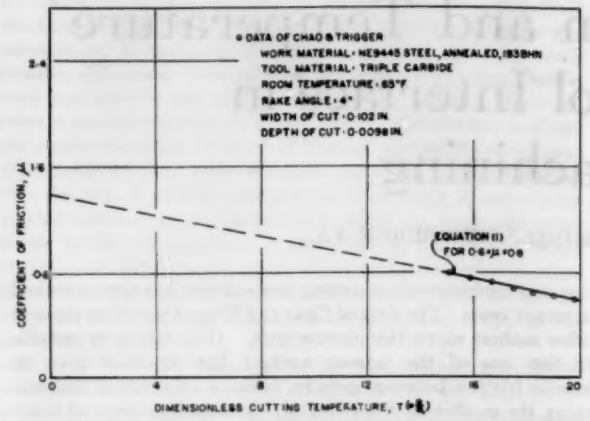

FIG. 2 COEFFICIENT OF FRICTION VERSUS DIMENSIONLESS CUTTING TEMPERATURE

the variation of μ with θ. Fig. 2 shows the data of Chao and Trigger (1), namely, μ plotted against $T(\equiv\theta/\theta_0)$ for $15 \leqslant T \leqslant 20$. The solid line is a curve faired through the experimental points by the authors. Expressed empirically it is given by

$$\mu = \mu_0 - \xi T = 1.4 - 0.04T \text{ for } 15 \leqslant T \leqslant 20 \quad [1]$$

The fact that $\mu(T)$ is unknown for $0 \leqslant T < 15$ is not important in the present study where only the steady-state temperature is concerned. However, to insure a unique solution the $\mu(T)$ relationship for $0 \leqslant T < 15$ has to be monotonic as in the range $15 \leqslant T \leqslant 20$.

CUTTING TEMPERATURE

Fig. 3 shows the condition of heat transfer at the chip-tool interface. The tool is viewed as a semi-infinite solid with a con-

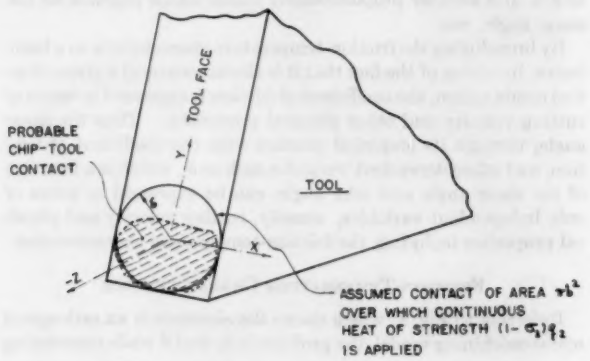

FIG. 3 CUTTING TOOL AS A SEMI-INFINITE SOLID

tinuous heat source of strength $(1 - \sigma_2)q_2$ applied over the surface. In the first approximation the temperature at the center of the fictitious circular heat source will be taken as the average temperature of the chip-tool interface. At first glance this might seem to be a crude choice but Blok (5) has shown that for $(Vb)/(4a) \geqslant 5$ the maximum temperature is $\sqrt{2} \times$ the temperature at the center. From known temperature distributions across diameter of the heat source the average temperature taken as $(1/\sqrt{2}) \times$ maximum temperature is a fair approximation. Henceforth θ will be taken to mean the surface at the center of the circular heat source. Other postulates are: (*a*) All the strain energy at the shear zone is dissipated in the form of thermal energy; (*b*) physical properties such as a, K, S_S are independent of temperature—average values evaluated at the range of temperatures concerned are used; (*c*) for simplicity and clarity no distinction is made between the thermal properties at the shear-zone temperatures and those at the chip-tool interface temperature; and (*d*) for finding the steady-state temperature σ_1 and σ_2, an evaluation based on Blok's work (6) as used by Loewen and Shaw (2) and Leone (7) can be employed.

According to Leone (7) the shear-plane temperature is expressed

$$\theta_S \doteq \sigma_1 q_1 b/K(\pi R)^{1/2} \quad [2]$$

where

$$\sigma_1 \doteq 1/(1 + 4r\pi^{-1/2}R^{1/2})$$

and the heat generated at the shear zone according to Chao and Trigger (4) is

$$q_1 = S_S \epsilon \sin \phi V \quad [3]$$

where

$$\epsilon = \cot \phi + \tan (\phi - \alpha)$$

Substituting Equation [3] into Equation [2] there results

$$\theta_S \doteq \frac{S_S/\gamma c}{r + \pi^{1/2}/4\,R^{-1/2}} \sin \phi \,[\cot \phi + \tan (\phi - \alpha)] \quad [4]$$

Using Lee and Shaffer's relation for shear angle (10), friction angle, and rake angle

$$\phi = \pi/4 - \tau + \alpha \quad \text{where } \tau = \tan^{-1}\mu$$

and considering the case where α is small, Equation [4] reduces to

$$\theta_S \doteq \frac{S_S \csc \pi/4/\gamma C}{r + \pi^{1/2}/4R^{-1/2}} \sec \tau/(1 + \mu) \quad [5]$$

If r in the denominator is replaced by an average value r_a the maximum error introduced in θ_S is estimated to be approximately 2 per cent for $R \geqslant 30$ and a variation of r of about ± 15 per cent. This is a reasonable variation. Thus

$$\theta_S \doteq \frac{S_S \csc \pi/4/\gamma C}{r_a + \pi^{1/2}/4R^{-1/2}} g_1(\mu) \quad [6]$$

where

$$g_1(\mu) = \sec \tan^{-1}\mu/(1 + \mu)$$

Considering conduction only on the tool with a heat source the heat equation

$$\nabla^2\theta = \frac{1}{a}\,\phi_t \quad [7]$$

applies, and the temperature at the center of surface due to a continuous disk source of strength $(1 - \sigma_2)q_2$ and size πb^2 according to Carslaw and Jaeger (8) is

$$\theta(t) = 2\int_0^t \frac{(1 - \sigma_2)q_2}{\gamma C\sqrt{\pi a(t - t')}} \{1 - \exp [-b^2/4a(t - t')]\}dt' \quad [8]$$

where t' is the time at which instantaneous heat is employed

$$q_2 = \frac{FV_c}{\pi b^2} = \frac{FVr}{\pi b^2} \quad [9]$$

and $(1 - \sigma_2)q_2$ can be obtained in a manner similar to Loewen and Shaw (2), thus

$$q_2(1 - \sigma_2) \doteq \frac{b/K[(\pi rR)^{-1/2}q_2] + \theta_S}{b/K\,[1 + (\pi rR)^{-1/2}]} \quad \ldots\ldots [10]$$

substituting Equation [9] into Equation [10]

$$q_2(1 - \sigma_2) \doteq \frac{4R^{1/2}Fr^{1/2}/\pi^{3/2}\gamma Cb^2 + \theta_S}{b/K[1 + (\pi rR)^{-1/2}]} \quad \ldots\ldots [11]$$

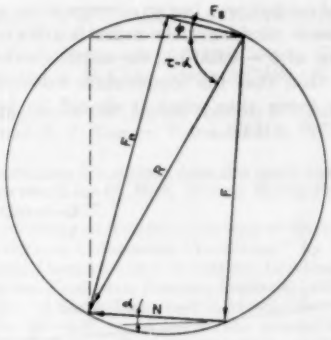

FIG. 4 FORCE CIRCLE IN ORTHOGONAL METAL MACHINING DUE TO MERCHANT

The system of equations governing the forces in orthogonal metal machining due to Merchant (9), Fig. 4, are

$$\left.\begin{aligned} F_n - F\cos(\phi - \alpha) - N\sin(\phi - \alpha) &= 0 \\ F_S + F\sin(\phi - \alpha) - N\cos(\phi - \alpha) &= 0 \\ F_n &= F_S\tan(\phi + \tau - \alpha) \\ F_S &= 2S_S b\delta\csc\phi \end{aligned}\right\} \quad \ldots\ldots [12]$$

Solving Equations [12] for F and remembering that α is small and $\phi = \pi/4 - \tau + \alpha$

$$F = 2S_S b\delta(\cot\phi - 1) \quad \ldots\ldots [13]$$

$$Fr^{1/2} = 2S_S b\delta(\cot\phi - 1)[\sin\phi/\cos(\phi - \alpha)]^{1/2} \quad \ldots\ldots [14]$$

Substituting in this equation Lee and Shaffer's shear-angle relation $\phi = \pi/4 - \tau + \alpha$ and again remembering that α is small

$$Fr^{1/2} \doteq 4S_S b\delta\,\mu(1 - \mu^2)^{-1/2} \quad \ldots\ldots [15]$$

Putting Equation [15] into Equation [11]

$$q_2(1 - \sigma_2) \doteq \frac{[16S_S\delta R^{1/2}/\pi^{3/2}\gamma Cb]}{b/K[1 + (\pi r_a R)^{-1/2}]}\, g_2(\mu) + \theta_s \quad \ldots\ldots [16]$$

where

$$g_2(\mu) = \mu(1 - \mu^2)^{-1/2}$$

Again r_a is substituted for r in Equation [16] and a maximum error of 2 per cent is estimated.

Substituting Equations [16] and [6] into [8] and using $T \equiv \theta/\theta_0$

$$T(t) = D\int_0^t [Eg_2(\mu) + Gg_1(\mu)]H(t, t')dt' \quad \ldots\ldots [17]$$

where

$$D = 2KS_S/\theta_0(\gamma C)^2 b[1 + (\pi r_a R)^{-1/2}]$$

$$E = 16\delta R^{1/2}/\pi^{3/2}b$$

$$G = \sec\pi/4/[r_a + \pi^{1/2}/4(R^{-1/2})]$$

$$g_1(\mu) = \sec\tan^{-1}\mu/(1 + \mu)$$

$$g_2(\mu) = \mu(1 - \mu^2)^{-1/2}$$

and

$$H(t, t') = \{1 - \exp[-b^2/4a(t - t')]\}/[\pi a(t - t')]^{1/2}$$

It will be found more expedient to solve for μ first and then to find T from Equation [1]. Now combining Equations [1] and [17]

$$\mu(t) = \mu_0 - \xi D\int_0^t \{Eg_2[\mu(t')] + Gg_1[\mu(t')]\}H(t, t')dt' \quad \ldots\ldots [18]$$

It should be pointed out that the solution sought is

$$\lim_{t\to\infty}\mu(t)$$

and that because of the assumptions made $\mu(t)$ does not represent the true transient value. Equation [18] is a nonlinear integral equation and it does not appear to be possible to get an exact solution at present.

APPROXIMATE SOLUTION OF EQUATION [18]

A search of the literature shows that the coefficient of friction in metal machining varies approximately between 0.6 and 0.8. If the problem is limited to a narrow range of values of μ as cited, an approximate solution seems possible. Figs. 5 and 6 show two

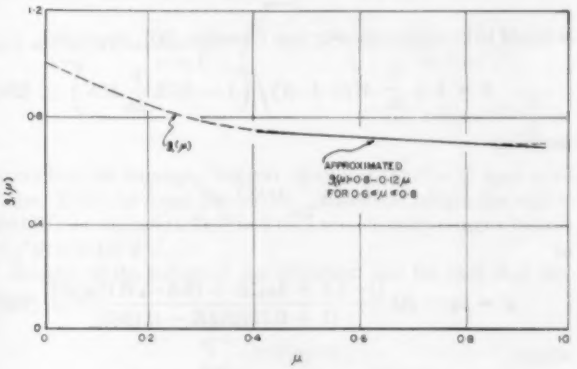

FIG. 5 APPROXIMATE $g_1(\mu)$ FUNCTION

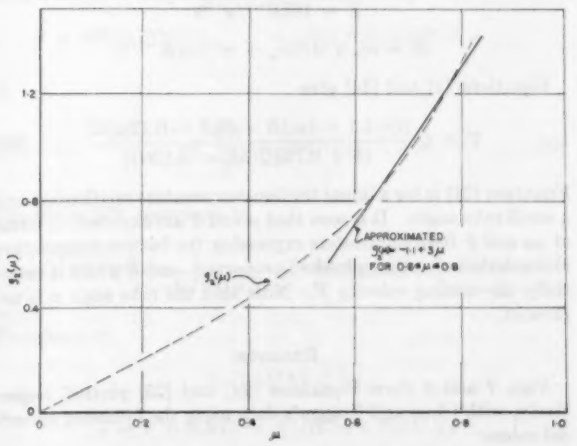

FIG. 6 APPROXIMATE $g_2(\mu)$ FUNCTION

linear functions replacing $g_1(\mu)$ and $g_2(\mu)$ approximately, for $0.6 \leq \mu \leq 0.8$, respectively. Thus

$$g_1(\mu) = 0.8 - 0.12\mu \quad \ldots\ldots [19]$$

and

$$g_2(\mu) = -1.1 + 3\mu \quad [20]$$

Putting Equations [19] and [20] into [18]

$$\mu(t) = \mu_0 - \xi D \int_0^t [(-1.1E + 0.8G) + (3E - 0.12G)\mu(t')] H(t, t')dt' \quad [21]$$

Letting $\bar{\mu}(t) = \mu(t)/\mu_0$, Equation [21] becomes

$$\bar{\mu}(t) = 1 + M \int_0^t [1 + N\bar{\mu}(t')]H(t, t')dt' \quad [22]$$

where

$$M = \frac{-\xi D}{\mu_0}(-1.1E + 0.8G)$$

and

$$N = \mu_0(3E - 0.12G)/(-1.1E + 0.8G)$$

Equation [22] is a linear integral equation known as Volterra's equation of the "second kind." The solution

$$\bar{\mu} = \lim_{t \to \alpha} \bar{\mu}(t)$$

is found to be approximately (see Equation [30], Appendix)

$$\bar{\mu} = 1 + \frac{b}{2a} M(1 + N) \Big/ \left(1 - 0.75 \frac{b}{2a} MN\right) \quad [23]$$

provided

$$\left| 0.75 \frac{b}{2a} MN \right| < |$$

or

$$\mu = \mu_0 - \xi Q \frac{[(-1.1 + 3\mu_0)E + (0.8 - 0.12\mu_0)G]}{[1 + 0.75\xi Q(3E - 0.12G)]} \quad [24]$$

where

$$Q = S_S/\theta_0\gamma C[1 + (\pi r_a R)^{-1/3}]$$

$$E = 16\delta R^{1/3}/\pi^{3/3}b$$

$$G = \sec \pi/4/[(r_a + \pi^{1/3}/4(R^{-1/3})]$$

Equations [1] and [24] give

$$T = Q \frac{[(-1.1 + 3\mu_0)E + (0.8 - 0.12\mu_0)G]}{[1 + 0.75\xi Q(3E - 0.12G)]} \quad [25]$$

Equation [24] is for a linear friction-temperature relationship and a small rake angle. It is seen that μ and T are expressed in terms of μ_0 and ξ (two parameters expressing the friction-temperature characteristics), other physical properties, and R which is essentially the cutting velocity V. Note that the rake angle α is not present.

Example

Figs. 7 and 8 show Equations [24] and [25] plotted, respectively, with Chao and Trigger's data using the following numerical values:

S_S = 65,000 psi
ξ = 0.04
μ_0 = 1.4
θ_0 = 65 F
b = 0.051
r_a = 0.33
τ_a = 0.7

$K_{1200\,F}$ = 4.82 lb/sec deg F
$a_{1200\,F}$ = 0.0096 sq in/sec
$\gamma C_{1200\,F}$ = 502.5 lb/sq in. deg F
} From Loewen and Shaw's data (2)

For the range of R-values $|0.75\xi Q(3E - 0.12G)| < |$, consequently Equations [24] and [25] are valid.

It is interesting to note that in Equation [25], T is approximately proportional to $b^{-1/3}$. From Chao and Trigger's data the so-called actual contact area has an average value of 0.0072 sq in. If a circular area is considered, the radius is 0.048 in. while in this analysis a value of $b = 0.051$ in., the width of cut, is used. One would expect then that the temperature calculation would be approximately lower than what it should be by a factor of $(0.051/0.048)^{-1/3} = 1.03$.

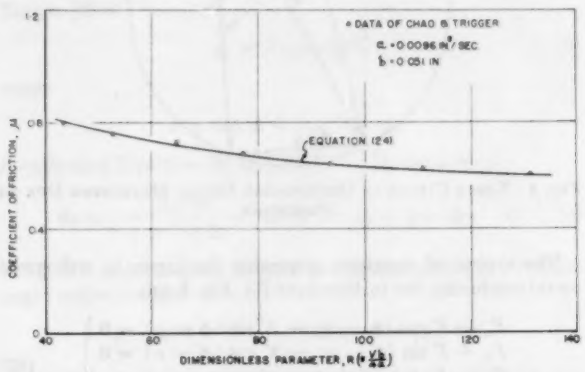

Fig. 7 Coefficient of Friction Versus Dimensionless Parameter R

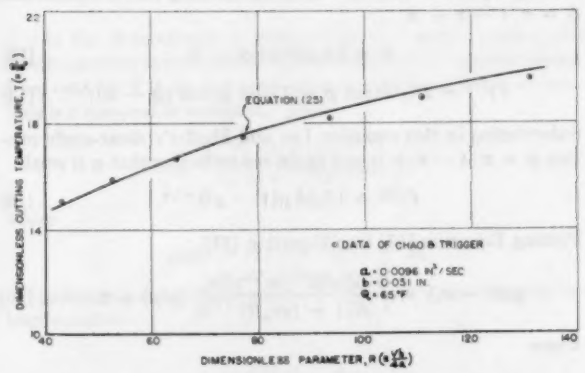

Fig. 8 Dimensionless Cutting Temperature Versus Dimensionless Parameter R

The fact that the calculated values of T, Fig. 8, are higher than the experimental values can be attributed to the fact that no heat losses through other means were considered and as pointed out earlier many simplifying assumptions have been made.

The primary purpose of this paper is to show a functional relationship between T and the independent variables when the friction-temperature characteristics are incorporated; and the quantitative check is only of secondary interest as there are so many uncertainties involved in the metal-machining theory.

Conclusions

For a linear friction-temperature relationship determined by two constants and for small rake angles, analytical expressions have been derived for cutting temperature and coefficient of fric-

tion. Both parameters are expressed in terms of the independent variables, namely, the physical properties of the problem and cutting speed.

BIBLIOGRAPHY

1 "Cutting Temperature and Metal-Cutting Phenomena," by B. T. Chao and K. J. Trigger, Trans. ASME, vol. 73, 1951, pp. 777–793.

2 "On the Analysis of Cutting Tool Temperatures," by E. G. Loewen and M. C. Shaw, Trans. ASME, vol. 76, 1954, pp. 217–231.

3 "An Analytical Evaluation of Metal-Cutting Temperatures," by K. J. Trigger and T. B. Chao, Trans. ASME, vol. 73, 1951, pp. 57–68.

4 "The Significance of the Thermal Number in Metal Machining," by B. T. Chao and K. J. Trigger, Trans. ASME, vol. 75, 1953, pp. 109–115.

5 "Les temperatures des surface dans des conditions de graissage sous pression extreme," by H. Blok, Second World Petroleum Congress, Paris, Section 4, 1937.

6 "Theoretical Study of Temperature Rise at Surfaces of Actual Contact Under Oiliness Lubricating Conditions," by H. Blok, Proceedings of General Discussion on Lubrication, Lubricants, The Institution of Mechanical Engineers, London, England, 1950.

7 "Distribution of Shear Zone Heat in Metal Cutting," by W. C. Leone, Paper No. 53—A-7, presented at the Annual Meeting, New York, N. Y., November 29–December 4, 1953, of THE AMERICAN SOCIETY OF MECHANICAL ENGINEERS.

8 "Conduction of Heat in Solids," by H. S. Carslaw and J. C. Jaeger, Oxford University Press, London, England, 1947, p. 220.

9 "Mechanics of the Metal Cutting Process I. Orthogonal Cutting and a Type 2 Chip," by M. E. Merchant, *Journal of Applied Physics*, vol. 16, 1945, pp. 267–275.

10 "The Theory of Plasticity Applied to a Problem of Machining," by E. H. Lee and B. W. Shaffer, Trans. ASME, vol. 73, 1951, pp. 405–413.

Appendix

SOLUTION TO EQUATION [22]

Equation [22] is written

$$\bar{\mu}(t) = 1 + M\int_0^t [1 + N\overline{\mu(t')}]H(t, t')dt' \ldots\ldots [26]$$

where

$$H(t, t') = \{1 - \exp[-b^2/4a(t - t')]\}/[\pi a(t - t')]^{1/2}$$

If $\bar{\mu}(t)$ is substituted into the right-hand side of Equation [26], we get

$$\bar{\mu}(t) = 1 + M(1 + N)g(t) + M^2N(1 + N)g'(t) + \ldots. + M^{n+1}N^n(|1 + N|)g^{(n)}(t) + \ldots.$$

or

$$\bar{\mu}(t) = 1 + M(1 + N)\sum_0^\infty (MN)^n g^{(n)}(t) \ldots\ldots [27]$$

where

$$g(t) = \int_0^t H(t, t')dt'$$

$$g'(t) = \int_0^t \int_0^{t'} H(t', t'')dt''dt'$$

$$\vdots$$

$$g^n(t) = \int_0^t \int_0^{t^{(n)}} H[t^n, t^{(n+1)}]dt^{(n+1)} \ldots\ldots dt'$$

$$g(t) = \int_0^t H(t, t')dt' = \beta\left[\frac{1 - e^{-\tau^2}}{\sqrt{\pi}\,\tau} + \text{erfc}\,\tau\right] \ldots [28]$$

where

$$\beta = b/2a \text{ and } \tau = b/2(at)^{1/2}$$

erfc is 1-error integral

$$\bar{g}(t) = \lim_{t\to\infty} g(t) = \beta$$

It is seen further that

$$g(t) \leqslant \beta, \quad g'(t) \leqslant \beta^2, \ldots., g^{(n)}(t) \leqslant \beta^n, \ldots.$$

and the series

$$\sum_0^\infty g^{(n)}(t)$$

is bounded by a power series in the constant β

$$\sum_0^\infty \beta^n$$

However, further investigation of

$$\overline{g(t)} = \lim_{t\to\infty} g'(t) = \lim_{t\to\infty}\left\{\beta\int_0^t H(t, t')\left[\frac{1 - \exp(-b^2/4at')}{\sqrt{\pi}\,b/2(at')^{1/2}} + \text{erfc}\,b/2(at')^{1/2}\right]\right\} dt$$

shows that the improper integral (singularly at $t' = t$) does converge. It is to be noted that $t' \leqslant t$. Numerical integration shows that $\bar{g}(t)$ converges to $0.75\beta^2$ and that a much steeper upper bound of $\bar{g}''(t)$ is $(0.75)^2\beta^3$.

Because of the nature of the integrand and the fact that the series

$$\sum_0^\infty (MN)^n g^{(n)}(t)$$

is an alternative one, it can be approximated by

$$\beta + MN(0.75)\beta^2 + \ldots. + (MN)^n(0.75)^n\beta^{n+1} + \ldots$$

or

$$\beta\sum_0^\infty (0.75MN\beta)^n \ldots\ldots [29]$$

The Series [29] converges to

$$\beta\frac{1}{1 - 0.75MN\beta} \quad \text{if} \quad |0.75MN\beta| < |$$

Therefore for

$$|0.75\beta MN| < |$$

$$\bar{\mu} = 1 + \beta M(1 + N)/(1 - 0.75\beta MN)$$

or

$$\bar{\mu} = 1 + \frac{b}{2a}M(1 + N)\Big/\left(1 - 0.75\frac{b}{2a}MN\right) \ldots [30]$$

Discussion

B. T. Chao[4] and K. J. Trigger.[5] The writers are very much interested in the analysis presented in this paper and are in complete sympathy with the intent of the authors to relate one of the fundamental problems in metal-cutting science, namely, the friction and temperature at the tool-chip interface. In spite of the many liberal assumptions used in the analysis, it is surprising to note that the predicted results agree so well with the experimental data. However, the writers cannot accept some of the postulates upon which the analysis is based. The following comments are submitted for clarification and consideration.

According to the authors, the dimensionless cutting temperature T, which is the ratio of the temperature rise (above ambient) at the tool-chip interface to the ambient temperature, can be computed from Equation [25] of the paper for a linear friction-temperature relationship and a small rake angle. Upon examination of the equation, the authors further noted that T should be approximately proportional to $b^{-1/3}$, b being the half-width of the chip or the *half-depth of cut in a conventional turning operation*. This means that reducing the depth of cut by half would increase T by a factor of $\sqrt{2}$ or 1.41 under otherwise identical conditions. Unfortunately, this is in direct contradiction to well-established experimental facts. Trigger[6] in his first progress report on tool-chip interface temperature showed that at a feed of about 0.01 ipr, and with a nose radius of $^3/_{64}$ (0.047) in., the cutting temperature increased slightly with *increase* but *not decrease* in depth of cut to about 0.100 in. Further increase in cutting depth up to 0.150 in. had virtually no effect on the interface temperature. The work material used was annealed NE9445 steel, 183 Bhn, and the tool material was triple carbide. The relationship between depth of cut and interface temperature is shown in Fig. 9 of this discussion.

Fig. 9 Effect of Depth of Cut on Interface Temperatures

It also has been observed in orthogonal cutting (the conditions for the authors' analysis) that there is no difference in the measured interface temperature for tube-wall thicknesses varying from 0.050 to 0.200 in. with other cutting conditions constant. Similar results have been obtained for conventional turning operations with small (0.015 in.) nose-radius tools. This phenomenon is attributed to the fact that once the depth of cut is significantly greater than the nose radius the heat concentration per unit length of cutting edge and per unit area of contact is substantially constant as are the interface temperatures.

Inasmuch as the main conclusion of the authors' analysis is in error, it may prove useful to re-examine the various assumptions adopted in the paper. Huxley once remarked that what one could get out of the mathematical mill depended solely on what one put into it. This appears to be the case in the formulation of Equations [24] and [25] of this paper. In the calculation of the tool-chip interface temperature, the authors postulated that the heat liberated due to rubbing of the hot chip on the top surface of the tool was distributed over a circular area whose radius was taken to be the half-depth of cut. Table 1 of this discussion shows the error involved in using such a hypothetical area for the tool-chip contact as compared to that determined by actual measurement under the cutting conditions selected by the authors for the construction of Figs 7 and 8.

TABLE 1 COMPARISON OF ACTUAL AND ASSUMED TOOL-CHIP CONTACT AREAS

Work material: NE9445 steel, mill-annealed, 183 Bhn
Tool material: Triple carbide
Tool rake: 4 deg
Feed: 0.0098 ipr
Tube-wall thickness: 0.102 in.
Orthogonal cutting

Cutting speed	Tool-chip contact area, in² × 10⁻³		
sfpm	By measurement	Assumed	Error, per cent
166	8.05	8.17[a]	1.5
204	7.7	8.17	6.1
249	7.32	8.17	11.6
298	7.02	8.17	16.4
360	6.75	8.17	21.0
428	6.50	8.17	25.7
504	6.35	8.17	28.7

[a] Since $b = 0.051$ in., $\pi b^2 = 8.17 \times 10^{-3}$ in.²

The role which the tool-chip contact area plays in affecting interface temperature has been explained elsewhere[7] and thus will not be repeated here. Suffice it to say that a decrease in contact area will result in a higher concentration of heat on the tool contact and hence an increase in interface temperature. It may be remarked further that if the feed is reduced beyond that indicated in Table 1, while the depth of cut is kept unchanged, the authors' hypothesis of a circular source will introduce an even larger error. Table 1 also indicates that the use of a single value of contact area for the computation of cutting temperature at various speeds cannot possibly yield an accurate result.

In the authors' analysis, the tool is viewed as a semi-infinite solid which, also, does not conform to the true situation. This and the previous postulate undoubtedly will lead to a calculated cutting temperature which is too low.

On the other hand, Equation [8] of the paper gives the temperature at the center of the hypothetical disk source and therefore represents the maximum rather than the average temperature. It is possible that for the case cited the positive error resulting from the use of Equation [8] is more or less canceled by the negative errors as explained in the foregoing paragraphs. This fact may serve to explain the apparent good agreement between the calculated values of T and the experimental data as shown in Fig. 8. However, the writers are inclined to believe that this is a case of happy coincidence and cannot be taken as evidence to justify the use of the various assumptions.

The writers want to point out that the dynamic shear stress S_s of annealed NE9445 steel is not 65,000 psi as the authors have indicated. It varies from 86,300 to 90,600 psi over the cutting-speed range of 166 to 504 sfpm, other cutting conditions being as listed in Table 1.

Finally, the writers also question the validity of not making

[4] Associate Professor of Mechanical Engineering, University of Illinois, Urbana, Ill.

[5] Professor of Mechanical Engineering, University of Illinois. Mem. ASME.

[6] "Progress Report No. 1 on Tool-Chip Interface Temperatures," by K. J. Trigger, Trans. ASME, vol. 70, 1948, pp. 91–98.

[7] Authors' Bibliography (1).

distinction between the thermal properties of the work material at the shear zone and at the interface, and those of the chip and tool material. The influence of temperature on the specific heat and thermal conductivity over the whole temperature range encountered is appreciable, at least for NE9445 steel.

The foregoing comments have been submitted in a spirit of constructive criticism in the hope that future analysis may be based upon more realistic conditions.

W. C. Leone.[8] The authors are to be complimented for making a novel attack on the difficult problem of metal-cutting temperatures.

With respect to the principal causes of lower frictional resistance, there are several remarks which should be clarified. Unfortunately, it is difficult to make simple general statements about a concept as complex as friction. For instance, it is not quite clear what the significance of a lower-yield-strength material is with regard to friction unless something is said about which of the rubbing surfaces has the lower yield strength.

The authors state that at higher temperatures lower frictional resistance is caused by more ready oxidation. On the other hand, Westphal and Glatter[9] say, ". . . it is sufficient to state that in all cases the friction was appreciably higher in water than when dry, except where lead and lead oxide powders were applied. A plausible explanation of this behavior is that oxidation takes place more readily in water than in air at the contact points where high temperatures are developed during motion. Since the oxides of most metals are abrasive, increased friction results."

With respect to the shear-angle relationship

$$\phi = \frac{\pi}{4} - \tau + \alpha \text{ where } \tau = \tan^{-1} \mu$$

Lee and Shaffer[10] assumed that (*a*) the material cut behaves as an ideal plastic which does not strain-harden, and (*b*) the shear stress and the normal stress on the shear plane are equal. As shown by Shaw, Cook, and Finnie,[11] this is generally not the case and the foregoing equation cannot be regarded as a general solution. It would seem appropriate to use a more complete relationship for ϕ such as that of Merchant which includes the so-called "machining constant."

E. G. Loewen.[12] In the past few years at least six groups of investigators both here and abroad have attacked the problem of temperature analysis of the metal-cutting process. Further proof of the importance of this subject is hardly necessary. Although all investigators agree on the basic energy sources the methods of analysis differ to a surprising degree. That the final results exhibit a corresponding divergence is only to be expected in such a complex problem. Obviously it will require experiments to decide which, if any, of the theories explains all the facts. Such experimental verification is not easy since, for example, the tool-work thermocouple method is not always precise enough and in any case tells us nothing about temperature distributions. Unfortunately, alternative methods require much more elaborate experiments, but these are now being performed in several laboratories. Recent results obtained at M.I.T. indicate, for instance, that the equation for σ_1 (just below Equation [2] in the paper), is approximately correct over at least part of the range of R, provided σ is more reasonably defined, as in Leone's original paper (7).

It must be pointed out that the present authors have defined their thermal number R as $Vb/4a$, while previous writers have defined it as $V\delta/a$. This change, the need for which is not made sufficiently clear, gives undue prominence in the final result to the width of cut, $2b$, although it is well known that once $2b$ exceeds $^1/_{32}$ in. a further increase has negligible effect on tool temperatures. It is not possible to revert simply to the older definition without changing the whole analysis.

A much more serious difficulty in applying the authors' solution in practice lies in the great importance that is assigned to the coefficient of friction, and, in particular, the value of μ_0 which has to be obtained from severely extrapolated experimental data. Furthermore, the basic plot is that of μ against T, which is also the final result to be obtained. It has been the writer's experience that the slope of μ versus T curve can be opposite to that shown in Fig. 2. Such slopes would lead to calculated tool temperatures far too low; in fact, may result in negative values for T. Perhaps it is better not to regard the coefficient of friction as a fundamental quantity of metal cutting at all. As Kronenberg[13] has pointed out, it represents little more than a convenient ratio between friction and normal forces on the tool face.

With many work materials the variations in thermal properties with temperature are too large for a single value to be satisfactory in both shear and friction zones. Recent experiments at M.I.T. showed that the specific heat of titanium increases markedly with temperature. Not until this fact was established was it possible to calculate cutting temperatures for titanium and obtain reasonable results, using the toolt-emperature analysis of the authors' reference (2).

Authors' Closure

The authors wish to thank the discussers for their constructive criticisms. Of the questions raised, most of them were concerned with the approximate assumptions which entered into the analysis. We agree that these assumptions, which we were careful to point out explicitly, lead to results which should be further refined. However, it was important to carry through an analysis of some sort to see what the interaction of friction and temperature at the chip-tool interface would lead to. The main results of the paper are those shown in Figs. 7 and 8 and, as may be seen, give good agreement between the theory and the data of Chao and Trigger for orthogonal cutting. We do not feel that references to conventional cutting are pertinent to the present discussion.

Regarding the comparison of actual and assumed tool-chip contact areas we have shown that the worst error in the numerical case we treat is 3 per cent in the temperature. The per cent error in the area of contact may be higher but we should not confuse error in the area with errors in the final result. We admit though that not being able to derive an exact value for the area of contact is a definite limitation on the method and we hope to improve and refine the theory to take care of this.

As to the question raised by Professor Loewen regarding the use of a dimensionless parameter $R = Vb/4a$ instead of the conventional one, $V\delta/a$, our reason was for the purpose of making the cutting velocity dimensionally homogeneous. So as not to cause any confusion we were careful not to refer to it as a thermal number.

---

[8] Member of the Technical Staff, Hughes Aircraft Company, Culver City, Calif.

[9] "The Wear and Friction Properties of Materials Operated in High-Temperature Water," by R. C. Westphal and J. Glatter, Paper No. 54—SA-13, presented at the Semi-Annual Meeting, Pittsburgh, Pa., June 20–24, 1954, of The American Society of Mechanical Engineers.

[10] "The Theory of Plasticity Applied to a Problem of Machinery," by E. H. Lee and B. W. Shaffer, Trans. ASME, vol. 73, 1951, p. 405.

[11] "The Shear-Angle Relationship in Metal Cutting," by M. C. Shaw, N. H. Cook, and I. Finnie, Trans. ASME, vol. 75, 1953, p. 273.

[12] Assistant Professor of Mechanical Engineering, Massachusetts Institute of Technology, Cambridge, Mass. Assoc. Mem. ASME.

[13] "Metal Cutting Friction Coefficient Needs Reinterpretation," by M. Kronenberg, *The Tool Engineer*, vol. 31, October, 1953, p. 49.

Regarding the question of Dr. Leone and Professor Loewen on the correlation of friction and interface temperature, one of the authors (Ling) had experimented with surface friction on a friction machine using surface conditions similar to that at the chip-tool interface. It was found that for a rough surface similar to a chip sliding on a hard surface (the tool), friction decreased with increase of sliding velocity. Furthermore, a corresponding phenomenon was observed when the interface temperature was raised by artificial means while sliding was kept constant, i.e., while frictional heating was simulated. This correlation of friction and temperature is quite pronounced. It was these experimental findings, leading to the use of Equation [1] and the metal-cutting data of Chao and Trigger, since our own was lacking, that initiated this work. In a case where the slope of the μ versus T curve is opposite to that of the authors the method still holds. It is not at all clear that Dr. Loewen's conjecture, that the calculated cutting temperature would be too low, is justified.

The authors wish to point out an error in the paragraph following Fig. 3 and in the table of values. The temperature at the center of the area of contact should be the maximum and the average over the surface can be shown to be approximately $2^{-1/4}$ of the maximum. The temperature curve, plotted in Fig. 8, was arrived at by using a mean value of S_s = 92,000 psi. As pointed out by Professors Chao and Trigger the averaged value should be somewhere between 86,300 and 90,600 psi. Thus, according to the present theory, the calculated temperature should be slightly lower than that shown if the proper mean value is used.

Dielectric Breakdown Properties of Thermosetting Laminates

By N. A. SKOW,[1] OAKS, PA.

Thermosetting laminated plastics are used extensively for electrical insulation because of their unusual combination of electrical, mechanical, and chemical properties. Excellent electrical insulators, these materials are also mechanically strong, light in weight, and easy to fabricate. They resist chemical corrosion, moisture, aging, heat, and temperature deterioration. To establish safe operating loads, tests for the endurance limits of dielectric strength were run on each of several grades of thermosetting plastic laminates plotting voltages against time. The data thus obtained indicate that for a given thickness and atmospheric condition, a maximum voltage exists below which failure will not occur. Tests of this type yield results which are valuable to the design engineer in determining the proper grade and thickness of material for use as insulating parts in electrical equipment.

Determining Insulating Properties

In selecting an electrical insulating material, the designer is primarily concerned with insulation resistance, dielectric loss, and dielectric breakdown. The relative importance of these various properties depends on the application involved, but dielectric breakdown is almost always a major consideration.

As defined by ASTM, the dielectric strength of an insulating material is the maximum potential gradient that the material can withstand without rupture. It is difficult to evaluate quantitively because its magnitude varies with temperature, thickness of material, moisture content, and time exposed to stress. In general, the dielectric strength of insulating materials decreases with time of exposure to the electrical stress.

For a quick determination of dielectric strength, the short-time test has been devised. For fairly rapid determinations, but laying more emphasis on the time factor, the step-by-step test has been arranged. These tests involving short exposures are primarily comparative and are not indicative of the breakdown of the materials under prolonged exposure to lower stresses. The limitations of these tests already have been pointed out in the appendix to the ASTM Standards on Electrical Insulating Materials.[2]

Since long service without breakdown is a primary requirement of electrical insulating materials, determination of the endurance limit is most essential. This can be measured by stressing the laminate with voltages less than the short-time value and recording the results at each voltage. When the maximum voltage that can be applied for an indefinite time without breakdown has been found, the endurance limit of dielectric strength has been established.

Differences between the dielectric breakdown properties of thermosetting laminates stressed parallel to laminations and those stressed perpendicular to laminations are sufficient to warrant investigation of behavior for each direction. The same dielectric strength and endurance characteristics do not exist where laminated sheets are used as insulating spacers (stressed perpendicular to lamination), and where laminates are used as terminal-board insulators (stressed parallel to lamination).

Grades of Plastics Tested

To obtain the results presented here, seven standard NEMA grades of laminated thermosetting plastics were tested: Grades X, XX, XXXP, LE, A, G-5, and N-1. Any other NEMA grade might be used in similar applications but those mentioned were selected because they are typical of the entire group. While this series of tests was made only upon laminates in the sheet form, the dielectric properties of tubes, rods, and molded parts are quite similar. Briefly, the materials tested can be described as follows:

Grades X, XX, and XXXP are paper-base laminates bonded with phenolic resin. Grade X is intended primarily for mechanical applications and should be used with discretion under high humidity conditions. Grade XX is made with a more absorbent paper and has a higher resin content than Grade X. Grade XX is better electrically, although slightly weaker mechanically, than Grade X. Grade XXXP, which has a still higher resin content, is one of the best electrical laminates produced. Grade LE has a cotton-fabric base and is bonded with phenolic resin. This grade is used on electrical applications requiring greater toughness than is provided by Grade XX.

Grade A is an asbestos paper-base laminate bonded with phenolic resin. It is more flame and heat-resistant than the cellulosic grades. Bonded with melamine resin, Grade G-5 is a glass-base laminate with very high mechanical strength, excellent electrical properties under dry conditions, and good heat, flame, and arc resistance. Grade N-1 is a nylon-fabric-base laminate bonded with phenolic resin. It has excellent electrical and mechanical properties even under high humidity conditions.[3]

Program of Tests

Fig. 1 indicates the sample size and test arrangements used to determine dielectric strength and endurance limit of plastic laminates in both directions (perpendicular and parallel to laminations). For testing perpendicular to laminations, 6 × 6-in. samples were selected at random from standard production sheets (36 × 36 × 1/16 in.). For the tests parallel to laminations, specimens 2 × 3 × 1/2 in. were cut from standard sheets 36 × 36 × 1/2 in. A hole, 2 in. in diam, was drilled along the 2-in. axis of each specimen to a depth of 1 3/4 in. The end of each hole was counterbored with a flat-bottom drill, leaving a 1/4-in. thickness of laminate between the bottom of the hole and the edge of the sample. While this is not a standard test specimen it was found very convenient in this study because it eliminated the problem of flashover. (To have used a specimen 6 × 6 in. would have

[1] Director of Research, Synthane Corporation, Oaks, Pa.

[2] Published by American Society for Testing Materials, 1916 Race Street, Philadelphia, Pa.

Contributed by the Rubber and Plastics Division and presented at the Semi-Annual Meeting, Pittsburgh, Pa., June 20–24, 1954, of The American Society of Mechanical Engineers.

Note: Statements and opinions advanced in papers are to be understood as individual expressions of their authors and not those of the Society. Manuscript received at ASME Headquarters, May 11, 1954. Paper No. 54—SA-67.

[3] For a description of the NEMA grades not included here see "Standards for Laminated Thermosetting Products," publication No. LP1-1951.

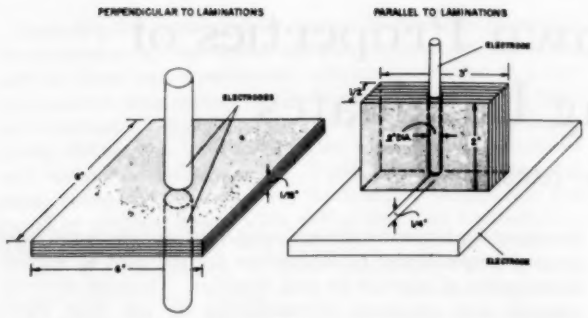

FIG. 1 SAMPLE SIZES AND TEST ARRANGEMENT FOR DETERMINING DIELECTRIC BREAKDOWN—PARALLEL AND PERPENDICULAR TO LAMINATIONS—IN THERMOSETTING LAMINATES

(Electrodes perpendicular to laminations are not drawn to scale—actually they are 2 in. diam.)

meant the production of a 6-in-thick sheet of laminate for each grade to be tested.)

Short-time dielectric-strength measurements perpendicular to laminations were made on the $6 \times 6 \times {}^{1}/_{16}$-in. specimens in oil as specified in ASTM Standard D149-44. The samples to be tested were first dried in an oven at 220 F for 1 hr and then cooled in a desiccator for 16 hr at 73 F. After conditioning, tests were made using five specimens of each grade.

Short-time dielectric-strength measurements parallel to laminations were made on the $2 \times 3 \times {}^{1}/_{2}$-in. specimens in oil. Because of the thickness of sample, these test pieces were conditioned at 220 F for 8 hr followed by 16 hr of cooling in a desiccator at 73 F. Five specimens of each grade were tested.

RESULTS OF TESTS

Results of tests in both directions are given in Table 1 for Grades XX, XXXP, and N-1 at temperatures from 65 to 256 F. Breakdown voltage versus temperature curves are given in Fig. 2 for both perpendicular and parallel directions for each of the three grades tested. Two significant facts are readily apparent: (1) Short-time dielectric strengths parallel to laminations are lower than those perpendicular to laminations (with the exception of Grade XX at temperatures above 180 F); and (2) the differences in dielectric strength versus temperature characteristics parallel to laminations are comparatively small.

Grade XXXP laminate has the highest dielectric strength perpendicular to laminations within the temperature range covered and the drop in breakdown voltages is very small between 90 and 180 F. This gradual change in breakdown voltage up to 180 F is of particular advantage when laminated-plastic components are subjected to hot-spot temperatures in electronic equipment. It is evident that there is a rapid decrease in the breakdown voltage of even Grade XXXP as the temperature is increased further. The breakdown characteristics of the three grades parallel to laminations are more nearly equal. This indicates that it makes little difference in regard to short-time dielectric strength which of the three grades is selected for operation at temperatures within the range covered.

The data in Table 1 indicate that parallel to laminations Grade N-1, nylon-base laminate, has the most rapid decrease in dielectric strength (short-time) with temperature, while the breakdown voltages of Grade XXXP, although it has a lower dielectric strength at lower temperatures, drop slightly between 65 and 256 F. The breakdown voltages of Grade XX appear between these two extremes throughout the temperature range.

Data in Table 2 are presented to indicate the effect of sample thickness on the short-time dielectric strength measured in both directions. The dielectric strength of Grade XX plastic laminate

TABLE 1 EFFECT OF TEMPERATURE ON DIELECTRIC STRENGTH—SHORT TIME—OF LAMINATES

Temperature Degrees F	DIELECTRIC STRENGTH (SHORT TIME) Volts/Mil					
	Grade XX		Grade XXXP		Grade N-1	
	Perpendicular[1]	Parallel[2]	Perpendicular[1]	Parallel[2]	Perpendicular[1]	Parallel[2]
65	700	154	900	160	520	240
77	484	150	850	156	498	228
91	416	156	825	160	486	224
100	339	158	800	158	483	220
121	282	144	775	154	480	204
139	240	140	778	152	455	180
170	160	140	750	148	317	140
184	138	142	743	144	275	132
202	120	128	719	150	213	104
210	103	120	675	140	170	92
226	98	116	500	132	155	72
238	87	108	490	138	145	60
244	85	104	--	129	140	52
256	82	--	--	148	134	--

[1] Average for five specimens conditioned for 1 hour at 220F

[2] Average for five specimens conditioned for 8 hours at 220F

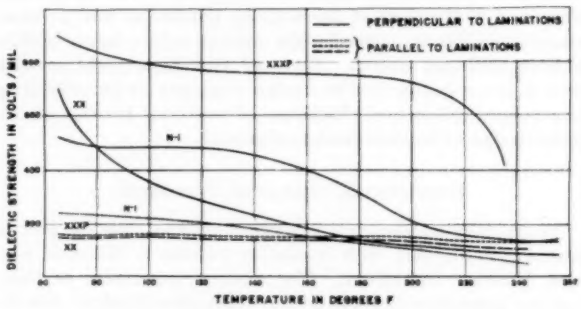

FIG. 2 EFFECT OF TEMPERATURE ON DIELECTRIC STRENGTH (SHORT TIME) OF LAMINATES

TABLE 2 EFFECT OF SAMPLE THICKNESS ON DIELECTRIC STRENGTH—SHORT TIME—OF LAMINATES; TESTED DRY AT 73 F

THICKNESS Inches	DIELECTRIC STRENGTH (SHORT TIME) Volts per Mil		
	PERPENDICULAR TO LAMINATIONS[1]	PARALLEL TO LAMINATIONS[2]	
	Grade XX paper-base	Grade X paper-base	Grade XX paper-base
1/32	940	--	--
1/16	695	360	530
1/8	515	270	275
1/4	--	180	190
3/8	--	120	130
1/2	--	110	120

[1] Average for five specimens, conditioned for 1 hr. at 220 F.

[2] Average for five specimens, conditioned for 8 hrs. at 220 F.

measured perpendicular to lamination is 515 vpm at a ${}^{1}/_{8}$-in. thickness or slightly more than half the magnitude for a ${}^{1}/_{32}$-in. sample thickness. The dielectric strengths parallel to laminations, measured at five thicknesses ranging from ${}^{1}/_{16}$ to ${}^{1}/_{2}$ in., are very close for Grades X and XX with sample thicknesses greater than ${}^{1}/_{8}$ in. In Table 2 the decrease in dielectric strength may be compared to the law of diminishing returns in that each additional thickness of laminate provides a smaller increase in the total dielectric-breakdown voltage of the sample.

Table 2 shows the necessity for maintaining equal sample thicknesses for all tests to obtain results for the purpose of comparison. For measurements perpendicular to laminations throughout this testing program a thickness of ${}^{1}/_{16}$ in. was selected because it is representative of the sheet thicknesses used in many electrical applications. A ${}^{1}/_{4}$-in. thickness was specified

for testing parallel to laminations because thinner sections were more difficult to machine to uniform dielectric gaps.

Effects of Conditioning

To determine the effects of conditioning, the dielectric strength (short-time) of Grade XX laminate was measured in both directions for various combinations of time, temperature, and moisture treatment. The results of these tests are given in Table 3 for each specified conditioning treatment. Conditioning for a maximum of 4 days for measurements perpendicular to laminations was sufficient, but 21 days were necessary to insure uniform moisture absorption for obtaining breakdown voltages parallel to laminations. Because dielectric strength varies widely with changes in conditioning treatment, considerable care was taken to standardize the sample conditioning prior to dielectric-strength tests. One-hour drying at 220 F was selected for samples to be tested perpendicular to laminations because it provided the most reproducible results.

These samples were removed from the conditioning chamber, placed between the electrodes of the testing equipment and immersed in an oil bath. In so far as possible, the samples of each grade of laminate were tested at 85, 70, 60, 55, 50, and 45 per cent of the short-time breakdown voltage measured previously. Voltage was applied at the rate of 10 kv/sec until the specified magnitude was reached and maintained until rupture occurred. The voltage applied and the time in minutes required for failure were then recorded.

Measurements parallel to laminations were made in oil with a metal pin and plate as electrodes, Fig. 1. All samples were conditioned in an oven for 8 hr at 220 F, and five specimens of each grade were tested for short-time dielectric strength in accordance with ASTM D149-44. Because of the $^1/_4$-in. thickness of the electrode gap, a longer conditioning period was necessary to insure uniform dryness.

The endurance limit of the dielectric strength parallel to laminations was determined by applying voltages at the rate of 10 kv/sec until 85, 70, 60, 55, 50, and 45 per cent of the short-time breakdown value was reached. After rupture occurred, the voltage and time for failure were recorded. For all tests, the samples and testing procedure were made as uniform as possible.

TABLE 3 EFFECT OF CONDITIONING TREATMENT ON DIELECTRIC STRENGTH—SHORT TIME—GRADE XX TESTED AT 73 F

	Conditioning Treatment	Dielectric Strength* (Short Time) Volts per Mil
Perpendicular	1 hour in oven at 220F	690
	96 hours at 90% RH and 95F	240
	48 hours in H2O at 122F	112
Parallel	21 days in desiccator at 73F	180
	21 days at 90% RH and 73F	100
	21 days in H2O at 73F	40

* Average for five specimens

Endurance Limits

The endurance limits, perpendicular and parallel to laminations, for the seven grades of laminates tested are given in Fig. 3. The dielectric strength of all grades in both directions decreases rapidly with time until it is approximately 60 to 70 per cent of the short-time dielectric strength. The curves show that the breakdown voltage, or upper limit of voltage gradient without rupture, gradually approaches a magnitude that is independent of time. The endurance limit of the material is considered approximately equal to the maximum dielectric strength which will not rupture after a 100-min exposure to stress. This assumption is based on tests on five samples which, after resisting breakdown for 100 min, continued to withstand the applied stresses for 18 hr.

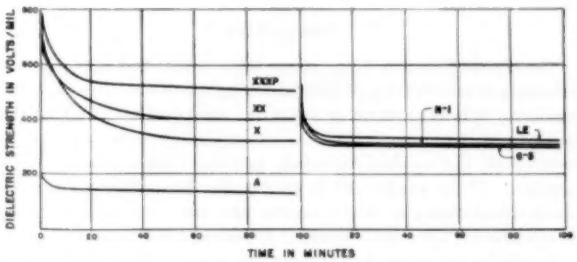

FIG. 3 ENDURANCE LIMITS OF DIELECTRIC STRENGTH—PERPENDICULAR TO LAMINATIONS

TABLE 4 SHORT-TIME DIELECTRIC STRENGTHS AND ENDURANCE LIMITS OF LAMINATES TESTED AT 73 F

Grade	Thickness	Conditioning	Perpendicular to Laminations: Short Time Diel. Str. Volts/Mil	Endurance Limits Volts/Mil	Endurance Limits Short Time Diel. Str. %	Parallel to Laminations: Short Time Diel. Str. Volts/Mil	Endurance Limits Volts/Mil	Endurance Limits Short Time Diel. Str. %	Grade	Thickness	Conditioning
A	X	Dry	849	320	49.3	124	92	74.2	X	1/8" Thick	Dry
	XX		685	390	56.1	176	106	61.3	XX		
	XXXP		780	500	64.2	172	124	72.0	XXXP		
	LE		434	320	73.8	206	134	65.0	LE		
	A		155	130	83.8	48	36	75.0	A		
	G-5		450	310	68.9	144	100	69.4	G-5		
	M-1		394	305	77.4	240	180	75.0	M-1		
B	XX	1/16", 96 hrs. at 90% RH 95F	240	150	62.5	100	80	80.0	XX	1/4", 21 days at 90% RH, 50C	
		1/16", 48 hrs. in H2O at 122F	112	55	49.5	38	18	47.4		1/4", 21 days in water at 50C	
C	XXXP	1/16", 96 hrs. at 90% RH 95F	700	400	84.2	112	96	85.7	XXXP	1/4", 21 days at 90% RH, 50C	
		1/16", 48 hrs. in H2O at 122F	680	375	57.2	56	28	50.0		1/4", 21 days in water at 50C	

Short-time dielectric strengths and endurance-limit values are compared in Table 4. In part A, where the seven grades of laminates are tested dry at 73 F, the ratios (per cent) of endurance limits to short-time dielectric strength are tabulated (data from curves in Fig. 3) to indicate the relative characteristics of the seven grades. Grade A, asbestos-base plastic laminate has the lowest dielectric strength and endurance limit in either direction but is recommended in high-temperature applications because

of its superior heat resistance. The six remaining grades tested are suitable for high-voltage applications, Grade XXXP having the highest breakdown voltages perpendicular to laminations and Grade N1 the highest parallel to laminations.

Safety Factor

For dry specimens, the endurance limits (in either direction) of the seven standard grades of laminates tested vary from 49 to 84 per cent of the corresponding short-time dielectric strength. Therefore the designer can consider a safety factor of 3, based on the short-time test, to be sufficient. For Grades XX and XXXP exposed to high humidity and elevated temperatures (Parts B and C of Table 4), the percentage ratio of endurance limit to short-time dielectric strength ranges from 47 to 86 per cent (including both directions). Again, a safety factor of 3 should be satisfactory. In actual practice, a designer may expect to use equipment under highly humid conditions, yet available data on the laminates may be limited to short-time dielectric strength under dry conditions. In these cases, a safety factor of 6, as recommended by NEMA,[4] may be necessary.

Conclusions

Conclusions drawn from these tests would indicate that for selecting thermosetting plastic laminates to be used as a dielectric medium, it is important to know the temperature at which the equipment is to be operated, the atmospheric conditions to be encountered, the mechanical strain and the dielectric stress to be applied. If the equipment is used under dry conditions and the mechanical-strength requirements are not severe, paper-base laminates are very satisfactory. If humid conditions are factors it would be advisable to use the more water-resistant paper-base grades such as Grade XXXP. Under dry conditions requiring high mechanical strength it may be necessary to use a fabric grade such as LE and under continuous humid conditions requiring high mechanical strength it may be necessary to use Grade N-1. If arc resistance is an important requirement Grade G-5 is indicated.

Acknowledgment

The tests described herein were conducted in the Research Laboratory of Synthane Corporation, Oaks, Pa.

Discussion

W. M. Lair.[5] The data presented and the conclusions drawn should be valuable to the design engineer in choosing laminates for insulating parts. The selection of grades for test was well made and gives representative laminates for different applications. The parallel dielectric-strength test method is an interesting one, and does eliminate flashover for thick sections. It also would have been worth while to include parallel measurements on the $^1/_{16}$-in. specimens used for the perpendicular testing. A more direct comparison of parallel and perpendicular breakdown values would have then been possible, providing flashovers did not occur. The retention of perpendicular dielectric breakdown on endurance tests depends on the type of filler material used, while parallel breakdown endurance is relatively independent of the various filler materials studied. The fabric grades have endurance values representing higher retention of the short-time dielectric strengths than do the paper-base grades, giving a rough correlation with ability to take mechanical strain.

G. H. Mains.[6] The author has presented a very interesting paper covering a considerable amount of data on dielectric-strength measurements of laminated materials made under various conditions of time, temperature, and humidity. His series of tests on endurance limits of dielectric strength provides a valuable contribution to the industry.

One point which might be emphasized more strongly is the variation in dielectric strength due to thicknesses. In general, it has been shown in the past that dielectric strength in volts per mil of thermosetting paper-base laminates varies inversely as the square root of the thickness. Consequently, we would expect the values for $^1/_4$-in. thickness, which is the gap between electrodes for the parallel tests, to be approximately one half of those for $^1/_{16}$-in. thickness, the gap used for the perpendicular tests. If the $^1/_4$-in. value for Grade XX (about 375 volts per mil) had been included in Table 2, the relation between dielectric strength in the perpendicular and parallel directions would be more clear.

In Table 2 changing the heading of the first column to "Thickness of Electrode Gap" instead of "Thickness" should serve to clarify the table.

In this same connection the statement is made under the heading Results of Tests: "The dielectric strengths parallel to laminations, measured at five thicknesses ranging from $^1/_{16}$ to $^1/_2$ in., are very close for Grades X and XX with sample thicknesses greater than $^1/_8$ in." This statement hardly seems correct since actually the ratio for Grade XX between the values of $^1/_4$ and $^1/_8$ in. is 275/180 or 1.53 to 1, and for $^1/_2$ and $^1/_4$ in. (again, the second sheet being one half the thickness of the first) is 180/120 or 1.50 to 1.

Under Conclusions, while the next to the last sentence might be true, there are no data given in the paper on the mechanical strengths of Grades LE and N-1 nor any data on electrical properties of N-1 under humid conditions; hence there is nothing to warrant including this statement as a conclusion. Likewise, there are no data given on arc resistance to substantiate the last sentence in the paragraph.

J. C. Pitzer.[7] We do not have any specific points of discussion in this paper but we are glad to see that the author has presented in graphic form a point which the laminated-plastics industry has known to exist for a good many years, namely, that there is some point below the dielectric-breakdown value at which laminated-plastic materials can be operated successfully over long periods of time. It would be a valuable contribution to the electrical-insulating field if similar information could be determined on other types of dielectric materials which are commonly used for electrical-insulating materials. The author has only touched the surface of a problem which requires much more extensive study.

Author's Closure

The author is grateful to the discussers for their valuable additions to the paper. Referring to the closing sentences of Mr. Mains' comment, any data added to prove his contention would be redundant, because it is common practice in the industry to make those same recommendations, and they may be found in the NEMA Standards for Laminated Thermosetting Products.

---

[4] NEMA Standards for Laminated Thermosetting Products Publication No. 46-118, August, 1946, paragraph LP-64.

[5] Chemical Divison, Laminated and Insulating Products Department, General Electric Company, Coshocton, Ohio.

[6] National Vulcanized Fibre Company, Kennett Square, Pa.

[7] Engineering Department, The Formica Company, Cincinnati, Ohio.

Thermodynamics of Supercritical-Pressure Steam-Power Plants

By JEROME BARTELS,[1] BROOKLYN, N. Y.

This paper deals with the efficiencies that are thermodynamically obtainable from a steam-power cycle by utilizing throttle pressures exceeding the critical pressure of steam. The analysis starts with Rankine cycles, and then successively presents simple cycles, multiple reheat cycles, and increasingly more complex feed-heating arrangements. Thermal efficiencies and heat rates for these cycles are established, and explanations are offered to show why the results turn out the way they do.

Constant-Pressure Processes

SEVERAL constant-pressure heat-transfer processes are presented on the temperature-entropy plane for water, Fig. 1. This plane shows the transferred heat during a constant-pressure process as an area underneath the constant-pressure line. Fig. 1 is made as a freehand sketch rather than an accurate graph so that certain relationships may be emphasized.

The required apparatus to conduct such constant-pressure heat-transfer processes consists of a cylinder filled with water atop of which there is a weighted piston.

Room-temperature water is first subjected to a pressure of 700 psia by making the piston adequately heavy, and then heat is supplied to the bottom of the cylinder to warm the contents. The water in the cylinder reaches its boiling temperature at approximately 500 F or 960 Rankine (R). Liquid water is readily identifiable up to the boiling temperature.

During the boiling process, the plateau in Fig. 1, heat is added with no change in temperature. At this temperature the heat added goes into boiling the water present. Each steam bubble forming in the water reveals that a mass of water has undergone a change of phase—from liquid to vapor. As the steam bubbles coalesce, a layer of steam forms between the water and piston. There is a sharp demarcation between the two phases present while boiling occurs; a free surface of the liquid is apparent.

Since steam occupies more space than the water from which it came, then this nonflow boiling process requires the restraining vessel to increase in size to accommodate the steam formed. Thus the piston undergoes movement so that the volume in the cylinder increases over 30 times during this boiling process at 700 psia.

After all the water boils, the additional transferred heat energy goes into superheating the vapor. The heavier the piston, the higher the cylinder pressure, the smaller the boiling plateau becomes before superheating starts.

The critical pressure provides the limiting condition as the boiling plateau approaches zero, or as the required latent heat of vaporization approaches zero. This constant-pressure line at 3206.2 psia has an inflection point of horizontal slope on top of the steam dome.

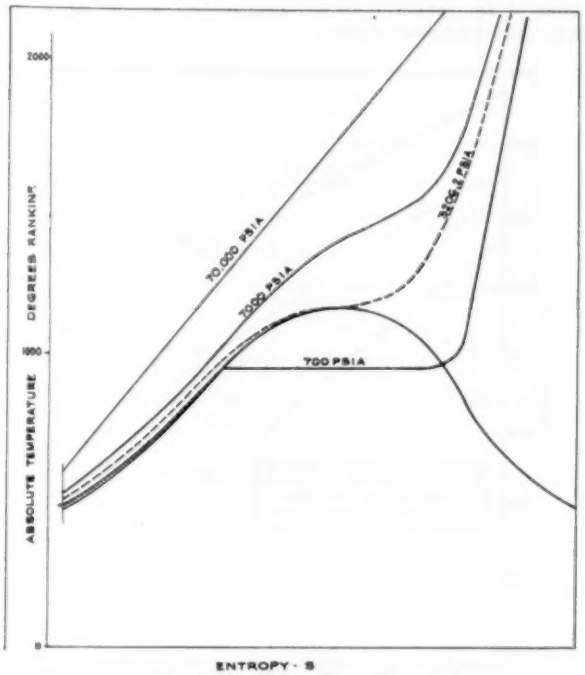

Fig. 1 Sketch of Constant-Pressure Heating Processes on Temperature-Entropy Plane for Water

At any pressure higher than the critical pressure, the physical properties of the working substance within the cylinder will follow a path with no change of phase, with no plateau, with no latent heat of vaporization.

Thus it would be, while applying weights to the top of the piston, during the pressurizing process applied to the cold working substance, that the critical pressure is surpassed, and the working substance is carried into a new monophase region. In this monophase region the working substance can now be raised to any final temperature without bubble formation. Above the critical pressure, the addition of heat causes the entire substance to expand smoothly and gradually to its final size.

By being heated, the working substance in this high-pressure monophase region can gradually acquire a large increase in its specific volume with no further change of phase, with no boiling. In everyday terms, one might think of a rubber band which is initially thick and completely opaque to light. As the rubber band is slowly stretched, it gradually becomes thinner and optically translucent. Who can say at what point the rubber band attains different optical properties, translucent in lieu of opaque? In a similar manner, the supercritically pressurized H_2O gradually changes its specific volume from values in the range of liquids to values comparable to superheated steam as its temperature is brought up to its final value.

A more discerning explanation of the behavior of the working substance is contained in the Appendix.

[1] Professor of Mechanical Engineering, Polytechnic Institute of Brooklyn, and associated with Gibbs and Hill, Inc., New York, N. Y. Mem. ASME.

Contributed by the Power Division and presented at the Fall Meeting, Milwaukee, Wis., September 8–10, 1954, of The American Society of Mechanical Engineers.

Note: Statements and opinions advanced in papers are to be understood as individual expressions of their authors and not those of the Society. Manuscript received at ASME Headquarters, July 19, 1954. Paper No. 54—F-37.

It is rather difficult to find available data on the physical properties of H_2O above the critical pressure. The present Keenan and Keyes' Tables[2] are adequate up to 5500 psia, barely over the new threshold.

In 1953, an article was published[3] which compared American, German, Russian, and Japanese steam tables, and evaluated the differences that exist among them. Unfortunately, the values presented from the foreign tables stop at pressures lower than those of the American tables, and so they are not useful for supercritical-pressure studies.

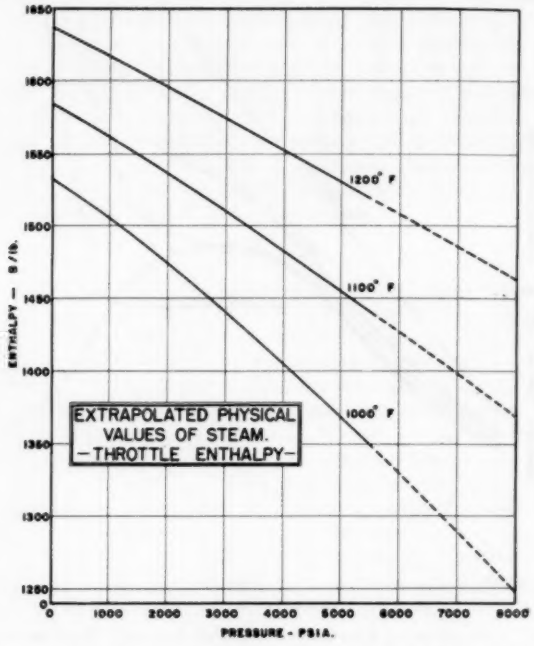

FIG. 2 EXTRAPOLATED PHYSICAL VALUES OF STEAM—THROTTLE ENTHALPY

The author resorted to extrapolating the Keenan and Keyes' Tables. A plot of enthalpy versus pressure was constructed for several temperatures, Fig. 2. Values of entropy were similarly plotted versus pressure for the same isotherm values, Fig. 3. These two sets of curves cover the properties of throttle steam over the range of pressures and temperatures investigated. Another set of curves, Fig. 4, gives the exhaust enthalpy values that would result if the various throttle steams were expanded isentropically through ideal turbines to a back pressure of $1^1/_2$ in. Hg abs.

Fig. 5 gives the enthalpy values for several supercritical pressures of H_2O over the lower temperature range. It is useful primarily for feed-pump and feed-heater calculations. This graph also is interesting because it shows a crossover point at 530 F for the two constant-pressure lines. This concludes the required data for the analysis.

RANKINE CYCLES

The Rankine cycle is the chosen starting point for the analysis of the steam-power cycles, for the Rankine cycle shows the effects of physical properties upon thermal efficiency without the distortions due to component efficiencies. The cycle arrangement

[2] "Thermodynamic Properties of Steam," by J. H. Keenan and F. H. Keyes, John Wiley & Sons, Inc., New York, N. Y., 1936.

[3] "New Steam Table Up to 700° C," by H. Erythropel, *Combustion*, March, 1953.

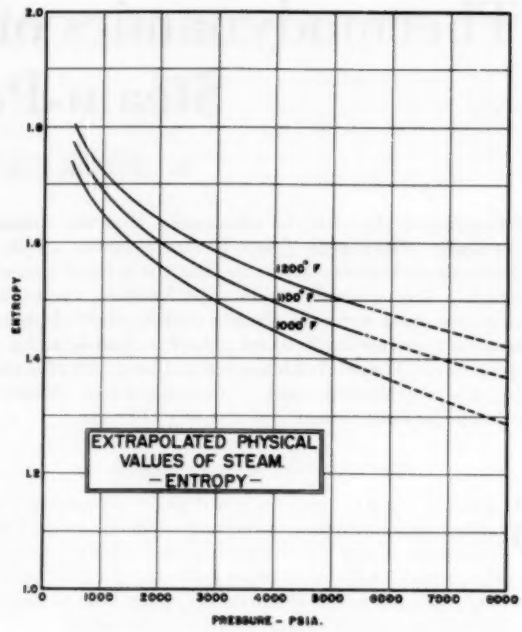

FIG. 3 EXTRAPOLATED PHYSICAL VALUES OF STEAM—ENTROPY

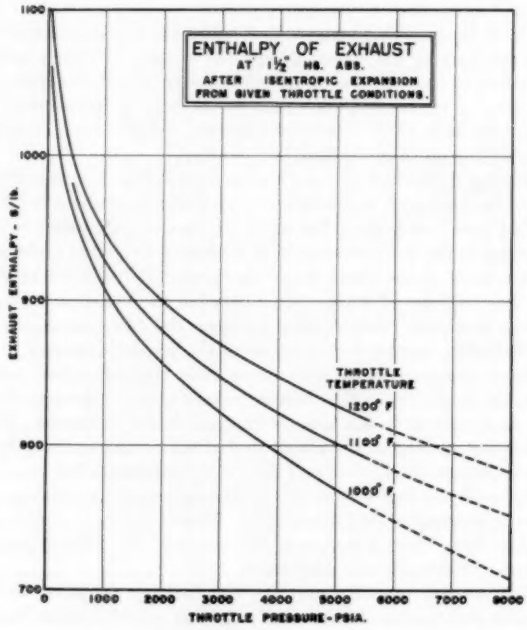

FIG. 4 EXTRAPOLATED PHYSICAL VALUES OF STEAM—ENTHALPY OF EXHAUST

consists of an ideal boiler followed by an ideal turbine, ideal condenser, and ideal feed pump. Throttle pressures cover the range of 0 to 8000 psia. Throughout the analysis, the condenser is assumed always to be at $1^1/_2$ in. Hg abs. Although the results can be presented as thermal efficiencies, we have adopted the cycle heat rate as the ordinate in Fig. 6, because the design engineer is more familiar with numerical values of heat rates than of thermal efficiencies.

Note that for any particular throttle temperature in Fig. 6,

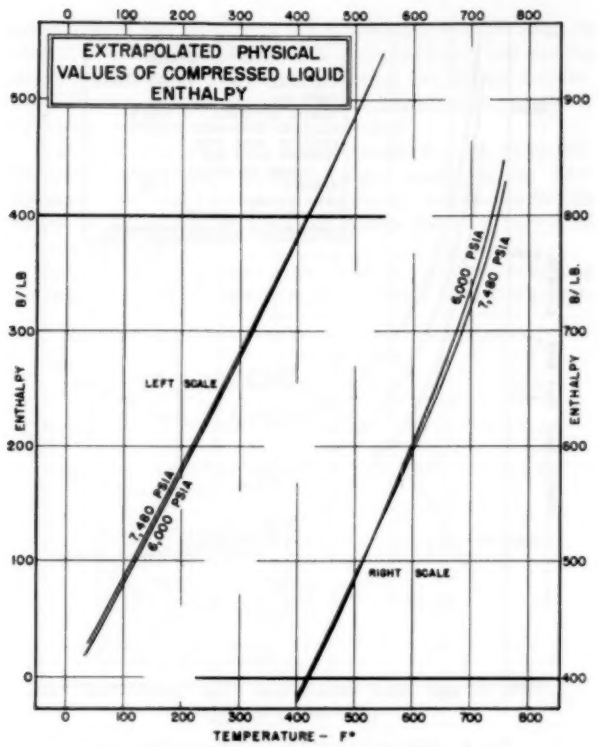

FIG. 5 EXTRAPOLATED PHYSICAL VALUES OF COMPRESSED LIQUID —ENTHALPY

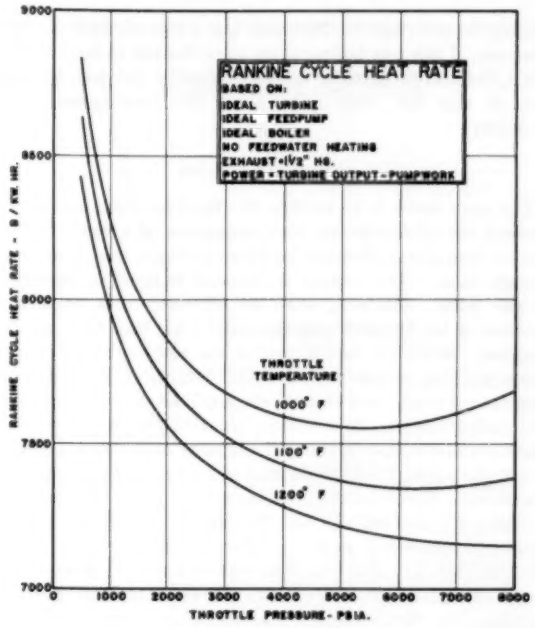

FIG. 6 RANKINE-CYCLE HEAT RATE

there is a definite throttle pressure which gives the lowest heat rate, or highest thermal efficiency. Also, the higher the throttle temperature, the higher will be the pressure at which maximum efficiency occurs. To find the reason why the results turn out this way, one must return to the sketches of constant-pressure lines on the temperature-entropy plane. The thermal efficiency of any Rankine cycle can be evaluated by substituting an equivalent Carnot cycle, i.e., a Carnot cycle accepting heat at a constant temperature equal to the average temperature at which the Rankine cycle receives heat, and rejecting heat at the same temperature that the Rankine cycle does. Fig. 7 first redraws the sketched processes of Fig. 1, and then adds two processes to complete the Rankine cycles, viz., a vertical isentropic expansion process through the turbine, followed by a horizontal line depicting constant-temperature heat rejection in the condenser.

Let the throttle temperature be limited to 1200 F, and compare the cycles formed from throttle pressures of 700 psia, 7000 psia, and 70,000 psia. Since the heat-rejection temperature of all three cycles is the same, then the thermal efficiency of each of the cycles is determined by the average ordinate of the heat-accepting process.

The reader is to act like a mental integrating machine, scan the areas of Fig. 7, and determine by inspection what these average ordinates are for the heat-addition process. Note that the 700-psia cycle is handicapped by the long plateau at 500 F or 960 R. Thus the average ordinate is just a little below the plateau, and is marked on the right side of the sketch.

The 7000-psia line has an average ordinate considerably higher than the 700-psia ordinate, and is approximately as shown on the sketch. The area for heat addition at 70,000 psia has a readily determined average ordinate located half way between initial and final temperature.

The reason why the 7000-psia average ordinate is higher than

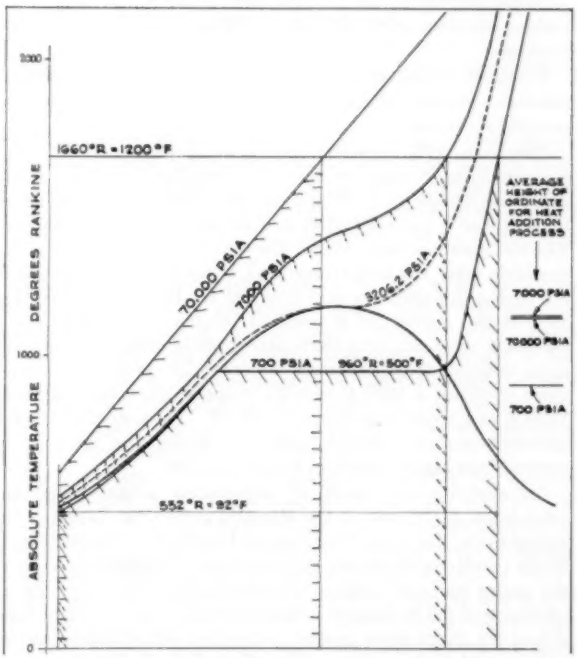

FIG. 7 SKETCH OF RANKINE CYCLES AND AVERAGE ORDINATE FOR HEAT-ADDITION PROCESS OF EACH CYCLE

the 70,000-psia average ordinate is that the 7000-psia pressure line has an upward bulge in its curve, whereas the 70,000-psia line is practically straight. Neglecting the effect of the feed pump, if the 7000-psia line were a straight line too, it would have the same average ordinate as the 70,000-psia line even though the slopes of the two lines were different. It is further noted that the closer a pressure line can "snuggle up" to the top limiting-temperature line of the cycle, the higher will be its average ordinate, and the higher will be its efficiency. Thus with a 1200 F

limiting temperature the 7000-psia line is located most favorably. However, if the top temperature were limited to only 500 F, or 960 R, the best pressure by far would now be 700 psia, for a good deal of this line runs right along the limiting-temperature boundary.

Nonideal Cycles

The next move is to modify the Rankine cycle to take into account the efficiencies of the components of a workable cycle. Let the feed-pump efficiency be taken as 75 per cent, a reasonable enough value. The turbine is assumed to have an efficiency of 86 per cent. Attaining such an efficiency with supercritical pressure at the throttle may represent a big task for the turbine designer. Since the first stages of the turbine handle a rather dense working substance, the radial heights of the nozzles and buckets are small, and turbine stage efficiency is proportional to this radial height. In addition, since turbine-wheel rotational losses are also proportional to the density of the steam, the head end of the machine will again tend to have somewhat poorer stage efficiencies. To counterbalance the effects at the head end of the machine, it is pointed out that the exhaust from cycles dealt with later in the analysis is much drier than conventional cycle exhaust. Thus the tail end of the machine can be expected to have better stage efficiencies than conventional turbines now have. In addition, the disadvantage of small radial height of the high-pressure nozzles and buckets can be overcome by going to units of larger output ratings. These are the bases for assuming a turbine efficiency of 86 per cent regardless of the throttle pressure studied.

It is further assumed that line losses cause a 10 per cent drop in pressure between the discharge nozzle of the feed pump and the throttle of the turbine.

This cycle with imperfect turbine and pump, and with a line pressure drop, is more realistic than the Rankine cycle, and is called the "simple cycle" by the author. Note that it is still based upon use of a perfect boiler, and it has no feedwater heating. The turbine-room heat rate for this cycle is based upon the power available after the feed-pump work is satisfied. The results of employing this cycle are shown in Fig. 8. It is again noted that each of the curves for a constant throttle temperature has a minimum heat rate at a particular throttle pressure. Also, the gains resulting from exceeding the critical pressure of steam are quite small for a 1000 F throttle temperature, become larger at 1100 F, and appear significant at 1200 F. Thus, as metallurgical advances permit higher-temperature levels, the gains to be derived from higher pressures become greater.

To evaluate the effect of introducing actual component efficiencies, the curves of the Rankine cycle, Fig. 7, and of the simple cycle, Fig. 8, are both repeated as Fig. 9. The inefficiency of the turbine in the simple cycle uniformly magnifies the value of the entire curve of turbine-room heat rates. However, the inefficiency of the feed pump increasingly penalizes the right-hand side of the curve since greater feed-pump contributions are involved at higher pressures. The effect of the feed pump, raising the right end of the curve for the simple cycle, is to shift the minimum points of the heat-rate curves to lower pressures.

In the remaining analysis, the necessary number of calculations can be reduced by restricting the throttle temperature to one value, 1200 F.

Now let one reheater be added to the simple cycle. The temperature of the steam returning from the reheater is assumed to be 1200 F, and the pressure drop in the reheat circuit is assumed to be 10 per cent. For one chosen value of throttle conditions, 6800 psia and 1200 F, a whole series of values is used in

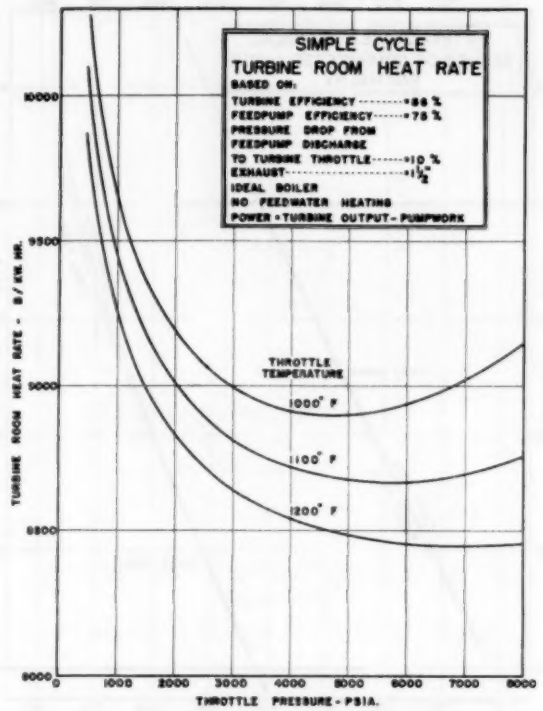

Fig. 8 Simple-Cycle Turbine-Room Heat Rate

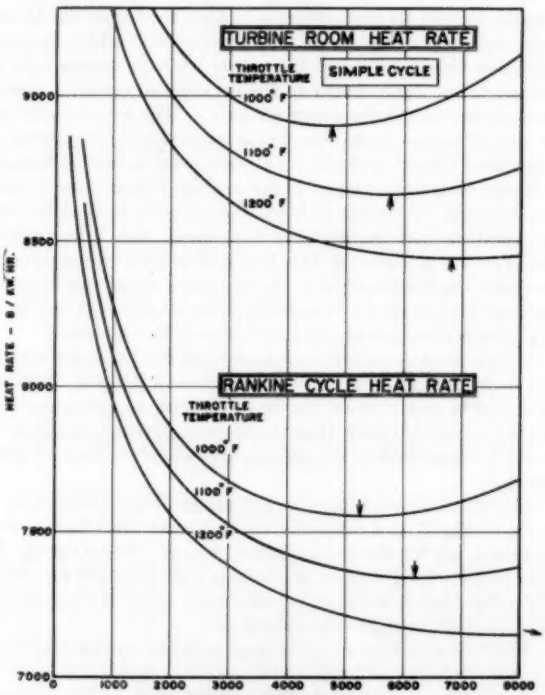

Fig. 9 Both Rankine-Cycle and Simple-Cycle Turbine-Room Heat Rates

succession for the pressure at the reheat-turbine inlet. Fig. 10 gives the resulting values for turbine-room heat rate, and also the moisture content in the exhaust leaving the reheat turbine. The best efficiency occurs with a reheat turbine-inlet pressure of 1100 psia, or 16 per cent of throttle pressure.

The initial throttle pressure is now changed to a new value, and the entire calculation to produce a curve similar to Fig. 10 is repeated. The final results appear in Fig. 11, and summarize the values at the maximum-efficiency points for the individual throttle pressures.

The analysis now turns to a cycle with two reheaters returning the temperature of the turbine-steam to 1200 F instead of a single

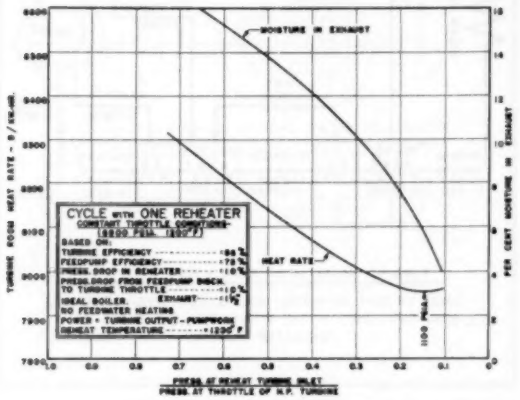

FIG. 10 CYCLE WITH ONE REHEATER—6800 PSIA THROTTLE
(Turbine-room heat rate and exhaust moisture versus ratio of reheat turbine-inlet pressure to throttle pressure.)

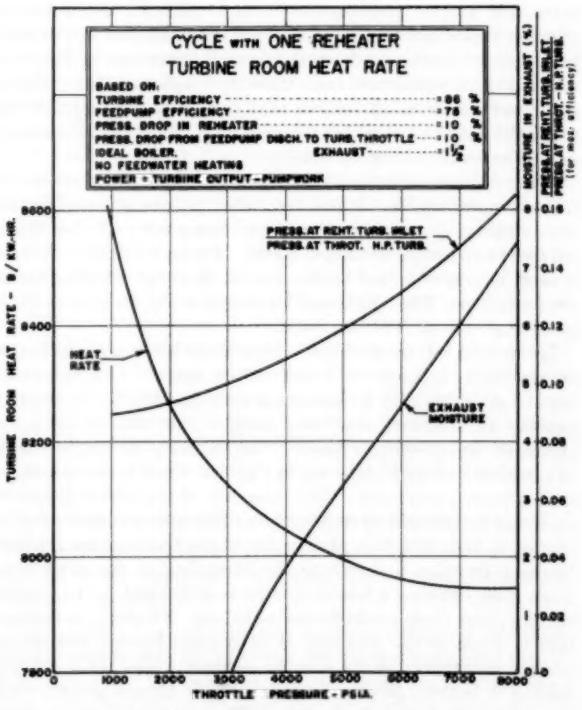

FIG. 11 CYCLE WITH ONE REHEATER
(Turbine-room heat rate, exhaust moisture, and optimum ratio of reheat turbine-inlet pressure to throttle pressure, all plotted versus throttle pressure.)

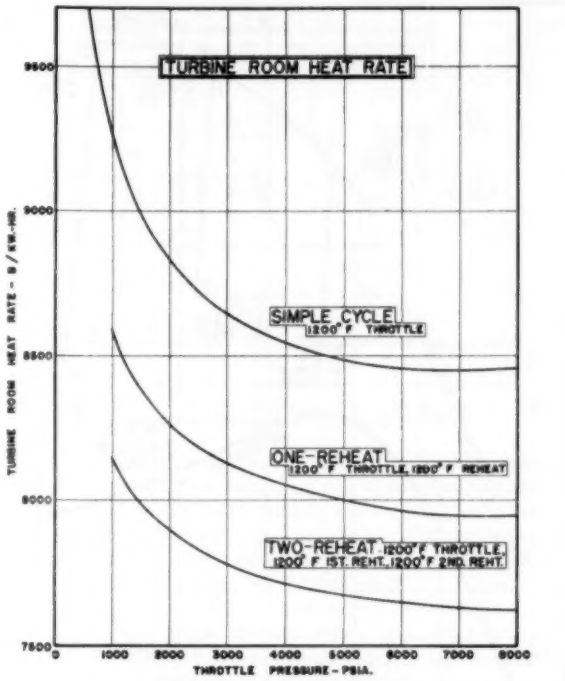

FIG. 12 TURBINE-ROOM HEAT RATES FOR SIMPLE CYCLE, FOR CYCLE WITH ONE REHEAT, AND FOR CYCLE WITH TWO REHEATS VERSUS THROTTLE PRESSURE

stage of turbine steam reheating. Fig. 12 shows that the incremental gains of the second reheater are not as large as those due to the first reheater, but they are still quite sizable. The bottom curve represents the maximum efficiency for each initial throttle pressure after surveying all combinations of pressures at the two reheat-turbine inlets.

The turbine-room heat-rate curve for the cycle with two reheaters does not hit a minimum point within the throttle-pressure range going up to 8000 psia. Since the curve shows extremely small cycle improvements at the upper end of the pressure range, the throttle pressure is arbitrarily dropped back to a chosen value of 6800 psia for the more complex cycle arrangements to follow. This pressure does happen to be the minimum point of the simple-cycle heat-rate curve for 1200 F.

The data obtained are now adequate to depict the turbine-expansion lines on a Mollier diagram for a cycle with two reheaters. The skeleton Mollier chart, Fig. 13, shows each of the three turbines sections with an efficiency of 86 per cent. Although the internal efficiency of the second reheat turbine is shown larger than that of the other two turbine sections, its assumed 15 Btu, leaving loss per lb of steam, re-establishes the 86 per cent value of efficiency. It is noted that the exhaust is far from being in the wet region, and has an enthalpy fully 72 Btu per lb above the saturation condition.

EXTRACTION CYCLES

To this cycle with two reheaters and the given steam conditions, shown on the Mollier diagram, there is now added one single stage of feedwater heating. The pressure drop between the turbine-extraction stage and the shell of the feedwater heater is taken as 10 per cent, and the heater terminal-temperature differences are fixed at 5 deg F at the feed exit, 10 deg F at the feed entrance, with drains cascading from drain cooler to the condenser.

At what extraction location is the cycle efficiency best? The

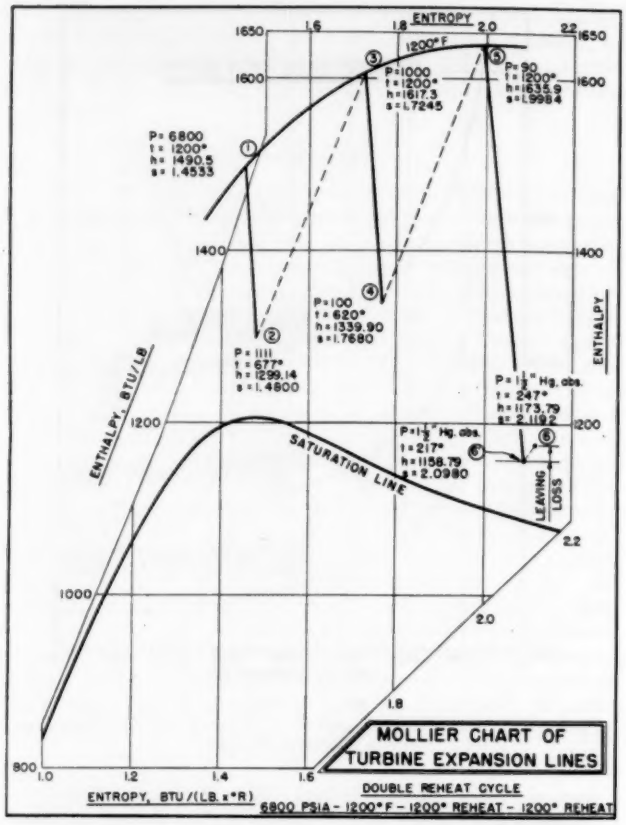

FIG. 13 MOLLIER CHART OF TURBINE-EXPANSION LINES FOR DOUBLE REHEAT CYCLE—6800 PSIA-1200 F-1200 F REHEAT-1200 F REHEAT

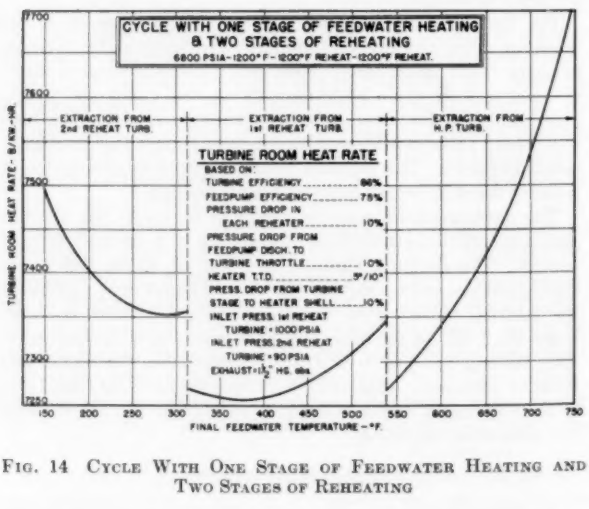

FIG. 14 CYCLE WITH ONE STAGE OF FEEDWATER HEATING AND TWO STAGES OF REHEATING

result of moving only the extraction point along the turbine-expansion line is shown in Fig. 14. The abscissa, final feed temperature, corresponds to the extraction location on the turbine with the higher feed temperatures coming from positions closer to the head end of the machine. The curve has sharp breaks occurring at the reheat points. An extraction taken close to the inlet of either of the two reheat turbines results in an extremely high

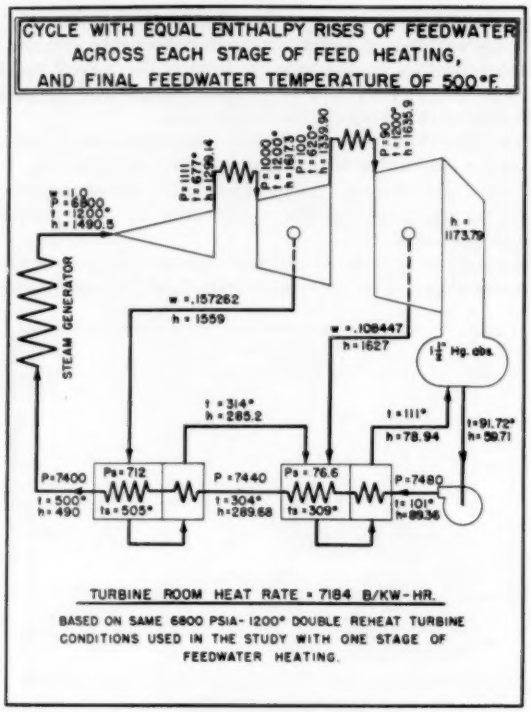

FIG. 15 HEAT-BALANCE DIAGRAM FOR CYCLE WITH TWO STAGES OF FEEDWATER HEATING AND TWO REHEATS

(Feedwater acquires equal enthalpy rises across each stage of feed heating and final feedwater temperature of 500 F.)

extraction steam temperature—close to 1200 F. Such hot extraction steam causes a large thermal irreversibility in the feed-heating process, and produces the upward distortions of the heat-rate curve for extraction from these two regions. The designer can generalize from this curve that extraction locations should avoid the head end of reheat turbines on thermodynamic grounds as well as for metallurgical reasons.

Some definite analytical techniques are required to proceed to more complex cycles. If two feedwater heaters are used in this same steam cycle, where shall the extraction points be? Let the final feed temperature be fixed at 500 F. First, an old rule of thumb is used, letting each feed heater provide an equal enthalpy rise to the feedwater. The resulting cycle shown in Fig. 15 has a turbine-room heat rate of 7184 Btu/kwhr.

Is this heat rate good or bad? Should the lower pressure heater be moved to a higher or lower turbine stage? Unfortunately, Fig. 15 does not help in answering such questions. In order to provide an adequate analytical insight, this same cycle is re-examined on an entropy basis. The method, extremely simple in actual execution, is depicted in Fig. 16. Each heater is treated as if it were a free body. The boundary of the heater system is extended so that the system includes the irreversibilities due to friction in the extraction piping, due to the temperature gradient for heat transfer, and due to the throttling of the drain trap. Each mass entering a heater system is multiplied by its specific entropy, and these products are added up. Similarly, a summation is made of the products of each mass leaving this heater system multiplied by its specific entropy. The total entropy leaving a system (after the processes) is always greater than the entropy entering the system. The net gain of the system's entropy is a direct index of the amount of imperfections involved in the processes.

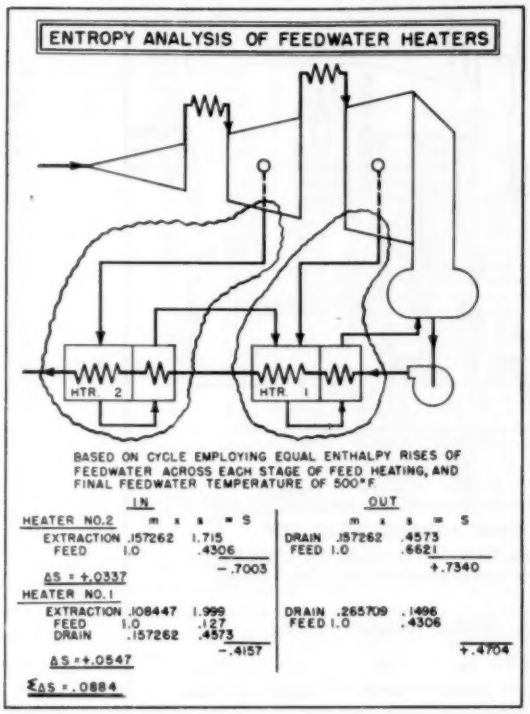

FIG. 16 ENTROPY ANALYSIS OF FEEDWATER HEATERS OF FIG. 15

The calculations listed in Fig. 16 show that the imperfection of heater No. 1 is much larger than that of heater No. 2. Now maximum efficiency for the cycle occurs when the imperfections of all heaters are approximately the same size.

In order to limit the analysis to handling one variable at a time, the final feed temperature had been stated as being fixed at 500 F, and this requirement prevents any change in the location of the extraction point for heater No. 2. However, the extraction point of heater No. 1 can be moved, and must be so changed that the imperfection of heater No. 1 becomes smaller. This is accomplished by making the feed-heating duty smaller on heater No. 1 by shifting its extraction point to a lower turbine stage. Simultaneously, such a move increases the duty on the top heater.

Let the extraction point of heater No. 1 arbitrarily be moved so that the rise in feedwater enthalpy across the heater is only 150 Btu instead of 200 Btu per lb. The calculations appear in Fig. 17. This arbitrary change in duty has overshot the mark, for the net change in entropy of heater No. 1 is now smaller than that of heater No. 2. However, the values of the net entropy changes are now much more nearly equal for heaters No. 1 and No. 2 than they had been when each heater supplied equal enthalpy rises. The result of this more equal distribution of heater imperfections is that the turbine-room heat rate is now 7160 Btu instead of 7184 Btu/kwhr.

Thus, there are two guides which aid in setting up a real cycle:

1 Avoid extraction near the top of reheat turbines.

2 Try to have approximately equal net entropy changes for all the feed heaters.

The analysis now moves along to consideration of the more complex cycle in Fig. 18, in which the turbine-room heat rate is 6825 Btu/kwhr. The steam-expansion lines of the previous two-heater cycle remain unchanged, but eight stages of feedwater heating are employed. In addition, the exhaust steam passes over a large finned heat exchanger in the neck of the condenser. Thus

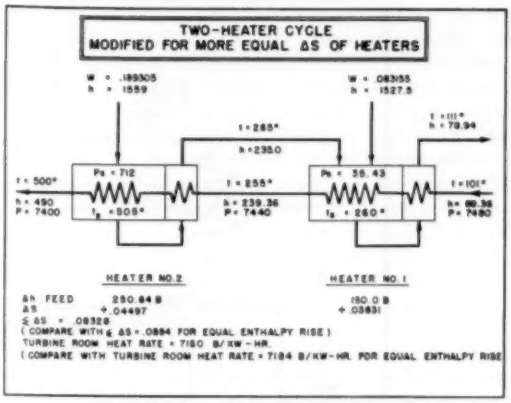

FIG. 17 TWO-HEATER CYCLE MODIFIED FOR MORE EQUAL NET ENTROPY CHANGES OF HEATERS

the condenser steam trunk in effect becomes a condenser desuperheating zone to reclaim some fraction of the 72 Btu/lb of exhaust superheat present in the steam leaving the turbine. The first feedwater heating is done by picking up 50 Btu/lb of condensate in this condenser desuperheating zone, thereby reducing the exhaust enthalpy by about 58 Btu/lb of exhaust.

Since the exhaust heat exchanger is a device commonly employed in gas-turbine cycles, it would appear appropriate to use the nomenclature of that field to evaluate this new exhaust heat exchanger in the condenser neck. Accordingly, regenerator effectiveness is defined as the actual heat energy transferred from the exhaust, divided by the ideal or maximum possible heat transfer therefrom. The condenser desuperheater in this cycle is assumed to transfer about 58 out of a possible 72 Btu/lb of exhaust. This performance amounts to a regenerator effectiveness of 80 per cent, which would be near the upper values of effectiveness now used in the gas-turbine field wherein pressure-drop penalties are extremely severe. No evaluation of the physical equipment required for desuperheating has been undertaken to date.

In the tabulation of data at the bottom of Fig. 18, the terminal temperature difference is listed in fractional form, with the numerator referring to the feed-exit end of the heater, and the denominator signifying the feed-entrance or drain-cooler end of the heater. A negative terminal temperature difference indicates that the feed leaves at a temperature above the saturation temperature of the extraction steam in the heater shell.

This cycle shown in Fig. 18 is presented as a starting point from which one could work toward crystallization of final design. The techniques developed earlier in the paper are now applied. In particular, the net-entropy changes listed in the tabulation should be more uniform in size for all heaters, and the following moves are indicated:

(*a*) Increase the duty on heater No. 1.

(*b*) Let heater No. 2 extraction point remain unchanged, for its duty will decrease as heater No. 1 carries the water to a higher temperature leaving heater No. 1.

(*c*) Move heater No. 3 extraction point down a stage lower in the turbine, thereby decreasing the irreversibility of heater No. 3 and increasing that of heater No. 4.

(*d*) Since heater No. 4 is conveniently located at the crossover point before the second reheater, it may be left unchanged.

(*e*) Extraction for heaters Nos. 6 and 7 may each be moved down somewhat.

(*f*) The most apparent fault in the cycle, as presented, is the very small entropy increase of the top heater, indicating that the final feedwater temperature should be made higher than it is.

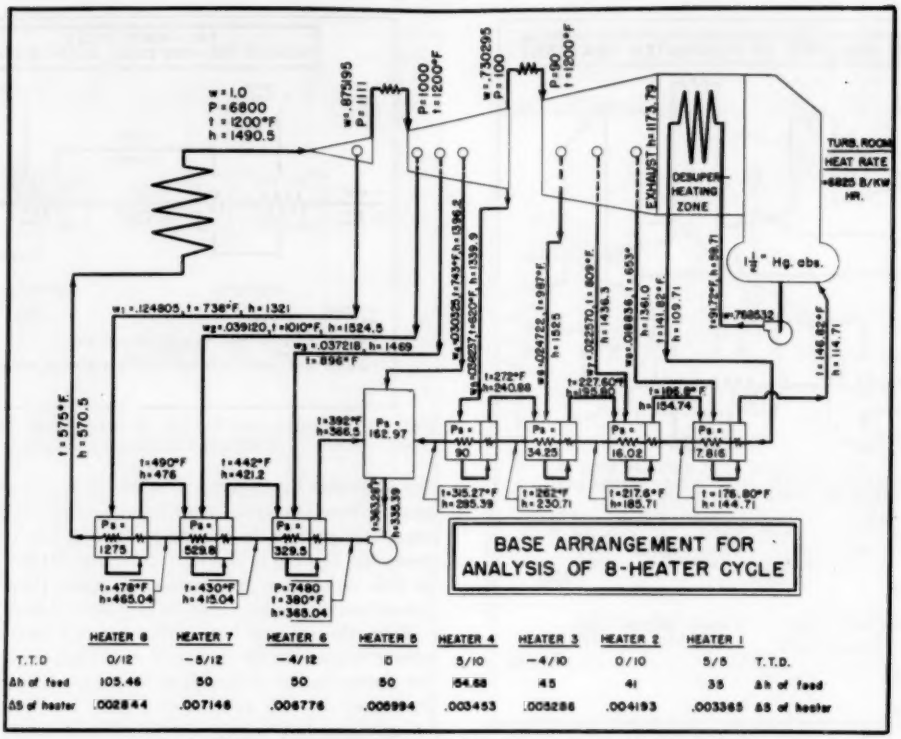

FIG. 18 BASE ARRANGEMENT FOR ANALYSIS OF EIGHT-HEATER CYCLE

Step (*f*) will be developed a little further because of its importance. Let the whole cycle be frozen as shown on the diagram, and change only the location of the top heater while observing the resulting change in turbine-room heat rate. It may be difficult to guess ahead as to what final feed temperature will give the greatest efficiency. Unfortunately, the old rule cannot be used that the best temperature rise is approximately $n/(n+1)$ fraction of the difference between condenser saturation temperature and steam-drum saturation temperature, for there is no steam-drum saturation temperature. By computation, the peak efficiency occurs, as shown in Fig. 19, when the final feed temperature is 610 F.

Several additional variations in the cycle arrangement have been worked out. For example, a change in 5 deg F in the terminal temperature difference at the feed-exit end of the top heater modifies the turbine-room heat rate by 3.2 Btu/kwhr. When the drain cooler on the lowest heater is eliminated, and the drains pumped ahead, there is an improvement of 1.0 Btu/kwhr. These changes are small compared to the result of eliminating the desuperheating zone in the condenser inlet. Omitting the exhaust desuperheater hurts the turbine-room heat rate to the extent of 46.6 Btu/kwhr.

Another interesting cycle modification was the use of a liquid-sodium reheat circuit to transfer heat from boiler gases to the two steam reheaters located adjacent to the turbines.[4] The turbine-room heat rate was improved fully 1 per cent as a result of reducing the reheat-circuit-steam pressure drops from 10 to 2 per cent.

There is no extensive experience concerning the behavior of the working substance in the immediate neighborhood of the critical pressure or the operation of equipment at these pressures. Thus designers would tend to set up a band of pressures which they would try to avoid. This pressure band would extend for several

[4] "Design and Economic Evaluation of Liquid Sodium Reheaters in Supercritical Pressure Steam Power Cycles," by I. Gabel, Master's thesis, Polytechnic Institute of Brooklyn, N. Y., June, 1954.

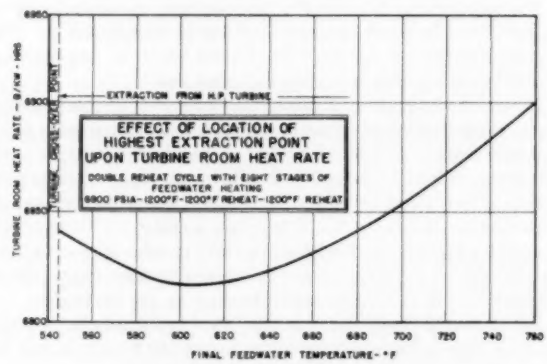

FIG. 19 EFFECT OF LOCATION OF HIGHEST EXTRACTION POINT UPON TURBINE-ROOM HEAT RATE

hundred pounds per square inch on either side of the critical pressure. If a plant operates in the supercritical-pressure region, the pressure should be high enough so that sudden load changes would not produce subcritical pressures and undesired bubble formation. With this thought in mind, Table 1 was constructed covering various cycle arrangements for three throttle pressures. The first pressure, 2600 psia, represents the approximate upper limit of subcritical-pressure operation. The second pressure, 4000 psia, would be about the lower limit of design for supercritical-pressure operation. The third pressure represents the point for maximum efficiency for the given turbine-inlet temperatures, namely, 5800 psia for 1100 F, and 6800 psia for 1200 F.

Throughout this paper, the turbine-room heat rate serves as a measuring stick of cycle performance because it is immune to the effects of using various fuels, boiler efficiencies, and auxiliary power requirements beyond that of the feed pump. It is interest-

TABLE 1 TURBINE-ROOM HEAT RATES FOR SUPERCRITICAL-PRESSURE-CYCLE ARRANGEMENTS

Cycle temp, deg F	No. of steam reheaters	No. of stages feedwater heating	Throttle pressure, psia	Turbine-room heat rate, btu/kwhr	Remarks
1200	2	8	2600	...	Exhaust too hot
1200	2	8	4000	6930	Exhaust desup'r used
1200	2	8	6800	6818	Exhaust desup'r used
1200	2	6	2600	...	Exhaust too hot
1200	2	6	4000	6940	Exhaust desup'r used
1200	2	6	6800	6829	Exhaust desup'r used
1200	1	8	2600	7348	Exhaust desup'r not req'd
1200	1	8	4000	7117	Exhaust desup'r not req'd
1200	1	8	6800	6922	Exhaust desup'r not req'd
1200	1	6	2600	7367	Exhaust desup'r not req'd
1200	1	6	4000	7150	Exhaust desup'r not req'd
1200	1	6	6800	6961	Exhaust desup'r not req'd
1100	2	8	2600	7307	Exhaust desup'r used
1100	2	8	4000	7127	Exhaust desup'r used
1100	2	8	5800	7057	Exhaust desup'r used
1100	2	6	2600	7319	Exhaust desup'r used
1100	2	6	4000	7163	Exhaust desup'r used
1100	2	6	5800	7079	Exhaust desup'r used
1100	1	8	2600	7508	Exhaust desup'r not req'd
1100	1	8	4000	7293	Exhaust desup'r not req'd
1100	1	8	5800	7186	Exhaust desup'r not req'd
1100	1	6	2600	7531	Exhaust desup'r not req'd
1100	1	6	4000	7326	Exhaust desup'r not req'd
1100	1	6	5800	7217	Exhaust desup'r not req'd

NOTE: The regenerative effectiveness of the exhaust desuperheaters, if used, is assumed to be 80.25 per cent.

ing, nevertheless, to follow the calculation down to the net station heat rate for a hypothetical installation. Let us take the best case listed in Table 1, a turbine-room heat rate of 6818 Btu/kwhr for throttle conditions of 6800 psia, 1200 F, with two steam reheats back to 1200 F, eight stages of feedwater heating, and an exhaust pressure of $1^1/_2$ in. Hg abs. The turbine-room heat rate is first increased by an assumed 2 per cent to account for fixed-turbine losses and generator-electrical losses. Then an assumed boiler efficiency of 89 per cent is taken for the case of the pulverized-coal plant. Lastly, the auxiliary power beyond that required for feed pumps is assumed to be $4^1/_4$ per cent. Then the cycle would have

$$\text{Net station heat rate} = \frac{6818 \times 1.02}{0.89 \times 0.9575} = 8160 \text{ Btu/kwhr}$$

This value is a reduction of 12 per cent below the reported 9300 Btu/kwhr rate representing the best present-day plant.

SUMMARY

This paper attempts to stake out the boundaries and to survey the level of efficiencies attainable in the area of supercritical-pressure plant design.

The paper points out the basic thermodynamic advantage of using H_2O at supercritical pressures in cycles which use high throttle temperatures.

Turbine-room heat rates of the Rankine cycle and the simple cycle are determined for throttle temperatures of 1000, 1100, and 1200 F over a range of throttle pressures of 0 to 8000 psia.

For a constant turbine-inlet temperature of 1200 F, the effects of adding one reheater and two reheaters are measured over a throttle-pressure range of 0 to 8000 psia with nonextraction operation.

The location of extraction points for feed heating is discussed, and a particular cycle is analyzed.

A tabulation of cycle performance is provided for designs encompassing various throttle pressures, temperatures, number of steam reheats, and number of stages of feedwater heating.

Appendix

The thermodynamics of power cycles, including supercritical-pressure cycles, is handled very satisfactorily by the macroscopic approach of measuring physical properties. Such an approach is entirely immune to the arrival or departure of various theories involving the atomic or molecular structure of the working substance. However, the working substance of the supercritical-pressure cycle undergoes changes which demand an explanation.

The microscopic point of view has been very helpful in predicting phenomena before they are measured, and in providing an insight concerning the behavior of the working substance. The kinetic theory provides a good model for the visualization of gases. Similarly, the solids are conceived as crystals in which the atoms are arranged in orderly space lattices. But what is the model for a liquid, and especially, what is the model for the monophase region above the critical pressure? The following few paragraphs lean heavily for answers upon the physicists' works listed.[5, 6]

With the melting of a solid to the liquid state, the orderly lattice formation of the solid is replaced by a relatively compact mass with a volume for most liquids but slightly (about 10 per cent) larger than that of the corresponding crystals. Water is an exception, and will be mentioned later. This liquid mass is permeated by interstices or fissures which appear and disappear, fluctuating throughout the mass. Increasing the temperature at constant pressure increases the number of fissures, thereby increasing the specific volume. The increasing temperature also increases the rate of fluctuation of the fissures.

At higher temperatures along a constant-pressure process, the continuum of liquid lattice structure interspersed by fluctuating fissures gives way to an arrangement characterized by groups or clusters of tens of molecules. The number of molecules in any particular group keeps fluctuating with time. Within a cluster, the molecules are held together in an orderly latticelike arrangement by strong potential binding forces of short-time duration. The clusters themselves may undergo relative rotations, thus giving rise to the characteristic of a liquid, namely, local orderly arrangement of molecules coupled with distant disorder and disarrangement.

In the case of water and ice, it is believed that each has a different lattice structure. The structure of ice is similar to that of tridimyte. Liquid water directly above the melting point has the more compact lattice structure resembling quartz. Thus, even though the observed density of water is greater than that of ice, there is still room for fissures to appear in the more compact lattice structure of liquid water. Everyday liquid water has the chemical formula $(H_2O)_x$ wherein x fluctuates as the fissures and cluster size keep changing.

Liquids may be subjected to an increase in pressure at constant temperature and undergo a slight reduction in volume. There are two aspects to this compressibility of liquids, the first being a geometrical aspect, and the second, structural. The geometrical consideration involves the simultaneous contraction of all intermolecular distances under the influence of the external pressure. The second aspect of the compressibility in liquids is the structural rearrangements involving an increased degree of regularity of molecules, and consequently increased compactness. It is interesting that the magnitude of each aspect can be measured by the use of high-frequency ultrasonic vibrations.

Evaporation consists of a surface molecule in a liquid cluster, acquiring adequate thermal energy to overcome the potential binding forces of its neighbors and to break away clear of the

[5] "Kinetic Theory of Liquids," by J. Frenkel, Clarendon Press, Oxford, England, 1946.

[6] "A General Kinetic Theory of Liquids," by Max Born and H. S. Green, Proceedings of the Royal Society of London, England, series A:

I—"Molecular Distribution Functions," vol. 188, 1947, p. 10.
II—"Equilibrium Properties," vol. 189, 1947, p. 103.
III—"Dynamical Properties," vol. 190, 1947, p. 455.
IV—"Quantum Mechanics of Fluids," vol. 191, 1947, p. 166.

cluster. The binding forces between the surface molecule and molecules well below the surface need not be considered, only the forces of adjacent neighbors, for potential forces drop off extremely rapidly with increasing distance. High pressures require higher thermal energy, and therefore higher temperature, for the surface molecule to break free of the cluster. At supercritical pressures, the potential forces no longer can be overcome by the thermal energy, and no molecules escape free of the clusters. The author proposes, however, that as the supercritical-pressure fluid undergoes a temperature rise, the average size of its clusters diminishes. At still higher temperatures, the clusters are reduced down to isolated molecules, and all traces of crystalline structure have disappeared. Thus the author suggests that the supercritical-pressure fluid acquires its steamlike qualities not by evaporation of isolated surface molecules, but rather by the gradual diminution in the size of the clusters.

An Introduction to the Thermal Problems of Turbojet Engines for Supersonic Propulsion

By A. J. GARDNER,[1] DAYTON, OHIO

An introductory summary of what temperature ranges are to be expected in planning the design of turbojet engines for use at supersonic flight speeds, and the effect of the expected temperatures on various basic engine components. The source and magnitude of the heat is first considered. The general effects of the high temperatures on engine materials, compressor performance, and energy, added in the form of fuel, are outlined. General requirements and possible design considerations for supersonic turbojets are summarized briefly.

Introduction

THE past decade has produced momentous advances in aeronautics. Piloted research aircraft have flown at more than twice the speed of sound. Tactical aircraft capable of supersonic speeds in level flight are coming off production lines in increasing numbers. With the breaching of the so-called sonic barrier, the rush for higher and higher supersonic speeds has begun in earnest. The initial advances into the supersonic-speed regime brought no appreciable change in the problems of engine design and construction from current practices. However, military aviation is one of the world's most competitive enterprises and the goals must constantly be raised to new and higher limits if U. S. air power is to maintain world leadership. Therefore we are moving into a new phase of supersonic flight where greater speeds and longer durations than those heretofore encountered must be made possible.

With this new phase, come old problems that are now of serious proportions and new problems which challenge the ingenuity of the many types of engineers who have a hand in the design, production, and use of aircraft engines. These problems might be grouped roughly under the headings of theoretical design considerations, engine performance, and mechanical considerations.

Problems of the Thermal Barrier

One serious, compelling, and vital problem transcends the limits of each of these groups and bids fair to be the most serious obstacle encountered to date if we are to have aviation power plants in the supersonic era comparable to present subsonic-era engines. That problem is the thermal barrier. Barrier is a misnomer. This is no specific point in the speed spectrum such as Mach 1 in the case of the sonic barrier. It is a barricade of infinite depth and the solution of its problems will merely push back the problem temporarily. *Time* magazine once expressed it as "through the sonic wall into the thermal thicket." This is an apt description for as speeds increase the problem is present again in greater proportions. There is no diminishing point. So long as flight of the vehicle is confined to the earth's atmosphere more speed results in more heat.

This paper will attempt to clarify briefly the supersonic-speed problem and discuss in simple terms its effect on the primary power plant. The discussion will be confined to turbojet engines although with proper modification for the unique circumstances concerned, the data can be applied to other forms of air-breathing propulsion systems. We may assume that, at present, man-carrying and some unmanned supersonic vehicles will be turbojet-powered for reasons of state of development, economy, and missions to be performed. The information presented is completely general and in no way can be construed to represent a specific aircraft or engine or to be indicative of the scope and limits of present-day investigations of the U. S. Air Force. The thermal problem is not one peculiar to a given aircraft or engine but varies with the particular equipment considered. Dealing with it reminds one of the fact that "alligators are considered less vicious than crocodiles and have shorter jaws. However, if the question ever came up, it would probably be at a time when you wouldn't have a tape measure along." Excessive heat is a serious thing and the danger lies in the excess more than the heat.

Supersonic Propulsion

In dealing with the results of supersonic propulsion, it is important to understand the relationships between propelling force, or thrust, and the resistance the thrust must overcome and exceed, or drag. In addition, an altitude-speed relationship arises as a result of the dynamic pressures which can be encountered, necessitating special consideration for structural requirements. A typical manner to present the relationship between thrust and drag for a given airplane-engine combination at a fixed altitude is to plot Mach number versus thrust required for the airplane and thrust available from the engine.

Fig. 1 is a typical plot of such information. Note that the slope of the thrust-required curve changes sharply through the transonic speed range from about 0.9 to 1.1 Mach number and

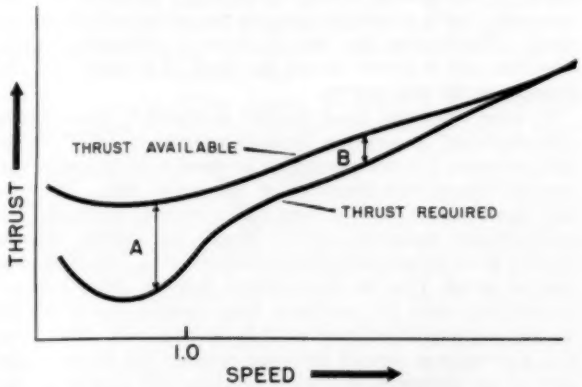

Fig. 1 Typical Thrust-Available Thrust-Required Curve for Supersonic Aircraft

[1] Major, USAF, Power Plant Laboratory, Wright Air Development Center, Air Research and Development Command, Wright-Patterson Air Force Base.

Contributed by the Aviation Division and presented at a joint session of the Aviation Division, American Rocket Society, and The Society of Automotive Engineers, at the Annual Meeting, New York, N. Y., November 28–December 3, 1954, of The American Society of Mechanical Engineers.

Note: Statements and opinions advanced in papers are to be understood as individual expressions of their authors and not those of the Society. Manuscript received at ASME Headquarters, September 28, 1954. Paper No. 54—A-155.

then increases at a lesser rate as supersonic speeds are established. The vertical distance between the curves at a given Mach number is indicative of the excess power available for acceleration, climb, and maneuver. At point A, during subsonic flight, a considerable amount of excess power is available. However, in supersonic flight, the characteristic shape of the curves is such that at point B not only is rapid acceleration impossible, but fuel supply may be exhausted before the required acceleration is completed owing to the small thrust versus drag differential. The theoretically possible high speed at the intersection of the curves may never be reached for this reason. It is readily seen that in regions where the curves run very close together, small thrust variations may cause the airplane to operate momentarily at available thrust less than required thrust.

High-Altitude Considerations

Aircraft structures of any type must be constructed in terms of the dynamic pressures, $q = 1/2\rho V^2$, and resulting loads that it can withstand. The engine likewise must be constructed in terms of the maximum dynamic and static pressures to be resisted. For these reasons one can readily see, by referring to Fig. 2, that in order to achieve a suitable combination of high strength

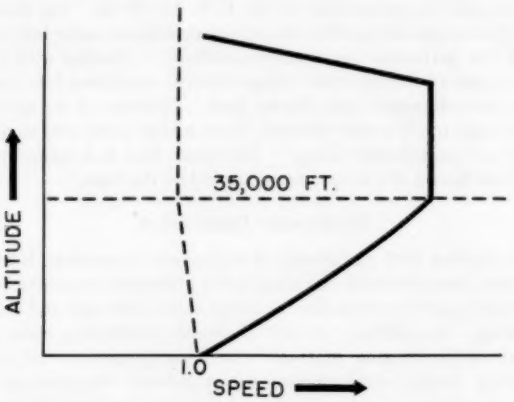

Fig. 2 Altitude-Speed Envelope for Supersonic Aircraft

and light weight (in addition to reasons of fuel economy), speeds appreciably above Mach number 1 will be above 35,000 ft. Referring to the curve, we will assume that the aircraft is capable of Mach number 1 at sea level. From sea level to 35,000 ft, the fall-off of atmospheric density allows higher speeds as altitude increases; that is, a constant q may be maintained with increasing speed. This limiting line may be either an air-frame or engine limitation and is almost always the result of dynamic or static pressure, as the case may be.

At some maximum Mach number at 35,000 ft, above which "standard-day" temperature becomes constant at —67 F as altitude increases, it is not uncommon for speed to be limited by the ram-rise temperature limitation of the engine inlet. The vertical line from 35,000 ft to some higher altitude represents this engine-limited supersonic speed. Finally, an altitude point is reached where the airplane-drag increase resulting from increasing angle of attack, plus the engine-thrust decrease due to increasing altitude, cause the maximum Mach number line to fall off sharply and very little further altitude can be gained. This curve then represents an aircraft operating envelope and indicates that most of our discussion of thermal problems will involve an ambient temperature of about —67 F and very low air densities at 35,000 ft and higher.

Magnitude and Source of Heat

Let us now examine the magnitude and source of the heat that causes the thermal problem. What causes the heat? In the engine the heat comes from the deceleration to rest of the onrushing air, from friction forces, from compression work, and from the burning of fuel. Fig. 3 is a plot of temperature attainable in sustained flight in the atmosphere above 35,000 ft and is plotted on the basis of isentropic stagnation of the onrushing air. Note that aluminum, steel, and titanium, our most common jet-engine materials, actually melt at less than Mach number 8. Realizing that the material exceeds its usefulness at low creep values which occur at temperatures far less than the melting temperatures, it is readily seen that easily attainable temperatures very rapidly cause difficulty. It is also startling to note that at Mach number 10 a diamond will vaporize. The vicious and increasing complexities of the thermal problem are readily apparent on the basis of the metal-melt comparisons and the shape of the curve. Each additional increment of speed results in higher temperatures and greater quantities of heat with which to cope.

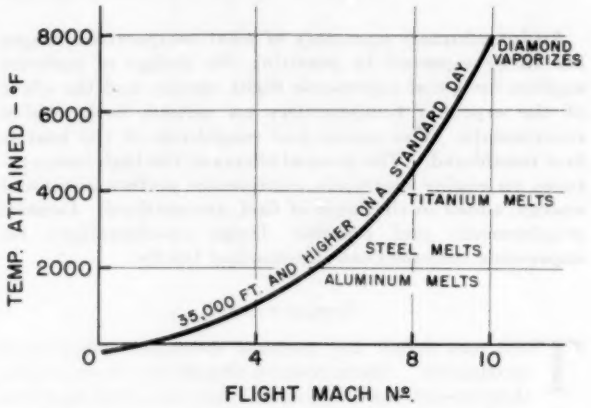

Fig. 3 Temperatures Attainable in Sustained Flight

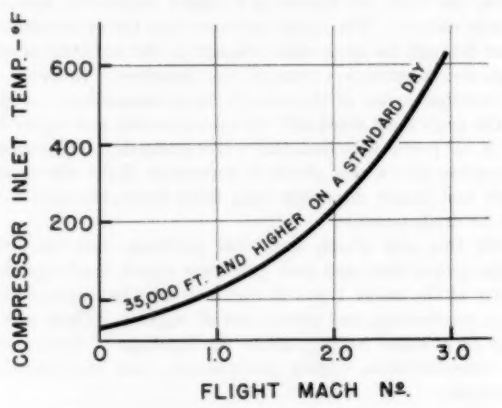

Fig. 4 Temperatures Attainable in Sustained Flight

Now let us reduce this heat rise to values easily attained today, and, in fact, to speeds generally already attained in research aircraft. Fig. 4 is in effect a blowup of the lower-speed portion of the previous figure and is a curve of temperatures which might be felt by portions of the turbojet compressor inlet which bring the incoming air to rest and represent the total temperature of the incoming air at any point in the intake. Immediately, the problem

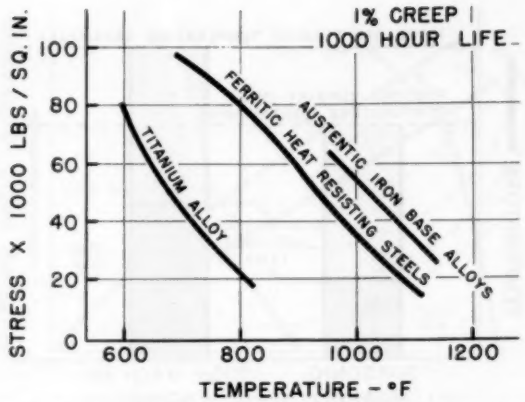

FIG. 5 CHARACTERISTIC RELATIONSHIP BETWEEN TEMPERATURE AND STRESS FOR 0.1 PER CENT CREEP IN 1000 HR

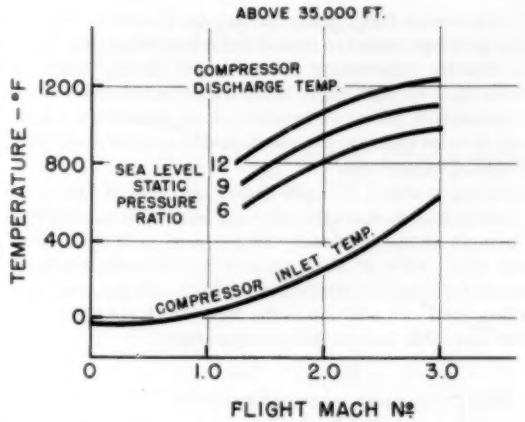

FIG. 6 TYPICAL INLET COMPRESSOR-DISCHARGE TEMPERATURES VERSUS FLIGHT MACH NUMBER

of materials to resist such temperatures comes to mind. It will be sufficient to note here that the heat rise is rapid, resulting in deterioration of the metal properties and creep which is a slow-rate permanent deformation of the structure. The nonuniform temperature distribution resulting from the rapid heating causes severe thermal stresses leading to buckling and reduced stiffness.

As an example of the deleterious effects of temperature increase alone, let us look at Fig. 5. Maximum stress for 0.1 per cent creep in 1000 hr is plotted against temperature. For the purposes of illustration the materials and values are unimportant at this time. The slopes of the curves are the points of interest for the purpose of this illustration. Note that a 100-deg F temperature increase drastically reduces the stress limit of the material. We already have seen that such a temperature increase will result from approximately $^1/_2$ of a Mach number in increased speed. This rapid fall-off of strength with temperature rise is typical of the various strengths considered in the choice of engine metals and vividly points out one of the designer's foremost problems in overcoming heat effects.

Temperature Rise Through Compressor

Having taken air on board the engine, it must now be compressed and this is where the temperature problem becomes acute. Fig. 6 is a plot of temperature rise through the compressor at various flight Mach numbers for compressors of several sea-level static design pressure ratios operating above 35,000 ft on a hot day, a hot day being our worst operating condition. For reference purposes the plot of standard-day inlet temperatures discussed earlier is reproduced as the lower curve. The sizable increase in temperature of the air as it passes from the inlet-compressor stages to the final stages is clearly evident and, as one would naturally expect, the rise is greater for the higher-pressure-ratio machine.

The plotted data take into account the decrease in effective compressor-pressure ratio due to aerodynamic heating at the inlet and are therefore accurately representative of actual temperatures which may be expected to be felt by the blades in the aft-compressor stages. For instance, a sea-level static 9:1 compressor operating at a flight speed of Mach number 1 above 35,000 ft will receive inlet air with a total temperature of about 60 F and discharge the air with a total temperature of about 500 F. These temperatures represent no problem in terms of today's designs. However, the same engine operating at Mach number 2.8 receives air at about 650 F and discharges it at about 1100 F. These discharge temperatures represent a very definite problem.

Considering the effect of temperature rise on metal strengths, previously discussed, it is obvious that a much more limited choice of materials is available and that the vibratory stresses caused by blade-flutter problems are more likely to complicate further the design problem. Considering that a high-performance compressor may have a thousand blades exclusive of stators and that the failure of one blade can completely wreck the engine and possibly destroy the airplane and crew, it will be appreciated that in high-temperature conditions the compressor appears as an old problem which has become more critical and difficult of solution. In addition, in spite of thermal expansions and creep, the designer must provide for the small clearances between blade tips and the casing which make for high-compressor efficiency. A further problem arises where temperatures and pressures are at a peak in providing satisfactory seals to prevent hot-air leakage to the interior of the engine. Therefore, for various reasons, the increase of problem areas in future compressor designs cannot be overemphasized.

Turbine a Critical Component

If we were arbitrarily to define some turbine-engine component as the most critical with respect to temperature, in all likelihood, it would be the turbine. In turbojets the principal function of the turbine is to produce sufficient shaft horsepower to drive the compressor. The maximum operating temperature which the turbine can withstand automatically acts as a limit to the amount of energy in the form of fuel which can be added to the gas stream upstream of the turbine. In an engine with a fixed maximum turbine-inlet temperature, as the compressor-discharge temperature increases, the allowable addition of fuel per pound of air must decrease.

Fig. 7 is a plot of fuel burned per pound of air versus flight Mach number for two turbine-inlet temperatures for an engine having a sea-level static compressor-pressure ratio of 12, operating above 35,000 ft. As the flight Mach number increases, the energy addition per pound of air diminishes rapidly. A point finally would be reached where the allowable energy addition is sufficient only to compensate for the losses in the compressor and turbine, resulting in zero thrust from the engine. If by some means the engine continued to move through the air, any increase in speed while turbine-inlet temperature remained constant would result in insufficient power to run the compressor and the compressor would begin to act as a turbine, extracting energy from the gas stream instead of adding energy to it.

Actually for what it is worth, one might plot compressor-pres-

sure ratio versus flight Mach number for a series of compressor-discharge temperatures to establish the line of limiting heat addition, thereby establishing pressure-ratio limits. Such a plot discloses that for high flight Mach numbers, relatively low compressor-pressure ratios are required if an appreciable amount of energy is to be added to the gas stream in spite of restrictive turbine-inlet temperatures.

Referring to Fig. 7, it can be determined that at Mach number 1 a turbine-inlet temperature increase from 1600 to 1800 F allows an increase of approximately 22 per cent in fuel addition per pound of air, while at Mach number 2.5, the same 200-deg F increase in turbine-inlet temperature allows a 44 per cent increase, pointing out a new addition to the facts which spur the quest for higher allowable turbine-inlet temperatures.

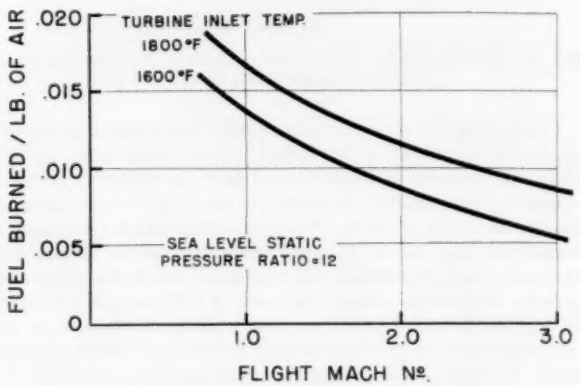

Fig. 7 Typical Fuel Burned Per Pound of Air Versus Flight Mach Number for Two Maximum Turbine-Inlet Temperatures

This same fact is illustrated in a schematic and qualitative fashion in Fig. 8. The vertical axis can be considered as temperature, enthalpy, or energy added per pound of air, whichever makes the point clear. For simplicity it is regarded here as temperature. In the case of the engine designed for relatively low speeds the difference between compressor-discharge temperature and turbine-inlet temperature allows sufficient differential to add enough fuel to provide compressor power and a significant amount of useful thrust for propulsion. It is important to note that as much as two thirds and more of the energy represented by the temperature differential is required to power the compressor.

Now consider the high Mach number engine operating at the same turbine-inlet temperature but the much higher compressor-discharge temperature. The differential, representing energy available for the compressor and thrust, has been considerably reduced. Power requirements, to make up compressor and turbine losses although probably reduced, will still consume a major portion of the available energy and can conceivably be of such magnitude as to allow no energy for thrust requirements, as previously mentioned. Therefore, excluding the use of afterburners and other thrust-augmentation devices, it is readily seen that to provide the same compressor-discharge turbine-inlet temperature differential as was provided by the low-speed engine, increased emphasis must be applied to allowing higher maximum turbine-inlet temperatures.

As in the case of the compressor the designer is again faced with creep and rupture-stress limitations, sealing problems, and fabrication difficulties. The turbine problem is one that was born with the turbine engine but whose magnitude increases tremendously as the thermal barrier is assaulted.

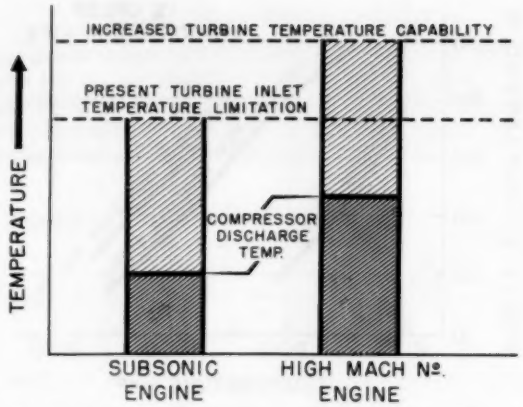

Fig. 8 Diagrammatic Representation of Energy Which Can Be Added to Turbojet-Engine Air Stream as Flight Mach Number and Turbine-Inlet Temperature Are Varied

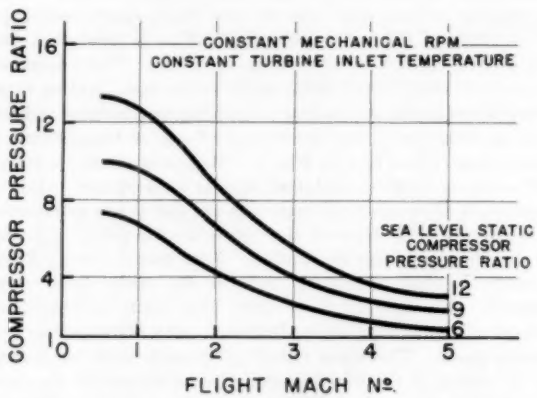

Fig. 9 Variation of Compressor-Pressure Ratio With Flight Mach Number for Several Sea-Level Static Compression-Ratio Engines Operating With Constant Mechanical Rpm and Turbine-Inlet Temperature

Compressor-Pressure Ratio

Mention already has been made of the reduction of effective compression ratio across the compressor as a result of aerodynamic heating at the inlet. This inlet heating effect is plotted in Fig. 9 for several sea-level static compressor-pressure ratios. The specific descriptions of the causes of the effect are unimportant here, beyond mentioning that the heating of the inlet air results in decreased density and decreased Mach number of the air moving through the compressor, leading to off-design operation and decreased compression ratio. Note that an engine with a sea-level static compressor-pressure ratio of 9, operating at constant mechanical rpm and constant turbine-inlet temperature, produces a pressure ratio of only 4 at Mach number 3. This effect is not entirely a disadvantage, as we shall see subsequently.

Economy of operation is partly a function of compressor-pressure ratio, and thrust output is partly a function of mass flow through the engine. Heating of inlet air not only decreases compressor-pressure ratio but sharply reduces mass flow through the engine. Fig. 10 is a simplified theoretical compressor characteristic and operating line, commonly referred to as a compressor map, which is a plot of compressor-pressure ratio versus per cent corrected air flow through the engine for a range of engine rpm and compressor efficiencies. The line at approximately 45 deg, marked surge line, is the compressor characteristic above which

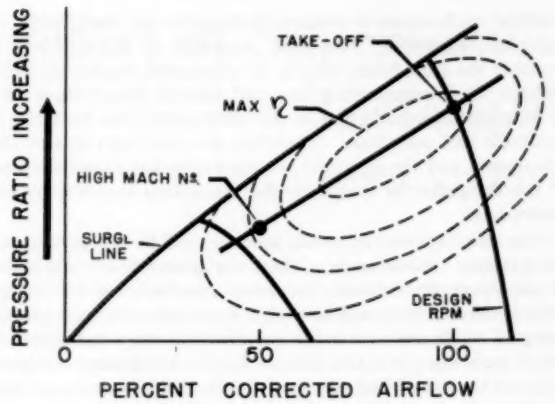

FIG. 10 SIMPLIFIED-COMPRESSOR CHARACTERISTIC AND OPERATING LINE FOR CONSTANT MECHANICAL RPM AND TURBINE-INLET TEMPERATURE

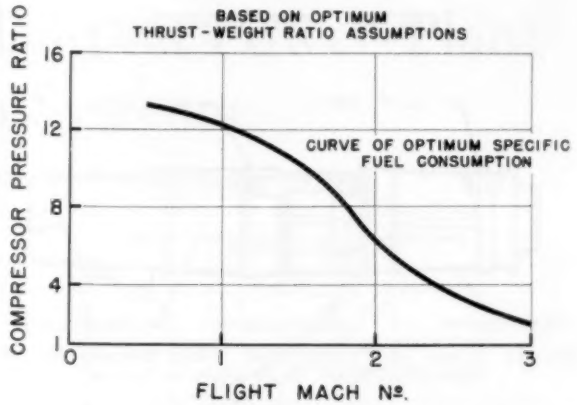

FIG. 11 OPTIMUM COMPRESSOR-PRESSURE RATIO FOR TURBOJET ENGINE WITH AFTERBURNER BASED ON CERTAIN THRUST, WEIGHT, AND FUEL-CONSUMPTION OPTIMUMS

the compressor will not operate. The dotted lines are efficiency contour lines, efficiency decreasing from the center outward. Corrected rpm decreases from left to right as inlet temperature increases and mechanical rpm remains constant. Assuming that the engine operates at design mass flow and rpm at take-off, some pressure ratio is produced across the compressor with high efficiency. Neglecting any cruise-operation point, as the engine operates at increasing flight Mach numbers, the locus of operating points on the compressor map will be approximately the line connecting the take-off point and the high Mach number point which is assumed to be in the region of Mach number 3. We now have a compound off-design operation problem. Using the scale of the figure, the engine is operating at decreased compressor efficiency, about half the design corrected mass flow, about half the design corrected rpm, and at a sharply reduced compressor-pressure ratio. Increasing the pressure ratio at the same mass flow, that is, moving the point vertically upward, results in compressor surge, while increasing the mass flow, moving the point to the right, requires an rpm increase or a larger inlet and consequently means that the potential take-off point could probably be moved upward and to the left. In fact, the basic engine would be changed. The over-all result of the inlet air heating at the high Mach number point is a limit to the thrust which the engine otherwise could produce and some loss of operating economy.

The loss of compressor-pressure ratio with increasing flight speed is not completely a disadvantage for several reasons. For example, an engine operating at Mach number 1 at sea level, at a 10:1 compressor-pressure ratio, excluding losses, would have to be capable of withstanding a pressure of 280 psi at the compressor outlet. The same engine at Mach number 3 at 35,000 ft and a 10:1 pressure ratio would have to withstand about 360 psi. This would result in a very heavy compressor casing and poor engine specific weight. If certain assumptions are made concerning optimum engine weight, thrust per pound of air, and specific fuel consumption, then a curve of flight Mach number versus optimum compressor-pressure ratio may be plotted.

Optimum Compressor-Pressure Ratio. Fig. 11 is a plot of optimum compressor-pressure ratio for afterburning turbojet engines as a function of flight speed. The exact shape of the curve is influenced by the weight, thrust, and fuel assumptions but the general shape and alignment, which are the important aspects, are as shown. The decrease of compressor-pressure ratio due to heating of the inlet air is not as great as the optimum curve indicates to be required. However, depending on engine application and mission requirements, a region of design-point operation can be chosen such that the two curves would be nearly identical in the chosen region. This choice, of course, then dictates the position of the rest of the compressor-pressure ratio versus flight-speed curve and indicates the attendant penalties in fuel consumption, weight, or thrust in the speed ranges where the curves are not coincident.

As an example, if cruise economy with only short-time high-speed capability were desired, then the high compression ratio, low Mach number end of the curve would be favored in compressor-design choice, resulting in a high flight Mach number compression ratio, higher than optimum for weight and fuel-consumption considerations but compromised for the sake of over-all performance. The existence of and relationship between the curves of Figs. 9 and 11 are two of the main reasons why the engine designer is able to provide engines of reasonable versatility in operation with acceptable economy and weight. For example, if optimum compressor pressure required an increase as flight Mach number increased, the designer would fight an almost hopeless and losing battle against either prohibitive weights or fuel consumption. The effect on the compressor of heating inlet air is one natural phenomenon that is the proverbial dark cloud with at least some silver lining.

PRACTICAL TEMPERATURE RANGES

So far the discussion has dealt with individual components and the cause and effects of temperature rise. To sum up the over-all engine problem and to provide a temperature frame of reference for the engine designer as well as the air-frame and accessory designer, an examination of the practical temperature ranges to be expected is necessary.

Fig. 12 is an outline drawing of a typical turbojet engine labeled with a general résumé of temperatures to be expected as we invade the thermal-barrier region. The temperatures are actually a summary of the foregoing discussion and are those which probably will be felt by the structural material. Today's compressor designer must now provide inlet-stage blades which might run at a temperature which yesterday's designer only considered for last-stage blades, and last-stage blades must operate in conditions as severe as the turbines endured in early engines. As allowable turbine-inlet temperatures are raised, combustor liners and tubes must resist the severe temperature extremes now applied to turbines. The turbine itself, long the real hotbed of thermal difficulties, forces the materials and design engineers into areas of effort where arithmetic-performance progress requires geometric effort expenditures.

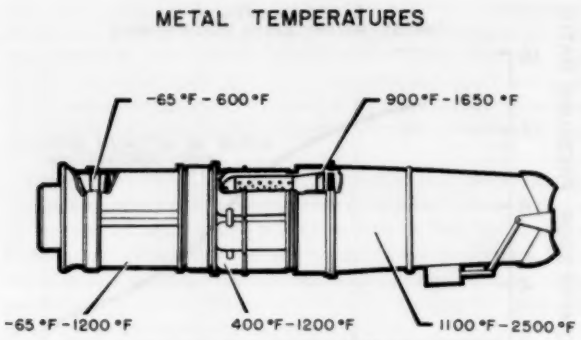

FIG. 12 RANGE OF TEMPERATURES WHICH TURBOJET-ENGINE COMPONENTS MIGHT BE REQUIRED TO ENDURE

Auxiliary Components. Downstream of the turbine, the constant quest for higher performance and lighter weight sustains the challenge to the designer of aft sections, afterburners, and propulsion nozzles. Many materials now employed in the main and auxiliary components of the turbojet engine can no longer be used where sustained operation at high flight Mach numbers is required. Many engine subsystems become extremely vulnerable as a result of the maximum temperatures shown in Fig. 12. Modern engines require extensive and complex hydraulic and electrical control systems using fluids, insulators, electronic equipment, seals, and the like, which cannot withstand such temperatures. Certain systems, such as starting or ignition, are used only on the ground but must be protected in flight from extreme soak temperatures without complicating the system beyond its break-even point of usefulness versus penalty. Bearings will be required to run at higher stabilized operating temperatures and lubricants must be provided to allow such operation. These few examples, together with other specialized and detailed comments about such subsystems, make it clear that the turbojet engine must enter a new era if substantial inroads into the accomplishment of supersonic flight are to be made.

SOLVING THE THERMAL-BARRIER PROBLEMS

The solutions to the thermal problems lie in research and the practical applications of research findings by the many types of engineers concerned. The basic approach to the problem is probably the most futile, that is, to accomplish supersonic flight without the accompanying ram and friction temperature rise. So long as the vehicle flies in the atmosphere the heat rise is inevitable and relentless. Therefore we must turn to new developments and the ingenuity, co-operation, and resourcefulness of the designers, to overcome the limitations imposed by excessive heat.

New and improved materials probably will be the keystone of any progress that is made. These materials will include metal alloys, synthetic rubbers, ceramics, plastics, and lubricants. Aiding new materials will be design techniques and innovations, many of which are now in the experimental stage and others of which have not yet taken definite form. Mechanical refrigeration and the use of fuel as a heat sink are already being investigated thoroughly. The cooling of turbine wheels and blades by passing gas or liquid through internal passages has been widely discussed and examined both theoretically and experimentally, here and abroad. Relocating certain engine accessories to avoid local regions of very high temperature will have value. The scope of basic theory concerning blade flutter, stress limits, off-design operation, combustion, and the like, for turbojet engines must be widened and given practical value. The engine designer must co-operate closely with the air-frame designer to achieve the most efficient results, most especially in the early design stages of the air vehicle. The military services must join hands with research organizations and industry to provide a full understanding of one another's problems and requirements, and to promote a working atmosphere of maximum co-ordination and co-operation.

The best turbojet-engine design will depend mainly on two factors, the total supersonic flight-time requirements of the design mission and the state of the art knowledge available to the designer. The problems are many and their solution will be costly in time, money, and manpower, but world conditions are such that we have no right, or time, to ponder whether we can produce worthwhile supersonic engines. We are faced with the absolute necessity of rolling up our sleeves and making a united assault on the common enemy—the thermal barrier.

Effect of Supersonic Flight on Power-Plant Installation Systems

By R. B. KEUSCH,[1] WRIGHT-PATTERSON AIR FORCE BASE, OHIO

This paper treats power-plant installation-system problems either brought on or aggravated by supersonic flight. These problems are in addition to those (treated elsewhere) of the basic engine; their magnitude and possible effect on the aircraft mission are treated. Among the power-plant installation-system areas considered are fuel systems, lubrication systems, power transmission, engine placement, air-induction systems, and cooling systems.

Introduction

EVEN though a supersonic power plant is available, it is obviously useless unless it can be utilized in an aircraft or missile to perform an assigned mission. Other authors (1)[2] have highlighted some of the problems involved in obtaining a supersonic engine—in other words, the "internal" propulsion system. This paper will be devoted to the multiplicity of problems involved "external" of the engine itself. The features to be discussed do not, of themselves, contribute to the thrust of the propulsion system, but they are essential to support that engine, and, if improperly designed or executed, may detract very greatly from the mission effectiveness of the aircraft or missile.

In the broad area of power-plant installations are included such items as fuel systems, lubrication systems, lines, fittings and seals, power transmission, engine placement, air-induction systems, and cooling systems.

Before proceeding to the various items to be discussed under these headings there are some broad considerations to which we should first direct our attention.

The most aggravating factor in supersonic flight is the temperature which is encountered. The familiar chart, Fig. 1, on temperature versus Mach number shows that the increase of effective aircraft skin temperature, with increasing Mach number, may be described as considerable. When ambient air is utilized for cooling, this is the temperature of this "cooling" air. Shown here are the stagnation temperature and an "effective" temperature, in which an 88 per cent recovery factor has been applied. It is quite true that the shape of the body, emissivity, absorptivity, solar radiation, and irradiation will affect these values somewhat (2 to 5).

Then there is the overriding materials problem. As shown in Fig. 2, at relatively modest speeds the usefulness of rubber materials, aluminum, and titanium ends. Our earnest hopes are with those engineers who work on development of new materials.

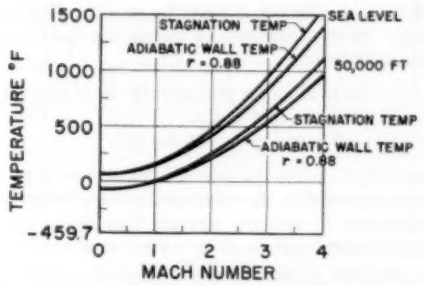

Fig. 1 Stagnation and Adiabatic Wall Temperature Versus Speed
(For variable specific heat.)

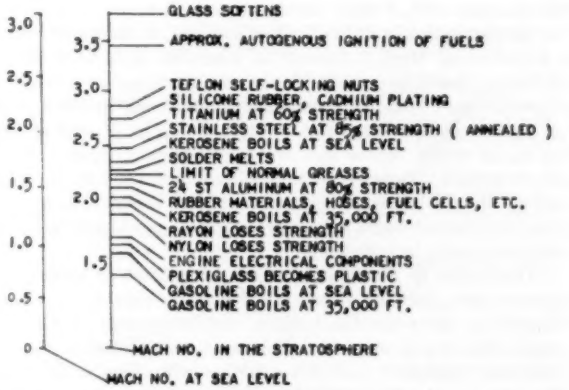

Fig. 2 Mach Numbers to Which Aircraft Materials Are Limited by Temperature
(Full stagnation temperatures are assumed.)

Also, there is the consideration of obtaining a properly integrated power-plant installation composed of the various systems involved. With the advent of high-speed aircraft, each power-plant system, or at least some phase of it, becomes dependent upon another power-plant system or systems. This makes the designer's job doubly difficult in that he is very often not able to solve his problem locally, but must solve it in relation to, or even with, other problems.

Fuel Systems

Of paramount importance and a predominant source of concern to the engineer who must consider supersonic power-plant installations, is the problem occasioned by the effects of high-speed flight upon fuel systems.

The importance of supersonic-flight performance on the propulsion-system characteristics is shown (6) rather clearly in Fig. 3. Here, airplane velocity has been plotted against percentage of airplane gross weight represented by the engine and fuel. We note that, as velocity is increased from 300 to 900 mph, the percentage of the airplane total weight required for the engine and fuel weight increases from about 20 to around 60 per cent.

---

[1] Special Assistant to the Chief, Installations Branch, Power Plant Laboratory, Wright Air Development Center, Air Research and Development Command, United States Air Force. Assoc. Mem. ASME.

[2] Numbers in parentheses refer to the Bibliography at the end of the paper.

Contributed by the Aviation Division and presented at a joint session of the Aviation Division, American Rocket Society, and The Society of Automotive Engineers, at the Annual Meeting, New York, N. Y., November 28–December 3, 1954, of The American Society of Mechanical Engineers.

Note: Statements and opinions advanced in papers are to be understood as individual expressions of their authors and not those of the Society. Manuscript received at ASME Headquarters, September 28, 1954. Paper No. 54—A-156.

While the figures are not intended to be precise, and would certainly be affected by the individual airplane design, the chart does impart to us the general magnitude of the problem.

Until the advent of high-altitude requirements for aircraft operation, and before extreme cold weather became a consideration, fuel served its basic function of combustion to produce power, and presented no particular problems. When flight above 40,000 ft became a reality, fuel volatility had to be maintained within certain limitations, so that considerable amounts of fuel would not boil away before it could be consumed by the aircraft power plant. Several methods of alleviating the situation were considered, including:

(*a*) Lower the Reid vapor pressure (RVP) of the fuel.
(*b*) Pressurizing the fuel tanks.
(*c*) Pre-take-off refrigeration of the fuel.

Each method, if used independently, introduced other problems and it has appeared that the solution is a compromise among the three. Operation of military aircraft from cold-weather bases loomed as an additional obstacle to be overcome, forcing the petroleum engineer to inject more "volatility" into the fuel—the antithesis of the demands of altitude and speed requirements.

It is obvious that heat will be conveyed to the stored fuel of a supersonic aircraft, with fuel stored in either the wing or fuselage. With hydrocarbon fuels of the JP-4 type (in accordance with Specification MIL-F-5624) certain losses will be encountered unless pressurization is utilized. For instance, as shown in Fig. 4, a hypothetical Mach 2 bomber, in sustained flight at 40,000 to 50,000 ft, would lose about 18 per cent of its fuel as a result of vaporization. This fuel is assumed to be initially at 100 F, with no tank pressurization. The addition of $^1/_{16}$ in. of cork around the tanks would reduce this loss to 8 per cent, again with no pressurization. However, with insulation and 4 to 5 psi pressurization, the fuel loss is negligible. Other configurations than that investigated might not be so favorable, and higher fuel-tank pressures might be necessary.

Temperature of Fuel Tanks. It is of interest to know what temperatures the fuel within tanks may be expected to reach. Obviously, under sustained flight, the temperature would approach the skin temperature; however, the particular type of structure, insulation, and other factors will cause a finite lag. Work done at the Wright Air Development Center (7) on heating of fuel may be found of interest. With certain restrictive assumptions, both a wing tank and a fuselage tank were considered; the calculations were made with JP-4 fuel, and a so-called limiting temperature of 120 F.

On the basis of these calculations, sufficient data were obtained to construct a series of graphs, several of which are shown herewith, demonstrating how fuel temperatures are affected by high-speed flight. In Fig. 5 we show the time for fuel in a full wing tank to reach 120 F versus Mach number. Meanwhile it is

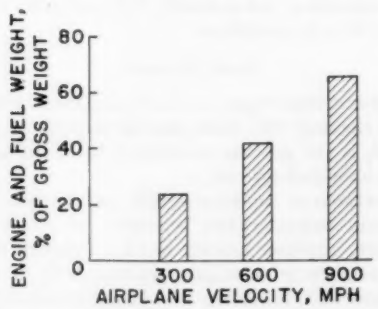

Fig. 3 Effect of Airplane Velocity on Total Propulsion System Weight

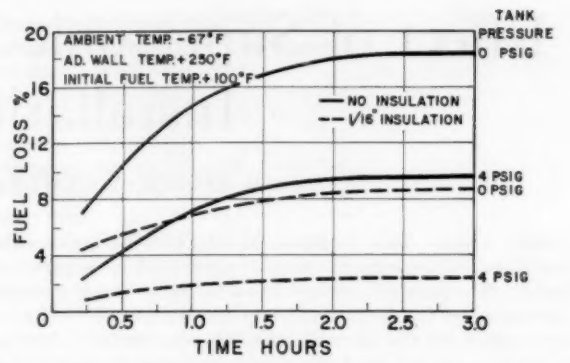

Fig. 4 Fuel Vaporization Losses for a Hypothetical Mach 2 Airplane
(Showing effect of tank pressurization and fuel cell insulation.)

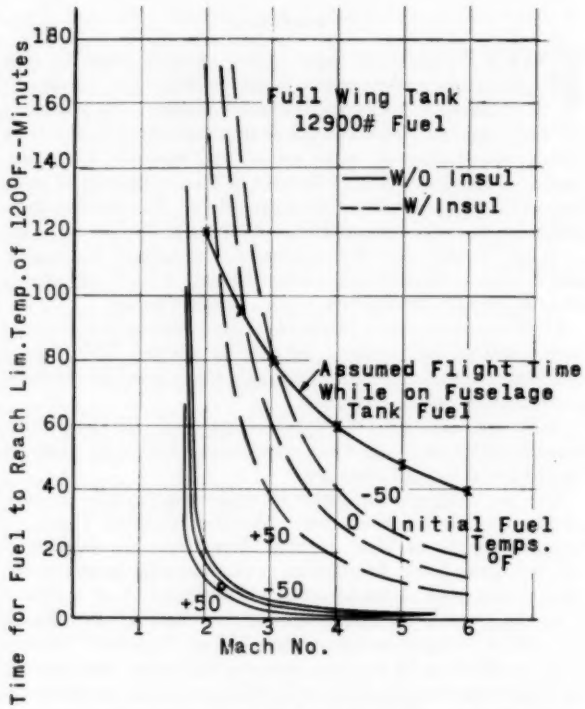

Fig. 5 Heating of Fuel in Full Wing Tank at 40,000 Ft

assumed that fuel is being utilized from a fuselage tank, as by X — X. Fig. 6 shows similar information for a full fuselage tank, with fuel being used from the wing tank. Figs. 7 and 8 give a time-temperature history for emptying fuselage tanks at Mach 2 and Mach 4.

We can see that, while insulation is important, it might have its optimum values under conditions which could penalize the mission of the aircraft. It would be necessary to perform, for the particular aircraft being considered, the laborious calculations of a "range trade," that is, a determination of reduction in range due to insulation (taking up space which could be utilized for fuel) compared to that due to loss of fuel.

The figure of 120 F for the "limiting" temperature was chosen because of a desire to limit tank pressures to about 5 psi, since the structure of transonic aircraft can withstand 5 psi internal gage

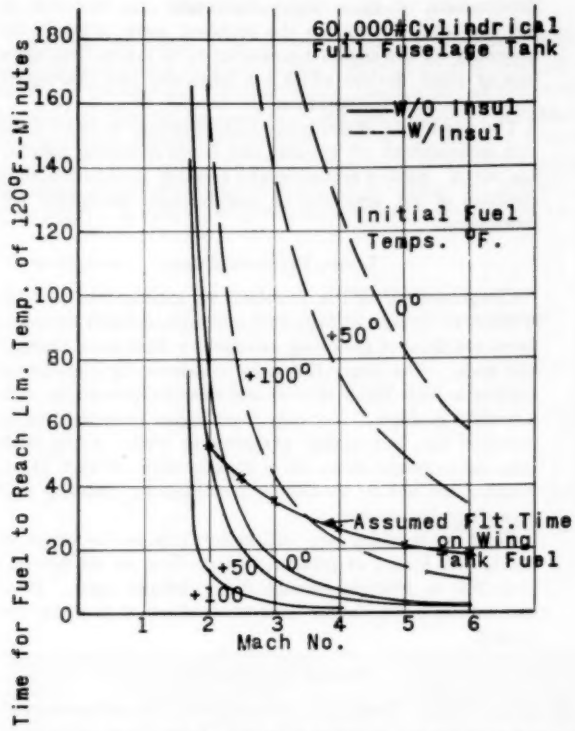

FIG. 6 HEATING OF FUEL IN FULL FUSELAGE TANK AT 40,000 FT

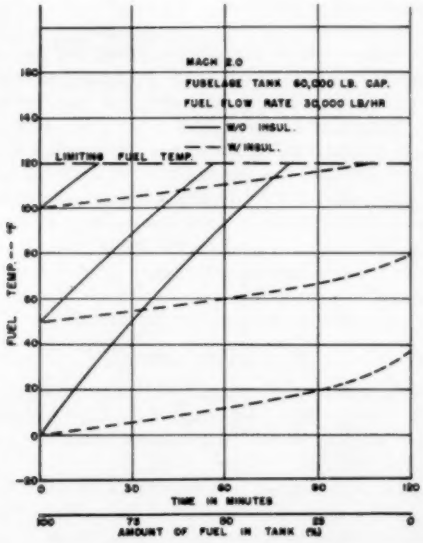

FIG. 7 HEATING OF FUEL IN EMPTYING FUSELAGE TANK
(Mach 2 at 40,000 ft; tank emptying at a constant rate.)

pressure with no additional weight penalty. Later work shows that somewhat higher pressures should be considered; however, the use of high temperatures is to be avoided, if at all possible. If fuel is in the tank at 120 F, it will be at considerably higher temperatures when it enters the fuel nozzles in the combustion chambers; heat will be added by each pump through which the fuel must pass by the fuel-oil heat exchanger

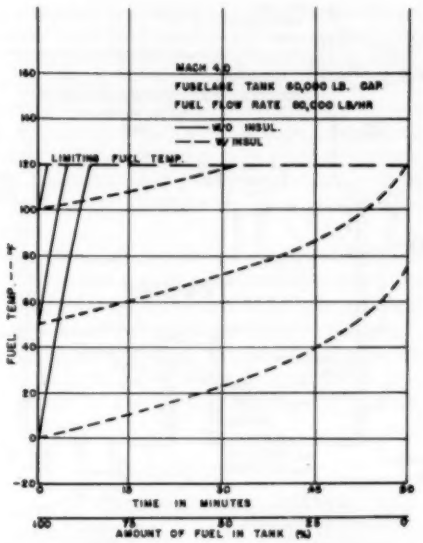

FIG. 8 HEATING OF FUEL IN EMPTYING FUSELAGE TANK
(Mach 4 at 40,000 ft; tank emptying at a constant rate.)

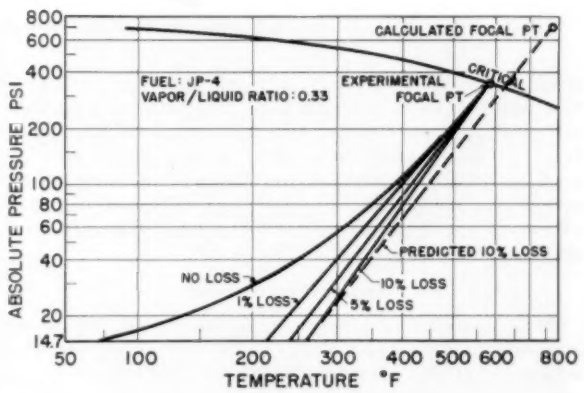

FIG. 9 FUEL-CELL PRESSURE AS A FUNCTION OF TEMPERATURE AND FUEL VAPOR LOSS

and by the fuel control. Further, hydrocarbon fuels are limited due to severe gumming tendencies if heated to the range of 250 to 300 F. This limitation may be lifted as a result of additives, but there will very likely be another and more severe difficulty at some higher temperature.

Fuel-Tank Pressure. Another way to look at the supersonic heating problem is to determine, if we resolve to lose a predetermined amount of fuel, what the fuel-tank pressure would be, as the fuel is heated. Fig. 9, extracted from recent work done by Thompson Products, Inc., under subcontract to the Aviation Fuels Division of the Coordinating Research Council, shows this relationship. With JP-4 fuel, as aerodynamic heating occurs, considerable tank pressures will be felt, if we insist on losing no fuel. If 1 per cent is lost, considerable reductions in tank pressures would be felt. On the other hand, taking as much as a 10 per cent loss will not reduce tank pressures significantly from those associated with 1 per cent loss.

The large quantity of fuel aboard supersonic aircraft (see Fig. 3) is looked at with covetous eyes by the engineers of many systems, as a panacea for their supersonic problems—the fuel

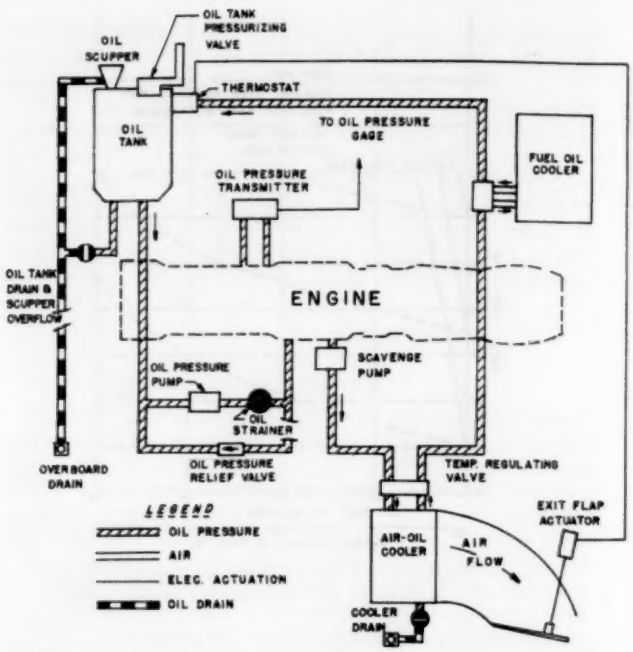

FIG. 10 TYPICAL LUBRICATION SYSTEM FOR TURBOJET ENGINE

system is the ideal heat sink, they say. However, the fuel-system designer has more than his share of problems under conditions of supersonic flight, without anyone else adding heat to the fuel. It must, in some instances, be so used—but all such heat additions must be integrated carefully into the design of the aircraft; otherwise, the fuel system, as it emerges on the actual vehicle, may prevent the aircraft from accomplishment of its mission.

LUBRICATION SYSTEMS

Since any lubrication system, such as the typical turbine-engine lubrication system shown in Fig. 10, is predicated upon some external mechanism for cooling the oil, improvement in this area is worthy of intensive effort. This problem is in addition, of course, to that of making a lubrication system operate at the extremely high altitudes of which supersonic aircraft are capable.

To investigate the parameters pertinent to the oil-cooling problem in high-speed aircraft, the Wright Air Development Center has contracted with the United Aircraft Corporation for a study. This study will consider various methods of oil cooling, under conditions up to Mach 2.5, sea level to 80,000 ft, and at various fuel and oil flows. It is expected that, as a result of this study, the air-frame manufacturer will be able to select the optimum oil-cooling system for his particular air frame-and-engine combination. The use of fuel to cool the oil looks increasingly disadvantageous, both owing to the complications of heat addition to the fuel, and the decreasing fuel flows which may be expected with higher altitudes.

The Ideal Oil Properties. It is quite true that oils capable of sustaining high temperatures will alleviate the lubrication-system problem significantly. Among properties which the oil should have is that of noninflammability and retention of lubricity at high operating temperatures. An ideal oil for modest supersonic speeds would be operational in the temperature range from about —65 to +800 F. In this connection it is of interest to note that placing less stress on the low-temperature oil requirement may help raise the upper temperature limits appreciably. The development of these high-temperature oils, however, is not the total solution to the problem, since it would be necessary for the engine manufacturers to insure that bearings or other devices which are lubricated can operate at these very high temperatures.

The possibility of designing main bearings to have their own independent oil system, and hence eliminate pumps, has merit. Such a system might possibly involve the substitution of air, graphite, or molybdenum disulphide for lubrication.

LINES, FITTINGS, SEALS

Companionate to the problems of getting fuel and oil systems to operate at high-fluid and high-ambient temperatures, are those of providing satisfactory fluid lines, fittings, and seals. The larger line sizes occasioned by high-thrust engines in high Mach aircraft and missiles, present us with a twofold problem. Not only must higher temperatures be provided for, but higher pressures as well. Along with this, light weight must be a consideration, if high Mach vehicles are not to be unduly penalized by "beefing up" present fitting designs.

Fluid seals which are satisfactory up to the range of 500 to 700 F and at pressures (depending on the system) from 700 to 4000 psi, would fill a definite need. Hose and tubing in the larger sizes (sizes above 6 in.) also are needed.

POWER TRANSMISSION

In this field the Wright Air Development Center sponsored a contract with the Armour Research Foundation to explore the basic parameters which should guide the selection of the method of driving aircraft accessories, namely, mechanical, hydraulic, pneumatic, or electrical. This study (8) will enable the aircraft manufacturer to state the locations of equipment, their power schedules, types of engines, and speed and mission of the aircraft—and obtain the resultant hp/lb of the transmission system. In this work an interesting concept of "mission weight" is utilized. Chargeable to the transmission system is not only the fuel necessary to carry the weight of the transmission system, but also the increased fuel flow necessary to obtain from the aircraft the same speed which it would have, if it were not burdened with power extraction for the particular transmission system.

It is quite true that the optimum method of power transmission might not be utilized, because of the necessity of having some particular items of equipment driven by one means, thus making that particular means the most logical for the aircraft.

ENGINE INSTALLATION

As shown previously, the weight of fuel and power plant will account for a rather high percentage of the total aircraft weight. But the power plant and related systems dominate the aircraft in yet another way.

It is rather obvious that any supersonic airplane must have thin wings and a clean fuselage, so that the volume of the engine and its installed fuel will tend to be the greatest factor in determining over-all airplane drag. Engine and engine-installation compromises have had small effects on subsonic aircraft, but these same compromises may very easily reduce the range of supersonic aircraft by 15 to 20 per cent. At the same time, various changes to types of wing (delta, straight, etc.) may be made, so long as the wings and fuselage stay thin and clean, and the reduction in range at supersonic speeds will be only 2 to 4 per cent (6).

Placement of the power plant and its systems must be viewed as a vital part of preliminary airplane design; further, the total envelope for the engine must be kept small.

Air-Induction Systems

Of particular significance in the installation of a supersonic air-breathing engine is the problem of getting air delivered efficiently to the engine. In other words, the pressure at the compressor face (for turbine engines) should be as high a percentage of free-stream pressure as possible; this is the recovery factor mentioned previously. Supersonic operation must insure that the shock waves generated at the inlet are positioned properly, as in Fig. 11, in order to obtain a high ram recovery, a low airplane drag, and an even pressure and velocity distribution across the compressor face (or burner inlet for ramjets). The inlet may be of great help in obtaining power for supersonic flight; for instance, at Mach 3, the compression across the necessary shock waves can be about 18 to 1. However, if the aircraft or missile is to operate effectively at other than a single design point (and by this term we include speed, back pressure, angle of attack, and altitude), the inlet must always position these shock waves properly (9). In addition, with varying air speed, the inlet area must be varied.

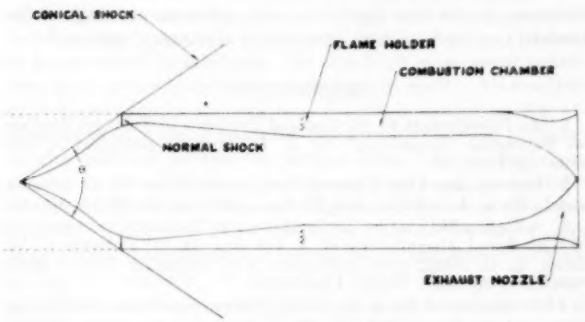

Fig. 11 Supersonic Inlet
(Applied to a ramjet.)

To date, most of the induction-system work has been accomplished by the air-frame or missile manufacturer, in applying the basic data obtained by the NACA. As speeds increase, optimization of the air-induction system over the speed range of the vehicle becomes imperative. In the field of variable-area inlets, the need for data, which can be developed into practical installations, jointly by the aircraft, engine, and controls people, is a very present one.

Cooling Systems

The acuteness of the problem of cooling the engine and its associated systems stems from the lack of suitable noncritical materials which will withstand the high temperatures necessarily encountered in high Mach aircraft. Consider that not only must the power-plant installation itself be cooled to obtain

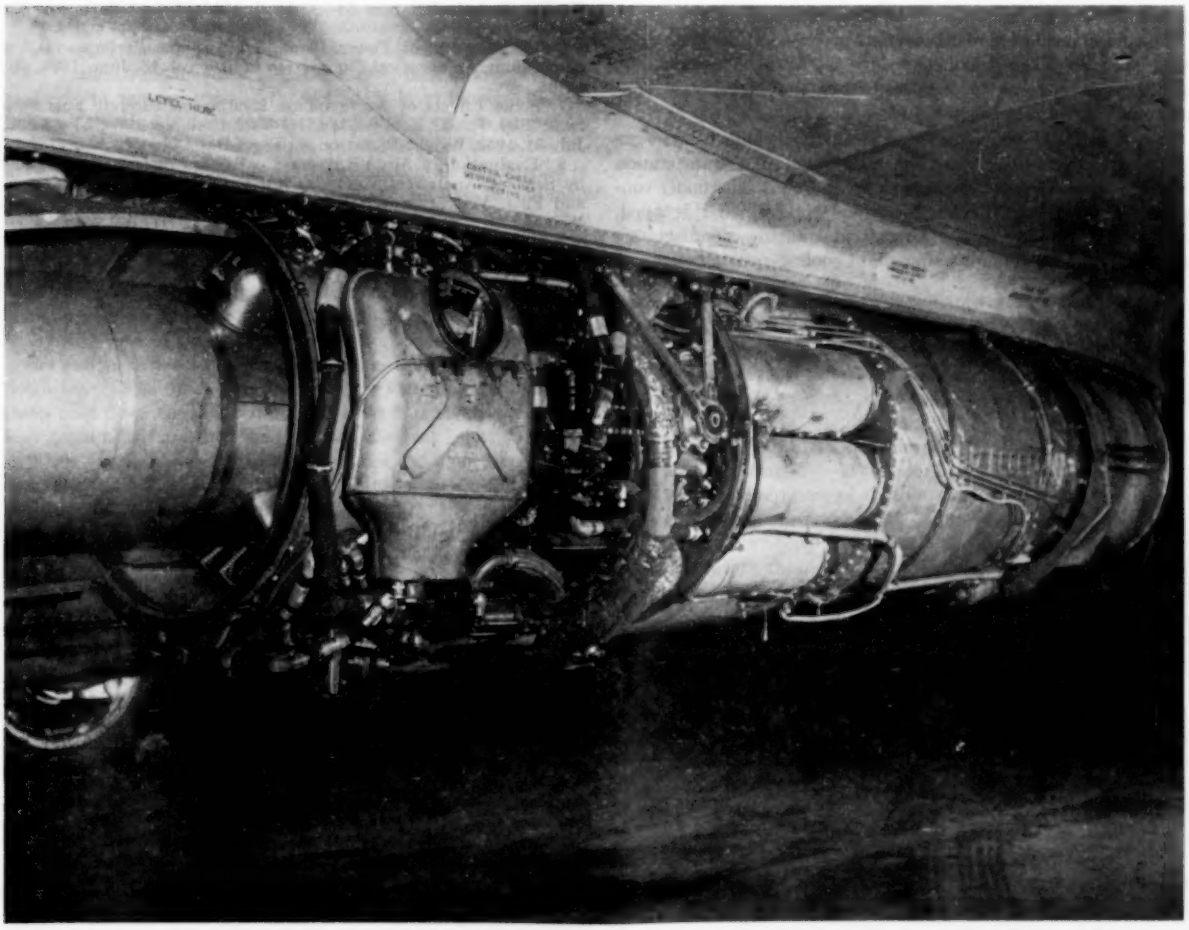

Fig. 12 Typical Engine Installation

satisfactory performance of the engine and accessories, but also the structure and aircraft skin surrounding the power plant must be kept within temperature limits (3, 4).

In subsonic flight, a sufficient temperature differential exists between the stagnation temperature and the limiting temperature of all power-plant components, to permit adequate cooling with air supplied by flight ram pressure, with small power losses chargeable to the cooling system. This, of course, is not the case with supersonic flight.

The cooling problem of a supersonic aircraft power-plant installation is further aggravated by an increased heat load that must be dissipated. The following factors are pertinent:

(*a*) Aerodynamic heating of the aircraft skin.

(*b*) The larger engines to be used in supersonic aircraft and missiles have, in many cases, greater compression ratios, and hence increased temperatures of the engine case over the last few stages of the compressor.

(*c*) The use of cooled turbine blades and afterburners (with the temperature of the latter running as high as 3500 F) will result in much higher temperatures for the "hot" parts of the engine.

A typical turbine-engine installation is shown in Fig. 12; while this is not from a supersonic aircraft, the problems are much the same. The amount of cooling air (expressed as a percentage of intake air) must be kept as low as possible; the surrounding aircraft structure must be kept within temperature limits; the components on the engine must be kept within their limits.

The use of insulation blankets offers promise at the lower supersonic speeds. These blankets reduce the air flow required, but result in an increase in temperature of the engine case (and possibly in greater engine weight).

Other methods which have some merit include exhaust-gas boundary-layer bleed, water-steam system, and transpiration cooling. The Wright Air Development Center has under contract with Northrop Aircraft, Inc., some work, which, it is hoped, will make available to the aircraft and engine manufacturers significant parameters for power-plant cooling-system design.

Conclusion

We have seen that the power plant and its installation systems, with increasing aircraft speed, account for increasingly larger percentages of the aircraft weight. The fuel system has been assessed as being particularly critical. Supersonic speed adds heat to the fuel system in such quantities that it gives the fuel-system designer many problems; the fuel system is not the ideal heat sink which, at first, it might appear to be. Other power-plant installation-system problems demand early consideration in the design of aircraft, for compromise in the solution of these problems, due to their high-percentage effect on the range of the aircraft, may well result in compromise of the total mission.

BIBLIOGRAPHY

1 "An Introduction to the Thermal Problems of Turbojet Engines for Supersonic Propulsion," by A. J. Gardner, published in this issue, pp. 715–720.

2 "Determining Skin Friction Temperature," by W. D. Murray and L. Slote, *Aero Digest*, vol. 68, June, 1954, pp. 33–36, 38, and 42.

3 "A Design Manual for Determining the Thermal Characteristics of High-Speed Aircraft," by H. A. Johnson, M. W. Rubesin, F. M. Sauer, E. G. Slack, and L. Possner, AAF Technical Report 5632, September 10, 1947, Wright Field, Ohio.

4 "A Method of Predicting Skin, Compartment, and Equipment Temperatures for Aircraft," by W. D. Murray and L. Slote, WADC Technical Report 53-119, July, 1953, Wright-Patterson Air Force Base, Ohio.

5 "Survey on Heat Transfer at High Speeds," by E. R. G. Eckert, WADC Technical Report 54-70, April, 1954, Wright-Patterson Air Force Base, Ohio.

6 "Optimization of Power Plant and Airplane Performance," a Symposium, *Aeronautical Engineering Review*, vol. 13, June, 1954, pp. 42–61.

7 "Some Effects of Aerodynamic Heating on Aircraft Fuel Systems," by R. B. Keusch, WADC Technical Note WCLP-53-227, July 31, 1953, Wright-Patterson Air Force Base, Ohio.

8 "Evaluation of Aircraft Accessory Power Transmission Systems by Selected Analytical Methods," by J. H. Bonin, R. A. Harmon, and F. J. Vodvarka, WADC Technical Report 53-36, July, 1953, Wright-Patterson Air Force Base, Ohio.

9 "Installation Is Critical for Mach 2 Jets," by D. A. Anderton, *Aviation Week*, vol. 61, July 12, 1954, pp. 28–30, 34.

An Investigation of the Melting of Bodies Due to Aerodynamic Heating

By C. H. McLELLAN,[1] LANGLEY FIELD, VA.

Various approaches to the aerodynamic heating problem of bodies re-entering the atmosphere are considered briefly. One approach to this problem is to allow the heat to be absorbed by the body. At very high supersonic velocities, part of the body can be expected to melt. An analysis of a high-density conical-nosed vehicle entering the atmosphere at a speed of 20,200 fps showed that, in addition to the melting at the tip of the cone, the temperature gradients through the skin become very large and, under some conditions, surface melting would occur on the cone as well. Since very little was known about the melting of bodies due to aerodynamic heating, an exploratory investigation was made in the Langley 11-Inch Hypersonic Tunnel. The results of melting tests of several bodies made of a low-melting-temperature alloy are discussed.

Introduction

At low supersonic speeds it is permissible to allow a vehicle structure to reach a temperature equilibrium with air in the boundary layer. As the flight Mach numbers are increased, the temperatures in the boundary layer increase to such large values that the structural integrity of a vehicle cannot be maintained when the temperatures approach those in the boundary layer. For example, the structure of a vehicle constructed of steel, flying at a low altitude for a long period of time, would melt at a Mach number less than 6. The melting point of all other structural materials is exceeded before a Mach number of 8 is reached. Long before these Mach numbers and temperatures are reached, the structural strength of materials begins to decrease and many other problems begin to plague the designer.

Vehicles can, of course, be operated for brief periods of time under far more severe heating conditions than for steady-state conditions. The operating time may be extended at high altitudes because of the reduced heating rates and also the radiation may more nearly balance the aerodynamic heat input.

When long-range ballistic-type vehicles are considered, however, the vehicle approaches the high-density air at high velocities and will be subject to enormous heat-transfer rates unless the vehicle is decelerated at high altitudes. These heat-transfer rates can be great enough to melt parts of the vehicle unless the surface is cooled. Actually, allowing parts of the vehicle to melt may be a satisfactory solution to the aerodynamic-heating problem in some cases. The problem then becomes one of determining whether or not the vehicle can reach the earth before being destroyed by the melting.

The aerodynamic-heating problem of long-range ballistic vehicles will first be reviewed, then an attempt to study experimentally the melting of a body by aerodynamic heating in the Langley 11-Inch Hypersonic Tunnel will be discussed.

The Problem of Aerodynamic Heating of Long-Range Vehicles Using a Ballistic Trajectory

In order to give an insight into the magnitude of the problem, Fig. 1 presents the initial velocities and Mach numbers that are required to obtain various flight ranges with a ballistic trajectory, assuming the duration of powered flight is negligible. The Mach numbers given are for an air temperature of —44 F, at which the speed of sound is 1000 fps. For trajectories with a range greater than 3500 miles, the initial trajectory velocity will be in excess of 20,000 fps, which is not much less than the initial velocity of 26,000 fps that is required to establish a satellite trajectory with infinite range.

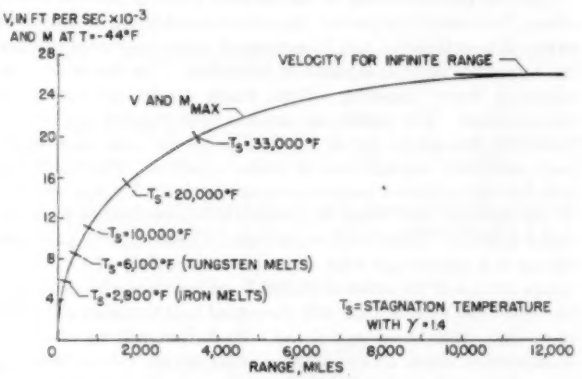

Fig. 1 Initial Velocity and Mach Number Required to Attain Various Ranges Using a Ballistic Trajectory

As the speed is increased, the air temperatures around the vehicle increase rapidly. If the air is considered a perfect gas, the increase in temperature of the air at any point around the vehicle will be proportional to the square of the velocity of the vehicle. At a velocity of 6000 fps, the stagnation temperature, the temperature ahead of a blunt surface where the air is at rest with respect to the vehicle, will be sufficiently high to melt iron or steel. At a velocity of 20,000 fps, the stagnation temperature is about 33,000 F. Dissociation, ionization, and radiation from the gas will alter these temperatures somewhat. The recovery temperatures, which are the temperatures that would be reached on an insulated surface, are not much lower for either the laminar or the turbulent boundary layers. Obviously, the surface temperatures must be kept far below the stagnation and recovery temperatures. Radiation of heat from the vehicle will be of considerable help in limiting the maximum temperature attained, particularly at high altitude where the heat transfer to the vehicle will be reduced because of the low density of the air.

A vehicle traveling in a ballistic trajectory at very high speeds is fortunately in the relatively high-density air where heat transfer and drag are important for only a short time. A typical trajectory for a range of 3450 miles with an initial acceleration of

---

[1] Head, 11-Inch Hypersonic Tunnel Section, Langley Aeronautical Laboratory, NACA.

Contributed by the Aviation Division and presented at a joint session of the Aviation Division, American Rocket Society and The Society of Automotive Engineers, at the Annual Meeting, New York, N. Y., November 28–December 3, 1954, of The American Society of Mechanical Engineers.

Note: Statements and opinions advanced in papers are to be understood as individual expressions of their authors and not those of the Society. Manuscript received at ASME Headquarters, September 28, 1954. Paper No. 54—A-157.

5 g's is shown in Fig. 2. The maximum altitude of the flight is over 650 miles above the earth's surface. For most of the flight, the heat transfer will be negligible since the air density at an altitude of 70 miles is less than one millionth of the sea-level value.

Typical heat-transfer rates to a station 4-ft back from the point of a 10-deg semi-apex angle conical nose are presented in Fig. 3 for this trajectory. In a practical flight plan for this range, the initial acceleration will be sufficiently small so that the vehicle will pass through this effective portion of the atmosphere before the velocity is high enough to create any important heating problem. For the trajectory considered, the maximum heat-input rate was only slightly over 20,000 Btu per hr per sq ft, assuming a laminar boundary layer. If the skin were 1 in. thick at this point, the temperature rise during the climb phase would be less than 100 deg F. Even a turbulent boundary layer would not increase seriously the heat transfer during this portion of the flight. After 80 sec, the air density is sufficiently low that the heat-transfer rates are negligible.

The real problem arises in the re-entry phase of the trajectory, where, for a very brief period, the vehicle is subjected to enormous values of heat transfer, and it becomes of vital importance whether the boundary layer is laminar or turbulent. For the re-entry, a relatively heavy low-drag vehicle which decelerated very little was assumed. The maximum laminar heat-transfer rate is over 2,000,000 Btu per hr per sq ft, which is on the order of 50 times that ordinarily encountered in modern boilers. The maximum rate for the turbulent boundary-layer case is 36,000,000, which is of the order of 1000 times that which is encountered in standard boiler practice. These values are based on calculations assuming the air is a perfect gas with a specific-heat ratio γ of 1.4. Since temperatures of the order of 30,000 F are involved, the air cannot be considered a perfect gas and the actual heat transfers will differ somewhat from those calculated. Radiation will be relatively unimportant since, at the melting point of iron (about 2800 F), the radiation of a black body would be only 190,000 Btu per hr per sq ft.

Since the heat-transfer rates during re-entry are many times greater than for any other part of the trajectory, only this part of the trajectory will be analyzed further.

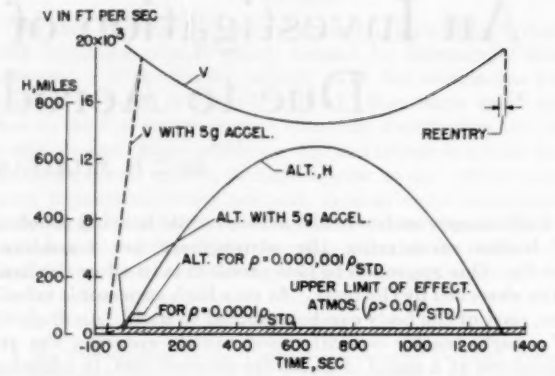

FIG. 2 VELOCITY AND ALTITUDE DURING A 3450-MILE TRAJECTORY

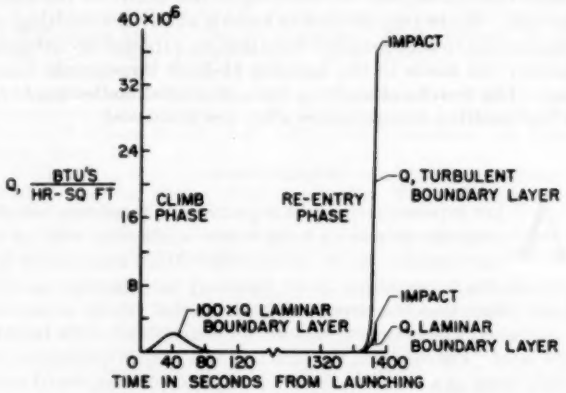

FIG. 3 HEAT-TRANSFER RATES TO A STATION 4 FT FROM NOSE OF 20-DEG CONE DURING 3450-MILE TRAJECTORY

POSSIBLE SOLUTIONS TO THE PROBLEM

Several possibilities of relieving the aerodynamic heating present themselves. One that probably first comes to mind is to avoid the high temperatures of the air around the body by decelerating the vehicle. Reverse thrust to decelerate the vehicle before it enters the high-density air would be usable if sufficient fuel could be carried along. However, the amount of fuel necessary to obtain any significant deceleration would require great increases in take-off weight. In fact, an increase in initial weight of at least one order of magnitude would not be unlikely. The vehicle also may be decelerated at high altitudes by the use of a large drag-to-weight ratio. This is the mechanism by which very small meteorites reach the earth's surface even though they have much higher entry velocities than those considered for man-made vehicles.

Whipple (1)[2] points out that meteorites less than 0.04 in. in radius are not destroyed by high heat transfer since their drag, which is high in comparison to their weight, decelerates them sufficiently at high altitude so that they enter the lower atmosphere with relatively low velocities. Application of the same principle to a large vehicle would require that the drag be very large at high altitudes even though the air densities are extremely small, so that the structure required would probably be large and heavy. Moreover, in some applications, the high drag may be undesirable at the lower altitudes after the desired deceleration is completed.

For some flight conditions, the structure probably can be protected to some extent by use of an insulating material applied to the exterior of the vehicle. The surface temperature would be greatly increased because of the low conductivity of the material. This increased temperature would decrease the heat transfer from the air and increase the heat that can be radiated from the body. However, there are no insulating materials known which can stand up under the high temperatures, thermal stresses, and aerodynamic forces that would be encountered at the higher Mach numbers.

Another possible approach is to cool the surface by some means, such as transpiration cooling where a fluid (possibly water) is forced through the surface. Although the use of a transpiration cooling system or, for that matter, any cooling system, involves considerable design complication both in the cooling system itself and in the vehicle structure, it is a promising approach.

As a further possibility, the structure of the vehicle may be used to absorb the heat, and parts of the vehicle may be allowed to melt, if necessary. This process is one which occurs in nature for very large meteorites. Very large meteorites reach the earth's surface because they are able to absorb large amounts of heat per unit of surface area. For these meteorites, the aerodynamic heat-transfer rates are high for a short time, but only a small part of the heat can be conducted to the interior so that melting occurs at the surface while the interior remains relatively cool. Between the

[2] Numbers in parentheses refer to the Bibliography at the end of the paper.

very small and the very large meteorites which are able to reach the earth's surface, are many which are destroyed by the heat they absorb as they enter the atmosphere.

Analysis of Temperature Gradients Through the Skin of a Vehicle

To estimate the magnitude of the temperature gradients which could be encountered when the skin of the vehicle is used to absorb the aerodynamic heat input, a very simple analysis has been made.

The heat balance across the surface of the skin neglecting radiation is

$$-k\frac{dT}{dy} = h(T_{aw} - T_w) = Q$$

where k is the thermal conductivity of the skin, dT/dy is the temperature gradient through the skin at the surface, h is the heat-transfer coefficient, T_{aw} is the adiabatic wall temperature or recovery temperature, T_w is the surface temperature of the skin, and Q is the heat input to the skin. Assuming an average k of 26 Btu per hr per sq ft per deg F

$$\frac{dT}{dy} = \frac{-Q}{26}$$

which will be in degrees F per foot when Q is in Btu per square foot per hour. For the vehicle considered earlier with the laminar boundary layer (Q = 2,000,000 Btu per hr per sq ft), the maximum temperature gradient through the surface would be 6400 deg F per in. For the turbulent case, where the maximum Q was 36,000,000 Btu per hr per sq ft, the maximum gradient would be 115,000 deg F per in. Obviously, with such high gradients at the surface, the surface will get very hot and may even melt while the interior is relatively cool. Therefore a more detailed analysis is required to determine the internal gradients in the skin.

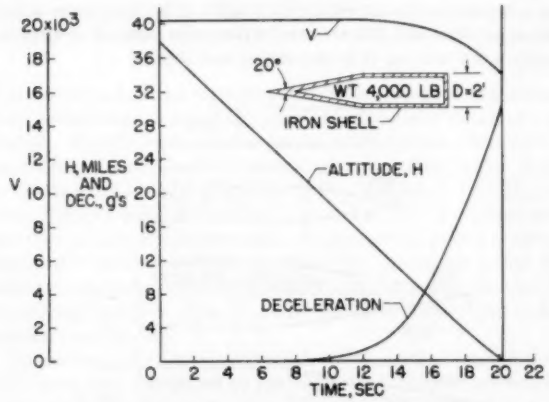

Fig. 4 Velocity, Altitude, and Deceleration of 4000-Lb 20-Deg Cone-Cylinder Vehicle During Re-Entry. $V_{entrance}$ = 20,200 Fps at 30 Deg to Horizontal

For this analysis, a 4000-lb vehicle, composed of a 10-deg semi-apex angle cone followed by a 2-ft-diam cylindrical afterbody, as shown in Fig. 4, is assumed to enter the atmosphere at 30 deg to the horizontal with a velocity of 20,200 fps at an altitude of 38 miles. This vehicle probably would be considered a relatively dense low-drag vehicle. Acceleration due to gravity has been neglected during the re-entry. The velocity, deceleration, and altitude of the configuration have been plotted against time in Fig. 4. In the absence of air, the vehicle would have reached the ground in 19.8 sec. The drag of the cone-cylinder configuration decelerates it to about 17,000 fps before it reaches the ground, 20.2 sec after passing the 38-mile level. At an altitude of about 22 miles, the vehicle began to decelerate noticeably and reached a maximum deceleration of 28 g's just before impact.

Heating of a Blunt Nose. An initially sharp nose could be expected to melt very early in the flight because very high heat-transfer coefficients will exist near the nose. To simplify the analysis, the very complex problem with the vehicle's heat-input rates and internal heat conduction at the tip of a cone has been replaced by a simple one, assuming one-dimensional heat flow in a rod with heat applied at one end. The heat input assumed is that at the stagnation point on a 1-in-radius hemisphere as calculated by the method of Sibulkin (2), which is based on incompressible flow theory applied to the stagnation point of the subsonic flow which exists between the front of a blunt body and the shock ahead of the body. The method used to obtain the temperatures in the metal was essentially the same as Dusinberre's numerical method with a variable heat input (3). The average metal characteristics used in these calculations are given in Table 1.

TABLE 1 AVERAGE METAL CHARACTERISTICS ASSUMED

	Wood's metal	Iron
Specific heat	0.04	0.15
Weight, lb/cu ft	586	487
Conductivity, Btu/hr, ft, deg F	7.7	26
Heat of fusion, Btu/lb	14	117
Melting temperature, deg F	158	2800

The variations of the temperature with time at various stations through the rod are shown in Fig. 5. At the end of about 6.5 sec,

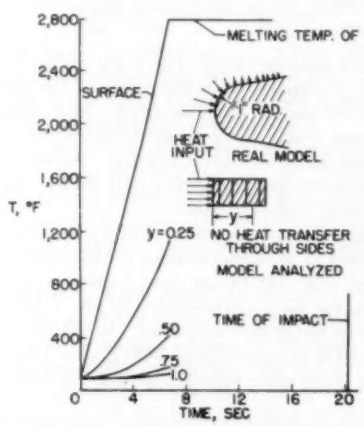

Fig. 5 Temperatures in a 1-In-Thick Iron Plate With Heat Input Corresponding to That at Stagnation Point of Vehicle Considered During Re-Entry

the end of the rod reached the melting temperature of iron (2800 F). From this time on, the metal would melt at the surface. Since the heat transfer increases rapidly with decreasing altitude, this melting would become more rapid as the simple model approached the earth. The hemispherical nose would melt at only a slightly lower altitude than this simple model.

Heating of the Side of a Cone. Of course, the tip of the cone is not the only part of the vehicle which could possibly melt. The heat-transfer rates over the remainder of the vehicle also must be considered. In order to give an idea of what might be expected over the rest of the vehicle, calculations have been made at the 4-ft station on the cone, assuming first a laminar, then a turbulent boundary layer. The heat-transfer rates are the same as those given in Fig. 3 which were based on local conditions around the

cone, with a recovery factor of 0.82 for the laminar flow and 0.88 for the turbulent flow. A ratio of specific heats of 1.4 was assumed for all calculations. A uniform initial skin temperature of 100 F was assumed since the temperatures of the vehicle would have sufficient time to equalize during the high-altitude part of the trajectory.

The calculations have been made for a 1-in-thick iron skin by the same method that was used for the nose calculations. For the laminar-flow calculation, the heat-transfer rates were obtained using the work of Van Driest (4), which is based on the Crocco method. For the turbulent case, Van Driest's work (5) was used.

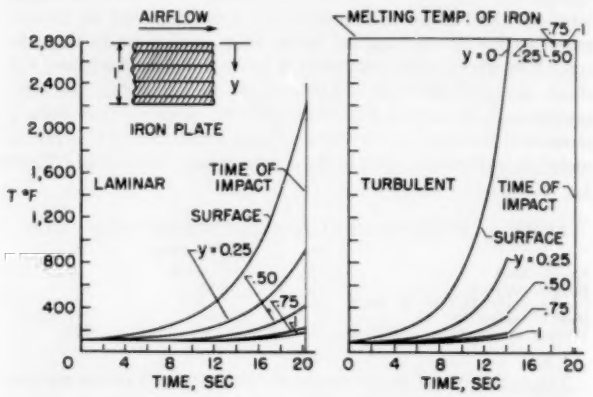

FIG. 6 TEMPERATURES IN A 1-IN-THICK IRON PLATE WITH HEAT INPUT CORRESPONDING TO THAT AT 4-FT STATION ON VEHICLE CONSIDERED DURING RE-ENTRY

With a laminar boundary layer, Fig. 6, the surface temperature reached 2200 F at impact, while the center of the plate reached only 400 F and the back of the plate 180 F. Such large temperature gradients can create many structural problems, such as distortion and even local structural failures. At stations further forward, the temperature gradients would be even greater and melting could occur before impact.

At least in the latter part of the trajectory the boundary layer would be expected to be turbulent since the Reynolds number becomes very high (125,000,000 per ft at impact). Therefore the temperatures in the plate are presented in Fig. 6 for a turbulent boundary layer for the complete re-entry. In this case, the surface reached the melting temperature of 2800 F after 14 sec, at which time the center of the plate was up to only 270 F and the back up to 140 F.

After melting has started at the surface, calculation of the heat conduction is more complicated. As a first approximation to the time required to melt each layer, all the heat is assumed to be absorbed in the outermost layer in raising the temperature to the melting point and melting that layer. These calculations also assume that, as the metal melts, it is blown from the surface so that it can no longer absorb heat. This may be true only at the very nose. Further back, there will probably be a layer of molten metal flowing over the surface.

Although these calculations indicate that the 1-in. plate would be completely melted away 1 sec before impact, the presence of the molten metal might allow the vehicle to reach impact before the plate is completely melted. Of course, the possibility of the melting process increasing the heat transfer through increased roughness should not be excluded. The time at which melting starts would not be affected materially by reducing the plate thickness to $^1/_2$ or by increasing it to an infinite thickness.

These calculations show that during the re-entry of a long-range ballistic-type vehicle, the heat-transfer rates can be high enough to melt parts of the vehicle. However, little is known about what happens when melting occurs. Meteorites which have been found, for example, have very irregular shapes. It would, therefore, be important to know, for a body in a controlled attitude, whether or not its melting is regular and predictable, and what shape it would assume. Furthermore, the melting could have an effect on the heat-transfer rates to the body and the aerodynamic forces could cause flow of the molten metal over the body which also could alter the heat transfer to the unmelted surface.

WIND-TUNNEL INVESTIGATION OF MELTING OF A BODY BY AERODYNAMIC HEATING

The problem of simulating the melting of a full-size vehicle in a wind tunnel is very complex, since the melting is influenced by the internal heat flow, the heat of fusion of the metal, the behavior of the molten metal on the surface, and the heat transfer between the liquid and solid phases of the metal. Ordinarily, the variable speed and altitude conditions obtained in flight cannot be simulated in a tunnel.

Too little is known about most of these factors to evaluate their relative importance in the relation between the melting process in the wind tunnel and in flight. However, wind-tunnel tests can be used to formulate a preliminary picture which will aid in the development of methods of analysis of the phenomena in flight vehicles. Such tests must be carried out with materials which will melt at temperatures below the recovery temperatures available in wind tunnels. Some supersonic tunnel tests have been made by Gruenewald (6), using models made from solid carbon dioxide. This material, however, sublimes rather than melts.

Testing Conditions and Configurations. An investigation was therefore undertaken to melt models by aerodynamic heating at a Mach number of 6.9, using Wood's metal which melts at 158 F. For these tests, the free-stream temperature was about —350 F while the stagnation temperature was about 700 F. The stagnation pressure for the investigation was 34 atm which gives a free-stream pressure of 0.009 atm and a Reynolds number of approximately 4,000,000 per ft in the tunnel test section.

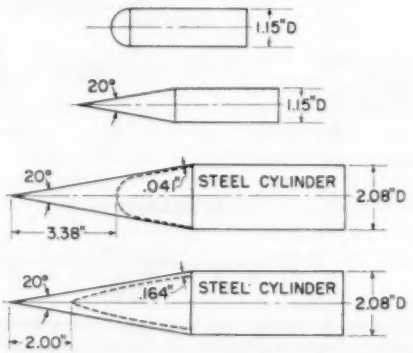

FIG. 7 WOOD'S METAL WIND-TUNNEL MODELS BEFORE MELTING

The configurations used in this investigation are shown in Fig. 7. They included a solid hemispherical-nosed cylinder, a solid cone-cylinder, a thin-walled cone, and a thick-walled cone. The solid models were 1.15 in. diam and were cast from Wood's metal. Models of these solid configurations were tested both as-cast and with machined surfaces. All the cone models had a 10-deg semi-apex angle. The thin and thick-walled models were 2.08 in. diam and were cast around cores of a low-conductivity material. The cylindrical afterbodies were made of steel. The thin-walled

model was designed to melt early in the test and the thick-walled model after about 40 sec of test time.

The melting of the models was recorded by both motion pictures and still pictures during the tests. Some pictures were taken directly, while others were taken through a Schlieren system in which density changes in the air, such as those occurring through shocks, are visible.

Analysis of Temperature Gradients in Model. In an attempt to test the validity of the methods used in determining the onset of melting in the vehicle, the same method was used to calculate the time of onset of melting in the tunnel models. Theoretical heat-transfer rates had not been verified previously for the high Mach number of these tests. Therefore a preliminary investigation of the heat transfer to hemispherical-nosed and conical-nosed bodies was carried out on hollow steel models. These heat-transfer rates have been applied to the two solid-nosed bodies and the results are presented in Fig. 8. The total

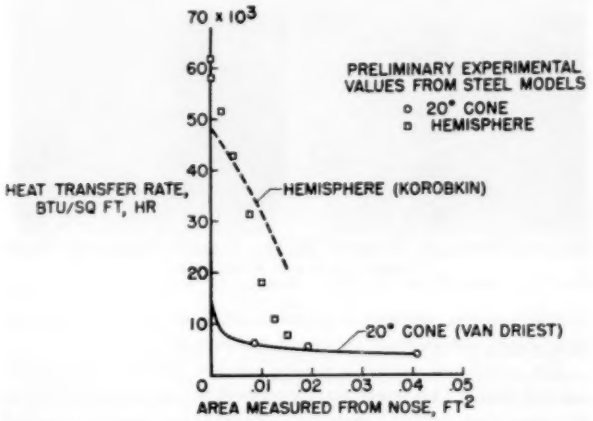

FIG. 8 THEORETICAL AND EXPERIMENTAL LAMINAR HEAT-TRANSFER RATES TO HEMISPHERE AND 20-DEG CONE AT MACH NUMBER 6.9

area under each curve represents the heat-input rate to the nose. Both experimental and theoretical heat-transfer rates are included. For the cone-cylinder model, a theoretical curve is presented which was calculated, assuming laminar flow (which would be obtained on a model of this size in the Langley 11-Inch Hypersonic Tunnel), using the work of Van Driest (4). A surface temperature of 158 F was assumed. Experimental points obtained from the steel cone-cylinder model of the same size under the same tunnel conditions are in excellent agreement with the theory. An average heat-flux value of around 5000 Btu per sq ft per hr was obtained on the cone.

On the hemispherical-nosed model, the theoretical heat-transfer rates have been calculated by use of the heat-transfer coefficients developed by Sibulkin and presented by Korobkin (7). This work is based on incompressible flow theory applied to the region of subsonic flow which exists in front of blunt bodies in supersonic flow. Recovery temperatures which were used with these heat-transfer coefficients were obtained by calculation of the pressures around the nose by Newtonian impact theory which has been found to be reasonably accurate for bodies at high supersonic Mach numbers (8). The Mach numbers were then calculated assuming isentropic flow on the streamline just outside the boundary layer. A recovery factor of 0.825 was used, based on the local conditions just outside the boundary layer. The maximum value of heat transfer at the nose is about 48,000 Btu per sq ft per hr from these calculations, Fig. 8.

The heat transfer to the hemispherical nose as obtained from experimental results from the hollow steel model was a maximum of about 62,000 Btu per sq ft per hr at the stagnation point and decreased more rapidly with distance from the stagnation point than the theoretical values. This disagreement between the theoretical and experimental heat-transfer rates is not surprising since the theoretical model of the subsonic-flow field without a shock does not accurately represent the real flow field at high supersonic speeds. The average heat-transfer rate on the hemispherical nose is about seven times the average value on the cone.

Since only an indication of the approximate time at which melting starts is required, a simple one-dimensional analysis of the variation of the temperature down the length of a flat-ended Wood's metal rod has been made with two constant heat-input rates applied to one end of the rod. One of these heat-input rates was approximately equal to the rate at the stagnation point of the hemispherical-nosed model and the other corresponded to the rate at a point near the nose of the cone models. The same type of numerical analysis that was applied to the nose of the full-size vehicle was used with the metal characteristics given in Table 1. With a heat input of 62,000 Btu per sq ft per hr, which is approximately the value at the nose from the hemispherical-model tests, the heated end of the rod reached the melting temperature in approximately 0.7 sec. The analysis also showed that on the blunt nose of the model, the melting temperature would be reached at the surface with little change in the internal temperatures of the model. The hemispherical-nosed model would be expected to start to melt in approximately the same length of time.

With a heat input of 8000 Btu per sq ft per hr, the temperature at the heated end of the rod was only 140 F at the end of 40 sec. Although the heat flow in the cone cannot be considered one-dimensional, inspection of the temperature gradients in the rod with this heat input, which is considerably greater than the average cone value of 5000 Btu per sq ft per hr, indicates that the rate of surface-temperature rise on the cone would be of the same order, and the model would not be expected to melt on the cone surface during the testing time of 40 to 50 sec.

Results of Melting Tests. The results of the melting tests of the solid models are presented in Figs. 9 and 10. These photographs of the models as they melted were obtained from the 16-mm motion-picture film. It must be emphasized that these tunnel tests were made at a constant Mach number, air temperature, and density.

The hemispherical-nosed model, as well as the cone cylinder, were observed to start melting almost immediately with the start of the air flow in the nozzle. Because of the short time involved, during which the air-flow conditions were not yet steady, it was impossible to determine if the onset of melting would have occurred exactly at 0.7 sec after the start of the flow as predicted by the calculations. On the hemispherical-nosed model, melting started at the center of the nose and rapidly spread to cover the entire hemisphere during the first 10 sec, after which the nose shape remained constant for the rest of the run. The stable shape was considerably blunter than the original hemisphere. The fact that the melting started on the blunt surface almost immediately with the start of the flow, indicated that the heat-transfer rate of about 62,000 Btu per sq ft per hr to the blunted surface was much greater than could be conducted away from the surface layer.

On the conical-nosed models, melting started on the tip, producing an approximately spherical-blunted nose, which grew in radius as it moved back on the cone. As predicted, the sides of the cone, where the heat-transfer rate is approximately $^1/_7$ that of the blunted surface, did not melt. If the heat-transfer rate were increased sufficiently, melting also would occur on the sides during the testing time. The melting rates of the noses of both of these models were regular and could be repeated.

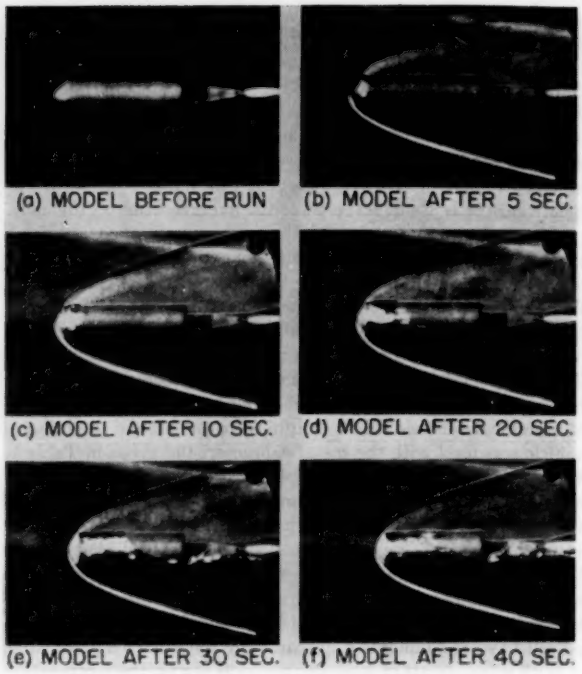

FIG. 9 MELTING OF SOLID HEMISPHERICAL-NOSED CYLINDER IN WIND TUNNEL AT MACH NUMBER 6.9

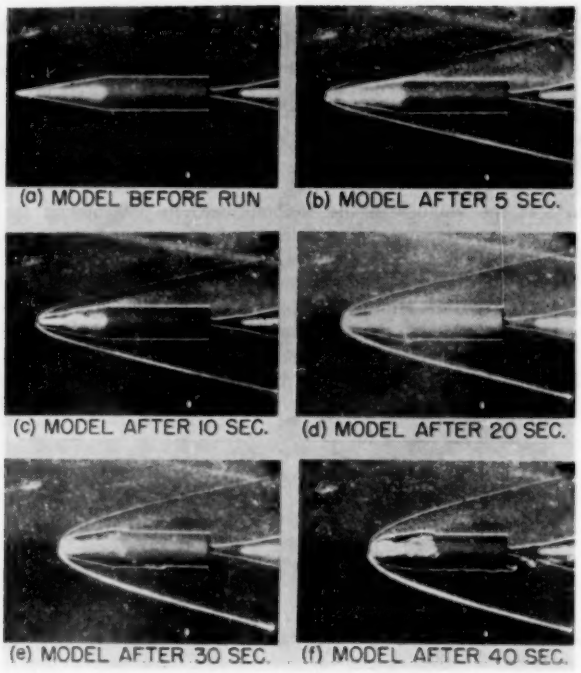

FIG. 10 MELTING OF SOLID 20-DEG CONE-CYLINDER IN WIND TUNNEL AT MACH NUMBER 6.9

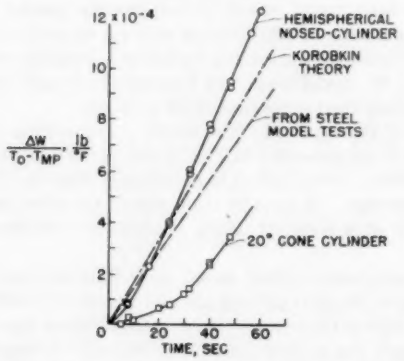

FIG. 11 WEIGHT LOSS OF MODELS DURING MELTING IN WIND TUNNEL

From profiles obtained from both still and motion pictures, the weight losses were calculated and these are presented in Fig. 11. The weight loss is divided by the temperature difference between the melting temperature and stagnation temperature in order to compensate for the variation of stagnation temperature between runs. The hemispherical-nosed model reached a constant rate of metal loss after about 10 sec. The change in shape of the curve in the first 10 sec is probably due to the heating of the entire nose up to the melting point and to the shape changes while establishing a stable shape. The cone showed an extremely low initial rate of loss of metal; however, at the end of the tests it was rapidly approaching the same rate of loss as the hemispherical-nosed model.

The rate of metal loss for the hemispherical-nosed model was calculated by the same theoretical procedure that was used for Fig. 8, and also from the experimental heat-transfer values obtained from the steel-model tests. All the heat input over the hemisphere was assumed to go into melting of the metal, and the nose shape was assumed to remain hemispherical.

The calculated values of weight loss are less than the experimental ones. This is not surprising because the actual shape of the nose, after melting has started, is more blunt than the assumed hemisphere. Since the disagreement is not large, it is clear that the melting of the surface has not resulted in a large increase in heat-transfer rate.

In order to obtain conditions in which melting would occur on some part of the model other than the blunted nose, a thin and a thick-walled conical-nosed model were tested. The melting of these models is shown in Figs. 12 and 13, which were obtained from 16-mm motion-picture films of the melting.

The melting of the thin-walled model, which was intended to melt on the cone surface early in the test, is shown in Fig. 12. The thin wall failed after about 18 sec. In contrast to the steady melting which was observed on the solid models, the entire thin wall failed very shortly after the melting of the outside of the wall had started, which indicates that the inner surface of the wall reached the melting point at approximately the same time as the outer surface. With a heat input of about 4000 Btu per hr per sq ft, a temperature difference of less than 1 deg F would be expected across this approximately 0.04-in-thick wall.

Fig. 13 shows the melting of the thick-walled model. The white ring around the model in Fig. 13(*a*) was a paper ring which was blown from the model at the start of the flow to indicate zero time on the film. Although actual melting had not started on the conical surface at 20 sec, a change in the surface texture can be seen in the $^3/_4$ front view. For these tests, the temperature on the inside of the cone shell was only a few degrees lower than on the outside surface. To simulate the large temperature gradients in the skin, much higher heat-transfer rates or a material with a much lower conductivity would be required. The core was just beginning to show at 36 sec and is plainly visible at the nose in

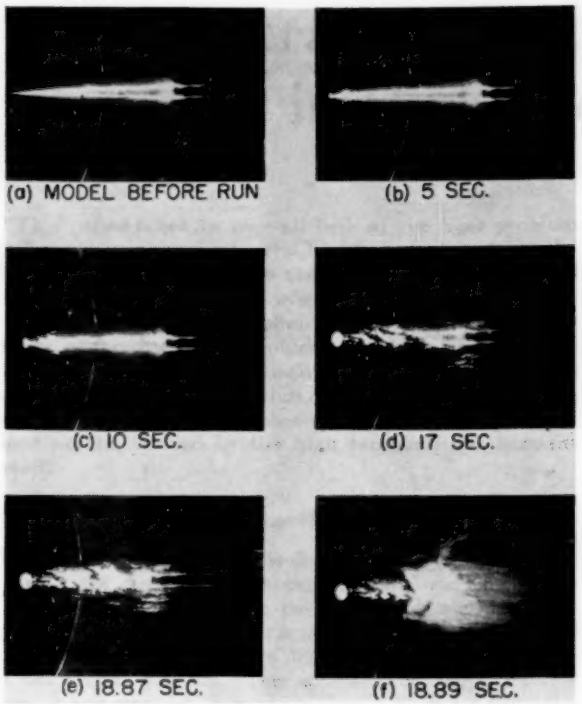

FIG. 12 MELTING OF THIN-SHELL MODEL IN TUNNEL AT MACH NUMBER 6.9

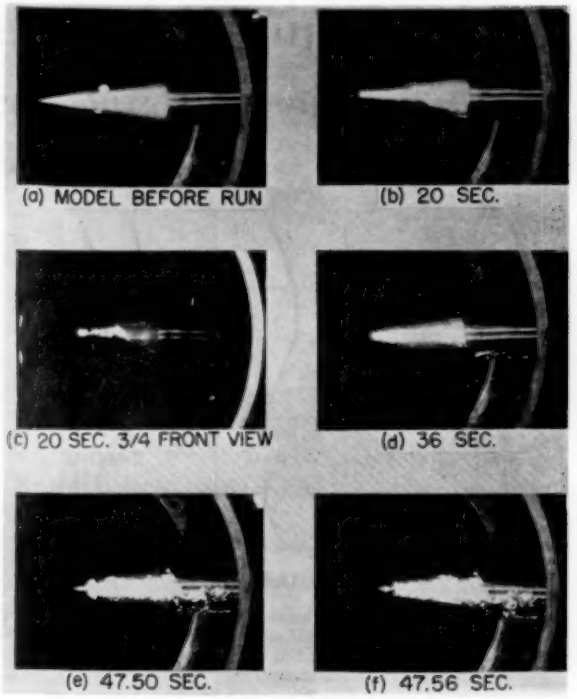

FIG. 13 MELTING OF THICK-SHELL MODEL IN TUNNEL AT MACH NUMBER 6.9

the two lower pictures. During the approximately 0.06 sec between Figs. 13(*e* and *f*), a considerable amount of molten metal was suddenly blown from the surface. This indicated that a thin layer of molten metal could be retained on the surface under the test conditions, but that when the layer became too thick, it was shed suddenly. In the case of an actual vehicle, the retention of molten metal on the surface could reduce the melting rate, since a part of the aerodynamic heat input could be absorbed in heating the liquid metal.

CONCLUDING REMARKS

Long-range vehicles using ballistic trajectories are subjected to enormous heat-transfer rates for very short periods of time during the re-entry into the earth's atmosphere. The heat-transfer rates may be great enough to melt the nose of the vehicle and, in some cases, the sides. Some aspects of the melting problem can be studied in wind tunnels by the use of low-melting-temperature materials. Preliminary tests in the NACA Langley 11-Inch Hypersonic Tunnel have shown that the melting is an orderly and reproducible process. Melting occurred only on the nose of the solid bodies in the tunnel because the heat-transfer rates were sufficiently low over the remainder of the bodies so that much of the heat could be conducted to the interior. In flight, where the heat-transfer rates can be very high, the melting might also occur at parts of the body other than the nose regardless of the skin thickness. In the tunnel tests the melting process on the blunt nose did not appear to alter greatly the heat-transfer rates.

BIBLIOGRAPHY

1 "Meteoritic Phenomena and Meteorites," by F. L. Whipple, Physics and Medicine of the Upper Atmosphere, A Study of the Aeropause, The University of New Mexico Press, Albuquerque, N. M., first edition., 1952, pp. 137–170.

2 "Heat Transfer Near the Forward Stagnation Point of a Body of Revolution," by M. Sibulkin, Readers Forum, *Journal of the Aeronautical Sciences*, vol. 19, no. 8, August, 1952, pp. 570–571.

3 "Heat Transmission," by W. H. McAdams, McGraw-Hill Book Company, Inc., New York, N. Y., third edition, 1954, p. 44.

4 "Investigation of Laminar Boundary Layer in Compressible Fluids Using the Crocco Method," by E. R. Van Driest, NACA TN 2597, January, 1952.

5 "Turbulent Boundary Layer on a Cone in a Supersonic Flow at Zero Angle of Attack," by E. R. Van Driest, *Journal of the Aeronautical Sciences*, vol. 19, no. 1, January, 1952, pp. 55–57.

6 "Drag and Evaporation of Dry Ice Models in Supersonic Air Flow," by K. H. Gruenewald, NAVORD Report 2954, September, 1953.

7 "Local Flow Conditions Recovery Factors and Heat-Transfer Coefficients on the Nose of a Hemisphere-Cylinder at a Mach Number of 2.8," by I. Korobkin, NAVORD Report 2865, May, 1953.

8 "Exploratory Wind-Tunnel Investigation of Wings and Bodies at M = 6.9," by C. H. McLellan, *Journal of the Aeronautical Sciences*, vol. 18, no. 10, October, 1951, pp. 641–648.

Temperature Problems of Equipment in High-Speed Aircraft

By H. W. ADAMS,[1] SANTA MONICA, CALIF.

This paper takes an over-all look at the heat problem facing the equipment in the high-speed aircraft of the future. It discusses briefly the basic problem—the high temperatures that result when a body moves rapidly through the air; the kind of airplane and equipment that might be faced with the problem; methods of combating the problem; and the alternatives that are available to the airplane designer. The author concludes that up to speeds of 2 or 3 times the speeds that we are now flying, aircraft need not be limited by the high temperatures encountered.

Introduction

WHEN considering equipment problems confronting the designer of high-speed aircraft, one must decide whether to consider the detail problems of the immediate future, or to take a more over-all look. Since the detail problems of every airplane are different, this paper looks more at the over-all problem. This approach, of course, involves broader and more nebulous assumptions. There are four parts to the over-all approach that will be discussed in this paper: (1) The basic problem, the high temperatures that result when a body moves rapidly through the air; (2) the kind of airplane and equipment that might be faced with this problem; (3) a brief look at probable methods of combating the temperature problem; and (4) the choice between the alternatives available to the airplane designer.

The Basic Temperature Problem

There are three factors in the basic temperature problem that appear significant: (*a*) The temperature of the air surrounding the moving aircraft, which is principally a function of the speed of the aircraft; (*b*) the rate of heat input which, for any given speed, depends on air density; and (*c*) the rate of heat loss due to radiation, which is important at high temperatures.

Fig. 1 shows the variation of temperature versus altitude at Mach numbers up to 6. These are the nearly vertical lines on the figure. The temperature variation with altitude at Mach 0 is the NACA standard temperature. At higher Mach numbers, the temperature versus altitude curves are simply displaced to the right, indicating that the temperature rise does not vary with altitude but only with Mach number. The temperature that is plotted here is the temperature of the layer of air passing over the skin of the aircraft and is assumed to be 88 per cent of the stagnation temperature.

It is apparent from these figures that we cannot get away from high temperatures by flying higher. The possible flight limits for future supersonic aircraft also are shown in Fig. 1. The curve,

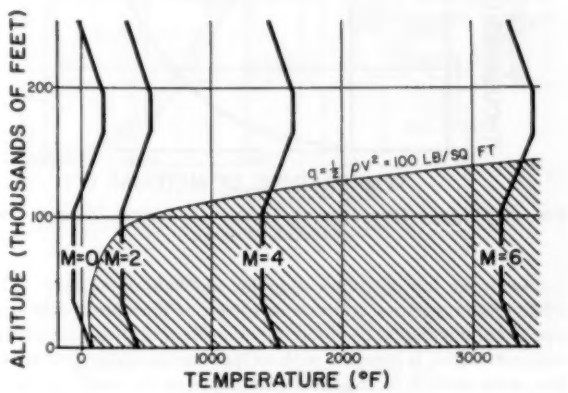

Fig. 1 Variation of Temperature Versus Altitude at Mach Numbers Up to 6

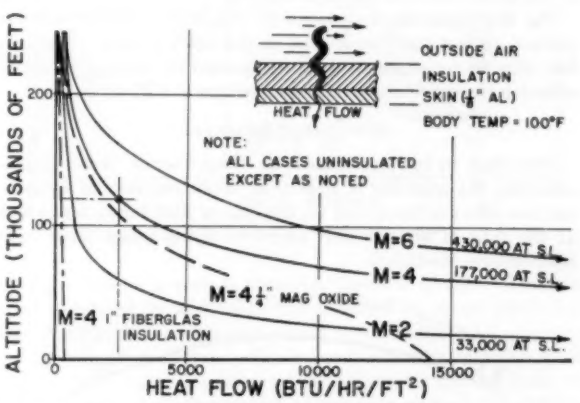

Fig. 2(*a*) Heat Input Into Airplane Versus Altitude for Mach Numbers 2, 4, and 6

q = 100 psf, is plotted at the altitude at which an airplane with a wing loading of 100 psf would stall with a lift coefficient of 1. Thus no reasonably proportioned airplane is likely to fly above this altitude.

Throughout this paper, most studies requiring fixed altitudes have been made at 20,000, 70,000, and 120,000 ft with the intent of bracketing the altitude range of future airplanes.

Heat Input Versus Altitude. Fig. 2(*a*) shows the heat input into the airplane plotted against altitude for Mach numbers 2, 4, and 6. The three solid curves show the heat transfer to the skin of a conventional uninsulated aircraft. It is apparent that the heat input varies tremendously with altitude. At Mach 4, for example, the heat input at 120,000 ft, about 2000 Btu per hr per sq ft, is only a little over 1 per cent of the heat input at sea level, which is 177,000 Btu per hr per sq ft. The dotted curves show the effect of insulating the outside skin of the aircraft; the effect is small at high altitudes but becomes large at low altitudes. At Mach 4, the effect of $^1/_4$-in. magnesium-oxide insulation is to reduce the heat flow slightly at high altitudes and

[1] Chief Design Engineer, Douglas Aircraft Company, Inc.

Contributed by the Aviation Division and presented at a joint session of the Aviation Division, American Rocket Society, and The Society of Automotive Engineers, at the Annual Meeting, New York, N. Y., November 28–December 3, 1954, of The American Society of Mechanical Engineers.

Note: Statements and opinions advanced in papers are to be understood as individual expressions of their authors and not those of the Society. Manuscript received at ASME Headquarters, September 17, 1954. Paper No. 54—A-131.

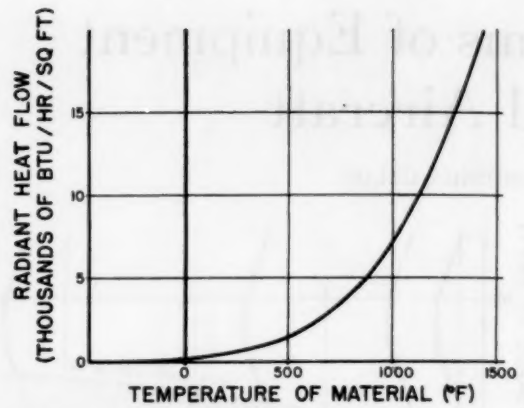

FIG. 2(b) HEAT LOSS DUE TO RADIATION VERSUS TEMPERATURE OF OUTER SURFACE

markedly at low altitudes over an uninsulated surface. The effect of an insulation equivalent to 1 in. of fiberglas is still more marked and it should be noted that the effect of altitude is greatly reduced. This is because, with so high an available heat input, the outer surface of the insulation heats up to nearly the same temperature at any altitude and the heat flow through the insulation is then a function of the temperature difference and not of the heat input into the outer surface.

Fig. 2(*b*) shows the heat loss from the airplane due to radiation plotted against the temperature of the outer surface. The high loss due to radiation at high temperatures is a major factor affecting the equilibrium skin temperature at high altitudes.

SUPERSONIC AIRCRAFT

Now that we have examined the "heat barrier" as to its temperature, the quantity of heat that it can put into an airplane, and the effect of insulation on the rate of heat input, let us look at the type of aircraft that might be flying under these high-temperature conditions.

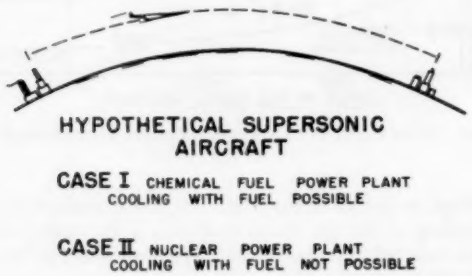

FIG. 3 TYPES OF SUPERSONIC AIRCRAFT DEFINED

Fig. 3 defines two different types of supersonic aircraft. In the first type a chemically fueled power plant is used, and in the second type a nuclear power plant is used. The reason for distinguishing between these types is that one possible system of cooling takes advantage of the heat capacity of the liquid fuel. This is possible in the aircraft of Case I, but not in the aircraft of Case II.

Two types of mechanical components in an airplane are affected by temperature. One is the type that might be called "passive" equipment similar to structure in that it does not generate heat of itself; the second is what might be called "active" equipment which does generate heat in operation—an engine and a radio set are equipment of the active type.

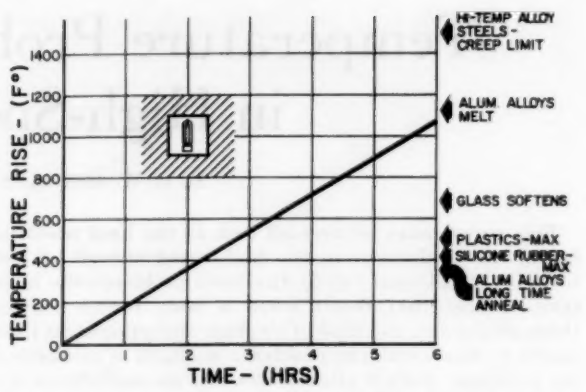

FIG. 4 RATE OF TEMPERATURE INCREASE VERSUS TIME FOR UNCOOLED AND PERFECTLY INSULATED ELECTRICAL UNITS

Fig. 4 shows the rate of temperature increase against time for electrical units if the units were uncooled and perfectly insulated so that their temperature increased linearly with time. Actually, electrical units may require cooling before they reach the limiting temperature because Fig. 4 assumes the temperature rise is absorbed evenly throughout the unit. One reason why the rate of heat increase is important is because at extremely high speeds the time of flight is quite short and in some cases transient effects must be considered. Significant temperature limits of materials also are shown in Fig. 4.

ATTACKING THE HEAT PROBLEM

There are two basic ways of attacking the heat problem of both active and passive equipment. The first approach is to design the aircraft to endure the high temperatures. This might be possible at low Mach numbers with some structural materials and with simple equipment. It is the simplest solution from the airplane designer's point of view because it avoids the necessity for cooling systems except for the pilot, but it appears at the present time to present almost insurmountable problems of equipment development at even moderately high Mach numbers. Since each airplane and its equipment present a different problem in this respect, this approach will not be pursued further.

The second approach is to keep the equipment cool so that conventional designs can be used. Even here the airplane designer is faced with two choices, the first being to insulate the airplane and equipment with no provision for cooling. The success of this method depends on a low rate of heat rise and a short time of flight to keep the equipment below its limiting temperature. The second approach is to provide some form of cooling system.

Insulation Without Cooling. Fig. 5 illustrates the first approach, that of using insulation without cooling. It shows the transient temperature of passive equipment or structure, plotted against time of flight, for various altitudes, at Mach 4.

At 20,000 ft the temperature of an uninsulated airplane skin reaches equilibrium in about 1 min; with $^1/_4$-in. magnesium-oxide insulation it takes nearly 10 min., and with insulation equivalent to 1 in. of fiberglas, the temperature after 20 min is 425 F.

At 120,000 ft with uninsulated structure, the skin temperature after 20 min would be about 510 F; with $^1/_4$-in. magnesium-oxide insulation, about 390 F; and with insulation equal to 1 in. of fiberglas the skin temperature after 20 min would be only about 225 F. The reduction in equilibrium temperature from the boundary-layer air temperature of 1440 F to about 1240 F at 20,000 ft is due to radiation heat loss. At 120,000 ft, because of the lower

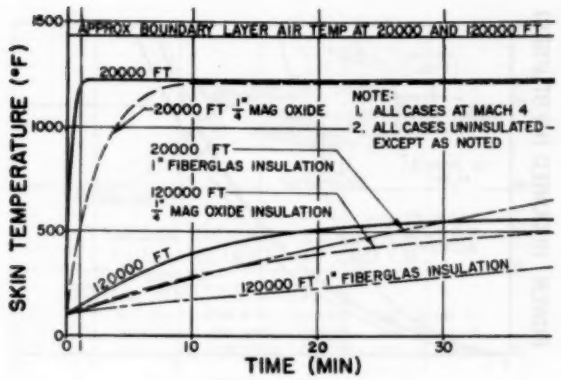

FIG. 5 USE OF INSULATION WITHOUT COOLING

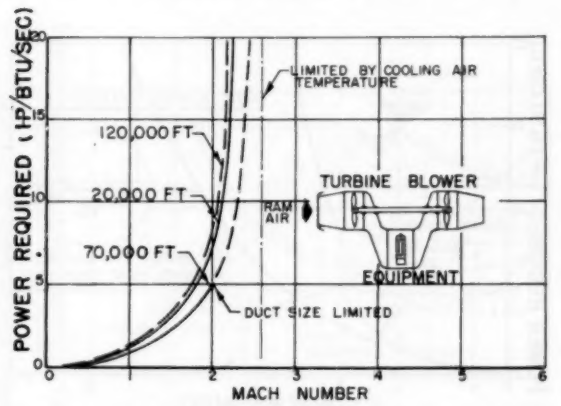

FIG. 6 COOLING HORSEPOWER VERSUS MACH NUMBER FOR SIMPLE FORMS OF AIR-CYCLE COOLING

heat input from the air stream, radiation reduces the equilibrium temperature from 1440 F to 570 F.

Cooling System Provided. The second approach is to provide some sort of cooling system. Some of the cooling systems that have been used in the past have been examined to determine their suitability for use in high-speed, high-altitude aircraft. These cooling systems fall into three general classes: (1) Air-cycle systems, (2) water-evaporation cooling systems, and (3) fuel cooling. Fuel cooling is possible of course only in chemically fueled aircraft.

Air-Cycle Cooling. Fig. 6 shows a plot of cooling horsepower required versus Mach number for one of the simple forms of air-cycle cooling. A turbine expands and cools ram air. Its power is absorbed by a blower which partially recompresses the expanded air. As speed increases, the minimum attainable cooling-air temperature rises. If a maximum permissible equipment temperature of 250 F is assumed, the cooling-air temperature reaches this value at about Mach 2.6 using the turbine and blower efficiencies assumed in this study. Because the cooling-air temperature approaches 250 F, the cooling airflow, and therefore the power required, approaches infinity as Mach 2.6 is approached. As temperatures and airflows increase, duct sizes also increase. If a reasonable duct-size limit is chosen (in this case 20 sq in. per Btu per sec) then systems operating at 70,000 ft will have excessive duct sizes if designed for operation at speeds above Mach 2. At 120,000 ft the duct sizes required to conduct the low-density air at this altitude are above the duct-size limit at any speed. Below the duct-size limit the curves are drawn solid; above the duct-size limit they are dotted.

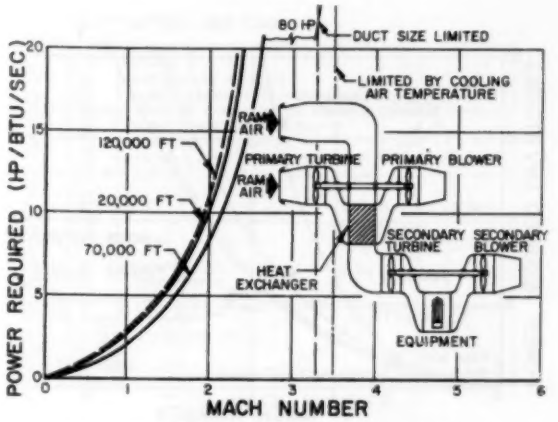

FIG. 7 TWO-STAGE VERSION OF SYSTEM IN FIG. 6

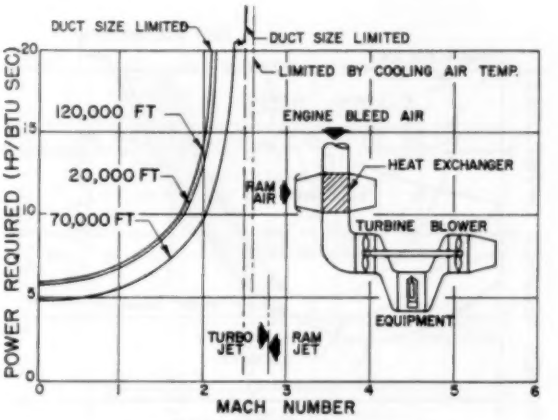

FIG. 8 TURBOJET BLEED SYSTEM

Fig. 7 shows a two-stage version of the same system. This system is limited by cooling-air temperature at about Mach 3.5. At 70,000 ft its duct-size limit occurs at about Mach 3.3.

Turbojet Bleed System. Fig. 8 shows a system in which air is bled from a turbojet engine, passed through a ram air-heat exchanger, then through a turbine-blower expansion cooling system. In this case, because the system uses compressed air from the engine, the duct-size limit is not reached until about Mach 2.1 at 120,000 ft and at about Mach 2.5 at 70,000 ft. The system is limited by minimum attainable cooling-air temperature at about Mach 2.6. A dividing line between turbojet and ram-jet airplanes is shown at about Mach 2.8. This speed was chosen as the speed where the turbojet compression ratio must be reduced to 1 in order that its turbine temperature, after fuel burning, does not exceed permissible turbine temperatures. Thus, above Mach 2.8, the engine bleed system becomes a ram system.

Water-Evaporation Cooling System. The second distinct type of cooling system is the water-evaporation cooling system. With some types of equipment direct water cooling may be possible. The horsepower required in this case would be zero although, of course, there is a weight penalty to the airplane as a result of the water consumption.

Fig. 9 shows a system in which a water evaporator in combination with a turbine-blower expansion cooling system is used to provide cold air for equipment cooling. It can be seen that the use of water evaporation permits the aircraft to go to higher Mach numbers before it reaches the limiting duct size or tempera-

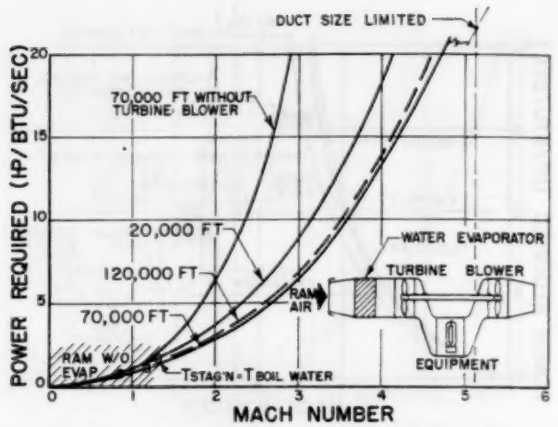

FIG. 9 WATER-EVAPORATION COOLING SYSTEM

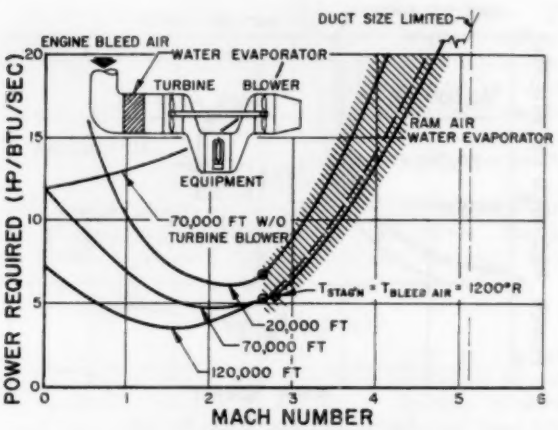

FIG. 10 WATER EVAPORATOR USED TO COOL ENGINE BLEED AIR

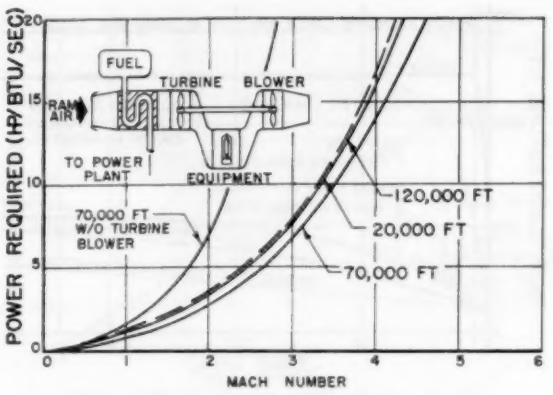

FIG. 11 TYPE OF FUEL AIR-HEAT EXCHANGER SYSTEM

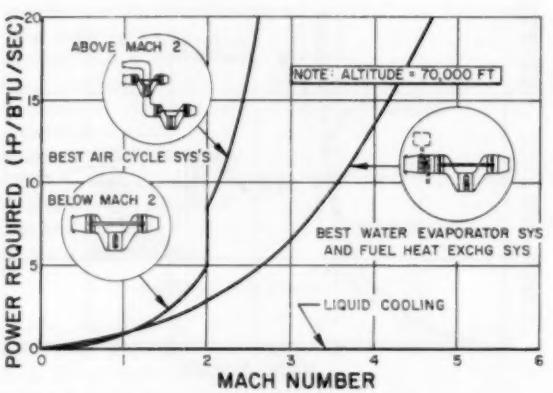

FIG. 12 SUMMARY OF THE BEST COOLING SYSTEMS

ture. At 70,000 ft the duct-size limit is reached at about Mach 5.1. The left-hand curve shows the effect of omitting the turbine and blower. The result is a higher horsepower consumption; this is because the air used for equipment cooling is not as cold and therefore a larger quantity is required than if a turbine blower is used.

Evaporator Used to Cool Engine Bleed Air. Fig. 10 shows a water evaporator used to cool engine bleed air rather than ram air. Since the engine becomes a ram jet above Mach 2.8, the curves in this region (cross-hatched in the figure) are identical with the ram air-water evaporator system of Fig. 9. Below about Mach 2, the horsepower required increases again because of the inefficiency associated with using high-pressure air.

Fuel Heat-Exchanger System. In the case of the chemically fueled airplane, one more system of cooling is possible. This is the use of a fuel heat exchanger where the heat capacity of the fuel is used as a "heat sink." As in the case of water-evaporation cooling, direct fuel cooling is possible and involves no horsepower penalty to the airplane. Where air, rather than liquid, is required for cooling, a system of the type shown in Fig. 11 is required. In this case, ram air passes through a fuel heat exchanger, then through a turbine-blower system. The horsepower curves here are identical with the horsepower curves for the water-evaporation system. Of course the weight penalty to the airplane resulting from the water consumption of the water-evaporation system is not present in the case of the fuel-air heat exchanger. The quantity of heat that can be absorbed is limited by the engine fuel flow and the maximum temperature rise permitted. A 400 F rise has been assumed throughout this paper, which requires fuel pressures on the order of 120 psi to avoid vaporization.

Fig. 12 summarizes the best cooling systems, from a horsepower standpoint, for altitudes of 70,000 ft. Below Mach 2, the best air-cycle system is the ram-turbine and blower system. Above Mach 2, the compound ram-turbine and blower system is better On this same basis, the water-evaporator and the fuel heat-exchanger systems are equal, and are better than air-cycle systems for all speeds above Mach 1.

THE DESIGNER'S CHOICE

Now that we have seen what performance might be expected from cooling systems, let us examine the choices facing the designer of a hypothetical high-speed aircraft of the future. This aircraft might look something like the aircraft shown in Fig. 13. Three wing loadings have been shown to give reasonable performance through a range of altitudes and Mach numbers.

Fig. 14 shows the performance of this family of hypothetical aircraft. It will be noted that the drag curves and the fuel-consumption curves are identical. The values are simply read from different scales. This is because a fuel consumption of 3 lb per lb thrust per hr was assumed for all Mach numbers. This is about the present fuel consumption of jet engines with afterburners at low supersonic Mach numbers, and theoretical considerations indicate that if efficient air intakes can be developed, fuel consumptions of this order are still possible at high Mach

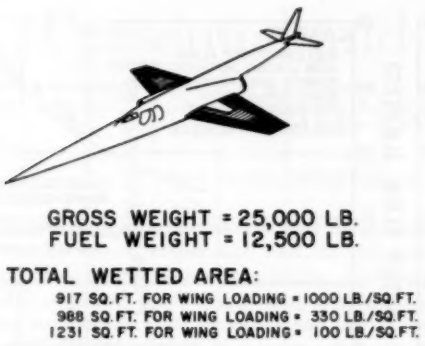

FIG. 13 TYPES OF AIRCRAFT OF THE FUTURE

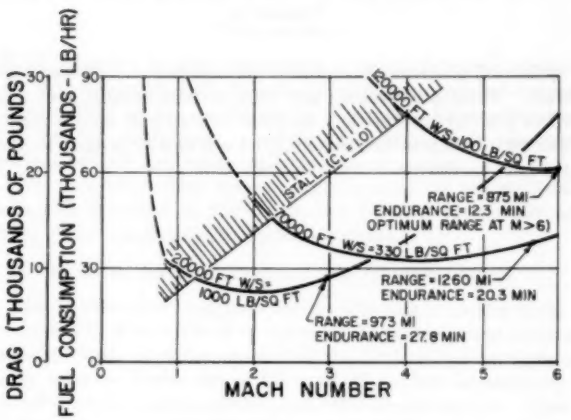

FIG. 14 PERFORMANCE OF HYPOTHETICAL AIRCRAFT

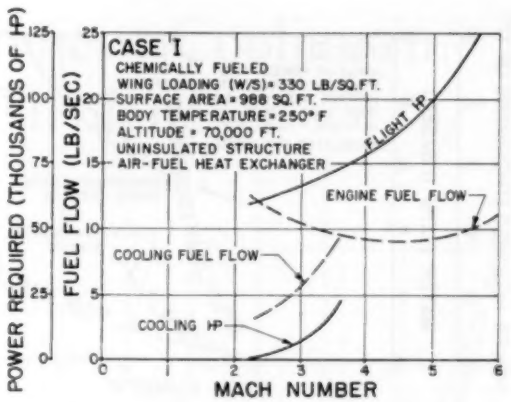

FIG. 15 DESIGN SUMMARY FOR CHEMICALLY FUELED AIRCRAFT

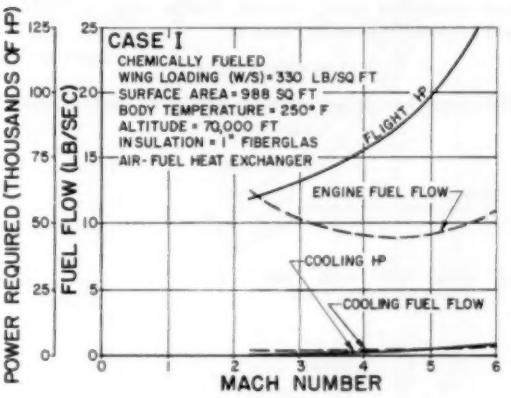

FIG. 16 AIRCRAFT INSULATED WITH EQUIVALENT OF 1 IN. OF FIBERGLAS

numbers. At Mach 6 this fuel consumption would correspond to 0.26 lb per hp hr, which is not impossible considering the high compression ratio associated with this speed.

The airplane with a wing loading of 1000 psf at 20,000 ft would have a stalling speed somewhat above Mach 1. Its minimum drag and fuel consumption occur at about Mach 2 and its maximum range occurs at about Mach 3.

At 70,000 ft the airplane having a wing loading of 330 psf would have a stalling speed above Mach 2, minimum drag and fuel consumption at Mach 4.5, and maximum range at a speed of Mach 5.6. It is interesting to note that this aircraft would have a range of about 1260 miles, which it would cover in 20 min.

The aircraft flying at 120,000 ft with a wing loading of 100 psf would have a stalling speed of Mach 4, have its minimum drag at Mach 5.8, and its maximum range at some higher Mach number. At Mach 6 the range would be 875 miles and it would be able to fly for 12 min.

Up to now we have looked at the basic heat problem and several kinds of airplane and equipment that might be encountering this problem; let us now look at the choices facing the airplane designer.

HORSEPOWER REQUIRED FOR COOLING

Fig. 15 shows a design summary for the chemically fueled aircraft with a wing loading of 330 psf, flying at an altitude of 70,000 ft. The horsepower required varies from less than 60,000 hp at Mach 2 to above 120,000 hp at Mach 6. The engine fuel flow is on the order of 10 lb per sec. With the aircraft uninsulated, the entire engine fuel flow would be required to cool the airplane at Mach 3.5, and the cooling horsepower, assuming an air-fuel heat exchanger, would be about 25 per cent of the horsepower required for flight.

If, as in Fig. 16, the aircraft were to be insulated with insulation equal to 1 in. of fiberglas, the cooling horsepower would be only a few per cent of the horsepower required for flight and the fuel flow required for cooling would be on the order of 10 per cent of the engine fuel flow.

It has been assumed that the whole aircraft is insulated because this is the critical case. If temperature-resistant materials are used for portions of the structure, and a smaller part of the aircraft is insulated, the horsepowers and fuel flows are lower.

In Fig. 17 the same data are presented for an uninsulated aircraft having a nuclear power plant, where fuel cooling is not possible. For this aircraft, it can be seen that the cooling horsepowers start to rise rapidly in the region of Mach 2 if air-cycle cooling systems are used. If a water-evaporator system is used, the cooling horsepower equals the flight horsepower at about Mach 4.9 and the water flow would be such that the airplane range would be limited to about 2400 miles, assuming half of the take-off weight of the airplane to be water.

If, as in Fig. 18, this same aircraft were to be insulated with insulation equal to 1 in. of fiberglas, the cooling horsepower would be on the order of 5 per cent of the flight horsepower and the re-

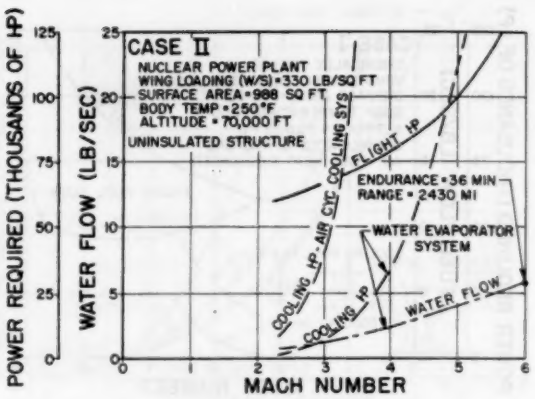

FIG. 17 UNINSULATED AIRCRAFT FOR A NUCLEAR POWER PLANT WHERE FUEL COOLING IS NOT POSSIBLE

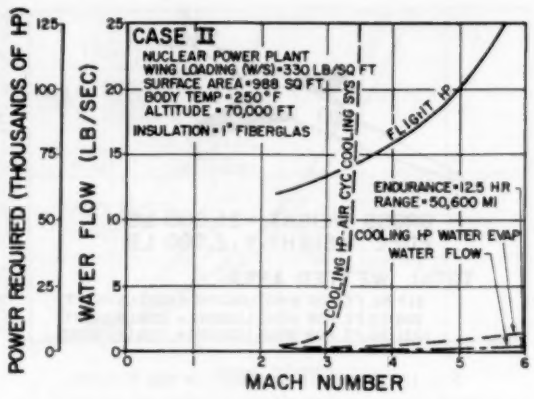

FIG. 18 AIRCRAFT OF FIG. 17 WITH INSULATION EQUAL TO 1 IN. OF FIBERGLAS

quired water flow would be such that a range of 50,000 miles would be possible even at Mach 6.

CONCLUSION

This paper has presented, very briefly, an over-all look at the equipment problems confronting the designer of high-speed aircraft. These problems do not seem insurmountable, and even when the day arrives that we think our aircraft speeds will be limited by temperature, certainly, we will find ways again to push the heat barrier out into the future.

Personnel and Equipment Cooling in Supersonic Airplanes

By J. MAKOWSKI[1] and V. L. WHITNEY, JR.,[2] BAY SHORE, L. I., N. Y.

Cooling of crew compartments and electronic equipment becomes more important and, at the same time, more difficult as airplane speeds increase. A sharp increase in capacity required from the cooling system takes place when the surrounding air becomes too hot to be a convenient direct heat sink. The successful use of water vaporization permits the design of compact cooling units which satisfy the requirements of supersonic airplanes.

Introduction

INCREASES in flight speeds over a period of years, together with the growing use of electronic equipment, present serious problems to the manufacturer of airplane air-conditioning and cooling equipment. Conventional simple-type air-cycle systems become inadequate in supersonic airplanes.

The air-cycle cooling system, supplemented by the artificial heat sink described in this paper, can be used successfully in today's and tomorrow's supersonic airplanes.

Several Factors Influencing Cooling Loads

The manufacturer of airplane air-conditioning or cooling equipment usually does not have to calculate the compartment cooling loads involved. In order to calculate the airplane cooling loads, a fairly accurate knowledge of the type of airplane is necessary, i.e., of its shape, speed, mission, and other similar factors. Most of this information is usually kept secret for new airplanes. Cooling-load values which are given to the manufacturer show an extremely fast increase as the speed of the airplane is increased.

Without going into details of the problems of the airplane itself, the reasons for the sudden increase of the cooling loads can be explained briefly. The stagnation temperature of air, in reference to the airplane speed, can be expressed as the sum of the ambient (static) temperature plus the square of the velocity divided by a constant. This is a parabolic curve, Fig. 1, in which the steepness increases with velocity. Consequently, the higher the velocity the more rapid the increase in stagnation temperature. The stagnation temperature determines heat transfer from the outside surface of the airplane to its inside. The temperature finally becomes so high that the air is no longer suitable for direct cooling of equipment, even if this equipment does not generate any heat but has only to be protected from high temperatures (for example, tires).

Although not discussed in this paper, the cooling of the aircraft structure is expected to become a problem in the near future. Another reason for the sharp increase in cooling requirement is

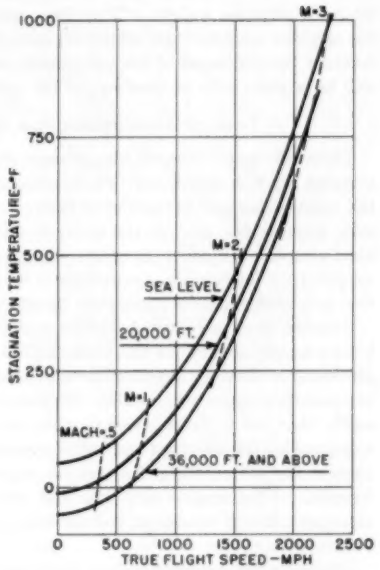

Fig. 1 Air Stagnation Temperature Variation With Flight Speed and NACA Standard Atmosphere

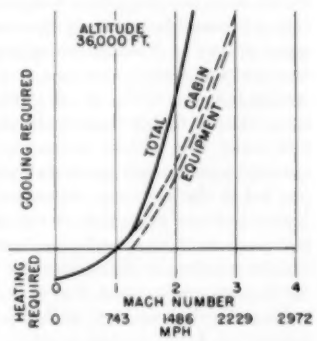

Fig. 2 Required Cooling Capacity Versus Speed

that supersonic airplanes use much more electronic equipment in connection with their operation and mission than is used in subsonic flight. Similar to equipment which is not producing heat, the direct cooling of electrical equipment by ram air becomes impossible when ram-air temperature is too high. Owing to these additional requirements, the cooling-load curve, Fig. 2, grows with speed much faster than the stagnation temperature.

Cooling-System Variables Affecting Airplane Performance

Partly because of the secrecy surrounding new airplanes and partly because of insufficient recognition of the importance of cooling, it has sometimes been difficult for the equipment manufacturer to obtain the proper data representing the penalties to the airplane which are attributable to the cooling system and its operation. In order to evaluate cooling systems properly and to find the most suitable system for an airplane, he should know the relative influence on airplane performance of additional equip-

---

[1] Chief Research Engineer, Stratos Division of the Fairchild Engine and Airplane Corporation.

[2] Research Engineer, Stratos Division of the Fairchild Engine and Airplane Corporation.

Contributed by the Aviation Division and presented at a joint session of the Aviation Division, American Rocket Society, and The Society of Automotive Engineers, at the Annual Meeting, New York, N. Y., November 28–December 3, 1954, of The American Society of Mechanical Engineers.

Note: Statements and opinions advanced in papers are to be understood as individual expressions of their authors and not those of the Society. Manuscript received at ASME Headquarters, October 11, 1954. Paper No. 54—A-206.

ment weight, amount of bleed air, and of cooling-air drag. These values can guide the designer in selection of a system. Depending on the airplane, in some cases weight saving is more important than cooling-air drag or conservation of bleed air and vice versa.

A convenient form for evaluating penalties is to convert all system losses into either miles of range or pounds of additional fuel necessary to carry the system and maintain the operational range of the aircraft. As an order of magnitude, we can say that saving of 1 lb of bleed air may be equivalent to the saving of 5 to 20 lb of airplane weight. Therefore information furnished by the airplane manufacturer which explains to the equipment manufacturer the influence of his equipment on airplane performance will be a great help in selection of the most suitable equipment.

Loss of Atmospheric Air Heat Sink

There are many reasons why present-day conventional cooling systems are not satisfactory for supersonic airplanes, but one of the most important is the loss of that extremely convenient heat sink, atmospheric air. In the air-cycle cooling systems which are used almost exclusively in military airplanes at present, the air supplied by jet-engine compressors is cooled in two basic steps, first in a heat exchanger and then by expansion in an air turbine.

Starting from a required turbine exit temperature sufficiently low to supply cooling to the cabin with a reasonable amount of air flow (the flow requirement becomes infinite when turbine exit temperature approaches cabin temperature), it can be shown easily that for a given pressure ratio across the turbine, as determined by the bleed air and cabin pressures, there is a temperature of the air entering the turbine above which cooling is not feasible. That means that the first step of cooling (heat exchangers) should be able to cool the bleed air at least down to this temperature.

With the ram-air temperature increased to the point where it is hotter than the temperature required at the turbine inlet it becomes impossible to satisfy the foregoing requirement. A schematic diagram, showing the relative variation of bleed-air pressure and temperature across a simple-type air-cycle refrigeration system is shown in Fig. 3. A cooling-air temperature (stagnation temperature) higher than the limiting line shown on the diagram will make this system impractical. The so-called "bootstrap system" uses turbine power to compress bleed air before it is expanded in the turbine; consequently, the turbine operates at a higher pressure ratio than in the simple system. However, with increased airplane speeds, the turbine-inlet-temperature limit is quickly reached as determined by the ram-air temperature used for the heat exchangers, Fig. 4.

Vapor-cycle systems, such as are used in mechanical refrigeration, face a similar problem. In order to operate a vapor system, a heat sink for the condenser has to be provided. Freons which are used at present are limited to a temperature of approximately 300 F and there is no other chemical at the moment which seems to be practical either from the pressure or from the handling safety standpoints.

Air leaving the crew compartment is usually at moderate temperature and can be applied usefully. The most common application is for direct equipment cooling. It also can be directed to additional heat exchangers or vapor condensers.

Use of surrounding air, the most easily accessible heat sink, becomes impractical at stagnation temperatures in excess of 300 F. Finding another heat sink in an airplane packed with equipment is not an easy matter.

Reduced Ambient Heat Sink

Before resigning completely from the use of outside air, however, we should consider decreasing the temperature of the ram air to lower values by expanding it through a ram turbine. This

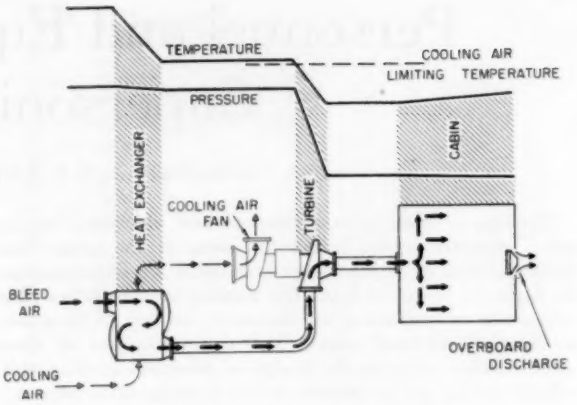

Fig. 3 Simple Air-Cycle Cooling System

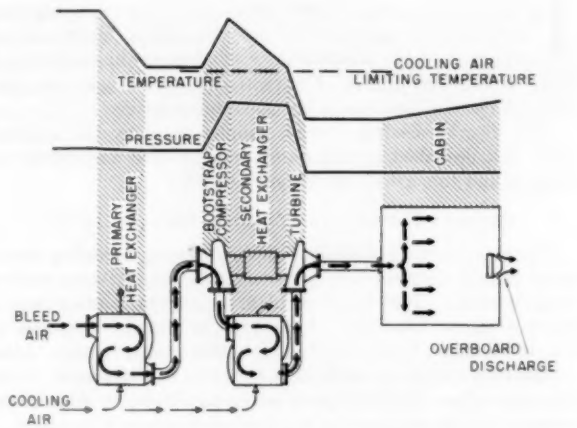

Fig. 4 Bootstrap Air-Cycle Cooling System

is theoretically possible and satisfactory; however, when practical application is considered, the size of a ram turbine which can satisfy high-altitude conditions becomes very large, and satisfactory control at lower altitudes difficult. Also, use of full ram pressure air at high airplane velocities adds considerably to the momentum drag of the airplane if this air is not reaccelerated to high velocity as it is returned to the atmosphere.

In general, a ram turbine would be used to supply cooled ram air to a heat exchanger as cooling air. The additional cooling capacity available from this heat exchanger-turbine combination would depend largely on the ram-turbine inlet pressure and temperature, the turbine outlet pressure, and the cooling-to-cooled-air flow ratio available. Since the last variable needs to be at least unity or greater to obtain reasonable heat-exchanger effectiveness, the ram-turbine flow passage areas become quite large at reduced high-altitude air densities resulting in large component sizes. Absorption of the ram-turbine power output constitutes another problem which would depend largely on the specific application.

Other Heat Sinks

Heat sinks which can be found in the airplane are the structure and the fuel. The airplane structure itself can be used satisfactorily for a short duration where its thermal lag and capacity are sufficient and cooling off follows a brief period of excessive temperatures. For any flight longer than a few seconds, the whole

structure will reach too high a temperature to be useful. Fuel is a very attractive heat sink and it can be used very conveniently if a heat exchanger between the fuel and the air is used downstream from the fuel pump.

Unfortunately, the claim for fuel as a heat sink is made by the engine manufacturer for oil cooling and, so far, the air-conditioning engineer has not been able to obtain fuel for his purposes. There are also certain objections because of possible deterioration of the fuel if it is heated to excessively high temperatures. If part of the fuel could be evaporated before burning, this heat of vaporization would provide a very convenient sink for the cooling system.

Artificial Heat Sinks

As there seems to be no other heat sink present in the airplane, we have to create an artificial one. Let us consider what should be the properties of the best artificially created heat sink. (*a*) It must be able to absorb heat at the proper temperature level; (*b*) it should be able to absorb the highest possible amount of heat at the smallest possible weight and volume penalty; (*c*) it should be easily available and have no poisonous or highly corrosive properties.

It seems that plain water is superior to other substances on the bases of heat-absorption capacity, availability, and chemical properties. The superiority of water is so great in these respects

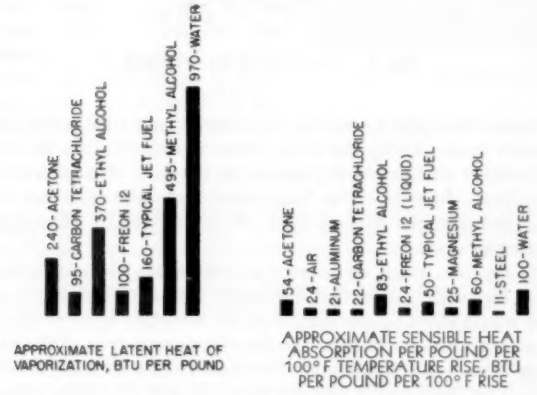

Fig. 5 Thermal Capacity Per Pound for Various Materials

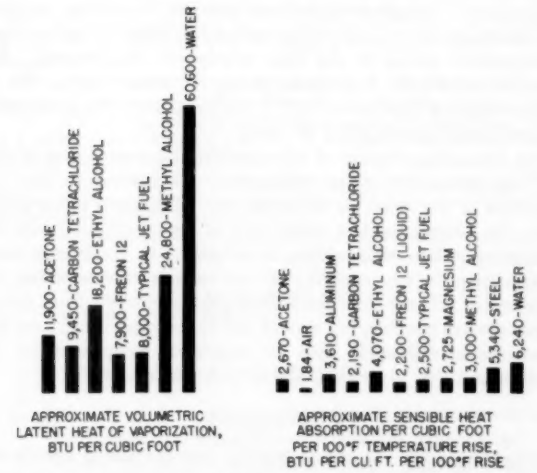

Fig. 6 Thermal Capacity Per Cubic Foot for Various Materials

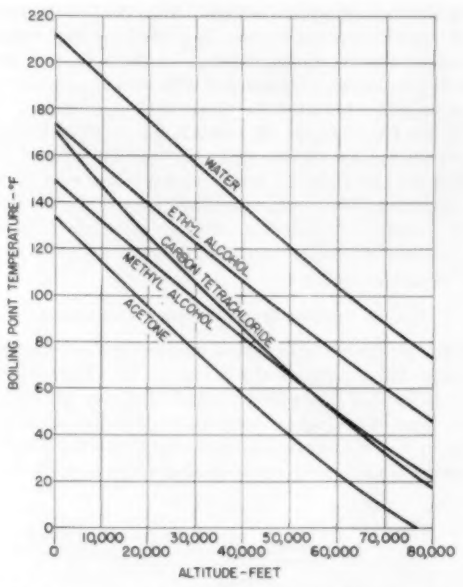

Fig. 7 Variation of Liquid Boiling-Point Temperature With Altitude

that the use of other materials having lower boiling-point temperatures at altitude is rarely justified in aircraft applications. In those cases where the lowest temperatures are required, another evaporative stage using a lower boiling-point liquid might be added after water evaporation.

Figs. 5 and 6 show latent heat of vaporization of different liquids at sea-level pressure and also, as a comparison, the heat which can be absorbed by increasing the temperature of different materials 100 deg F without change in state (1, 2, 7).[3] Boiling temperatures versus altitude are shown in Fig. 7 (1, 3, 4). After selecting water (or more exactly, the heat of vaporization of water) as a heat sink, a decision has to be made as to how to apply it to a cooling system.

The complete elimination of an air-to-air heat exchanger does not seem justified as it can be used for precooling the bleed air, thus reducing the amount of water which must be carried. Also, flight conditions may arise where cooling is required but where the evaporative component would be less effective than the air-to-air exchanger. Therefore an air-to-air heat exchanger will be used in addition to the water. Three possibilities arise here, as follows:

1 Evaporate the water into the cooling air.
2 Evaporate the water into the cabin (bleed) air.
3 Evaporate the water in a boiler without direct contact with the air being cooled and discharge the steam outside the airplane.

For all cases the amount of heat removed from the air per pound of water used (evaporated) is roughly the same, approximately 1000 Btu.

Some Systems Using Water Evaporation

Direct evaporation by spraying water into the air has the advantage that temperatures much lower than the boiling point of water can be obtained. The air temperature can be dropped close to the wet bulb temperature.

Spraying water into the cooling air has the disadvantage that a relatively large amount of air has to be cooled and, consequently,

[3] Numbers in parentheses refer to the Bibliography at the end of the paper.

the total water consumption is high. Also, the practical problem exists of vaporizing a water spray in a relatively high velocity air stream with a limited mixing length. In these circumstances the wet bulb temperature is not reached without a considerable excess of water consumption over the theoretical requirement. Direct injection into the bleed air will result in increased cabin humidity which, in some cases (at low altitude), may be objectionable.

Cooling the bleed air in a boiler or evaporator seems to be the best. There is no change in humidity of cabin air, the effectiveness of the boiler (for its size) is very high, and water consumption is low because of cooling only the bleed air which is a smaller amount than the cooling air.

Simple System With Water Evaporator

A typical air-cycle simple system employing a water evaporator is represented diagrammatically in Fig. 8. This type of system is installed in the X-3 high-speed research airplane. As can be seen from the lines of cooling-air temperature and boiling-water temperature in Fig. 8, the system can operate with the turbine inlet temperature considerably below cooling-air temperature.

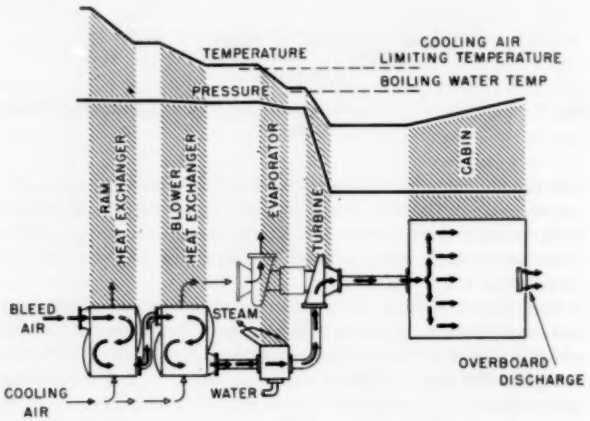

Fig. 8 Simple Air-Cycle Cooling System With Water Evaporator

The major components of the system are ram air-cooled heat exchanger, blower air-cooled heat exchanger, evaporator, air-cycle machine (turbocompressor). None of these components is new or revolutionary, but a logical analysis of the problem has led to their combination in a unique but simple manner which has produced a very satisfactory system for supersonic airplanes.

The blower and ram air-cooled heat exchangers are conventional air-to-air heat exchangers of a type which is now used in a great number of applications; therefore no detailed description is necessary.

There is no absolute reason for using two heat exchangers rather than one (either blower or ram). In this installation it was found convenient to use two. The ram heat exchanger removes a considerable portion of heat from the bleed air. The blower heat exchanger, as a result of this, removes less heat at a lower temperature level; consequently, the cooling air entering the blower has a reasonably low temperature. This is an important factor in the design of the blower itself and the bearing adjacent to it. The combined effectiveness of the blower and ram heat exchangers is high at all conditions. One depends on airplane speed, the other on engine setting. In most cases the gain of effectiveness in one heat exchanger compensates for loss in the other at different combinations of airplane speed and engine setting. On the ground when there is no ram available, the blower heat exchanger permits cooling to be obtained.

The evaporator design which has been used successfully for this application is illustrated in Fig. 9 (5). This unit is of brazed aluminum construction with extended surface on both the air and water sides. Tests of the water-filled core indicate that this evaporator can be frozen solid without damage. During operation, the water level is maintained constant by means of a dia-

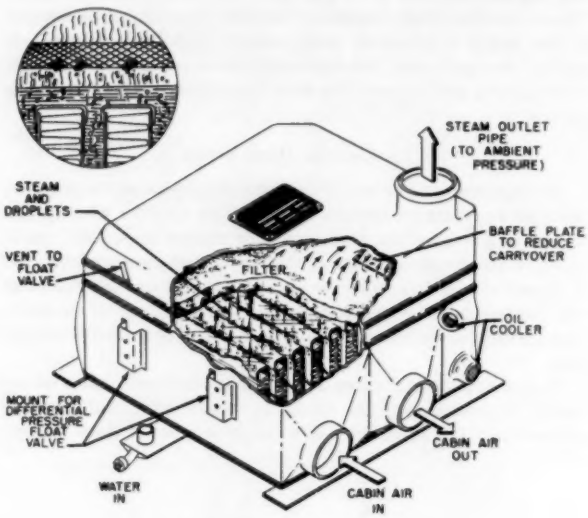

Fig. 9 Cutaway of Evaporator

phragm valve which controls the water supply from a remotely located tank. Using the boiler alone and eliminating the heat exchangers completely is feasible, in the case of a high-speed condition. In spite of the larger amount of water necessary, this may decrease the over-all drag of the system by eliminating cooling air drag.

The system which we describe used low-energy boundary-layer bleed for cooling air so that decreasing the amount of cooling-air flow would affect proper control of the boundary layer at the engine air entrance. In this case the momentum drag of the heat exchangers was not charged to the system as the air was available at no additional cost in airplane drag over and above the amount which had to be bled off for boundary-layer control.

Presence of the evaporator constitutes a safety feature of some importance. In case of mechanical failure of the turbine, the pilot will be subjected to an air temperature very close to boiling-water temperature owing to the high evaporator effectiveness. For example, at 36,000 ft altitude, during supersonic flight, this air temperature will be about 150 F, while without the evaporator it could easily reach 400 F or more.

An interesting feature of this particular system is that it does not require control of the evaporator. This is due to the temperature of the bleed air after the heat exchangers being higher than the boiling point of water only at the conditions (with one exception) when evaporation is needed. At conditions when evaporation is not needed, the air temperature entering the evaporator is lower than the boiling point of water. Such design is not always possible, but should not be forgotten when new systems are investigated. Fig. 10 represents components of the system and Fig. 11 the airplane in which it is used (6).

Conclusions

Flight through the atmosphere at ever-increasing speeds will continuously confront designers with cooling problems of greater

number and magnitude. The thermal barrier, unlike the sonic barrier, is not a fixed obstacle which one can jump over—the faster the speed the tougher the problem!

Cooling the supersonic airplane is so important in terms of performance of the airplane that the optimum system can be achieved only through the cooperative efforts of airframe and equipment designers starting with the preliminary design stage and continuing through the final acceptance of the airplane.

Logical analysis of the cooling problem of a supersonic airplane led to the simple water-evaporative system, which, in its basic concept, can find application in high-speed aircraft of the present and for some time in the future.

The excessive cooling loads associated with ever-increasing speeds eventually will lead to flight outside the earth's atmosphere. Although it might not necessarily be required, cooling under these conditions of flight also could be obtained by nature's oldest method of cooling man—water evaporation.

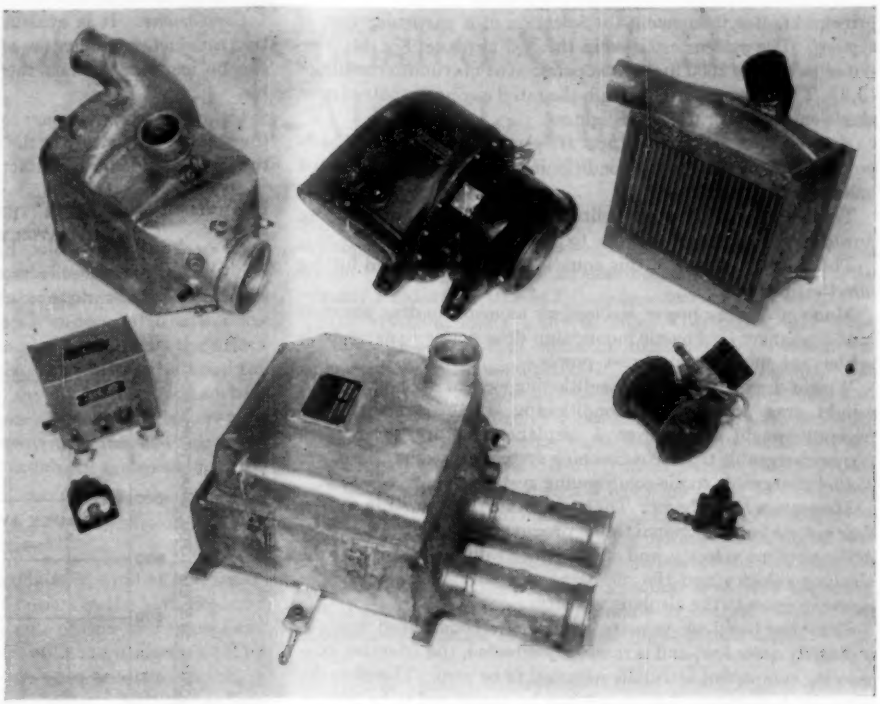

FIG. 10 COMPONENTS OF SIMPLE AIR-CYCLE COOLING SYSTEM WITH WATER EVAPORATOR

BIBLIOGRAPHY

1 "International Critical Tables of Numerical Data, Physics, Chemistry, and Technology," by the National Research Council of the United States of America, McGraw-Hill Book Company, Inc., New York, N. Y., 1926–1933.

2 "Mechanical Engineers' Handbook," edited by L. S. Marks, McGraw-Hill Book Company, Inc., New York, N. Y., fifth edition, 1951.

3 "Thermodynamic Properties of Steam," by J. H. Keenan and F. G. Keyes, John Wiley & Sons, Inc., New York, N. Y., 1936.

4 "Cooling of Electronic Apparatus at High Altitudes," by Harry Wilkie, Technical Data Digest, Central Air Documents Office, Wright-Patterson Air Force Base, Dayton, Ohio, December, 1950.

5 "Water Cools the Stiletto," by Herbert Olden, *Aviation Age*, Conover-Mast Publications, Inc., New York, N. Y., February, 1954.

6 "X-3 Cooling System Small But Powerful," by G. L. Christian, *Aviation Week*, McGraw-Hill Publishing Company, Albany, N. Y., January 4, 1954.

7 "Data Book on Hydrocarbons," by J. B. Maxwell, D. Van Nostrand Company, Inc., New York, N. Y., second printing, 1950.

8 "A New Method of Performance Analysis of Air Cycle Cooling of a High Speed Airplane," by D. E. Brimley, 1952 ASME Spring Meeting Paper No. 52—S-5.

9 "Operational Experience—Pneumatic Components of Cabin Pressurization and Accessory Drive Systems," by G. A. Lemke, SAE Paper (preprint) 382, New York, N. Y., 1954.

10 "Army Summer Atmosphere—Tables & Data," by Capt. R. M. Drake, Jr., AAF Technical Report No. 5540, Air Materiel Command, Wright Field, Dayton, Ohio, 1947.

11 "Aircraft Engines of the World 1953–1954," by P. H. Wilkinson, New York, N. Y., 1954.

Appendix

PRINCIPAL FACTOR INFLUENCING AIR-CONDITIONING-SYSTEM SELECTION FOR HIGH-SPEED TURBOJET AIRPLANES

The thrust horsepower needed to operate and carry the air-conditioning systems in modern high-speed airplanes is the

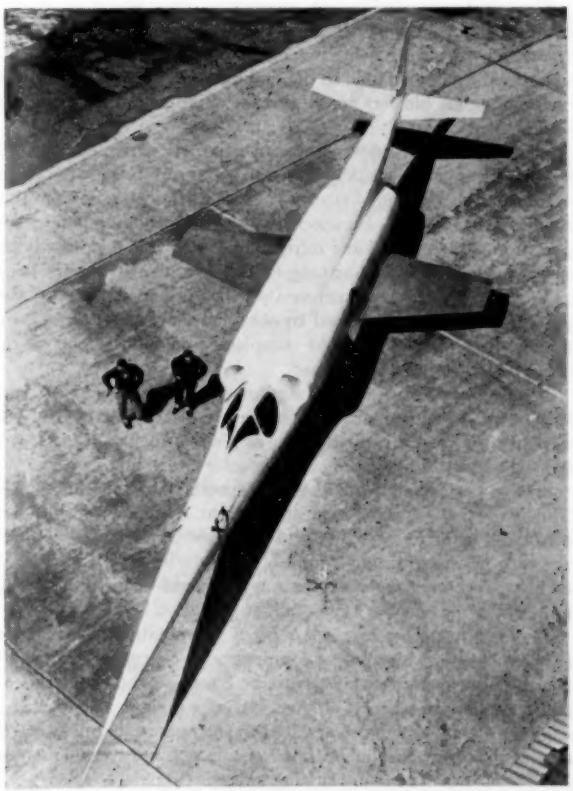

FIG. 11 X-3 HIGH-SPEED RESEARCH AIRPLANE; FIRST TO USE AIR-CYCLE SYSTEM WITH WATER EVAPORATOR

principal factor influencing the selection of a particular type of system. The system installed in the X-3 airplane, Fig. 11, is reputed to require 2600 hp for its operation at maximum conditions (5,6). This power is greater than the rated engine outputs of most single-engined World War II fighters.

Air-Conditioning-System Drag Horsepower. The drag horsepower chargeable to the air-conditioning system for unaccelerated level flight is as follows:

Total drag power = momentum drag power + weight drag power + engine power loss due to air bleed

The first two terms of this equation can be expanded further into the following:

Momentum drag power = bleed-air momentum drag power + heat-exchanger cooling-air momentum drag power — expendable refrigerant momentum thrust power

Weight drag power = air-conditioning system fixed-component weight drag power + air-conditioning system expendable refrigerant-weight drag power + airplane structural-weight drag power chargeable to air-conditioning system + weight drag power of fuel chargeable to air-conditioning system

Momentum Drag Power. The momentum drag power in a given flow system is proportional to the product of the weight flow rate, of the airplane velocity, and of the velocity difference between the airplane velocity and the discharge air velocity component opposite in sense to the airplane velocity.

Since the bleed-air velocity leaving the conditioned space is ordinarily quite low, and is randomly directed, the effective exit-velocity component is usually assumed to be zero. Therefore the bleed-air momentum drag power can be considered to be proportional to the product of the bleed-air weight flow rate and the square of the airplane velocity.

Heat-exchanger cooling-air momentum drag power is usually evaluated in a manner similar to the bleed-air drag power (8). Increasing efforts are being made to minimize cooling-air drag by utilizing the energy added to the cooling air in the heat exchangers and cooling-air blowers to obtain a positive net thrust from the cooling-air system.

Since the weight flow rate and velocity of expendable refrigerant vapor are usually quite insignificant relative to other system flow rates and velocities, the thrust available from this source is negligible. Furthermore, since the boiling-point temperature of the expendable refrigerant is dependent primarily on its pressure and this boiling temperature is ordinarily desired to be as low as possible commensurate with other limitations, the pressure differential required to obtain a significant thrust from the discharging vapor would completely defeat the purpose in using an expendable refrigerant.

Weight Drag Power. The drag power required to carry weight in an airplane is proportional to the product of the weight, the airplane drag-to-lift ratio, and the airplane velocity. This is perhaps the most difficult drag-power factor to evaluate without recourse to performance analysis of a specific airplane and engine. This is particularly true regarding weight components which are consumed in flight, i.e., fuel and expendable refrigerant. Since the rate of consumption of these items varies with the type of flight operation, proper evaluation of weight drag penalties requires that the effect of type of flight operation be known.

Engine Power Loss Due to Air Bleed. Evaluation of the engine thrust loss due to bleeding of compressor-discharge air for the air-conditioning system usually must be based on the results of engine manufacturers' tests of specific engine designs. Here, again, engine parameters must be related to the operational parameters of a specific airplane in order to obtain a proper evaluation of different types of air-conditioning systems (9).

Conclusions. It is evident from the foregoing considerations that satisfactory evaluation of an airplane air-conditioning system can be made only when the necessary airplane data are available.

Unfortunately, security considerations usually severely limit the amount and nature of the airplane data which are available to the air-conditioning manufacturer.

Example Illustrating the Effect of Adding a Water Evaporator to a Simple System

Fig. 12 shows the effect of adding a water evaporator to a simple system at various Mach numbers under otherwise identical

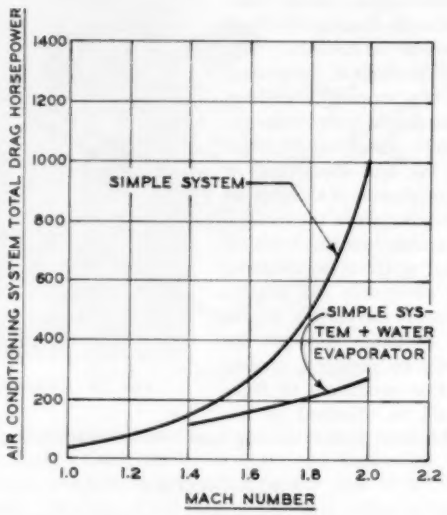

Fig. 12 Effect of Water Evaporator on Simple System Drag Power

conditions. Constant values of heat-exchanger effectiveness and flow ratio, water-evaporator effectiveness, turbine efficiency, and component specific weight were assumed throughout the comparison. The drag chargeable to the heat-exchanger cooling air was assumed to be effectively zero. This assumption is approximately true if the cooling air is drawn from a low-energy-level source such as boundary-layer bleed-off ducts.

The superiority of the system with the evaporator increases with the Mach number. This is due to the fact that in one case the sink temperature remains constant while in the other it increases as the square of the Mach number.

The values of significant airplane and engine parameters, Table 1 (except skin temperature), were assumed to be constant in the Mach number range considered. In actual practice these factors would vary with Mach number changes.

TABLE 1 LIST OF USEFUL PARAMETERS

Altitude: 36,000 ft
Conditions: Army summer day (10)
Inlet diffuser total pressure recovery: 0.7
Compressor pressure ratio: 5.0
Compressor efficiency: 0.85
Required cabin temperature: 75 F
Cabin pressure: ambient + 5.0 psi
Effective skin temperature: ambient + 0.85 ram temperature rise
Cooling load: 2.0 (effective skin temperature-required cabin temperature + 200, Btu per min)
Lift-drag ratio: 10.0 (2)
Specific fuel consumption (with reheat): 2.0 lb fuel per hr per lb thrust (11)
Bleed thrust loss: 2.0 lb thrust per lb per min bleed-air flow

Human Problems Associated With High-Speed and High-Altitude Flight

By R. A. McFARLAND,[1] BOSTON, MASS.

Human tolerance for heat and cold is outlined so that aeronautical engineers may have a better understanding of design problems related to cabin atmosphere. The hazards resulting from noxious gases and vapors also are considered. The need for air-crew indoctrination in the effective use of equipment is emphasized as well as the need for airmen to understand their own physical limitations while in flight. Finally, the need for more effective collaboration between the biological and engineering sciences is stressed in regard to improving the man-machine systems in high-speed, high-altitude flying.

Introduction

THE utilization of space as a medium of combat and transportation has opened up new frontiers in the biological and engineering sciences. Our concepts of time and space have been revolutionized with the advent of modern aircraft. The stresses imposed on airmen in flying such equipment are reaching tolerance limits in all realms of human behavior. Altitudes so high that human life is no longer possible may now be reached within a few minutes, and the full range of tolerable temperature is met within a single flight. Extremes in accelerative forces leading to loss of consciousness or to death may be encountered during maneuvers and in the sudden impact of crash landings. Currently the aeronautical engineer is solving many of the problems of high-altitude, high-speed flying by means of cabin pressurization and other advances. Much remains to be accomplished, however, to protect airmen and passengers from the adverse influences of the physical environment, not only in the event of failure of equipment but also in extending the operational efficiency of the newest types of aircraft.

One of the most important ways of improving flight safety and combat efficiency is to design equipment in terms of human capabilities and limitations. Aeronautical engineers should have an understanding of the sense organs and the characteristics of human perception if satisfactory information is to be supplied from pointer readings and sounds in the operation of the equipment which they design. Unreasonable demands should not be placed upon a pilot in regard to the physical responses involved. For example, if an instrument must be read within a fraction of a second while moving at the speed of sound, the dials must be very legible, or if a pilot is to survive a sudden loss of cabin pressure at altitudes where he will lose consciousness, supplementary oxygen must be provided. The environmental conditions relating to temperature, humidity, toxic gases, and many other factors must be considered or physiological limits may be exceeded. Thus there is great need for more effective collaboration between the engineering and biological sciences. Unless aircraft are designed around the characteristics of airmen it is hardly fair to attribute so many accidents to human failure as is usually the case (3).[2]

After spending many hours in flight with pilots, and while working with aeronautical engineers, an attempt was made in the author's book, "Human Factors in Air Transport Design," not only to study the relationships between the physical stimuli and the human responses to flying but also to suggest the most desirable limits within which the variables should be controlled (1). In a more recent study entitled "Human Factors in Air Transportation," primary consideration has been given to the health and safety features in flying modern aircraft (2). Although the demands placed upon airmen are being increased with the advent of newer models, the principles of human limitations and capabilities as developed in these two books remain essentially the same. In this paper an attempt will be made to analyze some of the human factors related to high-speed, high-altitude flight.

Fig. 1 Physical Variables Influencing Comfort and Safety During Flight

(Figure shows schematically magnitude of physical variables in relation to degree of comfort experienced. These values are only approximations since each variable is interdependent on one or more additional factors. McFarland, reference 2.)

A schematic interpretation of the various stimuli encountered in flight is given in Fig. 1 in terms of limits for comfort, discomfort, and unbearable zones. Marked discomfort might arise if the "psychological" boundary is exceeded, while more serious impairment might be expected if the "physiological" boundary is exceeded. If the human responses to these physical factors en-

[1] Associate Professor of Industrial Hygiene, Harvard School of Public Health.

Contributed by the Aviation Division and presented at a joint session of the Aviation Division, American Rocket Society, and The Society of Automotive Engineers, at the Annual Meeting, New York, N. Y., November 28–December 3, 1954, of The American Society of Mechanical Engineers.

Note: Statements and opinions advanced in papers are to be understood as individual expressions of their authors and not those of the Society. Manuscript received at ASME Headquarters, October 21, 1954. Paper No. 54—A-230.

[2] Numbers in parentheses refer to the Bibliography at the end of the paper.

countered in flight are plotted in terms of linear scales, an oversimplification of the problem may result. For example, all people may not respond in the same way, and usually there are several variables interacting together, requiring the use of nomograms in which the various factors are interrelated.

The difficulty of giving a single numerical value as a standard is exemplified in stating the maximum allowable limits for carbon monoxide for aircraft in flight. The generally accepted standard is 0.005 per cent carbon monoxide in the ambient air. This figure may be satisfactory for a person sitting quietly at sea level, but it should be reduced if the amount of exercise, degree of ventilation, or the length of time increases. An additional complication is introduced while in flight because of the combined effect of carbon monoxide and the oxygen want associated with high altitude. For example, if there is 0.005 per cent carbon monoxide in the ambient air at 9000 ft, the resultant physiological altitude is 15,000 ft (4). The same complexity characterizes almost every other function that will be discussed.

Stimuli Primarily Related to High-Altitude Flight

One of the most important variables which must be considered in flights to high altitude concerns the effect of oxygen want on performance. The nervous system is particularly sensitive to a deficiency of oxygen and an inadequate supply produces marked alterations in the entire organism. A brief statement will be given of the physical characteristics of the atmosphere, followed by a description of the effects of oxygen want on the body from the physiological point of view. This will enable the aeronautical engineer to understand the changes in behavior which might be expected to occur with increasing altitude, and the way in which breathing equipment and cabin pressurization will facilitate adaptation. One of the most important questions is to determine the approximate altitude where the initial effects on behavior might be expected to occur as well as the limits beyond which it is impossible to ascend without artificial aids. Also, consideration must be given to the effects of a sudden loss of pressure in the event of a failure in the equipment. The frequency with which there has been a sudden loss of pressure in transports will be reviewed.

The second part of the paper will deal with stimuli primarily related (*a*) to high-speed flight and (*b*) to cabin atmosphere, including extremes of temperature and toxic gases. Some of the more important developments in high-altitude flying cannot be discussed at this time because of the restricted nature of the reports.

Influence of a Diminished Oxygen Supply on Pilot Performance. When an airman ascends to high altitude during a flight, certain alterations take place in his environment which significantly influence his performance and well-being. These changes are brought about by the decrease in partial pressure of oxygen ($_pO_2$) with increasing altitude. In any mixture of gases, each component contributes a share of the total pressure in proportion to its concentration by volume. The pressure exerted by each gas is designated as its partial pressure and is computed by multiplying the total pressure by the proportion of the gas in the mixture. Dry atmospheric air by volume contains 20.94 per cent oxygen, 79.03 per cent nitrogen (including small amounts of rare gases of no physiological significance), and 0.03 per cent carbon dioxide. This relative composition does not vary appreciably with altitudes up to 70,000 ft. Since at sea level the atmospheric pressure is 760 mm Hg and approximately 21 per cent of this is oxygen, the partial pressure of oxygen in the atmosphere equals 760 times 0.21, or 160 mm Hg. As one rises above the level of the sea, the total pressure of the atmosphere falls, as does the partial pressure of its components (5).

The decrease in partial pressure with altitude influences the body by way of the respiratory mechanisms or the processes whereby the cells of the body obtain oxygen and eliminate carbon dioxide (CO_2). The most important physical principle involved is that any gas will pass from a region of high partial pressure to one in which the partial pressure is lower. As atmospheric air is inhaled, it eventually reaches the very thin-walled sacs of the lungs called alveoli. These are functionally related to the small blood capillaries of the lungs, and their walls are permeable to the respiratory gases, thus permitting the alveolar air to come into contact with the blood (2, 5).

The partial pressure of oxygen in the alveolar cavities is determined not only by the percentage of oxygen in the inspired air and the barometric pressure but also by the partial pressures of carbon dioxide and of water vapor in the lungs. The tension of alveolar carbon dioxide decreases slightly with altitude, but the water vapor in the lungs maintains a constant pressure of 47 mm Hg. Therefore, as the total pressure in the lungs decreases, the carbon dioxide and water vapor become proportionately larger in volume at the expense of oxygen and nitrogen, and the partial pressure of oxygen in the inspired air is reduced to about 100 mm Hg in the alveolar air. The increasing fraction of carbon dioxide and water vapor in the lungs results in lower and lower alveolar partial pressure of oxygen so that a level is finally reached at which it is impossible, even though breathing 100 per cent oxygen, to maintain a molecular concentration adequate to sustain consciousness or life. This critical "pressure altitude" is about 45,000 ft.

Breathing is normally under the automatic control of the respiratory center in the brain which reacts to the concentration of carbon dioxide rather than to that of oxygen in the blood. When the tension of carbon dioxide in the blood increases as in exercise or in holding the breath, the respiratory center is stimulated and the rate and depth of breathing are increased. The respiratory center is very sensitive to variations in carbon-dioxide tensions; an increase of carbon dioxide in the inspired air to about 4 per cent will increase ventilation of the lungs by 100 per cent.

Oxygen diffuses into the blood from the alveolar air and is taken up by the red blood cells. These cells contain a pigment called hemoglobin which has a relatively high affinity for oxygen. As the oxygen-laden blood circulates through the arteries, it comes into contact with tissues in which the partial pressure of oxygen is lower than in the blood. The hemoglobin then releases oxygen to the tissue of the body directly. The oxygen-carrying capacity of the hemoglobin is influenced not only by the partial pressure of oxygen but also by the acidity of the blood or especially by variations in carbon dioxide. When normal human blood is completely saturated, it holds about 20 cu cm of oxygen per 100 cu cm of blood (20 vol per cent). Under ordinary conditions, arterial blood is only about 95 per cent saturated; i.e., it contains only 19 vol per cent of oxygen.

The condition that is brought about by a lowered concentration of oxygen in the air breathed is commonly referred to as "anoxia," which by derivation means "without oxygen." The common usage of this term implies intermediate degrees of oxygen want; hence the term "hypoxia," denoting partial oxygen want, is preferred. As brought out in the foregoing, the condition most commonly noted among airmen depends on the reduction of the partial pressure of oxygen in the air breathed.

Effects of Acute Oxygen Want. The response of an airman to the oxygen want encountered at high altitude depends on (*a*) absolute height attained, (*b*) rate of ascent, (*c*) length of exposure, (*d*) amount of physical exertion, and (*e*) certain individual factors, such as degree of acclimatization, physical fitness, emotional adaptation, and degree of fatigue. The effects of a sudden and extreme, i.e., acute, oxygen want are very different from those of repeated or prolonged exposures, i.e., chronic oxygen want (2, 6).

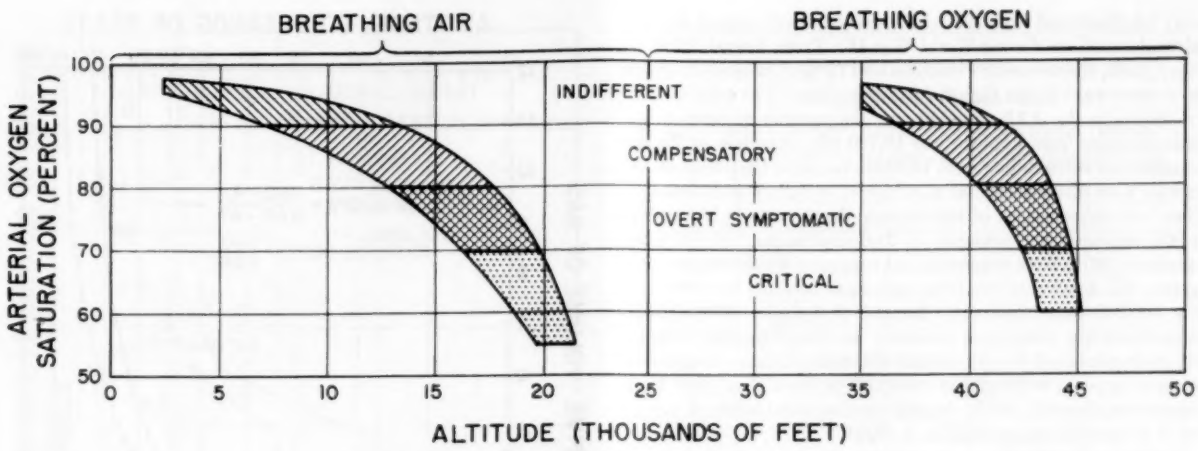

FIG. 2 EFFECT OF OXYGEN WANT AT VARIOUS ALTITUDES

(Figure demonstrates effect of oxygen want in relation to arterial oxygen saturation at various altitudes. Critical stage resulting in collapse after short exposure, corresponding to about 65 per cent arterial oxygen saturation, occurs between 20,000 and 23,000 ft while breathing air and between 44,800 and 45,500 ft while breathing 100 per cent oxygen. Reference 5 and McFarland, reference 2.)

The relationship between the onset of symptoms, approximate pressure altitudes, and arterial oxygen saturations encountered in rapid ascents to high altitude is shown graphically in Fig. 2. According to this presentation, the first or indifferent stage extends up to about 10,000 ft while breathing air and 39,000 ft while breathing 100 per cent oxygen. If the arterial oxygen saturation is lowered to about 85 per cent, many subjects show impairment in such mental functions as memory and reasoning. Frequent errors in judgment may be made by airmen in navigational problems or blind flying. If the arterial oxygen saturation falls below 85 per cent, an appreciable handicap is observable; below 75 per cent a danger zone is approached and the deterioration in behavior is marked. The compensatory mechanisms of the body begin to fail when the arterial oxygen saturation approaches 70 per cent; this stage occurs in most subjects at about 15,000 to 18,000 ft altitude. When it falls as low as 60 per cent, or the altitude is approximately 20,000 ft, collapse may be imminent. The critical stage for short exposures occurs between 20,000 and 23,000 ft while breathing air and between 44,800 and 45,500 ft while breathing 100 per cent oxygen with special pressure breathing devices (7).

One of the most sensitive tests for demonstrating the effect of oxygen want is to measure dark adaptation or light sensitivity at high altitude. Pilots have frequently reported a general darkening of the visual field while flying at high altitude without oxygen and a marked increase in the brightness of lights on inhaling oxygen. The ability of the eye to become dark-adapted is progressively impaired with increasing oxygen want. This phenomenon has been measured precisely by means of light thresholds obtained against backgrounds with various intensities of illumination. A reduction in an airman's ability to see at night takes place at altitudes as low as 5000 to 6000 ft, see Fig. 3 (references 8, 9). This loss in visual efficiency at high altitude tends to disappear at high illumination. The effects are caused by the influence of oxygen want on the neural elements of both the retina and the central nervous system. As discussed later, a demonstration of the effects of altitude on dark adaptation provides an effective means of showing airmen how they may benefit by inhaling oxygen at relatively low altitudes, especially at night.

Other psychological reactions are not influenced until somewhat higher altitudes are reached. The average number of words recalled in standardized tests for immediate memory shows a significant decrease at altitudes of approximately 10,000 to 12,000 ft.

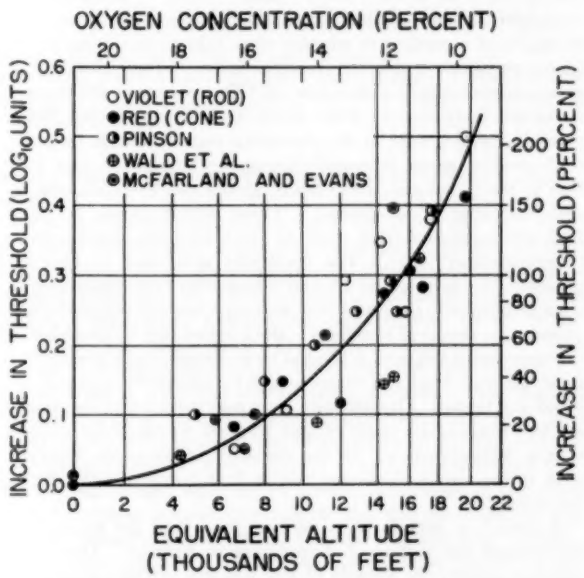

FIG. 3 EFFECT OF ALTITUDE ON LIGHT SENSITIVITY

(Curve shows increase in threshold for light, or decreased ability to see at night, in relation to altitude or oxygen pressure. Light sensitivity is impaired at altitudes as low as 5000 or 6000 ft. Percentage increase in light threshold at 15,000 ft is approximately 100 per cent; hence almost twice as much light would be required to see a given stimulus under this condition. Millikan, reference 9, and McFarland, reference 2.)

The psychological deterioration at high altitude is characterized not merely as a general slowing up of mental functions, and a greater amount of effort needed to carry out a task, but also by qualitative changes. The content of the associations is different, and the pattern of behavior is altered. Attention appears to fluctuate more easily. Calculations are unreliable, and judgment is faulty. An airman may feel unduly fatigued or may complain of sleepiness, headache, and breathlessness. Normal inhibitions may be released at higher altitudes, as in alcoholic intoxication. Such emotional reactions as euphoria, overconfidence, pugnaciousness, or moroseness may occur, depending on the basic personality traits of the individual and the length of the exposure.

The seriousness of the effects of acute hypoxia in military flying

may be illustrated from the AAF experience with regard to high-altitude missions during World War II. From August, 1942, to May, 1945, there were 388 nonfatal and 77 fatal cases attributable to oxygen want in the Eighth Air Force alone. The total number of deaths in the AAF was 110 and the number of cases of unconsciousness from hypoxia was 10,700 (5). Analysis of the circumstances surrounding each incident revealed that most of the causes were directly related to a lack of or failure in indoctrination. An examination of the hypoxic death rates in November, 1943, indicated an incidence of 21.6 deaths per 100,000 man-missions (10). With improved and expanded indoctrination programs, the death rate due to oxygen want declined to a level of 2 per 100,000 man-missions by the end of the war. The aircraft-manufacturing companies maintain an indoctrination program for their personnel who fly at high altitudes. In one company no serious hypoxic incident has occurred in more than 1300 hr of operations above 25,000 ft, despite the occasional failure of oxygen or of pressurization equipment in flight.

Influence of Changes in Barometric Pressure. A decrease in barometric pressure, in addition to giving rise to oxygen want, has other undesirable effects on the body. The symptoms, generally known as decompression sickness, occur even though the oxygen saturation of the arterial blood remains normal by the inhalation of oxygen. The effects due to changes in barometric pressure may be classified according to whether they take place during ascent (decompression) or descent (recompression). They also may be grouped according to their cause: (*a*) The expansion of free gases in certain body cavities from which ready escape is not always possible, causing pain in the abdominal region, sinuses, or teeth; or (*b*) evolved gases, principally nitrogen, which escape from solution in the blood and tissue fluids, giving rise to bends, chokes, and neurological symptoms. These disturbances, resulting from decompression from 1 atm to less than 1 atm, are known as "aeroembolism" (11). The syndrome is similar to that experienced by deep-sea divers and others who work under greater than atmospheric pressures and who experience bends on decompression to sea-level pressures. Both types can be classified as decompression sickness, activated by a change from a greater to a lesser pressure level and characterized by bubble formation in the blood and tissues. Occasionally, pain may originate in the middle ear and sinuses as a result of gas trapped within those cavities during decompression. In the majority of instances, however, pain in the ears and sinuses results from recompression during descents.

A review of certain physical laws may help the engineer to understand the causes of decompression sickness. During an airplane ascent, the volume of any free gas within the body increases in accord with Boyle's law; i.e., the volume of a gas is inversely proportional to the pressure exerted on it. Gases within the body, however, tend to expand more than Boyle's law demands when barometric pressure is reduced because (*a*) the gas remains saturated with water vapor at body temperature and (*b*) the tensions of oxygen and carbon dioxide decrease at altitude less rapidly than the barometric pressure. Abdominal pain is one of the most common manifestations of the expansion of gases, especially at very high altitudes (see Fig. 4 for comparative volumes of gas inside the body at various altitudes).

Another law relates to the formation of gas bubbles within the body similar to those released from a bottle of charged water when the cap is removed. The gas comes out of solution because its pressure is higher than that in the outside air. When the cap is replaced, pressure is built up in the space between it and the fluid level below until the gas in that space and the gas in solution are in equilibrium. At that time the bubbling ceases. The body contains about 1 to $1^1/_2$ liters of nitrogen in dissolved form at sea level. According to Henry's law, smaller proportions of this

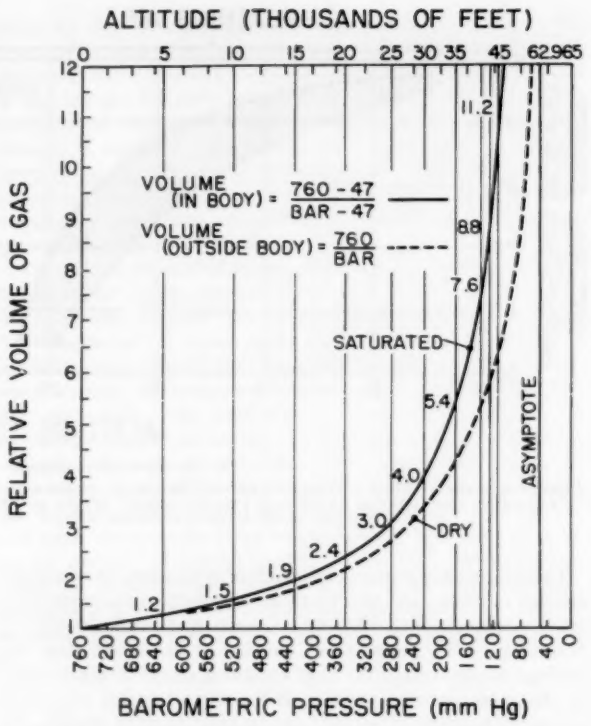

FIG. 4 COMPARATIVE VOLUME OF GASES INSIDE THE BODY AT VARIOUS ALTITUDES

(Figure shows comparative volumes of dry and saturated gases at various altitudes. As atmospheric pressure decreases during a plane ascent, gases trapped within enclosed spaces of the body tend to expand in accordance with well-known physical laws. Initial volume of 1 liter of gas would be 1.5 liters at 10,000 ft, 3 liters at 25,000 ft, and 7.6 liters at 40,000 ft. Lovelace and Gagge, reference 14, and McFarland, reference 2.)

gas are retained in solution as the barometric pressure decreases. When the tissues and fluids become sufficiently supersaturated in relation to the decreasing partial pressure of nitrogen in the atmospheric air, especially during rapid ascents to 30,000 ft or more, the dissolved nitrogen tends to come out of solution and form gaseous bubbles in the tissues and the blood. These bubbles, usually located in the connective tissue about the bones, joints, and muscles, produce the major symptoms of decompression sickness (5, 11).

Symptoms Related to Ascent. The most frequent manifestations of decompression sickness are bends, characterized by pain in and about the muscles and bone, especially in the joints. The larger joints, such as the knees and shoulders, are most frequently affected, but the small joints of the hands, wrists, and ankles are commonly involved. The pain may be mild at first but often becomes deep, gnawing, and so severe as to be intolerable, resulting in collapse. Occasionally, mild symptoms disappear after a period of a few minutes to one hour. Severe symptoms are unlikely below 23,000 ft, but for each 100 man-hours at 25,000 ft there is a single probable incident of decompression sickness serious enough for flight termination and ten incidents tolerable and not serious enough to terminate a flight. For each 100 man-hours at 30,000 ft, the serious incident rate is 3 and the tolerable incident rate is 30 (12).

There are several other variables in addition to rate of ascent, altitude attained, and amount of time at a given altitude which influence the incidence of aeroembolism. Amount of activity, exercise, and previous injuries facilitate the formation of bubbles. In general, bends occur more frequently when subjects are cold

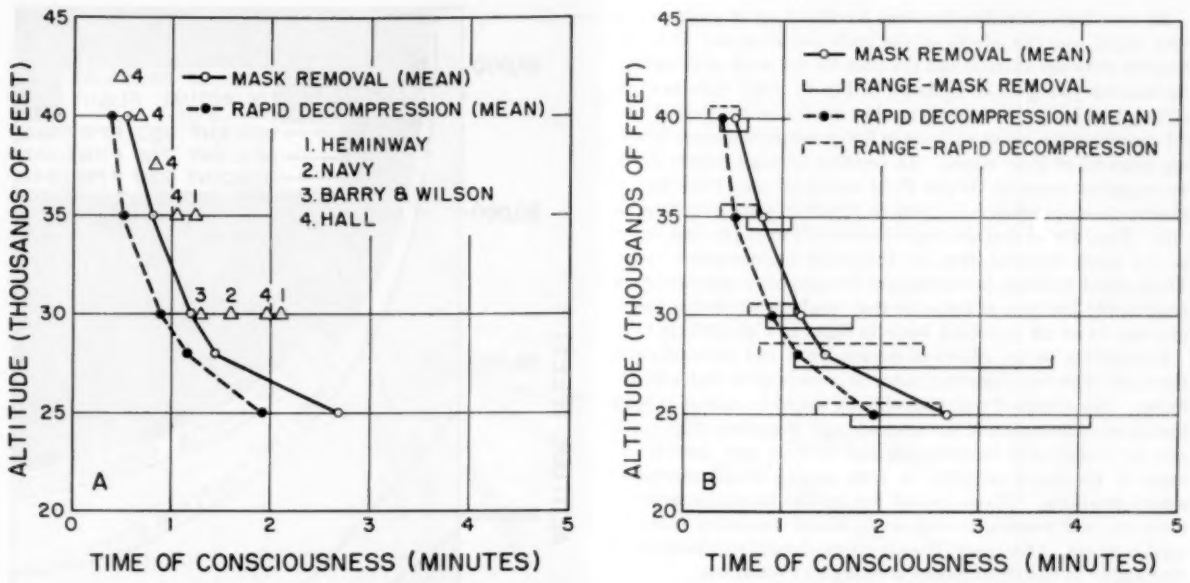

FIG. 5 DURATION OF USEFUL CONSCIOUSNESS IN RELATION TO ACUTE OXYGEN WANT

(Figure summarizes findings of several investigators regarding time limits within which a person can retain useful consciousness at various altitudes following removal of oxygen mask—solid curve—or rapid decompression at same altitude—dashed curve. Time of useful consciousness is greater in mask-removal experiments than following rapid decompression. Note wide range of individual reactions compared with mean response of subjects in part B of figure. Comfort and Wilson, reference 15.)

than when they are hot. The symptoms are capricious; for no apparent reason, a subject may experience bends one day and not another. Since fat per unit of mass dissolves 5 or 6 times more nitrogen than does blood, the tissues having the highest content of fat are most favorable to bubble formation. There are other unknown factors that account for the wide range of individual susceptibility.

The next most common manifestation of decompression sickness is referred to as "chokes." The symptoms comprise a group of disturbances beginning with a burning sensation in the substernal region of the thorax or deep respiratory passages. The burning pain becomes increasingly severe and persistent and is accompanied by the development of a nonproductive cough which becomes spasmlike. Once the burning sensations and coughing have begun, a viscious cycle is set up wherein increased ventilation of the lungs leads to coughing, which in turn leads to air hunger and results in more strenuous breathing. Breathing becomes progressively more shallow, and there is a sensation of suffocation followed by faintness or collapse.

Other symptoms occurring in aeroembolism as a result of the lowered barometric pressure are as follows: (*a*) Dermal reactions, including tingling, itching, cold and warm sensations, and small bubbles or blisters beneath the skin; (*b*) neurological symptoms, resulting in transient impairment of vision, especially blind spots, and persistent dull headaches; (*c*) abdominal distress, caused by expansion of gas in the digestive tract. These latter symptoms are characterized by a feeling of distention and at times by severe cramps. They are usually rapid in onset but are not serious in most persons in flights below 20,000 ft.

Effects of Rapid Decompression in Flight. The first hazard in rapid decompression is the fact that, if an astrodome, emergency hatch, or window fails, the pressure gradient is equalized rapidly and with great force. In such an event, an individual sitting or standing near the opening might be swept out of the plane; such cases are on record in both civilian and military operations. Thus the importance of indoctrinating the crew members in the necessity of keeping their safety belts fastened and their essential instruments and equipment securely attached at all times is emphasized.

A second hazard results from the direct effects of a very rapid rate of decompression. There are at least four important physical variables that must be considered: (*a*) The volume of the pressurized compartment, (*b*) the size of the opening, (*c*) the pressure differential, and (*d*) the flight altitude at which the decompression takes place (13, 14). Naturally, the most drastic decompression possible would be that occurring in the smallest cabin with the lowest cabin altitude at the highest possible flight altitude. Experiments have been made at Wright Field to test very extreme conditions in small military aircraft in flight at 35,000 to 40,000 ft (5). The results indicated that the average subject experienced a sense of inflation in the chest and abdomen as a result of expanded gas, and about 20 per cent of them suffered "bends" during the first 5 min at high altitude These conditions were much more acute than would be experienced in transports with larger pressurized areas.

By far the greatest and most serious hazard of a rapid decompression is that of acute oxygen want, since useful consciousness can be maintained no longer than about 1 min at 40,000 ft. This is an important consideration at all altitudes above 25,000 ft (see Fig. 5). The indicated time reserves in the figure are for subjects at rest and would be less for an active pilot carrying out a certain amount of emergency action. The air crews should don oxygen masks immediately on reaching an altitude of 8000 ft and should be thoroughly familiar with their use and accessibility. The masks should be of the oral-nasal type with a built-in intercommunication system to avoid loss of consciousness, which might occur if an airman talks while using a nasal-type mask. Until the possibility of pressure failure has been eliminated completely, at least one crew member should wear an oxygen mask at all times as an added safety measure. A potentially more serious problem of acute oxygen want exists (*a*) if a plane should be forced to remain at altitudes over 25,000 ft after loss of pressure due to weather or terrain and (*b*) if sufficient oxygen is not available for all crew members and passengers (1).

At very high altitudes, the time for the onset of symptoms is very rapid, and the effects on the body are extreme. The relationship between altitude and the time for the onset of symptoms for healthy young males is shown in Fig. 5. Such tests as card-sorting and handwriting were used as criteria of the time of useful consciousness, using subjects in low-pressure chambers following removal of their masks. In addition to mask removal, the investigation made at Wright Field employed tests following explosive decompression from 8000 to 10,000 ft while breathing air (15). They found that the time reserve is 29 to 49 per cent longer in the mask removal than in the rapid-decompression series. These latter findings are significant because they simulate more realistically the type of response that would occur during loss of pressure in an air transport while in flight at high altitude (16).

In addition to the effects of oxygen want and aeroembolism, there are other variables that must be considered in high-altitude flying. The effects of cold undoubtedly would be serious in some instances. Distention of the stomach and intestines might give rise to considerable disturbance, and persons with certain diseases of the heart or lungs or with anemia would experience severe reactions. Glasses would fog up due to condensation of moisture, and passengers with acute visual anomalies would be unable to see. Obviously, the air crews should be indoctrinated thoroughly to handle all phases of emergency situations.

Operating Experience With Pressurized Transports. Ten rapid-decompression failures occurred on U. S. scheduled transports as of January 1, 1950, in approximately 1,000,000 flying hours. Four took place on the Constellation in 511,038 hr of operation, five in the DC-6 in 441,262 hr, and one in the B-377 in 23,501 hr. Thus the rate of sudden compression failures has been 1 in about 96,000 hr of flying. All the incidents listed for the DC-6 were confined to door-latch mechanism failures. In the case of the L-49, one failure was caused by the loss of an astrodome, one by an incident in which a propeller went through the fuselage, and two by failure in the door mechanism. During 1950–1951 and the first 8 months of 1952, eight additional rapid decompressions occurred. Three involved the B-377; in two instances, the main cabin door blew open due to a failure of the lock, and in the other, cabin pressurization was lost when a piece of the propeller ruptured the fuselage. Two incidents on Constellations involved failure of the windows, and two on DC-6's resulted from the failure of a door and rupture of the fuselage by a propeller blade. A similar incident also took place on a CV-240.

Fig. 6 indicates the approximate altitude at which three of the explosive decompressions occurred and the general descent patterns followed. In all cases it was possible to descend to safe altitudes in approximately 10 to 12 min or less. In the event of a rapid decompression at higher altitudes, the rate of descent necessary for pilots breathing oxygen to avoid unconsciousness is shown in Fig. 7 (2). The report of the SAE Committee A-9 on "Air Conditioning of Aircraft at High Altitudes" should be consulted (14).

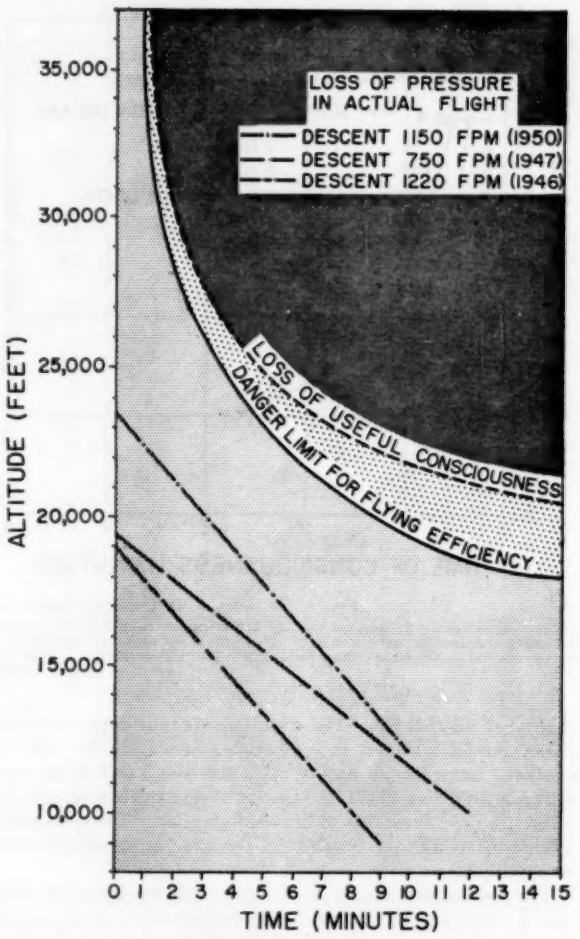

FIG. 6 EXAMPLES OF FORCED-DESCENT PATTERNS

(Figure shows patterns of descent from approximately 20,000 ft following a sudden loss of pressure on commercial air transports in relation to time for loss of flying efficiency and useful consciousness. No serious symptoms were experienced by flight crews or passengers, although it is obvious from figure that loss of pressure at 30,000 to 40,000 ft would be very serious. McFarland, reference 2.)

INFLUENCE OF OTHER VARIABLES AT HIGH ALTITUDES

Cosmic Radiation. The primary particles which make up cosmic radiation are protons, neutrons, alpha particles, and heavy nuclei. These particles come from outer space and travel at high velocities. Cosmic "rays" are much more penetrating than other radiations. Cosmic radiation can be measured by its ionizing effect with the aid of the same device used to measure other ionizing rays, such as x rays. Such measurements have been made by Millikan and his associates. On the basis of fairly extensive research with x rays and radium, the biological effects of cosmic radiation can now be estimated. Accurate predictions, however, are not possible since the densely ionizing cosmic radiation, consisting of neutrons and heavy primary particles, may differ in biological effect from the less densely ionizing x rays. Nevertheless, careful analysis of cosmic-radiation data indicates that its biological effectiveness definitely will be less than 10 times that of x rays.

It has been calculated that an aviator spending 1000 hr a year at 55,000 ft would receive in an average week only 0.015 unit of exposure. For the medical profession and Atomic Energy Commission 0.3 roentgen unit of exposure per week is considered safe, or a dosage 20 times that received by the pilot just mentioned. Even if the biological effects of cosmic radiation were 10 times that of x rays he would still receive only one half of the dosage considered safe for indefinitely continued exposure (5).

Visual Problems. The eyes can adjust to a great range of light intensities but the ability to read aircraft instruments falls off as light is reduced. In night flying it is often necessary to use the lowest light intensity at which instruments can be read safely. Below 0.01 foot-lambert (effective foot-candle) instruments cannot be read satisfactorily and pilots usually prefer slightly higher values. Lightning flashes create special problems in cockpit illumination and such blinding flashes destroy dark adaptation.

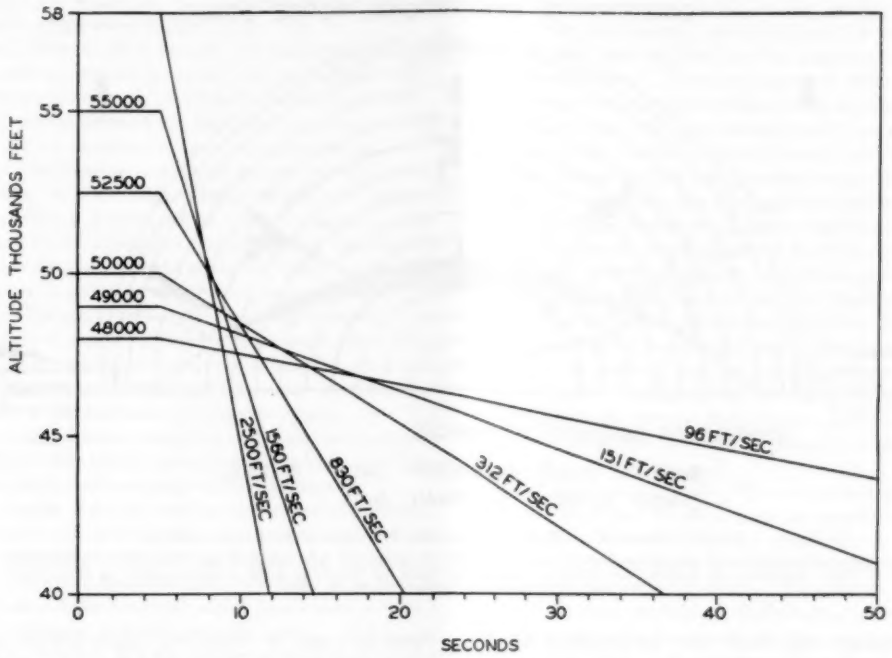

FIG. 7 RATE OF DESCENT NECESSARY FOR AIR CREWS BREATHING OXYGEN TO AVOID UNCONSCIOUSNESS AFTER RECOMPRESSION

(It is obvious from this figure that very rapid descents would have to be made if a loss of pressure occurred at high altitude. Committee A-9, Society of Automotive Engineers, reference 14.)

Under these conditions approximately 10 foot-candle power may be required which would destroy dark adaptation for seeing outside the plane at night.

There are interesting changes in the visual surroundings of the pilot in flight at very high altitudes. The quality of the light itself is changed; there are not enough dust particles to diffuse it. Also, with the clouds and earth far below him the pilot has no points of reference for judgment of distances in focusing on objects. The sun's rays become more intense and contain a higher proportion of ultraviolet light, the sky becomes darker, and there is less haze. The use of sunglasses becomes more necessary as protection against the ultraviolet radiation and the increased light intensities. However, because of the darkened sky, shadows become darker, instruments and shaded areas of the cockpit are darker, but sunlight areas are more glaring. The reading of instruments may become especially difficult where there are small windshields and glare shields over the panel. In such occasions white artificial lighting may be used or, on some occasions, sunglasses of graded density (5).

STIMULI PRIMARILY RELATED TO HIGH-SPEED FLIGHT

Flights at very high but uniform speeds and without change of direction have no adverse effects on man as long as he is protected against wind blast. Any considerable deviation in speed or direction, however, is immediately sensed. Man lives in an environment characterized only by gravitational forces when he is resting quietly. Additional forces imposed by change in motion under such ordinary circumstances as running, walking, and low jumping are not of practical importance. Accelerative forces may become limiting factors in performance or even survival in high-speed aircraft, however, during maneuvers, crashes, and related situations.

Influence of Acceleration and Motion. Acceleration is defined as a change in speed or direction of a moving body. It is designated as positive ($+g$) or negative ($-g$) according to whether the change in speed is an increase or a decrease or the change of direction results in forces acting from head to seat or seat to head. Forces also may act in the horizontal or transverse direction, i.e., from front to back, or vice versa (Tg). There are three general types of acceleration: (a) Linear, as in take-offs, landings, and crashes; (b) radial, as in turns; and (c) angular, as in spins and certain types of acrobatics. Type (a) involves a change in rate, (b) a change in direction, and (c) a change in both (2, 5).

Linear accelerations, which are best tolerated in the ordinary seated position, ordinarily will present few difficulties on transport planes. While the exact tolerance to linear acceleration when fully stretched out is not known, it is believed to be low. Thus possibly the passenger on sleeper planes reclining with his head toward the cockpit would have excessive positive g forces imposed on him, especially during highly accelerated take-offs. The problem of linear acceleration will become important in the positioning and protection of the air crews and passengers when future transports are equipped with jet or rocket-type propulsion. As speeds increase and flight durations are reduced greatly, however, sleeping accommodations may not be necessary.

Radial acceleration in aircraft is primarily a problem in combat-type military planes. Since aerial combat may require completion of extreme maneuvers at very high speeds, the planes must be highly stressed. In certain instances the personnel, even though carefully selected for physical fitness, must be given personal protective equipment and indoctrination in the methods of increasing their tolerance (17).

The relation of air speed to the production of various magnitudes of g should be considered for human tolerance to radial acceleration (1). If speed is held constant, the number of g increases as the radius of turn decreases. For example, at a speed of 300 mph, g increases from 3 to 6 as the radius of turn decreases from about 2000 ft to approximately 1000 ft. This problem is

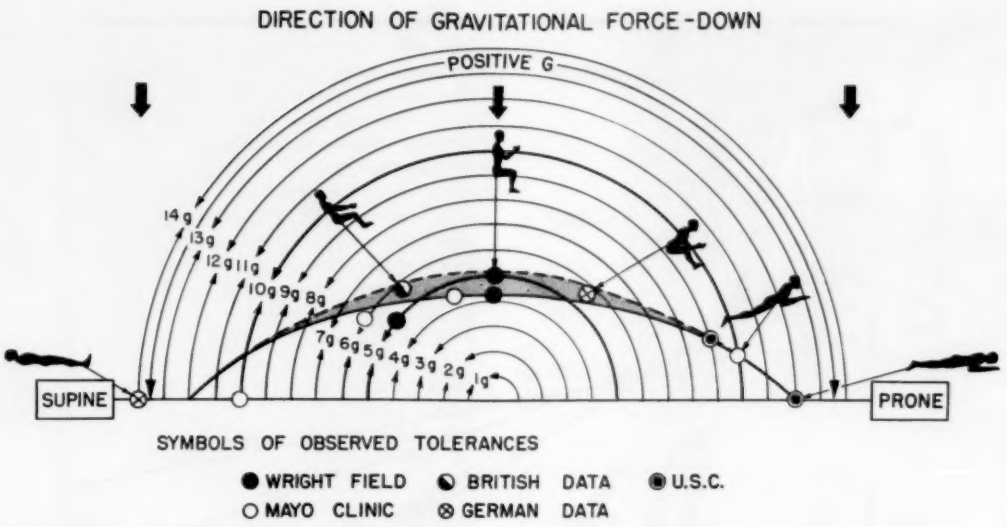

FIG. 8 EFFECTS OF BODY POSITION ON TOLERANCE TO ACCELERATION

(Figure summarizes results of several studies of human tolerance to sustained accelerations of 10 sec or more duration. Note extent to which resistance to positive acceleration may be increased by assuming body positions such as crouching or lying prone or supine. Gagge, reference 18.)

becoming increasingly important with jet-propelled aircraft.

Human Tolerance to Acceleration. Numerous experiments have been carried out to determine human tolerance to sustained accelerations of 10 sec or more duration. These data, shown graphically in Fig. 8, indicate that body position has an important influence on tolerance (18). The subjective effects of positive accelerations can be summarized as follows: At 2 g, the subject is pressed firmly into the cockpit seat; at 3 to 4 g, upward movements of the extremities become difficult or impossible, and the soft tissues of the face and body begin to sag. At a force of only 3 g a pilot will be immobilized in his seat and will need assistance or some kind of propulsive device if he is to escape from his plane. At 3.5 to 5 g, visual disturbances begin, characterized by dimming of vision. When the forces are relatively small, as 3 to 5 g, marked physiological effects are not produced for about 5 sec, and a continuance of the force beyond 10 sec probably will not increase the severity of the symptoms. At or above 5 or 6 g, unconsciousness may result within 5 sec. As accelerative force rises to about 7 to 9 g, the time required for blackout or unconsciousness to occur may be as low as 2 sec (5).

The dimming or complete loss of vision and consciousness that may result from exposure to high positive accelerations in aircraft or on the human centrifuge is caused by reduced amounts of oxygen in the retina and brain. The effects are the result of the marked decrease in arterial pressure at the level of the head produced by the centrifugal force. Since extreme oxygen want produces temporary functional or permanent histological damage to the brain and certain other tissues, the question has been raised whether test pilots or combat airmen might suffer permanent neurological damage. Many of the personnel of human centrifuge laboratories have served repeatedly as subjects in such tests. It has been found that repeated exposures of 5 to 10 sec duration have no untoward effects and that pilots have nothing to fear from the residual effects of repeated blackouts or similar episodes experienced in flight (19).

The limit of man's tolerance to negative acceleration is reached at the comparatively low values of —2 to —3 g. The flow of blood toward the head results in congestion and a sharp rise in blood pressure; gritting sensations occur in the membranes of the eyelids, and throbbing pains are felt in the head. At —3 g, the visual field may be colored red, retinal function may be impaired, and a persistent headache may develop. At values exceeding —3 g, such serious complications as retinal and cerebral hemorrhages can be anticipated.

In both positive and negative acceleration with the forces acting along the long axis of the body, the chief effects are on the cardiovascular system. The heart, which acts as a pump, must work against an excess pressure of about 120 mm Hg to force blood to the head during a positive acceleration of 5 g. The heart is unable to compensate for this added force, however, and the brain is deprived of its blood flow. If the deprivation is sustained, unconsciousness intervenes. In negative acceleration, the blood is forced into the head, and pressure may rise greatly since the bony structure of the head does not permit a ready expansion of the blood vessels. The effects on the nervous system are secondary to those effects resulting from changes in blood pressure and flow and have not been of as much concern to investigators.

In military flying, human tolerance to g-forces has been increased by the development of special devices, such as pneumatic suits which limit the flow of blood to the extremities, and by crouching or assuming other positions (see Fig. 8). In the unprotected pilot, a tolerance to Tg is 2 or 3 times as great as that to $+g$. Thus one method of increasing maneuverability has been to substitute Tg for $+g$ by placing the pilot in a prone position. In making a turn, the centrifugal force is directed across the body from front to back rather than along the long axis of the body. If a pilot is in the prone position, it is possible to turn within so small a radius of curvature that 12 to 15 g may develop, provided that the g-tolerance of the aircraft is great enough. Under such conditions, gross muscular disabilities may be so great as to impair breathing, and the arms and legs may become too heavy to be controlled. Obviously, it would be unwise to expose pilots or passengers to such forces during flights at supersonic speeds. By decelerating the aircraft quickly, a sharp turn can be accomplished without exceeding the tolerance of the pilot for $+g$. The rate at which the plane is decelerated, however, must be kept within the limits of the human tolerances for Tg-forces (5). A complete review of human tolerance to accelerative forces has recently been compiled from the literature and summarized in tabular

and graphic form by White of the Lovelace Foundation for Medical Education and Research (20).

Pilot Reaction Times at High Speeds. In high-speed aircraft additional demands are placed upon the pilot in so far as vision and reaction time are concerned. With high closing speeds only a few seconds may elapse between the sighting of another aircraft and its passing. Often the decision for action must be made and the correct control response initiated and carried out in a matter of seconds. Owing to these high closing speeds and reduced turning radii a jet pilot will often not be able to bring his aircraft into firing position unless a target is picked up at a considerable distance. In the same manner flight obstacles must be picked up at greater distances in order for the proper evasive action to be taken. Mid-air collisions, especially in the neighborhood of airports, are currently a serious problem. In recent years there have been 11 mid-air collisions involving scheduled air transports with other planes, resulting in 130 fatalities. Such hazards naturally increase while operating at greater speeds (2). The extent to which a lag in visual perception and reaction times may have been involved is not known but pilots flying high-speed aircraft must be indoctrinated in regard to this problem.

At supersonic speeds, if a pilot sees another plane approaching half a mile away, it will have passed him before the stimulus registers on the perceptive center of his brain. At 600 mph a plane travels a mile every 6 sec or about 880 fps. If a pilot is flying at 600 mph on a collision course with a fixed object, about 2 to 3 sec might be involved in taking evasive action. The latent period of the pilot involves 0.8 sec for recognition, 0.5 sec for visual accommodation, 0.07 sec for foveal perception, 0.05 sec for eye movements, and 0.175 sec for reaction time. In addition, the time required for the response of the plane itself must be considered. Thus a distance of 2000 to 3000 ft might be traversed before evasive action could be taken (2).

While pilots of high-speed aircraft carry out many of the same activities as they would in slower planes, there is often much less time and consequently a high premium is put upon reaction time. A moment's hesitation can have serious implications. However, it is under such conditions of stress requiring instantaneous decisions that human errors are most likely to occur in reading instruments or operating controls. A pilot may often do what seems "natural" rather than what he has been trained to do. For this reason all of the pilot's operational activities should be designed, in so far as possible, to coincide with what his natural reactions would be. Significant progress has been made along these lines in recent years. In Fig. 9 the distances traveled before a pilot can complete the process of perception and initiate a muscular reaction in response to a visual stimulus is shown graphically (21, 22, 23).

Visual Illusions in Flight. The designer should keep in mind the fact that visual illusions may be accentuated during high-speed flight. Illusory responses result from a wide variety of causes and are frequently classified according to whether they are visual or nonvisual in origin. The former are primarily related to the visual mechanism, while the latter arise from stimulation of the vestibular mechanism in the inner ear and the muscles, tendons, and joints. Misinterpretations may be caused by the

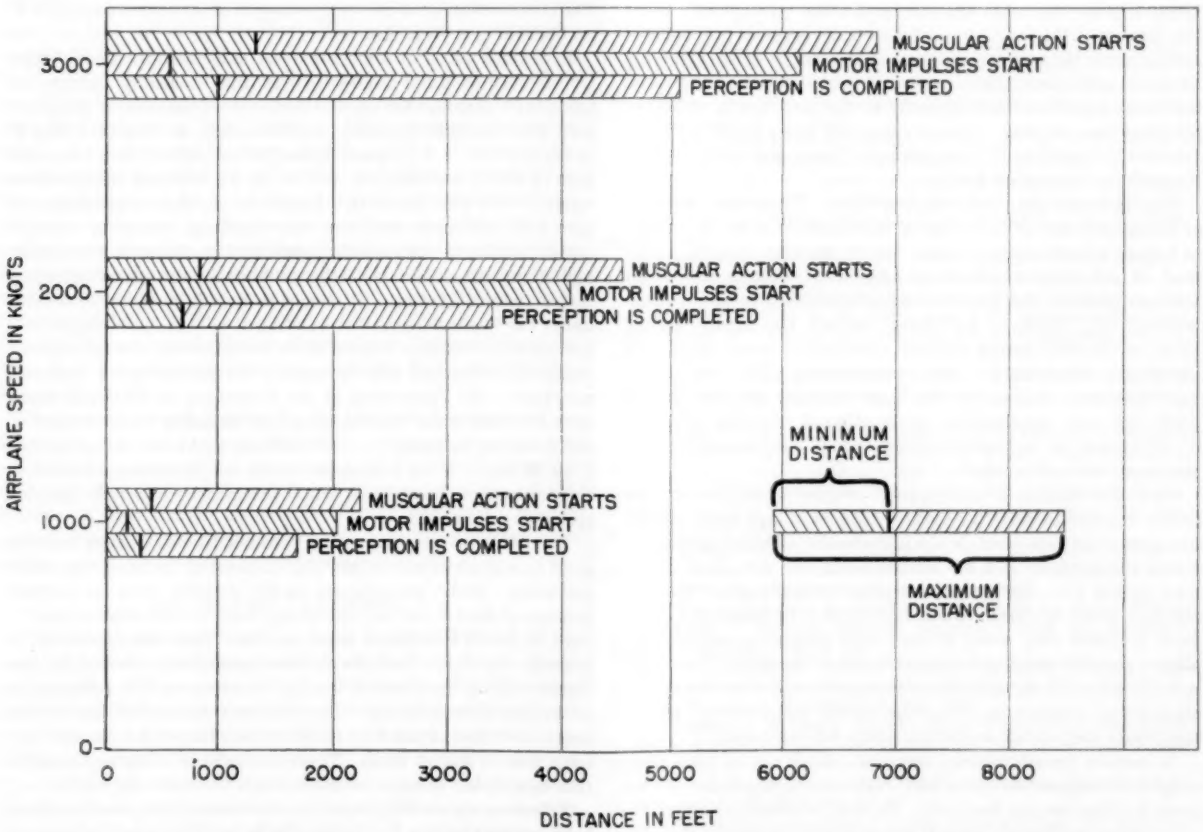

FIG. 9 DISTANCES TRAVELED BEFORE PILOT MIGHT PERCEIVE VISUAL STIMULUS AND INITIATE MUSCULAR RESPONSE
(Minimum distances represent bright visual stimulus in line of sight when subject is forewarned of conditions. Maximum distances represent faint stimulus slightly out of exact line of vision without previous warning. Strughold, Canfield, et al., references 21, 22, and 23.)

conflict of one visual cue with another or by various combinations of visual and nonvisual stimuli. A brief summary of representative illusions most commonly reported by airmen may be found in the author's most recent book, and a complete bibliography, including abstracts of experimental studies has been compiled by the U. S. Air Force (2, 24).

One of the most common visual illusions that has been the cause of many accidents in aviation as well as on the highways is the autokinetic illusion. It may be described as the tendency of a single fixed point of light to appear to move in a random fashion when looked at steadily against a dark background. When a subject is asked to localize such a source of light, he will report that he cannot do so with certainty because it appears to move. This apparent shifting of a light that is actually fixed is known as autokinetic movement. Conditions favorable to this phenomenon are (*a*) a dark environment, (*b*) a small single stimulus of low intensity, (*c*) steady fixation, and (*d*) ocular or general fatigue. In 1941 the CAB required the use of alternately blinking lights on the tail, wing tips, and fuselage of all air transports and since 1950 on all aircraft. Autokinesis is destroyed by such a design because steady fixation on a single point of light cannot be maintained.

The oculogyral illusion has its origin in the stimulation of the vestibular mechanism rather than in the eye alone (25). It may occur when a series of small angular accelerations are experienced by the pilot. For example, if propeller torque, rough air, or some other cause produces yawing movements of the plane, the deviations from the course can be corrected by successive applications of the rudder. During each such adjustment, however, the receptors of the semicircular canals of the ear react to the deviations, reflexly stimulate the eye, and cause nystagmus. Since the motion of the fluid caused by each deviation is not counteracted during the recovery because of the inertia of the fluid, the effects may be cumulative. As a result, the objects in the visual field will appear to rotate opposite to the direction in which the pilot has been moving. It is obvious that pilots should be indoctrinated in regard to the recognition of these and other illusory responses in high-speed flying.

Control Forces and Performance of Pilot. The present concepts of flying have incorporated within them a need for the application of human proprioceptive senses; that is, the pilot receives a good deal of information about his aircraft's attitude and speed through position and pressure stimuli presented to him through his controls. Pilots of high-speed aircraft rely greatly on the "feel" of the stick during gunnery attacks or evasive action, with occasional reference to other instruments. The feel of the back pressures exerted by the flight controls provides the jet pilot with early approximate information of what the plane will do as a result of his control actions before the plane and its instruments have responded.

As is well known to aeronautical engineers, the tremendous forces required to move the control surfaces of high-speed aircraft are so great as to necessitate the introduction of boost systems between the controls and the control surfaces. Jet pilots, therefore, do not have the same direct pressure feedback or "feel" on the stick which is present in slower aircraft. In addition, control-force reversals may occur at very high airspeeds, such as right aileron pressure causing the plane to roll to the left! Thus pilots must continually sample aircraft response and sense changes in stick forces because at very high speeds instability of control may cause the aircraft to disintegrate in a few seconds.

In certain recent models, however, which are of such great weight or designed to fly at such high speeds, the forces are too great to allow for any feedback. In such irreversible systems the pilot no longer flies his aircraft but adjusts a hydraulic metering valve which directs the desired forces. Attempts have been made to develop an artificial feel system to duplicate the positions and forces in the control system of the older-type aircraft. In this way the previously learned flying habits of the pilot are unimpaired. This requires a knowledge of human-response characteristics when the pilot is considered as a part of the total servoboost control system. Further research is indicated in regard to whether such systems should comprise feel alone, position or pressure alone, or simple visual stimuli (1, 26).

Stimuli Primarily Related to Cabin Atmosphere

Tolerance to High and Low Temperatures. The efficiency of flight crews may be influenced adversely if certain stimuli in the cabin atmosphere are not maintained within reasonable limits. Probably the most important variables are (*a*) ventilation, temperature, and humidity, and (*b*) noxious gases and vapors. Very cold or hot temperatures may be encountered in a forced landing in arctic or tropical regions. A failure of the heating system, window, or door would create an unusually cold environment in flight at even moderate altitudes.

A significant factor in the operation of high-speed aircraft is the high temperatures generated by (*a*) the frictional impact of air on their outer surfaces, (*b*) the power plant, (*c*) the compression of air for the ventilating systems, and (*d*) solar radiation. This aerodynamic heating is, in part, a function of the number of molecules of air encountered by the plane's surfaces during a given time period. Hence both high speeds and/or dense air will increase temperatures within the plane. In the absence of refrigeration, the temperature within the cabin of an aircraft travelling at 650 mph at sea level could be as much as 70 deg F above the outside ambient-air temperature. Temperatures as high as 160 F have been recorded in the cockpit of jet aircraft and 275 F on the skin of a V2 rocket.

In general, this problem is somewhat alleviated by the fact that jet aircraft or other high-speed vehicles normally operate at fairly high altitudes for there is a consistent decrease of temperature with altitude, equaling approximately a drop of 1 deg F in every 300 ft. A jet plane taking off at sea level in a temperature of 59 F, for example, will be in an external temperature range of —67 F at 36,000 ft. In spite of the decrease of temperature with altitudes, however, the dominant factor of aerodynamic heating at high speeds is sufficient to maintain reasonably high temperatures so that the problem is one of refrigeration rather than of heating. It should be noted, however, that even under the worst temperature conditions of high-speed flight, i.e., low altitude, hot day, failure of air conditioning, the anticipated temperatures would still be within the physiological limits of tolerance. Air Force tests at the University of California have revealed that under conditions of low humidity temperatures of 160 F can be tolerated for over an hour, and even as high as 240 F for 23 min. Even if practical limits for pilots were one half of these tolerance times, there would presumably be ample time for remedial action (26).

The limits of tolerance to cold are not so well defined and depend to a great extent on activity, amount of clothing, and other variables. Body temperature rarely departs from its normal average of 98.6 F, but prolonged exposure to cold weather can reduce it to 75 F without fatal results. This limit, however, is seldom exceeded. Such levels were apparently reached by the Nazis at Dachau in their inhuman experiments with prisoners in water just above freezing. Exposure to water at 50 F for 45 min can cause a fall of 5.5 F in body temperature and a state of collapse that is almost fatal. There seems to be some acclimatization to cold, but it is not so marked as is the case with heat.

Tolerance curves for aircraft environmental temperatures have been evolved by the Air Service Technical Command in terms of exposure times, using vapor pressure and amount of clothing as

parameters. For instance, a temperature of 100 F can be tolerated three times as long when the atmosphere is moderate as when it is humid, and while a zero temperature cannot be endured at all in light clothing it can be tolerated for 4 hr when dressed in very heavy clothing (27).

More recent developments in the field of protective clothing for military personnel consist of the anti-*g* equipment, high-altitude pressure suit, and thermal protection combined into one integrated unit. Difficulties in regard to visibility and mobility are being overcome, and such equipment offers great promise in the field of high-altitude and high-speed flying.

Tolerance to Toxic Gases and Vapors. Aeronautical engineers should be aware of the potential dangers of toxic gases and vapors or other substances airmen may encounter in all types of aircraft. Hazardous situations occasionally arise from the least suspected sources in spite of extensive flight tests of new equipment and careful appraisal of all fluids and other substances. The concentration of a gas expressed in terms of percentage or parts per million does not describe adequately the conditions encountered in aviation. The amount of bodily absorption can be determined accurately only when all the following factors are known: (*a*) The percentage concentration of gas in the ambient air; (*b*) the barometric pressure; (*c*) the temperature and humidity of the air in direct contact with absorptive surfaces of the body; and (*d*) the magnitudes of any gaseous exchange affecting concentrations in air in contact with the body.

Of the various hazards, smoke from insulation or overheated electrical equipment, carbon monoxide (CO) from cabin internal-combustion heaters and engine exhausts, and carbon dioxide (CO_2) from fire extinguishers and refrigeration equipment are the most common sources of trouble. Ten to twelve instances of a cockpit filling with smoke are reported to the CAA each month in U. S. airline operations, and approximately 60 per cent of them are attributable to overheated electrical equipment. There were over 250 such cases from October, 1948, through December, 1950. Adverse effects from exposure to gasoline fumes and vapors have been observed when the cabin or cockpit atmosphere has been contaminated by (*a*) leaking tanks or piping connections, (*b*) fuel transfer, and (*c*) fuel dumping. Pipes and gages carrying hydraulic fluid under pressure may be a source of contamination should leaks develop. Sometimes harmful fumes are produced when leaking oil comes in contact with hot surfaces. Representative incidents have been reviewed by the Committee on Aviation Toxicology of the Aero Medical Association in air transportation and similar reports are available from the Military Services (2, 5, 28).

The role of human factors in the operation of bombers on long-range missions has been studied by a team of scientists representing the engineering, operational, and medical personnel of the Air Research and Development Command of the USAF. Studies of this nature should be of great interest to aircraft manufacturers in assisting them to improve the effective integration of the air crews and their equipment (29).

Summary and Conclusions

The objective of this paper has been to review several of the more important human factors which are involved in the design and operation of high-speed and high-altitude aircraft. Considerable attention is devoted to a better understanding of the aircraft environment and the related limitations imposed on human performance especially by the adverse effects of high altitudes and the resulting functional limitations on the brain and sense organs. It is first shown that oxygen want at high altitudes gives rise to a progressive and insidious deterioration of performance. Although cabin pressurization and pressure-breathing equipment provide satisfactory solutions, much remains to be done in improving the comfort and reliability of such advances. Sudden loss of pressure is shown to be very serious, especially the symptoms related to aeroembolism which may occur during explosive decompression. The visual problems encountered at very high altitudes have introduced a number of unusual factors which are being brought under control by a redesign of cockpit illumination systems and other aids to the pilot.

The adverse stimuli relating to high-speed flight are shown to center around the accelerative forces which build up rapidly during sudden maneuvers, especially during combat flying. Some protection can be afforded the pilot with anti-*g* suits but the limiting factors remain serious ones and all pilots should be indoctrinated in regard to their physical responses from such maneuvers. The visual and motor reaction times of pilots are shown to impose serious limitations in high-speed jet flying. Also, the most satisfactory methods of designing the controls of modern aircraft to come within the range of human capabilities is shown to be deserving of further research. Human tolerance for heat and cold is outlined so that aeronautical engineers might have a better understanding of design problems related to cabin atmosphere. The hazards resulting from noxious gases and vapors also are considered. The need for air-crew indoctrination in the effective use of equipment is emphasized throughout the paper as well as the need for airmen to understand their own physical limitations while in flight. Finally, the need for more effective collaboration between the biological and engineering sciences is stressed in regard to improving the man-machine systems in high-speed, high-altitude flying.

Bibliography

1 "Human Factors in Air Transport Design," by R. A. McFarland, McGraw-Hill Book Company, Inc., New York, N. Y., 1946.

2 "Human Factors in Air Transportation—Occupational Health and Safety," by R. A. McFarland, McGraw-Hill Book Company, Inc., New York, N. Y., 1953.

3 "Human-Engineering Aspects of Safety," by R. A. McFarland, *Mechanical Engineering*, vol. 76, 1954, pp. 407–410.

4 "The Effect of Carbon Monoxide and Altitude on Visual Thresholds," by R. A. McFarland, F. J. W. Roughton, M. H. Halperin, and J. I. Niven, *Journal of Aviation Medicine*, vol. 15, 1944, pp. 381–394.

5 "Physiology of Flight," Air Force Manual, 160–30, Department of the Air Force, Washington, D. C., July, 1953.

6 "The Effects of Oxygen Deprivation (High Altitude) on the Human Organism," by R. A. McFarland, CAA Technical Development Report 11, Government Printing Office, Washington, D. C., 1941.

7 "Flight Surgeon's Reference File," AAF Manual 25-O-1, United States Army Air Forces, Washington, D. C., November 1, 1945.

8 "Visual Thresholds as an Index of Physiological Imbalance During Anoxia," by R. A. McFarland, et al., *American Journal of Physiology*, vol. 142(3), 1944, pp. 328–349; also, "The Relation Between Foveal Visual Acuity and Illumination Under Reduced Oxygen Tension," by R. A. McFarland and M. H. Halperin, *Journal of General Physiology*, vol. 23(5), 1940, pp. 613–630.

9 "Anoxia and Oxygen Equipment," by G. A. Millikan, Chapter 24 in "Advances in Military Medicine," by E. C. Andrus, Little, Brown and Company, Boston, Mass., vol. 1, 1948.

10 "Trend of Anoxia Accidents in the Eighth Air Force Heavy Bombardment," October, 1943, to November, 1944, *Air Surgeon's Bulletin*, vol. 2(3), 1945, p. 83.

11 "Decompression Sickness–Caisson Sickness, Diver's and Flier's Bends and Related Syndromes," edited by J. F. Fulton, W. B. Saunders Company, Philadelphia, Pa., 1951.

12 "Incidence of Bends Pain in Short Exposure to Simulated Altitudes of 26,000, 28,000, and 30,000 Feet," by H. A. Smedal and E. B. Brown, *BuMed News Letter*, vol. 8(5), 1947, p. 3.

13 "Explosive Decompression," by H. M. Sweeney, *Air Surgeon's Bulletin*, vol. 1(10), 1944, pp. 91–94.

14 "Aeromedical Aspects of Cabin Pressurization for Military and Commercial Aircraft," by W. R. Lovelace, II, and A. P. Gagge, *Journal of the Aeronautical Sciences*, vol. 13(3), 1946, pp. 143–150; also, "Air Conditioning of Aircraft at High Altitude," Aeronautical

Information Report No. 33, prepared by Committee A-9, Society of Automotive Engineers, New York, N. Y., 1953.

15 "Some Factors Affecting Time Consciousness at High Altitudes," by E. Comfort and J. W. Wilson, Air Materiel Command, United States Air Force, Wright-Patterson Air Force Base, Dayton, Ohio, Technical Report 5970, February, 1950.

16 "Times Available for Protective Measures in Emergencies at High Altitude," by B. G. King and J. J. Swearingen, Medical Division, Civil Aeronautics Administration, Washington, D. C., April, 1951.

17 "Effects of Acceleration in Relation to Aviation," by E. H. Wood, E. H. Lambert, E. J. Baldes, and C. F. Code, *Federation Proceedings*, vol. 5(3), 1946, pp. 327–344.

18 "Human Requirements for the Design of Supersonic Aircraft," by A. P. Gagge, paper presented at the meetings of the American Association for the Advancement of Science, Boston, Mass., December, 1946.

19 "Do Permanent Effects Result From Repeated Blackouts Caused by Positive Acceleration?" by E. H. Wood, E. H. Lambert, and C. F. Code, *Journal of Aviation Medicine*, vol. 18(5), 1942, pp. 471–482.

20 "Bibliographic Tolerances to Accelerative Forces," by C. S. White, Lovelace Foundation for Medical Education and Research, Albuquerque, New Mexico, 1954.

21 "The Human Time Factor in Flight," by H. Strughold, *Journal of Aviation Medicine*, vol. 22, 1951, pp. 100–108.

22 "A Study of Reaction Time to Light and Sound as Related to Increased Positive Radial Acceleration," by A. A. Canfield, A. L. Comrey, and R. C. Wilson, *Journal of Aviation Medicine*, vol. 20, 1949, p. 350–355.

23 "Basic Environmental Problems Relating to Man in the 'Aeropause' as Seen by an Aeronautical Engineer," by A. M. Mayo, Douglas Aircraft Company, Inc., El Segundo, Calif., 1951.

24 "Annotated Bibliography on the Psychological Aspects of Orientation as They Relate to Aviation," by T. G. Hermans and R. B. Loucks, AAF Report TSEAA-694-16A, Engineering Division, Air Materiel Command, Wright Field, Dayton, Ohio, December, 1947.

25 "The Oculo-Gyral Illusion: A Form of Apparent Motion Which May Be Observed Following Stimulation of the Semi-Circular Canals," by A. Graybiel and D. I. Hupp, *Journal of Aviation Medicine*, vol. 17(1), 1946, pp. 3–27.

26 "Synopsis of the Aero Medical Aspects of Jet Propelled Aircraft," Engineering Division, Medical Laboratory, Air Materiel Command, Wright-Patterson Air Force Base, Dayton, Ohio, January, 1949.

27 "Thermal Requirements for Aircraft Cabins," Engineering Division, Air Technical Service Command, Wright Field, Dayton, Ohio, AAF Mem. Report TSEAL-3-695-56, August, 1945.

28 "Aviation Toxicology," prepared under the direction of the Committee on Aviation Toxicology, Aero Medical Association, The Blakiston Company, New York, N. Y., 1953.

29 "A Report on Human Factors in B-47 Operation," Headquarters, Air Research and Development Command, Project No. R-318-001, Report No. L, November 17, 1952.

The Thermal Barrier—Structures[1]

By N. J. HOFF,[2] BROOKLYN, N. Y.

In the past few years the term "barrier" has become popular in aeronautics. Not so long ago we heard of the sonic barrier which in the minds of many laymen represented a solid wall of compressed air which would not let an airplane through at the speed of sound. More recently the expression "thermal barrier" has been coined to indicate that the heating effect of air will set a definite limit to the speed of aircraft that can never be surpassed. As far as the sonic barrier is concerned, events have shown that supersonic flight is well possible. As a matter of fact, bullets flew at supersonic speeds even during the last century, and if no law of nature prevented them from doing so, it was unreasonable to expect airplanes to be stopped by the sonic barrier. The author is convinced that in a similar manner the difficulties presented by the high temperatures accompanying flight at supersonic speeds will be overcome through research and development. Thus the thermal barrier is not a stone wall that will shatter all hopes of high supersonic flight.

Aerodynamic Heating

TO PERSONS who are not students of supersonic aerodynamics it may sound odd that a strong wind will heat the surface of a body when in our personal experience a breeze on a hot summer day has a most welcome cooling effect. This effect comes about mostly because our body is cooled through the evaporation of water through the pores of the skin. The evaporation ceases when the layer of air closest to the body becomes saturated with water vapor. The breeze carries away the vapor-laden air and replaces it with fresh, dryer air facilitating the natural process of cooling of the human body; this causes the well-known feeling of relief.

With an airplane this process of cooling does not exist unless, as proposed by some designers, the walls of the wing are made of a porous material through which cooling water is forced. An entirely different process takes place during which the surface of the airplane is heated. This aerodynamic heating is present even in low-speed flight but there it is so slight that it can hardly be noticed. At speeds of several times the velocity of sound it becomes a menace to flight.

Aerodynamic heating is essentially a transformation of macroscopic kinetic energy into kinetic energy on a molecular scale. Near the leading edge of a wing section of an airplane in free flight, where the air divides to flow over the wing and under the wing, there is a point with zero relative velocity between wing and air; this point is designated as the stagnation point. There the entire kinetic energy of the supersonic air flow is converted into kinetic energy of the random motion of the molecules of which air is composed, and the increased agitation of the molecules is indicated by a higher reading on the thermometer.

The temperature corresponding to a complete transformation of this kind of the energy, in the absence of heat losses through conduction and radiation, is designated as the stagnation temperature. In compressible fluid theory the following equation is derived for this temperature

$$T_s = T_a\,[1 + (M^2/5)] \qquad [1]$$

where T_s is the stagnation temperature, T_a the ambient temperature, both measured in Rankine degrees (Fahrenheit degrees plus 460), and M is the Mach number of the undisturbed flow, that is, the ratio of the air speed to the sonic speed under the ambient conditions. Values of T_s calculated for flight at an elevation of 33,500 ft are shown in Fig. 1.

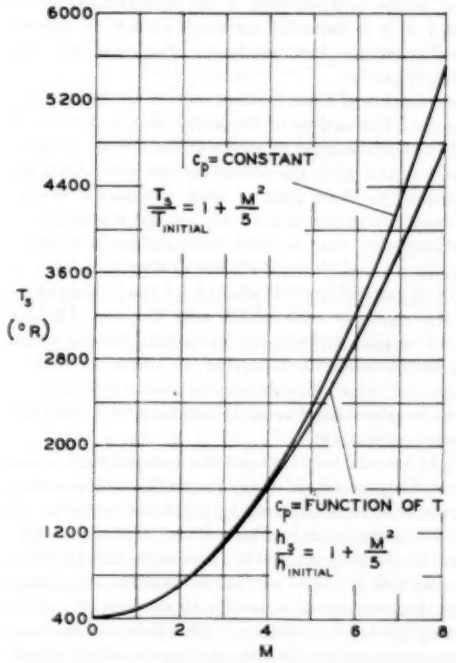

FIG. 1 STAGNATION TEMPERATURE FOR AN INITIAL TEMPERATURE OF 400 R

If the values indicated in the figure were the temperatures of the airplane structure, the maximum possible speed of flight would be very limited. Fortunately, heat is lost to the surrounding air by conduction and to outer space by radiation. A suitably designed airplane or missile may fly very fast at extreme altitudes where the density of air is practically zero and it can proceed at reduced speed while passing through lower altitudes. During the short periods of time it flies in the denser regions of the atmosphere even very high stagnation temperatures may not do much harm if the structure has a great deal of heat capacity, if it is protected by a layer of insulating material, or if it is cooled.

---

[1] A considerable portion of the information presented in this paper was obtained under Contract AF33(616)-116 sponsored at the Polytechnic Institute of Brooklyn, by the Wright Air Development Center of the Air Research and Development Command of the United States Air Force.

[2] Head of the Department of Aeronautical Engineering and Applied Mechanics, Polytechnic Institute of Brooklyn. Mem. ASME.

Contributed by the Aviation Division and presented at a joint session of the Aviation and Applied Mechanics Divisions, American Rocket Society, and The Society of Automotive Engineers, at the Annual Meeting, New York, N. Y., November 28–December 3, 1954, of THE AMERICAN SOCIETY OF MECHANICAL ENGINEERS.

NOTE: Statements and opinions advanced in papers are to be understood as individual expressions of their authors and not those of the Society. Manuscript received at ASME Headquarters, October 5, 1954. Paper No. 54—A-207.

A numerical value might be of some interest: When a thin wing is proceeding at a Mach number of 6 at an elevation of 40,000 ft, 74 Btu of heat are transmitted to each square foot of its area each second if the temperature of the wing is 340 F. This heating rate is calculated for an average distance of 1 ft behind the leading edge on the assumption that the boundary layer is turbulent.

Heat Transfer

To evaluate the effects of all these variables upon the heating of the structure and to calculate the temperatures of the structural elements, the engineer must be familiar with the theory of heat transfer. From the surface where the heat is generated it is transferred to the interior of the airplane structure by conduction. When the interior contains spaces filled with air or gasoline, heat is also transferred by convection and radiation. It is fortunate that the most important means of transfer in the structure is conduction, because this phenomenon has been extensively explored since 1822, when Fourier published his famous treatise on heat. The differential equation governing heat conduction in a rod is

$$(\partial T/\partial t) = a\,(\partial^2 T/\partial x^2) \quad \ldots\ldots\ldots\ldots\ldots\ldots [2]$$

where T is the temperature, x the longitudinal co-ordinate, t time, and a is a material constant known as diffusivity and measured in square feet per hour. For steel one may take $a = 0.46$ sq ft per hr.

In consequence of their random motion the molecules of hot air impinge upon the surface of the metal wing and excite the vibrations of the surface layer of atoms of the metal. These atoms in turn exert forces upon the atoms further away from the surface and transmit to them part of their vibrational energy. Thus atoms deep in the metal part are excited and begin to vibrate more vigorously; that is, their temperature is raised. Heat is thereby transferred through the metal structure.

The most astonishing fact about heat conduction along a metal rod is the slowness with which heat travels. Physicists have developed complicated theories to explain this but engineers can content themselves with accepting the empirical laws of thermodynamics and the results obtainable from a solution of Equation [2], or of its generalized versions valid for two and three-dimensional heat conduction.

It might be said here that solutions of practical interest of the equation of heat conduction are generally hard to obtain; nevertheless many have been found by mathematicians in the last 132 years. For instance, it has been shown that if one end of a long steel bar is suddenly heated to, and then maintained at, a temperature of 600 F above the initial uniform temperature of the bar, the temperature of a section 10 in. from the heated end is raised only 50 deg F in 15 min. This indicates that severe temperature gradients can be expected in the thick-walled or solid sections of supersonic aircraft structures.

Incidentally, our practical experience should warn us of the slowness of heat penetration. If heat were conducted much faster, we should not be able to use an iron poker to adjust the logs in a fireplace.

Thermal Stresses

A structural element made of a single homogeneous material expands uniformly when it is heated uniformly. But the wing of a supersonic airplane is heated only over its surface and its interior remains comparatively cool. Under these conditions the expansion of the material of the hot surface tends to force an expansion of the cooler interior which opposes such action. The result is that stresses, designated as thermal stresses, are set up which are compressive in the warm outer regions and tensile in the cool interior. The strains caused by these stresses render the changes in length of the various elements compatible.

As rapid heating gives rise to highly variable stresses in the structures of supersonic aircraft, large thermal stresses can be expected in them. Indeed a comparatively simple example calculated by the author showed this to be true. For the sake of simplicity the heating was assumed to be caused by a uniform speed of $M = 3.1$ at an elevation of 50,000 ft. A more realistic flight path involving changes in altitude as well as in speed would not have yielded significantly different results.

The wing structure was assumed to consist of two $^3/_8$-in-thick steel cover plates connected by a number of 0.1-in-thick steel shear webs. First the temperature distribution was calculated. It was found that about 6 min of flight were required to raise the temperature of the cover plates to 600 F; the uniform initial temperature was taken as 60 F. After 200 sec of flight the cover plates reached 540 F while the middle of the web was still at only 110 F. At that time the maximum stress in the structure was the longitudinal tensile stress in the web midway between the flanges; it was calculated to be more than 70,000 psi.

When tensile stresses of this order of magnitude actually appear in the comparatively cool portions of the structure the danger of fracture is evident. On the other hand, extreme thermal stresses in hot regions cannot be maintained for any length of time because plastic and viscous deformations take place which immediately reduce the thermal stresses. It seems advisable therefore to provide possibilities for the structure of supersonic aircraft to deform permanently and thereby to escape thermal stresses as far as possible.

At the same time care must be taken to maintain the deformations within those limits where safe operation is still possible. How best this can be achieved is one of the problems aeronautical engineers still have to solve.

Thermal Buckling

Thin elements subjected to compression do not fail by fracture, but buckle, that is, develop waves or bulges. The investigation of buckling by analytical methods must start out from the well-developed theory of structural stability but it must take into account the peculiar conditions prevailing when the stresses are the consequence of thermal expansion. Buckling obviously alters the state of strain in the structure; but the thermal stresses arise only because of nonuniform changes in length and thus they must change when the state of strain is altered. On the other hand, the loads of the classical theory of stability are predetermined, fixed quantities.

In order to understand the phenomenon of thermal buckling it is convenient to imagine the following experiment: A slender column, provided with knife-edges at its ends, is placed in a perfectly rigid testing machine. The loading head of the machine is fixed in its initial position and the column is heated while care is taken that the temperature of the machine remain unchanged. As the column warms up, its length would increase if the distance between its end points were not fixed by the rigid testing machine. The increase ΔL of a free column would be

$$\Delta L = \alpha L \Delta T$$

where α is the coefficient of thermal expansion, L is the length of the column, and ΔT is the increase in the temperature. Because of the unyielding supports, compressive stresses are set up in the column in the axial direction. If the material is perfectly elastic with an elastic modulus E, the shortening of the column is

$$\Delta L = PL/EA$$

where P is the compressive force and A the cross-sectional area

of the column. The shortening due to the compression must be equal to the extension caused by heating because the distance between the two ends of the column must remain unchanged. From this condition the compressive force P can be calculated

$$P = EA\alpha\Delta T \quad [3]$$

It can be seen from Equation [3] that the highest thermal stresses are likely to occur with a material for which the product of Young's modulus E and the coefficient of thermal expansion α is the greatest.

If initially the column was perfectly straight, it will remain straight until the force P becomes equal to the buckling load P_E of the column. This buckling load was first calculated by Euler in 1744, and is given by the formula

$$P_E = \pi^2 EI/L^2$$

where I is the moment of inertia of the cross section of the column.

Beyond this load the straight configuration is still possible theoretically but it is so unstable and unreliable that the slightest disturbance upsets it and causes a bowing of the column. Analysis has shown that the lateral deflections increase as the temperature rises and are always of such a magnitude that the relief they provide in the compressive strain just suffices to prevent increases in the compressive load. Hence the compression remains equal to the Euler buckling load when the temperature is further increased; at the same time the deviations from the initial straight configuration keep increasing.

In a numerical example the cross section of the column was assumed to be $^1/_4$ in. $\times$ $^1/_2$ in. and its length 10 in. With Young's modulus for steel taken as 28×10^6 psi, the Euler load was found to be 1800 lb and the corresponding compressive stress 14,400 psi. If the coefficient of thermal expansion is 7.5×10^{-6}, a rise in temperature of 68.6 deg F suffices to cause buckling. Hence in this particular case a change in temperature of 68.6 deg F is equally as dangerous as a compressive stress of 14,400 psi. These numerical values imply that nonuniform temperatures are most conducive to buckling.

When the deviations from straightness increase sufficiently, the combination of normal and bending stresses exceeds the yield point of the material and permanent deformations develop. As large-scale waviness in the walls of high-speed aircraft is most detrimental to the development of the proper aerodynamic forces, more information on thermal buckling is urgently needed.

Experiments carried out with the electromagnetic induction heating units of the Polytechnic Institute of Brooklyn produced large permanent bulges in the plating of box girders representative of the wing structures of low supersonic-speed aircraft. Solid wedge-type wings also showed waviness along the leading edge as may be seen from Fig. 2.

Effect of High Temperatures Upon Properties of Materials

Up to now the effect of the high temperatures upon the material properties has not been considered in this discussion of the structural problems of high-speed flight. It is well known, however, that metals soften when they are heated and become less capable of sustaining loads. For instance, a 24S-T4 extrusion maintained at 360 F for $^1/_2$ hr fails in tension at 90 per cent of its room-temperature tensile strength; when the heating is continued for 100 hr, the corresponding value is only 60 per cent. The same element kept at 600 F for $^1/_2$ hr shows a failing stress of only 21 per cent of the room-temperature value.

Besides the loss of strength, another phenomenon must be discussed in the high-temperature behavior of metals. It is the continued change in the shape of an element when it is subjected

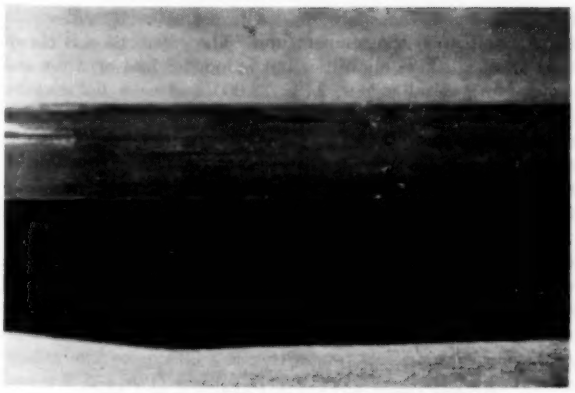

Fig. 2 Solid Wedge-Type Wing Showing Waviness Along the Leading Edge

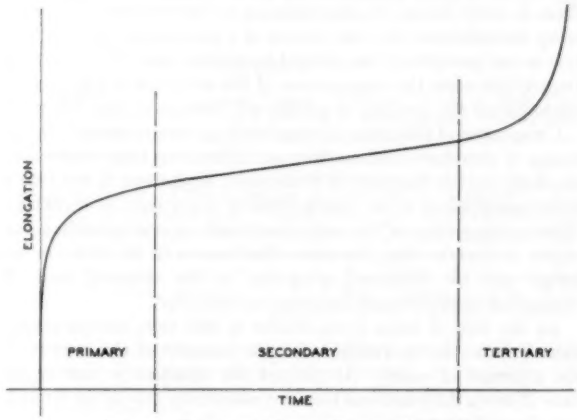

Fig. 3 Creep of Metal Rod in Tension

to constant loads. This phenomenon, known as creep, was first explored in some detail by Andrade in 1910. Some of its significant features are illustrated in Fig. 3.

When a tensile test specimen is placed in a testing machine provided with facilities for heating, its temperature is raised to, and subsequently maintained at, a predetermined high temperature, and finally a weight is suspended from its lower end, and the specimen elongates instantaneously. If the load and the temperature are sufficiently low, this elongation is purely elastic and can be regained upon removal of the load; otherwise part of the deformation is plastic and irrecoverable. If the load is not removed, the specimen continues to elongate but at a decreasing rate; this range of the deformations is known as the primary phase of creep. Eventually a steady rate of elongation is reached in the so-called secondary phase which is represented by a straight line in the strain-time plot. Finally, the deformations are accelerated once again before the specimen fails by fracture.

The best-known part of the creep phenomenon is the secondary phase. Many experimenters have determined the steady creep rates of various metals at various temperatures and under many loads. The most generally accepted creep law derived from these experiments can be written as

$$\dot{\epsilon} = (\sigma/\lambda)^n \quad [4]$$

where $\dot{\epsilon} = d\epsilon/dt$ is the time rate of strain, that is, the creep strain developing in unit time, σ is the applied stress, and λ is a constant

depending upon the material, its heat-treatment and strain history, and upon the temperature. The exponent n is also a function of all these quantities but is independent of stress and strain. As typical values, $\lambda = 22{,}000$ and $n = 6.2$ may be quoted for 52S-H32 aluminum alloy at 400 F when the stress is measured in psi and the strain rate in in. per in. per hr. According to Equation [4], a rod made of this material elongates to twice its original length if it is subjected to a tensile stress of 22,000 psi for 1 hr.

Metal physicists have proposed several mechanisms to explain the phenomenon of creep. It appears that the major contributing elements to the creep deformations are plastic slip in the crystals and viscous flow in the intercrystalline layers of the polycrystalline aggregates of which structural metals are composed.

Stress Distribution in Presence of Creep

If a modern fighter spends only a few hours of its total flying time at supersonic speeds, and if a guided missile is designed to hit the enemy after a flight of only a few seconds or a few minutes, there is every reason to allow stresses in its structure that cause creep deformations of a few tenths of a per cent in an hour. If this is not permitted, the allowable stresses must be chosen extremely low when the temperature of the structure is high, and in consequence the airplane or missile will become unduly heavy.

Creep rates of this order of magnitude are unprecedented in the design of structures and machinery. The creep rates studied extensively by the designers of heat-power equipment in the 1930's were measured in a few hundredths of a per cent in 10,000 hr. When creep strains of the same magnitude as, or greater than, the elastic strains develop, the stress distribution in the structure no longer can be calculated according to the accepted rules of strength of materials and the theory of elasticity.

As the idea of large creep strains is still new, comparatively little information is available for the analysis of the stresses in the presence of creep. At present the situation is best in the case of creep deformations that are essentially due to the secondary phase of creep.

The author was able to prove recently that the stress distribution in a body whose deformations are governed entirely by the creep law of Equation [4] is exactly the same as that in a body whose deformations obey the purely elastic stress-strain law

$$\epsilon = (\sigma/\lambda)^n \quad [5]$$

provided, of course, that the shape, loading, and the supports of the two bodies are the same. Equation [5] differs from Equation [4] only inasmuch as the strain appears in it instead of the strain rate. This analog is most helpful because it reduces the unexplored problems of creep-stress distribution to problems in the well-known field of ideal elasticity. All the rigorous and approximate methods developed in the theory of elasticity can thus be applied to the problem of the stress distribution due to creep. The only unfortunate thing about the analog is that it leads to nonlinear differential equations of which comparatively little is known. In ordinary elasticity theory $n = 1$; it is also customary to designate the constant in the denominator by the letter E. With these changes Equation [5] reduces to Hooke's law in its customary form.

It is hoped that solutions of the problems of nonlinear elasticity will become available in the future. One limiting case appears to be especially promising; when n is greater than about 6, little change in the stress distribution results from replacing $n = 6$ by $n = \infty$. But the latter reduces Equation [5] to the law of perfect plasticity in which no deformations are assumed to take place as long as the stress is less than the yield point of the material, and arbitrarily large deformations are considered possible when the stress is equal to the yield point. For this idealized rigid-plastic body, simple methods of approximate calculation have been developed under the name of limit analysis. They should be utilized in creep calculations.

For such simple structures as frameworks and rigid frames with a small number of redundancies the nonlinear stress-strain law of Equation [5] leads to simple solutions. Thus it has been shown that in a three-bar framework containing a vertical member as well as two members inclined at 60 deg, the vertical member carries 80 per cent of a vertical load when the structure is linearly elastic (Hooke's law is valid). When $n = 4$ in Equation [5], the share of the vertical bar is reduced to 58 per cent; when $n = 8$, the share is 53.5 per cent; and when $n = \infty$, it is 50 per cent. These results indicate that the stress is distributed more evenly when n is increased. For this reason stress concentrations are likely to be less severe in the presence of nonlinear creep than in a material following Hooke's law.

Creep Failure in Tension

It has been mentioned in connection with Fig. 3, that the rate of creep increases in the tertiary phase of creep before the bar fractures in consequence of tensile-creep deformations. With some metals this acceleration is due in part to metallographical changes. The major contributing factor, however, is the decrease in area, as Andrade discovered and experimentally proved in 1910.

When a bar elongates under a tensile load, its cross-sectional area decreases. Consequently, the average stress acting in the cross sections of the bar must increase to maintain equilibrium with the unchanged load. But an increase in stress by 1 per cent causes an increase in creep rate of about 8 per cent if $n = 8$ in the creep law of Equation [3]. Hence the creep rate increases catastrophically as soon as a noticeable reduction in the cross-sectional area develops.

On the basis of this consideration the author was able to derive the following theoretical formula for the time t_{cr} required for failure in tension

$$t_{cr} = 1/\dot{\epsilon}_0 n \quad [6]$$

In this equation $\dot{\epsilon}_0$ is the steady creep rate at the beginning of the test, before the cross-sectional area is noticeably reduced, and n is the exponent in the creep law of Equation [4]. The agreement between the predictions of Equation [6] and the results of experiments was found satisfactory.

The phenomenon of necking also can be explained easily with the aid of the nonlinear creep law. Any section of the bar that is weaker than the rest is subject to more rapid creep deformations than the other portions of the bar. As the cross section decreases, the differences in diameter along the bar are accentuated as long as n is greater than 1. Finally the bar fractures when one cross section becomes considerably smaller than the other sections. Necked shapes calculated theoretically were found to agree well with photographs of broken specimens.

Creep Buckling

Equally interesting phenomena can be observed when a bar is subjected to compressive rather than tensile loads. If the bar, designated as a column when subjected to axial compression, is of solid circular cross section and is perfectly straight and perfectly centered, the only changes taking place in its shape in consequence of creep are a decrease in length and an increase in diameter. After an indefinitely long time the column becomes a pancake, but its symmetry is undisturbed.

Of course in reality perfection is unknown, and any initial deviation from perfect symmetry is exaggerated by the creep deformations. Thus a slight initial curvature of the center line

of the column gives rise to bending moments which in any section are equal to the product of the compressive load by the deviation of the centroid of the section from the straight line of action of the force. Creep caused by the bending moment increases the curvature and hence the deviation from the straight line. A vicious circle begins, therefore, in which creep is increased by the increased deviations from the straight line and vice versa until the column folds up and becomes useless for structural purposes.

One interesting fact about creep buckling is that according to both theory and experiment it occurs suddenly. The experimenter may not notice any changes in the column for half an hour. At that time he gets the impression that one of his instruments begins to move; before he can make more than a few recordings the column snaps through and the test is over. This behavior pattern is a consequence of the nonlinearity of the creep law.

A second fact worth noting is that the buckling process just described takes place under any compressive load however small. Of course the column lasts much longer if the load is small. One cannot talk, therefore, of a critical load or of a critical stress in creep buckling. The significant quantity is the critical time, that is, the time necessary for the column to buckle. The structural designer must make sure that the critical time of his column is greater than the required lifetime of the structure.

Creep buckling has had a considerable literature in the past few years. Of the many formulas derived only the simplest one is quoted

$$t_{cr} = (2\pi^2/6)\,(\rho/L)^2\,[\lambda/(P/A)]^3 \log\left\{(2/e)\,[1 + (P/P_E)]\right\}. \quad [7]$$

Here t_{cr} is the time necessary for the column to buckle, (L/ρ) is the slenderness ratio of the column, A its cross-sectional area, P the load acting upon it (positive when compression), and e is the maximum initial deviation of the center line of the column from the ideal straight line divided by the radius of gyration ρ of the cross section. Equation [7] was derived on the assumption that the deformations were completely governed by the creep law of Equation [4] with $n = 3$.

More complete, and more complex, theories have been derived for the critical time in the past few years, as discussed in the references. Here it suffices to present Equation [7] as an indication of what might be expected of a column in creep buckling.

Conclusions

The high temperatures caused by aerodynamic heating have given rise to many interesting problems in the analysis of structures. A basic understanding of some of these problems is still lacking and a great deal more research work is needed before all the details are clarified and the best methods of structural design can be developed.

Perhaps the most novel feature of the behavior of structures at high temperatures is the time-dependence of failure. Both in tension and compression the structural element fails under any load if it is maintained for a sufficiently long time. In this respect structures at high temperatures differ fundamentally from those used only at ordinary temperatures. The designer of supersonic aircraft must become accustomed to the idea that each structural element must be calculated for a definite lifetime.

REFERENCES

1 "Structural Problems of Future Aircraft," by N. J. Hoff, Proceedings of the Third Anglo-American Aeronautical Conference, Brighton, England, September, 1951, published by the Royal Aeronautical Society, London, England, 1952, p. 77.

2 "The Structural Effects of Aerodynamic Heating," by N. J. Hoff, presented at the Third General Assembly of the Advisory Group for Aeronautical Research and Development (AGARD) of the North Atlantic Treaty Organization (NATO) in London, England, September 10, 1953. (To be published by AGARD).

3 "Rapid Creep in Structures," by N. J. Hoff, Polytechnic Institute of Brooklyn, Brooklyn, N. Y., PIBAL Report No. 254, May, 1954. (This paper will also be published in the *Journal of the Aeronautical Sciences.*)

4 "Buckling and Stability," by N. J. Hoff, the 41st Wilbur Wright Memorial Lecture, presented in London, England, on September 14, 1953, published in the *Journal of the Royal Aeronautical Society*, vol. 58, January, 1954, p. 3.

Some Structural Aspects of Thermal Flight[1]

By GEORGE GERARD,[2] NEW YORK, N. Y.

The trend of substantial increases in gross weight of modern high-performance aircraft designed for normal temperature operation is discussed. This trend has continued in spite of considerable improvements in physical properties of materials, more refined stress analyses, and improved fabrication techniques. With elevated temperatures as a consideration at Mach numbers greater than 2, the decrease in physical properties of materials will result in substantial weight increases due to this source alone. The evolution of thin-wing supersonic aircraft has resulted in a variety of proposed structural arrangements for wing and tail surfaces. The structural efficiencies of several designs are reviewed to indicate probable allowable compressive-stress levels. By use of probable stress levels, the efficiencies of various materials at elevated temperatures are considered for tension, compression, and shear components of the airframe. Based on such data, relative weight trends of aircraft designed for thermal flight are indicated. Additional considerations of life expectancy due to creep at elevated temperatures are presented.

Aircraft-Growth Trends

THE history of true airspeed and gross-weight trends for production fighter and bomber aircraft has been considered by Heinemann (1),[3] among others. These data are shown in a cross-plotted form in Fig. 1 with gross weight as a function of true airspeed. The substantial increases in gross weight associated with increases in velocity result from higher performance requirements in range and pay load, increasing complexity of equipment, and higher aerodynamic loads.

The addition of weight to an aircraft in the form of equipment, for example, is reflected in increased requirements for the propulsion system, decreased aerodynamic efficiency, and increased structural weight. The compounding of the aerodynamic, structural, and propulsion changes necessitated by an increase in weight has been referred to as the aircraft-growth factor by Heinemann (1). It has been found, for example, that if a weight increment of 10 per cent is added to an aircraft in the preliminary design stages, the additional aerodynamic, structural, and propulsion requirements increase the gross weight by 100 per cent if the original strength and performance characteristics are to be maintained. A growth factor of 10 has been found to be representative of several current jet aircraft. Values up to 15 and 20 have been obtained for individual high-performance fighters.

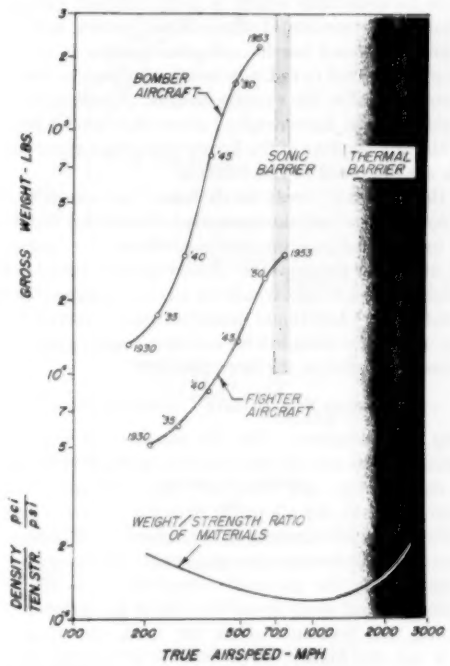

Fig. 1 Aircraft-Growth Trends and Weight/Strength Ratio Variations of Materials

The trend of increased weight with increased speed, such as shown in Fig. 1, is partly due to increased propulsion requirements and increased structural weight resulting from the demands of increased performance. Also, the weight increases reflect substantial increases in complexity of military equipment. While some control can be exercised over the latter, it is safe to state that the trend of weight increases with greater velocities will continue because of aerodynamic, structural, and propulsion requirements.

With the design of aircraft for Mach numbers greater than 2, substantial increases in structural weight are to be anticipated due to elevated-temperature effects. In addition to the natural trend of increased loads with increased velocities, the allowable strengths of the structural materials decrease at elevated temperatures and creep becomes a design consideration resulting in increased weight for given loading conditions.

Also shown in Fig. 1 are the weight-strength ratios of the various aluminum alloys used in aircraft between 1930 and today. Projected on this figure in the "thermal-barrier" region are the most efficient short-time weight-tensile strength properties of the materials which probably may be used in aircraft designed for thermal flight.

It can be observed that even with continued improvements in physical properties of the aluminum alloys since 1930, the gross weights of fighter and bomber aircraft have increased radically. With a reversal in the weight-strength trend of materials at elevated temperatures, the structures man possibly faces a truer barrier than the aerodynamicist did in the sonic barrier.

With this preview of some of the difficulties associated with this

---

[1] Portions of this paper constitute further developments of research originally sponsored by the Office of Naval Research and Aeronautical Research Laboratory, Air Research and Development Command, U. S. Air Force.

[2] Assistant Director, Research Division, College of Engineering, New York University, New York, N. Y. Mem. ASME.

[3] Numbers in parentheses refer to the Bibliography at the end of the paper.

Contributed by the Aviation Division and presented at a joint session of the Aviation and Applied Mechanics Divisions, American Rocket Society, and The Society of Automotive Engineers, at the Annual Meeting, New York, N. Y., November 28–December 3, 1954, of The American Society of Mechanical Engineers.

Note: Statements and opinions advanced in papers are to be understood as individual expressions of their authors and not those of the Society. Manuscript received at ASME Headquarters, June 9, 1954. Paper No. 54—A-40.

problem, it is pertinent to consider some of the structural aspects of thermal flight in greater detail. The evolution of modern thin-wing aircraft with its associated high loadings has resulted in a variety of proposed structural arrangements for wing and tail surfaces. It is necessary to analyze the various proposed configurations to determine which is most efficient for particular applications. The structural efficiencies of several such proposed designs are considered herein and some results of an extensive analysis are presented to indicate trends of allowable compression stress associated with the various designs. These forms of high-solidity construction have resulted in new fabrication techniques. Some of the implications of the heavy-press equipment soon to be available are discussed in this relation.

Once the probable stress levels have been established, it is possible to compare various materials to determine which is most efficient in elevated-temperature applications for tension, compression, and shear components. Based on these data it is possible to establish relative weight trends for aircraft designed for thermal flight conditions. Additional considerations involved in life expectancy of aircraft designed for elevated-temperature operation are discussed in terms of the creep problem.

Efficient Structural Configurations

Solidity Considerations. For the purposes of structural efficiency analysis, the aircraft structure can be divided generally into tension, compression, and shear-carrying structural components. In tension elements, the allowable strength is usually quite close to the ultimate tensile strength of the material. However, fatigue is a definite design consideration at normal temperatures and may lower considerably the allowable strength which may be used. In compression and shear structures which are generally subject to buckling, the optimum stress for minimum weight design usually is not the highest stress attainable because of the fact that certain geometrical details of the structure are fixed. It depends upon the magnitude of the loading, the thickness of the wing, and the arrangement of the supporting structure as well as the physical properties of the material.

The volume of tension, compression, or shear components can be given by

$$V = \bar{l}Lw \quad [1]$$

where

$\bar{l}$ = effective thickness
L = length
w = width

The applied axial loading acting on the tension and compression covers of wing and tail surfaces is prescribed by the bending moment M, the over-all height of the structural box h, and the width

$$N = M/khw \quad [2]$$

The coefficient k relates the centroidal height to the over-all height h, for the various types of construction.

In a structure of minimum weight, the applied stress is equal to the allowable stress. Therefore

$$N = \sigma\bar{l} \quad [3]$$

By substituting Equation [3] into [1]

$$V = NLw/\sigma \quad [4]$$

Instead of considering the volume of individual types of construction, it is more convenient to use the solidity Σ, which is a nondimensional term defined as follows

$$\Sigma = V/Lwh \quad [5]$$

The solidity represents the ratio of the volume of the structural material as compared to the volume enclosed by the outer dimensions of the structure. It is directly related to the weight of the structural material.

By substituting Equation [4] into [5]

$$\Sigma = \frac{(N/h)}{\sigma} \quad [6]$$

To compare the solidities of different structural arrangements for specified values of the structural loading parameter N/h, it is necessary first to determine the optimum stress.

Optimum Design. To attain structural efficiency within the limited geometry of the thin wings while supporting large compressive loadings of supersonic aircraft, it has been found desirable to have the skin act as the main load-carrying member. With the evolution of high-solidity structural configurations, stringer-panel construction no longer enjoys the universality of application it received in designs created before and during the recent world war. In its place, sandwich construction, in which the core may consist of end-grain balsa, expanded plastics, honeycombs, or possibly longitudinal corrugations, has been used. In other cases, multicell construction, in which relatively thick skins are stabilized by a series of webs, has been used with increasing frequency in thin-wing and tail designs. Post construction, which functions in a manner similar to a transversely stiffened plate, has been developed as an entirely new concept in structural design. The use of posts has been extended to post-stringer construction in which the stringer acts to enforce a longitudinal node in the skin in much the same manner as in multicell construction.

Attempts to define the regions of efficient application of the various types of structural configurations have appeared only recently. Stringer-panel and multicell construction were compared by the author (2) for typical ranges of parameters. In another study, stringer-panel-rib designs were compared with sandwich-panel construction (3).

To evaluate the available forms of construction from a structural efficiency standpoint, it is necessary to establish analytical methods for obtaining minimum weight designs of the various types of composite construction (compression cover plus supporting structure) for specified loading and geometric parameters. After the minimum weight designs have been established for each type of construction, it then becomes possible to compare the various types of construction on a common basis. From this procedure the ranges of efficient structural application of each form of construction can be established.

With this objective in mind, the various types of construction mentioned in the foregoing were analyzed (4). A considerable portion of this investigation was concerned with the optimum design of the various elements under specified loading conditions. These analyses specified the optimum rib, post, or web spacing for the afore-mentioned types of construction and also the optimum core properties of the various types of sandwich construction under bending loads. The optimum types of construction were then compared to obtain the ranges of efficient structural application for each. Included in the analysis were the weights of the supporting structures, the effects of the plasticity of the material, and the different centroidal heights of the various types of construction.

The results of this analysis are summarized in Fig. 2 which was calculated for 75S-T6 aluminum alloy at room temperature (4). It is important to observe that by the proper selection of a structural configuration for a prescribed value of M/h^2w, it is possible to achieve the compressive yield strength of the material for the high loadings associated with supersonic wing designs.

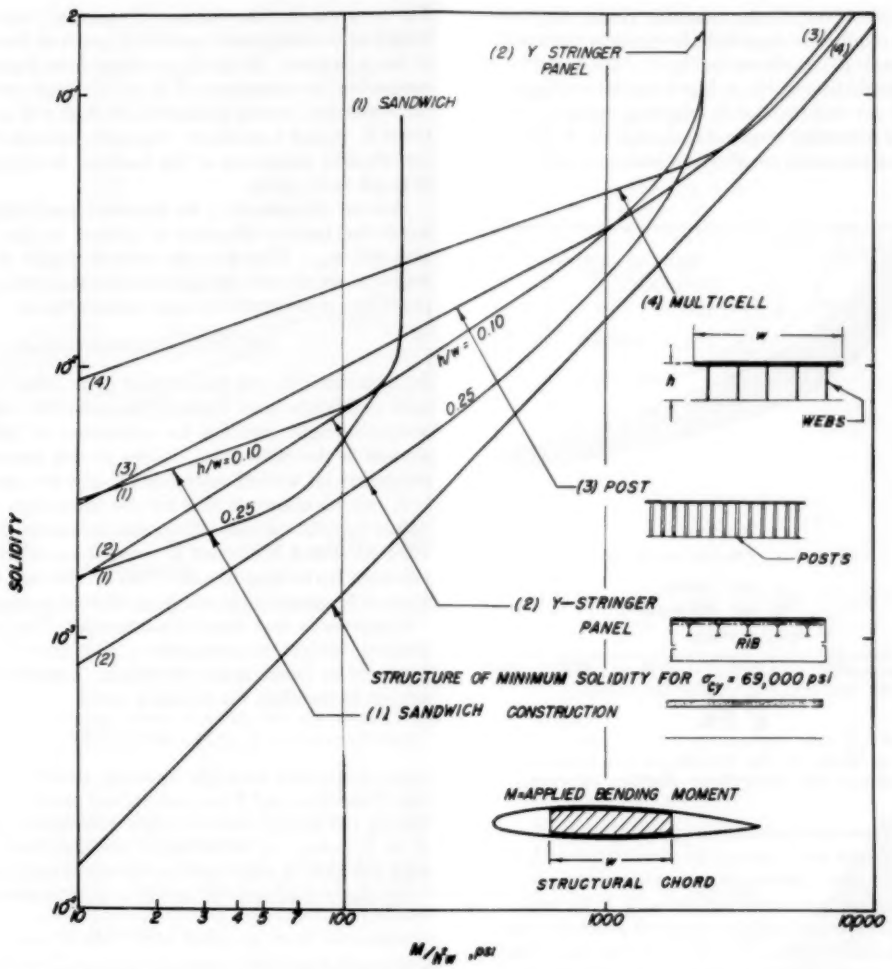

FIG. 2 STRUCTURAL EFFICIENCY OF WING AND TAIL COMPRESSION STRUCTURES OF 75S-T ALUMINUM ALLOY

Integral Construction. The development of efficient forms of new structural arrangements is closely associated with integral construction obtained by use of machining, forging, and extrusion techniques (5 to 8). The general advantages of integral construction are associated with considerable weight reduction through use of higher allowable stresses, the elimination of a large number of joints, and tapering of the structural components as required by design. From the production standpoint, substantial economies result from the reduction in a large number of parts.

From a structural point of view, the monolithic structure has considerably greater strength both in tension and compression than the riveted equivalent. Stress concentrations generally limit the fatigue strength of the high-strength aluminum alloys to the point where it may not be possible to take full advantage of the increase in static tensile strength of these alloys. As shown in Fig. 3, fatigue strength does not keep pace with the relative increase in static strength. Therefore, by the use of integral construction, many of the rivet holes, joints, and abrupt changes in section which contribute to lower fatigue strength may be eliminated, resulting in a monolithic structural component of greater fatigue strength. In this manner it may be possible to realize the full potential strength of such alloys as 78S-T.

For compression and shear structures subject to buckling, it

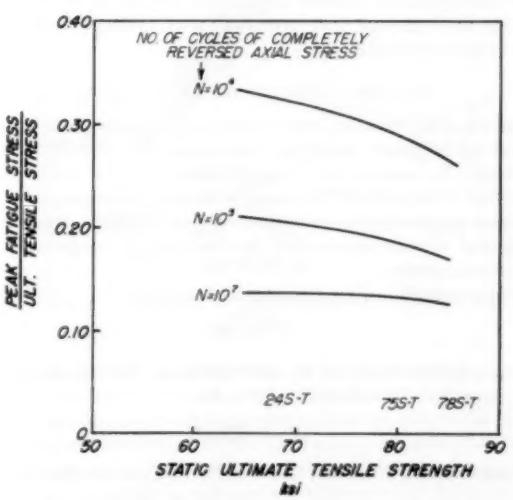

FIG. 3 COMPARATIVE NOTCH-FATIGUE STRENGTH OF ALUMINUM ALLOYS, CONCENTRATION FACTOR OF 3 (REFERENCE 5)

has been found that very large diameter rivets, very closely spaced, are often required to approach the strength characteristics of monolithic panels (9) as shown in Fig. 4. By use of integral construction it should be possible, in highly loaded components, to realize a 10 to 25 per cent increase in crippling strength, since the rivet pitches and diameters required to realize the full potential strength in fabricated panels are often not realistic from a production standpoint.

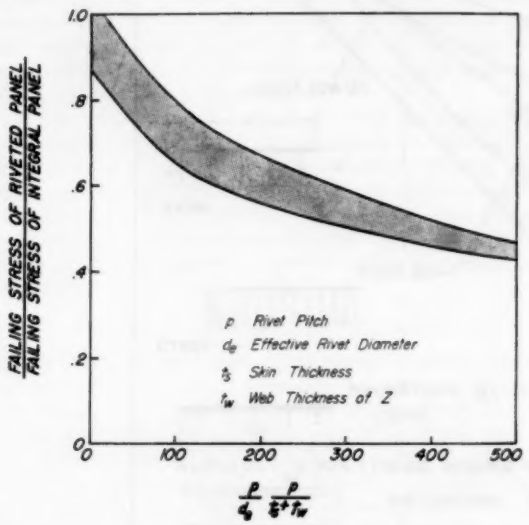

FIG. 4 EFFECT OF RIVET PITCH, DIAMETER, AND STRENGTH UPON CRIPPLING STRENGTH OF Z-STIFFENED PANELS (REFERENCE 9)

From some of these considerations it appears that heavy forging and extrusion presses are essential for development of integral high-solidity structures. Although some integral components are now being fabricated from machined slabs (5, 6, 8), use of forgings and extrusions result in higher physical properties than obtained with machined billets (7). It is to be noted that the high-solidity structures of aircraft designed for thermal flight require relatively thick-skin components for which the heavy presses are ideally suited. In fact, they are better suited for such structures than for current production aircraft in which the inability to forge very thin webs may limit realization of the full heavy-press potential.

RELATIVE EFFICIENCIES OF MATERIALS

In Fig. 2 the various types of structural configurations are compared for a specific material, aluminum alloy 75S-T6 which is currently in common use. As the second part of the efficiency problem, it is pertinent to consider various materials which may be used at elevated temperatures to determine the temperature ranges of efficient application for the tension, compression, and shear components.

The weight W, of any structural element is

$$W = \rho V \quad [7]$$

where ρ is the density of the material used. By use of Equation [5], Equation [7] can be rewritten as

$$W = \rho \Sigma Lwh \quad [8]$$

By substituting Equation [6] into [8] and rearranging terms

$$\varphi = \frac{W}{Lwh} = \left(\frac{N}{h}\right)\left(\frac{\rho}{\sigma}\right) \quad [9]$$

The term φ is the "structural density" and represents the weight of the structural material relative to the enclosed volume of the structure. It can be observed from Equation [9] that in comparing two structures of identical design except for material, the structural loading parameter, N/h as well as the geometrical terms L, w, and h are fixed. The only variable is concerned with the physical properties of the material as given by the weight-strength ratio (ρ/σ).

Tension Components. As discussed previously, the allowable stress for tension elements is related to the ultimate tensile strength, σ_{tu}. Therefore the relative weight of the tension elements of an aircraft designed for elevated temperatures as compared to one designed for room temperature is

$$(W/W_0)_t = (\rho/\sigma_{tu})/(\rho/\sigma_{tu})_0 \quad [10]$$

In Equation [10] the subscripts 0 and t refer to room-temperature conditions and tension, respectively. Since the proper weight-strength criterion for evaluation of materials used for tension is the ratio ρ/σ_{tu}, values of this parameter have been computed for several materials (5) and are shown in Fig. 5.

It can be observed that for the aluminum alloys, the ρ/σ_{tu} values rapidly increase above approximately 400 F. Titanium alloy RC-130-A is efficient at room temperature and retains this efficiency up to approximately 800 F. Beyond this temperature, Inconel X appears to be the most efficient material.

Compression and Shear Components. The strength of components subject to compressive and shear loads is generally governed by buckling considerations. For a compressive element subject to buckling, the critical stress is

$$\sigma_{cr} = K\bar{E}(t/b)^2 \quad [11]$$

where K depends upon the boundary conditions, b is a characteristic dimension, and $\bar{E}$ is a generalized plastic modulus. For predicting the failing stress of plate elements in the plastic range, $\bar{E} = E_s$ (where E_s is the secant modulus) is in good agreement with test data at both room and elevated temperatures.

By use of Equation [3] and $\bar{E} = E_s$, Equation [11] becomes

$$t = (Nb^2/KE_s)^{1/3} \quad [12]$$

Substituting Equation [12] into Equations [1] and [7] and forming the weight ratio

$$(W/W_0)_c = (\rho/E_s^{1/3})/(\rho/E_s^{1/3})_0 \quad [13]$$

For the thin wings and high loads of supersonic aircraft, the data shown in Fig. 2 indicate that it generally will be efficient to use the compressive and shear yield strengths as the allowable stress. This is valid for the heavily loaded members which contribute the major portion of the structural weight. At elevated temperatures, the decrease in physical properties of the materials probably will result in the use of the compressive yield stress as the allowable for the less highly loaded members also.

By taking the allowable stress in compression as the compressive yield stress σ_{cy}, the value of the secant modulus can be directly established from the relationship

$$(E_s)_{cy} = \frac{\sigma_{cy}}{0.002 + \sigma_{cy}/E} \quad [14]$$

Since the values of σ_{cy} and E generally are given as a function of elevated temperature, the secant modulus can be computed from Equation [14] without recourse to stress-strain curves.

For shear structures, the analysis is quite similar to that for compression structures. The only difference is associated with the value of the plastic shear modulus which can be taken as the shear secant modulus. In this case

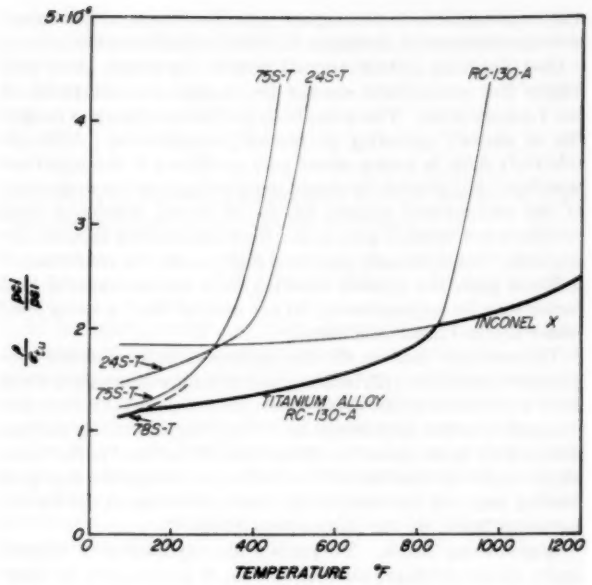

FIG. 5 WEIGHT-STRENGTH RATIOS OF TENSION SHEET MATERIALS (SHORT-TIME DATA)

$$(W/W_0)_s = (\rho/G_s^{1/3})/(\rho/G_s^{1/3})_0 \quad [15]$$

Since there is no well-established relation for the shear yield strength corresponding to Equation [14], it is assumed that

$$E_s/E_{s0} = G_s/G_{s0} \quad [16]$$

On this basis the results obtained by use of Equations [13] and [14] were applied to shear structural elements.

Based on the weight-strength criteria for plastic buckling, $\rho/E_s^{1/3}$, values computed for several materials (10) are shown in Fig. 6. It can be observed in contrast to similar data for tension shown in Fig. 5, that the aluminum alloys are markedly superior to titanium alloys and Inconel X for compression and shear up to temperatures of almost 700 F. The compression and shear structures generally comprise a larger proportion of the structural weight than tension structures. Therefore the apparent superiority of titanium alloys for short-time tension for the temperature range up to 700 F must be balanced carefully against the superiority of the aluminum alloys for short-time compression and shear up to temperatures of 700 F.

Relative Weight Analysis. Since the natural growth trends of future aircraft are difficult to establish with any degree of accuracy, an approach is attempted in which the weight increases due to elevated temperatures are isolated from the natural growth trends. This can be accomplished by considering the relative weights of two aircraft designed to the same performance specifications; the reference airplane is designed for room-temperature conditions whereas the other is designed for elevated-temperature conditions on the basis of short-time elevated-temperature strength data. It must be recognized that relative weight data obtained from such comparisons at best can reflect only a trend since the analysis precludes any detailed treatment of the aircraft design.

From the data shown in Figs. 5 and 6 it can be observed readily that the best material from a structural efficiency standpoint for use in aircraft designed for room-temperature operation would be 78S-T aluminum alloy. Consequently, in computing the relative structural weights according to Equations [10], [13], and [15], 78S-T aluminum alloy at room temperature was used as

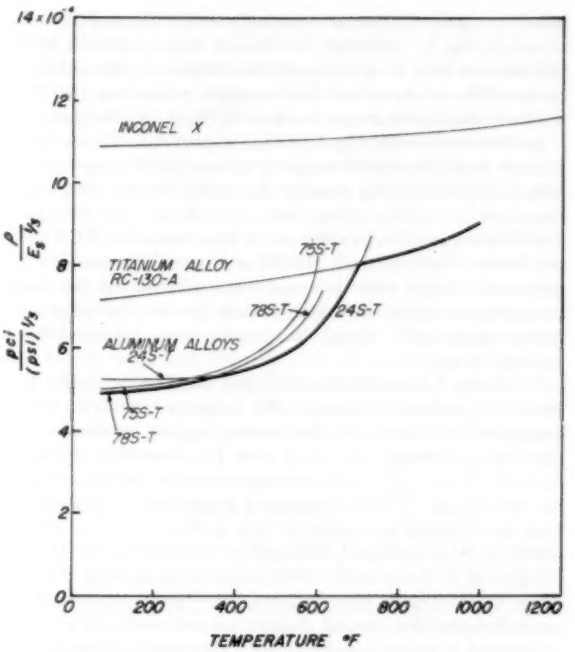

FIG. 6 WEIGHT-STRENGTH RATIOS OF COMPRESSION AND SHEAR SHEET MATERIALS (SHORT-TIME DATA)

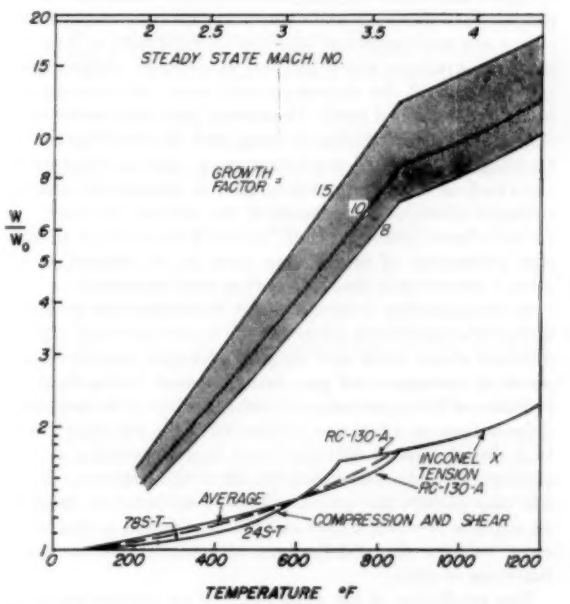

FIG. 7 RELATIVE WEIGHT OF AIRCRAFT DESIGNED FOR THERMAL FLIGHT

the standard of comparison. The relative weights computed on this basis are shown in the lower portion of Fig. 7.

The increment in weight necessitated by consideration of elevated temperatures must be multiplied by a suitable growth factor to account for the increased propulsive and aerodynamic requirements to achieve comparable performance of the room and elevated-temperature aircraft. Therefore the average relative weight of tension, compression, and shear components was multi-

plied by representative growth factors of 8, 10, and 15 and are shown in Fig. 7. Although the blanket use of a growth factor in this manner may be questioned, the purpose of this analysis was to establish trends rather than absolute values and therefore it appears permissible to use the growth factor for this purpose.

In connection with Fig. 7, it is of importance to note that the average trend of relative weight as a function of temperature was obtained by averaging roughly the trends for the most efficient materials in tension, compression, and shear. For example, at 500 F this would lead to the use of titanium alloy RC-130-A as the tension material and 24S-T4 as the compression and shear material. If the same material were selected for the tension, compression, and shear material, then the relative weights for a given temperature would be greater than indicated by the average trend.

From Fig. 7 it can be observed that tremendous weight penalties are apparently involved in the design of aircraft for elevated temperatures in terms of what is now required for the usual temperature conditions associated with the operation of transonic aircraft. It is to be noted that the trends indicated in Fig. 7 do not include the trend of increased weight with increased speed such as indicated by statistical data in Fig. 1, and the extensive use of cooling equipment, although presumably the use of a suitable growth factor provides some means of estimating this trend. Thus weight trends may indicate even larger penalties for aircraft designed for thermal flight than indicated in Fig. 7 which attempted to isolate penalties due to elevated temperatures only.

Life Expectancy of Aircraft

Up to this point the analysis has been based on short-time properties of materials and no mention has been made of the fact that a new and significant aspect of thermal flight is that the design of a structure which operates at elevated temperatures entails analysis of the time-dependent creep deformations which occur under applied load. Depending upon the service application of the aircraft, various criteria, such as stress rupture, creep buckling, initiation of third-stage creep, and specified deformations such as 0.02 strain may be used to indicate the time of retirement of major components of the aircraft structure. In a survey of such problems, Hoff (11) has indicated that an entirely new philosophy of design may have to be adopted in which piloted aircraft may be considered as semi-expendable.

In the operation of an aircraft at Mach numbers greater than 2, the structure during its service life is intermittently exposed to different stress levels and different elevated temperatures as a result of maneuver and gust loads imposed during flight. The problem of life expectancy, therefore, is one of determining the deformations as a function of time when the structure is subject to a distribution of different stress levels operating at various elevated temperatures during the life of the structure. In effect, one may picture the ordinary velocity-acceleration diagram for an airplane to which a time axis has been added so that at a constant velocity the distributions of accelerations are given as functions of time.

The prediction of life expectancy of an aircraft flying under elevated-temperature conditions entails an intimate knowledge of the applied stress and temperature distributions as well as a complete understanding of the behavior of materials under the complex loading conditions associated with the aircraft operation. From a physicist's and metallurgist's point of view, the phenomenon of creep even under simple loading is rather incompletely understood. Thus the engineer in facing the problem of predicting life expectancy of aircraft under elevated-temperature conditions is forced to adopt a wholly phenomenological viewpoint. With this approach, hypotheses which may ignore certain features of creep of significance to the physicist or metallurgist, may be acceptable to the engineer provided the results obtained are commensurate in accuracy with the initial data used.

Gust Loadings. With aircraft now in operation, it is well known that intermittent stresses due to gusts are superposed on the 1 g stress level. This is the basis for life expectancy or fatigue life of aircraft operating at normal temperatures. Although relatively little is known about gust conditions in the upper atmosphere, it is possible to obtain some estimate of the magnitude of the intermittent stresses by use of theory developed from relatively low-altitude gust data. Such calculations indicate, for example, that in straight and level flight under the conditions of a 30-fps gust, the stresses resulting from the incremental load factor may be approximately 50 per cent of the 1 g stress level under thermal flight conditions.

The available data on alternating stresses under elevated temperature conditions (12) indicate that when the alternating stress level is a fraction of the mean stress, the creep curves remain unchanged to a first approximation. Since the alternating stresses due to gust loads appear to be less than 50 per cent of the mean stress under the conditions of a 30-fps gust it appears that gust loading may not decrease to any appreciable extent the life expectancy based on the mean stress levels.

Maneuvering Loads. To predict life expectancy of aircraft under elevated-temperature conditions, it is necessary to determine the time required to satisfy a given failure criterion under complex loading conditions which may involve both varying stresses and temperatures. The initial information for the analysis of life expectancy under elevated-temperature conditions consists of basic creep data for the material and the relative frequency distribution of applied stress resulting from maneuvers which the airplane is to experience. Such data are shown in Fig. 8 in which the creep spectrum for a given temperature and failure criterion, such as 0.02 in/in. total creep, is plotted with σ_i/σ_u as a function of time, t. The term, σ_u, is the short-time stress at ultimate-load factor and σ_i is the applied stress.

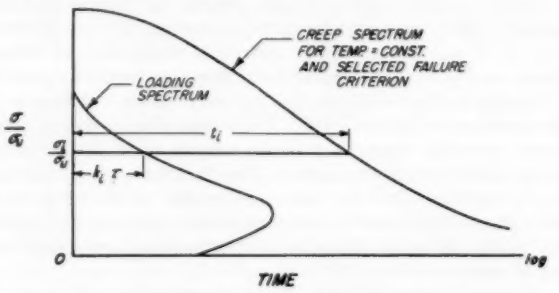

Fig. 8 Initial Data for Life-Expectancy Analysis

Similarly, the loading spectrum is plotted using the same ordinate versus the time $k_i\tau$, where k_i is the ratio of the time at a given stress-ratio level to the life expectancy τ. To determine τ, it is necessary to introduce an hypothesis which combines both the loading and physical property data.

The hypothesis to be considered proceeds from the following assumptions which have as their basis limited experimental evidence on alternating and cyclic loading (12).

(a) Under constant elevated temperature and varying stress conditions, the total creep is the sum of the creep increments due to the net time spent at each stress level.

(b) The varying loads are randomly applied.

As indicated in Fig. 8, the ratio of time of applied stress to time for failure, at a given stress level σ_i, is $k_i\tau/t_i$. In the simple case where $\sigma_i = \sigma_1$ and all other stress levels are zero, then $k_1 = 1.0$ and the life expectancy τ is simply equal to t_1. In more complex

cases, such as for the loading spectrum depicted in Fig. 8, the assumption that the total creep results from the net time spent at each stress level leads directly to the following cumulative creep hypothesis

$$\Sigma \frac{k_i \tau}{t_i} (\sigma_i) = 1 \quad [17]$$

where the parentheses (σ_i) indicates a function of stress σ_i. By rearranging Equation [17], the life expectancy

$$\tau = 1/\Sigma \frac{k_i}{t_i} (\sigma_i) \quad [18]$$

In the most general case, aircraft operation under elevated temperature conditions will involve both variable stresses and temperatures. Although few data are available under cyclic temperature conditions, it appears plausible that the cumulative creep hypothesis may be extended to this most general case.

The initial data for this problem are similar to those given in Fig. 8, although the stress-relative time curves and the basic creep data for a selected failure criterion are given for the series of temperatures T_j, pertinent to the problem. The life expectancy, by extension of Equation [18], becomes

$$\tau = 1/\Sigma_j \Sigma_i \frac{k_i}{t_i} (\sigma_i, T_j) \quad [19]$$

This method of analysis for life expectancy under variable stress and variable temperature conditions is based upon rather limited experimental evidence which suggests the cumulative creep hypothesis as a first approximation. The proposed method of analysis requires extensive testing and verification before it can be applied with confidence to the prediction of aircraft life expectancy.

Conclusions

On the basis of trends established by the relative weight analysis, it appears that sustained flight in the region where aerodynamic heating is of importance may be limited seriously by the tremendous weight problem. Although the upper limit for utilization of current engineering materials is in the neighborhood of 1800 F, the weight penalty due to decreased material properties resulting from aerodynamic heating may limit sustained flight to the region below 800 F. This corresponds to a steady-state Mach number of approximately 3.5 without cooling, or correspondingly higher Mach numbers with cooling. Flight at higher Mach numbers without cooling would be limited to operations of very short duration in order that the structure would not aerodynamically heat up to the steady-state temperature. At altitudes where aerodynamic heating is no longer of importance, solar heating will be of importance. Although rocket-powered flight at such altitudes is beyond the scope of this paper, some of the considerations discussed herein may pertain to this problem.

In connection with the weight problem, it appears that extensive use of integral construction may result in substantial weight savings for the high-solidity structures required for thermal flight. The availability of the large forging and extrusion presses of the heavy-press program probably will show to best advantage in permitting new techniques for fabrication of such high-solidity structures.

The life expectancy of aircraft at room temperature is governed by fatigue considerations. Under thermal flight conditions fatigue may not be of importance in determining life expectancy. In its place, the problem of creep will be the determining factor in establishing the usable life of the aircraft. To design the airframe for an unlimited life will, even if possible, result in additional weight to the already tremendous weight penalties associated with static loading. Therefore limited-life expectancy of aircraft designed for thermal flight may be expected as one solution to this problem.

Bibliography

1 "Airplane Weight and Cost Can Be Reduced," by E. H. Heinemann, *Aeronautical Engineering Review*, vol. 12, January, 1953, pp. 20–23.

2 "Efficient Applications of Stringer Panel and Multicell Wing Construction," by G. Gerard, *Journal of the Aeronautical Sciences*, vol. 16, January, 1948, pp. 35–40.

3 "Relative Structural Efficiencies of Flat Balsa—Core Sandwich and Stiffened Panel Construction," by R. E. Hubka, N. F. Dow, and P. Seide, NACA TN 2514, October, 1951.

4 "Comparative Efficiency in Bending of Structural Elements of Various Designs and Solidities," by G. Gerard, New York University Report to Office of Naval Research, April, 1952.

5 "Structures for High Speed Aircraft," by H. L. Hibbard and J. F. McBrearty, Fourth Anglo-American Aeronautical Conference, 1953, preprint.

"Structures—Theory, Materials, Methods," by H. L. Hibbard, *Aeronautical Engineering Review*, vol. 12, December, 1953, pp. 96–107, 131.

6 "Integral Construction," by E. D. Keen, *Journal of the Royal Aeronautical Society*, vol. 57, April, 1953, pp. 215–227.

7 "Design Considerations Associated With Large Aluminum Forgings," by C. W. Andrews, *Mechanical Engineering*, vol. 75, 1953, pp. 777–784.

8 "Machining Integrally Stiffened Structures," by J. C. Borger, *Mechanical Engineering*, vol. 75, 1953, pp. 871–874.

9 "Effect of Variation in Rivet Strength on the Average Stress at Maximum Load for Aluminum Alloy, Flat, Z-Stiffened Panels That Fail by Local Buckling," by N. F. Dow, W. A. Hickman, and B. W. Rosen, NACA TN 2963, June, 1953.

10 "Structural Efficiencies of Various Aluminum, Titanium and Steel Alloys at Elevated Temperatures," by G. J. Heimerl and P. J. Hughes, NACA TN 2975, July, 1953.

11 "Structural Problems of Future Aircraft," by N. J. Hoff, Third Anglo-American Aeronautical Conference, 1951, pp. 77–114.

12 "Life Expectancy of Aircraft Under Elevated Temperature Conditions," by G. Gerard, U. S. Air Force, WADC TR 53-493, October, 1953.

Problems in the Design of Aircraft Subjected to High Temperature

By F. R. STEINBACHER[1] and LOUIS YOUNG,[2] BURBANK, CALIF.

Design problems associated with the high temperatures of supersonic flight are discussed. Factors, affecting choice of materials, significant changes in methods of analysis and allowable loads, and the need for a new safety criterion, are covered. The importance of the various factors influencing high-temperature design are evaluated and some indication of the direction, future research should take, is given.

Introduction

SUSTAINED supersonic flight depends on the successful solution of major high-temperature problems in the fields of aerodynamics, thermodynamics, aeroelasticity, equipment, materials, production, and structures. In the supersonic range, temperature is a fundamental variable, which specialists in every phase of aircraft design must learn to handle. While the authors touch upon many of these problems in the presentation of the over-all picture, their affiliation with Structures Research and Development naturally places primary emphasis on the high-temperature behavior of aircraft structures.

Two sources of heat which aircraft designers have not had to contend with until recently are aerodynamic heating and nuclear explosions. The first is a function of velocity and, as such, will always exist as a challenge until some other barrier develops. From a thermal point of view, however, the second is minor by comparison, but nevertheless important, for in order to survive an atomic explosion, an aircraft must not be damaged by the heat at some reasonable distance from the center of the blast, say, 1 mile. At this distance, the heat produced per unit area is only about 4 per cent of that produced in 1 min at 2000 mph by aerodynamic heating.

Temperature is not entirely a new problem to aeronautical engineers since it has long affected the design of structure near the engines, de-icing, and other thermal equipment. Here, however, its effects are highly localized. At speeds above 1500 mph, temperature rapidly becomes an over-all problem in design and with the entire aircraft hot, the difficulties arising are compounded. Solutions to these thermal problems are complicated further by many other design considerations since each possible solution must be evaluated in the light of aerodynamic, aeroelastic, weight, producibility, space requirements, and so on.

Aerodynamic Heating—High Temperatures and Large Quantities of Heat

Two aspects of aerodynamic heating appear startling to the structural engineer who until recently has had little or no experience with thermoaerodynamics. First and best-known is the temperature rise associated with high speeds. The adiabatic increase in the temperature of the boundary layer is given very closely by

$$\Delta T = \frac{9}{5}\left(\frac{V}{100}\right)^2$$

where ΔT is in degrees Fahrenheit and V is in miles per hour. There is an adiabatic temperature rise of 720 deg F at 2000 mph and of 1620 deg F at 3000 mph. From Figs. 1 and 4, it is easily seen that at speeds above 2500 mph the temperatures developed are so high that material strengths fall well below satisfactory working limits.

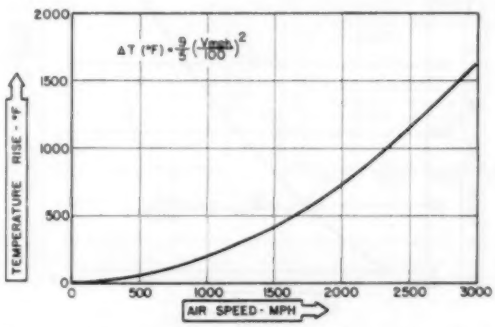

Fig. 1 Adiabatic Temperature Rise at Any Altitude

Equally impressive is the rate at which heat is produced. For example, at 2000 mph approximately 1200 Btu per min (more than enough to heat a five-room house) are theoretically generated in each square foot of the boundary layer. In fact, the majority of all drag on the airplane is converted into heat.

These large temperature increases and heating rates make it obvious that any method of preventing the primary structure from heating up for more than a short period of time is, at best, only palliative. Figs. 2 and 3 make this point in a different way. They give an idea of the weight penalties that must be accepted in insulating or cooling the structure. Further considerations of the use of insulation, heat storage, cooling, and other methods, make it clear that sooner or later the aircraft engineer will have to face the task of designing primary structure to carry loads while hot.

Material Considerations—Reduced Allowables—Weight Penalties

Fortunately throughout certain temperature and time ranges (which vary for different materials), current methods of analysis can be used with short-time material data and reduced allowables. For example, conventional methods are applicable for aluminum alloy loaded for $\frac{1}{2}$ hr or less at temperatures up to 250 F, or 17-7PH steel loaded for as long as 500 hr at 600 F. For some idea of the weight penalties involved in this range see Fig. 4.

Short-time tensile data such as these are, however, only a small

---

[1] Group Engineer, Structures Research and Development, Lockheed Aircraft Corporation.

[2] Research Engineer, Lockheed Aircraft Corp.

Contributed by the Aviation Division and presented at a joint session of the Aviation and Applied Mechanics Divisions, American Rocket Society, and The Society of Automotive Engineers, at the Annual Meeting, New York, N. Y., November 28–December 3, 1954, of The American Society of Mechanical Engineers.

Note: Statements and opinions advanced in papers are to be understood as individual expressions of their authors and not those of the Society. Manuscript received at ASME Headquarters, August 30, 1954. Paper No. 54—A-100.

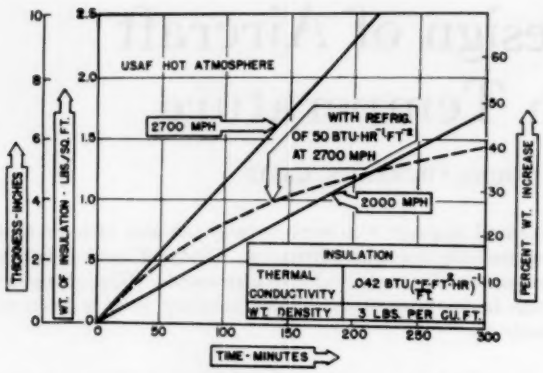

FIG. 2 THICKNESS AND WEIGHT OF INSULATION PER SQUARE FOOT OF SURFACE REQUIRED TO KEEP THE TEMPERATURE OF A 1/4-IN-THICK ALUMINUM PLATE UNDER 200 F FOR SPECIFIC TIME INTERVAL AT ALTITUDE OF 40,000 FT

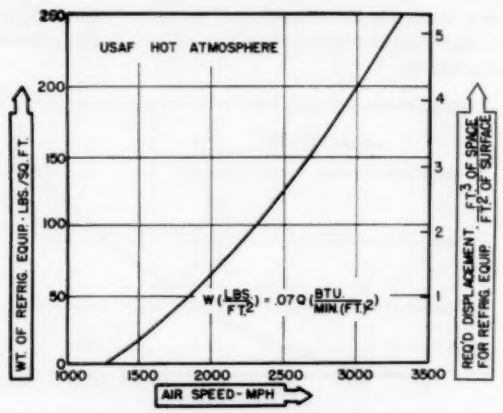

FIG. 3 WEIGHT AND DISPLACEMENT OF REFRIGERATION EQUIPMENT REQUIRED TO KEEP EACH SQUARE FOOT OF SURFACE AT 200 F AT AN ALTITUDE OF 40,000 FT

part of the enormous amount of data required in the design of a high-temperature aircraft. In general, the primary structure of the aircraft is subjected to various combinations of compressive, bending, shear, and bearing loads and is made up of such structural elements as columns, plates, and panels. Some work of this type, which is summarized in Fig. 5, has been done by the NACA in determining the efficiency of different materials under various loadings at temperatures up to 1200 F.[3] These data were obtained for isolated elements and have been incorporated in a preliminary design evaluation of the weight penalties that can be expected in an aircraft at various temperatures. These data are shown in Fig. 6 for five materials along with the benefit of using the optimum material for each type of structural element.

CREEP—A MAJOR HIGH-TEMPERATURE DESIGN PROBLEM

In subsonic aircraft, creep is a relatively unimportant factor in design. At elevated temperatures, however, creep becomes a major consideration, especially if both temperature and stress levels are high. Fig. 6 in the preceding section gives the weight penalties based on short-time material data and is, of course, only applicable for short-time loading. When creep is important, the use of long-time material data is required and, in

[3] "Structural Efficiencies of Various Aluminum, Titanium and Steel Alloys at Elevated Temperatures," by G. J. Heimerl and P. J. Hughes, NACA TN 2975, July, 1953, p. 16.

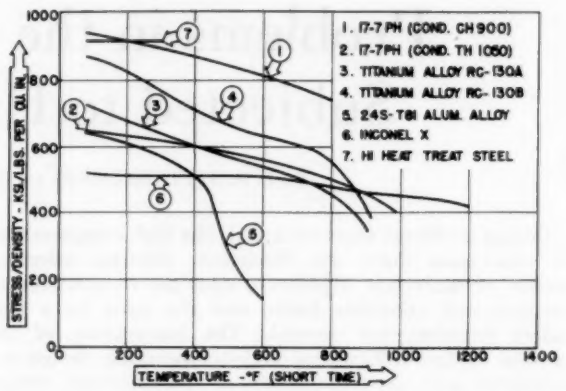

FIG. 4 SPECIFIC STRESS VERSUS TEMPERATURE FOR SHORT-TIME LOADING. CURVES ARE BASED ON MINIMUM STRENGTH SPECIFICATIONS

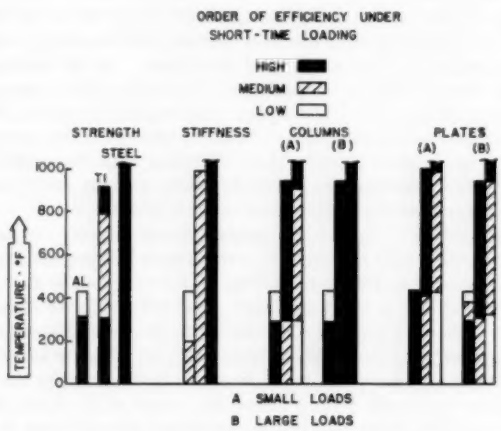

FIG. 5 COMPARISON OF EFFICIENCIES OF THREE MATERIALS FOR STRENGTH, STIFFNESS, AND COLUMN AND PLATE BUCKLING

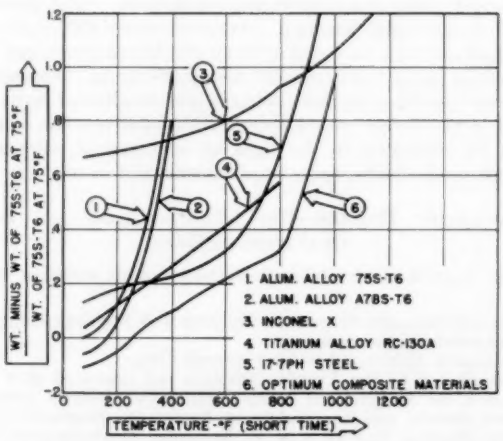

FIG. 6 COMPARISON OF WEIGHT INCREASES WITH TEMPERATURE RESULTING FROM USING SINGLE MATERIAL THROUGHOUT AND BEST MATERIAL FOR EACH TYPE OF LOADING. CURVES ARE BASED ON MINIMUM STRENGTH SPECIFICATIONS

(Prepared by B. J. Saelman, Lockheed Weight Research Engineer.)

general, will result in larger weight penalties. This is brought out in Table 1 which compares, for a different distribution of structural elements than used in Fig. 6, the weight penalties that accrue from using long-time data with those that develop using short-time data. Increases in time and temperature or some reduction in the allowable deformation will increase the increments shown in Table 1.

TABLE 1 COMPARISON OF WEIGHT OF SEVERAL AIRCRAFT STRUCTURAL MATERIALS AT 400 F WITH ALUMINUM STRUCTURE AT 75 F

	Per cent weight increase for short-time loading	Per cent weight increase for long-time loading—100 hr	
		2 Per cent deformation	Rupture
Aluminum.....	65	280	230
Titanium.....	23	39	37
17-7PH Steel...	16	..	18

To some extent, if either the temperature or the stress level is low, creep can be taken care of by merely reducing the allowables. At the higher temperatures and higher stress levels, however, this method of circumventing the creep problem leads to such large reductions in material allowables and imposes such large weight penalties that it is no longer feasible and the use of creep data in design becomes mandatory. Some idea of the weight penalties involved may be obtained from Fig. 7.

One interesting and important bit of information should be brought out at this time. A comparison of creep data for wrought and cast materials shows that at the higher temperatures some cast materials have larger allowable creep stresses than wrought. If this proves to be generally true, it could mean a radical change in design and fabrication methods and, of course, lead to the economies associated with castings.

Creep affects not only the allowable loads, but also the distribution of the applied load. With both the allowables and the distribution of the applied load a function of "time," conventional methods of analysis are no longer valid. But determining what the loads are throughout the structure at any instant is certainly not an easy thing to do. It depends not only on instantaneous values, but on the time-temperature-stress history of the structure. This means that a complete and accurate analysis must be based on the sum total of all variant effects integrated over the expected life of the aircraft. The foreknowledge required for such an analysis must include at the very minimum a spectrum of the total time the aircraft will spend at each temperature, and the time-temperature history of each flight, such as shown in Fig. 8.

Judging by the number and variety of papers devoted to it creep is a familiar phenomenon. But how to handle the effects of creep in the analysis of a structure is far from familiar. In fact, the development of a simple analysis that takes into account creep is sure to be a major contribution in the field of structural analysis.

Temperature gradients, stress variations, thermal-induced stresses, stress and thermal cycling, stress-strain temperature-time histories, and many other factors affect both the stress distribution in a structure and the allowable stresses the various components will carry. While these problems are all receiving some attention, it appears that it may be years before simple, practical methods of handling them are available to the engineer.

To get an idea how much creep can affect the stress distribution in a structure, consider the very simple case of a tension panel with portions, as shown in Fig. 9, at two different temperatures. (For the sake of simplicity, thermal-induced stresses are ignored.) In this simplified illustration, it is assumed that the panel is so loaded and restrained at the ends that each portion is forced to deform at the same rate. This condition is not too

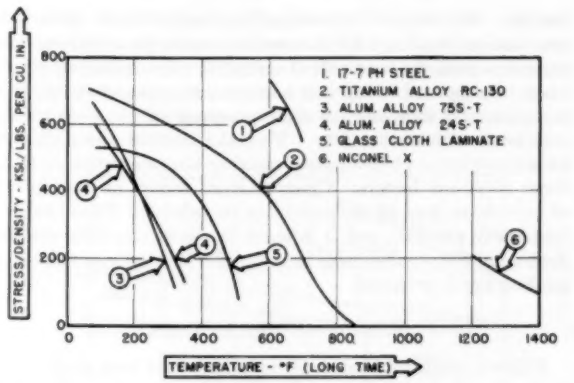

FIG. 7 SPECIFIC STRESS VERSUS TEMPERATURE FOR MINIMUM CREEP RATE OF 10^{-4} PER CENT PER HR (0.01 PER CENT PER 100 HR)

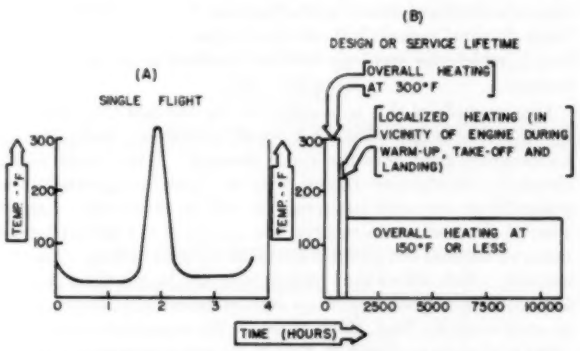

FIG. 8 (*a*) TEMPERATURE-TIME SPECTRUM FOR OVER-ALL STRUCTURAL HEATING DURING SINGLE FLIGHT. (*b*) SPECTRUM SHOWING TOTAL TIME AT TEMPERATURE DURING SERVICE LIFE OF AIRCRAFT

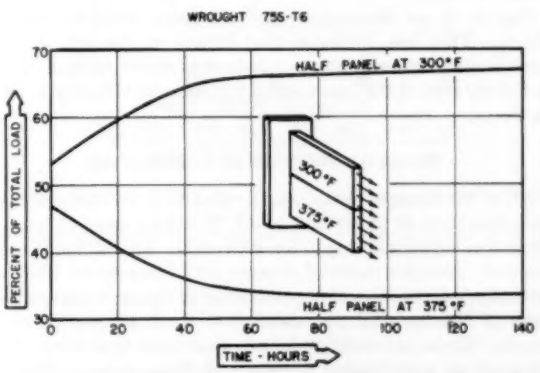

FIG. 9 REDISTRIBUTION OF LOAD DUE TO CREEP IN A SIMPLE PANEL

far-removed from that which actually exists in the tension surface of a wing.

The hotter portion, which is capable of creeping at a faster rate than the panel as a whole, will gradually unload and the cooler strip will load up. Fig. 9 shows how this distribution varies with time.

Redistribution of the load as a function of time for a structure with a nonuniform temperature distribution is the heart of the creep problem. In general, problems involving uniform temperature and no major concentrations of stresses can be handled in a more or less straightforward manner. Changes in tolerances and clearances due to creep are, for example, relatively simple to

handle. But the problems arising from redistribution of the load and changes in allowables that occur at other than uniform temperatures have not been solved except for a few extremely simple cases. In general, creep is a nonlinear function of stress, temperature, and time and, as such, possesses all the complexities associated with nonlinearity. To make matters worse, creep is an accumulative phenomenon requiring the integration of all of these nonlinear factors. Creep analysis today, in the absence of any clever way of circumventing its inherent difficulties, is a formidable problem, and is in much the same condition that indeterminate structures were in before the Hardy Cross relaxation method was introduced.

Fatigue—A Minor Factor

Failures resulting from material fatigue have long plagued the engineer. In fact, as a result of several recent airline catastrophies which have been traced to fatigue, it is now a far greater consideration in design than ever. In the case of a high-temperature structure, however, the engineer may be more fortunate. Tests on some materials show that fatigue may be, at least, one field in which the problems are not amplified as the temperature increases.

One example of this is brought out by the fact that for many materials the fatigue strength drops off more slowly with increased temperature than does the static strength. This means that a structure satisfactory fatigue-wise at room temperature and statically at elevated temperatures will be satisfactory fatigue-wise at elevated temperatures, too, provided the cyclic plus the mean stress does not produce a critical creep condition. Another example which shows that fatigue may not be a serious problem in high-temperature structures was brought out as early as 1927 in some work by Prof. H. F. Moore.[4] He found that at temperatures in the range of 850 to 1000 F the fatigue strengths of low-carbon steels were higher than their rupture strengths. Consequently, in this case, creep and not fatigue was the important factor in design.

Fig. 10 is an interaction curve between creep and fatigue effects. This, too, indicates that fatigue at elevated temperatures is not a serious problem. Note that cyclic stresses as high as 100 per cent of the mean (creep) stress have virtually no effect on the creep stress.

Material Stability at Temperature

All of the changes in material properties so far discussed have been functions of stress and could, to some extent at least, be circumvented by working to lower stresses. In addition to these, however, there are material changes with temperature which are virtually independent of stress and limit the working temperatures of the material no matter how much allowables are reduced. These are stability factors that have their roots in the chemical or metallurgical structure of the material. Titanium RC-110A, for example, after ½ hr exposure to 1800 F becomes extremely brittle and loses about 20 per cent of its strength when returned to room temperatures.

In general, most structural materials lose stability and deteriorate at an accelerated rate at elevated temperatures. There are two basic reasons for this: (1) The deleterious chemical reactions, that cause corrosion and loss of stability, progress more rapidly at elevated temperatures. (2) The added elements which increase the strength and stability of a material may, at certain temperatures, either precipitate out or unite chemically with

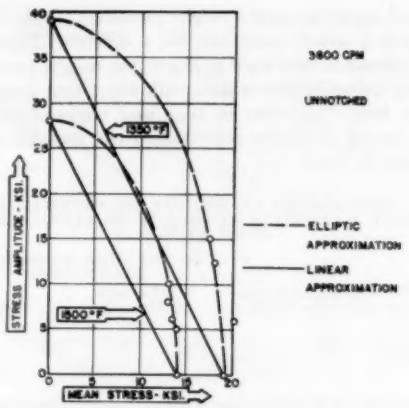

Fig. 10 Design Curves for N-155 Alloy, 150-Hr Lifetime With Cyclic Load Applied at 3600 Cpm; Failure by Fatigue or 0.5 Per Cent Elongation

other elements and thereby prevent their further functioning in the intended manner.

Losses in strength due to corrosion are generally controlled by either coating the exposed surfaces (as clad aluminum is) to prevent the basic alloy from contacting the atmosphere or by adding elements that retard corrosion such as titanium or columbium in stabilized stainless steels.

Both of these methods appear to have their limitations. At extreme temperatures (above 2000 F) there is a point beyond which alloys, no matter how skillfully blended, no longer can be considered structural material.

This critical point is reached at much lower temperatures in the case of protective coatings. Most paints and the more promising nylon-type plastic coatings, for example, lose their effectiveness above 300 F. Cadmium plate as a protection for steel ceases to be useful above 500 F. Ceramic coatings go to higher temperatures, but until recently their brittleness and the effects of differential expansion introduced other problems.

Titanium's corrosion resistance is excellent, in fact, under many conditions superior to stainless steel. But as previously indicated by Fig. 4, the use of titanium in preference to 17-7PH steel entails weight penalties (above 400 F).

Beyond metals, the engineer must turn to refractory ceramics (particularly oxides of aluminum, magnesium, silicon, and zirconium). Already fully reacted with oxygen, these oxides can resist corrosive atmospheres and do not weaken appreciably until near their melting points (as high as 5000 F). More work is needed however, because present-day ceramics are far from being a satisfactory structural material.

Low-Expansion Alloys Promise Weight Savings

Exact solutions for nonuniform-temperature problems are available only for very simple cases. Yet, unfortunately, a nonuniform temperature of even a continually varying temperature distribution is sure to exist in a supersonic aircraft many times during each flight. Hoff and other investigators have pointed out the seriousness of the problem by showing that the stresses induced by such temperature variations can be of the same order of magnitude or larger than the stresses normally developed from loads.[5]

However, the problem is much more serious than has been

[4] "Progress Report on Fatigue Tests of Low Carbon Steel at Elevated Temperatures," by H. F. Moore and N. J. Alleman, ASTM Proceedings, part 1, vol. 31, 1931, pp. 114–121.

[5] "Structural Problems of Future Aircraft," by N. J. Hoff, Proceedings, Third Anglo-American Aeronautical Conference, Brighton, England, The Royal Aeronautical Society, 1951, pp. 77–114.

brought out. Thermally induced stresses depend on the temperature gradient and thus they cannot be reduced or eliminated by merely adding more material. Another method of attack, which on the surface seems to have merit, is to reduce the thermal gradient by improved material-thermal properties. This method merely reduces the length of time a gradient will last but alters its magnitude very little.

The unfortunate fact is that improving the thermal properties offers little hope of reducing the magnitude of the temperature gradient to a point where they are negligible. This follows from the fact that the initial temperature distribution has much more effect on length of time the critical initial temperature gradient will last than the thermal properties of the material.

Another, and perhaps more lucrative approach, is to tackle the problem from an entirely different angle. Thermally induced stresses are produced by differential expansion; consequently, instead of attempting to reduce the temperature gradient, perhaps it might be better to reduce the coefficient of expansion. In fact, it would be ideal if a structural material could be found or developed which has zero coefficient of expansion. For such a material no thermal stresses would develop regardless of the temperature distribution.

There are some materials that have nearly zero expansion. Invar, for example, has a coefficient of expansion only 1/30 as large as steel. This means that for the same temperature gradient the stresses induced in Invar would be only about 3 per cent as large as those induced in steel. Invar, however, does not retain this low coefficient of expansion at all temperatures, for example, at low temperatures or above 500 F.

Nickel is one of the alloys which, when added to steel in the proper proportion, tend to reduce the coefficient of expansion. Invar has 36 per cent nickel. Alloys with different nickel content behave slightly differently. For example, an alloy with 43.5 per cent nickel has a coefficient of expansion one half that of steel and retains this low coefficient up to 800 F. Fig. 12 shows the effect of different nickel content on the coefficient of expansion of steel.

High-nickel alloys with large amounts of chromium added, Elinvar (36 per cent Ni, 12 per cent Cr), for example, have, in addition to a relatively low coefficient of expansion, an invariable modulus of elasticity over a considerable range of temperature. This would be an advantage in a structure exposed to nonuniform temperatures, since it would eliminate the redistribution of the load due to differences in E that takes place at the instant the structure is loaded.

The development of low-expansion alloys might well make the difference between a practical aircraft and a structure too heavy to fly. At present, no other metallurgical contribution to high-speed flight appears to offer greater promise or is more within the realm of possibility.

A New Criterion of Structural Safety Is Required

In the design of aircraft structures, just as in the design of any structure, some sort of margin of safety is required to take care of variations in materials, manufacturing techniques, design uncertainties, etc. At present, both commercial and military aircraft are designed using a factor of safety of 1.5 which is defined as the ratio of the maximum load the structure can carry to the limit (or actual applied) design load. All structural parts (unless otherwise specified) are designed to meet this requirement.

Many engineers feel, however, that applying this 1.5 factor indiscriminately to all parts is somewhat unrealistic. They point out that methods of analysis, inspection, quality control, etc., have improved greatly since this criterion of safety was first set up nearly 20 years ago. Mangurian,[6] for example, presents many powerful arguments in favor of this stand and makes some recommendations for revisions. However, high-temperature structure requires an entirely new approach to design and under these different conditions a complete restudy of the safety criteria should be made.

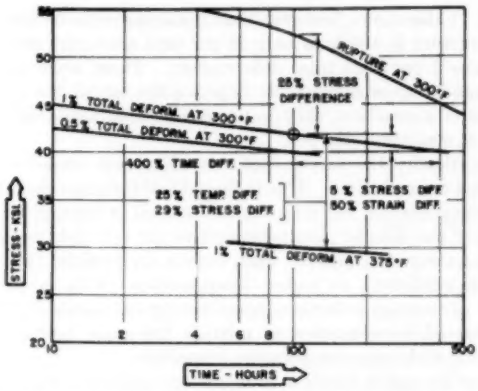

Fig. 11 Creep Curves for 24S-T3 Showing Various Ways of Applying a Safety Factor and How They Affect Allowables

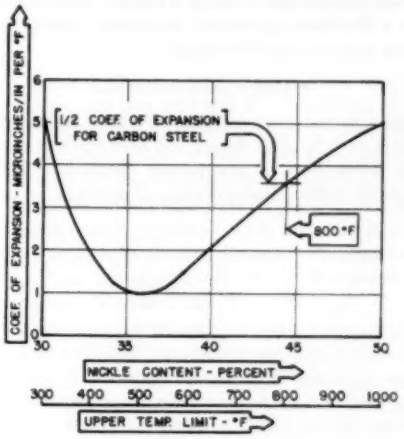

Fig. 12 Nickel Content (in Nickel-Iron Alloy) Versus Coefficient of Expansion

The temperature scale indicates upper limit to which alloy can be heated and retain the indicated coefficient of expansion.)

The present margin of safety is based on load-carrying ability. In a high-temperature aircraft, however, four important variables are involved, creep or creep rates, time, temperature, and stresses, any of which can be critical. Fig. 11 shows how confused the margin-of-safety concept becomes when creep factors are considered. These curves are drawn using 24S-T3 aluminum alloy at 300 F and indicate that a structure subjected to a stress of 42 ksi would produce a total deformation of 1 per cent in 100 hr.

The interesting point is that small reductions in stress either appreciably increase the useful life of the structure or decrease the resultant total deformation. Notice that a 5 per cent reduction in the stress, for example, permits either using the structure 400 per cent longer or reducing the total deformation 50 per cent.

[6] "Is the Present Aircraft Structural Factor of Safety Realistic?" by G. N. Mangurian, paper presented at IAS Annual Summer Meeting in Los Angeles, Calif., June 21–24, 1954. IAS Preprint No. 478.

The conventional 1.5 safety factor applied to the stress is almost ridiculous under these conditions since it is considerably more than enough to insure "indefinite" creep life. Applying a safety factor to the temperature is equally ridiculous because even small factors can reduce the stress level as much as, or more than, the conventional 1.5 safety factor used at room temperatures.

Fig. 11 also shows, however, that the stress required to rupture the structure in 100 hr is only 25 per cent above the stress that produces 1 per cent total deformation. Thus, while small reductions in stress appreciably improve the useful life or deformation of a structure, they do not compensate much for inaccuracies in structural analysis.

Statistically, the safety factor is also more complicated at elevated temperatures. If it is thought of (among other things) as a compensation for variation in material properties, then the shape of the normal distribution curve for test data becomes a consideration. In general, such curves are broader (and show greater variation) at higher temperatures. This means that larger percentage reductions from the typical values are needed at elevated temperatures to provide the same confidence we associate with room-temperature properties.

Since the safety factor is so intimately associated with weight, a co-ordinated effort between industry, the Military, and the CAA, is needed to study this problem with the aim of establishing a practical and standardized safety criterion for elevated temperatures that will remain applicable even after new types of high-temperature material are developed.

Other Considerations

In addition to the more obvious effects of increased temperature, there is sure to arise during the first flight at each increase in speed a whole host of unexpected problems. The effect of temperature on flutter, the operation of controls, armament, and instruments, the safety and comfort of the crew, and many other such factors, might give trouble.

There are also in addition to purely technical problems many economic, educational, and administrative considerations which are just as formidable. The problem of selecting a material to be used for the next 10 to 15 years of supersonic development illustrates the nature and magnitude of these problems.

At the present, aluminum alloy is the backbone of the aircraft industry. Relatively speaking, practically all design information and production facilities are geared to its use. Yet aluminum must soon be discarded in favor of some high-temperature alloy.

Such a change to a new material means that much of the data, experience, background, and contacts, accumulated over the past 20 years will become useless and the accumulation of design data, production know-how, the acquisition of shop equipment, and the training of personnel will have to start anew. A new material will lead to new vendors and subcontractors, changes in purchasing, and inspection. It is obvious that the cost and far-reaching effects of such a change make it necessary that the correct material be chosen the first time. While this will not place management in a unique position, it will call for a much more important and far-reaching decision than the average they are called on to make. And, at the very minimum, it will require a comprehensive evaluation of the field to determine the relative importance of various factors and the accumulation of enough test data and experiences to substantiate the evaluation.

Conclusion

Traditionally, the burden of long-range basic research has always been carried by the universities, government laboratories, and others, with industry generally concentrating on reducing the significant results into design principles. Both fields of activities are important and with continued well co-ordinated effort the thermal barrier will be slowly pushed back.

Carbon-Molybdenum Steel Steam Pipe After 100,000 Hours of Service

By R. J. SINNOTT,[1] I. A. ROHRIG,[2] J. W. FREEMAN,[3] and A. I. RUSH[3]

Rarely does the engineer or metallurgist have an opportunity to evaluate design considerations and laboratory data in terms of creep in service. Carbon-molybdenum steam pipe, carefully measured for service creep during 100,000 hr of operation at 900 F, was subjected to laboratory examination after removal from service. The purpose was to check calculated service creep rates, assess creep damage, and to compare long-time performance prediction based on short-time laboratory data. Remarkable correlation was observed between calculated service creep rates and those established by subsequent laboratory creep testing. Full agreement with average values used by the Subgroup on Allowable Stresses for Ferrous Materials of the ASME Boiler Code Committee in setting allowable stresses for this material was established for both creep and stress-rupture properties.

Introduction

WHEN Unit No. 14 was being erected at the Delray Power Plant of The Detroit Edison Company in 1938, the lack of reliable data on service-life properties of metals subjected to high-temperatures was felt acutely. The practice of basing design on stresses obtained by 1000-hr high-temperature laboratory tests extrapolated to 100,000 or more hours has repeatedly been questioned. Designers accepted such data only because no better method of property prediction of high-temperature characteristics has been available. It is the purpose of this paper to present (*a*) the results of creep measurements made on carbon-molybdenum pipe subjected to 100,000 hr of actual power-plant service, (*b*) results of after-service laboratory testing, and (*c*) a discussion of service results as compared to properties predicted by laboratory testing prior to service.

Service History. With the installation of Unit No. 14, a service creep-measurement program was initiated. Stainless-steel measuring points were arc-welded on the external surfaces of two 10-in. nominal diam carbon-molybdenum steel pipes connecting the turbine emergency stop valve to the upper and lower steam chests of the turbine. The two Schedule 80 steam leads were designated as "north" and "south" indicating their position with respect to the turbine. The stainless-steel buttons were located to provide both diametral and axial measuring stations and were ground to give accurate measuring surfaces. Fig. 1 illustrates the measuring stations.

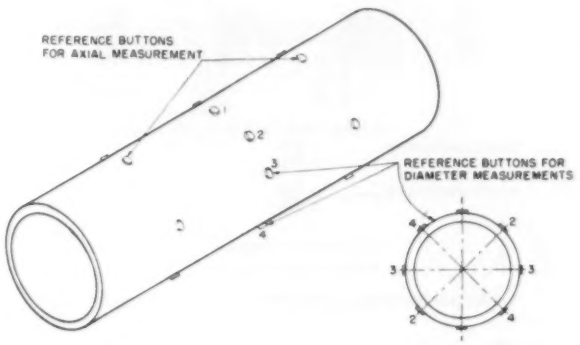

Fig. 1 Sketch Showing Location of Stainless-Steel Reference Buttons Used for Axial Length and Diameter Measurements During Service of C-Mo Pipe

Weighted average pressures and temperatures during the operating period are 835 psig and 900 F. Maximum temperature fluctuations of ±20 deg F represent normal operating conditions.

Measurements were made at prevailing temperatures during five outage periods and were taken after the unit had cooled down and the thermal insulation removed from the locations undergoing test. Dimensions were measured with an outside micrometer caliper and a special micrometer trammel. Readings taken were corrected to a base temperature of 68 F. The results of these measurements are shown in Table 1.

Plotted service creep calculations based on diametral measurements indicated a typical low-stress creep versus time curve over the first 67,000 hr of operation, viz., a relatively rapid initial creep rate followed by a reduction in rate of creep, which is characteristic of material operating under stress conditions producing creep at a low rate. Total diametral elongation at this time was observed to be in the order of 0.1 per cent, a relatively low value. The total axial elongation during the 67,000-hr period as determined by axial measurements did not exceed 0.03 per cent and in most cases was considerably less.

After 75,500 hr of operation, weld samples removed from the valve-to-pipe and pipe-to-pipe joints of the south connection indicated the presence of graphite ranging from dispersed nodular in the valve joint to chain type in the pipe-to-pipe joints. At shutdown intervals during the next 5000 hr of operation, all the welded joints in the turbine leads were first normalized at 1725 F, and shortly thereafter all welds were gouged out, rewelded, and normalized. After 100,135 hr of operation, the carbon-molybdenum turbine leads were removed and replaced with chromium-molybdenum pipe, which is highly resistant to graphitization.

Final service creep measurements were made just prior to the removal of the carbon-molybdenum pipe from service. Calculations based on diametral measurements indicated a drastic increase in creep rate over the rate established at the end of the fourth period. Concern over the carbon-molybdenum pipe remaining in service in other portions of the system indicated the

[1] Mechanical Engineer, The Detroit Edison Company, Detroit, Mich. Mem. ASME.

[2] Engineering Department, The Detroit Edison Company, Detroit, Mich.

[3] Engineering Research Institute, University of Michigan, Ann Arbor, Mich.

Contributed by the Joint ASTM-ASME Committee on Effect of Temperature on the Properties of Metals and presented at the Annual Meeting, New York, N. Y., November 28–December 3, 1954, of The American Society of Mechanical Engineers.

Note: Statements and opinions advanced in papers are to be understood as individual expressions of their authors and not those of the Society. Manuscript received at ASME Headquarters, August 2, 1954. Paper No. 54—A-73.

TABLE 1 DIAMETRAL MEASUREMENTS OF 10-IN. SCHEDULE-80 CARBON-MOLYBDENUM PIPE DURING AND AFTER 100000 HR OF SERVICE

Location	November, 1938	August (12789 hr), 1940	March (26937 hr), 1942	July (43832 hr), 1944	June (66987 hr), 1947	August (100135 hr), 1951	Tot. change 5 periods	Cold relaxed position after removal/line (100135 hr)
Diametral Over Stainless-Steel Reference Buttons, In.[a]								
North position								
1–1	11.2876	11.2921	11.2933	11.2948	11.2984	11.3046	+0.0170	11.3052
2–2	11.2756	11.2791	11.2808	11.2818	11.2844	11.2887	+0.0131	11.2912
3–3	11.3161	11.3201	11.3213	11.3218	11.3244	11.3277	+0.0116	11.3292
4–4	11.3536	11.3581	11.3608	11.3608	11.3644	11.3734	+0.0198	11.3740
South position								
1–1	11.2304	11.2453	11.2512	11.2548	11.2593	11.2945	+0.0641	11.2732
2–2	11.3044	11.3103	11.3137	11.3153	11.3193	11.3305	+0.0261	11.3332
3–3	11.4924	11.4873	11.4852	11.4798	11.4783	11.4785	−0.0139	11.4812
4–4	11.3794	11.3813	11.3812	11.3808	11.3823	11.3865	+0.0071	11.3892

Inside Diameters After Sectioning, In.

	1–1	Between 1–2	2–2	Between 2–3	3–3	Between 3–4	4–4	Between 4–1
North connection.....	9.665	9.666	9.665	9.659	9.666	9.646	9.646	9.657
	9.666	9.654	9.665	9.658	9.661	9.645	9.633	9.653
South connection.....	9.564	9.575	9.598	9.651	9.683	9.678	9.648	9.612
	9.525	9.539	9.611	9.673	9.697	9.676	9.641	9.583

Circumferential Length Covered by Reference Points, In.

North connection—5.090
South connection—5.075

[a] All measurements corrected to 68 F.

advisability of laboratory tests as a check on calculated service creep rates.

Description of Material. The pipe was ASTM A158-36 grade P1, Schedule 80, made from National Tube Company's Heat 10043. The reported chemical composition was as follows:

	Per cent
Carbon	0.13
Manganese	0.45
Silicon	0.131–0.135
Molybdenum	0.60–0.62

The pipe was 10.75-in. OD × 0.593-in. wall. After bending and upsetting the ends, it had been given a full anneal at 1900 F for 2 hr. Physical properties were reported as follows:

Tensile strength, psi	60880
Yield strength, psi	39730
Elongation in 2 in., per cent	45

Experimental Procedure

Creep Testing

"North Connection." Creep tests were run on both tangential and longitudinal specimens at the operating temperature of 900 F and under the estimated operating stress of 7500 psi. In addition, tests were made under the present 12,500-psi allowable stress of the ASME Boiler Code.

"South Connection." One tangential specimen and one longitudinal specimen were taken from the pipe. Creep tests of these two specimens were run at 900 F under a stress of 7500 psi.

Rupture Testing

"North Connection." A stress-rupture curve was established at 900 F for time periods up to nearly 1800 hr. Longitudinal specimens were used for this test. In addition, a check test was run on a tangential specimen which was tested at 37,000 psi, a stress intended to cause rupture in about 1400 hr.

"South Connection." Tests were run on longitudinal and tangential specimens at a stress of 37,000 psi.

Impact Tests

"North Connection." Charpy V-notch tests were made on both longitudinal and tangential specimens. Similar tests were made on the pipe material after it had been reheated 2 hr at 1900 F and furnace-cooled. All of the Charpy V-notch specimens were tested at 80 F. No impact tests were made on material from the south connection.

Tensile Tests

"North Connection." Room-temperature tensile tests were run on longitudinal specimens. No tensile tests were made on material from the south connection.

Hardness Tests

"North Connection." Brinell hardness tests were run on eight sections representing the entire circumference of the pipe section.

"South Connection." The Brinell hardness was determined on one section representing the south connection.

Metallographic Examination

"North Connection." A metallographic examination was made on sections through the center line of the measuring buttons representing the four quadrants of the north connection and, in addition, samples were taken adjacent to all of the test specimens.

"South Connection." Samples were taken at one measuring button and also adjacent to the creep and rupture specimens.

Results

Dimensional Measurements on the North and South Connections. The measurements shown in Table 1 were made across the diameters of the pipe at the reference buttons. It should be noted that, at the time the reference buttons were attached, no attempt was made to keep the height of the measuring buttons uniform. Accurate inside-diameter measurement of the pipes was not readily obtainable with the equipment available at the time of installation. Therefore any initial ellipticity of the pipes which may have existed was not detected, and was not indicated by the diametral measurements made during service. No changes in diameter due to sectioning were observed. The inside diameters were measured at both ends of the pipe ring containing the reference buttons and are recorded also in Table 1. Measurements were made on the pipe diameters containing the reference buttons and at diameters between each button. Further, the circumferential length covered by the buttons was determined as a matter of record with the results shown in Table 1.

From these data it was observed that the minimum diameter of the north connection was at the (4-4) axis and at the (1-1) axis of the south connection. These diameters correspond to those

TABLE 2 CALCULATED CREEP RATES OF SCHEDULE 80 C-Mo PIPE DURING 100000 HR SERVICE AT 900 F UNDER A NOMINAL STRESS OF 7500 PSI

Period	Duration, hr	Accumulated time, hr	Circumferential creep rates per cent/1000 hr	
			North connection	South connection
First	12789	0 to 12789	0.00315	0.00365
Second	14148	12789 to 26937	0.00165	0.00220
Third	16895	26937 to 43832	0.00020	−0.0015
Fourth	23155	43832 to 66987	0.00140	0.00130
Fifth	33148	66987 to 100135	0.00165	0.00470[a]

[a] Cutting out welds and rewelding may have influenced measurement and creep during the fifth period.

TABLE 3 TENSILE PROPERTIES AT ROOM TEMPERATURE FROM NORTH CONNECTION C-Mo PIPE AFTER 100000 HR OF SERVICE AT 900 F

Specimen location	Tensile strength, psi	Yield point,[a] psi	Proportional limit, psi	Elongation in 1.5 in., per cent	Reduction of area, per cent
2BT	53000	35300	27500	43.3	71.5
2BB	53400	32600	....	42.0	71.8
4BT	53400	32100	27000	41.3	71.8
4BB	53900	38000	32500	42.0	71.0

[a] Specimens showed a very sharp yield point so that this value also is the same as the offset-yield-strength values.

showing the greatest increase from creep as judged by the diametral measurements taken during service. Consequently, it must be concluded that the pipes were originally elliptical in shape and were becoming round during service.

The wall-thickness measurements indicated that both sections varied by a maximum of approximately 0.025 to 0.030 in., a variation which was well within the specified allowances for the size of pipe. However, it should be emphasized that these measurements were made after 100,000 hr of service and that original wall thicknesses were unknown.

Creep Rates During Service. The average rates of creep during service were calculated from the measurements taken on the measuring points during service. The results obtained from such measurements were used to calculate the creep rates by two separate and different approaches, namely, changes in diameter of the pipe, and changes in the perimeter of an ellipse having the dimensions established by the changes in diameter. The latter method is preferred; therefore the results given for creep during service are based upon changes in the perimeter of an ellipse having the dimensions established by the measurements of the pipe given in Table 1. The results of these calculations are given in Table 2. Fig. 2 shows graphically the changes in circumference of the pipes as a function of time and service.

The average circumferential creep rates during service show the following:

1 During the first period the creep rate of both sections was somewhat higher than 0.003 per cent per 1000 hr.

2 During the next three periods the rates were less than 0.0022 per cent per 1000 hr. However, the minimum creep rates were observed for both sections during the third period.

3 During the fifth period the average rate for the south connection apparently increased to 0.0047 per cent per 1000 hr, whereas the creep rate for the north section was essentially the same as for the second and fourth periods.

It should be emphasized that the measurements made during service reflected very small changes in the diameters as shown by Table 1. Consequently, it would not appear that too much significance should be placed on the minor differences in creep rates observed for the different periods, i.e., the low creep rates calculated for the third period of operation. The somewhat higher average creep rates during the first period might have been expected owing to the combined effects of primary creep and possible relief of stress concentrations. The apparent increased creep rate of the south connection during the fifth period is clouded by the effects of the removal of the old welds and the rewelding. It does appear highly significant, however, that, in general, the creep rates and total deformations are of the order expected from the extrapolation of laboratory data.

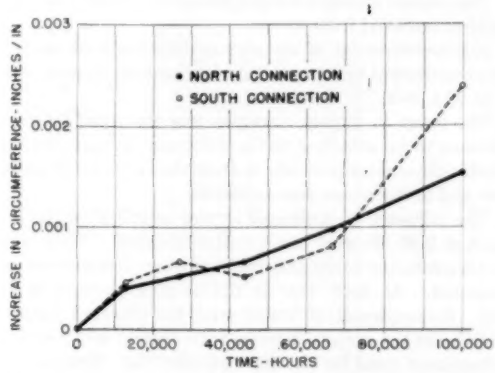

FIG. 2 CHANGE IN CIRCUMFERENCE OF 10-IN. C-MO PIPE DURING 100,000 HR OF SERVICE AT 900 F UNDER AN OPERATING STRESS OF 7500 PSI

Tensile and Hardness Properties. Tensile tests conducted at room temperature gave the data shown in Table 3. Material from all four quadrants had very uniform tensile strengths and ductility values. Yield strengths and proportional limit values varied somewhat. There did not, however, appear to be a consistent relationship between specimen location and variation in these values.

Lack of specific comparative data raises the question of whether the low tensile strength was the result of service or if it is characteristic of the somewhat high temperature and slow rate of cooling during the original heat-treatment. This heat-treatment might be expected to give somewhat lower tensile strengths than those usually used for reported data for 0.5 Mo steel. For similar reasons the yield strengths might have been expected to be low. It, therefore, appears that service may have raised the yield points somewhat as would be expected.

Brinell hardness determinations were as follows:

Connection	Location	Brinell hardness no.
North	Top, side, and bottom of pipe	103–107
South	Side of pipe	101

There did not appear to be a significant variation in hardness around the pipe circumference. The hardness values, like the tensile strength, appear to be somewhat low for 0.50 Mo steel. Apparently the hardness was characteristic of the original heat-treatment, because reheat-treatment at 1900 F for impact testing resulted in a Brinell hardness of 101 to 106. There is, therefore, no real evidence of softening during service.

Impact Properties. Charpy V-notch tests were made at 80 F

TABLE 4 CHARPY V-NOTCH IMPACT PROPERTIES AT 80 F FOR PIPE METAL FROM NORTH CONNECTION

	Impact strength, ft-lb
As removed from service	
Tangential	10, 11
Tangential	7, 8
Longitudinal	11, 9.5
Longitudinal	8, 9
Heated 2 hr at 1900 F, furnace-cooled	
Tangential	19, 22.5
Tangential	20, 23
Longitudinal	18, 20.5
Longitudinal	20, 22

NOTE: Specimens were held 16 hr at 200 F after machining. Before testing specimens were equalized to a temperature of 80 F by holding in a water bath at 80 F.

on specimens taken from the pipes as removed from service and after sections of the pipe had been given the original heat-treatment. The data obtained, Table 4, indicate the following:

1 The impact strength ranged from 7 to 11 ft-lb for the pipe material as removed from service.

2 Reheat-treatment of the pipe material with the same nominal heat-treatment as the original pipe gave an impact strength of 18 to 22.5 ft-lb.

3 The range in impact strengths was too small for any real significance to be attached to the difference in specimens taken longitudinally and tangentially or from the locations of estimated highest and lowest stress concentrations.

4 The influence of prolonged service at 900 F on the impact strength of 0.50 Mo steel is not well established. Such information as is available would indicate that some deterioration would be expected. At least that is the usual experience in creep-testing. Consequently, it would seem the observed values of 8 to 11 ft-lb do not appear unusual for material with the original heat-treatment used for the pipe in question. However, if the pipe had been normalized from 1650 F in place of 1900 F, it is probable that the values would have been higher than 8 to 11 ft-lb.

Laboratory Creep-Test Properties. The creep-rate data obtained from the individual tests are shown in Table 5 and the log-stress log-creep-rate curves derived from the creep-test data are shown in Fig. 3. The curves in Fig. 3 indicate that the stress for a creep rate of 0.01 per cent per 1000 hr was 12,500 psi.

Tests were run at two stress levels as follows:

(*a*) At 7500 psi—the stress corresponding to the operating stress during service calculated by The Detroit Edison Company. The measured creep rates ranged from less than 0.001 to 0.002 per cent per 1000 hr. These rates are not considered as precisely established because the sensitivity of the extensometer system, particularly for the 1-in. gage lengths of the tangential specimens, was too low to give exact values. There is no doubt, however, that the creep rates were of the order of 0.001 per cent per 1000 hr.

(*b*) At 12,500 psi—the stress corresponding to the present allowable stress under the ASME Boiler Code. Both a longitudinal and a tangential specimen from the north connection gave final secondary creep rates of 0.01 per cent per 1000 hr.

Tangential, as well as longitudinal, specimens were tested because the creep during service was largely circumferential and it was felt that creep characteristics should be established for material with the same orientation as the service creep. The absence of any substantial difference between the two types of specimens appears somewhat unusual, because specimens taken across the direction of metal flow during working usually have slightly higher creep resistance. The absence of specific data on this point for pipe produced and heat-treated in the same way as the pipe tested, however, make this uncertain for the particular case.

The tangential specimens tested at 7500 psi showed a decrease in length during the first few hours of testing. The reason for this is uncertain. It could have been due to relief of some complex internal-stress system or to testing-technique variables. Careful review of the testing procedure showed no reason to believe that it was testing technique.

The 7500-psi tests on specimens from the north and south connections did not show a significant difference in creep rate. The

TABLE 5 CREEP-TEST DATA AT 900 F FOR 0.50 Mo STEEL PIPE AFTER 100000 HR OF SERVICE

Section	Direction	Stress, psi	Creep rate—per cent/1000 hr at indicated time: 1000 hr	2500 hr
North	Longitudinal	7500	0.002	...
North	Tangential	7500	(1)	...
South	Longitudinal	7500	0.002	...
South	Tangential	7500	(1)	...
North	Longitudinal	12500	0.012	0.010
North	Tangential	12500	0.013	0.010

(1) These specimens showed a decrease in length during the first few hours of testing and no measurable creep thereafter out to 1000 hr.

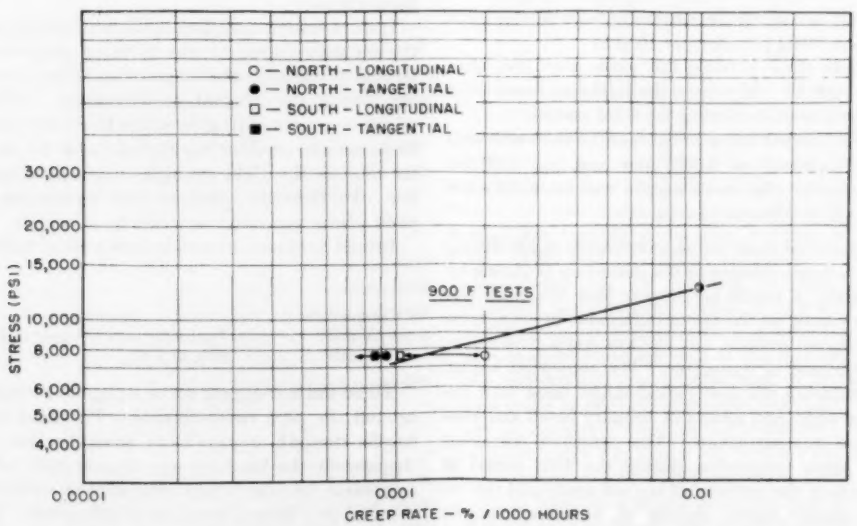

FIG. 3 STRESS-CREEP-RATE DATA FOR 0.5 Mo STEEL STEAM PIPE AFTER 100,000-HR SERVICE AT 900 F

TABLE 6 RUPTURE-TEST DATA AT 900 F FOR 0.50 Mo STEEL PIPE AFTER 100000 HR OF SERVICE

Specimen location	Stress, psi	Rupture time, hr	Elongation, per cent in 1.5 in.	Reduction of area, per cent
		NORTH CONNECTION		
2 CB—longitudinal	42700	S.T.T.T.	38.7	76.8
2 CT—longitudinal	40000	3.5	44.0	76.2
2 CB—longitudinal	38000	775	30.0	39.6
2 CT—longitudinal	36000	1803	21.3	26.2
NA2 B3—tangential	37000	1482	25.0[a]	31.4[a]
		SOUTH CONNECTION		
SA3 L2—longitudinal	37000	1558	20.0	26.1
SA3 R1—tangential	37000	1349	23.0[a]	29.8[a]

[a] Tangential specimens were 0.250 in. diam with a 1-in. gage length.

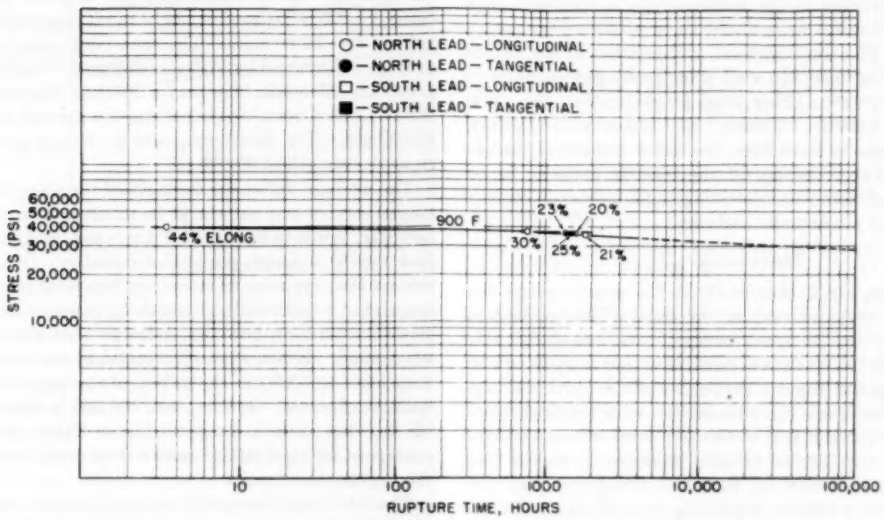

FIG. 4 STRESS-RUPTURE-TIME CURVE FOR 0.5 STEEL STEAM PIPE AFTER 100,000-HR SERVICE AT 900 F

creep rates were so low, however, that it is not certain that some difference in creep resistance did not exist.

Rupture-Test Properties. The data obtained from the rupture tests are given in Table 6 and are plotted as the usual log-stress log-rupture-time curve in Fig. 4. From this curve the following rupture strengths at 900 F have been estimated:

STRESS FOR RUPTURE IN INDICATED TIME PERIODS AT 900 F (PSI)

100 hr	1000 hr	10000 hr	100000 hr
37500	37000	33000	29000

The extrapolation to 10,000 and 100,000 hr appears somewhat uncertain in that there seems to be a break in the slope of the stress-rupture curve at about 1000 hr. The tests at longer-time periods are insufficient to define the slope of the curve for longer-time periods with certainty. The curve has been extended using the greatest slope (lowest strengths) indicated by the available data.

Elongation and reduction-of-area values decreased with rupture time. The short-time elongation was approximately 40 per cent. Tests between 1000 and 2000 hr in duration showed elongations between 30 and 20 per cent. There was no significant difference between longitudinal and tangential specimens or between the two pipe sections.

Metallographic Examination. Test specimens were taken adjacent to or between measuring buttons. The microstructures typical of the test specimens were as follows:

1 The microstructures were ferrite and slightly spheroidized pearlite. In addition, there were apparently fairly massive carbides in the grain boundaries and a light general precipitation throughout the matrix. Scattered graphite nodules were present.

2 The grain size was mainly 5 to 8. No areas of larger grains were observed in the north connection. Occasional nodules of graphite could be found, and it was noted that the massive carbides were absent in the presence of graphite.

3 No significant variations in structure around the circumference of the north connection were observed. The examination of the south connection was less extensive. However, all samples were similar to the north connection, except for the occurrence of small patches with grain sizes up to grain size No. 3, ASTM Designation E 19.

4 A rather general graphitization was observed on both the inside and outside wall surfaces of both connections. The graphite was quite fine and appeared to be concentrated in the grain boundaries.

The microstructures beneath the stainless-steel buttons had the following characteristics:

1 Segregated graphite approaching "chain" graphite was present under all buttons. In most instances the chain graphite was either parallel to the surface of the pipe and approximately halfway between the inside wall and the heat-affected zone of weld or progressed diagonally in the wall near one end of the button.

2 Only a few isolated nodules of graphite were observed in the heat-affected zone of the welded stainless-steel buttons.

The microstructure of the material reheat-treated for impact tests revealed the following:

1 The structure of the reheat-treated material was similar to that of the pipe as removed from service except that there was somewhat less spheroidization of the carbides.

2 The massive carbides observed in the grain boundaries of the pipes also were present in the reheat-treated material.

It was concluded from the metallographic examination that, where the metal was not influenced by the stainless-steel measuring buttons, little graphitization had occurred. There also seems to be little question but that the original carbide lamellae in the pearlite had spheroidized slightly. The presence of what appears to be massive carbides in the grain boundaries was somewhat surprising in view of the relatively slight spheroidization of the pearlite and raises some doubt as to whether they are actually carbides. The slight general precipitation in the matrix was characteristic of 0.50 Mo steel after prolonged exposure to stress and temperature. Other than graphitization, the slight spheroidization, "massive carbides," and characteristic general precipitation appear to have been the major structural changes during service. The resistance of the massive carbides to removal by heat-treatment was interesting and indicates an unusual composition if they are actually carbides.

Discussion

The creep curves, Fig. 2, obtained from the measurements during service are a very unusual set of data. The engineer or metallurgist rarely has an opportunity to evaluate design considerations and laboratory data in terms of actual creep in service.

The exact creep and rupture prpperties of the particular pipe material at the time it was placed in service were not established. There are, in fact, very few laboratory tests which establish stresses for creep rates as low as those measured in service (less than 0.002 per cent per 1000 hr, Table 2). Creep strengths of C-Mo steel are rather variable, depending on heat-treatment and melting practice. The exact creep rate for the service stress of 7500 psi at 900 F is therefore not well established. Extrapolation of the available laboratory creep data at higher stresses back to 7500 psi, however, suggests that on an average, rates of the order of 0.001 per cent per 1000 hr might be expected, see Fig. 5. The observed creep in service, therefore, is considered to be in good agreement with the predictions of laboratory data.

The creep rates measured in service and those measured in the laboratory for tests at 7500 psi on coupons cut from the pipes after they were removed from service are in good agreement. This confirms the service creep measurements. It would be expected that, after a brief period of adjustment, the two creep rates should agree.

The stress for a creep rate of 0.01 per cent per 1000 hr established in the laboratory, 12,500 psi, and the stress for rupture hours, 29,000 psi, turned out to be in exact agreement with average values for new steel. The observed creep strength is the average value found by Miller and Heger (1)[4] and used by the Subgroup on Allowable Stresses for Ferrous Materials of the ASME Boiler Code Committee in setting the present allowable stress of 12,500 psi. The same group also developed an average value for rupture strength of 29,000 psi.

The average values for strength of the pipe material after prolonged service may appear to be somewhat surprising. Actually, however, this is to be expected if it is assumed that the pipe metal had nearly average properties initially. It is generally considered that exposure to stress and temperature will permanently use up the available life of metals by creep. Consideration of the service conditions, however, indicates that this should have been very small. If the stress-rupture-time curve of Fig. 4 was extrapolated to 7500 psi, the indicated rupture time would be many millions of hours. On this basis, 100,000 hr of service was negligible in comparison to the total life available. Certainly the percentage of life used on this basis was too small to alter significantly the rupture-test results.

The laboratory creep data show no evidence of weakening from the 100,000 hr of service. As previously discussed, the creep

[4] Numbers in parentheses refer to the Bibliography at the end of the paper.

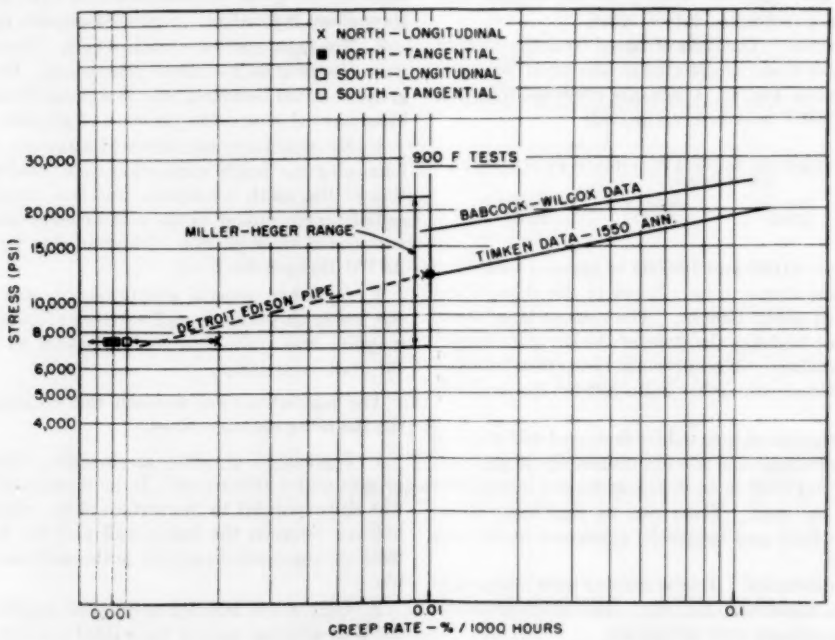

Fig. 5 Creep Data at 900 F From C-Mo Pipe of Delray Station, Detroit Edison Company, After 100,000 Hr of Service Compared With Data for C-Mo Steel Reported by The Timken Roller Bearing Company (5) and The Babcock & Wilcox Tube Company (4)

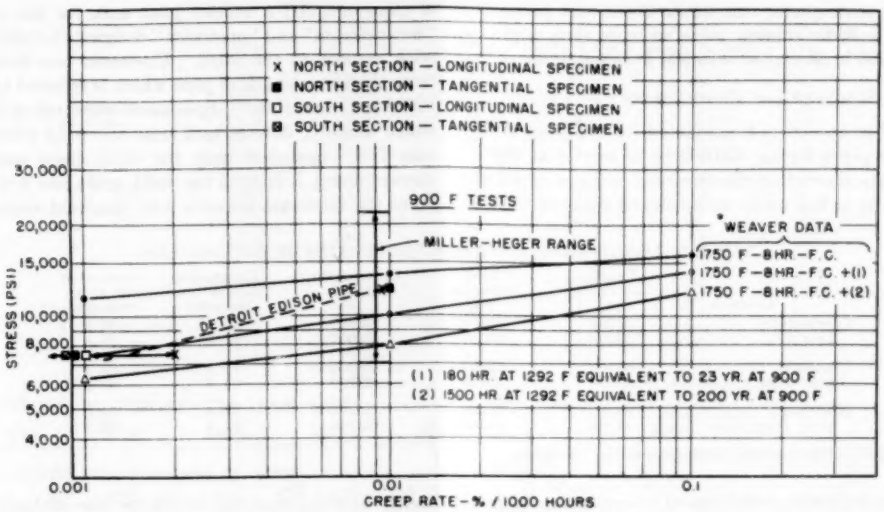

FIG. 6 CREEP DATA AT 900 F FOR C-MO PIPE AFTER 100,000 HR OF SERVICE COMPARED WITH DATA FOR SPHEROIDIZED C-MO STEEL, AS REPORTED BY WEAVER (2)

rates were the same as those existing during service. Creep rates from laboratory tests, however, would be expected to show evidence of structural deterioration only if so-called third-stage creep had started during service. There is no precedent of which the authors are aware for estimating when third-stage creep should become evident in such prolonged time periods and at such low creep rates as existed in service. General laboratory experience indicates that, in the absence of substantial loss of strength by structural alteration due to temperature, third-stage creep would not be expected before the total creep deformation reached 1 per cent. The creep deformation during service, Fig. 2, was of the order of 0.2 per cent and the probability is that the onset of third-stage creep was remote. The test results support this view. The rates observed were average for the steel and there was no indication of increasing creep rates during the tests or in service at either 7500 or 12,500 psi.

The possibility exists that structural alteration under the influence of temperature and stress during the prolonged service could have altered substantially the creep properties from those characteristic of the new pipe. Unfortunately, creep data for the particular pipe samples before service are not available. The data obtained from the tests on the pipe after service are compared in Fig. 6 with those presented by Weaver (2) in which he attempted to estimate the effect of spheroidization during service. At 0.01 per cent per 1000 hr, the creep strength was in between that for the annealed condition and for a condition of spheroidization equivalent to 23 years of service at 900 F. Actually, the strength indicated is almost exactly that which would be estimated from Weaver's data. The 100,000 hr of service represents about one half the 23 years estimated by Weaver to attain the degree of spheroidization of his test bars and the creep strength of the pipe material is also about halfway between his two conditions. The microstructure also showed about the degree of spheroidization consistent with the creep strength in comparison to Weaver's data.

The creep strength of the pipe at 7500 psi in both service and laboratory tests did not agree as well with Weaver's data. Both showed a stress for a creep rate of 0.001 per cent per 1000 hr of about 7500 psi or a little less. This corresponded to Weaver's material spheroidized for an equivalent of 23 years of service, rather than to his annealed stock, which showed a stress of 11,600 psi for 0.001 per cent per 1000 hr. Because the pipe showed creep rates from early in its service life of the order of 0.001 per cent per 1000 hr, the indications are that the pipe material had different stress–creep rate relations than Weaver's test stock. Weaver annealed his stock from a lower temperature than was used for the Detroit Edison pipe. White and Crocker (3) reported creep data at 925 F for C-Mo pipe given the same heat-treatment but from different heats as the pipe used for the service creep tests. Extrapolation of their data to 900 F indicated strengths of 11,000 and 12,500 psi for 0.01 per cent per 1000 hr. In view of such variation, there seems sufficient precedent to assume that the service creep data reflect initial properties more than changes during service.

The similarity of creep and rupture properties of tangential and longitudinal specimens indicated that there was no great difference from this source in the properties of the pipe after service. Because creep in service was circumferential, it could be expected that any damage effect might be most evident in the tangential specimens. The absence of any difference between the longitudinal and circumferential specimens then could be further support to the indication that the 100,000 hr of creep in service had used up only a small fraction of the available service life of the pipe. Without supporting data on the probable relative strengths of longitudinal and tangential specimens for new pipe or for pipe subjected to creep, there is uncertainty in these conclusions.

The elongation and reduction-of-area values for the rupture-test specimens were not as low as have been observed for C-Mo steel. The change from 40 to 20 per cent elongation as the time for fracture increased to 2000 hr is not at all unusual. Certainly there is nothing in these values to suggest undue deterioration during the 100,000 hr of service.

The impact values after service were low. However, impact values of 10 ft-lb are not at all unusual for C-Mo steel, particularly when heat-treated at a relatively high temperature, as was the pipe. The difference in relation to the samples reheat-treated after service does not represent an unexpected change. The absence of any difference between longitudinal and tangential specimens again supports the view that creep damage during service was very slight.

The tensile properties after service possibly show some evidence of structural change during service. There is some uncertainty in this observation, because the comparative data for

new material are inadequate. In either event, the properties were satisfactory and the changes were no more than might be expected for 100,000 hr of exposure to 900 F under stress.

Summary and Conclusions

A unique set of creep curves is presented for the creep of two C-Mo steel steam pipes during 100,000 hr of service at 900 F. Analysis of the data shows that the observed creep rates of 0.002 per cent per 1000 hr or less under an operating stress of 7500 psi were in accordance with the predictions of laboratory creep data.

Laboratory creep and rupture tests were carried out on coupons cut from the pipe after the 100,000 hr of service. The creep rates under 7500 psi agreed with the rates observed in service. The creep strength of 12,500 psi for a rate of 0.01 per cent per 1000 hr and the stress for rupture in 100,000 hr of 29,000 psi are the same as the average values for new C-Mo steel.

Analysis of the service conditions indicated that 100,000 hr of service at 900 F under 7500 psi would have been expected to use up only a negligible amount of the available creep-rupture life of the steel. All laboratory test results support this conclusion. Deterioration of creep strength due to structural changes, such as spheroidization, was certainly no greater than might have been expected.

The general conclusion is that the pipes performed in service to a remarkable degree in accordance with the predictions of laboratory data.

BIBLIOGRAPHY

1 "Report on the Strength of Wrought Steels at Elevated Temperatures," by R. F. Miller and J. J. Heger, American Society for Testing Materials, Special Technical Bulletin No. 100, 1950.

2 "The Effect of Carbide Spheroidization Upon the Creep Strength of Carbon-Molybdenum Steel," by S. H. Weaver, Proceedings of the American Society for Testing Materials, vol. 41, 1941, p. 608.

3 "Effect of Grain Size and Structure on Carbon-Molybdenum Steel Pipe," by A. E. White and Sabin Crocker, Trans. ASME, vol. 63, 1941, pp. 749–764.

4 "Properties of Carbon and Seamless Alloy Steel Tubing for High Temperature High-Pressure Service," The Babcock & Wilcox Company, Technical Bulletin, No. 6E, 1948.

5 "Digest of Steels for High Temperature Service," Timken Roller Bearing Company, Steel and Tube Division, 1946.

Discussion

T. H. McCunn.[5] As the authors point out, the data presented in this paper do indeed show a remarkable correlation between long-time service creep measurements and subsequent laboratory creep testing. They make a substantial addition to the small fund of long-time test data available for verification of extrapolated long-time strengths obtained from short-time laboratory tests.

The company with which the writer is associated also conducted a few tests on a section of the replaced piping. The section of pipe included a welded joint and, for the results to follow, "downstream" and "upstream" designate location of test material with respect to the joint. Upstream test material was taken from the same length of pipe which is referred to in the paper as "North Connection." Specimens were taken from three locations, namely, downstream near the weld where the grain size was 7–8; upstream near the weld, grain size 6–7; and upstream about 3 ft from the weld, grain size 4–6. Test material from the upstream location near the weld appeared to be more nearly like the material tested by the authors than any other material tested by the writer's company.

TABLE 7 LONGITUDINAL TENSILE PROPERTIES OF PIPE SECTION

Location	Tensile strength, psi	Yield strength, psi	Proportional limit, psi	Elongation in 1.4 in., per cent	Reduction of area, per cent
Downstream,	59200	33400	32300	32.9[a]	66.2
near weld	58200	33400	32600	32.9[a]	66.4
Upstream,	55500	32200	35000	41.4	69.4
near weld	56700	39700	39700	42.2	69.4
Upstream,	61700	35200	30100	31.4	73.0
away from weld	62000	35200	32100	31.4	73.0

[a] Bench mark within necked-down region.

The longitudinal tensile properties are given in Table 7.

Charpy impact strengths are given in Table 8.

TABLE 8 CHARPY IMPACT TESTS OF PIPE SECTION

Location	Direction	Keyhole, ft-lb	60° V-notch, ft-lb
Downstream, near weld	Longitudinal	18, 36	...
Upstream, near weld	Longitudinal	36, 30	...
Upstream, away from weld	Tangential	40, 39	82, 46

Note: All fractures were partly fibrous, partly crystalline.

Longitudinal stress-rupture results, using the Larson-Miller "parameter" method,[6] are given in Table 9 and plotted in Fig. 7 of this discussion. Also plotted are the 900 F rupture-test data given in the paper and the recent data compiled by ASTM.[7]

Considering the apparent heterogeneity of the pipe, it is believed that differences between our test data and the test data of the authors are not significant, except for the impact-strength values. The writer does believe, however, that the difference between the log-log extrapolated 100,000-hr rupture strength of the authors and the values obtained by the writer with the Larson-Miller method are significant, as illustrated in Fig. 8, herewith. Our experience has been that the Larson-Miller method will usually yield more realistic predictions of long-time rupture strength.

Authors' Closure

Mr. McCunn's presentation of the results of tests on a section of pipe from the same system as that covered by the paper constitutes a valuable extension of the information in the paper. It should, however, be clearly recognized that the welded joint examined by Mr. McCunn has been solution-treated at 1700 F after 75,000 hr of service. Under the conditions of the heat-treatment the material designated "upstream-away from weld" should not have been subjected to this heat-treatment and therefore should be directly comparable with the material covered by the paper. The evident difference in properties and microstructure between the materials indicates that the two materials were not similar and it is presumed that it represents

[5] Metallurgical Engineer, General Electric Company, Schenectady, N. Y.

[6] "A Time-Temperature Relationship for Rupture and Creep Stresses," by F. R. Larson and James Miller, Trans. ASME, vol. 74, 1952, pp. 765–775.

[7] "Report on the Elevated-Temperature Properties of Chromium-Molybdenum Steels," ASTM Special Technical Publication No. 151, 1953, p. 15.

TABLE 9 STRESS-RUPTURE TEST DATA ON C-0.5 Mo PIPE

Location	Temp, deg F	Stress, psi	Time, hr	$T(20 + \log t) \times 10^{-3}$	Elong. in 2 in., per cent	Reduction of area, per cent
Downstream, near weld.....	1000	36000	5	30.2	23	71
	1050	30000	50	32.8	28	45
	1100	22000	40	33.7	33	60
	1150	15000	40	34.8	39	79
	1200	10000	33	35.7	63	95
	1200	6000	208	37.0	35	95
Upstream, near weld.....	1000	34000	135	32.3	18	33
	1050	26000	87	33.1	18	39
	1100	20000	112	34.3	30	59
	1150	15000	52	35.0	45	84
	1200	10000	13	35.1	63	93
	1200	6000	258	37.2	40	91
Upstream, away from weld...	1050	30000	2	30.7	35	81
	1050	25000	28	32.4	37	73
	1100	20000	28	33.4	40	74
	1150	15000	78	35.2	36	73
	1200	10000	79	36.3	34	68
	1300	6000	76	38.5	47	74

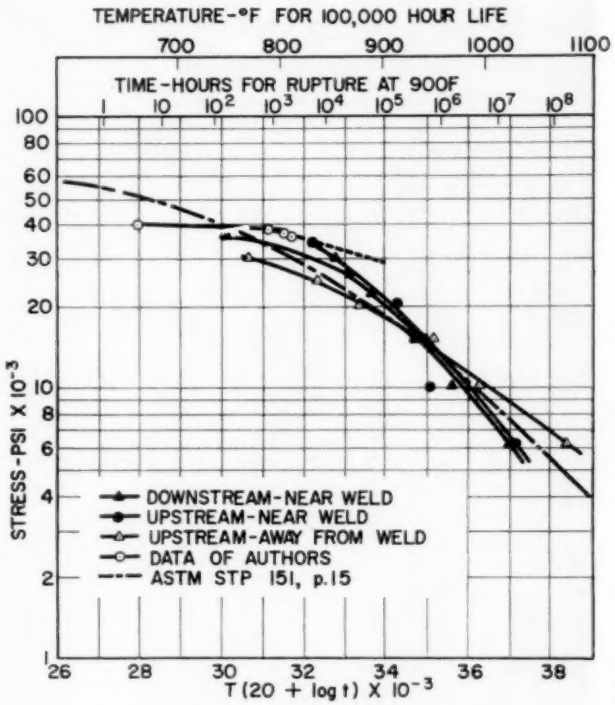

FIG. 7 RUPTURE STRENGTH OF C-0.5 Mo STEEL

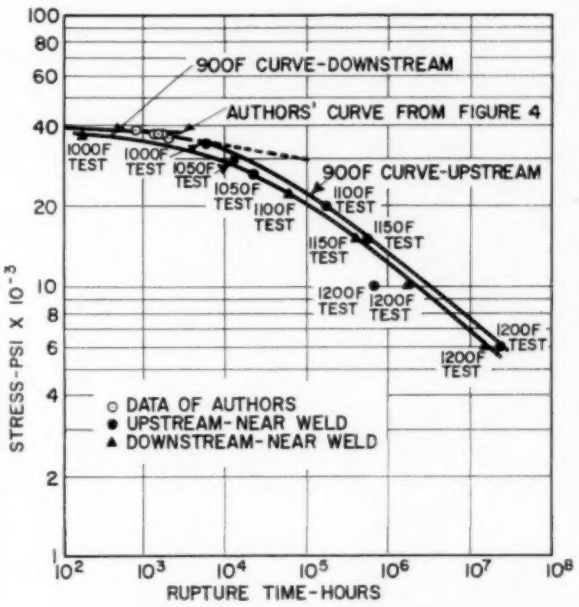

FIG. 8 RUPTURE STRENGTH OF C-0.5 Mo PIPE AT 900 F

the heterogeneity to be expected in the large section sizes involved in the pipe. The apparent similarity of the "upstream-near the weld" material appears to be happenstance rather than similarity in history.

In view of the variations which may occur in notched bar-impact testing, we are not in a position to explain the differences in Charpy impact-test values other than to point out that there was a difference in specimens. Mr. McCunn used a 60-deg V-notch while the data in the paper were for the ASTM standard 45-deg V-notch.

The rupture data presented in the discussion were reviewed carefully and no evidence of measurable damage in service was found. The comparison with data compiled by the ASME-ASTM Joint Committee on the Effect of Temperature on Metals for C-Mo, not available at the time the paper was prepared, substantiates that loss in strength did not occur during the 100,000 hr of service.

The question of extrapolation of the stress-rupture-time curve at 900 F, in the authors' opinion, remains unanswered in detail as was stated in the paper. Perhaps the most important point is that the extrapolation used by the authors followed common practice in evaluating C-Mo steel and thus more closely agrees with literature values for 100,000-hr strength than the relatively new parameter method. In view of the divergence in the three parameter curves reported by Mr. McCunn, the authors were reluctant to rely on them as a guide, especially when the curve which appeared to agree with the data in the paper was for reheat-treated pipe. It would have been useful to have had parameter-data tests on the material from the section covered by the paper along with a longer duration test at 900 F.

The authors believe that a major conclusion to be drawn from the work of both laboratories is that heterogeneity existed in the material tested and that with this fact in mind the results were well within the range of values indicated for new material.

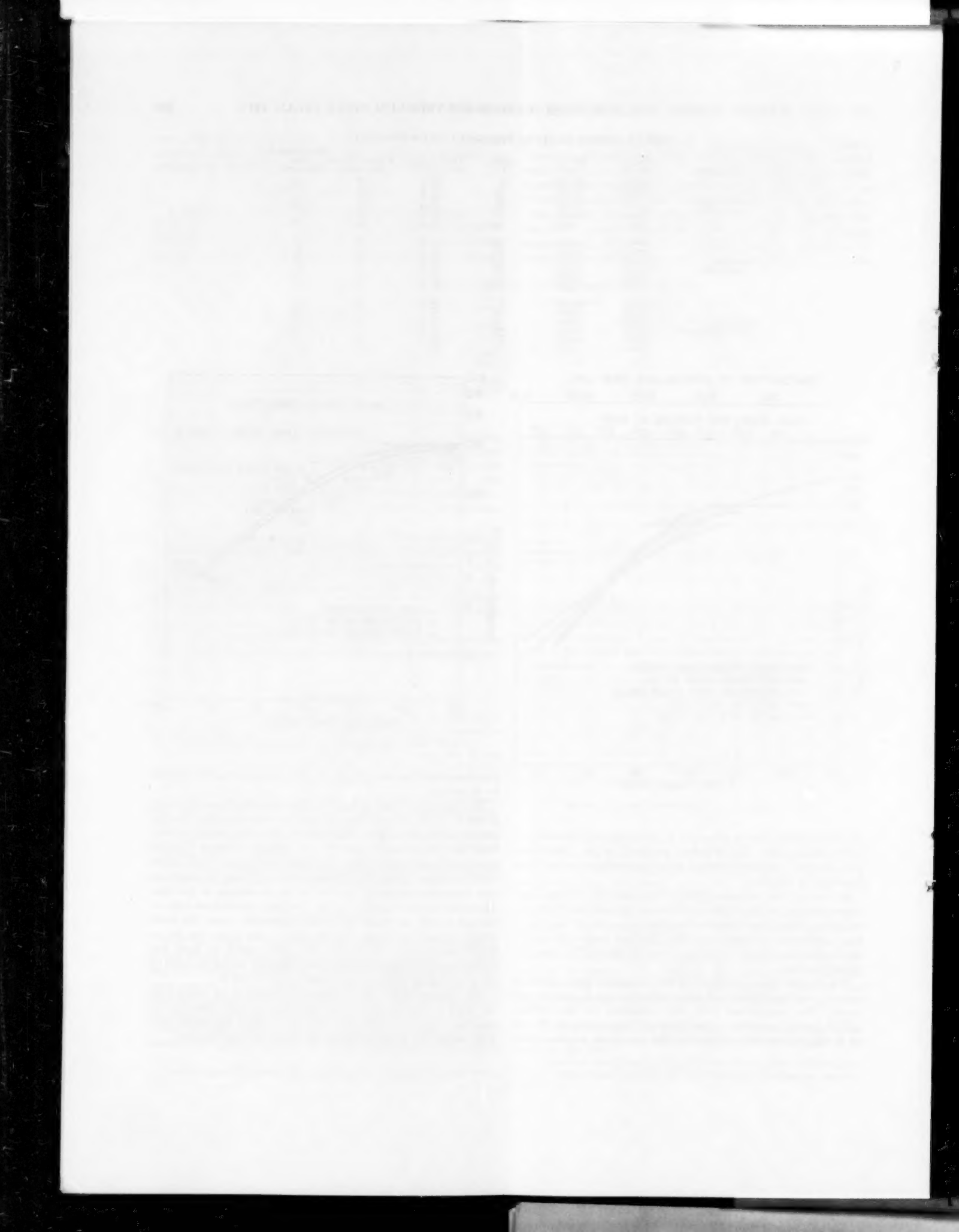

For practical help in solving problems of immediate or long-range importance, consult ASME publications. The following list illustrates the range of subjects covered. For a copy of the complete listing, write to The American Society of Mechanical Engineers, 29 W. 39th St., New York 18, N. Y.

PROCEEDINGS, SECOND U. S. NATIONAL CONGRESS OF APPLIED MECHANICS
Pub. 1955
$9.00 to members and nonmembers

The ninety-five technical papers and four general lectures in this 825-page volume form an invaluable record of recent advances made in connection with many of the significant problems associated with kinematics, dynamics, vibrations, wave motion, mechanical properties of materials and failures, stress analysis, elasticity, plates and shells, plasticity, fluid flow, aerodynamics, and heat transfer

ASME TRANSACTIONS FOR 1954
$15.00; $7.50 to ASME members

The experience, ideas, and practical know-how of over 400 specialists are available to you through this 1900-page reference. Specifically it gives quick access to the findings of important researches, information on new materials and their applications, details of product and equipment design, suggestions for improving procedures, and descriptions of new processes. Important problems dealt with in its 207 papers and discussions are those encountered in the fields of applied mechanics, automatic control, fuels, fluid flow, gas turbine power, heat transfer, hydraulics, lubrication, machine design, metal cutting, power plants, and other branches.

SMALL PLANT MANAGEMENT
Pub. 1950
$7.00

Here is the guidebook to consult for sound advice on organizing, operating, and supervising the small plant; rating products; selecting a process; controlling manufacturing expense; obtaining best facilities, materials, and productivity; labor relations; etc.

INDUSTRIAL ENGINEERING TERMINOLOGY
Pub. 1955
$1.50

In this handy 50-page Glossary are listed and defined some 500 terms used by industrial and management engineers. Subjects range from elementary definitions to an entire series of complex production terms. Definitions were formulated by the ASME Work Standardization Committee and have been reviewed and approved by the Terminology Committees of Australia, Canada, South Africa, the United Kingdom, and the American Standards Association.

SELF-APPRAISAL FORM
Pub. 1947
75c

This ASME Standard contains an appraisal form which an industrial manufacturing plant may use to measure the degree of progress it makes from a safety standpoint. It also shows how to use the form.

PLANT LAYOUT TEMPLATES AND MODELS
Pub. 1949
50c

Recommendations in this ASME Standard cover the engineering details to be incorporated in the design and construction of two-dimensional one-plane templates and three-dimensional equipment models.

DEFINITIONS OF OCCUPATIONAL SPECIALTIES IN ENGINEERING
Pub. 1951
$2.50

In addition to defining approximately 500 engineering fields of specialization and activities, this publication indicates the knowledge required to work in each field, the accessory techniques needed, and the duties and responsibilities of those engaged in various engineering activities.

GENERAL DISCUSSION ON HEAT TRANSFER
Pub. 1951
$10.00

The ninety-three contributions and discussions in this 500-page volume cover a decade's development in heat transfer and in the design of apparatus relating thereto and provide a fund of information on heat transfer with change of state; heat transfer between fluids and solids; conduction in solids and fluids; radiation, instrumentation, and measurement techniques; and on a number of special problems.

VISCOSITY OF LUBRICANTS UNDER PRESSURE
Pub. 1954
$5.00

This publication reviews and co-ordinates twelve experimental investigations of 148 lubricants comprising twenty-five fatty oils, ninety-four petroleum oils, seventeen compounded oils, and twelve other lubricants. Data are co-ordinated by means of sixty tables in which the results originally appearing in diversified units are compared. Conclusions and recommendations are also presented.

MANUAL ON CUTTING OF METALS
Pub. 1952
$10.00

Look to this book for information on the mechanical characteristics and structures of the metals to be cut; on the influence of the composition and microstructures of each metal on the wear of the cutting tool and surface finish; on the types and functions of cutting fluids; on the forces, power, and cutting speeds for specific cutting conditions when turning a variety of metals; for illustrations of tool shapes which have proved most efficient; and for tabular data on the feeds, speeds, and depths of cut to be used when machining steels and cast irons.

ASME SCREW THREAD MANUAL
Pub. 1952
$2.50

This Manual supplies essential information on threads up to 1½" nominal diameter such as the limits of size of the coarse, fine, and 8-pitch series of Classes 2A and 2B; their gage limits; basic dimensions; tolerances and allowances for standard threads; and formulas for all major, pitch, and minor diameters for the six unified classes of threads. In short, all the specific information a shopman needs about screw threads in general use.

NATIONAL PLUMBING CODE
A40.8—1955
$3.50

Here is a guide for the design, installation, inspection, testing, and maintenance of plumbing systems which is based on the best technical advice and experiences in the plumbing field. In its pages are the correct engineering provisions for safeguarding the water supply, for the fixtures to be used, and for the removal of liquid wastes from buildings. Additionally, it recommends a simple means of stack venting, presents administrative data for law enforcement agencies, and provides standards for sanitary installations within a trailer coach and for trailer park sanitary facilities.

GAS TRANSMISSION AND DISTRIBUTION PIPING SYSTEMS
B31.1.8—1955
$2.50

Consult this Standard for data and requirements applying to the design, fabrication, installation, inspection, testing, and safety aspects of operation and maintenance of gas transmission distribution systems; as well as to the conditions of use of the elements of the piping systems.

SURFACE ROUGHNESS, WAVINESS, AND LAY
B46.1—1955
$1.25

This Standard classifies roughness, waviness, and lay; includes the symbols for use on drawings, specifications, and reports; gives specifications for surfaces intended as precision roughness specimens of roughness height, and for surface finish specimens intended to illustrate machined surfaces; the requirements for tracer type instruments; the methods of producing, controlling, and inspecting surfaces; and criteria for selection of surface qualities.

SAFETY CODE FOR INDUSTRIAL POWER TRUCKS
B56.1—1955
$1.00

The safety requirements in this American Standard cover industrial trucks of both the driver-ride and driver-load type such as platform trucks, tractors, low- and high-lift trucks, fork trucks, and special industrial trucks. Part I covers design and construction features. Operation and maintenance rules are given in Part II, while Part III lists 34 rules and regulations for truck operators.

20% discount to ASME members